# Defining the Post-Chemotherapeutic Immune Landscape in Pancreatic Cancer

Assya Legrini
BSc (Hons)

Submitted in fulfilment of the requirements of a PhD degree

School of Cancer Sciences
College of Medical, Veterinary and Life Sciences

February 2024

# Author’s Declaration

The work presented in this thesis has been performed by the author, except in instances where it has been acknowledged. This thesis has not been submitted for another degree.

Assya Legrini
February 2024

# Acknowledgement

First, I would like to thank my primary supervisor, Professor Nigel Jamieson, for all the guidance, encouragement, and life lessons. I have thoroughly enjoyed my time spent in his lab, and all the leaning opportunities provided. I am grateful to have Nigel as my supervisor, to show me that ambition should never be shied away from. Thank you to my second supervisor, Professor David Chang, for offering an open door, philosophical discussions and fired chicken recommendations.

A huge thank you to all members of the Jamieson Spatial Lab, both past and present, for fostering a hardworking and joyful environment. In particular, thank you Holly Leslie for providing help, endless laughter and sharing food whilst we initially set up the lab. Colin Wood, you're star, I'll never be able to thank you enough for the automated pipeline, or the quirky emails. Thank you Tengyu Zhang and Ritika Nara for helping me out with time consuming tasks. Also, thank you Claire Kenndey and Yoanna Doncheva for helping out with the last few experiments when time was running low.
A huge thank you to Professor Joanne Edwards for her kindness, and her lab for providing a warm and friendly environment. Especially, a huge thanks to Dr Jean Quinn and Dr Kathryn Pennel for being the best story tellers around, and going above and beyond to help finish this thesis. I'll never be able to thank you enough. C and Molly, you're both sunshines, thank you for all the support, friendship and tea.

Thank you Dr Tomoko Iwata for initially training me up for multiplex assays, and all the mentoring and advice given. Also, thank you Glasgow Tissue Research Facility, especially Dr Jennifer Hay and Dr Hannah Morgan for providing access to all the tissue used, as well as producing tailor made, complex TMAs to fit with specific technologies. Additionally, thank you to all the NHS and Australian Pancreatic cancer Genome Initiative patients for providing tissue, and thank you to the Glasgow Biorepository. Thank you to the John Le Quesne lab, especially Leah Office-Jones, Dr Ian Powley, Rachel Pennie and Silvia Martinelli for all the help and advice throughout the years. Thank everyone at the CRUK Scotland centre histology department for all their help.

Finally, thank you to all my friends, family, and everyone in between. Matt and Hannah, thank you for the belly laughs, and for dragging me out of Glasgow. Zuzia, thank you for the unexpected gifts, and ridiculous conversations. Thank you to my mum, without her support and dry humour, I would not be where I am now. Thank you to my dad for reminding me nothing is ever as serious as it seems.

To everyone else, past and present, who has helped me along this journey, thank you.

# Abstract

Pancreatic ductal adenocarcinoma (PDAC) is the 5th most common cause of cancer death in the western world, with a 5-year survival of <7% [1, 2]. Surgical resection remains the best treatment option, although the 5-year survival remains <25% [3] .Most patients are ineligible for resection as they present with metastatic disease. These patients undergo systemic chemotherapy, which offers only a modest improvement in survival [4]. Compared to similar solid tumours, PDAC is a relatively poorly characterised disease, with few treatment improvements. This is due, in part, to its complex, heterogenous landscape, defined by a dense fibrotic stroma, low immunogenicity and low mutational burden. These factors make it highly chemo resistant and offers few options for targeted treatments. Of the few treatment improvements, the switch from Gemcitabine based to FOLFIRINOX based chemotherapy, offers a paradigm shift by doubling survival to almost 12 months in high performance patients [3]. Similarly, the introduction of neoadjuvant therapy in locally advanced and borderline resectable disease has resulted in improved prognosis [4, 5].

The tumour microenvironment is relatively well established in pancreatic cancer, with studies predominantly focused on naïve patients. Both an anti-tumorigenic and pro-tumorigenic role has been reported in pancreatic cancer. This is highly dependent on the types of immune and stromal cells present [6]. Traditionally, T helper and cytotoxic T cells are associated with immunosurveillance, increased tumour cell death and improved prognosis [7, 8]. Whereas, macrophages, fibroblasts and Tregs tend to inhibit the immune response and are primarily associated with poor prognosis [9, 10]. Furthermore, B cells fall into both the pro and anti-tumour categories due to contradictory reports [11-13]. Until recently, the number of immune cells investigated at one time was limited due to technology. This has resulted in the majority of studies reporting density-based metrics. The introduction of spatial biology and deep phenotyping assays has resulted in studies focused on co-expression, and inter-phenotypic distance relationships being established. Carstens et al reported one of the first upfront resected PDAC studies focused on single cell deep spatial phenotyping [7]. They found cytotoxic T cells within 20μm of cancer cells exhibited increased anti-tumour effects and correlated positively with increased survival. Immunohistochemistry (IHC) based studies demonstrate an immunogenic switch in neoadjuvant therapy patients. A depletion of pro-tumorigenic immune cells, recruitment of anti-tumour immune cells and alteration in the functional states in subsets of immune cells has been reported [6, 14, 15]. Again, these studies predominantly rely on single-plex technologies, with no consideration to spatial relationships within the tumour microenvironment. Furthermore, little is known regarding the biological pathways responsible for this immunogenic switch.

Characterization of pancreatic ductal adenocarcinoma in treatment naïve and neoadjuvant patients represents a niche research field with limited associated literature. The main aim of this thesis was to address this issue. The primary aim was to establish the protein immune cell landscape in treatment naïve and neoadjuvant human pancreatic cancer in terms of content, cellular density and spatial orientation of different phenotypes. The first step was to confirm the IHC prognostic benefit of the most common prognostic associated immune cells. Elevated CD3 ($p=0.015$) and CD8 ($p=0.043$) cells positively correlated with improved disease specific survival (DSS) in naïve PDAC tissue microarrays (TMAs). Subsequently, deep spatial phenotyping was initially separately established in treatment naïve and neoadjuvant setting, then compared. The immune cells explored included T cells, macrophages, fibroblasts and epithelial cells. Improved DSS in naïve patients correlated with increased CD3 T cell ($p=0.004$) and reduced CD68 ($p=0.008$) macrophage density. Additionally, increased proximity from CD68 macrophages to tumour cells ($p=0.005$), and decreased proximity from CD68 macrophages to CD3 T cells ($p<0.001$) also presented in longer survivors. Contradictory to the hypothesis, improved DSS in neoadjuvant patients correlated with reduced CD3 T cells ($p=0.004$) and CD68 macrophages ($p=0.001$). Furthermore, increased proximity from CD68 macrophages to PanCk ($p=0.001$), increased proximity from CD3CD8 cytotoxic T cells to CD3 T cells ($p=0.018$), and reduced proximity to FOXP3CD3 from CD3CD8 ($p<0.001$) correlated with survival. Additionally, this assay established distinct immune differences across chemotherapy versus chemoradiotherapy, and FOLFIRINOX treated versus Gemcitabine treated patients. The deep phenotyping assay lacked functional markers, prompting use of a larger regional protein assay, revealing a prognostically relevant, epithelial compartment specific immune checkpoint marker, B7-H3 ($p=0.026$).

Subsequent Spatial Transcriptomic characterisation was established in order to gain insight into underlying immune related biological mechanisms, something severely lacking in PDAC. Naïve intra-segment heterogeneity demonstrated two unique epithelial signatures, with a non-significant prognostic trend. A variety of potentially targetable significant genes and pathways appeared when integrating mIF findings into Spatial Transcriptomics. These included angiotensin, type I INF, JAK/STAT and IL-2 pathways, which also suggest potential mechanisms responsible for the immune phenotypes observed. Furthermore, transcriptomic B7-H3 expression validated the regional protein result, and was replicated in the neoadjuvant cohort, demonstrating distinct signature profiles between the ranked expression. Interest is growing within the cancer field regarding B7-H3 expression as an immune checkpoint marker [16]. This molecule has, reportedly, limited expression in normal tissue, and high expression in pancreatic cancer, with elevated expression correlating with poor survival and metastasis [17-19]. The results demonstrate potential targetable treatment options for PDAC. Three main immune cell

estimates were repeatedly associated with the better outcome group. These were T cells, B cells and dendritic cells. Taking into consideration variable protein translation from RNA, these results were investigated using a single cell ultra-high plex CosMx assay, with only CD4 and CD8 cell clusters validated. In-depth B7-H3 clustering demonstrated a range of immune cell and epithelial markers co-expressing with B7-H3 across naïve and neoadjuvant patients, with naïve exhausted T cell cluster 12 ($p=0.003$) and neoadjuvant T cell cluster 27 ($p=0.022$) negatively correlating with survival.

In conclusion, comprehensive protein and transcriptomic characterisation of pancreatic cancer spanning both naive and neoadjuvant setting reveals novel patterns. This established inter-phenotypic spatial relations, demonstrated significant differences between naïve and neoadjuvant patients, and has begun to explore complex biological mechanisms within PDAC. These results, if validated, represent potential novel predictive biomarkers, and novel targetable therapies, developments critically needed in pancreatic cancer.

# Graphical Abstract

## Aim 1: Deep immune phenotyping of the naïve and neoadjuvant pancreatic landscape

### a). Prognostic associated density and spatial patterns in naïve and neoadjuvant PDAC

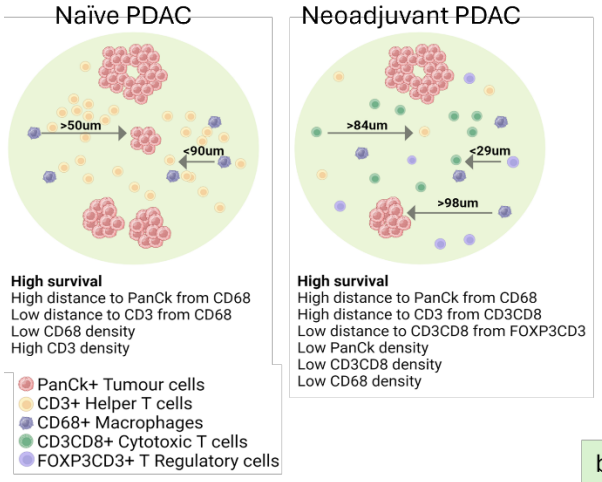


### b).B7-H3 regional Spatial Protein signature negatively corelates with prognosis

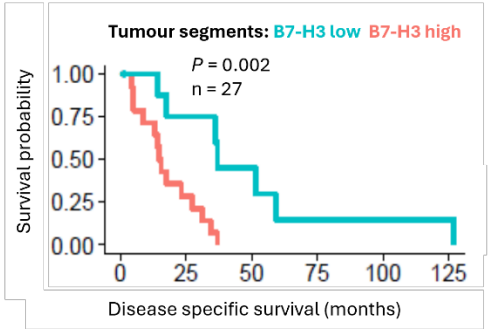


## Aim 2: Characterizing the impact of neoadjuvant therapy on the spatially resolved transcriptome in pancreatic cancer

### a). Distinct naïve epithelial signatures generated

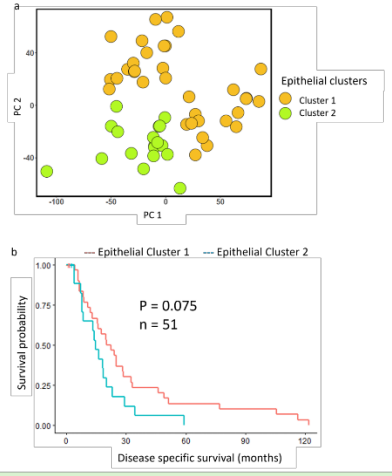


### b). Transcriptomic alterations across numerous naïve and neoadjuvant comparisons

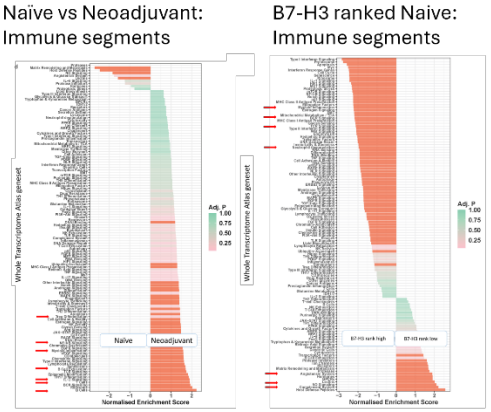


## Aim 3: Multi-omic, orthogonal characterisation of the naïve and neoadjuvant pancreatic landscape

### a). Orthogonal data integration identifies potential biological pathways influencing immune infiltration

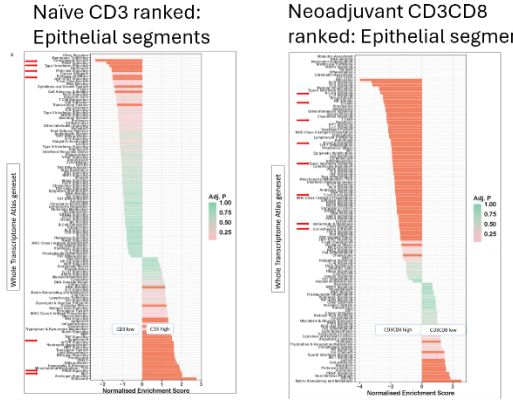


### b). Single cell proteomic clustering identifies numerous possible B7-H3 related clusters co-expressing with a variety of markers

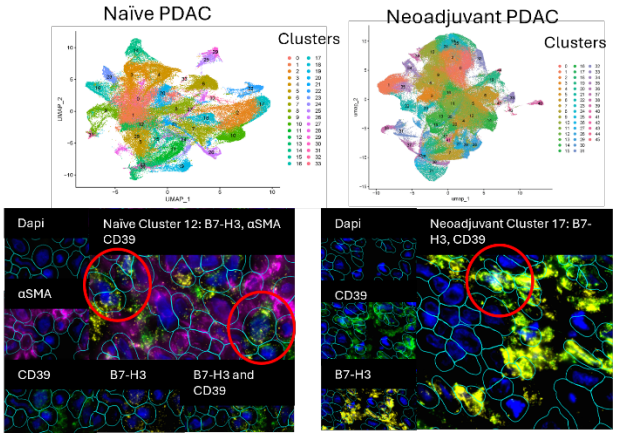

# List of Accompanying Material

Dreyer, S.B., Upstill-Goddard, R., **Legrini, A**., Biankin, A.V., Allison, S., Beraldi, D., Cameron, E., Chang, D.K., Cooke, S.L., Cunningham, R. and Dreyer, S., 2022. Genomic and molecular analyses identify molecular subtypes of pancreatic cancer recurrence. Gastroenterology, 162(1), pp.320-324.

Wood, C.S., Pennel, K.A., Leslie, H., **Legrini, A**., Cameron, A.J., Horgan, P., Edwards, J., Steele, C.W. and Jamieson, N.B., 2023. Spatially resolved transcriptomics deconvolutes histological prognostic subgroups in patients with colorectal cancer and synchronous liver metastases. Cancer Research, 83(7_Supplement), pp.4691-4691.

*In preparation* **Legrini, A**., Leslie, H., Dreyer, S., Edwards, J., Biankin, A., Chang, D. and Jamieson, N.,. High plex proteomic prognostic marker discovery for patients with pancreatic adenocarcinoma using digital spatial profiling.

*In preparation* **Legrini, A**., Wood, C.S., Leslie, H., Cameron, A., Zhang, T., Nara, R., Pennie, R., Martinelli, S., Officer-Jones, L., Powley, I., Le Quesne, J., Jamieson, N. Spatial Multi-omic characterisation of Human Pancreatic ductal adenocarcinoma in Naïve vs Neoadjuvant treated patients.

## Poster presentations

**Legrini, A**., Wood, C.S., Leslie, H., Cameron, A., Zhang, T., Nara, R., Pennie, R., Martinelli, S., Officer-Jones, L., Powley, I., Le Quesne, J., Jamieson, N. Spatial Multi-omic characterisation of Human Pancreatic ductal adenocarcinoma in Naïve vs Neoadjuvant treated patients. International Spatial Biology Congress 2023 – Rotterdam, Netherlands

**Legrini, A**., Leslie, H., Dreyer, S., Edwards, J., Biankin, A., Chang, D. and Jamieson, N. High plex proteomic prognostic marker discovery for patients with pancreatic adenocarcinoma using digital spatial profiling. AACR 2022 – New Orleans, US

**Legrini, A**., Wood, C.S., Leslie, H., Pennie, R., Martinelli, S., Officer-Jones, L., Powley, I., Le Quesne, J., H., Dreyer, S., Edwards, J., Biankin, A., Chang, D., Jamieson, N. Deep phenotype immune cell spatial characterisation in Pancreatic cancer. Glasgow Bioinformatics & Computational Biology Conference 2022 – Glasgow, UK

# Contents

# List of Figures

# List of Tables

# Definitions/Abbreviations

| | |
|---|---|
| AOI | Area of illumination |
| aSMA | alpha smooth muscle action |
| BCR | B cell receptor |
| BRCA1/2 | Breast cancer gene 1/2 |
| DDR | DNA damage repair |
| DEA | Differential expression analysis |
| DSP | Digital spatial profiler |
| DSS | Disease specific survival |
| EMT | Epithelial-to-mesenchymal transition |
| Epi | Epithelial |
| FFX | FOLFIRINOX |
| Gem | Gemcitabine |
| GemAbx | Gemcitabine plus Abraxane |
| GemCap | Gemcitabine plus Capecitabine |
| GSEA | Geneset enrichment analysis |
| ICB | Immune checkpoint blockade |
| IHC | Immunohistochemistry |
| IKK | IκB kinase |
| IL | Interleukin |
| IPMNs | Intraductal papillary mucinous neoplasms |
| ITPN | Intraductal tubular papillary neoplasms |
| JAK | Janus kinase |
| KPC | KrasG12D/+; Trp53R172H/+; P48-Cre |
| KRAS | Kirsten rat oncogene homolog |
| LAPC | Locally advanced pancreatic cancer |
| LOF | Loss of Function |
| LogFC | Log2 fold change |
| LTS | Long term survivors |

MCNs Mucinous cystic neoplasm

mDC Memory dendritic cell

MET Mesenchymal epithelial transition

mFFX Modified FOLFIRINOX

MHC Major histocompatibility complex

mIF Multiplex immunofluorescence

mIHC Multi-colour immunohistochemistry

mNN Mutual nearest neighbour

mTOR Mammalian target of rapamycin

MYC Myelocytomatosis oncogene

NAT Neoadjuvant therapy

Neoadj Neoadjuvant

NeoadjXRT Neoadjuvant treatment type

NES Normalized enrichment score

NF-kB Nuclear factor Kappa B

NK Natural killer

NN Nearest neighbour

NO Nitric oxide

padj P adjusted

PanCk Pan cytokeratin

PanINs Pancreatic intraepithelial neoplasms

PARP Poly-ADP ribose polymerase

PBT Platinum based therapy

PCA Principle component analysis

PDAC Pancreatic ductal adenocarcinoma

pDC Plasmacytoid dendritic cells

PDGF Platelet-derived growth factor

PI3K-Akt Phosphatidylinositol 3-kinase/protein kinase B

PPAR Peroxisome proliferator-activated receptors

PTB Presumed tumour bed

RFS Recurrence free survival

ROI Region of interest

ST Spatial Transcriptomics

STAT Signal transduction and transcription activation

STS Short term survivors

TC Tumour core

TCR T cell receptor

TGF-β Transforming growth factor-beta

TLS Tertiary lymphoid structure

TMA Tissue microarray

TME Tumour microenvironment

TNF Tumour necrosis factor

TNM Tumour, lymph node, metastasis

Tregs T regulatory

Type I INF Type I interferons

Type II INF Type II interferons

UFR Up front resected

UMAP Uniform manifold approximation and projection

VEGF Vascular endothelial growth

WTA Whole Transcriptome Assay

# 1 Chapter 1: Introduction

## 1.1 Pancreatic Cancer Epidemiology

With a 5-year survival of <7%, pancreatic ductal adenocarcinoma (PDAC) is currently the 5th most common cause of cancer death [1, 2]. Mortality rates in the past 10 years have remained stable for females, and a slight increase was seen in males, with 51% of rates associated with patients above 75 years old [20]. Surgical resection remains the best treatment method, although the 5-year survival remains <25% [21]. The vast majority of patients present with metastatic disease thus systemic chemotherapy offers only a modest improvement in survival [22]. The average number of cases from 1990s to 2016-2018 has increased 17%, resulting in approximately 10,500 new cases every year in the UK. It is currently the 10$^{th}$ most common UK diagnosed cancer, accounting for 3% of new cases [20].

## 1.2 Clinical presentation, symptoms and diagnosis

The poor outcome associated with PDAC is linked to several factors. One major factor being late presentation due to ambiguous symptoms such as back pain, fatigue and nausea, which are often ignored by the patients or attributed to other causes [23]. More specific symptoms include jaundice and new-onset diabetes [24]. Treatment is heavily dictated by the stage of disease [25]. Patients are split into four categories;

1. Resectable – surgery with pre or post operative chemotherapy/chemoradiotherapy
2. Borderline resectable - surgery with pre or post operative chemotherapy/chemoradiotherapy
3. Locally advance – preoperative treatment and surgery
4. Metastatic – systemic chemotherapy

Surgical resection is the only potentially curative method currently available, yet only 10-20% of patients present early enough to undergo surgery, with the remainder of patients presenting with metastatic disease [21]. Anatomical location of the cancer dictates the likely symptoms and potential prognostic outcomes [26]. Tumours located at the head/neck of the pancreas (70%) are more likely to present earlier with obstructive jaundice among other symptoms [26, 27]. Tumours located at the body (15%), tail (10%) and multifocal (10%) are associated with late-onset diabetes and non-specific symptoms leading to lower resectability rate and poor survival (figure 1.1) [26, 28].

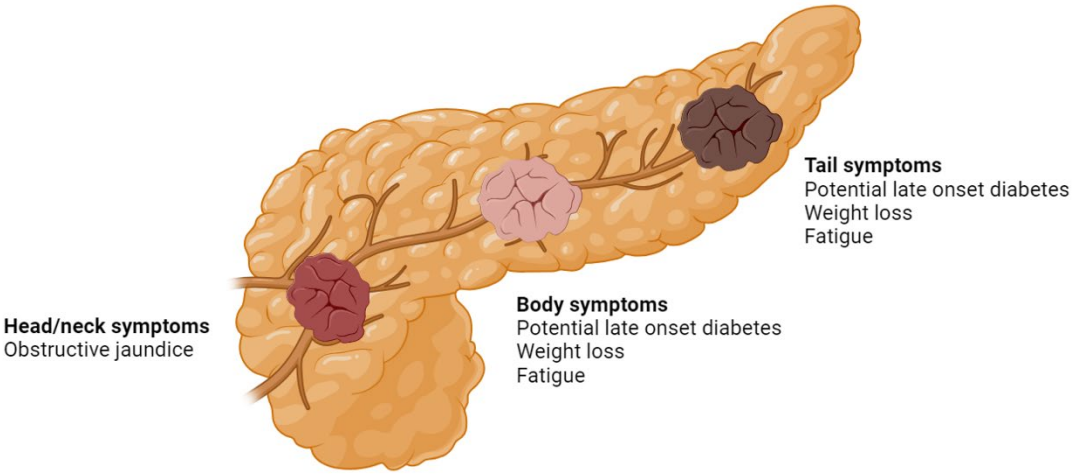


**Figure 1.1 Location of pancreatic ductal adenocarcinoma tumours and most common associated symptoms**. *Illustrative figure showing location of tumours in the pancreas with common symptoms. Locations include head and neck, body and tail. Figure created with BioRender*

A wide range of diagnostic tools can be implemented including non-invasive/invasive imaging techniques and serum markers. Initial steps are carried out using non-invasive methods, multidetector computed tomography (MDCT) angiography has a sensitivity of at least 90%, used in early detection of tumours between 2-5mm. Invasive methods such as endoscopic ultrasonography with fine needle aspiration have higher accuracy [29, 30]. Additionally, carbohydrate antigen 19-9 (CA19-9) is a validated biomarker with sensitivity of at least 70% and a specificity of 90% in symptomatic patients [31]. This biomarker can also be used to monitor treatment response, resection and survival outcome. It is important to note that elevated levels of CA19-9 are not specific to PDAC and can be seen in biliary obstructed patients [32].

## 1.3 Clinical pathology

Multiple clinical factors have been significantly associated with prognosis in pancreatic cancer. These have been limited to the most reported common factors.

### 1.3.1 TNM staging

TNM based staging from the American Joint Committee on Cancer (AJCC) 8th edition is a benchmark method for PDAC cancer classification. This classifies patients according to tumour (T), lymph node (N) and metastasis (M) [33]. Briefly, T Stage 1-3 indicates that the tumour is located within the pancreas with increasing size across the groups (Stage 1: 0-2cm, Stage 2: 2-4cm, Stage 3: >4cm), and T Stage 4 indicates the cancer has spread into neighbouring blood vessels. Nodal staging ranks from 0-2, with N0 indicating no contamination of nodes and N2 meaning at least 4 lymph nodes are involved [33]. Metastasis is ranked by presence (M1) or absence (M0) of metastasis. Patients with high stages across all categories tend to have worse outcome [33].

### 1.3.2 Lymph Node status

Lymph Node status defines whether there is confirmed nodal involvement. Patients are split into LN0 or LN1, where LN0 indicates no lymph node invasion and is typically associated with better survival. LN1 patients indicate presence of lymph node metastasis and is associated with worse prognosis [34, 35].

### 1.3.3 Resection margin status

Margin status indicates the level of cancer cells present at the edge of the tissue. Margin positivity (R1) indicates the presence of cancer cells either microscopically or macroscopically, and margin negative (R0) indicates no cancer cells are present [36]. R1 patients tend to be significantly associated with poorer survival outcomes [37-40].

### 1.3.4 Grade

Histological grade ranks the level of differentiation in pancreatic cancer, ranging from poor, moderate and good [41]. Patients with poor differentiation have worse outcomes [42, 43].

### 1.3.5 Vascular Invasion

Vascular invasion is defined by the presence of tumour cells within blood vessels, resulting in circulating tumour cells. Vascular invasion positive groups (V1) are dictated by multiple criteria and can be used to stratify patients. These patients tend to be associated with more aggressive tumours, with increased cell dissemination and poor survival [44]

### 1.3.6 Perineural Invasion

Perineural invasion is characterised by the presence of invaded or encompassed nerves by tumour cells. This phenomenon is present in 70-95% of PDAC patients, and tends to correlate with poor prognosis, metastasis and recurrence [45, 46].

## 1.4 Risk factors

There are few known risk factors for pancreatic cancer. However, medical conditions such as chronic pancreatitis may have an association with the development of PDAC [47]. It is estimated that around 5-10% of patients with pancreatic cancer have a familial association. However, the exact genetic basis for this association is unknown [48]. Reports of mutations in a variety of genes including, *BRCA2, CDKN2A* and *FANCG*, suggest that they may be associated with a predisposition to pancreatic cancer [49, 50]. Smoking is by far the most common modifiable risk factor reported, with studies demonstrating cancer development risk doubles amongst frequent smokers [51].

## 1.5 Pancreatic pathology and pathogenesis

The normal pancreas is made up of two glandular tissues, exocrine and endocrine, which have different functions. The exocrine compartment, which makes up the majority of the pancreas, produces eosinophilic zymogen granules in functional acinar cells located in lobular units. These enzymes, which are necessary for digestion, are secreted into intercalated ducts and then into the major pancreatic ducts. [52]. The endocrine pancreas is made up of islets of Langerhans, which are responsible for insulin production and blood glucose regulation [53]. Although there are a range of pancreatic cancer types, 90% of reported cases are pancreatic ductal adenocarcinomas [54]. These cancers stem from the exocrine pancreas, and the most likely cells of origin are either pancreatic acinar or somewhat controversially, ductal cells [55-57].

Pathogenesis of sporadic PDAC has yet to be fully characterised, however four main precursors have been established; pancreatic intraepithelial neoplasms (PanINs),

intraductal papillary mucinous neoplasms (IPMNs), intraductal tubular papillary neoplasms (ITPN) and mucinous cystic neoplasm (MCNs) [58]. Following the PanIN hypothesis, normal epithelium progresses through the different grades of PanIN lesions (from low grade 1A/B to high grade 3). Within this progression, multiple genetic mutations and gain/loss of function events take place [59, 60]. Low grade PanINs are associated with *KRAS* mutations, intermediate lesions are associated with telomere shortening and *p16/CDKN2A* inactivation, and high grade lesions have inactivation of *TP53*, *BRCA2* and *SMAD4*, and finally high grade PanINs progress into invasive carcinoma (figure 1.2) [61].

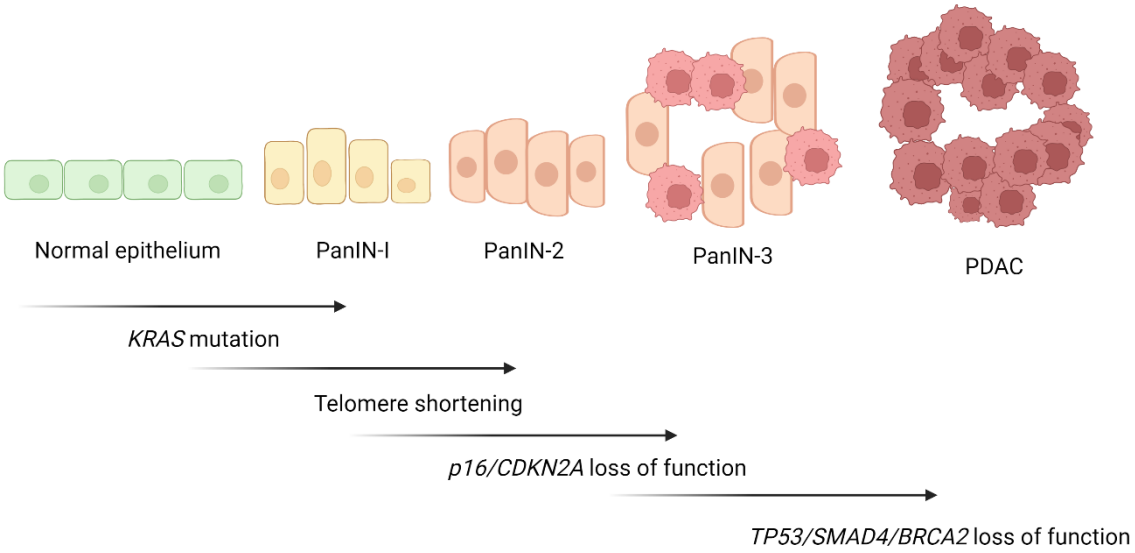


**Figure 1.2 Pathogenesis from pancreatic intraepithelial neoplasms (PanINs) to pancreatic ductal adenocarcinoma.** *Diagram showing development of PDAC from normal epithelium using the PanIN hypothesis. KRAS mutation leads to PanIN-I development, then accumulation of telomere shortening, p16/CDK2A loss of function results in PanIN-3. Progression into ductal adenocarcinoma occurs after loss of function of TP53/SMAD4/BRCA2. Figure created with BioRender.*

## 1.6 Molecular pathways associated with PDAC

A wide range of signalling pathways have been associated with pancreatic cancer. The most relevant pathways have been selected and described below. Where appropriate, a diagram has been included.

### 1.6.1 *KRAS* pathway

*KRAS* mutations are found in ~90% and one of the first genetic aberrations seen, indicating that it plays a critical role in neoplastic initiation. Missense mutations are most common, with *KRAS*$^{G12D}$ and *KRAS*$^{G12V}$ being the most prevalent [62-64]. These mutations are located in the GTP binding domain of RAS, resulting in a constitutively active *KRAS*. In normal cells, inactive *KRAS* is bound to guanosine diphosphate (GDP) until epidermal growth factors (EGFs) bind to their receptors, and GDP undergoes phosphorylation, resulting in the higher affinity molecule guanosine triphosphate (GTP) (figure 1.3). Active *KRAS* mediates multiple signalling pathways including RAF-MEK, TGF-β and PI3K associated pathways [65, 66].

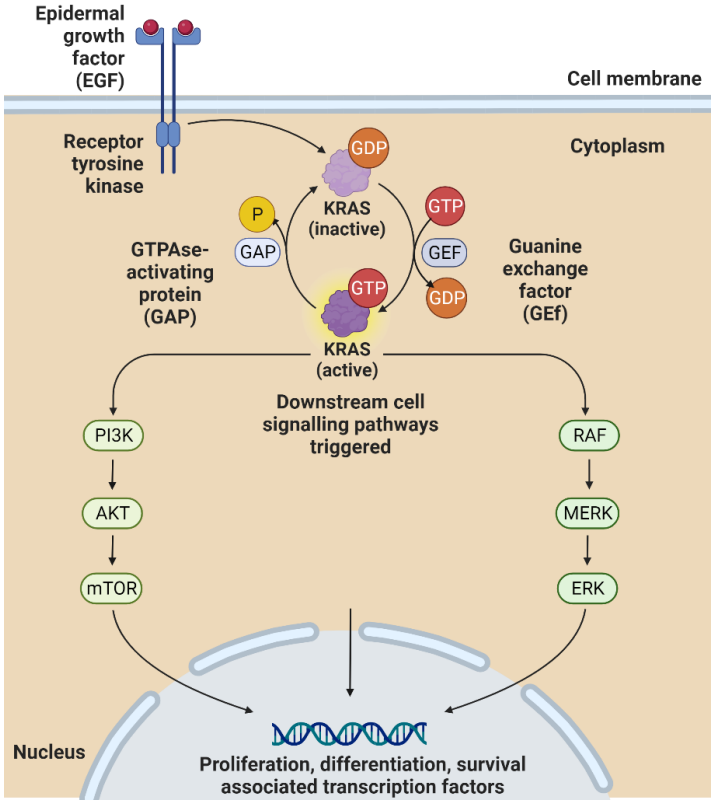


**Figure 1.3 KRAS cell signalling pathway**. *Epidermal growth factor (EGF) binds to receptor tyrosine kinase leading to phosphorylation (P) of guanosine diphosphate (GDP) into guanosine triphosphate (GTP) via guanine exchange factor (GEF). Active KRAS mediates multiple pathways including RAF and PI3K, resulting in transcription of important factors including proliferation, differentiation and survival associated factors. In normal cells, GTPase activating protein dephosphorylating KRAS ensuring it doesn't stay constitutively active. Figure adapted from BioRender template.*

## 1.6.2 TGF-β canonical pathway

TGF-β can be activated either via a SMAD-dependent or independent process. As one of the few prevalent PDAC genetic mutations, the focus will be on the canonical, SMAD-dependent pathway (figure 1.4) [67]. Signalling is mediated via TGF-β specific receptors, e.g. TGFβ-I and TGFβ-II. Ligands bind directly to TGFβ-II, which in turn phosphorylates TGFβ-I, leading to propagation of the signal via phosphorylation of SMAD proteins in their SXS C-terminal serine motif (figure 1.4). TGFβ-I activates a range of receptor dependent SMADs, and subsequently forms a heterodimer with the co-mediator SMAD4, translocates to the nucleus where it acts as both a co-activator and co-repressor for gene transcription [68, 69]. As for many proteins in pancreatic cancer, TGF-β has been reported as both a tumour suppressor via differentiation and apoptosis [70, 71], and a tumour promoter via chronic inflammation, metastasis and immune evasion [70, 72-74].

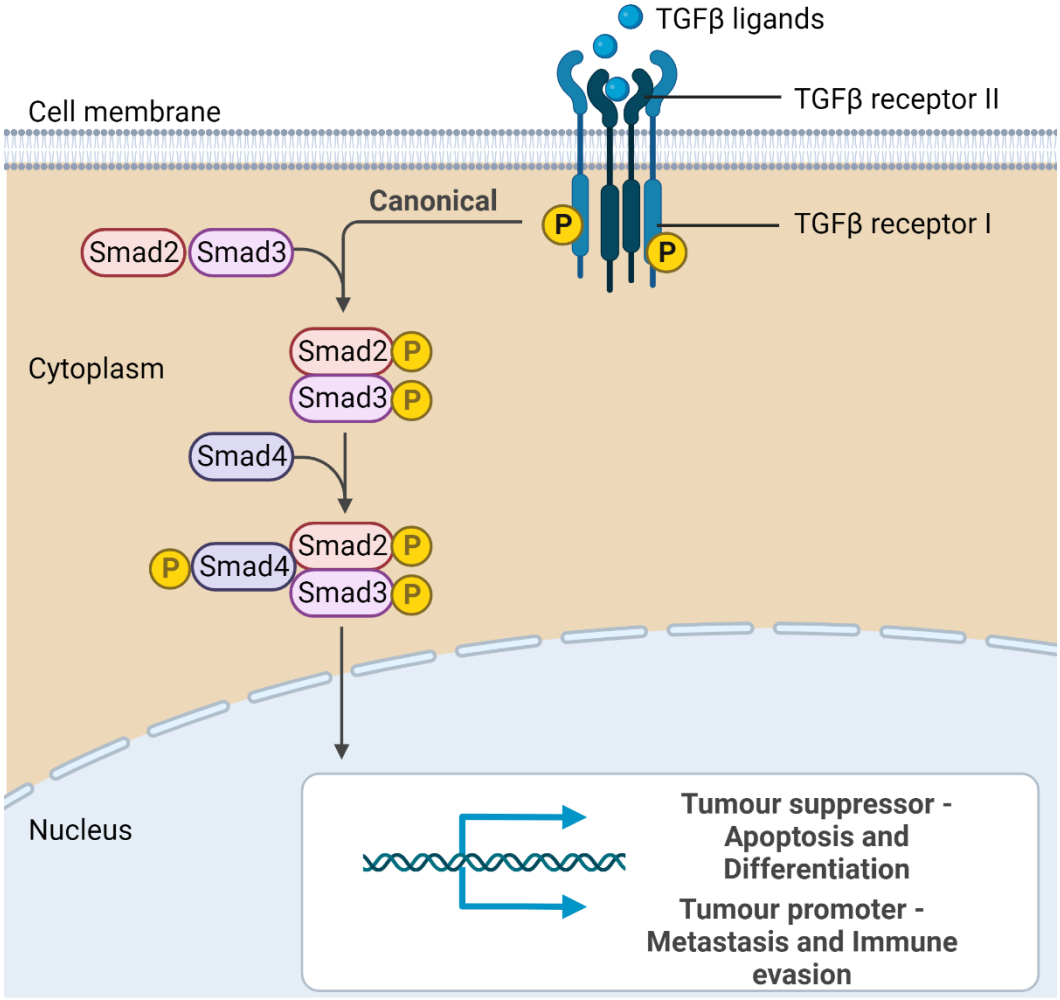


**Figure 1.4 TGF-β canonical signalling pathway**. *Schematic diagram showing SMAD-dependent TGF-β canonical pathway. TGF-β ligands bind to TGF-β receptor II, triggering receptor I phosphorylation (P). Cascade phosphorylation of SMAD proteins resulting in formation of SMAD4/SMAD3/SMAD2 heterodimer, translocation to the nucleus and subsequent activation or suppression of transcription factors. Canonical pathway suppresses apoptosis and differentiation, and promotes metastasis and immune evasion. Figure adapted from BioRender template.*

### 1.6.3 NF-κB associated pathway

NF-κB transcription factor is heavily involved in multiple immune/inflammatory responses and constitutively active in pancreatic cancer [75]. In the canonical pathway, upon activation via IKK phosphorylation, the NF-κB complex (p50/p65) translocates to the nucleus resulting in increased expression of inflammatory target genes such as interleukin-6 (IL-6) and interleukin-18 (IL-18) [76, 77]. This generates a positive feedback loop, leading to further NF-κB signalling. Excessive pathway activation is also linked to epithelial-to-mesenchymal transition (EMT) and neural invasion [78, 79].

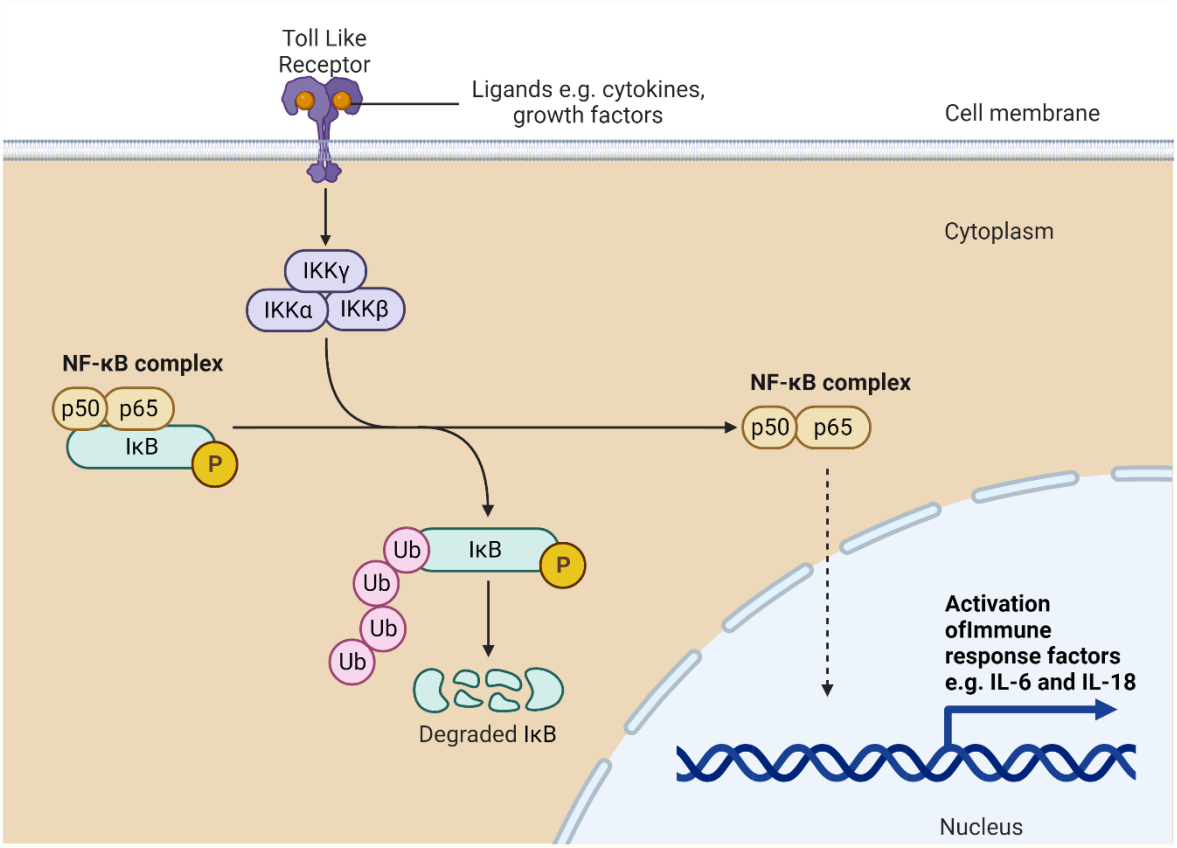


**Figure 1**.5 **NF-κB canonical pathway.** *Schematic diagram showing NF-κB canonical pathway. Appropriate ligand binds to toll like receptors triggering phosphorylation of the NF-κB complex via the IKK complex. Subsequent ubiquitination of NF-κB regulatory subunit results in translocation of NF-κB complex into the nucleus and activation of transcription factors. The canonical pathway associates with inflammatory immune response factors such as IL-6. Figure adapted from BioRender template.*

### 1.6.4 JAK2/STAT3 pathway

Sustained JAK/STAT activation in pancreatic cancer correlates with chronic inflammation and reduced cytotoxic T cells [80, 81]. Specifically, increased JAK2 expression significantly correlates with worse prognosis in resectable patients [82]. Activation of this pathway in the pancreas remains unclear, however insight can be drawn from various studies. STAT3 is reportedly vital for PDAC tumour progression, as demonstrated in *KRAS* cell and mouse models [83-86]. Upon ligand binding, transphosphorylation of JAK induces tyrosine phosphorylation of the receptor forming a STAT docking site (figure 1.6). STAT3 binds, is phosphorylated, dissociates and forms dimers which translocate to the nucleus (figure 1.6) [87]. A wide range of biological phenomena are influenced by this pathway including immune regulation [86, 88, 89]. Upon inhibition of STAT3 in PDAC mouse models, a subsequent downregulation of suppressive cytokines was seen, as well as increased activated T cells [81].

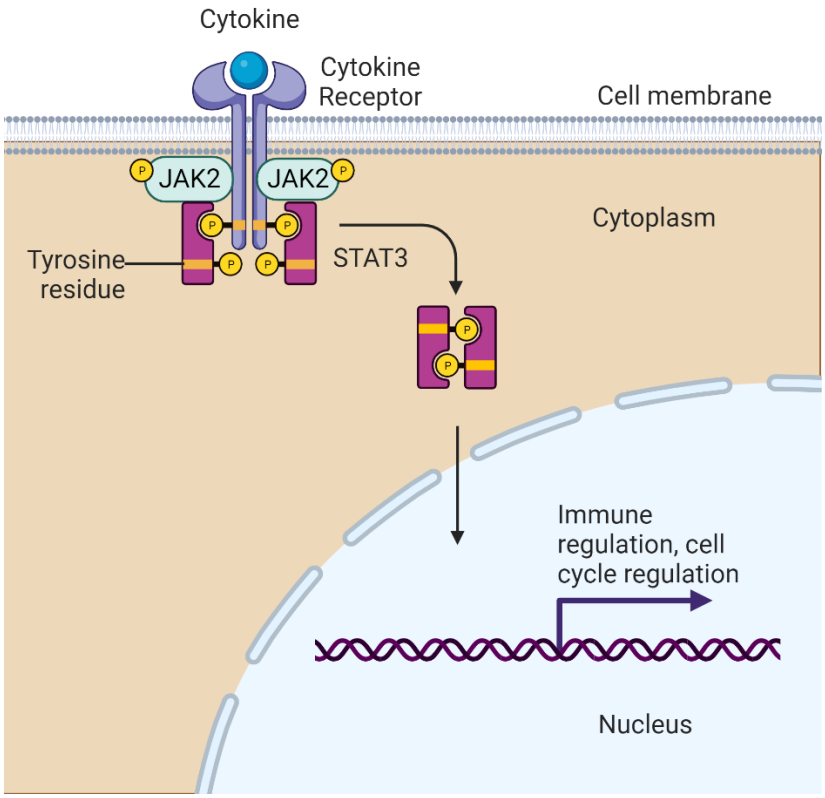


**Figure 1.6 JAK2/STAT3 pathway.** *Schematic diagram showing JAK2/STAT3 pathway. Appropriate cytokines e.g. IL6, binds to cytokine receptor resulting in recruitment and transphosphorylation of JAK2, and formation of STAT 3 docking site. Subsequent phosphorylation and dimerization of STAT3 occurs, leading to translocation to the nucleus and activation of transcription factors. JAK/STAT pathway associates with immune regulation and cell cycle regulation factors. Figure adapted from BioRender template.*

### 1.6.5 DNA damage repair

Up to 20% of patients may have some form of Loss Of Function (LOF) aberration, including BRCA1/2 resulting in inhibition of homologous recombination pathway. Cells become reliant on the DNA damage repair (DDR) pathway and are termed homologous recombinant-deficient (HRD) phenotype [15]. Patients with these BRCA1/2 mutations are of particular interest for targeted therapy and are by far the most promising targeted therapy option for pancreatic cancer patients [90].

### 1.6.6 Epithelial to Mesenchymal Transition

Although EMT is not strictly a signalling pathway, it is particularly important in pancreatic cancer and is thought to be essential for oncogenesis. It is regulated by a huge number of networks including TGF-β signalling, which is thought to be a primary inducer of this transition [91]. High levels of Zeb-1, a transcriptional suppressor of E-cadherin, is inversely correlated with E-cadherin. Studies have demonstrated Zeb-1 suppression resulted in increased E-cadherin expression and reversed drug resistance in pancreatic cell lines [92]. Vimentin, a well-known mesenchymal marker, was positively associated with tumour budding, reinforcing the hypothesis that EMT is a vital step in PDAC progression [93].

### 1.6.7 Angiogenesis

Angiogenesis is one of the hallmarks of cancer and is required for novel vasculature development for metastasis [94]. The angiogenic landscape in pancreatic cancer is complex, with low levels of vasculature found compared to other solid cancers. The dense, fibrotic stroma generates elevated interstitial fluid pressure, resulting in the collapse of vasculature, resulting in chemoresistance due to lack of access to the tumour core [95, 96]. However, elevated levels of angiogenesis markers and pathways are frequently reported in PDAC, including BICC1, VEGFR-1 and STAT3 regulated pathways [97-99]

# 1.7 Pancreatic cancer subtypes: molecular and genomic characterisation

## 1.7.1 Molecular subtyping

Pancreatic cancer demonstrates significant heterogeneity at an inter and intra tumoural level. This is, in part, due to its complex mutational landscape. *KRAS* mutation is seen in >90% of tumours, and aberration of *TP53*, *SMAD4* and *CDKN2A* (>50%) are also frequently present in PDAC [14, 15]. The frequency of other aberrations reduces significantly (<10%), resulting in the mutational landscape being dominated by rare mutations [15]. Recent developments in molecular profiling of PDAC have resulted in a more detailed understanding of the underlying heterogeneity of this disease. Attempts to subtype PDAC by gene expression have resulted in three major models; Collison, Moffit and Bailey classification, along with other important models, such as Raphael and Puleo (table 1.1) [100-104]. The first major molecular subtyping break through was published in 2011 by Collison et al [100]. This utilised gene expression microarrays, generating a bulk RNA signature defining three subtypes;

1. Classical
2. Quasi-mesenchymal
3. Exocrine-like

Classical subtypes were associated with the best outcome. This subtype had increased *GATA6* expression (an adhesion associated gene), and was *KRAS* dependent. Quasi-mesenchymal had, as the name suggests, increased mesenchymal associated genes and the poorest outcome. Exocrine-like subtypes demonstrated elevated neoplastic cell derived digestive enzymes and represented the middle outcome group [100]. In 2015, Moffit et al used a similar method, however with the added step of separating out tumour, stromal and normal pancreatic gene expression, producing histopathological distinct subtypes [101]. Two tumour epithelial and two stromal specific subtypes were generated;

1. Classical – tumour subtype
2. Basal-like – tumour subtype
3. Normal Stroma
4. Activated Stroma

Moffit Classical subtype and the Collison Classical subtype are highly interchangeable, with the majority of the genes classifying these subtypes overlapping including *GATA6* [100, 101, 105]. The Basal subtype was classified as the poor outcome subtype (median survival: 11 months), although interestingly these patients seem to respond better to

adjuvant therapy. Normal stroma exhibited a simpler geneset pattern with increased pancreatic stellate cells, smooth muscle actin, vimentin and desmin markers. In contrast, activated stroma had a complex geneset enrichment with increased macrophage, fibroblast activation and pro-tumorigenic inflammatory stromal response resulting in worse overall outcome [101]. Interestingly, the tumour subtypes were associated with both stromal subtypes. In 2016, Bailey et al investigated the transcriptional and mutational landscape of pancreatic cancer and discovered four subtypes;

1. Squamous
2. Pancreatic Progenitor (Progenitor or PP)
3. Abnormally Differentiated Endocrine Exocrine (ADEX)
4. Immunogenic

Squamous overlaps with both Collison's Quasi-mesenchymal and Moffit's Basal, and Progenitor overlaps with Classical [102, 105]. As expected, Squamous is associated with poor prognosis, potentially as a result of increased *TP53* and *KDM6A* mutations, and increased gene expression in inflammatory and hypoxic pathways [106]. Upregulation of TP63deltaN and downregulation of genes determining pancreatic endodermal cell fate are also a key feature, leading to increased EMT [102]. Pancreatic Progenitor, ADEX and immunogenic are typically associated with a relatively better prognosis. Progenitor subtypes express transcription factor *PDX1*, which plays a vital role in pancreatic cell development from embryonic progenitor cells. ADEX and Immunogenic subtypes were associated with increased *KRAS* activation and increased immune suppression and immune infiltration respectively [102].

Various other molecular subtypes have been established, the majority of which have continued to focus on tumour specific subtypes and generated some sort of variation of the Basal/Classical subtypes [103, 104]. Of interest, Puelo et al produced 5 subtypes from a mixture of tumour and stromal subtypes based on Moffit et al subtypes (table 1.1) [104]. For the remainder of this thesis, the terms Squamous (Bailey) and Classical (Collison and Moffit) will be employed. The Classical subtype will be a mixture of all the 'Classical-like' subtypes, and would be more accurately named Rest, however for simplicity the umbrella term 'Classical' will be used.

| Author | Method | Classification | Survival association (months) | Overlap |
|---|---|---|---|---|
| Collision [78] | Global Gene expression profiling | Classical | Best group (23) | Classical (Moffit) Progenitor (Bailey) |
| | | Exocrine-like | Middle group (19.7) | ADEX (Bailey) |
| | | Quasi-Mesenchymal | Worst group (6.6) | Squamous (Bailey) |
| Moffit [79] | Global Gene expression profiling and RNAseq | Classical (tumour) | Best tumour group (19) | Classical (Collision) Progenitor (Bailey) |
| | | Basal-like (tumour) | Worst tumour group (11) | Squamous (Bailey) |
| | | Normal Stroma | Best stromal group (24) | |
| | | Activated Stroma | Worst stromal group (15) | |
| Waddel [72] | Whole genome sequencing | Stable | NA | NA |
| | | Locally rearranged | NA | NA |
| | | Scattered | NA | NA |
| | | Unstable | NA | NA |
| Bailey [80] | Whole Genome and Transcriptome (RNAseq) | Immunogenic | Best group (30) | |
| | | ADEX | Middle group (25.6) | Exocrine-like (Collision) |
| | | Pancreatic Progenitor | Middle group (23.7) | Classical (Collision) Classical (Moffit) Quasi-Mesenchymal (Collison) Basal-like (Moffit) |
| | | Squamous | Worst group (13.3) | |
| Raphael [81] | Genome, Transcriptome and protein analysis | Classical/Pancreatic Progenitor | Best group | |
| | | Basal-like/Squamous | Worst group | |
| Puelo [82] | Genome, Transcriptome and protein analysis | Pure Classical | Best group (43.1) | Classical tumour, Normal and Activated stroma (Moffit) |
| | | Immune Classical | Middle high group (37.4) | Classical tumour, and Activated stroma (Moffit) |
| | | Desmoplastic | Middle group (24.3) | Basal-like or Classical tumour, and Normal stroma (Moffit) |
| | | Stroma activated | Middle poor group (20.2) | Basal-like or Classical tumour, and Activated stroma (Moffit) |
| | | Pure Basal-like | Worst group (10.3) | Basal-like tumour, and Activated stroma (Moffit) |

**Table 1.1 Pancreatic cancer molecular subtypes**. *Summary table includes methods used to establish molecular subtypes, subtype associated survival and overlap between different subtypes. Comparison made between Collison, Moffit, Waddel, Bailey, Raphael and Puelo. Table generated from appropriate references as indicated in author column.*

### 1.7.2 Genomic subtypes

In addition to transcriptome characterisation, Wadell et al characterised the genomic alterations in PDAC using whole genome sequencing on 100 primary tumours [15]. Four genomic subtypes were described according to chromosomal rearrangements;

1. Stable (30%)
2. Locally rearranged (30%)
3. Scattered (36%)
4. Unstable (14%).

This study revealed a potentially actionable target for treatment for patients with unstable tumour subtypes. Mutations in BRCA1/2, PALB2, and BRCA mutational signatures were significantly associated with these patients, indicating possible sensitivity to DNA-damaging treatments such as Platinum based therapies [106]. Combining the unstable subtypes along with patients with DNA damage repair deficiencies results in approximately 20% of diagnosed patients that may have a viable targeted treatment option [15].

Molecular and genomic subtyping has uncovered many biological insights that underlie biological pathways in pancreatic cancer, providing potentially actionable treatment targets, discovery of novel biomarkers and could be used as an independent prognostic tool. The differences seen within the different studies indicates that more research is needed on a larger representative cohort to test the robustness of using molecular subtyping in the clinic.

## 1.8 Spatial Biology

Spatial Biology is the study of high-plex biological phenomena at a 2 dimensional level whilst maintaining the spatial context from where the data originates from. This can be split into 1). Spatial Transcriptomics, and 2). Spatial Proteomics [107]. Both groups can generate spatially resolved, high output data at a scale reminiscent of single cell transcriptomics. Multiple academic groups and companies have attempted to create a range of spatial technologies. With the exceptions of a few companies, these techniques have mostly stayed within the parent institute, due to the requirement of niche expertise, highly specialised equipment and extensive personnel labour [108]. This has resulted in a selection of companies and their associated assays dominating the field and consistently appearing in Spatial Biology publications.

### 1.8.1 Spatial Transcriptomics

Spatial Transcriptomics (ST), Nature's method of the year 2020, primarily investigates regions within tissue samples and extracts data in either an imaging-based fashion or a sequencing-based fashion [109-114]. Fresh frozen and formalin fixed paraffin embedded (FFPE) tissue can be used depending on the technology. Until recently, imaging-based technologies have only worked with limited RNA panels. Use of fresh frozen tissue severely limits the types of cohorts explored and requires a specialised histology department. Due to these limitations, the main focus will be on FFPE and sequencing based technologies. There are arguably two major companies that excel in ST;

1. Nanostrings® – GeoMx™ assay
2. 10X Genomics® – Visium™ assay

GeoMx™ works by using digital optical barcoding for a range of panels including the whole transcriptome [113]. Multifluorescent imaging is carried out using a mixture of immune and morphology oligo-conjugated antibodies to visualise tumours and aid selection of regions of interest (ROI). Oligo tags are cleaved using ultraviolet light, hybridized to barcodes and sequenced [113]. Visium™ methodology works by using fixed oligonucleotide barcoded spots to spatially resolve the whole transcriptome of tissues found within the spots [114]. Both these technologies have benefits and limitations. GeoMx™ allows for generation of 'pure' regional transcriptomic signatures, and prior visualisation of tissue to select precise regions. However, it requires ideally 100 nuclei per region, resulting in the generation of a 'mini-bulk' signature. As this technology is ROI based, whole section work is costly, however it is ideal for Tissue Microarrays (TMAs). Visium™ is ideal for whole section work, as the slides have 55µm fixed spots across the

capture area, and requires no specialist equipment. Transcript resolution sensitivity is higher in Visium™, although both are classed as multicellular and can be outcompeted by other technologies with better resolution and capture [115, 116]. Selection bias in both technologies means establishing a robust experimental question is essential to ensure the correct samples are chosen.

### 1.8.2 Spatial Protein

Spatial Proteomics (SP) biology differs to its RNA counterpart primarily due to limitation of the plex. The suffix ‘omic’ strictly refers to the entire profile of the type of data, e.g. proteomics would technically refer to the full protein landscape, and would use techniques such as mass spectrometry detection [117]. A drive to focus data generation to specific panels has resulted in spatial biology taking the liberty of calling high-plex protein panels Spatial Proteomics or Spatial Protein. Spatial Protein techniques can be split into;

1) Imaging-based techniques
2) Oligo-tagged antibody with DNA barcoding

By far, the most popular imaging-based technique utilises Akoya Biosciences® assays. Akoya Biosciences® has two major techniques, PhenoImager™ (formerly Phenoptics) and Phenocycler™ (formerly CODEX) [118, 119]. PhenoImager™, a multiplex immunofluorescence (mIF) assay, is a multi-antibody staining strategy to enable quantification of multiple markers simultaneously on one tissue section providing the benefit of colocalization. As multiple antibodies are being utilised, different fluorophores, each with a specific excitation and emission spectra, are used to distinguish between epitopes. Akoya® specialises in linear spectral unmixing, which extracts the true signal of each fluorophore, allowing for up to 9 markers to be imaged on the same section at the same time [118, 119]. PhenoCycler™ utilizes super-resolution microscopy to image up to 100 protein markers on the same slide using cyclical imaging methods [119].

The second spatial protein technique works primarily with oligonucleotide tagged antibodies via DNA barcoding. This can be done using pre-determined panels such as GeoMx™ protein panels (up to 100plex) or the Visium™ co-detection protein expression panels (up to 31 plex) [113, 120] . Perhaps the most important benefit of the Akoya® techniques is the single cell resolution and the customisability. However, this requires a significantly longer optimisation time, with access to ample optimisation tissue required, as well as access to specialised equipment.

Spatial Protein technologies, though incredibly insightful, fundamentally remain characteristic in nature with limited direct investigation of underlying biological

mechanisms. Biological pathways can start being unpicked by combining Spatial Transcriptomics to specific cohorts. There has been a sharp rise in the number of Spatial Biology papers published between 2020 and 2024, with over 100 papers investigating human oncology Spatial Transcriptomics [121]. These will be explored throughout this thesis.

## 1.9 Pancreatic Cancer Treatment strategies

### 1.9.1 Adjuvant Chemotherapy: Single and Combination therapies

PDAC therapy has had few clinically relevant improvements in the past 50 years. This can be explained by two major factors, 1) heterogeneity 2) low mutation percentages [106].

#### 1.9.1.1 Gemcitabine based treatments

Gemcitabine is classed as an anti-neoplastic/anti-metabolite and works by inhibiting the tumour progression by substituting the endogenous pyrimidines cytosine or thymidine [122]. For over 20 years, single agent Gemcitabine was used as first line therapy in metastatic disease, with no other treatment options offering any improvement. However, the survival times remain moderate at best, with the median survival ranging from 5-8 months [123]. In an effort to improve the poor survival rates seen in pancreatic cancer, multiple studies have been carried out testing different Gemcitabine combination therapies, including drugs such as nab-Paclitaxel (Abraxane) and Fluorouracil derivative Capecitabine [124-128]. Abraxane is classed as a cytotoxic drug, made up of albumin bound Paclitaxel. It works by targeting and stabilizing microtubules, thereby inhibiting dynamic reorganization and the mitotic process [129]. Capecitabine is a pro-drug that interferes with DNA, RNA and protein synthesis, thereby inhibiting tumour growth [130]. Initial evidence for this combination approach was provided by the ESPAC-1 trial. The disease specific survival (DSS) benefit of adjuvant chemotherapy vs. chemoradiotherapy in resectable patients demonstrated that chemotherapy had a better 2 year survival (19.7 months - 95% CI 16.4-22.7) when compared to chemoradiotherapy (15.5 months – 95% CI 13.5-17.4) and no adjuvant treatment (14.0 months and 16.1 months respectively) [131]. These results led to a shift from routine single agent to multi-agent Gemcitabine therapy. Two major combinations were established, GemCap and GemAbraxane.

A phase 3 study was undertaken testing efficacy and possible toxicity of Gemcitabine plus Abraxane compared to single agent Gemcitabine in metastatic patients. 861 patients were treated with either mono or combination therapy and survival analysis was carried out. Significant differences were observed in DSS when comparing monotherapy vs

combination (6.7months and 8.5 months respectively (95% CI 0.62-0.83)). Combination therapy resulted in an increased occurrence of side effects such as peripheral neuropathy and myelosuppression [132]. The randomised, multi-centre ESPAC-4 trial looked at the survival differences and toxicity levels of 366 patients treated with either monotherapy Gemcitabine or GemCap. Increased overall survival was observed in GemCap patients (28months (95% CI 23.5-31.5)) compared to Gemcitabine (25.5months (95% CI 22.7-27.9)). As above, patients treated with combination had significantly increased reports of adverse toxicity events [126]. Both these trials confirm that patients experience the best outcomes following resection plus combination adjuvant cytotoxic chemotherapy, at the risk of increased side effects.

#### 1.9.1.2 FOLFIRINOX based treatment

In 2010, FOLFIRINOX (made up of folinic acid (leucovorin), fluorouracil (5FU), irinotecan and oxaliplatin) demonstrated a paradigm shift by doubling survival to almost 12 months in high performance patients and has shown significant benefit in localised and metastatic disease [3]. Subsequently, the PRODGE-24 trial demonstrated that resected patients treated with adjuvant treatment, modified FOLFIRINOX (mFOLFIRINOX), had better DSS compared to Gemcitabine alone. However, different criteria were used for patient stratification and salvage therapy thresholds. This could explain the contradictions seen. Patients treated with mFOLFIRINOX had increased toxicity, indicating that only a subset of ‘fit’ patients should be treated with these drugs [133].

### 1.9.2 Targeted Treatments: Platinum based therapies

Loss of function BRCA1/2 breast and ovarian cancer patients respond well to poly ADP ribose polymer (PARP) inhibitors [133]. This LOF results in inhibition of the homologous recombination pathway, making cells reliant on the DNA damage repair (DDR) pathway. PARP inhibitors are thought to function by inhibiting PARP dissociation from DNA, preventing DNA replication fork formation [103]. Platinum-based therapies (PBTs) cause double stranded breaks in DNA, cells lacking BRCA1/2 are unable to undergo homologous repair, resulting in apoptosis [134]. PBTs are routinely used in patients with ovarian cancer, and are associated with a higher DSS particularly in patients with BRCA mutations [135]. While germline and somatic mutations in BRCA1/2 and PALB2 are found rarely in PDAC, genomic analysis has extended this DDR cohort to almost 20% , indicating PARP inhibitors may offer viable options to this subset of patients [3, 15, 133].

If BRCA1/2 mutations in PDAC confer the same vulnerabilities seen in other cancers, PARP inhibitors and PBTs could be an effective, targeted treatment. The POLO trial

examined metastatic BRCA-positive PDAC and treatment with PARP-inhibitors. This was beneficial as second line therapy after progression on platinum chemotherapy. The median RFS was significantly longer in the Olaparib group [90]. At present, only BRCA1/2 can be used as biomarkers to identify patients that would benefit from PBTs. However, the unstable genomic subtype may unveil additional biomarkers [15]. It is anticipated that molecular analysis of either primary or metastatic tumour biopsies including genomic and transcriptomic assays currently being employed in clinical trials (e.g. PRIMUS-001) will result in future clinically relevant biomarkers.

### 1.9.3 Neoadjuvant Chemotherapy

It was hypothesized a subset of patients with more advanced non-metastatic pancreatic cancer (borderline resectable/locally advanced (LAPC)) would have the potential to undergo successful surgery if treated neoadjuvantly with the treatments explored above. A meta-analysis focusing on the effect of preoperative therapy in PDAC showed a third of initially classified “non-resectable” LAPC became eligible for resection when treated neoadjuvantly. Additionally, patients treated with combination neoadjuvant therapy demonstrated a significantly higher estimated response and resection probability [4]. This has translated in the routine treatment with neoadjuvant therapy for a subset of patients in an effort to increase the number of potentially curative surgeries. Although multiple papers reported an increase in both DSS and Recurrence Free Survival (RFS) in patients treated with neoadjuvant FOLFIRINOX, there are major issues with toxicity e.g. neutropenia and thrombocytopenia, resulting in strict filtering of patients eligible for this treatment option [5]. Large scale trials are needed to clarify the risk- benefit ratio of neoadjuvant treatment and the optimal treatment modalities employed.

### 1.9.4 Radiotherapy in Pancreatic cancer

The role of neoadjuvant radiotherapy in PDAC patients remains controversial. This is partly due to lack of studies fully classifying the effects of tumour regression, survival and toxicity. As with neoadjuvant chemotherapy, neoadjuvant radiotherapy is mainly used in borderline resectable and LAPC patients in an effort to pull these groups into the resectable category [136]. A SEER database analysis investigated the effect of upfront resection, neoadjuvant and adjuvant radiotherapy and resection with adjuvant chemotherapy. Patients were split into different pathological factors. Neoadjuvant radiotherapy seemed to result in the best survival for only one patient subset. T stage 4, margin 0 patients were significantly associated with better survival (median survival: 17months 95% CI 0.215-0.532) compared to resection plus chemotherapy (median survival: 10months 95% CI 0.411-0.683) [137]. Another study examined the survival

differences between neoadjuvant chemotherapy and radiotherapy. Overall survival analysis did not show any significant improvement for radiotherapy patients, and the 90 day mortality rate indicated that radio patients had a higher mortality probability rate (odds ratio 1.81, p <0.001) [138]. These studies provide insight into the complex decisions doctors must make to decide the treatment options for patients. Arguably, the bleak survival rates of PDAC make even the slightest increase in prognosis beneficial, providing adverse effects are acceptable.

### 1.9.5 Immunotherapy potential for PDAC

The interaction between molecular subtype, tumour microenvironment and treatment and disease prognosis is a pioneering research topic that, if exploited, could answer vital questions about cancer progression. Despite years of research in PDAC, targeted treatment and immunotherapy studies are lagging behind when compared to other major cancer types. However, certain aspects have been studied and important lessons can be learnt from similar cancers. Achieving significant progress in PDAC will likely require multimodal strategies targeting epithelial, stromal, and immune tumour components and using strategies to identify subgroups of patients at a genomic, immunological and transcriptomic level [139]. Biomarker development is needed to stratify patients for effective immunotherapy combinations at appropriate time points. PD-L1 expression is used in NSCLC to select patients who benefit from frontline PD-1 inhibitor immunotherapy ahead of chemotherapy [140]. However, the situation is more challenging in pancreatic cancer. PDAC transcriptomic molecular subtypes, may have the potential to identify which subtypes respond to specific treatments including immunotherapies [102]. The immunogenic subtype is of particular relevance, demonstrating upregulated immune avoidance mechanisms including CTLA-4 and PD-1. A further study has shown that >50% of pancreatic tumours with upregulated PD-L1 were the squamous subtype, indicating potential sensitivity to anti-PD-L1 inhibitors [141]. Classification of patients according to molecular subtype may identify those patients who would benefit from immunotherapy. Notably, recent studies have investigated the efficiency of targeting the immune checkpoint molecule B7-H3 in similar solid cancers, although it has yet to be tested on PDAC [142-146].

While most immune therapies are being developed for post chemotherapy, there is little understanding of the molecular pathology of “post-chemotherapy” tumours in PDAC. The complex anti-tumour immune response, coupled with the failure of Immune Checkpoint Blockade (ICB) has prompted the concept of combination chemotherapy strategies. Gemcitabine-based chemotherapy is often used in these combination immunotherapy trials, as there is evidence of an increased tumour antigen availability, coinciding with

transiently depleted immunosuppressive T regulatory cells (Tregs) in the TME [147]. The beneficial effect of neoadjuvant therapy, therefore, may not rely on direct cytotoxicity on epithelial cells, but rather on the restoration of the immune cell–mediated antitumour response.

Radiotherapy has a role in the neoadjuvant setting and in the management of LAPC, therefore in combination with ICB it may be a promising strategy for PDAC. Radiotherapy induces an immune response that mediates regression of metastatic lesions lying outside the radiation fields. Radiotherapy could therefore activate the immune system, increase T cell tumour trafficking, and elicit an antitumour response following ICB. Initial evidence for synergism has been demonstrated in PDAC possibly related to increased immunogenicity [148]. By increasing tumour visibility, radiotherapy may synergise with immune therapy. Characterisation of the immune landscape in the context of different neoadjuvant therapies needs to be explored to provide extra insight this combination therapy.

# 1.10 The Pancreatic cancer tumour microenvironment

## 1.10.1 Tumour core and the Tumour microenvironment compartments

The tumour immune microenvironment (TME) of PDAC is a complex and often contradictory subject to study. The tumour microenvironment, as the name suggests, is the immediate environment in which the tumour cells find themselves. It is a diverse and dynamic landscape made up of three major components (figure 1.7) [149];

1. Tumour compartment
2. Stromal compartment
3. Immune compartment

It is worth noting that although stroma and TME are often used interchangeably, they are distinct concepts and should be studied as such. TME encompasses both stromal and immune compartments. Additionally, the tumour compartment or tumour core is not strictly part of the TME, but as the TME tends to surround tumour cells, it has been included here.

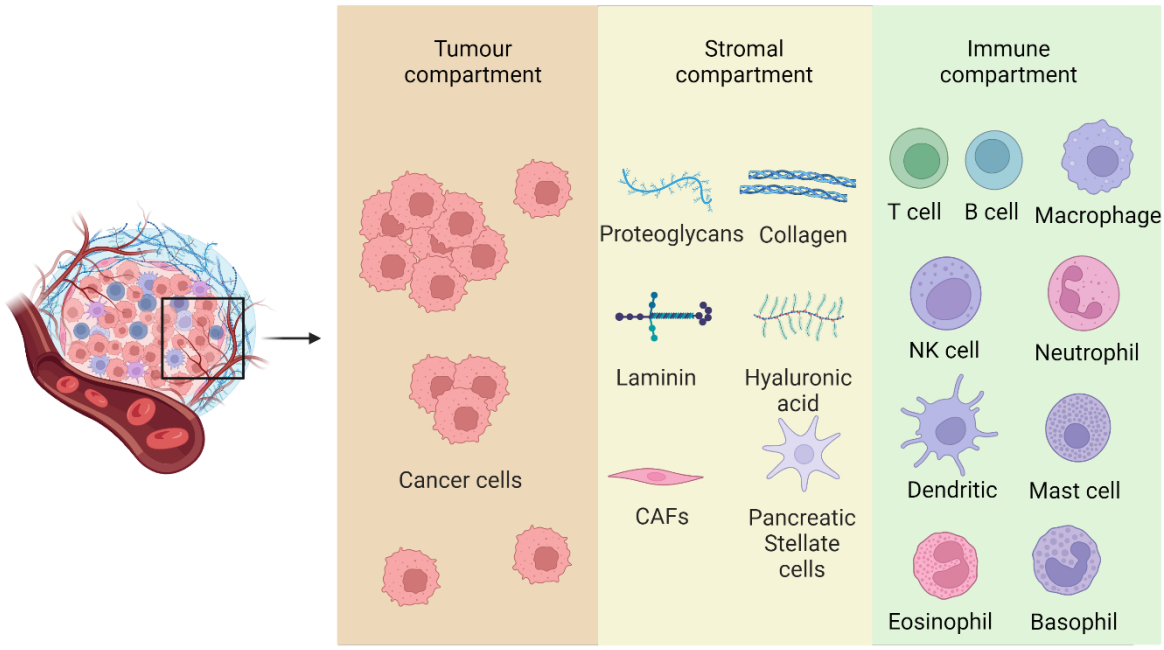


**Figure 1.7 Tumour and tumour microenvironment compartments in pancreatic cancer.** *Three compartments example cell types and molecules frequently seen. Tumour compartment is made up of epithelial cancer cells. Stromal compartment is made up of cancer associated fibroblasts, pancreatic stellate cells and a range of extracellular matrix molecules including collagens, proteoglycans. Immune compartment encompasses all immune cells including T and B cells, macrophages, natural killer (NK) cells among others. Figure adapted from BioRender template.*

#### 1.10.1.1 The Tumour compartment

The tumour compartment is made up of epithelial tumour cells (figure 1.7). Unusually, in pancreatic cancer the tumour compartment makes up a small proportion of the tumour, with reports of tumour cells making up approximately 20-25% of the tumour mass. Tumour cells exhibit a vastly heterogenous histological expression pattern, with a scattered cellular pattern [150].

#### 1.10.1.2 The Stromal compartment

The stromal compartment makes up the vast majority of the tumour mass, consisting of fibroblast and pancreatic stellate cells rich regions and extracellular matrix (ECM) (figure 1.7) [151, 152]. The ECM is a vital component that provides structural and regulatory support within the tissue. Comprised of a range of collagens, laminins and proteoglycans (among others), it has been reported to have a mutualistic relationship with the cells that reside within it (figure 1.7) [153]. In particular, fibroblasts are thought to vastly influence how the ECM is arranged, resulting in a highly dynamic, heterogenous compartment [154]. The majority of proteins found in the extracellular matrix are produced by cancer associated fibroblasts (CAFs). This combination results in a densely packed, stiff, 3D mesh which is thought to act as a barrier to chemotherapy. This desmoplastic stroma is linked to several cancer hallmarks including the creation of a hypoxic environment, limiting nutrient delivery and reducing immune cell infiltration, creating highly resilient PDAC cells [94]. Increased Epithelial-to-Mesenchymal transition is a major pathway associated with multiple pancreatic cancer processes such as tumorigenesis and drug resistance [155]. As described above, cancer cells that undergo EMT possess increased ‘stem-like’ properties manifesting an invasive and metastatic abilities [92, 156]. The stromal compartment is packed with cells and secretions that help drive the transition to a mesenchymal PDAC cell. Various cytokines, TGF-β, IL-6 and IL-1α/β, are all involved in cellular pathways that promote EMT and are upregulated in PDAC [151, 157-159]. It is worth noting that TGF-β is dependent of context, and whether it is SMAD-dependent or not. Altogether, the stroma exhibits multiple pathways that severely inhibit the benefits of treatment.

#### 1.10.1.3 The Immune compartment

Although the immune compartment could technically be placed within stroma, it plays a distinct role, therefore the stromal and immune compartments will be considered separately. The immune compartment refers to a collection of traditional immune cells (figure 1.7) [160, 161]. This compartment displays perhaps the most contradictory processes in pancreatic cancer, due to recruitment of different type of immune cells. It

plays an important role in immunosurveillance and the anti-cancer immune response. Counterintuitively, it also plays a role in immunosuppression and cancer progression. This is highly dependent on the types of immune cells present, and these fall into pro-tumour and anti-tumour cell types [6]. Traditionally, T helper and cytotoxic T cells are associated with immunosurveillance and increased tumour cell death [7, 8], whereas, macrophages and Tregs tend to inhibit the immune response [9]. Interestingly, B cells fall into both the pro and anti-tumour categories due to contradictory reports [11-13]. A full exploration of the immune cells associated with PDAC is contained in section 1.11

#### 1.10.1.4 Interaction and influence between compartments

The tumour microenvironment and stromal composition of cancer is a widely researched topic that can be explored in a multitude of ways. For the majority of cancer phenomena explored, characterising interactions between tumour cells and the surrounding environment will deepen biological underpinnings, as cancer cells are seldom self-contained. In addition to these cellular interactions, there is the added complexity of the extracellular matrix. This means that not only do we have to take into account the heterogeneity of the individual compartments themselves, but the interaction between the cells and these regions must also be considered [94]. A variety of studies in different cancers have explored these complex interactions. For example, ECM proteins MMP-9 and Tenascin-C bind to their respective cell-surface receptors on tumour cells, resulting in increased invasive properties and metastatic behaviour, as well as reduced survival times [162]. CAFs secreting TGF-β, recruit a range of pro-tumorigenic immune cells such as macrophages and neutrophils, in parallel, blocking cytotoxic T cell recruitment [163-166]. Poor oxygenation and high levels of acidity, due to a build-up of lactic acid from glycolysis, results in limited recruitment and proliferation of T cells [167-169]. This creates a hostile environment, in which cancer cells thrive, filtering which immune cells can infiltrate the microenvironment. Studies into PDAC specific interactions are required to determine if these findings can be replicated.

## 1.11 Pancreatic immune and stromal cell landscape

The protein immune and stromal landscape has been relatively well established in pancreatic cancer, with studies predominantly focused on naïve patients. It is characterized by a dense desmoplastic stroma, large infiltration of cancer associated fibroblasts and immunosuppressive leukocytes, and a low level of effector T cells [6].The tumour microenvironment plays an important role in the progression and aggressiveness of tumours, with much research carried out to define it. The TME in PDAC is characterized by many immune and stromal cells. There are two broad categories of cells (figure 1.8);

1. Effector cells
2. Suppressor cells.

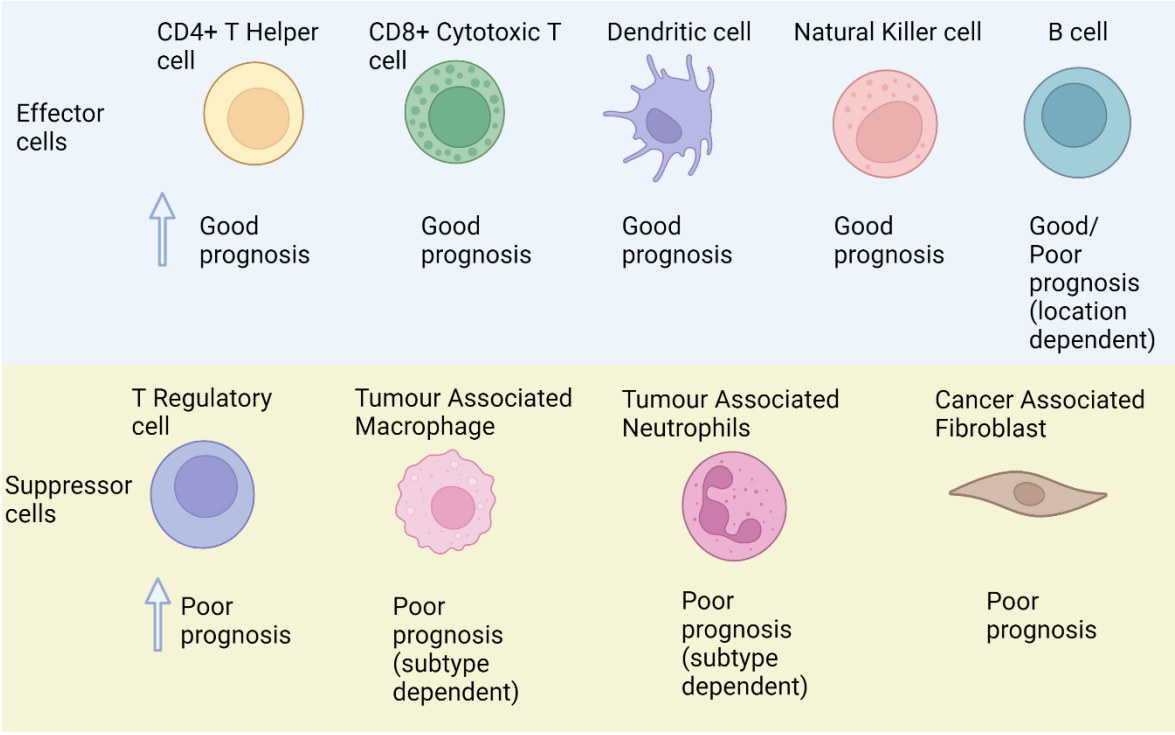


**Figure 1.8 Main cell types in PDAC**. *Illustrative diagram showing the most common tumour effector and suppressor cells in pancreatic cancer and their prognostic association. Tumour effector cells encompass CD4+, CD8+ T cells, dendritic, natural killer and B cells. Tumour suppressor cells encompass T regulatory cells, tumour associated macrophages, tumour associated neutrophils and cancer associated fibroblasts. Figure adapted from BioRender template.*

### 1.11.1 Naïve protein landscape

Tumour infiltrating lymphocytes (TILs) including CD8+ cytotoxic and CD4+ helper T cells, B cells and dendritic cells are the main effector cells found in naïve pancreatic cancer (figure 1.8) [170-174]. Additionally, tumour associated macrophages (TAMs), Tregs and CAFs, are the most common suppressor cells (figure 1.8) [6, 164, 175-177]. It is important to note that these immune cells have been split into these categories based on the current literature, however with cells such as macrophages and neutrophils, their effect is greatly dependent on polarization and activation. Macrophages have reportedly been split into M1 and M2, whereby M1 macrophages are associated with proinflammatory cytokines, and M2 are associated with increased immune suppressive cytokines [178]. This nomenclature has been criticized for being overly simplistic. Whilst these terms may be used for ease, the marker expression should be employed e.g. CD68+ or CD163+ macrophages. Neutrophils have also been split according to their activation into anti-tumorigenic TAN1 or pro-tumorigenic TAN2 cells [179].

#### 1.11.1.1 The role of T lymphocytes in naïve PDAC

The presence of CD8+ and CD4+ cells is arguably the most reported immune signature in PDAC. Classified as tumour effectors, an increased density of these cells is associated with better prognosis in treatment naïve cancer [8, 180-183]. A shift in the microenvironment was reported when the disease progressed from IPMN to a primary pancreatic lesion [184]. In low grade IPMNs, the immune phenotype observed was varied, with an abundance of tumour infiltrating immune cells such as CD8+, CD4+ helper T cells and high levels of Th1/Th2 cells. Once the transition to PDAC occurs, an immune switch is observed. A suppressive phenotype dominated by T-regulatory cells and decreased intratumoral infiltration of effector cells is observed. As the malignancy progresses, immunosuppressive lymphoid structures appear in the surrounding stroma. These results suggest that an oncogenic switch is achieved once immune surveillance is bypassed [184].

A study investigating preoperative immune cell ratios in peripheral blood found prognostic immune cell ratios [185]. Neutrophil: Lymphocyte and Lymphocyte:Monocyte ratios were found to have a significant effect on patients' survival. A Neutrophil: Lymphocyte (N:L) ratio of <5 and a Lymphocyte:Monocyte (L:M) of ≥ to 3 were associated with a significant increase in median survival. High N:L and a low L:M ratio were shown to be independent poor prognostic markers. Results also indicated increased N:L and decreased L:M ratios correlate with a 2-fold decreased count of T, B and natural killer cells [185].
In contrast, suppressor immune cells are often tumour beneficial and therefore are

associated with poor prognosis [6]. Much research has gone into understanding the role of TAMs and Treg cells in PDAC. CD68+ macrophages (M2) and a low Treg:CD4+ ratio is significantly associated with poor prognosis, whereas a high percentage of M1 and CD68+ cells was associated with better prognosis [9]. Immune profiling can be used as a prognostic tool, giving additional information on tumour characteristics that cannot be ascertained using standard prognostic tools.

#### 1.11.1.2 The role of CAFs in naïve PDAC

Cancer associated fibroblasts have been continuously linked with EMT, immune evasion and production of an inhospitable stroma [186-188]. Studies have shown there are at least three subtypes of CAFs, myofibroblastic, inflammatory and antigen presenting, each with distinct markers associated with them [189]. However, each subtype has markers associated with alpha smooth muscle actin (αSMA) expression and is commonly used to identify myofibroblasts. [190]. High levels of CAFs in pancreatic cancer is consistently associated with worse overall prognosis [191, 192]. Stromal composition has been classified by using the ratio of stained αSMA and all collagen areas. This is referred to as the activated stromal index (ASI). Patients with low collagen deposition and low ASI, had a worse prognosis. This was classified as a fibrolytic stroma. High collagen and low ASI was associated with better prognosis, and this was classified as fibrogenic stroma [193]. The general consensus is that dense stroma promotes tumorigenesis, but research has shown that the opposite is true in PDAC. Reduction of stromal cells by Sonic hedgehog (Shh) deletion in mouse models, resulted in increased proliferation, as well as a poorly differentiated tumour. This increase in aggressiveness indicates that Shh activated stroma has a tumour suppressor role in PDAC [194]. Using tumour microarrays from 93 resected patients, prognostic signatures were categorized based on leukocyte subtypes and stromal compositions. Patients with a fibrolytic stroma and a CD3lowCD8lowCD68high immune signature were associated with worse RFS. Longer RFS was associated with fibrogenic stroma and a CD3highCD206high signature [195]. The use of combination signatures reduces the risk of false-positives associated with single signatures, mimicking the heterogeneity of PDAC. Immune profiling could potentially inform specific treatment stratification.

A study using ESPAC-3/1 samples investigated the effect of stromal composition and immune cell infiltration in resected pancreatic cancer [196]. Adjuvant chemotherapy patients were split according to their treatment, gemcitabine or 5-flourouracil/folinic acid. No differences were seen between the two treatments in terms of survival and immune cell signatures investigated. However, in both cohorts, high expression levels of CD3+ T cells had the most significant independent predictive power for RFS. Two histological

predictive signatures were established in this study, 1). Increased CD3 and CD206 expression - associated with increased median RFS (16.6 months), 2). Decreased CD3/CD8 and increased CD68 expression – associated with decreased median RFS (7.9 months). Stromal composition was characterised using Erkan's ASI ratio [193]. Although this study found a correlation between RFS and the different stromal types, no relationship was found between stromal composition, immune marker expression and RFS [196].

#### 1.11.1.3 The role of B lymphocyte in naïve PDAC

The role of B cells in PDAC remains highly controversial with reports associating them with anti-tumour and pro-tumour responses [197-203]. Multiple studies have demonstrated B cells with increased cytokine IL-35 expression, traditionally responsible for immune system maintenance, promote neoplastic development, and support cancer proliferation [198, 202, 203]. Tertiary Lymphoid Structures (TLS) are a common phenomenon seen in a multitude of cancers [204]. They can be defined as lymphoid structures that usually develop in chronically inflamed, non-lymphoid tissues such as cancer. Visually, they appear circular, and are characterised by the presence of dispersed High Endothelial Venules (HEVs), an inner B-cell follicle and an outer T-cell zone [205, 206]. The location of these structures is indicative of levels of immune cell infiltration in pancreatic cancer [11, 207]. Intratumoral TLSs were associated with increased levels of T and B cells, as well as decreased immunosuppressive cells, and was significantly associated with better survival compared to patients without (Presence Vs Absence - median survival: 42.67 vs 15.53, p =0.002, 95% CI 1.8 (1.2-2.6) [171].

#### 1.11.1.4 Spatial Biology in naïve PDAC

Until recently, the number of immune cells investigated at one time was limited due to technology. Immunohistochemistry was one of the most popular and robust methods to characterise protein expression in human samples. The development of multiplex technologies has enabled co-localisation of multiple immune cells on one tissue section [118, 119]. Carstens et al investigated the role of desmoplastic stroma on immune cell infiltration and found that PDAC had a heterogenous mix of T cell populations. Cytotoxic T cells with a close proximity to cancer cells exhibited increased anti-tumour effects and correlated positively with increased survival. Surprisingly, there was no significant correlation with immune cell infiltration and the Collagen-I/αSMA presence [7]. Both the Mahajan et al and Carstens et al papers contradict the widely accepted hypothesis that the dense fibrotic PDAC stroma creates a physical barrier 'protecting' the tumour core from the immune system and even chemotherapy [7, 196, 208]. These contradictory results are suggestive of the interactions between stroma, immune cells and tumour cells

being much more complex than expected.

#### 1.11.1.5 Molecular biology immune pathways in naïve PDAC

Certain well established cellular pathways have been associated with immune cell density, particularly linked with cytotoxic T cells. Chronic inflammation is a well reported driver for pancreatic cancer progression, with the JAK/STAT and NF-κB pathways being associated with this. Continual activation of the JAK/STAT pathway has been associated with inhibition of cytotoxic T cell activation, and indirectly inducing inflammatory CAFs [81, 209]. Moreover, NF-κB increases CXCL12 expression in pancreatic stellate cells, leading to reduced cytotoxic T cell infiltration [210]. This transcription factor is also linked with suppression of macrophage surveillance in early tumorigenesis via regulation of growth differentiation factor 15 (GDF-15) in macrophages [211].

Immune evasion mechanisms are a repeating hallmark seen across the PDAC literature, although there has been little successful exploration of the biological mechanisms. In 2020, a paper investigating immune evasion in PDAC demonstrated downregulation of MHC-I may have an important role in immune evasion. Cell surface MHC-I expression seems to be targeted for lysosomal degradation via NBR1, an autophagy cargo receptor, resulting in lack of antigen presentation and subsequent immune evasion. Inhibition of autophagy was carried out in vivo, demonstrating a significant decrease in tumour mass and an immunogenic switch seen by the increased expression of CD8+ T cells. Importantly, they found that autophagy inhibition sensitized the tumour to dual immune checkpoint blockade therapy, offering a precise, actionable therapeutic target [212].

## 1.11.2 Neoadjuvant treated protein cell landscape

Highly immunogenic cancers are traditionally associated with better prognosis and indicate sensitivity to immunotherapy. PDAC is considered a non-immunogenic disease, although classical and immunogenic subtypes have considerably higher epithelial and stromal immune infiltration. It is hypothesised that Neoadjuvant Therapy (NAT) works by remodelling the tumour immune microenvironment via depletion of pro-tumorigenic immune cells [132, 147, 213, 214]. If tumours were able to undergo an immunogenic switch, a subsequent increase in tumour suppression would result in apoptosis of cancer cells, subsequently increasing neoantigen targets enabling potential vulnerability to immunotherapies.

### 1.11.2.1 The role of T lymphocytes in neoadjuvant PDAC

Research on the this 'immunogenic switch' has predominantly focused on characterisation rather than exploring biological pathways and most reports are Gemcitabine focused. A study looking at borderline resectable PDAC patients investigated the difference between naïve and Gemcitabine/radiation treated patients [147]. An increased CD4CD8+ signature correlated with neoadjuvant chemotherapy treated patients and a corresponding increase in overall survival was seen compared to treatment naïve patients [147]. This increase in cytotoxic T cell expression correlating with increased overall survival is a frequent phenotype observed across multiple cancer types. The observed elevated level of expression in treated compared to naïve indicates that treatment with Gemcitabine/radiation may play a role in triggering an immune response.

### 1.11.2.2 Effect of neoadjuvant Gemcitabine based therapies on the TME

The effect of treatment on the tumour microenvironment has also been demonstrated *in vivo*. One study investigated two different KrasG12D/+; Trp53R172H/+; P48-Cre (KPC) treatment cohorts: 1). combination Gemcitabine and a Particle-mediated epidermal delivery (PMED) NY-ESO-1 targeting vaccine, 2). PMED vaccine alone [132]. Prior treatment with Gemcitabine appeared to increase vaccine induced cytotoxic T cell response compared to vaccine only treated mice. Gemcitabine treated mice also had significantly reduced FOXP3CD4+ T cells, potentially due to the increased rate of proliferation seen in Tregs cells compared to other T cells. These murine models further reinforce the hypothesis that pre-treatment, especially by Gemcitabine, triggers an immune response and produces a cumulative affect when used in combination with vaccinations [132]. This double hit effect may partially explain the increased survival seen with combination treatments, such as Nab-paclitaxel/Gem [215].

Chemotherapeutic resistance is a prevalent issue seen in pancreatic cancer, contributing to the limited effect observed in the majority of treatments. There are many possible contributing factors that lead to chemoresistance, including the tumour microenvironment. The effect of prolonged Gemcitabine treatment was investigated in invasive tumour KPC models and replicated *in vitro* using a Panc1 cell line [213]. It was found that prolonged Gemcitabine exposure resulted in increased antigen presentation, immune checkpoint inhibitors PD-L1/2, CCL/CXCL chemokine expression and TGF-β associated signals [213]. TGF-β is a well-known immune regulator and has been reported to play an important role in immune evasion in advanced pancreatic cancer. Increased expression of this cytokine in the stroma may limit the full immunomodulatory effect of Gemcitabine, preventing tumour-infiltrating lymphocytes from efficiently targeting the tumour core. In vivo treatment of combined Gemcitabine/anti-PDL1 produced a limited immune response and a moderate delay in mortality [213]. In contrast, models pre-treated with the TGF-β inhibitor Galunisertib, and subsequent Gem/anti-PD-L1 treatment showed a uniform increased expression of CD3+ and CD8+ T cells. Apoptotic markers Granzyme B and caspase 3 were also present in neoplastic regions indicating the continued cytotoxic effect stimulated by this treatment combination [213]. Other beneficial phenomena such as improved vasculature and significant delay in mortality was observed. These observations indicate an immunogenic switch that is mediated by prolonged Gemcitabine treatment, from a cold phenotype in the control models, to a hot immune phenotype in the treated models [213]. Further research into the effect of Gemcitabine on the TIME is required to fully investigate this phenomenon in humans.

The effect of Gemcitabine on the tumour associated IgG antigen repertoire was investigated in pancreatic cancer models [214]. Treatment resulted in elevated recognition of antigens by IgG and a shift in expression from suppressor to effector tumour associated antigens e.g. α-Enolase (ENO1). The immune landscape prior and post treatment was compared, demonstrating a significant increase in tumour infiltrating CD8+ and CD4+ T cells in post-treatment analysis. An increased T cell response correlated with increased overall survival. In an effort to increase the therapeutic response, Gemcitabine and ENO1 combination treatment was used. Results showed a significant increase in CD4+ cells, corresponding with anti-tumour activity and subsequent impaired tumour progression was elevated in the combination therapy treated mice models. Singular treatment with either Gemcitabine or the vaccine failed to give the same levels of immune response [214]. The development of multiple synergistic combination targeted therapies is essential to treat this highly heterogenous, ever evolving disease. It is worth noting that although KPC models are the gold standard PDAC models, there are major differences in morphology and biology compared to human PDAC. It would be beneficial to produce a more robust model to improve translation from murine to human.

Importantly, the immune cell functional state of the reported cells has not been explored. This is a significant gap in knowledge when exploring the effects chemotherapy and radiotherapy have on the neoadjuvant landscape. Studies in other cancers such as breast and oesophagus have shown that immune cell density is not always increased. Rather there is a shift in functional state as indicated by marker expression, as well as the ratio of cell types [216, 217]. These studies also demonstrated initial depletion of T, B and NK cells lasting for up to 9 months [216]. This suggests that when samples are taken from the patient may be important. To fully understand the effects of neoadjuvant therapy on the TME, a combination of high-plex protein and transcriptome technologies should be used to characterize the differences observed.

## 1.12 Project Aims and objectives

It is hypothesised that neoadjuvant therapy works by remodelling the tumour immune microenvironment either via depletion of pro-tumorigenic immune cells or altering the functional states in subsets of immune cells [6, 14, 15]. Tumours that undergo this immunogenic switch, show an increase in tumour suppressor cells and subsequent apoptosis of cancer cells. Until now, technology was unable to adequately explore these phenomena. With the rise of Spatial Biology, the spatial interactions that define cancer can be investigated. This thesis aims to robustly characterise the tumour immune microenvironment in both treatment naïve upfront resected and post neoadjuvant settings in human pancreatic ductal adenocarcinoma. To fully explore the differences between naïve and neoadjuvant patients, the main objectives were as follows;

1). Establish the protein immune cell landscape in treatment naïve and neoadjuvant human pancreatic cancer separately in terms of content, cellular density and spatial orientation of different phenotypes.

2). Comparison of content, density and spatial relationships in naïve and neoadjuvant patients using the established protein landscape.

3). Explore the Spatial Transcriptomic signature in distinct tissue compartments (epithelial tumour, αSMA positive fibroblast, and immune compartments) in treatment naïve and neoadjuvant treated patients.

4). Multi-omic, orthogonal data comparison of treatment naïve and neoadjuvant cases using Spatial Omic data and deep immune phenotyping technologies.

Consideration will be given to important clinical subgroups within these aims.

# 2 Chapter 2: Materials and Methods

## 2.1 FFPE tissue studies

To characterize the tumour microenvironment across the naïve and neoadjuvant pancreatic cancer, archival formalin fixed paraffin embedded (FFPE) tissue microarrays were used, each associated with clinical pathology data. Serial sections were used and a variety of techniques including immunohistochemistry (IHC), multiplex immunofluorescence (mIF), Spatial Transcriptomics (ST) and single cell Spatial Protein assays were undertaken. All sections were cut by the Glasgow Tissue Research Facility (GTRF) at 5μm, baked overnight at 60◦C, and stored at 4◦C for up to a week.

### 2.1.1 Clinical cohorts

#### 2.1.1.1 Discovery cohort

The discovery cohort was made up of 9 treatment naïve TMAs, 8 of which come from the Australian Pancreatic cancer Genome Initiative (APGI) cohort, part of the International Cancer Genome Consortium (ICGC), and 1 Glasgow naïve cohort (SD-PAN-TMA). The APGI group consisted of 216 patients that had undergone resection between 2010 to 2017, and the Glasgow naïve cohort consisted of 28 patients that were resected between 2006 to 2011. The APGI/ICGC cohort had approximately 3x1mm cores per patient, and the Glasgow naïve cohort had approximately 4x0.6mm cores per patient. Cores were selected from epithelial rich regions by a pathologist. To establish patient characteristics for the cohort, disease specific survival (DSS) and recurrence free survival (RFS) analysis using clinical data was carried out (table 2.1). Median DSS survival for this cohort was 23 months. Approval for use of the Glasgow cohort was obtained through NHS QEUH Biorepository, application number 662, research ethic committee (REC) number 16/WS/0207. Ethical approval for the APGI cohort was obtained from the appropriate Human Research Ethics committee.

| Discovery naïve cohort | | | | | |
|---|---|---|---|---|---|
| **Characteristic** | ***n = 238*** | **Median DSS (months)** | ***P (Log-Rank)*** | ***RFS*** | ***P (Log-Rank)*** |
| **T Stage (AJCC 8th)** | | | | | |
| T1 | 21 | 20 | 0.005 | 17 | 0.01 |
| T2 | 114 | 23 | | 10.73 | |
| T3 | 48 | 15.5 | | 7.93 | |
| T4 | 0 | | | | |
| Unknown | 55 | | | | |
| **Lymph Node** | | | | | |
| LN0 | 48 | 30 | 0.001 | 13.3 | 0.01 |
| LN1 | 149 | 19.3 | | 9.5 | |
| Unknown | 41 | | | | |
| **Resection Margin** | | | | | |
| R0 | 158 | 27 | 0.003 | 12.2 | <0.001 |
| R1 | 80 | 17.4 | | 9.5 | |
| Unknown | 0 | | | | |
| **N Stage (AJCC 8th)** | | | | | |
| N0 | 55 | 42 | <0.001 | 17 | <0.001 |
| N1 | 177 | 20.3 | | 10 | |
| N2 | 0 | | | | |
| Unknown | 1 | | | | |
| **Grade / Tumour Differentiation** | | | | | |
| I / Well | 20 | 40 | <0.001 | 13.33 | <0.001 |
| II / Moderate | 148 | 27 | | 11.6 | |
| III / Poor | 57 | 15.2 | | 8 | |
| IV/Undifferentiated | 6 | 11.7 | | 4.81 | |
| Unknown | 2 | | | | |
| **Vascular Invasion** | | | | | |
| Negative | 84 | 34 | <0.001 | 13.33 | |
| Positive | 142 | 19.3 | | 9.77 | 0.01 |
| Unknown | 7 | | | | |
| **Molecular subtype** | | | | | |
| Classical | 122 | 29 | <0.001 | 12.2 | <0.001 |
| Squamous | 53 | 13.6 | | 7 | |
| Unknown | 63 | | | | |

**Table 2.1 Discovery naive cohort patient characteristics**. *Table showing the Discovery cohort patients with clinical characteristics associated with disease specific survival (DSS) and recurrence*

*free survival (RFS). Clinical features include T Stage (AJCC8th), resection margin status, lymph node status and molecular subtype*

#### 2.1.1.2 Validation naïve cohort

The Validation cohort was made up of 12 multi-regional Glasgow cohort TMAs (NJ-PANC-TMA and PDAC-PAN-TMA). This cohort comprised 192 patients who had undergone resection between 1992 to 2011. The NJ-PANC-TMA and PDAC-PAN-TMA had approximately 5x0.6mm and 4x0.6mm cores per patient respectively, and demonstrated a mixed histology with epithelial and stromal heavy cores. Patient survival characteristics were established for DSS and RFS analysis (table 2.2). Median DSS survival for this cohort was 18.5 months. Approval for use of the Glasgow cohort was obtained through NHS QEUH Biorepository, application number 662, REC number 16/WS/0207.

| Validation naïve cohort | | | | | |
|---|---|---|---|---|---|
| **Characteristic** | ***n = 192*** | **Median DSS (months)** | ***P (Log-Rank)*** | **Median RFS (months)** | ***P (Log-Rank)*** |
| **T Stage (AJCC 8th)** | | | | | |
| T1 | 24 | 29.3 | <0.001 | 17.8 | <0.001 |
| T2 | 117 | 21.5 | | 14.5 | |
| T3 | 48 | 10.5 | | 7 | |
| T4 | 0 | | | | |
| Unknown | 3 | | | | |
| **Lymph Node** | | | | | |
| LN0 | 33 | 26.6 | <0.001 | 17.8 | <0.001 |
| LN1 | 156 | 18.4 | | 12.3 | |
| Unknown | 3 | | | | |
| **Resection Margin** | | | | | |
| R0 | 50 | 26.5 | <0.001 | 21.2 | <0.001 |
| R1 | 139 | 16.3 | | 11.2 | |
| Unknown | 3 | | | | |
| **N Stage (AJCC 8th)** | | | | | |
| N0 | 31 | 22.9 | 0.02 | 17.1 | 0.02 |
| N1 | 150 | 18.4 | | 12.3 | |
| N2 | 1 | 20.9 | | 14.9 | |
| Unknown | 10 | | | | |
| **Grade / Tumour Differentiation** | | | | | |
| I / Well | 10 | 26.7 | 0.006 | 19.97 | 0.003 |
| II / Moderate | 115 | 20.1 | | 14.33 | |
| III / Poor | 59 | 13.4 | | 9.13 | |
| IV/Undifferentiated | 0 | | | | |
| Unknown | 8 | | | | |
| **Vascular Invasion** | | | | | |
| Negative | 86 | 23.6 | <0.001 | 15.1 | <0.001 |
| Positive | 85 | 15.6 | | 11.2 | |
| Unknown | 21 | | | | |
| **Molecular subtype** | | | | | |
| Classical | 19 | 34.3 | 0.4 | 18.73 | 0.3 |
| Squamous | 9 | 9 | | 7.83 | |
| Unknown | 164 | | | | |

**Table 2.2 Validation naive cohort patient characteristics.** *Table showing Validation cohort patients with clinical characteristics associated with disease specific survival (DSS) and recurrence free survival (RFS). Clinical features include T Stage (AJCC8th), resection margin status, lymph node status and molecular subtype.*

#### 2.1.1.3 Glasgow naïve cohort 1

The Glasgow naive cohort was made up of single multi-core TMA (SD-PAN-TMA). This cohort comprised of 28 patients who had undergone resection between 2010 to 2017. This cohort had approximately 4x0.6mm cores per patient and demonstrated an epithelial rich histology. Patient survival characteristics were established for DSS and RFS analysis (table 2.3). Median DSS survival for this cohort was 17.2 months. Approval for use of the Glasgow cohort was obtained through NHS QEUH Biorepository, application number 662, REC number 16/WS/0207.

| Glasgow naïve cohort 1 | | | | | |
|---|---|---|---|---|---|
| **Characteristic** | ***n = 28*** | **Median DSS (months)** | ***P (Log-Rank)*** | ***RFS*** | ***P (Log-Rank)*** |
| **T Stage (AJCC 8th)** | | | | | |
| T1 | 2 | 9.09 | 0.04 | 7.95 | 0.3 |
| T2 | 9 | 22.25 | | 15 | |
| T3 | 3 | 16.7 | | 10 | |
| T4 | NA | | | | |
| Unknown | 14 | | | | |
| **Lymph Node** | | | | | |
| LN0 | 2 | 62.9 | 0.5 | 60.5 | 0.4 |
| LN1 | 11 | 18.55 | | 14.65 | |
| Unknown | 15 | | | | |
| **Resection Margin** | | | | | |
| R0 | 24 | 16.45 | 0.3 | 13.45 | 0.2 |
| R1 | 4 | 73.5 | | 62.9 | |
| Unknown | 0 | | | | |
| **N Stage (AJCC 8th)** | | | | | |
| N0 | 2 | NA | 0.07 | NA | 0.07 |
| N1 | 21 | 17 | | 11.7 | |
| N2 | NA | | | | |
| Unknown | 5 | | | | |
| **Grade / Tumour Differentiation** | | | | | |
| I / Well | 3 | 36 | 0.2 | 18.9 | 0.3 |
| II / Moderate | 20 | 17.1 | | 11.7 | |
| III / Poor | 5 | 9.75 | | 4.6 | |
| IV/Undifferentiated | NA | | | | |
| Unknown | 0 | | | | |
| **Vascular Invasion** | | | | | |
| Negative | 10 | 27.5 | 0.5 | 19.5 | 0.2 |
| Positive | 18 | 16.9 | | 10.7 | |
| Unknown | 0 | | | | |
| **Molecular subtype** | | | | | |
| Classical | 6 | 30.9 | 0.01 | 23 | 0.04 |
| Squamous | 4 | 15 | | 8 | |
| Unknown | 18 | | | | |

**Table 2.3 Glasgow naive cohort 1 patient characteristics.** *Table showing Glasgow naïve cohort 1 patients with clinical characteristics associated with disease specific survival (DSS) and recurrence free survival (RFS). Clinical features include T Stage (AJCC8th), resection margin status, lymph node status and molecular subtype.*

#### 2.1.1.4 Glasgow naïve cohort 2

The Glasgow naive cohort 2 was comprised of a single multi-core TMA (PDAC-PAN-TMA). The cohort was comprised of 79 patients who had undergone resection between 1992 to 2011. This cohort had approximately 4x0.6mm cores per patient and demonstrated a mixed histology with tumour centre and stromal cores. Patient characteristics were determined from DSS and RFS analysis (table 2.4). Median survival for this cohort was 19.2 months. Approval for use of the Glasgow cohort was obtained through NHS QEUH Biorepository, application number 662, REC number 16/WS/0207.

| Glasgow naïve cohort 2 | | | | | |
|---|---|---|---|---|---|
| **Characteristic** | ***n* = 79** | **Median DSS (months)** | ***P* (Log-Rank)** | ***RFS*** | ***P* (Log-Rank)** |
| **T Stage (AJCC 8th)** | | | | | |
| T1 | 8 | 25.4 | | 18.2 | |
| T2 | 42 | 25 | 0.02 | 14.2 | 0.03 |
| T3 | 18 | 10.9 | | 8.9 | |
| T4 | | | | | |
| Unknown | 11 | | | | |
| **Lymph Node** | | | | | |
| LN0 | 10 | 36.5 | 0.04 | 25.9 | 0.03 |
| LN1 | 63 | 20 | | 12.2 | |
| Unknown | 6 | | | | |
| **Resection Margin** | | | | | |
| R0 | 21 | 25.8 | 0.1 | 16.1 | 0.05 |
| R1 | 52 | 17.5 | | 11 | |
| Unknown | 6 | | | | |
| **N Stage (AJCC 8th)** | | | | | |
| N0 | 8 | 23.1 | 0.5 | 14.8 | 0.8 |
| N1 | 60 | 21.2 | | 12.2 | |
| N2 | 0 | | | | |
| Unknown | 11 | | | | |
| **Grade / Tumour Differentiation** | | | | | |
| I / Well | 4 | 24 | | 11.6 | |
| II / Moderate | 41 | 19.1 | | 11 | |
| III / Poor | 28 | 19.1 | 0.9 | 27.4 | 0.1 |
| IV/Undifferentiated | 0 | | | | |
| Unknown | 6 | | | | |
| **Vascular Invasion** | | | | | |
| Negative | 39 | 24.5 | 0.2 | 15.1 | 0.2 |
| Positive | 34 | 16.3 | | 10.2 | |
| Unknown | 6 | | | | |
| **Molecular subtype** | | | | | |
| Classical | 13 | 46 | 0.3 | 20.87 | 0.3 |
| Squamous | 6 | 11.9 | | 6.25 | |
| Unknown | 60 | | | | |

**Table 2.4 Glasgow naive cohort 2 patient characteristics**. *Table showing Glasgow naïve cohort 2 patients with clinical characteristics associated with disease specific survival (DSS) and recurrence free survival (RFS). Clinical features include T Stage (AJCC8th), resection margin status, lymph node status and molecular subtype.*

#### 2.1.1.5 Naïve combined cohort

The combined naive cohort consisted of a total of 436 pancreatic cancer specimens combined from the discovery (1.1.1.1) and validation (1.1.1.2). Patient survival characteristics were established for DSS and RFS analysis (table 2.5). Median DSS survival for this cohort was 20.3 months. Approval for use of the Glasgow cohort was obtained through NHS QEUH Biorepository, application number 662, REC number 16/WS/0207.

| Naïve combined | | | | | |
|---|---|---|---|---|---|
| **Characteristic** | ***n = 436*** | **Median DSS (months)** | ***P (Log-Rank)*** | ***RFS*** | ***P (Log-Rank)*** |
| **T Stage (AJCC 8th)** | | | | | |
| T1 | 42 | 29.6 | <0.001 | 17 | <0.001 |
| T2 | 229 | 22 | | 12.2 | |
| T3 | 96 | 13 | | 7.3 | |
| T4 | | | | | |
| Unknown | 69 | | | | |
| **Lymph Node** | | | | | |
| LN0 | 78 | 25.2 | <0.001 | 13.3 | <0.001 |
| LN1 | 290 | 18.9 | | 11.3 | |
| Unknown | 68 | | | | |
| **Resection Margin** | | | | | |
| R0 | 207 | 26.6 | <0.001 | 14.9 | <0.001 |
| R1 | 210 | 15.8 | | 10.3 | |
| Unknown | 19 | | | | |
| **N Stage (AJCC 8th)** | | | | | |
| N0 | 86 | 36.7 | | 17 | |
| N1 | 329 | 19.6 | <0.001 | 11.3 | <0.001 |
| N2 | 1 | 20.9 | | 14.9 | |
| Unknown | 21 | | | | |
| **Grade / Tumour Differentiation** | | | | | |
| I / Well | 30 | 36.2 | | 1.2 | |
| II / Moderate | 263 | 23.9 | | 12 | |
| III / Poor | 116 | 14 | <0.001 | 8 | <0.001 |
| IV/Undifferentiated | 6 | 11.7 | | 5.45 | |
| Unknown | 21 | | | | |
| **Vascular Invasion** | | | | | |
| Negative | 175 | 26 | <0.001 | 14.5 | <0.001 |
| Positive | 235 | 17 | | 10.2 | |
| Unknown | 26 | | | | |
| **Molecular subtype** | | | | | |
| Classical | 141 | 29 | <0.001 | 12.9 | <0.001 |
| Squamous | 62 | 14.1 | | 7 | |
| Unknown | 233 | | | | |

**Table 2.5 Naïve combined cohort patient characteristics**. *Table showing naïve combined cohort patients with clinical characteristics associated with disease specific survival (DSS) and recurrence free survival (RFS). Clinical features include T Stage (AJCC8th), resection margin status, lymph node status and molecular subtype.*

#### 2.1.1.6 Neoadjuvant Glasgow cohort

The neoadjuvant Glasgow cohort is composed of 6 multi-core TMAs (Neoadj-MAL-TMA batch 1 and batch 2), with 72 patients who had undergone treatment and resection between 2009 to 2020. This cohort had approximately 3x0.6mm cores per patient. Cores were selected from tumour centre. Patient survival characteristics were established from DSS and RFS analysis (table 2.6). Median DSS survival for this cohort was 24.5 months. This cohort includes neoadjuvant chemotherapy treated (n=46) and neoadjuvant chemoradiotherapy (n=24) patients. Patients received either Gemcitabine based chemotherapy (n=20) or FOLFIRINOX based chemotherapy (n=53). Approval for use of this cohort was obtained through NHS QEUH Biorepository, application number 706, REC number 18/SS/0076.

| Neoadjuvant Glasgow | | | | | |
|---|---|---|---|---|---|
| **Characteristic** | ***n = 72*** | **Median DSS (months)** | ***P (Log-Rank)*** | ***Median RFS (months)*** | ***P (Log-Rank)*** |
| **T Stage (AJCC 8th)** | | | | | |
| T1 | 20 | 56.9 | 0.011 | | 0.01 |
| T2 | 9 | 26.5 | | 16.9 | |
| T3 | 1 | 9.9 | | 6.5 | |
| T4 | 14 | 21.3 | | 12.8 | |
| Unknown | 28 | | | | |
| **Lymph Node** | | | | | |
| LN0 | 29 | 39 | 0.001 | 37.1 | 0.001 |
| LN1 | 34 | 19.7 | | 14 | |
| Unknown | 9 | | | | |
| **Resection Margin** | | | | | |
| R0 | 32 | 33.1 | 0.04 | 30.1 | 0.075 |
| R1 | 30 | 20.5 | | 16.3 | |
| Unknown | 10 | | | | |
| **Vascular Invasion** | | | | | |
| Negative | 43 | 28 | 0.05 | 27.2 | 0.2 |
| Positive | 27 | 20.7 | | 16.3 | |
| Unknown | 2 | | | | |
| **Tumour Regression** | | | | | |
| Good | 30 | 33.1 | 0.005 | 34 | <0.001 |
| Poor | 31 | 19 | | 12.3 | |
| Unknown | 11 | | | | |
| **Treatment type** | | | | | |
| Chemotherapy | 46 | 20.7 | 0.02 | 16.3 | 0.05 |
| Chemoradiotherapy | 24 | 39 | | 30.1 | |
| Unknown | 2 | | | | |
| **Chemotherapy type** | | | | | |
| FFX based | 53 | 22.6 | 0.7 | 30.1 | 0.04 |
| Gemcitabine based | 20 | 24.6 | | 14.2 | |
| Unknown | 2 | | | | |

**Table 2.6 Neoadjuvant Glasgow cohort patient characteristics.** *Table showing neoadjuvant cohort patients with clinical characteristics associated with disease specific survival (DSS) and recurrence free survival (RFS). Clinical features include T Stage (AJCC8th), resection margin status, lymph node status, tumour regression, treatment type and chemotherapy type.*

#### 2.1.1.7 Neoadjuvant combined cohort

The neoadjuvant combined cohort is comprised of 7 multi-core TMAs (Neoadj-MAL-TMA batch 1 and batch 2, and PRIMUS-MAL), with 85 patients who had undergone treatment and resection between 2009 to 2021. The Neoadj-MAL-TMAs had approximately 3x0.6mm cores per patient (n=72). PRIMUS-MAL TMAs had approximately 3x1mmcores per patient (n=13) and were part of the PRECISION-Panc clinical trial from the PRIMUS002 arm. Cores were selected from the tumour centre. Patient characteristics were determined from DSS and RFS analysis (table 2.7). This cohort includes neoadjuvant chemotherapy treated (n=46) and neoadjuvant chemoradiotherapy (n=27) patients. Patients received either Gemcitabine based chemotherapy (n=21) or FOLFIRINOX based chemotherapy (n=54). Median survival for this cohort was 20.4 months. Approval for use of this cohort was obtained through NHS QEUH Biorepository, application number 706, REC number 18/SS/0076.

| Neoadjuvant combined | | | | | |
|---|---|---|---|---|---|
| **Characteristic** | ***n = 85*** | **Median DSS (months)** | ***P (Log-Rank)*** | ***Median RFS (months)*** | ***P (Log-Rank)*** |
| **T Stage (AJCC 8th)** | | | | | |
| T1 | 22 | 50.4 | | NA | |
| T2 | 11 | 25 | <0.001 | 16.9 | <0.001 |
| T3 | 1 | 9.9 | | 6.5 | |
| T4 | 27 | 21.3 | | 12.8 | |
| Unknown | 24 | | | | |
| **Lymph Node** | | | | | |
| LN0 | 35 | 44.4 | <0.001 | NA | <0.001 |
| LN1 | 40 | 23.6 | | 14 | |
| Unknown | 10 | | | | |
| **Resection Margin** | | | | | |
| R0 | 39 | 33.1 | 0.03 | NA | 0.04 |
| R1 | 35 | 20.9 | | 16.3 | |
| Unknown | 11 | | | | |
| **Vascular Invasion** | | | | | |
| Negative | 46 | 31.1 | 0.03 | 30.1 | 0.1 |
| Positive | 29 | 21.1 | | 16.3 | |
| Unknown | 10 | | | | |
| **Tumour Regression** | | | | | |
| Good | 37 | 34.3 | 0.005 | 32 | <0.001 |
| Poor | 34 | 19 | | 12.3 | |
| Unknown | 14 | | | | |
| **Treatment type** | | | | | |
| Chemotherapy | 46 | 20.7 | 0.02 | 16.3 | 0.05 |
| Chemoradiotherapy | 27 | 39 | | 30.1 | |
| Unknown | 12 | | | | |
| **Chemotherapy type** | | | | | |
| FFX based | 54 | 22 | 0.8 | 36 | 0.05 |
| Gemcitabine based | 21 | 24.6 | | 14.2 | |
| Unknown | 10 | | | | |

**Table 2.7 Neoadjuvant combined cohort patient characteristics**. *Table showing neoadjuvant combined cohort patients with clinical characteristics associated with disease specific survival (DSS) and recurrence free survival (RFS). Clinical features include T Stage (AJCC8th), resection margin status, lymph node status, tumour regression, treatment type and chemotherapy type.*

#### 2.1.1.8 PRIMUS 002 whole section cohort

Two matched biopsy and post neoadjuvant chemotherapy resected whole sections from the PRIMUS-MAL TMA (chapter 2.1.1.7) were selected for spatial transcriptomics validation. PP00144 and PP00171 samples were used. Approval for use of this cohort was obtained through NHS QEUH Biorepository, application number 706, REC number 18/SS/0076.

## 2.2 Immunohistochemistry

### 2.2.1 Staining and scanning

All Immunohistochemistry (IHC) was performed prior to the start of this thesis on Discovery TMAs (chapter 2.1.1.1) which were supplied to the CRUK Scotland Institute histology department. All sections were stained using an Agilent pre-treatment module and autostainer link 48 for CD3, CD8, CD68 and CD163 (table 2.8). To complete the IHC staining sections were rinsed in tap water, dehydrated through graded ethanol's and placed in xylene. The stained sections were coverslipped in xylene using DPX mountant (SEA-1300-00A, CellPath). TMAs were imaged using the Leica Aperio AT2 slide scanner at x20 magnification.

| Marker | Company (catalogue number) | Retrieval conditions | Antibody dilution | Secondary |
|---|---|---|---|---|
| CD3 | Agilent (A0452) | High pH TRS buffer (K8004, Agilent) | 1:50 | EnVision rabbit (K4003, Agilent) |
| CD8 | Leica (NCL-L-CD8-4B11) | High pH TRS buffer (K8004, Agilent) | 1:75 | EnVision mouse (K4001, Agilent) |
| CD68 | Agilent (M0876) | High pH TRS buffer (K8004, Agilent) | 1:500 | EnVision mouse (K4001, Agilent) |
| CD163 | Leica (NCL-L-CD163) | High pH TRS buffer (K8004, Agilent) | 1:300 | EnVision mouse (K4001, Agilent) |

**Table 2.8 IHC conditions for antibody of interests.** *Description of antibody marker (CD3, CD8, CD68, CD163), retrieval conditions, antibody dilution.*

### 2.2.2 Scoring

Images were analysed at x20 magnification using the digital imaging platform HALO® (Indica Labs, Albuquerque, USA). Specific thresholds were developed for whole cell staining per marker and a weighted histoscore (H score) generated for individual cores. H scores are calculated as follows; (1x% weak stain) + (2x % moderate stain) + (3x % moderate stain), generating scores ranging from 0-300. An average H score was calculated per patient.

### 2.2.3 Survival and cumulative incidence analysis

Log-rank survival and univariate cox regression analysis was performed to establish associations between marker expression and disease specific survival (DSS) with RStudio (RStudio, Boston, MA, USA) using survminer and survival packages. Cutoff was established per variable using surv_cutpoint function (table 2.9). This method finds the optimal statistically relevant cut point of selected variables using maximally selected rank statistics. Fine Grays mode was generated by R packages cmprsk and bshazard. This was used to investigate the cumulative incidence of recurrence. This is the instantaneous rate of occurrence of the given event in cases that have not experienced an event. Recurrence type was classed as the event of interest. A density heatmap was generated per marker per pattern of recurrence, Kruskal-Wallis test was performed via package ggpubr. Statistical significance for all tests mention was set to p≤0.05 and reported to 3 decimal places.

**Survival cut-off point per phenotype density in discovery**

| Phenotype | Region | Cohort | Time (months) | Number | Cut-off method | Cut-off point | Rank number |
|---|---|---|---|---|---|---|---|
| CD3 | Whole core | Discovery | DSS | 238 | LQ | 100 | High - 179<br>Low - 59 |
| CD8 | Whoel core | Discovery | DSS | 238 | LQ | 100 | High - 179<br>Low - 59 |

**Table 2.9 Rcutoff scores for Kaplan-Meier DSS IHC analysis.** *Table illustrates the markers and their associated cut-off method and cut-off point per time variable, disease specific survival (DSS). Number of patients generated per rank is indicated by rank number column. Table is limited to markers that are frequently referred to throughout the thesis.*

## 2.3 Multiplex

To perform deep phenotyping of the pancreatic cancer landscape and explore cellular spatial relationships, a multiplex immunofluorescence assay using the PhenoImager™ from Akoya Biosciences® (Akoya Biosciences, Marlborough, MA, US) was developed. The entire process is split into three phases; optimisation and image generation, image analysis for data extraction, and data analysis (figure 2.1).

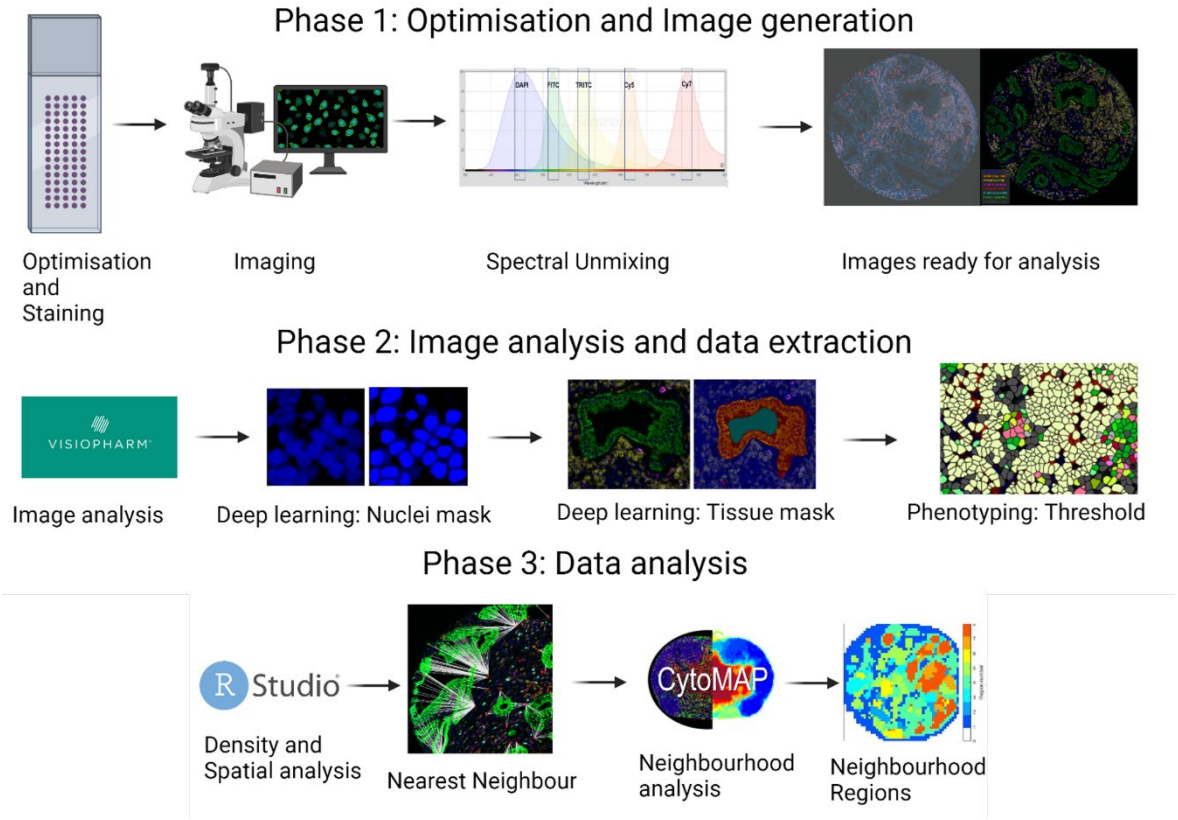


**Figure 2.1 Phases of PhenoImager™ workflow**. *Diagram showing the full workflow from optimisation to in-depth analysis. Phase 1 encompasses antibody optimisation to spectral unmixing of images, phase 2 encompasses image analysis with Visiopharm® using artificial intelligence generated algorithms, and phase 3 encompasses data analysis with multiple platforms including RStudio for single cell spatial metrics, CytoMAP for neighbourhood analysis.*

Multiplex immunofluorescence (mIF) is a cyclic multi-antibody staining technique based on a Tyramide Signal Amplification-Horse Radish Peroxidase (TSA-HRP) reaction. The assay works similarly to standard HRP based signal amplification assays. A secondary antibody conjugated to TSA-HRP is used to indirectly amplify the primary antibody. As multiple antibodies are being utilised, different fluorophores, each with a specific excitation and emission spectra are needed to distinguish between epitopes. HRP amplifies the fluorophore (Opal) signal by catalysing the reaction of labelled tyramide into free radicals, forming covalent bonds with tyrosine sites present on the endogenous protein. This assay was validated and performed in collaboration with John Le Quesne's lab, including Silvia Martinelli and Leah Officer-Jones. An automated staining procedure using the Ventana

Discovery ULTRA™ (Roche Diagnostic, Oro Valley, AZ, US) was established and images were generated by Akoya Vectra Polaris™ (Version 1.0.13, Akoya Biosciences, Marlborough, MA, US).

## 2.3.1 Phase 1: Optimisation and image generation

### 2.3.1.1 Panel design

A panel was generated in collaboration with Joanne Edwards lab, consisting of T cells ( CD3, CD8, FOXP3), macrophage (CD68), fibroblast (αSMA) and tumour cell (PanCk) markers (table 2.10). Markers were selected as they represent the most commonly expressed cells within the pancreatic landscape, and there is limited information regarding the spatial interactions between these cells. Antibodies selected were either diagnostic grade or sourced from in reputable papers (table 2.11). Antibody concentrations and panel locations were validated on test tonsil and PDAC tissue.

| Marker | Co-expression expected | Cell lineage | Phenotype (single) | Immune classification (single) | Co-expressed Phenotypes | Immune cell classification |
|---|---|---|---|---|---|---|
| PanCk | No | Epithelial | PanCk+ | Epithelial tumour | NA | NA |
| αSMA | No | Tissue resident myofibroblasts/ vascular smooth muscle cells | αSMA+ | Fibroblast/ myofibroblast | NA | NA |
| CD3 | Yes | Common lymphoid progenitor | CD3+CD8- | Effector T cell/ Helper T cell | CD3CD8+ | Cytotoxic T cell |
| CD8 | Yes | Common lymphoid progenitor | CD8+CD3- | Cytotoxic T cell/ potential NK cell | CD3CD8+ | Cytotoxic T cell |
| FOXP3 | Yes | Common myeloid progenitor | FOXP3+ | T regulatory cell | FOXP3CD3+ | T regulatory cell |
| CD68 | No | Common lymphoid progenitor | CD68+ | Macrophage (proinflammtory) | NA | NA |

**Table 2.10 Multiplex immune panel markers.** *Summary table showing the markers selected for the PhenoImager™ assay, including PanCk, αSMA, CD3, CD8, FOXP3 and CD68. Co-expression status, cell lineage, phenotype and immune classification is shown for single expressing and co-expressing markers.*

### 2.3.1.2 Automated staining

An automated staining procedure was performed on the Ventana Discovery ULTRA™ (Roche Diagnostic, Oro Valley, AZ, US) using the protocol Imm Phentype 4950. To generate a Discovery and validation cohort, two batches were stained at separate time points, the same antibody lot numbers were used. Briefly, slides were baked at 60◦C, and antigen retrieval (950-124, Roche Diagnostic) performed (table 2.11). Slides were

incubated with the appropriate blocking buffer to prevent non-specific binding, and first primary antibody was dispensed (table 2.11). The appropriate secondary antibody (Roche Diagnostic) was dispensed and washed (Discovery wash, Roche Diagnostic) and opal fluorophore (NEL821001KT, Akoya Biosciences) applied (table 2.11). This staining process is repeated from the antigen retrieval step for all 6 antibodies. Notably, the first retrieval step is to expose the epitopes induced by paraffinization, the subsequent retrieval steps are focused on stripping the primary antibody to allow the next primary to bind. After the final fluorophore step, the counterstain DAPI was applied. Slides were washed and cover slips mounted using Diamond ProLong™ (P36970, ThermoFisher Scientific).

| Marker | Assay type | Company | Catalogue number | Retrieval buffer | Blocking buffer | Antibody dilution | Secondary (catalogue number) | Opal | Location | Channel |
|---|---|---|---|---|---|---|---|---|---|---|
| CD3 | mIF | Roche Tissue Diagnostics | 5278422001 | Cell conditioning buffer Tris-EDTA based buffer pH 7.8 | Roche Tissue Diagnostic Goat Ig block | RTU | OmniMap anti-Rt HRP (760-4311) | 570 | 4 | TRITC |
| CD8a | mIF | Cell Signaling Technology | 70306 | Cell conditioning buffer Tris-EDTA based buffer pH 7.8 | Roche Tissue Diagnostic Goat Ig block | 1:100 | OmniMap anti-Ms HRP (760-4310) | 520 | 5 | FITC |
| FOXP3 | mIF | Abcam | 20034 | Cell conditioning buffer Tris-EDTA based buffer pH 7.8 | Roche Tissue Diagnostic Goat Ig block | 1:20 | OmniMap anti-Ms HRP (760-4310) | 690 | 2 | Cy5 |
| CD68 | mIF | Cell Signalling Technology | 76437 | Cell conditioning buffer Tris-EDTA based buffer pH 7.8 | Roche Tissue Diagnostic Goat Ig block | 1:200 | OmniMap anti-Rt HRP (760-4311) | 620 | 1 | Texas Red |
| aSMA | mIF | Roche Tissue Diagnostics | 5268303001 | Cell conditioning buffer Tris-EDTA based buffer pH 7.8 | Roche Tissue Diagnostic Goat Ig block | RTU | OmniMap anti-Ms HRP (760-4310) | 540 | 3 | FITC |
| PanCk AE1/AE3 | mIF | Leica Biosystems | AE1/AE3-601-L-CE | Cell conditioning buffer Tris-EDTA based buffer pH 7.8 | Roche Tissue Diagnostic Goat Ig block | 1:250 | OmniMap anti-Ms HRP (760-4310) | 650 | 6 | Cy5 |
| DAPI | mIF | Roche Tissue Diagnostics | 5268826001 | Cell conditioning buffer Tris-EDTA based buffer pH 7.8 | NA | RTU | NA | NA | 7 | DAPI/780 |

**Table 2.11 mIF conditions per marker.** *Summary table includes primary antibody details, retrieval and blocking buffers used. Primary antibody dilutions range from 1:20 to 1:250, or are ready-to-use (RTU). Opal refers to the fluorophore matched to the secondary, location indicates what cycle the antibody is used. Channel per opal is indicted.*

#### 2.3.1.3 Slide visualization and spectral unmixing

Multiplex stained TMAs were scanned at 20x using the Vectra Polaris™ (Akoya Biosciences, Marlborough, MA, US). An unmixing library was created using single stain images per marker plus DAPI counterstain. The spectra per marker was extracted via InForm® (Version 2.5.1, Akoya Biosciences, Marlborough, MA, US) and used to create a true emission spectra. An unstained PDAC TMA was used as an autofluorescence reference. This library was used to unmix raw images, generating component images for image analysis. When using multiple markers simultaneously on the same section, spectral bleed through becomes an issue. This is when fluorophores with a specific excitation-emission spectra corresponding to the wavelength of a set channel, are detected in another channel. This is due to overlap between the peripheral ends of the wavelengths in different channels (figure 2.1). The spectral library created is essential to correct this overlap.

## 2.3.2 Phase 2: image analysis and data extraction

### 2.3.2.1 Cell segmentation

A U-NET Deep Learning APP was trained for DAPI nuclear detection using the Author™ module on VISIOPHARM® (VISIOPHARM, Hørsholm, Denmark). A base template established by members of the John Le Quesne lab was used as a starting point. Using PDAC images with variable DAPI pixel intensity, regions of interest were selected, and nuclei annotated. An iterative training proceeded as follows;
annotate > train app > run on example cores > correct U-NET annotations > re-train.
The APP was trained until at least 90% of the images across discovery and validation were correctly segmented, 20% of the cohorts were reviewed. Reviewing process was aided by Rachel Pennie and Leah Officer-Jones. The final APP was trained for approximately 2.0 million iterations and had ~7% error rate. Post processing steps were included to remove artefacts, classed as objects <3µm, and a 35 pixel cell expansion was added, generating a whole cell label. Additional post-processing steps included producing pixel intensities per Opal, X Y coordinates per cell, and cell count per core.

### 2.3.2.2 Tissue segmentation

A Deep Learning APP was trained using a DeepLabv3+ module for tissue segmentation using the Author™ module on VISIOPHARM® (VISIOPHARM, Hørsholm, Denmark). The APP was trained from scratch to select epithelial and non-epithelial tissue. The PanCk opal 650 was trained as the tumour segment feature, and the remaining tissue was annotated as tumour microenvironment. The same training steps as in chapter 2.3.2.1 were followed. The APP was trained until at least 90% of the images across discovery and validation cohorts were correctly labelled, 20% of the cohorts were reviewed. Reviewing process was aided by Rachel Pennie and Leah Officer-Jones. The final APP was trained for approximately 1 million iterations and had ~3% error rate. Post processing steps were included to fill small unlabelled gaps found within masks and remove miscellaneous tissue labels <3µm.

### 2.3.2.3 Phenotyping

Biased phenotyping was carried out using a thresholded pixel intensity per marker (figure 2.3). Co-expressing phenotypes were cytotoxic T cells, defined by CD3+CD8+ cells, T cells defined by CD3+CD8- and T regulatory cells defined by FOXP3+CD3+. Single expressing phenotypes were CD68+ macrophages, αSMA+ fibroblasts, PanCk+ epithelial cells. Additionally, a single expressing CD8+CD3- population was observed, possibly a natural killer cell subpopulation or due to assay limitations and CD3 masking. Phenotypes

were reviewed on VISIOPHARM® (VISIOPHARM, Hørsholm, Denmark).

## 2.3.3 Phase 3: Analysis

### 2.3.3.1 Survival analysis

Log-rank survival and univariate cox regression analysis was performed to establish associations for disease specific survival (DSS) and recurrence free survival (RFS) with RStudio (RStudio, Boston, MA, USA) using survminer and survival packages. At the time of analysis, no established cutoff methods had been reported in pancreatic cancer. Cutoff was determined per averaged variable per patient using a variety of cutoff methods for exploratory purposes. All variables were tested with surv_cutpoint function (Rcutoff), Lower Quantile (LQ), Upper Quantile (UQ) and Median (Med), the best method was selected (table 2.12). Notably cutoff methods established in the discovery naive cohort were replicated in the validation naïve cohort. In Kaplan-Meiers with over two curves, pairwise comparison over strata was used. Statistical significance was set to $p \leq 0.05$, and reported to 3 decimal places.

### 2.3.3.2 Cellular density and ratios

Cellular density per phenotype was generated to establish the base immune landscape in naïve and neoadjuvant cohorts. Comparisons were made using p value adjusted Bonferroni T test. This was done using ggplot and ggpubr package from RStudio (RStudio, Boston, MA, USA). Density ratios were generated between two previously ranked phenotypes. Survival analysis and cut-offs were generated as stated in 1.3.3.1 (table 2.12).

### 2.3.3.3 Spatial distance metrics and survival analysis

Three main spatial metrics were explored to establish the spatial immune landscape in both naïve and neoadjuvant settings. Nearest neighbour (NN) analysis calculates the nearest neighbour of individual cells to a specific phenotype in a set distance e.g., distance of cell x to cell y. Mutual nearest neighbour (mNN) calculates the distance between mutual pairs. Radius analysis explores the density of cells from a set distance to the central cell. These metrics were generated between all phenotypes using the PhenoptR package. The average boxplots and comparisons were made using p value adjusted Bonferroni T test, using ggplot and ggpubr package from RStudio (RStudio, Boston, MA, USA). Survival analysis and cut-offs were generated as stated in 1.3.3.1 (table 2.12)

Survival cut-off for most significant phenotype density and nearest neighbour for disease specific survival

| Phenotype pattern | Region | Treatment | Cohort | Time (months) | Group | Number | Cut-off method | Cut-off point | Rank number |
|---|---|---|---|---|---|---|---|---|---|
| CD3 | Whole core | Naïve | Discovery | DSS | All patients | 238 | LQ | 178 | High - 179<br>Low - 60 |
| CD68 | Whole core | Naïve | Discovery | DSS | All patients | 238 | LQ | 270 | High - 179<br>Low - 60 |
| PanCk | Whole core | Neoadjuvant | Neoadjuvant | DSS | All patients | 72 | Rcutoff | 447 | High - 42<br>Low - 28 |
| CD3CD8 | Whole core | Neoadjuvant | Neoadjuvant | DSS | All patients | 72 | Rcutoff | 334 | High - 37<br>Low - 33 |
| CD68 | Whole core | Neoadjuvant | Neoadjuvant | DSS | All patients | 72 | Rcutoff | 1204 | High - 31<br>Low - 39 |
| Distance to PanCk from CD68 | Whole core | Naïve | Discovery | DSS | All patients | 238 | Med | 50 | High - 116<br>Low - 116 |
| Distance to CD3 from CD68 | Whole core | Naïve | Discovery | DSS | All patients | 238 | Med | 90 | High - 116<br>Low - 116 |
| Distance to PanCk from CD68 | Whole core | Neoadjuvant | Neoadjuvant | DSS | All patients | 72 | Rcutoff | 98 | High - 39<br>Low - 31 |
| Distance to CD3 from CD3CD8 | Whole core | Neoadjuvant | Neoadjuvant | DSS | All patients | 72 | Rcutoff | 84 | High - 38<br>Low - 34 |
| Distance to CD3CD8 from FOXP3CD3 | Whole core | Neoadjuvant | Neoadjuvant | DSS | All patients | 72 | Rcutoff | 29 | High - 44<br>Low - 26 |

**Table 2.12 Density and nearest neighbour cutoff scores for Kaplan-Meier DSS analysis.** *Summary table illustrates the most important density and nearest neighbour markers across naïve and neoadjuvant cohorts, their associated cut-off method and cut-off point per time variable disease specific survival (DSS). Number of patients generated per rank is indicated by rank number column. Table is limited to markers that are frequently referred to throughout the thesis.*

#### 2.3.3.4 Multivariate cox regression and decision tree analysis

Multivariate cox regression and decision tree analysis were performed on density and nearest neighbour significant patterns in naïve and neoadjuvant cohorts. This was done to filter for patterns with the best chance of biological significance. Multivariate cox regression and decision tree analysis were performed using four main packages, survival, survminer, rpart.plot and partykit.

#### 2.3.3.5 CytoMAP neighbourhood analysis

Raw pixel intensity per opal data and cell X Y coordinates were entered into MATLAB® CytoMAP (MathWorks, Natick, MA, US) to validate biased phenotypes generated in chapter 2.3.2.3. Normalization was carried out using the standardize method across each sample (subtract mean, divide by standard deviation). Number of neighbourhood regions was calculated using the Davies Bouldin method and clustering was carried out using the nearest neighbour self-organizing map algorithm.

#### 2.3.3.6 Ripley's K function

The well-known spatiotemporal point pattern analysis method 'Ripley's K function' was repurposed for single cell analysis. This method determines the pattern of distribution of points (in this case cells) within a set boundary. It classes points into three categories;

1. Random distribution – complete random distribution of points with no predictable pattern, estimated by Poisson process
2. Clustered – points clumped together, and the curve produced lies above the Poisson curve
3. Dispersed – points are scattered but have a predictable pattern, curve lies below the Poisson

The pattern of distribution was established per phenotype within naïve and neoadjuvant cohorts using the R package spatstat.

## 2.4 PhenoCycler

To establish the single cell protein landscape for T cells, B cells and dendritic cells, Akoya Biosciences® (Akoya Biosciences, Marlborough, MA, US) ultra-high plex assay PhenoCycler™ was trialled. This was part of a technology access program, using a ready-to-use panel, STEP core plus enhancement (Akoya Biosciences, Marlborough, MA, US). A Glasgow naïve cohort 2 (chapter 2.1.1.4) TMA section was sent to Akoya Biosciences®,

the assay was performed, and images were sent back for analysis. Briefly, after antigen retrieval and panel incubation, samples are placed in the PhenoCycler-Fusion™ and undergo cycles of fluorescent bound oligonucleotide flushed into the flow cell, binding to antibodies, image capture, then probe cleavage and removal. This cycle occurs 16 times as individual imaging cycles are restricted to 4 channels at any one time. Phenotyping was performed using the open-source platform QuPath (QuPath, Edinburgh, UK) on a filtered dataset. Markers were split into cytotoxic T cells (CD3e+CD8+), active T cells (CD3e+CD8+ICOS+), inactive T cells (CD3e+CD8+TIM3+), helper T cells (CD3e+CD4+), B cells (CD20) and dendritic cells (CD11b). Survival analysis was performed as outlined in chapter 2.3.3.1, using R function surv_cutpoint as the cutoff method.

## 2.5 GeoMx assays

### 2.5.1 Assay overview

GeoMx® DSP (NanoString, Seattle, WA, US) is spatial-resolved transcriptomic and proteomic method which works using digital optical barcoding. The assay was performed according to manufacturer's protocol and differs slightly between transcriptome and protein panels. The day before starting the assay, samples were re-baked overnight at 60◦C. Antigen retrieval was performed using the Leica BOND™ (Leica BIOSYSTEMS, Wetzlar, Germany) at HIER 20 minutes with ER2 and a 15 minute incubation at 37◦C with recombinant Proteinase K (AM2546, Invitrogen) at 1µg/ml. This step was performed in collaboration with CRUK Scotland Institute histology department. Samples undergo overnight *in situ* hybridization (ISH) at 37◦C using an oligonucleotide probe panel. Probes are composed up of a target oligo and an indexing oligo, bound together by an ultraviolet (UV) linker. Unbound probes are removed using a series of stringent washes at 37◦C. Two different probe sets and mIF panels were used for protein and transcriptomic assays, see chapter 2.5.1 and chapter 2.5.2 respectively. A mini multiplex immunofluorescence (mIF) panel using a mixture of immune and morphology oligo-conjugated antibodies was used to visualise pancreatic tissue and aid selection of regions of interest (ROI) and areas of illumination (AOIs) (figure 2.2). After cocktail primary antibody staining using the appropriate mIF panel, samples were loaded onto the GeoMx® machine for ROI selection. Localised ultraviolet light cleaves the indexing oligo tags at the UV linker site. Tags are aspirated and dispensed into a 96-well collection plate. Tags are hybridized to region specific barcodes and sequenced using either the nCounter® (NanoString, Seattle, WA, US) for protein, or the NextSeq 1000/2000 sequencer (Illumina, San Diego, CA, US) for RNA (figure 2.2).

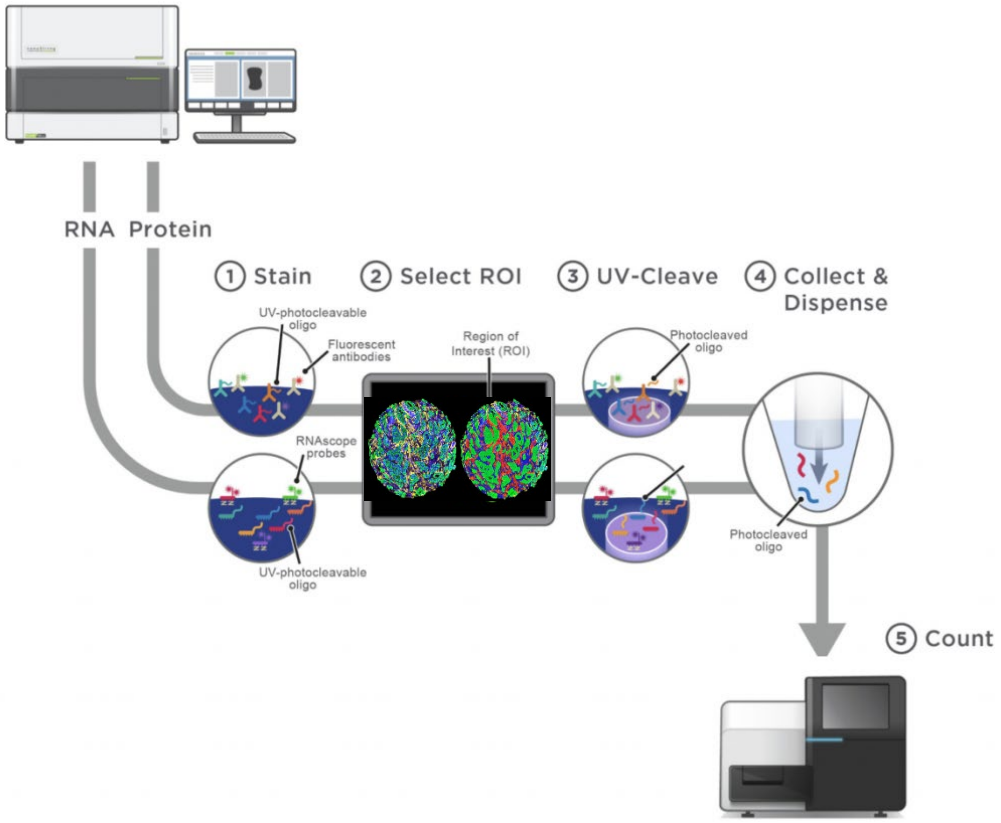


**Figure 2.2 Overview of GeoMx® DSP workflow.** *Overview of NanoString DSP workflow adapted with permission from NanoString®. Workflow is split into panel in situ hybridization, mIF staining, ROI selection and mask generation, oligo tags cleaved and collection for sequencing.*

## 2.5.2 Immune oncology protein panel

A combined GeoMx® Immuno-oncology (NanoString) panel was used on the Glasgow naïve cohort 1 (see chapter 2.1.1.4) to further establish the immune landscape and explore immune functional status. This was completed as part of a technology access program, with the assistance of NanoString® scientists. This panel is composed of 60 proteins, split into 5 modules defined by broad function, including Pan-tumour (GMX-PROMOD-NCT-HPT-12, NanoString), immune cell profiling (GMX-PROCO-NCT-HICP-12, NanoString), immune activation status module (GMX-PROMOD-NCT-HIAS-12, NanoString), IO drug target module (GMX-PROMOD-NCT-HIODT-12, NanoString) and PI3K/AKT signalling (GMX-PROMOD-NCT-HPI3K-12, NanoString) modules. The mIF panel was a ready-to-use technology access program immune morphology panel (NanoString, Seattle, WA, US), consisting of nuclear stain Syto13, PanCk, CD3 and αSMA (NanoString) (table 2.13). A total of 48 geometric ROIs were selected, 48 epithelial AOIs and 48 TME AOIs, encompassing all 28 patients from the Glasgow naïve cohort 1 (chapter 2.1.1.4). Approximately two ROIs were taken per patient. ROI diameter was

660µm. AOIs were created using the native thresholding method on GeoMx® DSP control centre, with epithelial AOIs generated from PanCk+ staining, and TME AOIs generated from PanCk- stain.

| Marker | Assay type | Company | Dilution | Channel |
|---|---|---|---|---|
| Syto13 | IO panel | NanoString | 1:10 | FITC |
| PanCk | IO panel | NanoString | 1:40 | Texas Red |
| CD3 | IO panel | NanoString | 1:40 | Cy3 |
| αSMA | IO panel | NanoString | 1:40 | Cy5 |

**Table 2.13 mIF panel for immuno-oncology panel in Glasgow cohort 1.** *Summary of marker, company it is produced by, and the dilution. The assay panel (immuno-oncology) and fluorescent channel used is also indicated*

#### 2.5.2.1 QC, filtering and normalization

Quality control (QC), housekeeping normalization and filtering was performed on this dataset using the R package GeoMxTools. Housekeeping markers were defined by GAPDH, Histone H3 and RPS6. QC and filtering methods were performed following the manufacturer's guidelines. All 98 AOIs passed technical QC. Targets with signal-to-noise ratio below 1.3 were reviewed and filtered as appropriate.

#### 2.5.2.2 DSP marker concordance analysis

Concordance between IHC markers (chapter 2.2) and matched DSP markers was performed with Spearman Rank correlation using the ggplot2 R package. Statistical significance was set to $p \leq 0.05$, and reported to 3 decimal places. Coefficient value, denoted by Rho, of ≥0.8 demonstrates strong concordance.

#### 2.5.2.3 Differential expression analysis

Differential expression analysis (DEA) was carried out to establish the differences between two comparison groups. DEA and volcano plots were generated by EdgeR and EnhancedVolcano R package. Statistical significance was set to p adjusted ≤0.05 and log2 fold change 1.5/-1.5, and reported to 3 decimal places. Naïve epithelial AOIs and TME AOIs were compared.

#### 2.5.2.4 Unbiased clustering heatmap

Unbiased clustering of averaged protein expression per patient was visualised using a heatmap. Annotations were included for immune high and immune low patients. Heatmaps were drawn using ComplexHeatmap R package.

#### 2.5.2.5 Survival analysis

Survival analysis was performed for CD3 and CD8 DSP protein markers to validate the protein prognostic trend. Prognostic value of immune high and immune low was tested. Further analysis was performed on all markers per AOI. Survival analysis and cutoff method was performed as outlined in chapter 2.3.3.1 (table 2.14).

**Survival cut-off for most significant phenotype in disease specific survival**

| Variable | Region | Treatment | Cohort | Time (months) | Group | Number | Cut-off method | Cut-off point | Rank number |
|---|---|---|---|---|---|---|---|---|---|
| CD3 | TME | Naïve | Glasgow cohort 1 | DSS | All patients | 28 | Med | 7.4 | High - 14<br>Low - 13 |
| CD8 | TME | Naïve | Glasgow cohort 1 | DSS | All patients | 28 | Med | 7.5 | High - 14<br>Low - 13 |
| B7-H3 | Tumour | Naïve | Glasgow cohort 1 | DSS | All patients | 28 | Rcutoff | 10.2 | High - 5<br>Low - 22 |

**Table 2.14 Cutoff scores for Kaplan-Meier DSS analysis.** *Summary table illustrates the markers and their associated cut-off method and cut-off point per time variable, disease specific survival (DSS) and recurrence free survival (RFS). Number of patients generated per rank is indicated by rank number column. Table is limited to markers that are frequently referred to throughout the thesis.*

## 2.5.3 WTA panel

The GeoMx® whole transcriptome atlas panel (GMX-RNA-NGSHuWTA-4, NanoString) was used on the Glasgow naïve cohort 2 (chapter 2.1.1.4) and neoadjuvant combined cohort (chapter 2.1.1.7) to determine the spatial transcriptomic landscape. This panel is composed of 18,000+ genes, excluding non-functional genes. The mIF panel was partially made up of ready-to-use NanoString® morphology kit antibodies (GMX-RNA-MORPHHST-12, NanoString), Syto13 and PanCk, and in-house conjugated antibodies, CD45 (M087629-2, ThermoFisher Scientific) and αSMA (53-9760-82, ThermoFisher Scientific). Antibody-fluorophore conjugation was carried out using Alexa Fluor™ kits as per manufacture protocol (table 2.15). Antibodies were approved for use by NanoString®. Concentrations were optimised on control tonsil and PDAC tissue, trialling a range of dilutions (1:50-1:500) until the final conditions of 1 hour incubation at room temperature with 1:200 dilution for both CD45 and αSMA were validated. This was completed in-house with the assistance of Holly Leslie. TMAs were used throughout the course of this thesis, resulting in different methods used to generate AOIs due to technological advancements. These are discussed in chapter 2.5.2.1. The same AOI types were generated, producing an epithelial PanCk+ AOI, fibroblast rich αSMA+ AOI, and immune AOI made up of the remainder of the ROI. Three main studies were performed;

1. Base naïve Spatial Transcriptomic landscape - investigating inter and intra tumour heterogeneity, and relevant clinical subgroup comparisons.

2. Base neoadjuvant Spatial Transcriptomic landscape - investigating inter tumour heterogeneity, distinct histology, and alterations between neoadjuvant treatment methods

3. Naïve versus neoadjuvant - comparison of matched segments/AOIs, exploring Spatial Transcriptomic shift between clinically relevant groups.

| Marker | Assay type | Company | Dilution | Conjugation kit (catalogue number) | Channel |
|---|---|---|---|---|---|
| Syto13 | WTA | NanoString® | 1:10 | NA | FITC |
| PanCk | WTA | NanoString® | 1:40 | NA | Cy3 |
| αSMA | WTA | ThermoFisher Scientific® | 1:200 | Alexa Fluor 594 (A20185) | Texas Red |
| CD45 | WTA | ThermoFisher Scientific® | 1:200 | Alexa Fluor 647 (A20186) | Cy5 |

**Table 2.15 mIF panel for WTA panel in Glasgow cohort 1.** *Summary of marker, company it is produced by, and the dilution. The assay panel (whole transcriptome atlas) and fluorescent channel used is also indicated*

#### 2.5.3.1 Area of interest selection process

As the Glasgow naïve cohort 2 (chapter 2.1.1.4) was one of the first experiments performed, the selection process relied on the native GeoMx® DSP control centre pixel threshold method. A total of 167 geometric ROIs were selected, 51 epithelial AOIs, 41 αSMA AOIs, 53 immune AOIs, and 3 whole core AOIs. A total of 58 patients were included. The neoadjuvant combined cohort (chapter 2.1.1.7) was performed at a later date, after considerable technological improvements. A deep learning U-NET tissue segmentation approach was developed using the Author™ module on VISIOPHARM® (VISIOPHARM, Hørsholm, Denmark). This method followed the same training steps as outlined in chapter 2.3.2.2. The tissue segmentation APP was initially trained on PDAC optimisation tissue, then further optimised on the actual stained sample on the day of ROI collection. A total of 310 geometric ROIs were selected, 95 epithelial AOIs, 95 αSMA AOIs, 81 immune AOIs, and 15 whole core AOIs . 71 out of 85 patients were included. Due to the cost per run, only 1 ROI per patient was taken for the naïve and neoadjuvant

TMA cohorts. As a small validatory experiment of TMA work, the GeoMx® whole transcriptome atlas (WTA) panel was performed on two matched biopsy and neoadjuvant treated resections from the clinical trial PRIMUS 002 cohort (chapter 2.1.1.8). A total of 20 ROIs were taken for PP00144 across biopsy and resection, 9 epithelial AOIs, 7 αSMA AOIs,13 immune AOIs and 4 whole core AOIs. 11 total ROIs were selected for PP00171 across biopsy and resection, 8 epithelial AOIs, 6, αSMA AOIs, 9 immune AOIs, and 1 whole core AOI. A mixture of geometric circle ROIs and polygon ROIs were drawn across the above cohorts. Geometric ROI diameter was set to 660μm diameter, and the maximum polygon size was 660μm x 785μm.

#### 2.5.3.2 QC, filtering and normalization

The first QC steps were performed out on the GeoMx® DSP control centre. The initial dataset was visually inspected to ensure correct overall deduplication of read counts. Most technical and biological QC parameters were carried out as per manufacturer suggestions. The two parameters altered were RNA specific technical background QC, negative probe count geomean, and nuclei count. Negative probe count checks the level of non-specific binding probes per AOI to ensure the floor of detection is reached. This parameter is highly dependent on tissue type and disease state. The count was set to 4 for PDAC FFPE tissue. Nuclear count per AOI was set to 100. AOIs that fell below these set thresholds were flagged and investigated via methods including principle component analysis (PCA). After QC steps, the total number of AOIs for the Glasgow naïve cohort 2 was 148/167 and the neoadjuvant combined cohort was 286/310. Using a lenient filtering approach, targets with values below median positive probe count in 5% of AOIs were filtered. Normalization was carried out using the Q3 method and batch correction was applied. Notably multiple different filtering and normalization methods were explored and can be implemented (supplementary 8.1)

#### 2.5.3.3 Differential expression analysis

Differential expression analysis was performed on all comparison groups as outlined in chapter 2.5.1.3.

#### 2.5.3.4 Geneset enrichment analysis

Geneset enrichment analysis (GSEA) determines the aberrated pathways between two comparison groups. All comparisons were made. GSEA and bar charts were generated by the fgsea R package. Statistical significance was set to p adjusted ≤0.05 and normalised enrichment score (NES) 1.5/-1.5, and reported to 3 decimal places.

#### 2.5.3.5 Survival

Survival analysis was performed for intra-AOI clustering (chapter 2.5.2.5) and B7-H3 expression (chapter 2.5.2.9). Survival analysis was generated as outlined in chapter 2.3.3.1. B7-H3 cut-off method was replicated from the immune oncology protein panel (chapter 2.5.2.5), resulting in a 20high-80low split used.

#### 2.5.3.6 Inter and intra tumour clustering analysis

Clustering was explored between all AOIs to confirm inter-tumour differences. Intra-tumour clustering was performed to determine heterogeneity within epithelium, αSMA and immune AOIs. Principle component analysis (PCA) determines the similarity of samples inputted by clustering. PCA and plots were generated by Cairo, ggplot2 and VennDiagram R packages.

#### 2.5.3.7 Immune cell deconvolution

Immune cell deconvolution estimates the immune cells present within the bulk transcriptomic context using validated single cell signatures. SpatialDecon, a NanoString® (NanoString, Seattle, WA, US) tool specifically designed for Spatial Transcriptomic data, was implemented using R package SpatialDecon. Immune cell count per 100 cells was generated, and all groups were compared. Statistical analysis was performed using Wilcoxon test, and significance threshold set to $p \leq 0.05$, reported to 3 decimal places.

#### 2.5.3.8 Molecular subtyping

Molecular subtyping was performed with epithelial AOIs, using a filtered Squamous/Classical gene list. A total squamous score was generated per epithelial AOI to determine squamous signature strength. Bulk molecular subtyped samples were classed as true subtypes. Suitability of molecular subtyping using spatial epithelial AOIs was determined by comparing it to bulk subtyping, epithelial cluster ranks (chapter 2.5.2.5) and total squamous score. Bulk was previously carried out by Rosie Upstill-Goddard as part of a larger cohort. This analysis was performed using ConsensusClusterPlus, singscore and ComplexHeatmap R packages.

#### 2.5.3.9 B7-H3 expression

To investigate the transcriptomic expression of B7-H3 across the naïve and neoadjuvant pancreatic cancer setting, epithelial and averaged whole core expression was explored. Survival analysis (chapter 2.5.2.5), DEA (chapter 2.5.2.3) and GSEA (chapter 2.5.2.4) were performed. Average AOI boxplots were drawn with ggplot2 R package, and

statistical analysis was performed using Kruskal-Wallis test, with significance threshold set to $p \leq 0.05$.

#### 2.5.3.10 Sankey plot

To visualize the immune cell switch in matched biopsy and neoadjuvant treated PRIMUS whole sections, a Sankey plot was generated. The percentage estimated cell population (chapter 2.5.2.6) from biopsy immune AOIs to neoadjuvant treated immune segments was determined. Sankey plots were generated using networkD3 R package.

#### 2.5.3.11 mIF integration with Spatial Transcriptomics

To determine the underlying transcriptomic landscape of relevant prognostic mIF protein ranked trends (chapter 2.3), matched samples were integrated into GeoMx® data. DEA (chapter 2.5.1.3), GSEA (chapter 2.5.2.4) and immune cell deconvolution (chapter 2.5.2.6) was performed.

Batch analysis for DEA, GSEA, immune cell deconvolution and PCA plots were performed using Colin Woods GeoMx automated pipeline R script.

# 2.6 CosMx

## 2.6.1 Sample preparation and probe incubation

The CosMx™ immune-oncology protein panel (CMX-H-IOP-64P-P, NanoString) was used on the Glasgow naïve cohort 2 (chapter 2.1.1.4) and neoadjuvant combined cohort (chapter 2.1.1.7) to determine the spatial single cell proteomic landscape. This panel was composed of 64 proteins, including B cell, T cell, dendritic cell and B7-H3 markers. The assay was performed as per manufacturers protocol with the help of Claire Kennedy and Yoanna Doncheva. Sections were placed in Leica BOND PLUS slides within the approximate gasket area (20mmx15mm). Slides were baked overnight at 60◦C the day before. A semi-automated tissue prep protocol was run on the Leica BOND™ in collaboration with the CRUK Scotland Institute histology department. Antigen retrieval was performed at HIER 20 minutes with ER2 at 100◦C and tissue permeabilization using recombinant Proteinase K (AM2546, Invitrogen) at 37◦C using 3µg/ml for 15 minutes. Subsequently, an incubation frame (NanoString, CMX-FCA) and fiducial mixture (CMX-FFPE-SP-P, NanoString) was applied to allow for future image registration on the CosMx™. A series of post fixation and Sulfo-NHS-Acetate (26777, ThermoFisher Scientific) steps were carried out to prepare the samples for overnight *ISH* of the protein probe mix at 37◦C. A series of stringent washes at 37◦C were carried out to remove unbound probes.

## 2.6.2 mIF staining and CosMx™ machine preparation

Manual staining was performed as per the manufacturers protocol. Briefly, a ready-to-use immunofluorescence panel was applied to PDAC TMAs. Nuclear staining, 1:40 DAPI (CMX-H-UCS-12-P, NanoString) dilution, was incubated first at room temperature and subsequent staining at 1:25 dilution for cell segmentation mix CD298/B2M (CMX-H-UCS-12-P, NanoString), PanCk (CMX-H-IO-PCKCD45- MM34-P, NanoString) and CD45 (CMX-H-IO-PCKCD45- MM34-P, NanoString). After a final Sulfo-NHS-Acetate (26777, ThermoFisher Scientific) incubation, the flow cell was assembled, slides were placed into the CosMx™, and machine preparatory steps were complete. Pre-bleaching configuration C profile and cell segmentation configuration A human tissue profile were selected on the machine. The CosMx™ cell segmentation is based on the Cellpose algorithm, using a nuclear segmentation and cell expansion method. This was optimised by NanoString® for CosMx™ experiments.

### 2.6.3 FOV selection

The field of view is currently limited to 500x500µm squares. Due to limited size of the imaging gasket, 20mmx15mm, not all Glasgow naïve cohort 2 and neoadjuvant combined cohort cores could be selected. A total of 38 patients were selected for Glasgow naïve cohort 2, and 58 patients for neoadjuvant combined cohort. Using the grid method, multiple FOVs were placed to cover the whole core (figure 2.3). A total of 150 FOVs were selected for Glasgow naïve cohort 2 and 337 FOVs were selected for neoadjuvant combined cohort.

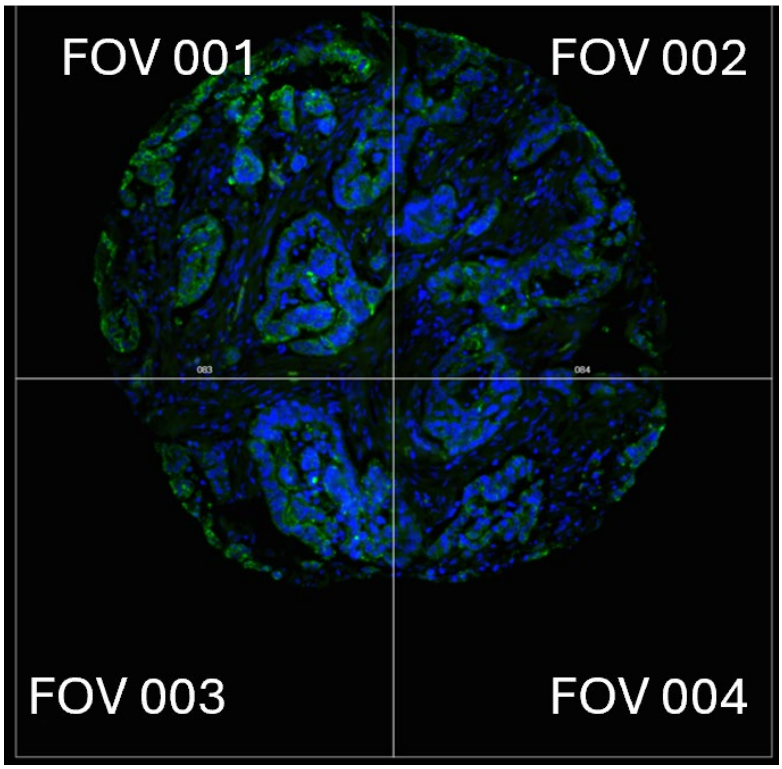


**Figure 2.3 Example FOV selection on Glasgow naïve cohort 2.** *Demonstrating four FOVs selected to cover the entire core. DAPI (blue) and PanCk (green) are shown.*

### 2.6.4 Cyclical fluorescent oligonucleotide imaging

The CosMx™ immune-oncology protein panel is an imaging-based assay. Once *ISH* probes are bound to the PDAC tissue and samples are placed in the machine, fluorescent readout reported probes are dispensed into flow cells. *ISH* probes have a readout domain that allows four reporters to bind sequentially, detecting unique proteins. Each reporter set produces a Z stack image with X, Y and Z coordinates generated by location oligonucleotide probes within each segmented cell. Images are subsequently flattened, and probes are assigned per cell with X and Y coordinates.

### 2.6.5 Data extraction

Data download, compilation, reviewing and QC was performed as recommended by NanoString®. This was done by Tengyu Zhang and Ritika Nara.

### 2.6.6 Seurat clustering

Using Seurat R package, normalization was performed using the SCTransform function, accounting for both normalization and variance stability across FOVs and batches. Cell clustering was performed using Seurat's PCA and UMAP embedding function. To define cell types found within UMAP clusters generated, B cells (CD20, CD19, IgD), T cells (CD3, CD4, CD8), dendritic cells (CD11b, CD11c, CD123) and B7-H3 probe expression were visualized. Additionally, top differentially expressed markers per cluster were extracted, and co-expression was visually confirmed across the appropriate samples. Several B cell, T cell and dendritic cell heavy clusters were observed, these were combined. This generated 3 overall clusters with heavy B cell, T cell and dendritic cell signatures. Multiple B7-H3 clusters were generated associated with other top expressing markers, these clusters were kept separate.

### 2.6.7 Cluster density

Seurat clusters were filtered to only include B cell, T cell, dendritic call and B7-H3 related clusters and overall density was explored. Boxplots were generated using R package ggplot2, and statistical analysis performed using a Kruskal-Wallis test with significance threshold set to $p \leq 0.05$.

### 2.6.8 Nearest neighbour

Nearest neighbour was performed as outlined in 2.3.3.3. This was carried out on the filtered cluster data set, focused on B7-H3 nearest neighbours and visualised using R package ComplexHeatmap.

### 2.6.9 Survival analysis

Survival analysis was performed for filtered clustering data for both the Glasgow naïve cohort 2 (chapter 2.1.1.4) and neoadjuvant combined cohort (chapter 2.1.1.7) (table 2.17). Survival analysis and cut-offs were generated as outlined in chapter 2.3.3.1.

**Survival cut-off for most significant phenotype density in disease specific survival**

| Variable | Region | Treatment | Cohort | Time (months) | Group | Number | Cut-off method | Cut-off point | Rank number |
|---|---|---|---|---|---|---|---|---|---|
| CD4 T cell cluster | Whole core | Naïve | Glasgow cohort 1 | DSS | All patients | 38 | Rcutoff | 161 | High - 13<br>Low - 25 |
| CD8 T cell cluster | Whole core | Naïve | Glasgow cohort 1 | DSS | All patients | 38 | Rcutoff | 18 | High - 27<br>Low - 11 |
| B7-H3 cluster 12 | Whole core | Naïve | Glasgow cohort 1 | DSS | All patients | 38 | Rcutoff | 38 | High - 12<br>Low - 23 |
| CD4 T cell | Whole core | Neoadjuvant | Neoadjuvant combined | DSS | All patients | 58 | Rcutoff | 130 | High - 31<br>Low - 27 |
| CD8 T cell | Whole core | Neoadjuvant | Neoadjuvant combined | DSS | All patients | 58 | Rcutoff | 31 | High - 39<br>Low - 19 |
| B7-H3 cluster 4 | Whole core | Neoadjuvant | Neoadjuvant combined | DSS | All patients | 58 | Rcutoff | 133 | High - 30<br>Low - 23 |
| B7-H3 cluster 27 | Whole core | Neoadjuvant | Neoadjuvant combined | DSS | All patients | 58 | Rcutoff | 3 | High - 38<br>Low - 15 |

**Table 2.16 Cutoff scores for Kaplan-Meier DSS analysis.** *Summary table illustrates the markers and their associated cut-off method and cut-off point per time variable, disease specific survival (DSS). Number of patients generated per rank is indicated by rank number column. Table is limited to markers that are frequently referred to throughout the thesis.*

All RStudio analysis was performed on version 4.3.2 (RStudio, Boston, MA, USA). A wide range of packages were implemented for analysis, the most relevant ones are mentioned above. HALO® version 3.0.311 was used for IHC analysis, VISIOPHARM® version 2021.09.2.10918 and QuPath version 0.4.0 was used for mIF image analysis, and CytoMAP version 1.4.21 was used for unbiased phenotyping and neighbourhood analysis.

# 3 Chapter 3: Deep immune phenotyping in naïve human pancreatic ductal adenocarcinoma

## 3.1 Introduction

Pancreatic cancer is the 5th most common cancer in the UK, accounting for 6% of all cancer deaths. The 5 year survival remains dismal at <7%, with limited improvements seen in the last 50 years [1, 2]. Increased research into this disease has resulted in biological insights robustly established such as molecular subtypes. Characterisation of the tumour immune cell microenvironment in pancreatic cancer has been limited by multiple factors including technology and tissue access. Of the work undertaken, the vast majority of papers focus heavily on the same cell types, namely T cells and macrophages, and limited to exploration of naïve patients [8, 141, 167, 182, 218]. This is most likely due to the difficulty in acquiring neoadjuvant tissue. Naïve patients have not been treated with neoadjuvant chemotherapy or chemoradiotherapy, and have undergone upfront resection. Of these naïve patients, most have had adjuvant therapy that was either FOLFIRINOX or Gemcitabine based.

The PDAC landscape is traditionally thought of being immune barren making it difficult to study. However, new technologies that allow high-plex phenotyping have enabled the TME to be studied with a view to discovering new biomarkers [177, 219-223]. Fibroblast, macrophage and T cell populations are by far the most prevalent populations in pancreatic cancer, and therefore have been studied most [8, 141, 167, 182, 186, 194, 209, 218, 224]. Recently, B cell interactions with T cells in cancer have gained popularity, particularly when investigating tertiary lymphoid structures [201, 225-227]. Immunohistochemistry, using FFPE tissue, has been the gold standard technique used to study immune cell protein expression. [228]. Although other technologies such as Mass Spectrometry have also been routinely used, IHC is largely more popular and is easily translatable to the clinic [229].

T lymphocytes are a major player in the adaptive immune pathway. Originating from bone marrow progenitor and maturing in the thymus into either CD4+ or CD8+ cells, they are released into the periphery as naïve T cells, and subsequently differentiate into either cytotoxic effector cells (CD8+), helper effector cells (CD4+) and regulatory cells (FOXP3+) [230]. Cytotoxic effector cells are associated with apoptosis of antigen presenting MHC-I cells, and increased expression of these cells is consistently positively correlate with increase survival in treatment naïve PDAC patients [8, 182, 231, 232]. Helper effector cells (CD4+) are associated with almost every adaptive immune response, activating B cell, CD8 cells and macrophages, and secretion of a range of cytokines resulting in pro-inflammatory, anti-inflammatory and regulatory functions [233]. These cells tend to correlate positively with survival, however specific subtyping would be beneficial as the regulatory subtype is also part of the helper T cell umbrella [8, 182, 234]. Regulatory T

cells, as the name indicates, regulate the immune cells, in theory to help prevent chronic inflammation. This results in reducing anti-tumour immunity in pancreatic cancer, and correlate with worse survival [235]. Macrophages play a significant role in the innate immune pathway, and originate from haematopoietic cells [236]. Multiple pathways of differentiation into macrophages have been hypothesized. A school of thought is the polarization of macrophages according to their external environment into either M1 (classically activated) or M2 (alternatively activated) subsets [178]. This hypothesize has been criticised by immunologists for being reductive, it may be beneficial to refer to subsets by their marker expression. CD68 macrophages are involved in phagocytosis, however the role is yet to be fully determined. Nonetheless, high expression of these cells is associated with worse prognosis in PDAC [237, 238]. Fibroblasts are located within the extracellular matrix, where they secrete a vast array of macromolecules that create and maintain this structural network [154]. There are 3 distinct cancer associated fibroblasts, with alpha smooth muscle actin (αSMA) expression commonly being used to phenotype myofibroblasts, which are normally responsible for wound contraction [190]. Continued expression of these cells results in fibrosis, correlating with a dense fibrotic stroma in PDAC which is linked to poor survival [163, 193]. The vast majority of studies have focused on the cellular density of these immune cells, with a new drive to maintain spatial interactions.

## 3.2 Aims

To first establish the prognostic value of T cell and macrophage subsets using singleplex immunohistochemistry in naïve pancreatic cancer. Explore the spatial immune cell landscape in terms of T cell, macrophage, and fibroblast content, density, and spatial orientation. Distinct histopathological regions for tumour and stroma explored when appropriate. The immune landscape will be characterised first with consideration given to appropriate clinical subgroups.

## 3.3 Clinical cohorts

Naive cohort consisted of a total of 436 pancreatic cancer specimens (table 3.1). These were split into discovery (n = 244) and validation (n = 192) cohorts. Median survival for these patients was 23 months for discovery, 18.5 months for validation, and 20.3 months for naïve combined cohorts. The naïve Glasgow cohort (n=28) refers to the subgroup of naïve patients used, median survival was approximately 17.2 months. Associated clinical data is found in chapter 2.1.

| Study | Cohort name | TMA | TMA number | Patient number | Treatment type |
|---|---|---|---|---|---|
| PhenoImager 7 plex assay | Discovery | APGI/ICGC TMA | 8 | 244 | Naïve |
| | | SD-PAN-TMA | 1 | | |
| | Validation | PDAC-PAN-TMA | 5 | 192 | Naïve |
| | | NJ-PANC-TMA | 7 | | |
| | Naïve combined | APGI/ICGC TMA | 8 | 436 | Naïve |
| | | SD-PAN-TMA | 1 | | |
| | | PDAC-PAN-TMA | 5 | | |
| | | NJ-PANC-TMA | 7 | | |
| GeoMx DSP Immune-oncology protein assay | Naïve Glasgow 1 | SD-PAN-TMA | 1 | 28 | Naïve |

**Table 3.1 Naïve clinical cohorts and associated study.** *Summary table showing the study and associated TMAs used, patients number and treatment type. The cohort name column refers to the cohort name in chapter 2.1.*

## 3.4 T cell signature offers prognostic value in naïve PDAC

Immunohistochemistry (IHC) is a robust method, routinely used to investigate immune populations in cancer (figure 3.1.a). T lymphocytes and macrophages, perhaps amongst the most popular immune cell populations, are routinely explored in pancreatic cancer using this gold standard method, with elevated T cell levels and reduced macrophages correlating with prognostic benefit. This was used to establish these subsets within treatment naïve pancreatic cancer. A naïve PDAC cohort (discovery cohort) was characterised using CD8, CD3, CD68 and CD163 single plex chromogenic staining. The digital imaging platform HALO® was used to score the sections. Survival analysis was

performed showing favourable prognosis associated with increased CD8+ (p=0.043) and CD3+ (p=0.015) (figure 3.1.b-c). Next, any association between immune infiltration and pattern of recurrence was investigated. Patients with no recurrence within 24 months of diagnosis demonstrated elevated CD3+ (p=0.009). Conversely, patients with liver metastasis, traditionally associated with aggressive disease, had elevated CD68+ expression (p=0.034) (figure 3.1.d). Furthermore, patients who developed liver metastasis recurred significantly quicker than all other recurrence patterns (p<0.001) (figure 3.1.e).

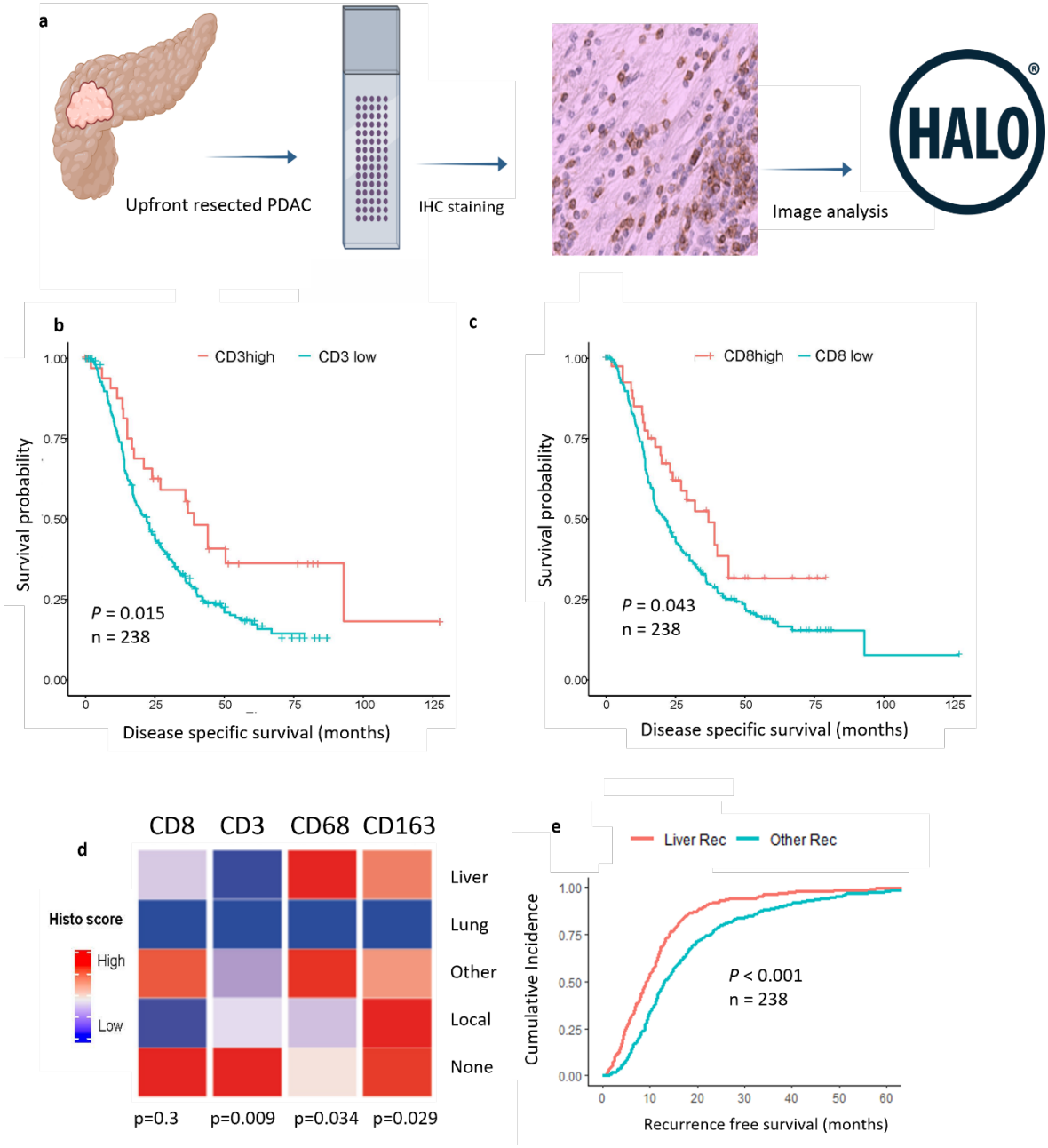


**Figure 3.1 Immunohistochemistry on naïve cohort** *a). Overview from resection to data analysis for IHC. Kaplan-Meier curves (disease specific survival) stratified by IHC protein marker expression (Log-Rank test) for b). CD3 and c). CD8 d). Immune cell density heatmap using Histoscores per recurrence pattern with Kruskal-Wallis test e). Fine Gray model looking at probability of recurrence over time for liver recurrence vs rest. Cut-off method established per variable (chapter 2.2.3)*

## 3.5 Deep phenotyping and cellular density landscape in naïve pancreatic cancer

Single plex IHC demonstrates high levels of T cell related markers had prognostic value. To further investigate cell-to-cell interactions, a 7 plex immunofluorescence panel was generated using Akoya Biosciences® PhenoImager™ to stain multi-regional treated naive Discovery (n=244) and Validation (n=192) TMA cohorts (table 3.1). The panel consisted of an epithelial tumour marker PanCk (AE1/AE3), an omnipresent T cell receptor marker CD3, cytotoxic T cell marker CD8, T regulatory marker FOXP3, pro-inflammatory macrophage marker CD68, myofibroblast marker αSMA, and DAPI as a counter stain (figure 3.2.a). Cells were phenotyped according to either single or co-localisation of markers. Phenotypes observed were (figure 3.2.b);

1. αSMA+ fibroblasts
2. CD3+CD8- T cells
3. CD3CD8+ cytotoxic
4. CD8+ cells
5. FOXP3CD3+ T regulatory cells
6. CD68+ macrophages
7. PanCk+ cancer cells

Biologically, cytotoxic T cells should always co-express both CD3 and CD8, therefore single expressing CD8+ cells could be indicative of a natural killer cell subtype, or due to limitations of the assay.

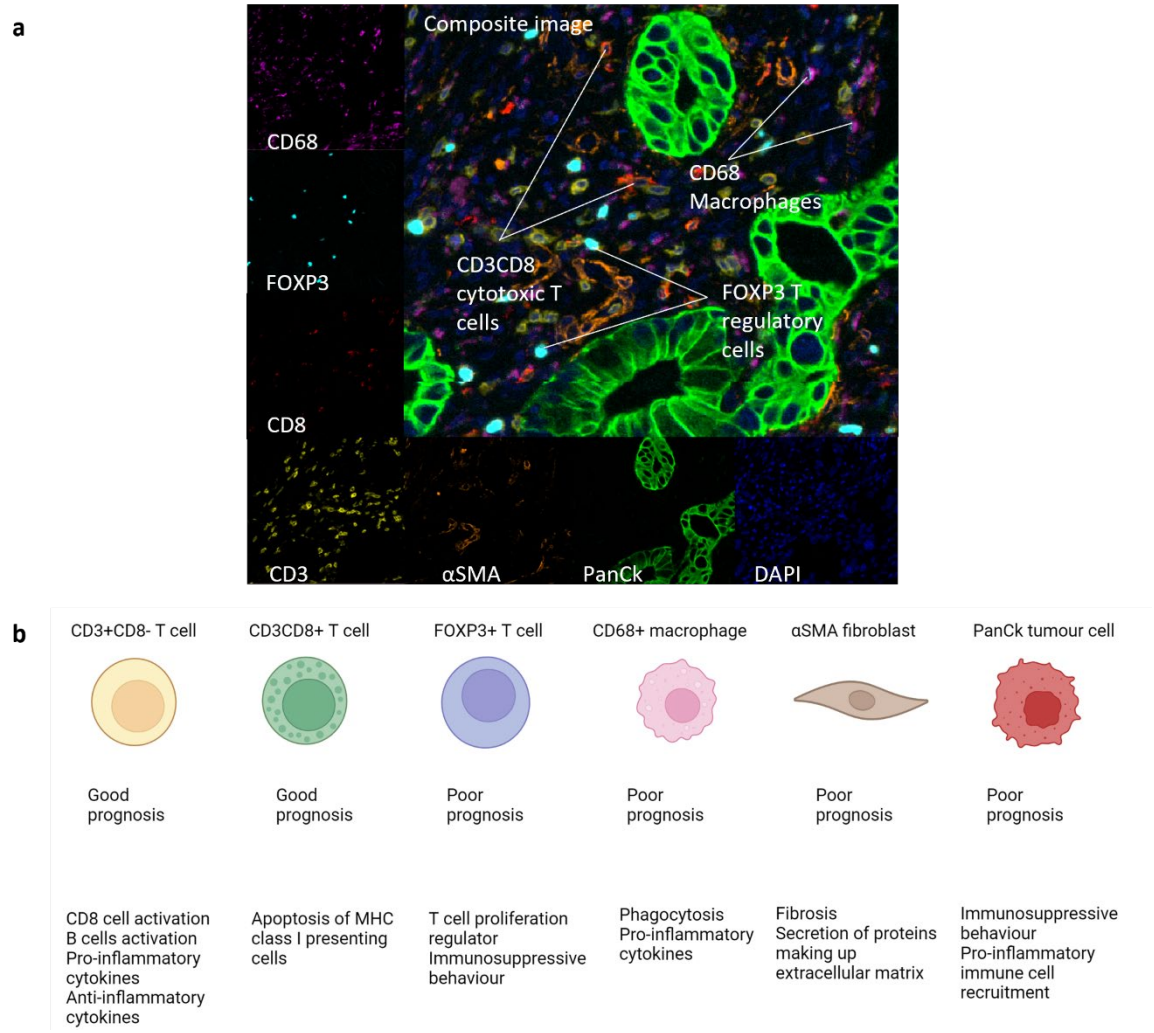


**Figure 3.2 Phenotyped cell population within mIF panel**. *a). Example of mIF panel on naïve core stained for DAPI, PanCk, αSMA, CD3, CD8, FOXP3 and CD68 b). schematic diagram showing the phenotyped immune cells explored in pancreatic cancer, main associated functions and the overarching prognostic relevance*

Total cell content for combined discovery and validation cohorts was measured to establish a base immune landscape in treatment naïve patients (table 3.1). Overall, the highest cell populations observed in naïve pancreatic, as expected, were PanCk+ and αSMA+ cells (figure 3.3.a). When considering only the immune subset, the highest cell population was CD3+ and CD68+ cells and the lowest cell population was FOXP3CD3+ population (figure 3.3.a). When patients were sub-categorised by molecular subtype, CD3+ levels were found to be significantly elevated (p=0.04) in classical naïve PDAC patients (figure 3.3.b).

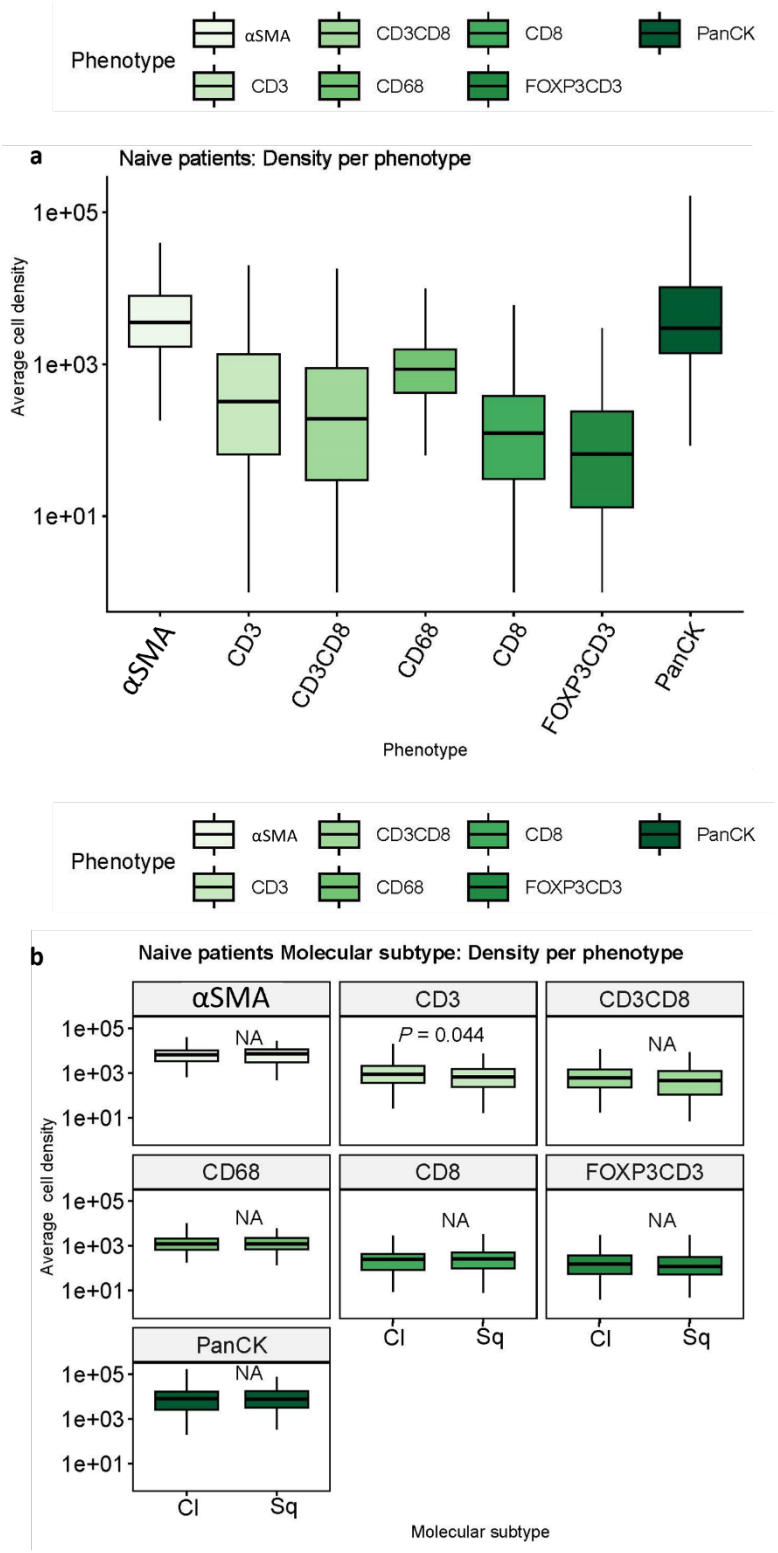


**Figure 3.3 Average cellular density boxplots of phenotypes in combined naïve pancreatic cohort** *across a). All patients, n=436 b). Molecular subtypes classical (Cl) (n=141) and squamous (Sq) (n=62) using Bonferroni p adjusted T-test*

## 3.6 Immune Cell density associates with survival in naïve PDAC

Validation of the predictive power of CD3+ as seen in previous IHC analysis (chapter 3.4) was observed in discovery (p=0.004) and validation (p=0.011) cohorts (table 3.2). In addition, elevated CD3CD8+ (p=0.001) was also prognostic in the discovery cohort (table 3.2). Elevated CD3+ (p=0.008) and CD3CD8+ (p=0.001) correlated with recurrence free survival (RFS) in the discovery cohort (table 3.2). Furthermore, a reduction in CD68+ cells in the discovery cohort was significantly associated with DSS (p=0.008) and RFS (p=0.02), with the RFS trend replicated in the validation cohort (table 3.2). The TMA core into tumour and TME compartments were investigated for compartment specific markers associated with prognosis. In TME discovery compartments, elevated FOXP3CD3+ correlated with disease specific (p=0.049) and recurrence free (p=0.03) survival (table 3.2). Within the discovery cohort molecular subtype groups, an enriched CD3+ and CD3CD8+ density in classical subtype naïve patients correlated with better disease specific and recurrence free survival (table 3.2). Conversely, reduced density of CD68+ in squamous patients was observed in those with better survival (table 3.2). This trend was not replicated in the validation cohort.

| Phenotype density in discovery and validation for disease specific and recurrence free survival | | | | | | | | |
|---|---|---|---|---|---|---|---|---|
| **Phenotype** | **Region** | **Cohort** | **Time (months)** | **Group** | **Cut-off method** | **Number** | **HR (95% CI)** | **P value** |
| CD3 | Whole core | Discovery | DSS | All patients | LQ | 238 | 0.61 (0.44-0.85) | 0.004 |
| CD3CD8 | Whole core | Discovery | DSS | All patients | LQ | 238 | 0.58 (0.41-0.81) | 0.001 |
| CD68 | Whole core | Discovery | DSS | All patients | LQ | 238 | 1.60 (1.13-2.27) | 0.009 |
| FOXP3CD3 | TME | Discovery | DSS | All patients | LQ | 238 | 0.72 (0.51-1.00) | 0.045 |
| CD3 | Whole core | Discovery | DSS | Classical | LQ | 122 | 0.53 (0.33-0.85) | 0.008 |
| CD3CD8 | Whole core | Discovery | DSS | Classical | LQ | 122 | 0.53 (0.33-0.86) | 0.009 |
| PanCk | Whole core | Discovery | DSS | Squamous | LQ | 53 | 2.19 (1.01-4.78) | 0.048 |
| CD68 | Whole core | Discovery | DSS | Squamous | LQ | 53 | 2.39 (1.14-5.03) | 0.021 |
| CD3 | Whole core | Discovery | RFS | All patients | LQ | 238 | 0.64 (0.46-0.89) | 0.008 |
| CD3CD8 | Whole core | Discovery | RFS | All patients | LQ | 238 | 0.56 (0.40-077) | 0.001 |
| CD68 | Whole core | Discovery | RFS | All patients | LQ | 238 | 1.53 (1.08-2.17) | 0.016 |
| FOXP3CD3 | TME | Discovery | RFS | All patients | LQ | 238 | 0.69 (0.50-0.96) | 0.03 |
| CD3 | Whole core | Discovery | RFS | Classical | LQ | 122 | 0.59 0.37-0.94) | 0.027 |
| CD3CD8 | Whole core | Discovery | RFS | Classical | LQ | 122 | 0.49 (0.30-0.78) | 0.003 |
| CD68 | Whole core | Discovery | RFS | Squamous | LQ | 53 | 3.35 (1.56-7.21) | 0.002 |
| CD3 | Whole core | Validation | DSS | All patients | LQ | 192 | 0.66 (0.48 -0.91) | 0.011 |
| CD68 | Whole core | Validation | RFS | All patients | LQ | 192 | 1.42 (1.00 - 2.03) | 0.05 |

**Table 3.2 Summary of density-based biomarkers in for disease specific and recurrence free survival in discovery and validation cohorts in whole core and TME segments**. *Cut-off method established per phenotype (chapter 2.3.3.3) in discovery cohort. Pattern reported per phenotype, region and patient group indicated, along with number of patients in each group. Log Rank (Mantel-Cox) p value and Univariate cox regression hazard ratio (HR) shown with 95% confidence interval (CI).*

## 3.7 Density interaction between phenotypes in naïve pancreatic cancer

Until recently, protein characterisation of immune cells in PDAC has predominantly been conducted via IHC methods. Studies have reported on the generation of numerous profiles for different immune cells resulting in the production of cell ratios that appear to perform better than cell density alone. Within the combined naive cohort (table 3.1), phenotypes were ranked into low or high and all possible pairs were tested. Log-rank survival analysis on overall survival of a ratio was performed, then pairwise comparison was performed to look at inter-curve differences between the different ranks within the same ratio. Multiple trends were seen. The proportion of PanCk+ and CD3+ cells significantly correlated with survival ($p<0.001$) in naive patients (figure 3.4.a), revealing patients with CD3high/PanCklow proportions did better than those with CD3low/PanCkhigh ($p=0.013$) and CD3low/PanCklow ($p=0.008$) (table 3.3). Surprisingly, CD3high/PanCkhigh patients did relatively well, outperforming CD3low/PanCkhigh ($p=0.008$) (table 3.3). Additionally, levels of CD3 and Tregs associated with survival (Log Rank $p<0.001$) (figure 3.4.c), CD3low/FOXP3CD3low naïve patients were associated with poor survival compared to CD3high/FOXP3CD3high ($p=0.001$) and CD3low/FOXP3CD3high ($p=0.02$) (table 3.3). Significant differences were also observed between CD3 helper T cell and macrophages proportions ($p<0.001$) (figure 3.4.b), with CD3high/CD68low patients outperforming all other ratios in terms of disease specific survival (table 3.3).

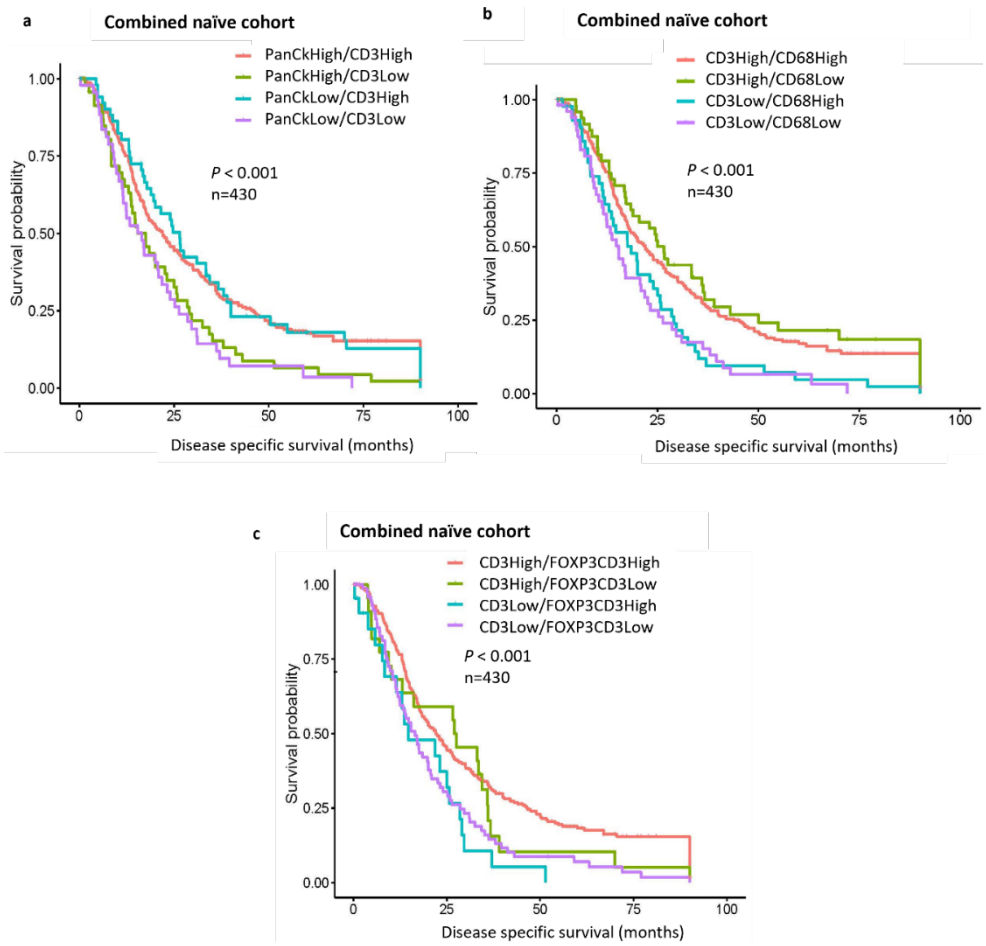


**Figure 3.4 Survival analysis of naïve cellular density ratio** *Kaplan-Meier curves (disease specific survival) stratified by ratio expression in combined treatment naïve PDAC (Log-Rank test) for a). PanCk/CD3 ratio b). CD3/CD68 ratio c). CD3/FOXP3CD3.*

| Ratio pair | Ratio comparison group 1 | Ratio comparison group 2 | P value |
|---|---|---|---|
| CD3/CD68 | CD3High/CD88Low | CD3High/CD68High | 0.329 |
| | CD3Low/CD68High | CD3High/CD68High | 0.329 |
| | CD3Low/CD68Low | CD3High/CD68High | 0.004 |
| | CD3Low/CD68High | CD3High/CD68Low | 0.010 |
| | CD3Low/CD68Low | CD3High/CD68Low | 0.004 |
| | CD3Low/CD68Low | CD3Low/CD68High | 0.586 |
| PanCk/CD3 | PanCkHigh/CD3Low | PanCkHigh/CD3High | 0.008 |
| | PanCkLow/CD3High | PanCkHigh/CD3High | 0.586 |
| | PanCkLow/CD3Low | PanCkHigh/CD3High | 0.007 |
| | PanCkLow/CD3High | PanCkHigh/CD3Low | 0.014 |
| | PanCkLow/CD3Low | PanCkHigh/CD3Low | 0.586 |
| | PanCkLow/CD3Low | PanCkLow/CD3High | 0.008 |
| CD3/FOXP3CD3 | CD3High/FOXP3CD3Low | CD3High/FOXP3CD3High | 0.513 |
| | CD3Low/FOXP3CD3High | CD3High/FOXP3CD3High | 0.021 |
| | CD3Low/FOXP3CD3Low | CD3High/FOXP3CD3High | 0.001 |
| | CD3Low/FOXP3CD3High | CD3High/FOXP3CD3Low | 0.186 |
| | CD3Low/FOXP3CD3Low | CD3High/FOXP3CD3Low | 0.284 |
| | CD3Low/FOXP3CD3Low | CD3Low/FOXP3CD3High | 0.513 |

**Table 3.3 Pairwise comparison between naïve cellular density ratios** *taken from Kaplan Meier*

*plots above (figure 3.6) ratio pairs are CD3/CD3CD8, PanCk/CD3 and CD3/FOXP3CD3. Log Rank (Mantel-Cox) pairwise comparison over strata.*

## 3.8 Single cell spatial analysis in the PDAC TME

After cellular content and density was established above, the differences in the spatial relationship between phenotypes in relation to clinical parameters was investigated. Two broad types of spatial analysis were explored, single cell analysis and clustering analysis. These analysis methods provide ideal tools for the data generated in the multiplex assay, allowing for deep immune characterisation of the TME. Three major forms of analysis were used, nearest neighbour, mutual nearest neighbour and radius distances.
Nearest neighbour (NN) analysis calculates the nearest neighbour of individual cells to a specific phenotype in a set distance e.g., distance of cell x to cell y. This can be used to estimate cell-cell interactions. It is important to note, this analysis does not compute mutual nearest neighbours. For example, if the nearest neighbour from cell X, was found to be cell Y, this doesn't mean the inverse relationship is the same, e.g. nearest neighbour from cell y might be cell Z (figure 3.5.a). Mutual nearest neighbour analysis can be thought of as a branch of NN, this solely looks at pairs of cells which are mutually neighbours (figure 3.5.b). Radius analysis explores the density of cell Y from a named cell X at a set distance from X e.g. number of CD68+ cells at 30μm from CD3+ cells (figure 3.5.c). As this metric works best with incremental distances, filtering for segments was avoided to prevent too many phenotypes from being discarded. 10μm increments were set from 0-50μm, then anything above 50μm was pooled together. This type of analysis produces vast amounts of significant data, later steps in the analysis pipeline provide robust filtering and marker selection.

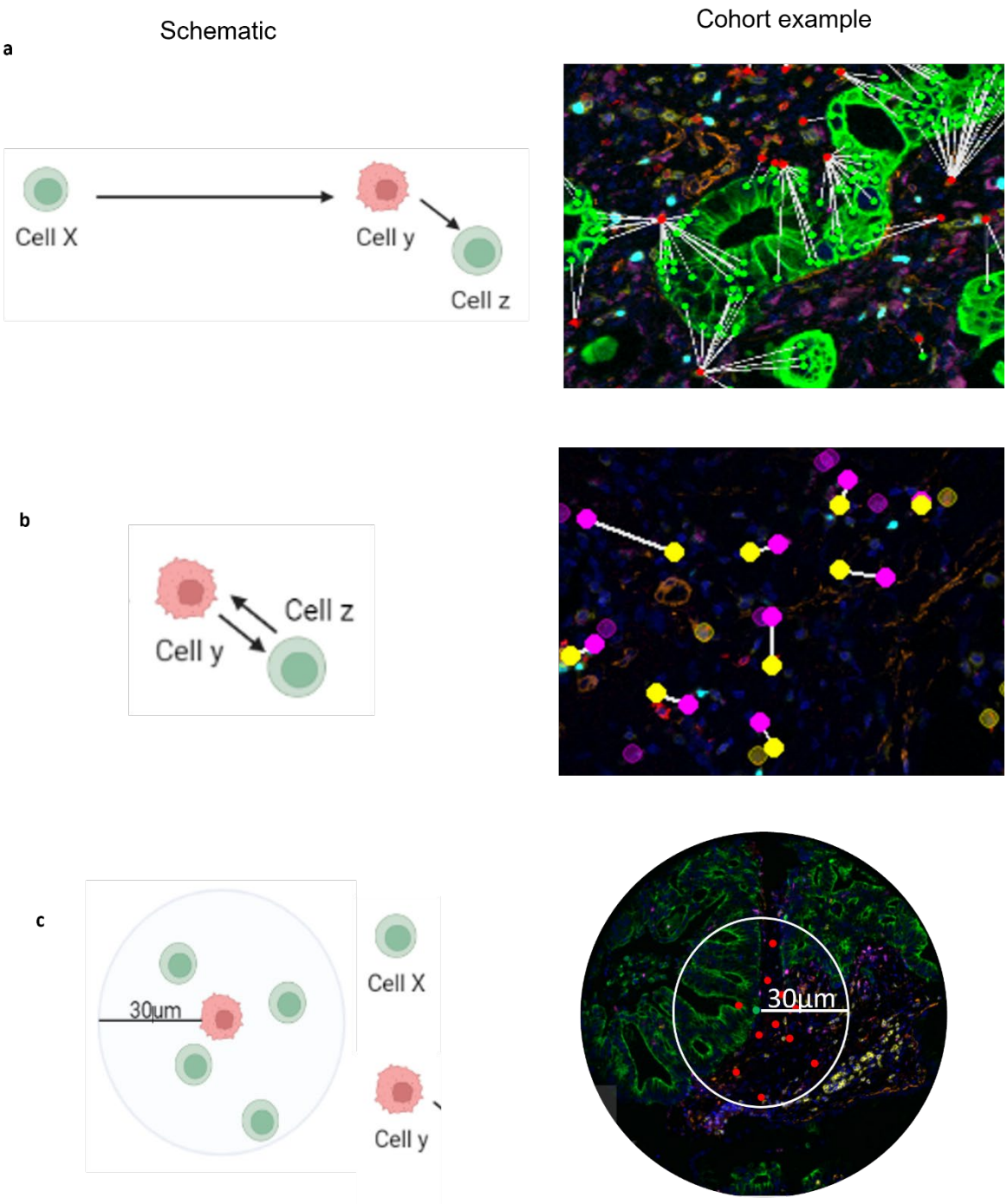


**Figure 3.5.a-c Schematic and real life examples of single cell spatial analysis in naïve PDAC** *a). Nearest neighbour analysis schematic calculates the distance of the nearest type from a cell e.g., cell X nearest neighbour is cell Y, but cell Z is cell Y nearest neighbour. Cohort example shows naïve core distance from PanCk+ (green dots) to CD3CD8+ (red dots) b). Mutual nearest neighbour analysis schematic calculates the distance between the mutual nearest neighbour pairs. Cohort example CD68+ (magenta dots) and CD3+ (yellow dots) mutual nearest neighbour c). Radius analysis schematic calculates density of cells from the chosen central cell type at a given radii e.g., density of cell X at 30µm from cell Y. Cohort example shows density of CD3CD8+ (red dots) from PanCk+ (green dots), images not to scale.*

### 3.8.1 Prognostically favourable nearest neighbour tumour immune landscape in all treatment naïve patients

To determine the level of interaction between phenotypes, the average distance between all phenotypes was explored. Average distance demonstrated tumour cells tended to be further away from CD3CD8+, CD3+ and FOXP3CD3+ T cells, with CD68+ and αSMA+ cells closest to tumour cells. This indicates the reduced likelihood of tumour cells interacting with CD3 helper and CD3CD8 cytotoxic T cells, and increased chances of interacting with immunosuppressive immune cells instead (figure 3.6).

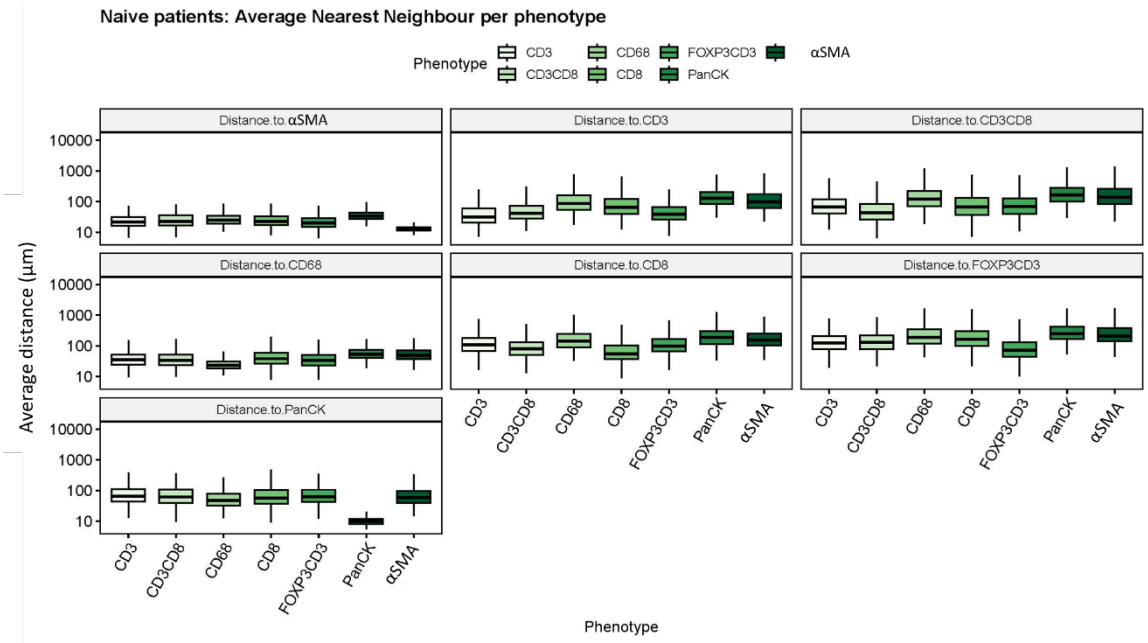


**Figure 3.6 Average nearest neighbour distance of combined naïve pancreatic cohort.** *Boxplots are faceted by distance to phenotype, with each 'from' phenotype displayed along the x axis, and average distance in µm along the y axis.*

Cellular density, although prognostically relevant, fails to provide insight into cell-to-cell patterns. Nearest neighbour analysis was performed to establish the significant interacting phenotypic relationships within naïve pancreatic cancer, this was carried out separately on the discovery and validation cohorts (table 3.1). Naïve patients with highest survival were associated with low distances from PanCk+ to CD8+ (p=0.004), and high distances to αSMA+ cells (p=0.022). Increased distance from CD3+ to αSMA+ (p=0.023) and from CD3CD8+ to PanCk+ (p=0.019) also associated with improved prognosis (table 3.4). These patterns were replicated in the validation cohort (table 3.4). Furthermore, increased distance to αSMA+ (p=0.019) from CD3CD8+ cells in TME compartments of naïve patients positively correlated with survival in the discovery cohort. New prognostic relationships emerging from tissue segment analysis further reinforces the need to carry

out extensive spatial analysis in highly heterogenous solid cancers like PDAC. CD68 associated nearest neighbour relationships had by far, the most number of trends. Naive patients with increased distances from CD68+ to PanCk+ (p=0.005), and short distances to CD3+ (p<0.001) and to CD3CD8+ (p=0.005) demonstrated improved survival (table 3.4). The sheer number of nearest neighbour relationships demonstrated reveals the extent of which macrophages interact with neighbouring cells and the potential influences they have on each other.

| Nearest neighbour trends in disease specific survival in naive cohorts | | | | | | | |
|---|---|---|---|---|---|---|---|
| **Nearest neighbour pattern** | **Region** | **Cohort** | **Group** | **Cut-off method** | **Number** | **HR (95% CI)** | **P value** |
| Distance to αSMA from PanCk | Whole core | Discovery | All patients | LQ | 233 | 0.67 (0.48 - 0.95) | 0.022 |
| Distance to CD8 from PanCk | Whole core | Discovery | All patients | LQ | 233 | 1.75 (1.20-2.55) | 0.004 |
| Distance to CD3 CD8 from αSMA | Whole core | Discovery | All patients | UQ | 233 | 1.42 (1.01-1.99) | 0.045 |
| Distance to CD3 from αSMA | Whole core | Discovery | All patients | UQ | 233 | 1.7 (1.22-2.38) | 0.002 |
| Distance to αSMA from CD3 | Whole core | Discovery | All patients | Med | 233 | 0.7 (0.52-0.95) | 0.023 |
| Distance to PanCk from CD3CD8 | Whole core | Discovery | All patients | Med | 233 | 0.69 (0.51-0.94) | 0.019 |
| Distance to PanCk from CD68 | Whole core | Discovery | All patients | Med | 233 | 0.64 (0.47-0.87) | 0.005 |
| Distance to CD3CD8 from CD68 | Whole core | Discovery | All patients | Med | 233 | 1.56 (1.15-2.11) | 0.004 |
| Distance to CD3 from CD68 | Whole core | Discovery | All patients | Med | 233 | 1.73 (1.28-2.35) | <0.001 |
| Distance to αSMA from CD3CD8 | TME | Discovery | All patients | Med | 233 | 1.43 (1.06-1.94) | 0.019 |
| Distance to αSMA from PanCk | Whole core | Validation | All patients | LQ | 192 | 0.71 (0.51-0.99) | 0.040 |
| Distance to CD8 from PanCk | Whole core | Validation | All patients | LQ | 192 | 0.65 (0.46-0.92) | 0.017 |
| Distance to CD3CD8 from αSMA | Whole core | Validation | All patients | UQ | 192 | 1.45 (1.06-1.98) | 0.020 |
| Distance to CD3 from αSMA | Whole core | Validation | All patients | UQ | 192 | 1.87 (1.12-3.12) | 0.016 |
| Distance to PanCk from CD3CD8 | Whole core | Validation | All patients | Med | 192 | 0.62 (0.45-0.85) | 0.003 |
| Distance to PanCk from CD68 | Whole core | Validation | All patients | Med | 192 | 0.59 (0.42-0.83) | 0.002 |
| Distance to CD3CD8 from CD68 | Whole core | Validation | All patients | Med | 192 | 1.60 (1.12-2.30) | 0.011 |
| Distance to CD3 from CD68 | Whole core | Validation | All patients | Med | 192 | 1.83 (1.33-2.53) | <0.001 |

**Table 3.4 Nearest neighbour patterns associated with disease specific survival in naïve cohorts looking at whole core and stromal tissue segments**. *Cut-off method established per pattern (chapter 2.3.3.3) in discovery cohort and replicated in validation cohort. Nearest neighbour pattern reported per cohort and region, patient group indicated, along with number of patients in each group. Log Rank (Mantel-Cox) p value and Univariate cox regression hazard ratio (HR) shown with 95% confidence interval (CI).*

Classical subtypes are traditionally associated with a higher immune infiltration. These findings have mostly come from IHC and RNA studies, with few spatially resolved metrics being described. The patterns seen in subtyped patients with better outcomes is described below. When taking subtype into consideration, high survival Classical subtypes demonstrated shorter distance from αSMA+ to CD3+ cells (p=0.031) (supplementary table 8.1). Furthermore, patients with improved survival and longer recurrence free survival demonstrated reduced distances from CD68+ to CD3+ (p<0.001 and p=0.004), and from CD68+ to CD3CD8+ (p<0.001 and p=0.002) (supplementary table 8.1). Different trends

were observed in Squamous subtypes. Increased distance from PanCk+ to CD68+ (p=0.018 and p=0.033) associated with improved survival and longer recurrence free survival, as well as large distance from CD68+ to CD3CD8+ cells correlating significantly with better DSS (p=0.046) (supplementary table 8.1).

### 3.8.2 Prognostically favourable mutual nearest neighbour pairs in the tumour immune landscape in treatment naïve patients

Mutual nearest neighbour analysis branches  from nearest neighbour, consequently many of the results seen should replicate those seen in NN, but with an added layer of classifying the distance in both directions. To establish the overarching phenotype interactions in naïve PDAC, the highest density pairs and their spatial relationship was investigated. Of note, the closest mutual neighbour to tumour cells was CD68+ and αSMA+ and macrophages were closest with αSMA. Additionally, the furthest CD3 T cell pair were tumour cells (figure 3.7). This reveals an immune suppressive and fibrotic environment surrounding tumour cells, with any potential beneficial T cell effect not reaching the tumour core.

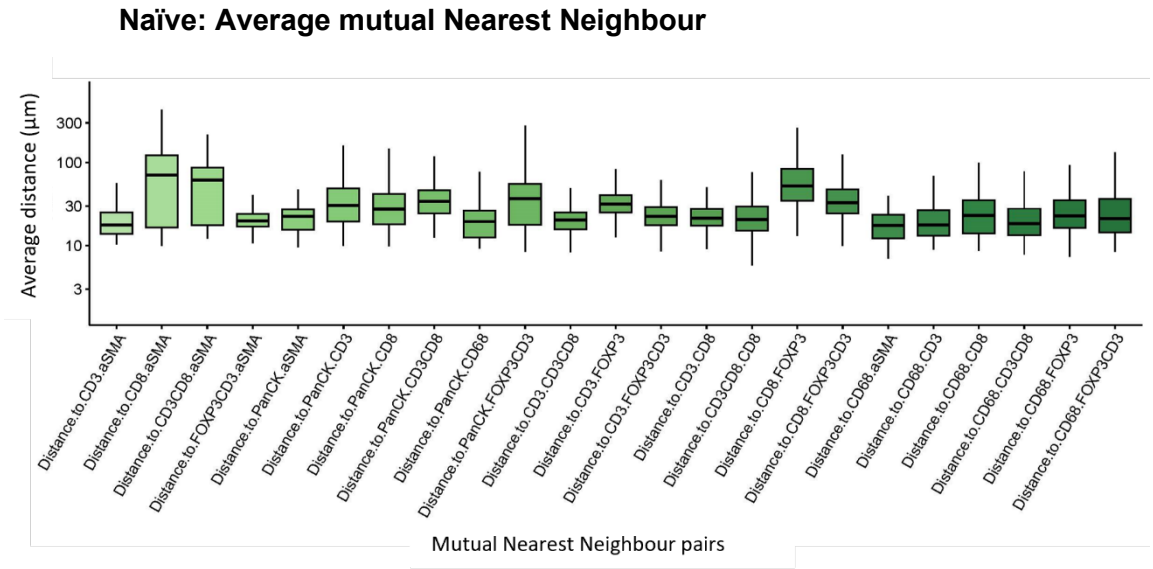


**Figure 3.7 Average mutual nearest neighbour distance of combined naïve pancreatic cohort.** *Boxplots shows the mutual relationship displayed along the x axis, and average distance in µm along the y axis.*

Naïve pancreatic cancer patients with better prognosis presented with large distances between PanCk-αSMA (p=0.040) and PanCk-CD68 (p=0.025) (table 3.5). Likewise naïve patients with longer survival associated with larger distances between αSMA-FOXP3CD3 (p=0.033) and CD3-αSMA (p=0.052) (table 3.5). These findings help confirm phenomena seen within naïve nearest neighbour findings. The pancreatic TME has a meaningful role indicated by the prognostic patterns seen in the naïve setting, with distance metrics playing an important role.

| Mutual nearest neighbour trends in disease specific survival in naive cohorts | | | | | | | |
|---|---|---|---|---|---|---|---|
| **Mutual nearest neighbour pair** | **Region** | **Cohort** | **Group** | **Cut-off method** | **Number** | **HR (95% CI)** | **P value** |
| Distance between PanCK and CD68 | Whole core | Discovery | All | Rcutoff | 233 | 0.70 (0.51-0.96) | 0.025 |
| Distance between FOXP3CD3 and αSMA | Whole core | Discovery | All | Rcutoff | 233 | 0.68 (0.48-0.97) | 0.033 |
| Distance between PanCK and αSMA | Whole core | Discovery | All | Rcutoff | 233 | 0.72 (0.52-0.99) | 0.040 |
| Distance between CD3 and αSMA | Whole core | Discovery | All | Rcutoff | 233 | 0.73 (0.53-1.00) | 0.052 |

**Table 3.5 Mutual nearest neighbour patterns associated with disease specific survival in naïve cohorts.** *Cut-off method per pair, region and patient group indicated, along with number of patients in each group. Log Rank (Mantel-Cox) p value and Univariate cox regression hazard ratio (HR) shown with 95% confidence interval (CI).*

### 3.8.3 Prognostically favourable tumour immune landscape in all treatment naïve patients at different radii

Radius analysis has the unique property of incorporating density of cells with distance metrics. To avoid this metric from turning into solely density based, the radii of focus was 0µm-50µm. The average surrounding immune cell population for all phenotypes within the immediate environment was defined as 50µm radius from the central cell. The immediate microenvironment of tumour cells was densely populated with αSMA fibroblasts and CD68 macrophages, in contrast limited cytotoxic T cells were present (figure 3.8). Additionally, in the surrounding macrophage environment, high numbers of tumour cells, αSMA fibroblasts and CD3 T helper were observed. This was confirmed when looking at the immediate cytotoxic T cell microenvironment, showing large density of CD68 macrophages, as well as CD3 T helper cells and low levels of tumour cells (figure 3.8).

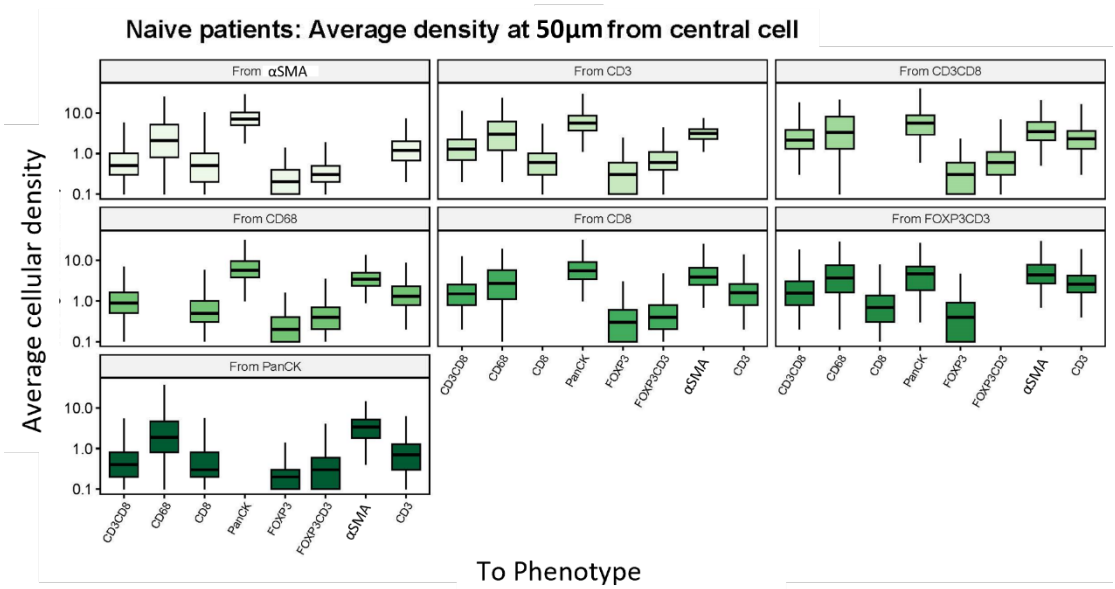


**Figure 3.8 Average immune cell population density at 50µm from central cell in combined naïve pancreatic cohort.** *Boxplots are faceted central cell ('from' phenotype), with each 'to' phenotype displayed along the x axis, and average cellular density along the y axis.*

Treatment naïve PDAC patients with good prognosis were associated with enriched density of CD3+ ($p<0.001$), CD3CD8+ ($p<0.001$) and low levels of CD68+ cells ($p=0.021$) within the surrounding tumour environment (30µm) (table 3.6). Yet again, spatial relationships associated with macrophages are heavily prognostic, relating to both disease specific survival and recurrence, replicating trends seen within nearest neighbour (chapter 3.8.1) and mutual nearest neighbour (chapter 3.8.2) analysis. Patients with high levels of CD3+ (DSS: $p<0.001$ and RFS: $p=0.003$), CD3CD8+ (DSS: $p=0.002$ and RFS: $p=0.002$) and FOXP3CD3+ ($p=0.021$) and low levels of PanCk+ ($p=0.015$) within 50µm of CD68+ macrophages associated with better outcome (table 3.6). The CD68-CD3 trend

was replicated in the validation cohort (table 3.6).

| Radius trends in disease specific survival and recurrence free survival in naïve patients | | | | | | | | | |
|---|---|---|---|---|---|---|---|---|---|
| From Phenotype | To Phenotype | Distance (µm) | Cohort | Group | Cut-off method | Time (months) | Number | HR (95% CI) | P value |
| PanCk | CD3 | 30 | Discovery | All patients | LQ | DSS | 233 | 2.00 (1.43-2.80) | <0.001 |
| PanCk | CD3CD8 | 30 | Discovery | All patients | LQ | DSS | 233 | 1.84 (1.31-2.57) | <0.001 |
| PanCk | CD68 | 30 | Discovery | All patients | LQ | DSS | 233 | 0.66 (0.46-0.94) | 0.021 |
| CD68 | CD3 | 50 | Discovery | All patients | LQ | DSS | 233 | 1.87 (1.34-2.60) | <0.001 |
| CD68 | CD3CD8 | 50 | Discovery | All patients | LQ | DSS | 233 | 1.71 (1.22-2.40) | 0.002 |
| CD68 | CD3 | 50 | Discovery | All patients | LQ | RFS | 233 | 1.65 (1.19-2.31) | 0.003 |
| CD68 | CD3CD8 | 50 | Discovery | All patients | LQ | RFS | 233 | 1.72 (1.23-2.40) | 0.002 |
| CD68 | FOXP3CD3 | 50 | Discovery | All patients | LQ | DSS | 233 | 1.50 (1.06-2.10) | 0.021 |
| CD68 | PanCk | 50 | Discovery | All patients | LQ | DSS | 233 | 0.64 (0.45-0.92) | 0.015 |
| CD68 | CD3 | 50 | Validation | All patients | LQ | DSS | 192 | 1.59 (1.15-2.19) | 0.005 |

**Table 3.6 Radii patterns associated with disease specific survival and recurrence free survival in naïve cohorts looking at whole core**. *Cut-off method established per radius pair in discovery cohort and replicated in validation cohort. Radii reported using 'from phenotype' column, indicating the central phenotype, and 'to phenotype' indicating the surrounding phenotype. Reported by distance (µm), cohort, patient group, along with number of patients in each group. Most significant radii is reported. Log Rank (Mantel-Cox) p value and Univariate cox regression hazard ratio (HR) shown with 95% confidence interval (CI) for disease specific survival (DSS) and recurrence free survival (RFS).*

## 3.9 Filtering prognostic markers

As seen above, multiplex spatial analysis has the ability to produce enormous amounts of significant descriptive data. Although all these findings may provide biological insight, it is important to start with those that have the highest probability of doing so. Therefore, only the markers and relationships seen in both discovery and validation cohorts were taken into consideration and placed into two different models. The first being a multivariate cox regression model (supplementary 8.2.2), and the second being a decision tree model. This was done with the aim of identifying the most relevant, robust variables that not only have the best predictive prognostic potential, but also will be robust enough to translate into future Spatial Transcriptomic experiments (Chapter 5). Consequently, biological mechanisms can begin to be elucidated from these purely characteristic results. The model cohort was limited to all patients and variables from density and nearest neighbour analysis and adjusted for resection margin and lymph node status. These were the most statistically relevant and validated methods.

### 3.9.1 Decision tree analysis

Decision tree analysis is perhaps one of the most simple supervised machine learning algorithms that can easily be employed for multiplex data due to its ability to support continuous and categorical data. Only variables from the final multivariate models (supplementary 8.2.2) were used. Three major models run were;

1. Full data – all significant variables included from density and nearest neighbour
2. Grouped data – variables split according to NN pairs (including density variables)
3. Filtered – CD68 related nearest neighbour variables with all density variables

Combination of density and nearest neighbour pairs generated interesting results in model 1 (figure 3.9.a). Unexpectedly, the root node seen was a nearest neighbour metric. Distance to CD3+ from CD68+Low (CD3-from-CD68) (Node 2: probability = 0.46, p=0.003), and CD3-from-CD68:CD68Low (Node 4: probability = 0.48, p<0.001) associated with highest survival probability. Lowest survival probability was associated with distance to CD3 from CD68High:CD68High (Node 5: probability = 0.14, p<0.001) (figure 3.9.a).
Looking only at cellular density in model 2, CD68Low patients had the best disease specific survival probability (Node 2: probability = 0.54, p=0.009), and CD68High:CD3Low had the lowest (Node 4: probability = 0.1, p=0.002) in naïve pancreatic cancer patients

(figure 3.9.b). Finally, CD68 specific nearest neighbour trends were input with all significant density markers. Highest survival probability was seen in naïve patients with CD68Low (Node 2: probability = 0.54, p=0.014), replicating trends seen above, and lowest survival probability was associated with CD68High:PanCk-from-CD68High:CD3Low (Node 6: probability = 0.08, p=0.042) (figure 3.9.c).

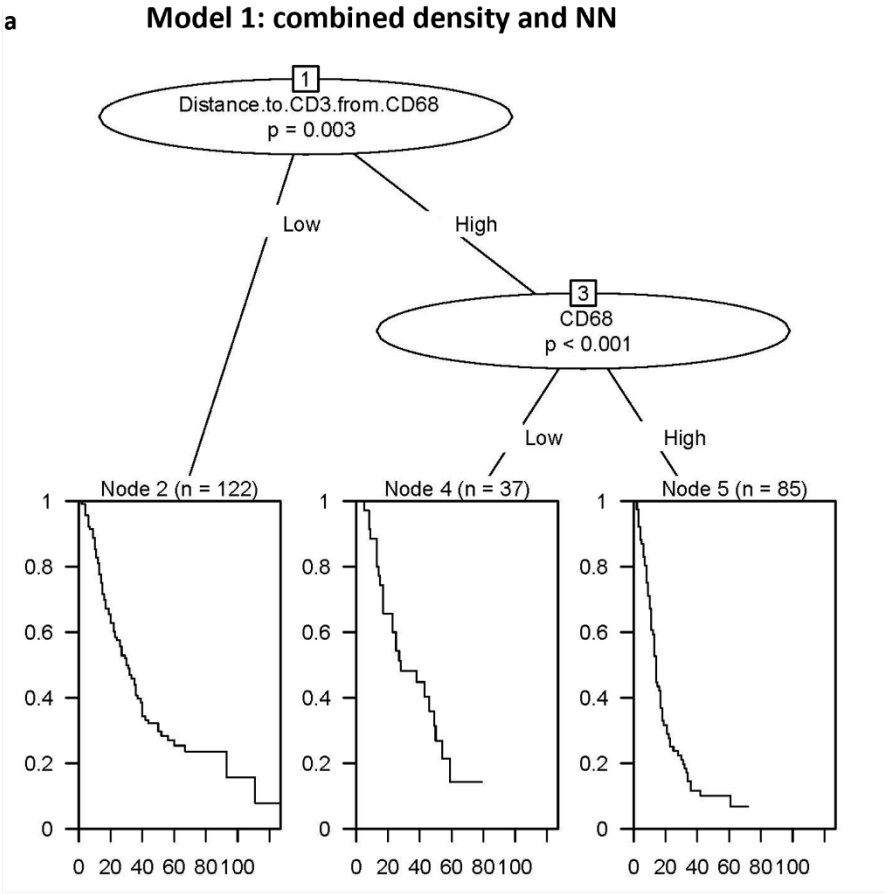


| Node Number | Number at risk | Number of events | Survival Probability | Censored Probability | Lower CI (95%) | Upper CI (95%) |
|---|---|---|---|---|---|---|
| 2 | 120 | 45 | 61 | 0.46 | 0.05 | 0.38 | 0.56 |
| 4 | 37 | 15 | 18 | 0.48 | 0.08 | 0.34 | 0.68 |
| 5 | 82 | 13 | 65 | 0.14 | 0.04 | 0.08 | 0.25 |

**Figure 3.9.a Density and nearest neighbour decision tree model with matching survival probability table in naive** *for a) Combined density and nearest neighbour variables. Nodes split according to rank, number of patients per node indicated and associated p value in decision tree model. Survival probability with confidence intervals (CI) and associated nodes reported in survival table.*

**b** **Model 2: Density alone**

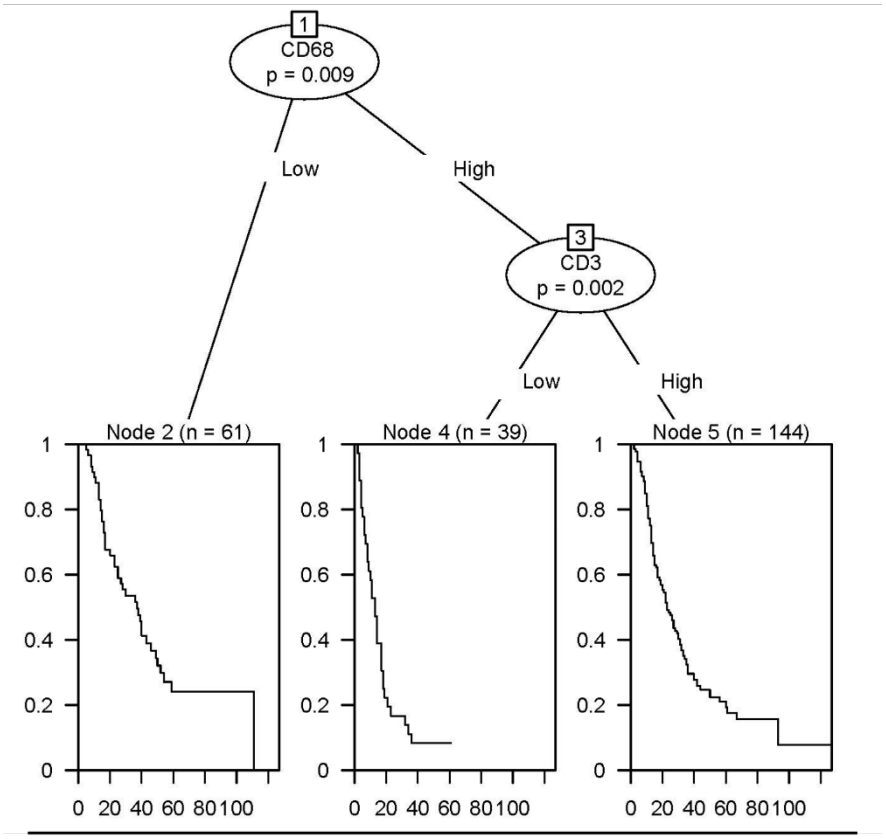


| Node | Number | Number at risk | Number of events | Survival Probability | Censored Probability | Lower CI (95%) | Upper CI 95%) |
|---|---|---|---|---|---|---|---|
| 2 | 61 | 28 | 27 | 0.54 | 0.07 | 0.41 | 0.68 |
| 4 | 37 | 5 | 32 | 0.11 | 0.05 | 0.04 | 0.28 |
| 5 | 141 | 40 | 85 | 0.34 | 0.04 | 0.27 | 0.44 |

**Figure 3.9.b Density and nearest neighbour decision tree model with matching survival probability table in naive** *for b) Density alone. Nodes split according to rank, number of patients per node indicated and associated p value in decision tree model. Survival probability with confidence intervals (CI) and associated nodes reported in survival table.*

**c** **Model 3: Distance from CD68 pairs and density**

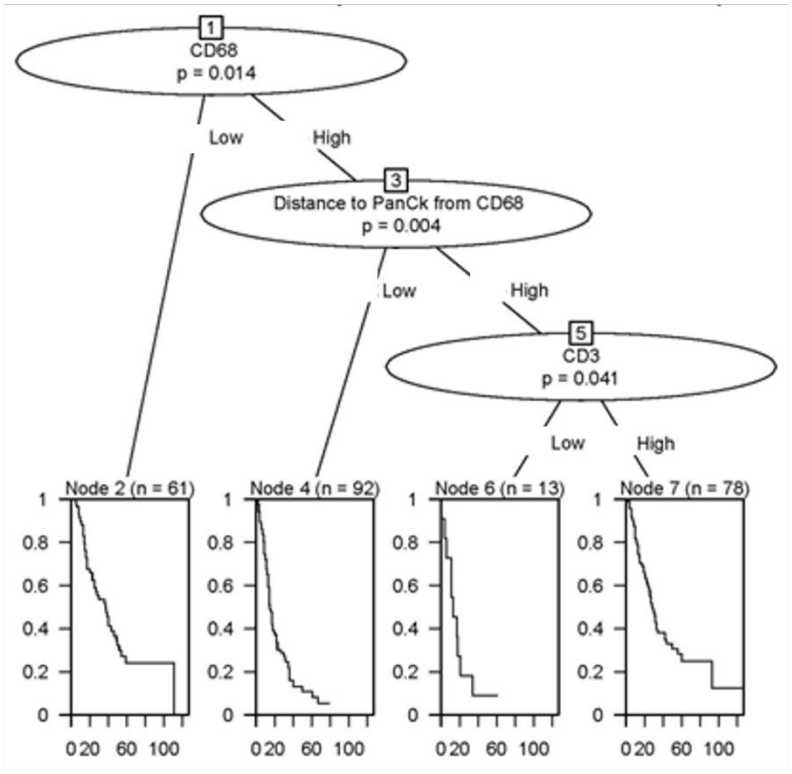


| Node | Number | Number at risk | Number of events | Survival Probability | Censored Probability | Lower CI (95%) | Upper CI (95%) |
|---|---|---|---|---|---|---|---|
| 2 | 61 | 28 | 27 | 0.53576 | 0.065646 | 0.42138 | 0.681189 |
| 4 | 90 | 17 | 64 | 0.246665 | 0.047508 | 0.169108 | 0.359791 |
| 6 | 11 | 2 | 10 | 0.090909 | 0.086678 | 0.014029 | 0.58911 |
| 7 | 77 | 26 | 43 | 0.38151 | 0.058791 | 0.282057 | 0.516032 |

**Figure 3.9.c Density and nearest neighbour decision tree model with matching survival probability table in naive** *for c). Distance from CD68 pairs with density metrics. Nodes split according to rank, number of patients per node indicated and associated p value in decision tree model. Survival probability with confidence intervals (CI) and associated nodes reported in survival table.*

## 3.10 Spatial clustering analysis in naïve pancreatic cancer

To further categorise the tumour immune microenvironment, clustering spatial metrics were investigated. These help to define the different cellular regions or neighbourhoods within naïve pancreatic cancer. Two methods were used, Ripley's K function and neighbourhood analysis. The well-known spatiotemporal point pattern analysis method 'Ripley's K function' determines the pattern of distribution of points (in this case cells) at increasing radii, was repurposed to establish intracellular phenotypic patterns (figure 3.10.a). The analysis was limited to a set boundary, looking at the overall pattern of distribution (figure 3.10.b). The average K function per phenotype was generated and compared to the average theoretical random distribution (Poisson's curve). Patterns of distribution are classed random, clustered and dispersed (figure 3.10.a) (chapter 2.3.3.6). Neighbourhood analysis determines the phenotypes that cluster together and creates neighbourhoods according to the frequency of the same clustering patterns occurring. This was done using CytoMAP hierarchical clustering (figure 3.10.c).

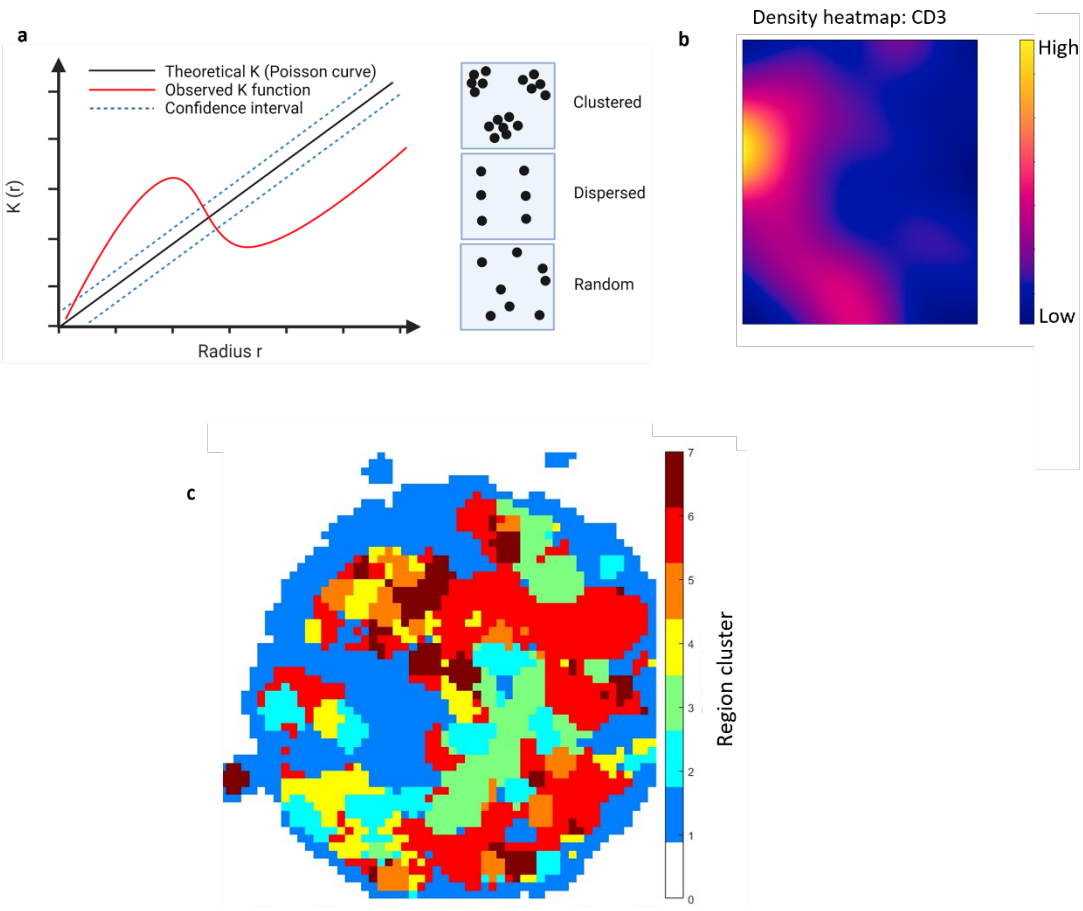


**Figure 3.10.a-c Clustering spatial analysis methods** *a). Ripley's K function graph showing theoretical Poisson curve and the observed K function. Observed K function above the theoretical indicates clustered pattern, below the theoretical indicates dispersed, and along the theoretical indicates random patterns of distribution b) Example density pattern heatmap for CD3 in naive core indicating clustered pattern of distribution c). Example naïve core with neighbourhood regions generated from MATLAB® CytoMAP, colour denotes the neighbourhood region*

### 3.10.1 Distribution pattern of immune cells in pancreatic cancer tumour microenvironment

To fully establish the spatial relationships within the TME, it is important to also take into consideration the relationships between the same phenotypes and their pattern of distribution. This was done using Ripley's K function (chapter 2.3.3.6). As above, discovery and validation cohorts were kept separate. On average, Ripley's K function in both discovery and validation upfront resected patients was consistently above the average theoretical value for each phenotype, revealing a clustered pattern of spatial distribution within TMA cores. Visual inspection of the TMA images when initial image analysis was being undertaken confirm these results. The distance from the K function score from theoretical is an indication to how clustered the phenotypes are. T-test using Bonferroni adjusted methods was performed to check significance of clustering and differences were found between the K function and Theoretical values for all phenotypes in discovery and validation cohorts (figure 3.11.a-b). The largest differences in both cohorts were seen between PanCk+, CD3CD8+ and FOXP3CD3+ phenotypes, signifying these markers have increased clustering expression compared to αSMA+ and CD68+ which have K function values closer to the theoretical cohorts (figure 3.11.a-b).

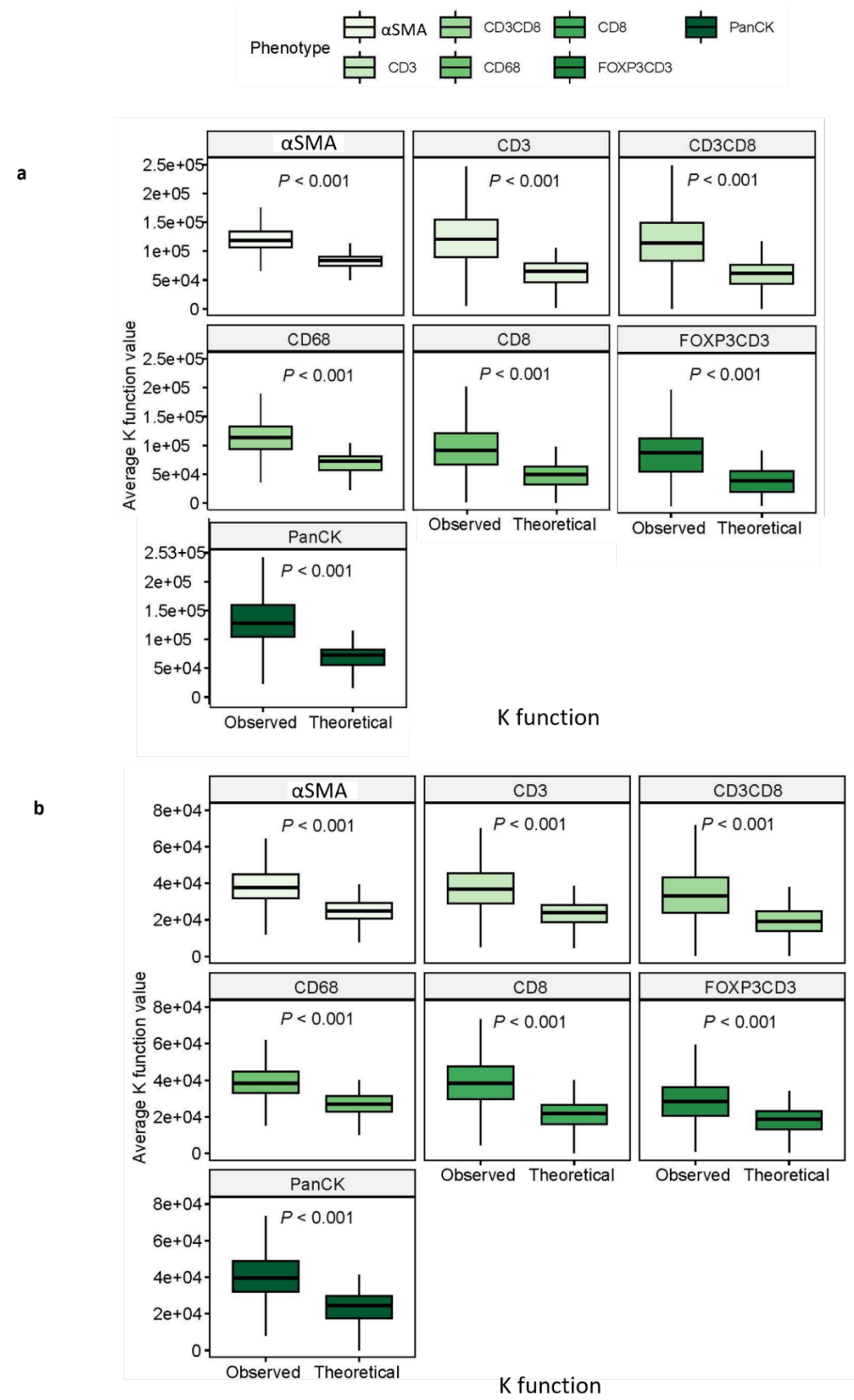


**Figure 3.11.a-b Average Ripley's K function and theoretical Poisson function values for all naïve phenotypes across discovery and validation cores**. *Boxplot faceted by phenotype, comparing observed K function to theoretical K function in a). Discovery cohort cores (n=776) using Bonferroni p adjustment T-test b). Validation cohort cores (n=815) using Bonferroni p adjustment T-test.*

### 3.10.2 Unbiased phenotyping and Neighbourhood generation

To confirm phenotypes generated via biased phenotyping, explore how different phenotypes cluster together and create regional neighbourhoods, MATLABs® CytoMAP was used on the combined naïve cohort. Unbiased phenotype cellular clustering produced 9 cell type clusters, 8 of which matched biased cell typing (chapter 3.5). In unbiased cell typing, a new cell type cluster, FOXP3CD3PanCk was observed, which was not selected for in biased phenotyping. The presence of this cluster was observed in ~5.5% of overall cell types (figure 3.12.a). These cell clusters were then made into neighbourhoods and clustered into regions. Overall, 8 regions were observed within naïve pancreatic cancer. Notably, neighbourhood 3 composed of FOXP3CD3PanCk cells clustered with CD3 (as expected) and slightly with CD68 cells, and neighbourhood 6 demonstrating clustering of CD3, CD3CD8 and CD68 (figure 3.12.b). All other regions were composed of expected single phenotypes. It is worth noting due to the small panel number, there is limited neighbourhood clustering, and it is constrained to the phenotypes present.

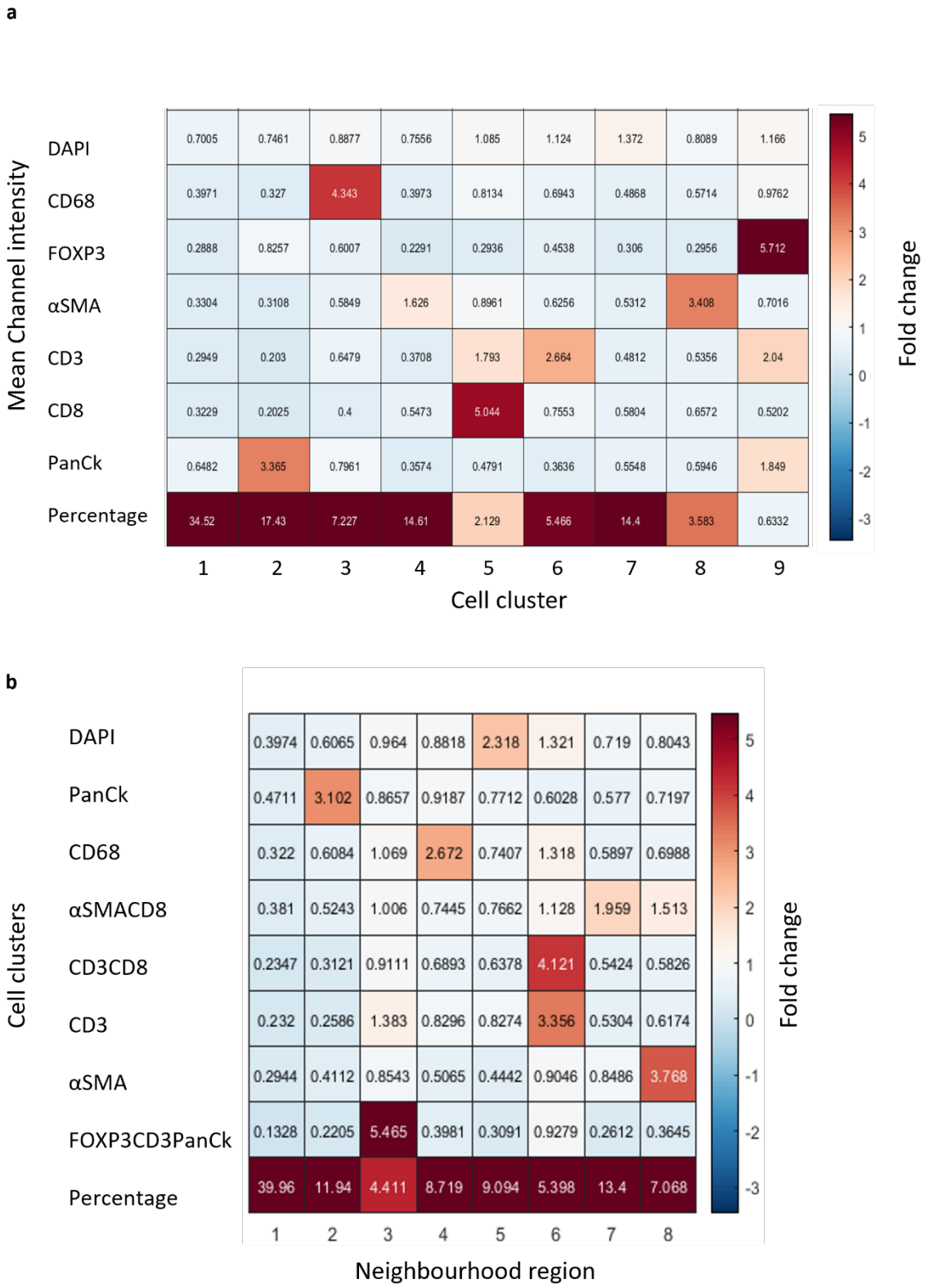


**Figure 3.12.a-b Neighbourhood generation in naïve PDAC combined cohort using CytoMAP**
*a) Cell typing heatmap showing fold change differences across channels to generate cell clusters b) neighbourhood regions generated by fold change of cell clusters associating with each other. Heatmap coloured by fold change.*

## 3.11 Regional protein phenotyping across the naive landscape

T lymphocyte and macrophage populations offer robust prognostic biomarkers within the naïve pancreatic cancer landscape as shown above. Although this is routinely reported in PDAC, the importance of lymphocyte subsets, their associated protein expression and activation status is less well characterised [239]. Deep immune regional phenotyping was carried out to help elucidate this. The Nanostring GeoMx DSP® platform enables high plex regional proteomic profiling of FFPE tissue sections with the regions of interest (ROIs) selected according to both morphological (histological) and phenotypic characteristics (figure 3.13.a). ROIs were selected according to PanCk+ staining, resulting in epithelial rich (PanCk+) and tumour microenvironment (TME) areas of interest (AOIs) (figure 3.13.b). Regional protein signatures were generated using a 60 plex immune-oncology panel, with 5 modules. This was carried out using a subset of the naïve cohort, named the naïve Glasgow cohort (table 3.1). Comparison with chromogenic IHC generated above (chapter 3.4) validated the protein DSP TME expression for CD3 ($R = 0.83$, $p < 0.001$) and CD8 ($R = 0.84$, $p < 0.001$) and showed strong concordance and relatively strong concordance for CD68 ($R= 0.68$, $p < 0.001$), between GeoMx™ protein panel and gold standard IHC methods (figure 3.13.e-g). Furthermore, the prognostic value of CD3 and CD8 within the TME compartment was tested. Elevated expression of both CD3 ($p= 0.027$) and CD8 ($p=0.009$) correlated with survival, recapitulating trends seen in IHC (figure 3.13.c-d).

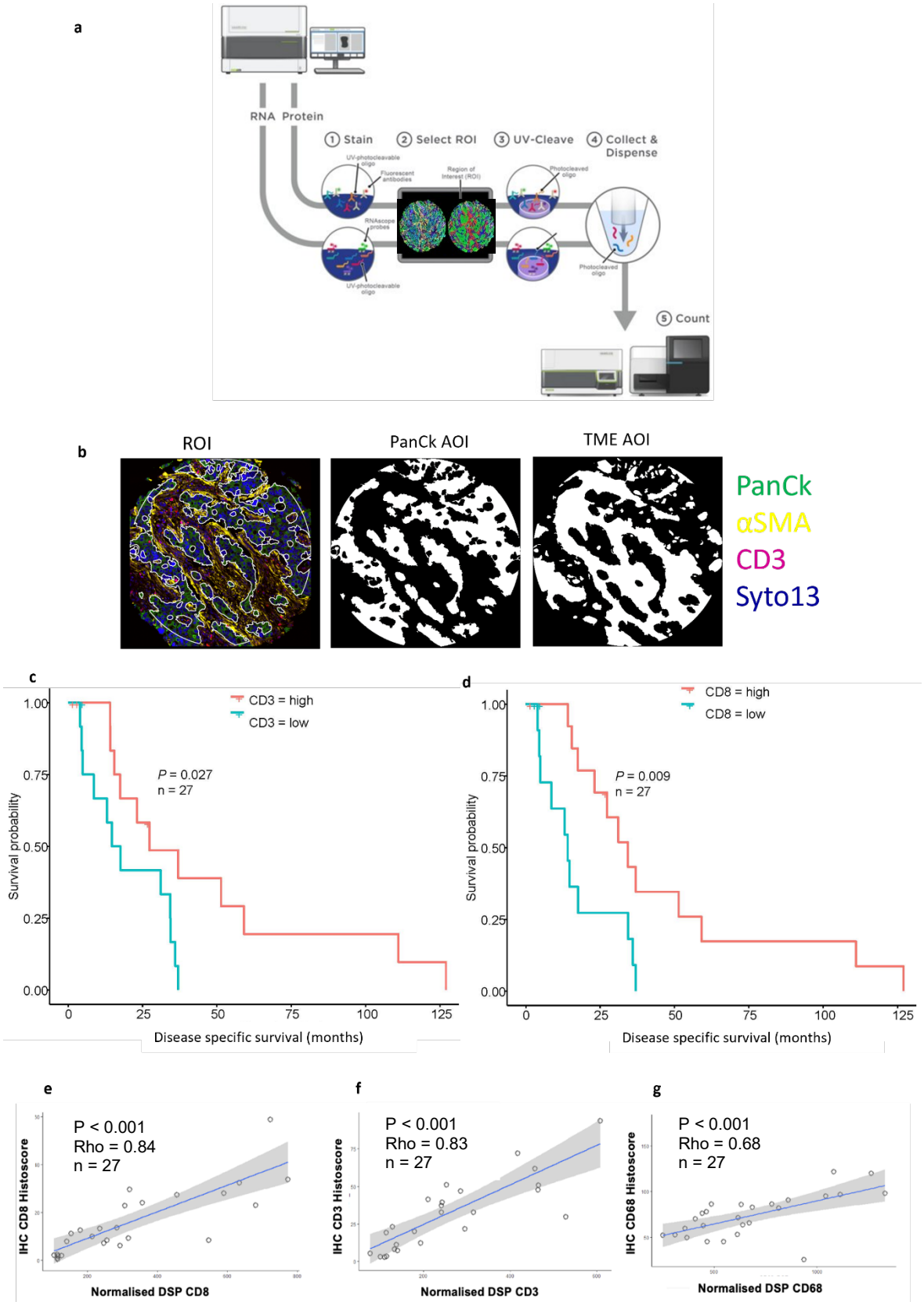


**Figure 3.13.a-g Correlation between IHC and Regional proteomics in naïve PDAC** *a). Overview NanoString™ DSP assay, full details provided in chapter 2, schematic adapted from NanoString technologies b). Example region of interest (ROI), with PanCk+ mask and tumour microenvironment mask (PanCk-), stained for PanCk (green), αSMA(yellow), CD3 (magenta) and Syto13 (blue). b). Kaplan-Meier curves (disease specific survival) stratified by DSP CD3 protein*

*marker expression (Log-Rank test) c). Kaplan-Meier curves (disease specific survival) stratified by DSP CD8 protein marker expression (Log-Rank test). Regression plots comparing e) CD8 f) CD3 g) CD68 positivity staining in each core (evaluated by IHC) assessed by automated scoring (HALO) with normalized DSP protein marker expression (averaged across all 48 cores). Spearman correlation coefficient and p-value presented. Grey shading denotes 95% confidence interval (CI) of correlation coefficient.*

Initial regional analysis confirmed that epithelial and TME ROIs within TMA cores had distinct patterns of DSP protein expression consistent with the predicted cell types in each region. In addition to PanCk expression being higher in epithelial ROIs, as expected, expression of CD3, CD4, CD8, αSMA along with immune checkpoint protein B7-H3 were significantly elevated in TME compartments (figure 3.14.a). Furthermore, unbiased clustering demonstrated differences within TME compartments vary from immune-rich to immune-void (figure 3.14.b), with immune-void patients negatively associating with survival (figure 3.14.c). The prognostic power of markers within tumour and TME regions was assessed for biomarker discovery. In total, 9 DSS and 3 RFS TME specific, and 3 DSS and 2 RFS tumour specific markers demonstrated prognostic significance (table 3.7). In TME segments, enriched expression of fibronectin was observed, CD3, CD4, CD8, Bcl-2, HLA-DR, GZMB, PD-1 and Tim-3 correlated with prognosis, and enriched fibronectin, CD8 and Bcl-2 correlated with recurrence (table 3.7). Tumour segments with reduced B7-H3, and enriched 4-1BB, Bcl-2 expression associated with better survival, and increased 4-1BB and reduced Her-2 correlated with longer recurrence free survival (table 3.7). A strong correlation between overlapping protein expression in IHC and DSP, validates the prognostic benefit of select immune T cell subsets, and the utility of this regional proteomic technology in novel biomarker discovery.

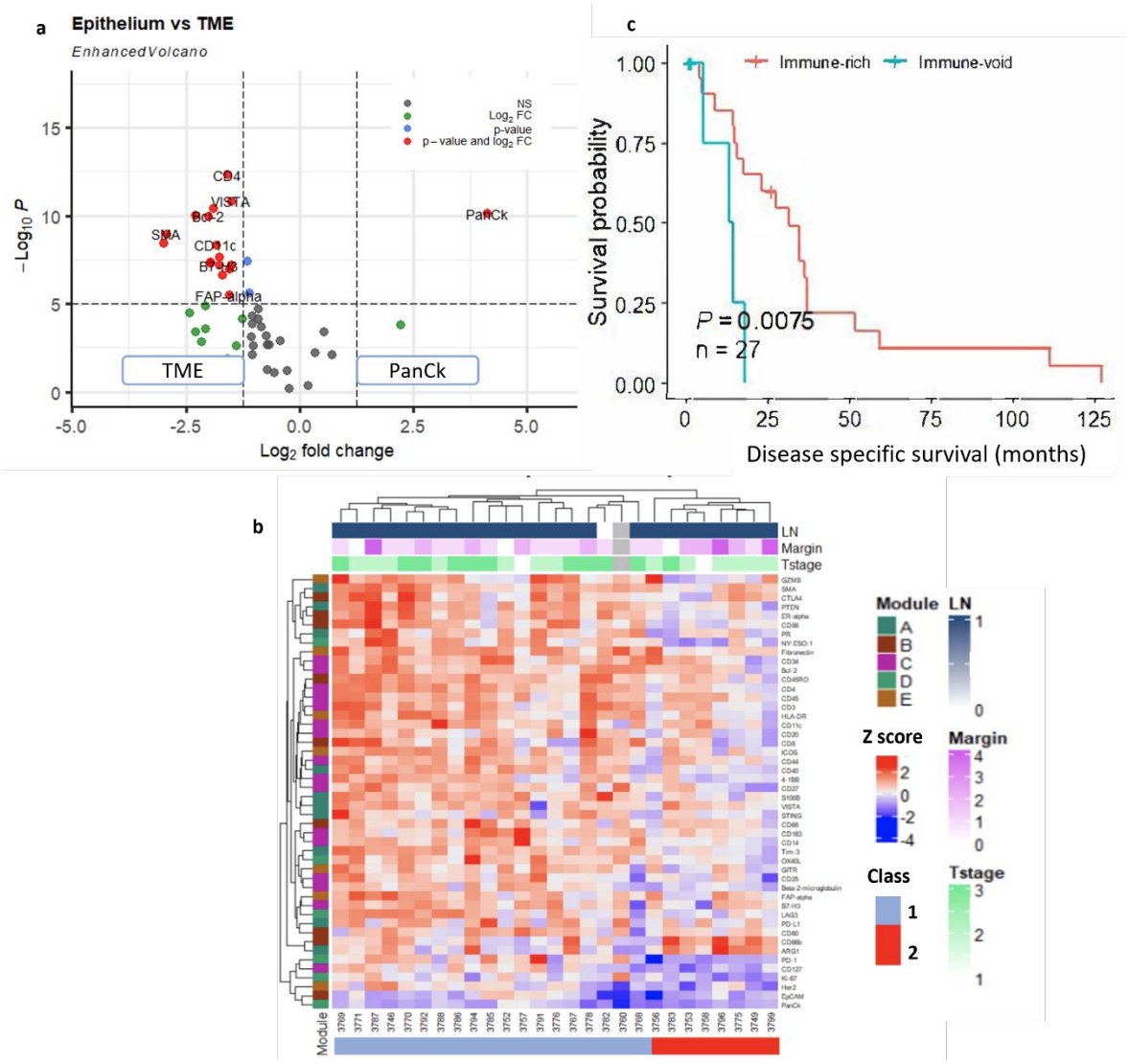


**Figure 3.14.a-c Segment specific protein expression across naïve PDAC** *a). Volcano plot demonstrating protein marker differential expression levels based on comparison of PanCk versus tumour microenvironment (TME) regions. Dashed line indicates significance thresholds, NS = non-significant, FC = fold change. b) Unsupervised analysis of DSP data in the tumour microenvironment regions identified 2 classes: Class 1 High immune signalling (blue); Class 2 Low immune signalling (red). c) Kaplan–Meier analysis of patient survival stratified by immune class; immune-rich (Class 1) and immune-void (Class 2)*

| Biomarker signature density in diseases specific and recurrence free survival | | | | | |
|---|---|---|---|---|---|
| **Biomarker signature** | **Segment** | **Cut-off method** | **Time (months)** | **HR (95% CI)** | **P value** |
| 4-1BB | Tumour | Median | DSS | 0.35 (0.14-0.88) | 0.026 |
| Bcl-2 | Tumour | Rcutoff | DSS | 0.33 (0.10-1.04) | 0.047 |
| B7-H3 | Tumour | Rcutoff | DSS | 3.67 (1.17-11.6) | 0.026 |
| 4-1BB | Tumour | Median | RFS | 0.40 (0.16-0.97) | 0.043 |
| Her-2 | Tumour | Rcutoff | RFS | 2.57 (0.02-1.87) | 0.039 |
| Fibronectin | TME | Rcutoff | DSS | 0.04 (0.00-0.71) | 0.028 |
| CD3 | TME | Median | DSS | 0.35 (0.13-0.91) | 0.031 |
| CD4 | TME | Rcutoff | DSS | 2.29 (0.11-0.76) | 0.012 |
| CD8 | TME | Median | DSS | 0.30 (0.12-0.77) | 0.012 |
| Bcl-2 | TME | Median | DSS | 0.32 (0.12-0.81) | 0.016 |
| HLA-DR | TME | Median | DSS | 0.28 (0.10-0.76) | 0.012 |
| GZMB | TME | Rcutoff | DSS | 0.25 (0.07-0.85) | 0.027 |
| PD-1 | TME | Rcutoff | DSS | 0.31 (0.11-0.89) | 0.03 |
| Tim-3 | TME | Rcutoff | DSS | 0.26 (0.09-0.73) | 0.011 |
| Fibronectin | TME | Median | RFS | 0.34 (0.13-0.92) | 0.033 |
| CD8 | TME | Median | RFS | 0.36(0.15-0.87) | 0.024 |
| Bcl-2 | TME | Median | RFS | 0.36 (0.15-0.85) | 0.021 |

**Table 3.7 Summary of naïve spatial protein biomarker signature density for disease specific survival and recurrence free survival in tumour and TME segments.** *Cut-off method established per phenotype and segment generated (chapter 2.5.1.5.). Log Rank (Mantel-Cox) p value and Univariate cox regression hazard ratio (HR) shown with 95% confidence interval (CI) for disease specific survival (DSS) and recurrence free survival (RFS).*

## 3.12 Discussion

Several studies have investigated the role of T lymphocytes, macrophages and fibroblast cells in naïve pancreatic cancer. Until recently these studies have been primarily focused on single stain immunohistochemistry. To begin to fully characterise the naïve pancreatic landscape, confirmation of prognostic relevance of major T cell and macrophage markers in the chromogenic setting had to be established. As expected, elevated levels of helper (CD3) and cytotoxic (CD8) T cells significantly correlated with survival, in addition to pro-inflammatory CD68 macrophages correlating with recurrence at the most aggressive site. These results replicated the general consensus established for naïve PDAC patients regarding cellular density. Increased levels of cytotoxic and helper T cells are consistently reported to have a positive association with survival. Due to the cytotoxic role of CD8 cells, increased levels are hypothesized to lead to increased apoptosis of tumour cells, resulting in longer survival [8, 182, 231, 232]. Helper T cells play a potentially more complex role. Patterson et al demonstrated these T cells help differentiate monocytes into tumour-suppressive macrophages, and also dampen the effect of T regulatory cells [234]. CD68+ macrophages fall into the pro-tumour category, with high expression routinely associated with poor survival [237, 238].

Within IHC studies, investigation into ratios between cell types using serial sections or using multi-colour IHC (mIHC) has provided pseudo interaction analysis with cellular ratios shown to outperform density alone in PDAC. Specifically, high expression of combined CD8+/CD4+ was found to be an independent prognostic marker which out competes individual density of each marker [8]. This ratio was also seen within the naïve cohort, although median survival was the same for both CD3high/CD3CD8high ratio and CD3high density (22.5months). Furthermore, low proportions of CD3/Tregs correlated with poor prognosis in PDAC patients [9], with the naïve cohort replicating the pattern.

Until recently, the vast majority of immune cell protein PDAC profiling has been carried out using IHC, and occasionally mIHC, though this was limited to a maximum of 3 markers [240]. However, with the accessible development of specialist technology, this is no longer the case. Tailor-made immune panels have been developed to stain for a large number of markers on the same section allowing for phenotyping via co-localization, and the ability for complex spatial analysis, which was previously unmanageable. Deep immune phenotyping in pancreatic cancer reveals  novel spatial immune interactions previously unknown. Highly defined cell clusters associated with survival have been discovered using a 27-plex marker panel, including PD-1 expressing CD4 T cells clustering with IL10 expressing myelomonocytes and CD8 T cells clustering with B cells [241]. With extensive panels such as these, characterization of the PDAC TME and biomarker discovery

becomes increasingly manageable.

The major advantage of multiplex panels is the ability to perform distance metric analysis. Our naïve cohort produced a large number of significant spatial relationships, with dominant trends observed. Naïve patients with a better survival associated with highly anti-tumour microenvironment, defined by reduced distances from tumour cells to cytotoxic T cells and CD3+ helper, and large distances to macrophages and fibroblasts. This trend has previously been reported. Carstens et al, investigated the spatial distribution of T lymphocytes in relation to pancreatic cancer cells and found high expression of cytotoxic T cells within 20μm of cancer cells significantly correlated with survival [7]. These immune cell interactions with tumour cells were further accentuated in radius analysis. Large numbers of effector T cells and a reduced number of macrophages within 30μm of tumour cells significantly associated with favourable prognosis. Naïve patients revealed a powerful prognostic distance metric validated across both cohorts. Reduced distance to CD3+ helper T cells from macrophages associated with longer disease specific and recurrence free survival. This phenomenon maybe due to density of T cells dampening macrophage effects.

To establish an integrated characterization of density and the role of inter-cellular interactions according to distance, varied multivariate cox regression and decision tree models were performed. Naïve patients with high survival probability were associated with either low inter-cellular distances from macrophages to CD3+ helper cells, or larger inter-cellular distances coupled with low density of CD68+ cells. As macrophage related spatial relationships were abundant in the naïve setting, these NN pairs along with density were investigated. Patients with highest survival probability were characterized by low CD68+ expression, or if patients had elevated CD68+, large distances between macrophages to tumour cells, couple with enriched CD3+ population seemed to provide prognostic benefit.

The established markers were validated using spatial bulk proteomics, with the two assays demonstrating high correlation. Furthermore, a substantial number of prognostic biomarkers within the naive landscape were predominantly associated with T cell related functions, providing insight into region specific cellular subtypes found within naïve pancreatic cancer. Within the epithelial compartment, the immune checkpoint and potential targetable marker B7-H3 had prognostic value. Interest is growing within the cancer field regarding B7-H3 expression as an immune checkpoint marker [16]. This molecule has, reportedly, limited expression in normal tissue, and high expression in pancreatic cancer, with elevated expression correlating with poor survival and metastasis [17-19]. Additionally, it has been correlated with advanced pathological stage, as well as lymph node metastasis [242]. Multiple pathways have been associated with B7-H3,

including both co-inhibitory and co-stimulatory T cell related pathways. It can both inhibit and stimulate the proliferation of helper and cytotoxic T cells and has been associated with one of the cancer hallmarks, immune evasion [243-246]. Blockade of this checkpoint alone using an anti-B7H3 monoclonal antibody in murine models resulted in increased cytotoxic T cell infiltration. Furthermore, combination therapy with Gemcitabine demonstrated vastly reduced tumour volume compared to either treatment alone [242] .

A shift of focus can be seen in the pancreatic cancer research field to study the tumour immune microenvironment using sophisticated technologies that facilitate robust, complex characterization with high through-put biomarker discovery potential. However, there is much to learn, with published literature in pancreatic cancer remaining relatively limited compared to other solid cancers such as colorectal or breast cancer. Multiplex immunofluorescence, remains at its core, a descriptive assay, limited to characterization, and although biological interactions can be inferred, a complementary Spatial Biology technique that will delve deeper into the underlying immune mechanisms is required.

# 4 Chapter 4: Deep immune phenotyping in neoadjuvant human pancreatic ductal adenocarcinoma

## 4.1 Introduction

Of the 10-20% of patients eligible to undergo surgical resection, a medically fit proportion undergo neoadjuvant therapy prior to surgery [21]. These patients are treated with FOLFIRINOX based therapy, Gemcitabine based therapy or chemoradiotherapy prior to surgical resection. This introduction of neoadjuvant treatment was based on evidence that neoadjuvant treatment in borderline resectable and locally advanced PDAC patients associated with improved survival outcomes [247-250]. Furthermore, it has been reported that preoperative treatment has the ability to convert unresectable patients into resectable [4, 250]. The great benefit of neoadjuvant therapy lies in its ability to make surgery a possibility. By increasing the number of patients eligible for resection, the likelihood of overall survival for PDAC is increased.

To date, few studies have robustly established the effect of neoadjuvant therapy on the tumour microenvironment or have directly explored the phenotypic differences between treatment naïve and neoadjuvant treated pancreatic tumours. Of the studies that have attempted this characterisation, analysis primarily remains focused on cellular densities and ratios, with little exploration in the spatial field [8, 251-253]. This is due to a multitude of factors, including limited access to human patient samples and lack of suitable technology. Even in cases where access to tissue is available, a delicate balance is needed to prevent wasting precious tissue, whilst having adequate representation of the patient sample. The added complication of expensive and labour intensive technologies has limited this exploration until recently. Multi-regional tissue microarrays allow for high patient throughput at a fraction of the cost (both reagent and personnel), whilst the multi-core aspect accounts for sufficient tissue input [254]. Combining this tissue resource with relatively novel multiplexing assays, results in a large amount of data generated with reduced tissue input. It would not be unreasonable to assume these types of studies will become increasingly accessible as time progresses.

There is emerging evidence in the literature that chemotherapy alters the tumour immune microenvironment, triggering an immunogenic switch from immune barren and pro-tumorigenic, into an immune rich landscape. The majority of immune cells explored in this context remain T cells and macrophages [132, 213, 214, 255]. Notably, elevated cytotoxic T cell proportions are seen within the stromal compartments of patients treated with neoadjuvant therapy, as well as reduced Treg populations [252, 253, 256]. The role of macrophages in the neoadjuvant treatment setting is less clear than in treatment naïve patients, with increased M1 polarized macrophages associated with improved survival [252]. In order to establish the validity of this hypothesis, the aim was to characterise a

neoadjuvant cohort using the same multiple immunofluorescent assay as describe in chapter 3.

## 4.2 Aims

Explore the spatial immune cell landscape in terms of T cell, macrophage, and fibroblast composition in neoadjuvant treated human pancreatic cancer. Investigate content, density, and spatial orientation in distinct histopathological regions. Base immune landscape will be characterised first, and subsequent comparisons between naïve and neoadjuvant cohorts will be carried out. Consideration will also be given to appropriate clinical groups.

## 4.3 Clinical cohorts

Neoadjuvant cohort consisted of 72 pancreatic cancer specimens within a TMA with clinical data associated (table 4.1). Median survival for these patients was 24.5 months. The combined naïve cohort, as seen in chapter 3, was used as a comparison group (table 4.1). Notably, these naïve and neoadjuvant patients are unmatched. Median survival for these patients was 20.3 months. Clinical data associated with these cohorts is found in chapter 2.1.

| Study | Cohort | TMA | TMA number | Patient number | Treatment type |
|---|---|---|---|---|---|
| PhenoImager 7 plex assay | Neoadjuvant Glasgow | Neoadj-MAL-TMA batch1 | 3 | 72 | Neoadjuvant |
| | | Neoadj-MAL-TMA batch2 | 3 | | |
| | Naïve combined | APGI/ICGC TMA | 8 | 436 | Naïve |
| | | SD-PAN-TMA | 1 | | |
| | | PDAC-PAN-TMA | 5 | | |
| | | NJ-PANC-TMA | 7 | | |

**Table 4.1 Neoadjuvant and naïve clinical cohorts and associated study.** *Summary table showing the study and associated neoadjuvant and naïve TMAs used, patient number and treatment type. The cohort name column refers to the cohort name in chapter 2.1.*

## 4.4 Deep phenotyping and cellular density landscape in neoadjuvant pancreatic cancer

The neoadjuvant pancreatic cancer has a considerably less well defined tumour immune microenvironment compared to its naïve counterpart. Substantially increased survival was observed upon introduction of pre-operative treatment, thought to be partly due to an immune rich phenotype. This hypothesis was investigated using a Glasgow based neoadjuvant treated cohort (n=72), recapitulating the same 7 plex immune assay (chapter 2.3), selecting for the same phenotypes and following the same analysis pipeline as in the naïve cohort (chapter 3). Phenotypes observed were;

8. αSMA+ fibroblasts
9. CD3+CD8- T cells
10. CD3CD8+ cytotoxic
11. CD8+ cells
12. FOXP3CD3+ T regulatory cells
13. CD68+ macrophages
14. PanCk+ cancer cells

Total cell density of all neoadjuvant patients was measured to establish a base immune landscape. The highest cell population observed were CD68+, αSMA+ and CD3+ cells and the lowest cell population were single stained CD3CD8+ and CD8+ populations (figure 4.1.a). Next, density of relevant clinical pathology subgroups was compared. Patients treated with chemotherapy had significantly elevated CD68+ ($p=0.019$) and PanCk+ ($p=0.005$) levels compared to patients treated with chemoradiotherapy (figure 4.1.b). No significant immune cell differences were observed across chemotherapy treatment type (figure 4.1.c) nor tumour regression status (figure 4.1.d).

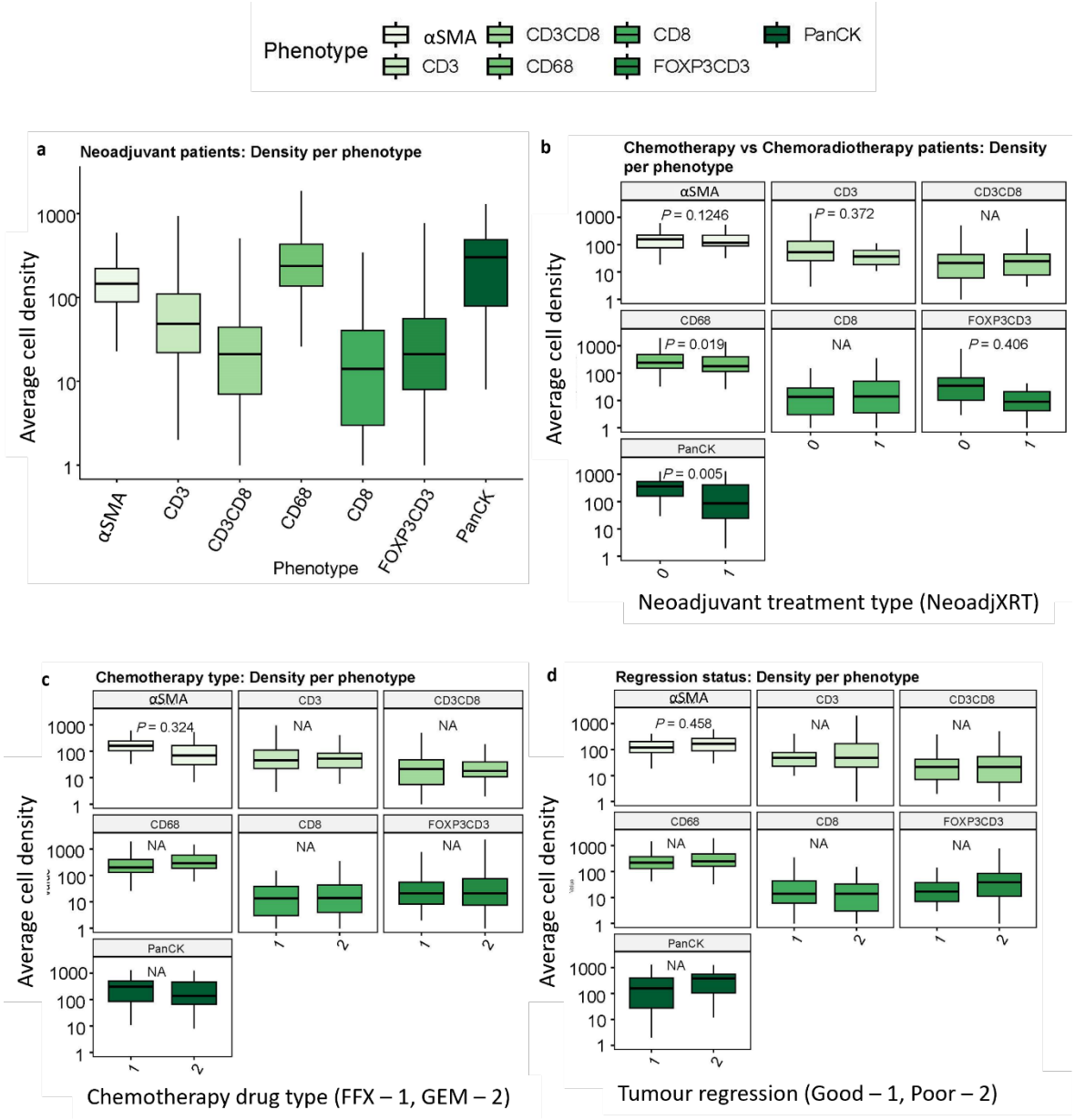


**Figure 4.1.a-d Average cellular density phenotype boxplots across neoadjuvant patients and in clinical pathological subgroups** *a). All neoadjuvant patients, n=72, b). Neoadjuvant treatment type (NeoadjXRT), chemotherapy (0) and chemoradiotherapy (1) using Bonferroni p adjusted T-test, chemotherapy n=46, chemoradiotherapy n=24, c). Neoadjuvant chemotherapy drug type, FOLFIRINOX (FFX = 1) and Gemcitabine (GEM = 2) using Bonferroni p adjusted T-test, FFX n=52, GEM n=18, d). Tumour regression status, good regression (1) and poor regression (2) using Bonferroni p adjusted T-test, good n=35, poor n=33*

## 4.5 Density survival analysis in neoadjuvant PDAC

Survival analysis was carried out using ranked densities. In the patients treated with neoadjuvant therapy low density of CD3+ (p=0.004), CD3CD8+ (p=0.001), CD68+ (p=0.001) and FOXP3CD3+ (p=0.003) cells associated with better disease specific survival (table 4.2), contrary to what was hypothesised. To confirm these findings, well-known clinically relevant prognostic groups were examined. When clinical subgroups were investigated, similar trends appeared. Low expression of CD3CD8+, CD3+, CD68+ and FOXP3CD3+ associated with better survival in chemoradiotherapy treated patients, FOLFIRINOX (FFX) treated patients, and patients with good regression (table 4.2). In addition, reduced infiltration of CD3CD8+ and CD68+ in Gemcitabine treated patients correlated with improved survival (table 4.2). As expected, reduced density of tumour cells (PanCk+) in chemotherapy treated, FFX treated and poor regression patients associated with better outcome (table 4.2). Each clinical group confirmed the counterintuitive density results, indicative that the neoadjuvant landscape is more complex than expected. Cellular density alone may be insufficient to explain the prognostic benefit of neoadjuvant patients.

| Phenotype density in neoadjuvant cohort for disease specific survival | | | | | | |
|---|---|---|---|---|---|---|
| **Phenotype** | **Region** | **Group** | **Cut-off method** | **Number** | **HR (95% CI)** | **P value** |
| CD3 | Whole core | All patients | Rcutoff | 72 | 2.14 (1.28-3.59) | 0.004 |
| CD3CD8 | Whole core | All patients | Rcutoff | 72 | 2.28 (1.41-4.00) | 0.001 |
| CD68 | Whole core | All patients | Rcutoff | 72 | 2.35 (1.39-3.97) | 0.001 |
| FOXP3CD3 | Whole core | All patients | Rcutoff | 72 | 2.53 (1.37-4.66) | 0.003 |
| PanCk | Whole core | Chemotherapy | Rcutoff | 46 | 2.91 (1.36-6.23) | 0.006 |
| CD3CD8 | Whole core | Chemoradiotherapy | Rcutoff | 24 | 4.78 (1.37-1.67) | 0.014 |
| CD3 | Whole core | Chemoradiotherapy | Rcutoff | 24 | 5.95 (1.56-22.6) | 0.009 |
| CD68 | Whole core | Chemoradiotherapy | Rcutoff | 24 | 6.17 (1.71-22.3) | 0.006 |
| FOXP3CD3 | Whole core | Chemoradiotherapy | Rcutoff | 24 | 2.91 (1.13-7.51) | 0.028 |
| CD3CD8 | Whole core | FOLFIRINOX | Rcutoff | 52 | 2.14 (1.18-3.87) | 0.012 |
| CD3 | Whole core | FOLFIRINOX | Rcutoff | 52 | 1.93 (1.07-3.49) | 0.029 |
| CD68 | Whole core | FOLFIRINOX | Rcutoff | 52 | 2.06 (1.12-3.78) | 0.020 |
| FOXP3CD3 | Whole core | FOLFIRINOX | Rcutoff | 52 | 2.23 (1.12-4.44) | 0.023 |
| PanCk | Whole core | FOLFIRINOX | Rcutoff | 52 | 2.44 (1.31-4.52) | 0.005 |
| CD3CD8 | Whole core | Gemcitabine | Rcutoff | 18 | 3.50 (1.06-11.6) | 0.040 |
| CD68 | Whole core | Gemcitabine | Rcutoff | 18 | 4.49 (1.20-16.7) | 0.025 |
| CD3CD8 | Whole core | Good regression | Rcutoff | 35 | 6.66 (2.42-18.3) | <0.001 |
| CD3 | Whole core | Good regression | Rcutoff | 35 | 3.64 (1.47-9.02) | 0.005 |
| CD68 | Whole core | Good regression | Rcutoff | 35 | 2.86 (1.01-8.06) | 0.047 |
| FOXP3CD3 | Whole core | Good regression | Rcutoff | 35 | 2.27 (1.01-5.11) | 0.047 |
| PanCk | Whole core | Poor regression | Rcutoff | 33 | 12.8 (2.88-57.2) | <0.001 |

**Table 4.2 Summary of significant density-based biomarkers in neoadjuvant cohort for disease specific survival in whole core**. *Cut-off method established per phenotype (chapter 2.3.3.3), region and patient group indicated, along with number of patients in each group. Log Rank (Mantel-Cox) p value and Univariate cox regression hazard ratio (HR) shown with 95% confidence interval (CI) ) for disease specific survival.*

## 4.6 Density interaction between phenotypes in neoadjuvant pancreatic cancer

To start deciphering intercellular dynamics between immune cells in the neoadjuvant microenvironment, density ratios between all phenotypes were investigated. As in chapter 3.7, Log-Rank survival analysis was performed on overall ratio, then pairwise comparison was used to look at inter-curve differences within the same ratio pair. Proportions between cytotoxic T cells demonstrated multiple significant ratios. Ratio between CD3CD8+ cells and tumour cells significantly correlated with survival ($p<0.001$) (figure 4.2.a). Pairwise comparison demonstrated CD3CD8high/PanCkhigh patients did considerably worse than all other groups, with CD3CD8low/ PanCklow groups associated with the best outcomes ($p<0.001$) (table 4.3). Significant relationships were also observed between cytotoxic T cells and T regulatory cells ($p=0.002$) (figure 4.2.b), with favourable outcome expressed CD3CD8low/FOXP3CD3low ratios, compared to patients with worse survival expressing CD3CD8high/ FOXP3CD3high ($p=0.001$) (table 4.3). Finally, cytotoxic T cell and macrophage ratio was observed to correlate with disease specific survival ($p =0.004$) (figure 4.2.c). Favourable prognosis was seen in patients with CD3low/CD68low, compared to CD3high/CD68high ($p=0.006$) (table 4.3). Neoadjuvant ratios confirm results seen with cellular density, indicative of immune cell interactions within the treated tumour immune microenvironment.

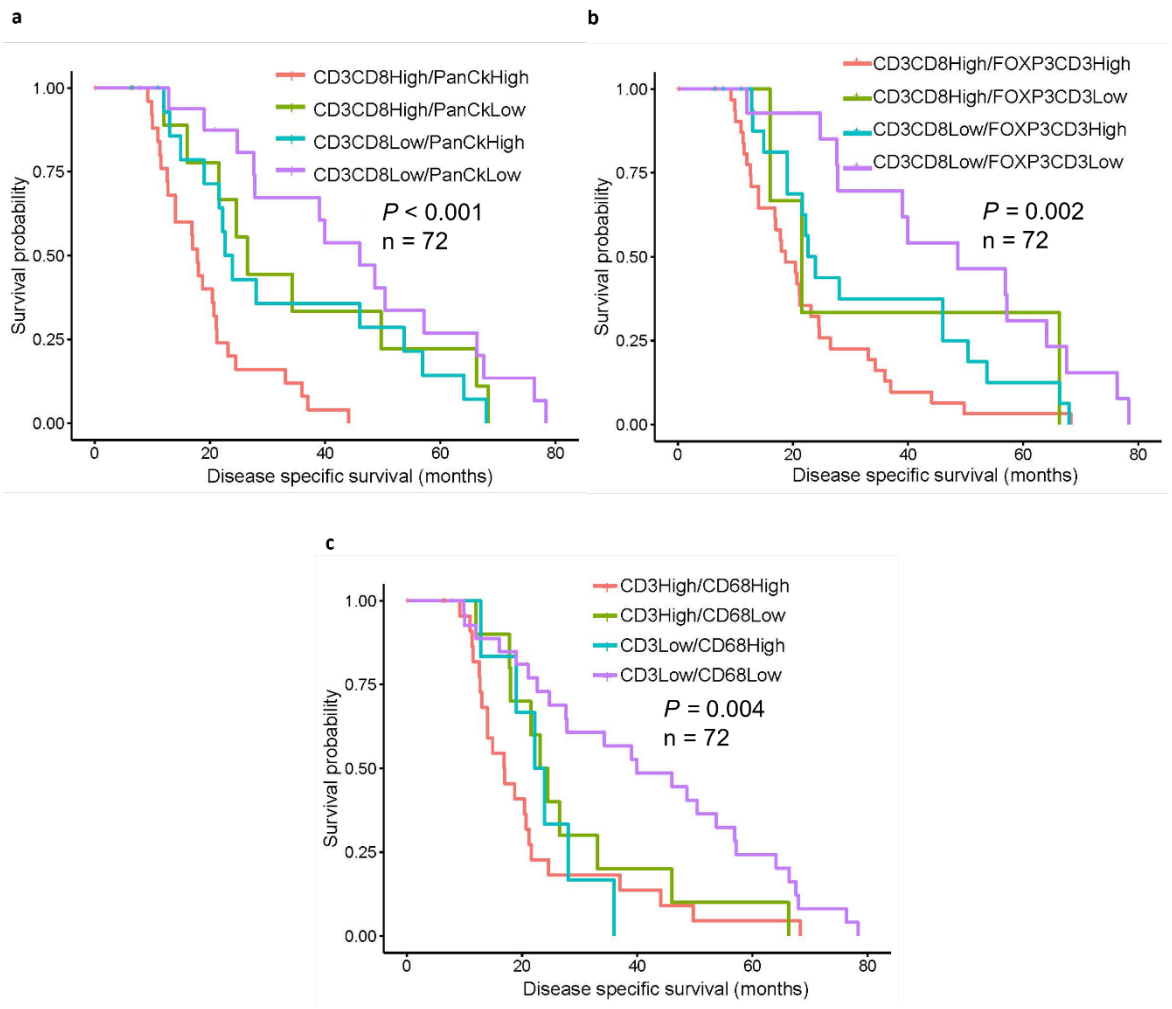


**Figure 4.2.a-c Survival analysis of cellular density ratio in neoadjuvant cohort.** *Kaplan-Meier curves (disease specific survival) stratified by ratio expression in neoadjuvant treated PDAC (Log-Rank test) for a). CD3CD8/PanCk ratio b). CD3CD8/FOXP3CD3 ratio c). CD3/CD68 ratio. Log Rank (Mantel-Cox) pairwise comparison over strata.*

| Ratio group | Ratio comparison group1 | Ratio comparison group2 | Pairwise P value |
|---|---|---|---|
| CD3CD8/PanCk | CD3CD8High/PanCkLow | CD3CD8High/PanCkHigh | 0.019 |
| | CD3CD8Low/PanCkHigh | CD3CD8High/PanCkHigh | 0.013 |
| | CD3CD8Low/PanCkLow | CD3CD8High/PanCkHigh | <0.001 |
| | CD3CD8Low/PanCkHigh | CD3CD8High/PanCkLow | 0.527 |
| | CD3CD8Low/PanCkLow | CD3CD8High/PanCkLow | 0.274 |
| | CD3CD8Low/PanCkLow | CD3CD8Low/PanCkHigh | 0.169 |
| CD3CD8/FOXP3CD3 | CD3CD8High/FOXP3CD3Low | CD3CD8High/FOXP3CD3High | 0.503 |
| | CD3CD8Low/FOXP3CD3High | CD3CD8High/FOXP3CD3High | 0.133 |
| | CD3CD8Low/FOXP3CD3Low | CD3CD8High/FOXP3CD3High | 0.001 |
| | CD3CD8Low/FOXP3CD3High | CD3CD8High/FOXP3CD3Low | 0.832 |
| | CD3CD8Low/FOXP3CD3Low | CD3CD8High/FOXP3CD3Low | 0.503 |
| | CD3CD8Low/FOXP3CD3Low | CD3CD8Low/FOXP3CD3High | 0.133 |
| CD3CD8/CD68 | CD3High/CD68Low | CD3High/CD68High | 0.403 |
| | CD3Low/CD68High | CD3High/CD68High | 0.635 |
| | CD3Low/CD68Low | CD3High/CD68High | 0.006 |
| | CD3Low/CD68High | CD3High/CD68Low | 0.635 |
| | CD3Low/CD68Low | CD3High/CD68Low | 0.093 |
| | CD3Low/CD68Low | CD3Low/CD68High | 0.047 |

**Table 4.3 Pairwise comparison between neoadjuvant cellular density ratios** *from Kaplan Meier's above (figure 4.2), ratio pairs are CD3CD8/PanCk, CD3CD8/FOXP3CD3 and CD3/CD68.*

## 4.7 Single cell spatial analysis in the neoadjuvant PDAC TME

The spatial immune cell landscape in neoadjuvant patients was explored to characterise the cellular interactions within the treated setting. The same spatial analysis methods used in chapter 3.8 were used to explore the neoadjuvant tumour immune microenvironment. Consideration was given to clinical variables treatment type (chemotherapy/chemoradiotherapy and FFX/GEM treated) and regression status, as reported in supplementary 8.3.1 for nearest neighbour and supplementary 8.3.2 for radii analysis.

### Prognostically favourable nearest neighbour tumour immune landscape in neoadjuvant patients

Overall cellular interaction in the neoadjuvant landscape demonstrates tumour cells interact primarily with αSMA and CD68 as seen by reduced average distance, and limited cytotoxic T cell interaction. Additionally, fibroblasts had mostly CD3 helper T cells and cytotoxic T cells in the immediate environment (figure 4.3).

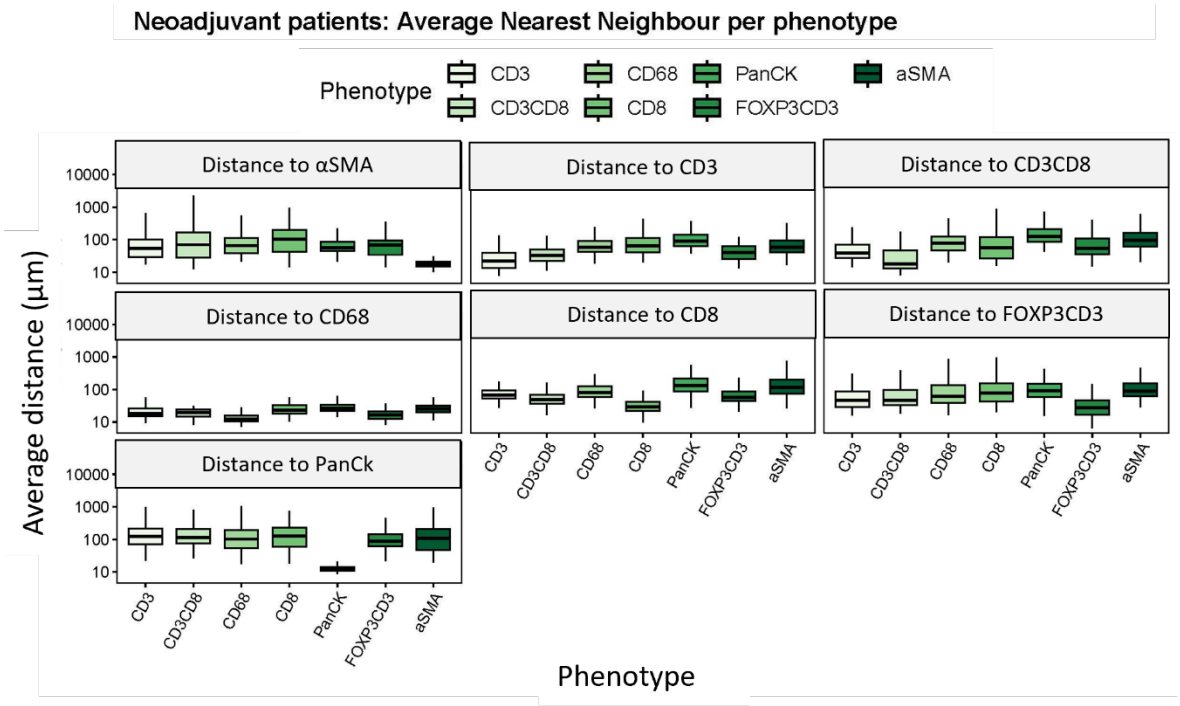


**Figure 4.3 Average nearest neighbour distance of neoadjuvant pancreatic cohort.** *Boxplots are faceted by distance to phenotype, with each 'from' phenotype displayed along the x axis, and average distance in µm along the y axis.*

Neoadjuvant patients with better outcomes demonstrated multiple significant intercellular spatial nearest neighbour patterns associated with prognosis. Short distances from PanCk+ cells to CD8+ ($p<0.001$), and short from αSMA+ cells to CD8+ ($p=0.002$), and

increased distance from αSMA+ to tumour cells (p<0.001) and CD68+ macrophages (p=0.009) were seen in high survival patients. Counterintuitively, improved disease specific survival correlated with large distances to PanCk+ cells from CD3DC8+ (p=0.023) and from CD3+ cells (p=0.013) (table 4.4). As expected, multiple trends associated with macrophages. Increased distance from CD68+ cells to PanCk+ (p=0.001), CD3CD8+ (p=0.046), CD3+ (p=0.006) and FOXP3CD3+ (p=0.002) all positively correlated with survival (table 4.4). T regulatory cells seem to play an important role in prognosis in neoadjuvant treated patients. Reduced distance from FOXP3CD3+ cells to αSMA+ (p=0.041) and CD8+ (p=0.048), and increased distance from FOXP3CD3+ to PanCk+ (p=0.002) correlated with increased survival (table 4.4). Additional trends are reported in table 4.4.

| Nearest neighbour trends in disease specific survival in neoadjuvant cohort | | | | | | | |
|---|---|---|---|---|---|---|---|
| **Phenotype** | **Region** | **Cohort** | **Group** | **Cut-off method** | **Number** | **HR (95% CI)** | **P value** |
| Distance to CD8 from PanCK | Whole core | Neoadjuvant | All pateints | Rcutoff | 72 | 3.73 (1.91-7.29) | <0.001 |
| Distance to PanCK from αSMA | Whole core | Neoadjuvant | All pateints | Rcutoff | 72 | 0.36 (0.20-0.63) | <0.001 |
| Distance to CD8 from αSMA | Whole core | Neoadjuvant | All pateints | Rcutoff | 72 | 3.40 (1.58-7.33) | 0.002 |
| Distance to FOXP3CD3 from αSMA | Whole core | Neoadjuvant | All pateints | Rcutoff | 72 | 0.23 (0.08-0.68) | 0.007 |
| Distance to CD68 from αSMA | Whole core | Neoadjuvant | All pateints | Rcutoff | 72 | 0.48 (0.28-0.83) | 0.009 |
| Distance to FOXP3CD3 from CD3 | Whole core | Neoadjuvant | All pateints | Rcutoff | 72 | 0.35 (0.20-0.62) | <0.001 |
| Distance to CD68 from CD3 | Whole core | Neoadjuvant | All pateints | Rcutoff | 72 | 0.36 (0.18-0.73) | 0.004 |
| Distance to PanCK from CD3 | Whole core | Neoadjuvant | All pateints | Rcutoff | 72 | 0.50 (0.29-0.87) | 0.015 |
| Distance to FOXP3CD3 from CD3CD8 | Whole core | Neoadjuvant | All pateints | Rcutoff | 72 | 0.31 (0.17-0.55) | <0.001 |
| Distance to CD68 from CD3CD8 | Whole core | Neoadjuvant | All pateints | Rcutoff | 72 | 0.41 (0.24-0.70) | 0.001 |
| Distance to PanCK from FOXP3CD3 | Whole core | Neoadjuvant | All pateints | Rcutoff | 72 | 0.38 (0.21-0.70) | 0.002 |
| Distance to CD3 from CD3CD8 | Whole core | Neoadjuvant | All pateints | Rcutoff | 72 | 0.54 (0.32-0.90) | 0.018 |
| Distance to PanCK from CD3CD8 | Whole core | Neoadjuvant | All pateints | Rcutoff | 72 | 0.54 (0.31-0.92) | 0.023 |
| Distance to PanCK from CD68 | Whole core | Neoadjuvant | All pateints | Rcutoff | 72 | 0.39 (0.22-0.69) | 0.001 |
| Distance to FOXP3CD3 from CD68 | Whole core | Neoadjuvant | All pateints | Rcutoff | 72 | 0.42 (0.24-0.73) | 0.002 |
| Distance to CD3 from CD68 | Whole core | Neoadjuvant | All pateints | Rcutoff | 72 | 0.45 (0.26-0.80) | 0.006 |
| Distance to CD3CD8 from CD68 | Whole core | Neoadjuvant | All pateints | Rcutoff | 72 | 0.55 (0.30-0.99) | 0.046 |
| Distance to PanCK from FOXP3CD3 | Whole core | Neoadjuvant | All pateints | Rcutoff | 72 | 0.38 (0.21-0.70) | 0.002 |
| Distance to CD68 from FOXP3CD3 | Whole core | Neoadjuvant | All pateints | Rcutoff | 72 | 0.53 (0.31-0.90) | 0.019 |
| Distance to αSMA from FOXP3CD3 | Whole core | Neoadjuvant | All pateints | Rcutoff | 72 | 1.79 (1.01-3.17) | 0.045 |

**Table 4.4 Nearest neighbour patterns associated with disease specific survival in neoadjuvant cohorts looking at whole core**. *Cut off generated (chapter 2.3.3.3) per nearest neighbour pattern, cohort, patient group and number indicated. Log Rank (Mantel-Cox) p value and Univariate cox regression hazard ratio (HR) shown with 95% confidence interval (CI).*

### 4.7.2 Prognostically favourable tumour immune landscape in all neoadjuvant patients at different radii

As described in chapter 3.8.3, radius analysis considers both distance and density metrics. Investigation was limited to increments of 10μm from 0-50μm to maintain the spatial component of this analysis type. Of note, an elevated density of macrophages was found within 50μm from CD3+ cells, from PanCk+ cells, and from FOXP3CD3+ cells (figure 4.4).

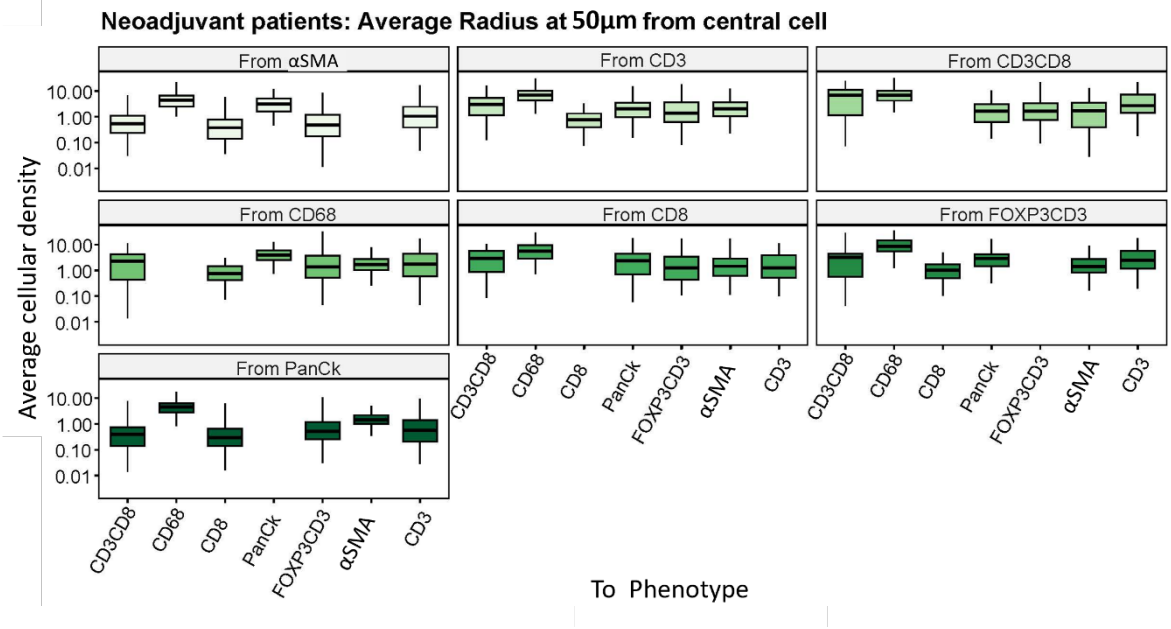


**Figure 4.4 Average immune cell population at 50μm from central cell in neoadjuvant pancreatic cohort.** *Boxplots are faceted central cell ('from' phenotype), with each 'to' phenotype displayed along the x axis, and average cellular density along the y axis.*

Neoadjuvant patients associated with favourable prognosis at variable distances. At 20μm, patients with low density of CD68+ (p=0.014) and PanCk+ (p=0.04) from CD3+ were seen in longer survival patients (table 4.5). They also presented with low density of CD3+ (p=0.035), CD3CD8+ (p=0.036), CD68+ (p=0.025) and PanCk+ (p=0.003) cells within 20μm from αSMA+ cells (table 4.5). Additionally, low density of CD3CD8+ (p=0.016), PanCk+ (p=0.009) and FOXP3CD3+ (p<0.001) at 30μm from CD68+ cells was also observed in better outcome patients (table 4.5). Reduced density of CD3+ (p=0.035), CD68+ (p=0.01) and FOXP3CD3+ (p=0.009) at 50μm from tumour cells correlated with survival (table 4.5).

**Radius trends in disease specific survival in neoadjuvant patients**

| From Phenotype | To Phenotype | Distance (μm) | Cohort | Group | Cut-off method | Number | HR (95% CI) | P value |
|---|---|---|---|---|---|---|---|---|
| PanCk | CD3 | 50 | Neoadjuvant | All patients | Rcutoff | 72 | 1.82 (1.04-3.18) | 0.035 |
| PanCk | CD68 | 50 | Neoadjuvant | All patients | Rcutoff | 72 | 2.36 (1.23-4.54) | 0.010 |
| PanCk | FOXP3CD3 | 50 | Neoadjuvant | All patients | Rcutoff | 72 | 2.09 (1.20-3.64) | 0.009 |
| αSMA | CD3 | 20 | Neoadjuvant | All patients | UQ | 72 | 1.74 (1.04-2.91) | 0.035 |
| αSMA | CD3CD8 | 20 | Neoadjuvant | All patients | UQ | 72 | 1.75 (1.04-2.94) | 0.036 |
| αSMA | CD68 | 20 | Neoadjuvant | All patients | UQ | 72 | 1.86 (1.08-3.20) | 0.025 |
| αSMA | PanCk | 20 | Neoadjuvant | All patients | UQ | 72 | 2.26 (1.32-3.89) | 0.003 |
| CD3 | CD68 | 20 | Neoadjuvant | All patients | Rcutoff | 72 | 2.58 (1.21-5.47) | 0.014 |
| CD3 | PanCk | 20 | Neoadjuvant | All patients | Rcutoff | 72 | 1.79 (1.03-3.13) | 0.004 |
| CD68 | CD3CD8 | 30 | Neoadjuvant | All patients | Median | 72 | 1.87 (1.12-3.11) | 0.016 |
| CD68 | PanCk | 30 | Neoadjuvant | All patients | Median | 72 | 2.54 (1.26-5.13) | 0.009 |
| CD68 | FOXP3CD3 | 30 | Neoadjuvant | All patients | Median | 72 | 2.90 (1.63-5.15) | <0.001 |

**Table 4.5 Radii patterns associated with disease specific survival in neoadjuvant cohorts looking at whole core**. *Cut-off method was established as indicated. Radii reported using 'from phenotype' column, indicating the central phenotype, and 'to phenotype' indicating the surrounding phenotype. Reported by distance (μm), cohort, patient group, along with number of patients in each group. Most significant radii is reported. Log Rank (Mantel-Cox) p value and Univariate cox regression hazard ratio (HR) shown with 95% confidence interval (CI) for disease specific survival (DSS) and recurrence free survival (RFS).*

# 4.8 Filtering Neoadjuvant prognostic markers

A substantial number of significant patterns were detected in neoadjuvant patients. To begin to make sense of these, a filtering process, replicating the one described in chapter 3.9, was performed to select robust variables with the highest likelihood of biological importance. As no validation cohort was available for the neoadjuvant patients, all significant variables from density and nearest neighbour analysis were used. Multivariate cox regression results are reported in supplementary 8.3.3

## 4.8.1 Decision tree analysis

Verification of significant density and nearest neighbour variables was carried out using decision tree models. Model input was limited to significant ranked variables found in the multivariate model above. Grouping density and NN pairs generated interesting results. As in the naïve  cohort (chapter 3.9.1), the root node was a nearest neighbour spatial metric, distance to CD3CD8 from FOXP3CD3 (CD3CD8-from-FOXP3CD3) (figure 4.5.a). Patients with lowest survival probability demonstrated CD3CD8-from-FOXP3CD3High:CD3-from-CD3CD8Low:PanCkHigh (Node 6: probability = 0.67 , p=0.038), and the highest survival probability patients associated with either were CD3CD8-from-FOXP3CD3Low (Node 2: probability = 0.97, p<0.001) or CD3CD8-from-FOXP3CD3High:CD3-from-CD3CD8High (Node 7: probability = 0. 93, p<0.001) (figure 4.5.a). Limiting the data type to significant density variables, patients with the lowest survival probability were CD3CD8High:PanCkHigh (Node 7: probability = 0.7, p=0.026) and highest survival probability was CD3CD8Low:CD68Low (Node 3: probability = 0.96, p=0.024) (figure 4.5.b). Focusing on nearest neighbour variables alone, a new nearest neighbour specific model was generated with distance to CD3CD8 from FOXP3CD3 (CD3CD8-from-FOXP3CD3) as the root node (figure 4.5.c). Patients with the highest survival probability were those with low distances to CD3CD8 from FOXP3CD3 (Node 2: probability = 0.97 , p<0.001) and CD3CD8-from-FOXP3CD3High:CD3-from-CD3CD8High:CD3CD8-from-PanCkHigh (Node 7: probability = 0.94, p=0.023) (figure 4.5.c). In contrast, patients with the lowest probability demonstrated CD3CD8-from-FOXP3CD3High:CD3-from-CD3CD8Low (Node 4: probability = 0.72 , p<0.001) (figure 4.5.c).

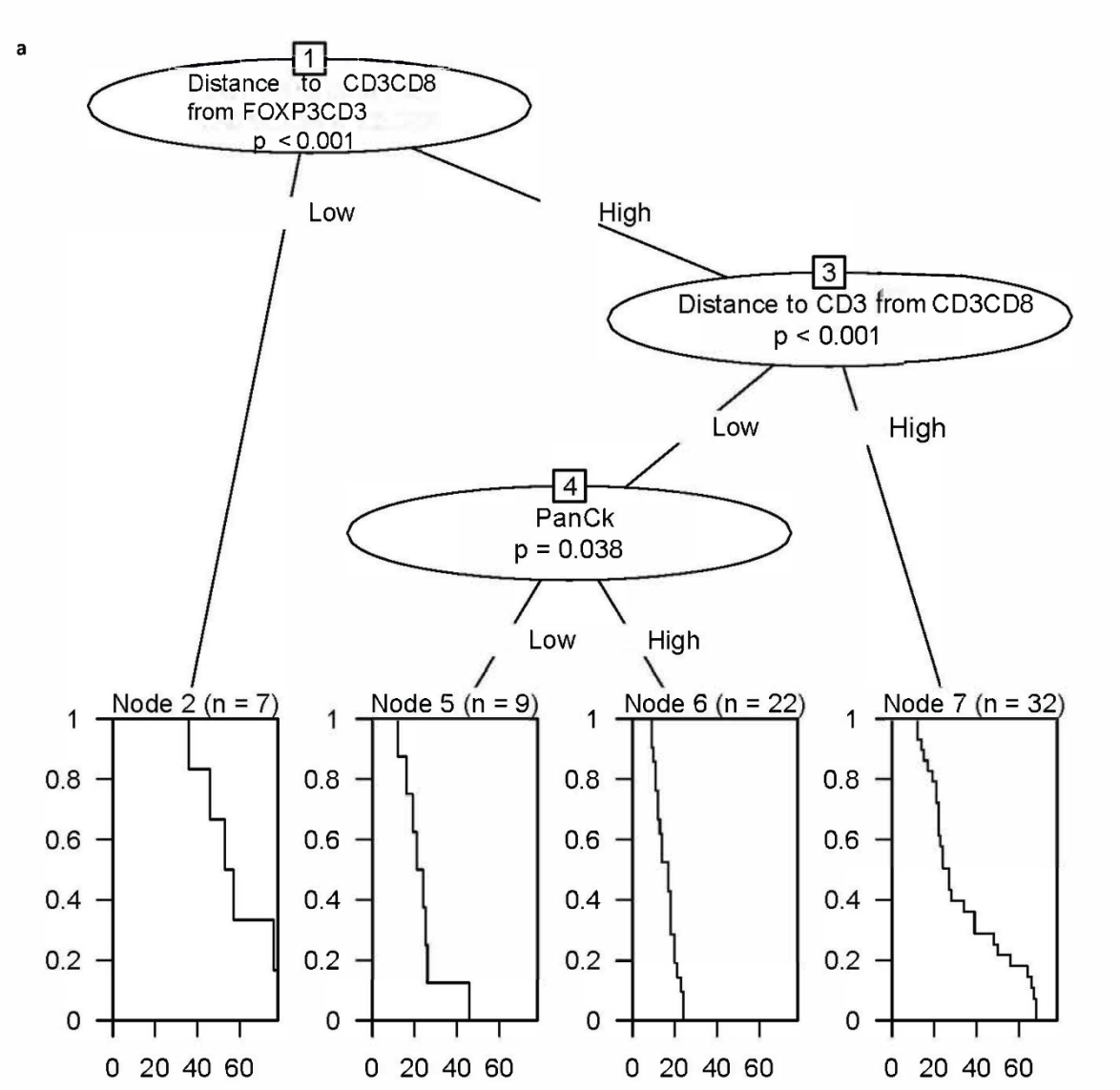


| Node | Number | Number at risk | Number of event | Survival Probability | Censored Probability | Lower CI (95%) | Upper CI (95%) |
|---|---|---|---|---|---|---|---|
| 2 | 7 | 6 | 0 | 0.97 | 0 | 1 | 1 |
| 5 | 9 | 8 | 1 | 0.88 | 0.12 | 0.67 | 1 |
| 6 | 22 | 16 | 7 | 0.67 | 0.10 | 0.49 | 0.90 |
| 7 | 32 | 29 | 2 | 0.93 | 0.05 | 0.84 | 1 |

**Figure 4.5.a Density and nearest neighbour decision tree model with matching survival probability table in neoadjuvant cohort** *for a) Combined density and nearest neighbour variables. Nodes split according to rank, number of patients per node indicated and associated p value in decision tree model. Survival probability with confidence intervals (CI) and associated nodes reported in survival table.*

b

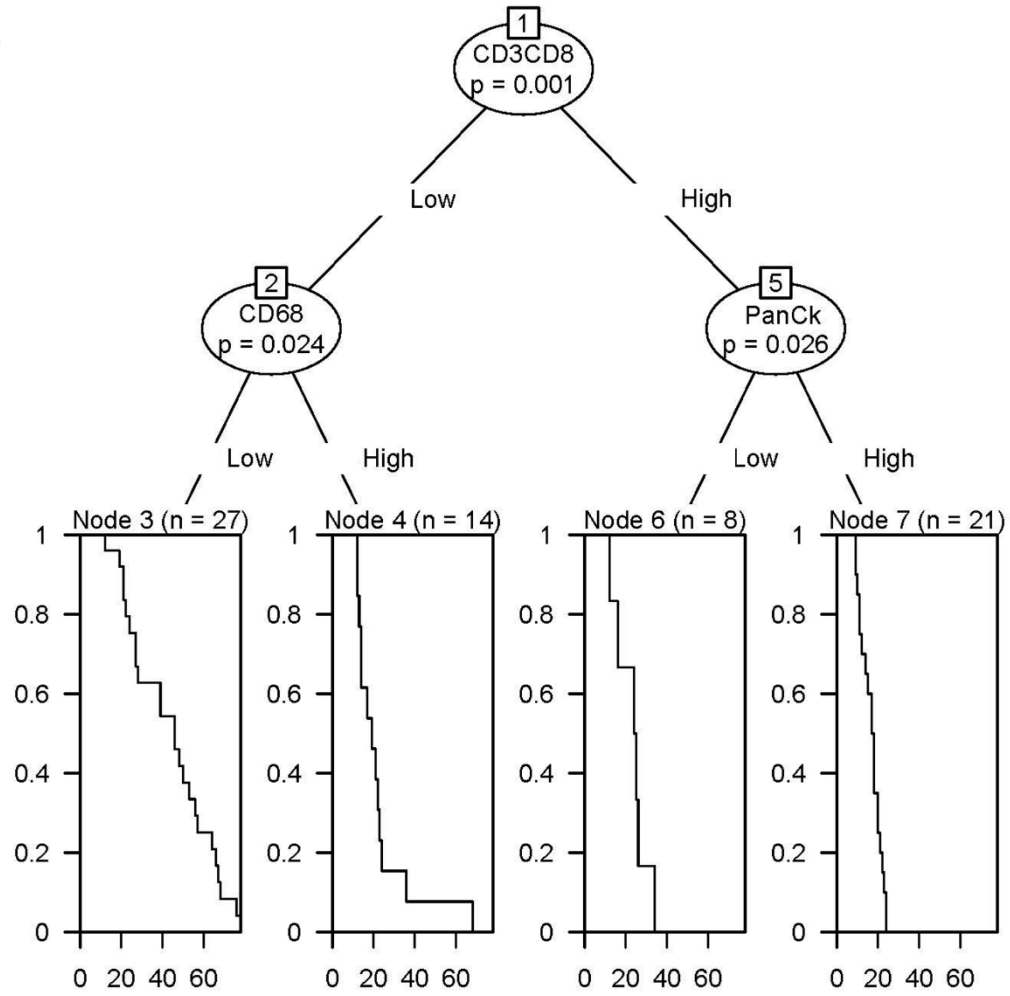


| Node | Number | Number at risk | Number of events | Survival Probability | Censored Probability | Lower CI (95%) | Upper CI (95%) |
|---|---|---|---|---|---|---|---|
| 3 | 27 | 25 | 1 | 0.96 | 0.04 | 0.89 | 1 |
| 4 | 14 | 13 | 2 | 0.85 | 0.10 | 0.67 | 1 |
| 6 | 8 | 6 | 1 | 0.83 | 0.15 | 0.58 | 1 |
| 7 | 21 | 15 | 6 | 0.7 | 0.10 | 0.53 | 0.93 |

**Figure 4.5.b Density and nearest neighbour decision tree model with matching survival probability table in neoadjuvant cohort for** *b) Density alone. Nodes split according to rank, number of patients per node indicated and associated p value in decision tree model. Survival probability with confidence intervals (CI) and associated nodes reported in survival table.*

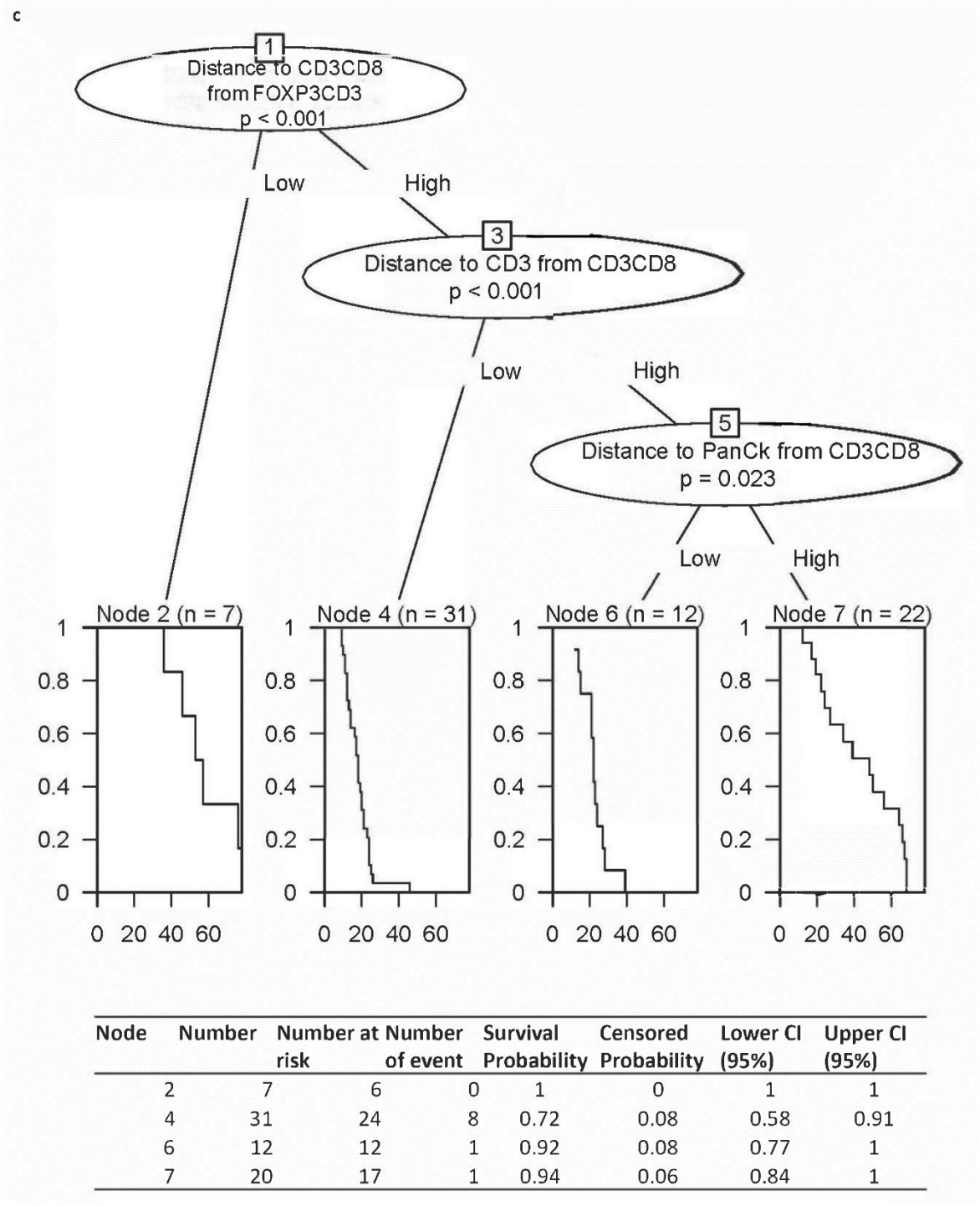


| Node | Number | Number at risk | Number of event | Survival Probability | Censored Probability | Lower CI (95%) | Upper CI (95%) |
|---|---|---|---|---|---|---|---|
| 2 | 7 | 6 | 0 | 1 | 0 | 1 | 1 |
| 4 | 31 | 24 | 8 | 0.72 | 0.08 | 0.58 | 0.91 |
| 6 | 12 | 12 | 1 | 0.92 | 0.08 | 0.77 | 1 |
| 7 | 20 | 17 | 1 | 0.94 | 0.06 | 0.84 | 1 |

**Figure 4.5.c Density and nearest neighbour decision tree model with matching survival probability table in neoadjuvant cohort for** *c). All nearest neighbour significant variables from multivariate model. Nodes split according to rank, number of patients per node indicated and associated p value in decision tree model. Survival probability with confidence intervals (CI) and associated nodes reported in survival table.*

## 4.9 Distribution pattern of immune cells in pancreatic cancer tumour microenvironment

As in chapter 3.10.1, spatiotemporal point pattern analysis method ‘Ripley’s K’ was used to determine the pattern of distribution of cells within the TMA cores. Much like the naïve cohort, the Ripley’s K function was always above the average theoretical value for each phenotype, and therefore phenotypes had a clustered pattern of distribution. Upon investigation on the level of clustering, clustering trends remained the same as in treatment naïve patients. Significant differences were observed in all phenotype pairs between K function and theoretical. On average, the most clustered markers were PanCk+, CD3+, CD3CD8+ and FOXP3CD3+, and least clustered were αSMA+ and CD68+ cells (figure 4.6). It is worth noting that this analysis was performed using TMA cores, and therefore spatiotemporal pattern of expression maybe biased due to the limited area investigated.

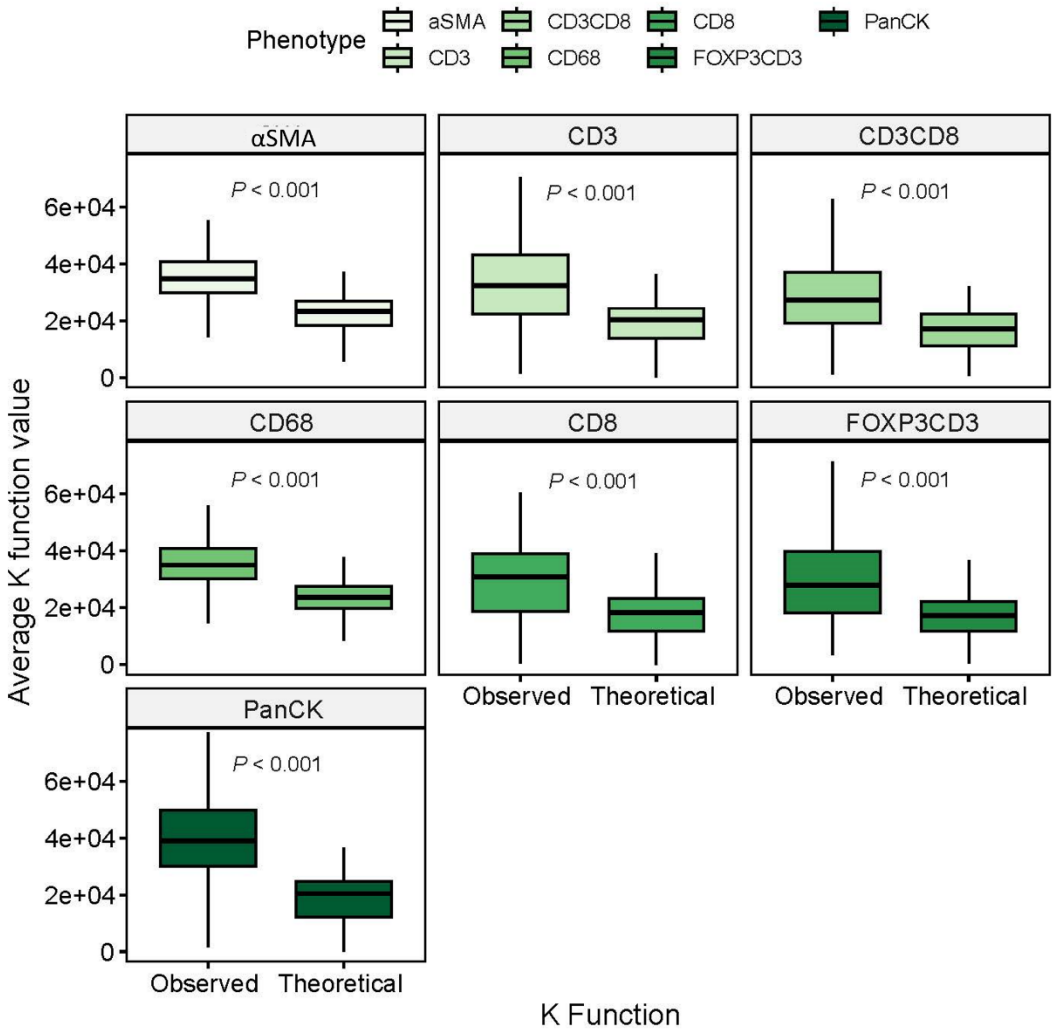


**Figure 4.6 Average Ripley’s K function and theoretical Poisson function values for all phenotypes across neoadjuvant cores.** *Boxplot faceted by phenotype, comparing observed K function to theoretical K function in all cores (n=253 ) using Bonferroni p adjustment T-test.*

## 4.10 Unbiased phenotyping and neighbourhood generation

Validation of phenotyping in neoadjuvant TMAs was carried out using CytoMAP unbiased clustering and subsequent neighbourhood region generation was established (chapter 2.3.3.5 and chapter 3.10). Nine cell cluster regions were produced (figure 4.7.a), most of which overlapped with biased phenotyping. Nonetheless, this clustering method produced two unexpected clusters in regions 7 and 8, comprising of CD3+CD8+FOXP3+ and CD3+CD8+FOXP3+CD68+ markers (figure 4.7.a). These cell clusters were then used to create neighbourhood region clusters, with five regions produced. Cluster 4 is of particular interest, as it presents a T regulatory and cytotoxic T cell and macrophage heavy region (figure 4.7.b). The remaining neighbourhoods were as expected.

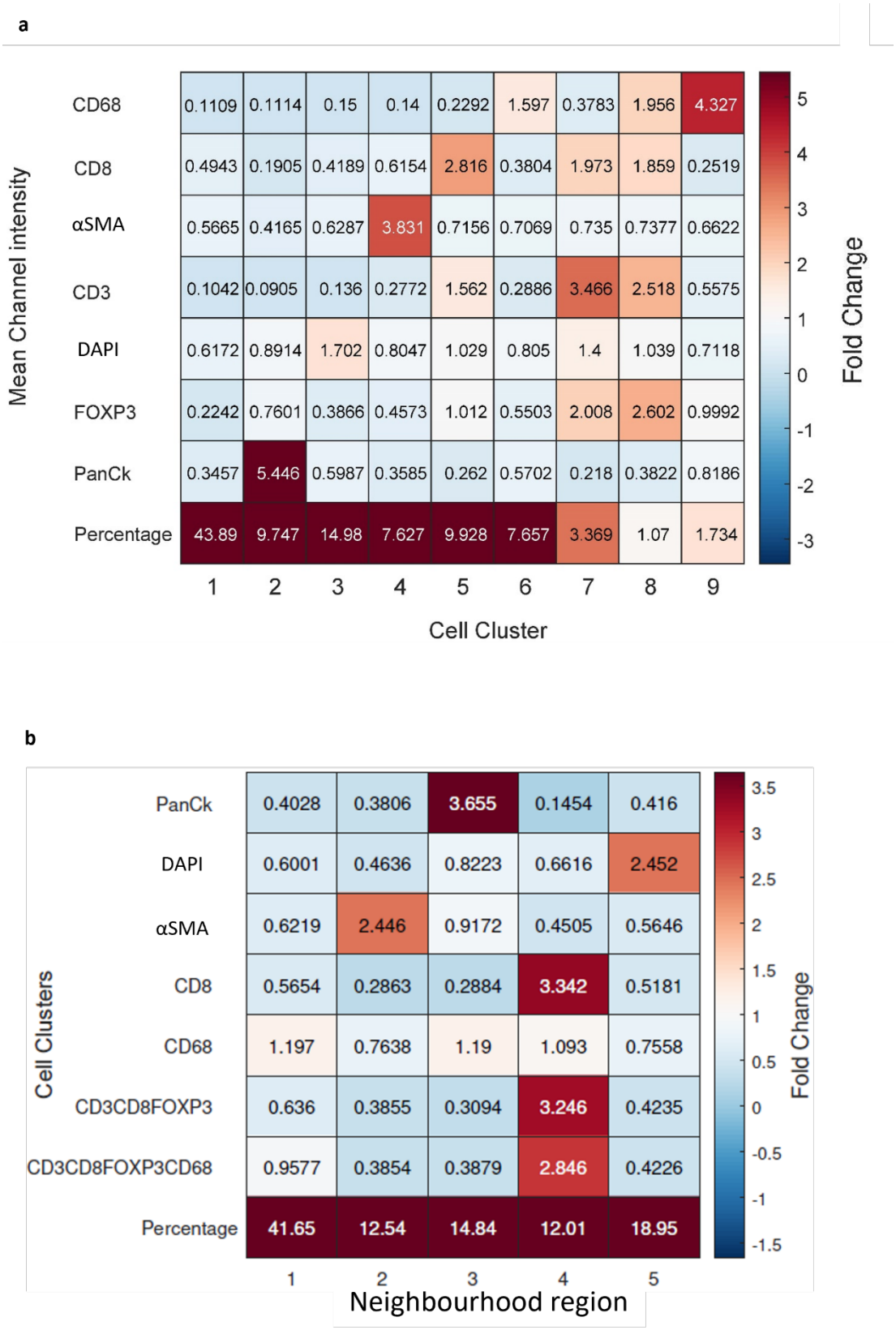


**Figure 4.7 Neighbourhood generation in neoadjuvant PDAC combined cohort using CytoMAP** *a) Cell typing heatmap showing fold change differences across channels to generate cell clusters b) neighbourhood regions generated by fold change of cell clusters associating with each other. Heatmap coloured by fold change.*

## 4.11 Characterising the tumour microenvironment in naïve versus neoadjuvant pancreatic cancer

Both naïve and neoadjuvant immune landscapes have been established in chapter 3 and chapter 4 (above). In order to explore the differences between naïve and neoadjuvant, the discovery and validation naive cohorts were combined, and compared to the neoadjuvant cohort (table 4.1). Previously established ranking was used.

### 4.11.1 Deep phenotyping and cellular density landscape in naïve vs neoadjuvant pancreatic cancer

The overall percentage phenotype population of naïve and neoadjuvant patients found elevated CD68+ and FOXP3CD3+ cell in the neoadjuvant cohort (figure 4.8). Additionally, elevated PanCk+ cells were observed in naïve cohorts as expected (figure 4.8).

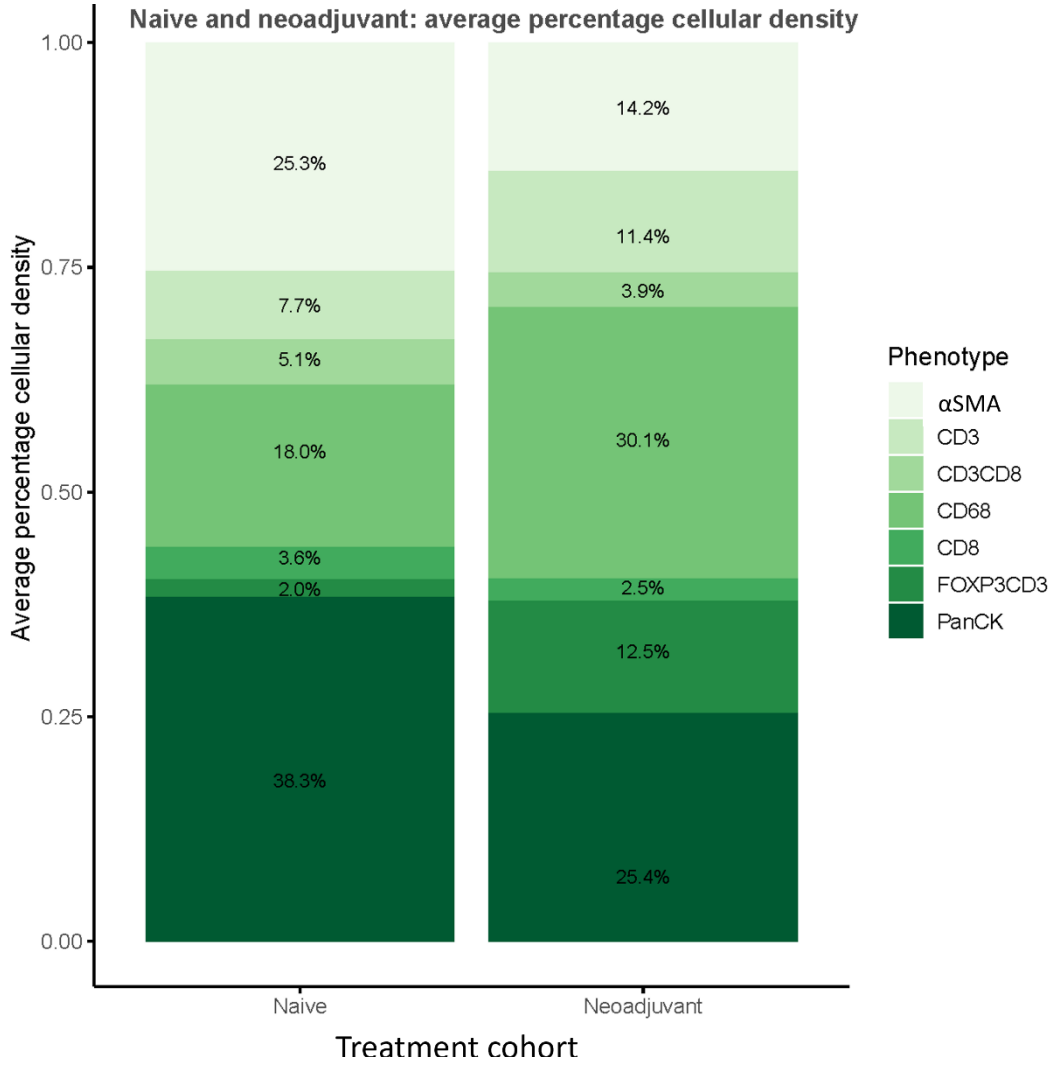


**Figure 4.8 Average percentage cellular density boxplots of phenotypes in combined naïve and neoadjuvant pancreatic cohort** *across all phenotypes. Percentage per phenotype per treatment shown.*

Subsequent investigation into whether the neoadjuvant cohort, along with its counterintuitive prognostic trends, would demonstrate improved survival when compared to the combined naïve cohort. Neoadjuvant patients with low expression of CD3+ ($p<0.001$), CD8+ ($p=0.03$), FOXP3CD3+ ($p=0.003$) and CD3CD8+ ($p=0.001$) consistently associated with the highest median disease specific survival times (figure 4.9.a-d). The comparison was strictly done between tumour core/centre, therefore these observations are limited to this histopathological region.

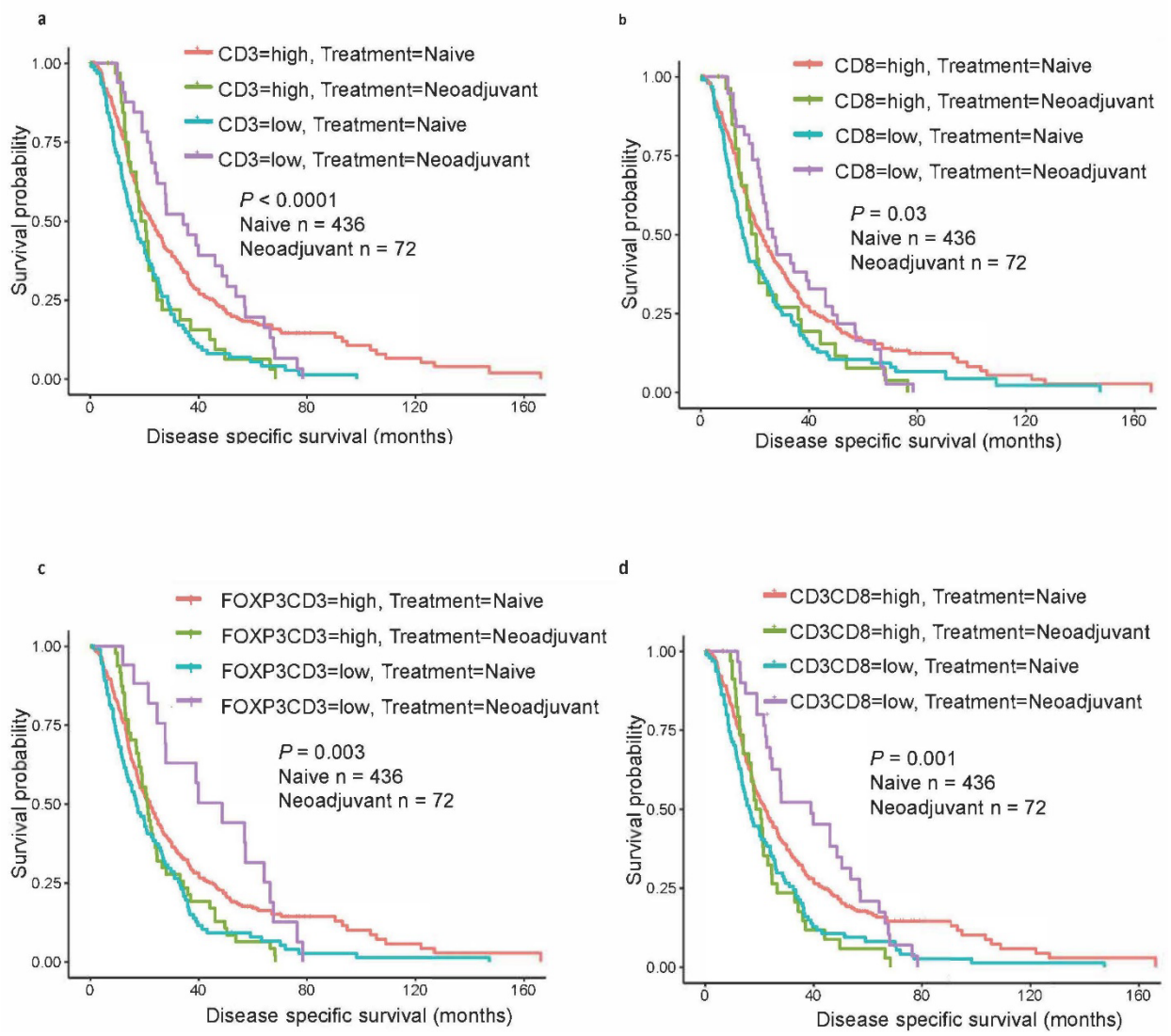


**Figure 4.9.a-d Survival analysis of cellular density in combined naïve and neoadjuvant PDAC cohorts,** *Kaplan-Meier curves (disease specific survival) stratified by protein marker expression (Log-Rank test) for a). CD3+ b). CD8+ c). FOXP3CD3+ d). CD3CD8+*

### 4.11.2 Prognostically favourable nearest neighbour tumour immune landscape in naïve vs neoadjuvant patients

Differences between nearest neighbour metrics in naïve and neoadjuvant patients were explored. First, the average distances were established to investigate whether the surrounding phenotypic environment was altered according to treatment status. Notably, neoadjuvant cohorts demonstrated significant reduced distances from CD68+ to CD3+ (p=0.037), from PanCk+ to FOXP3CD3+ (p=0.001), and from αSMA+ to FOXP3CD3+ (p=0.04) among others (figure 4.10). Furthermore, neoadjuvant patients also exhibited reduced average distance from all phenotypes (bar CD8+) to CD68+ macrophages compared to naïve patients (figure 4.10).

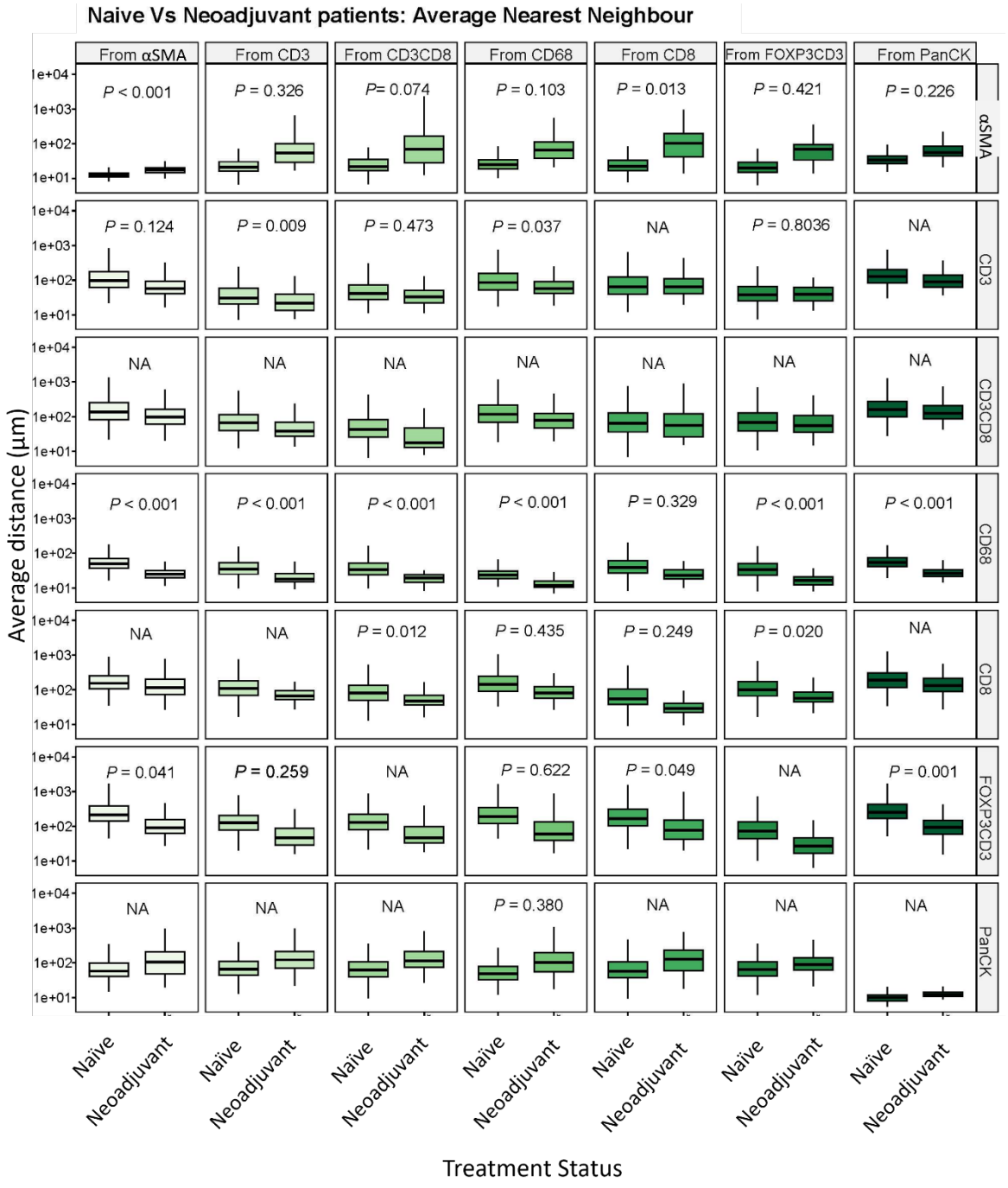


**Figure 4.10 Average nearest neighbour distance of combined naïve and neoadjuvant**

**pancreatic cohort.** *Boxplots are faceted by distance to phenotype, with each 'from' phenotype displayed along the top x axis, each 'to' phenotype displayed along the right y axis, and average distance in μm along the left y axis.*

Comparisons between the established base naïve and neoadjuvant samples were made to determine alterations in spatial interactions between treatment type. Overlapping distance metrics observed in both cohorts were investigated. Two survival clusters were observed, the better survival naïve and better survival neoadjuvant patients, and the poor survival naïve and poor survival neoadjuvant patients. Matching patterns were seen in a range of nearest neighbour pairs. Large distances to PanCk+ from αSMA+ (p=0.003), from CD3CD8+ (p=0.045), from FOXP3CD3+ (p=0.028), and from CD68+ (p=0.027) in both neoadjuvant and naïve cohorts correlated with increased disease specific survival. Neoadjuvant patients associated with best outcome (table 4.6). Interestingly, many nearest neighbour patterns differed between treatment status. Decreased distance to αSMA+ from CD3CD8+ (p=0.003) and to CD3CD8+ from CD68+ (p=0.008), in neoadjuvant patients associated with improved survival, with the opposite trend demonstrated in high survival naïve patients (table 4.6). Similarly, large distances to PanCk+ from CD3+ (p=0.024), to FOXP3CD3+ from CD68+ (p=0.003) and to CD3+ from CD68+ (p=0.010) in neoadjuvant correlated with improved survival, with the reverse trend seen in naïve patients (table 4.6).

| Nearest neighbour trends in disease specific survival in naïve and neoadjuvant cohorts | | | | | | |
|---|---|---|---|---|---|---|
| **Nearest neighbour pattern** | **Region** | **Cohort** | **Group** | **Number** | **HR (95% CI)** | **P value** |
| Distance to PanCK from αSMA | Whole core | Naïve and Neoadjuvant | Neoadjuvant<br>Naïve | 72<br>436 | 0.36 (0.20-0.63)<br>0.76 (0.59-0.97) | 0.003 |
| Distance to PanCK from CD3 | Whole core | Naïve and Neoadjuvant | Neoadjuvant<br>Naïve | 72<br>436 | 0.50 (0.29-0.87)<br>0.81 (0.65-1.00) | 0.024 |
| Distance to CD68 from CD3CD8 | Whole core | Naïve and Neoadjuvant | Neoadjuvant<br>Naïve | 72<br>436 | 0.41 (0.24-0.70)<br>0.83 (0.67-1.03) | 0.018 |
| Distance to αSMA from CD3CD8 | Whole core | Naïve and Neoadjuvant | Neoadjuvant<br>Naïve | 72<br>436 | 1.63 (0.97-2.75)<br>0.71 (0.57-0.89) | 0.003 |
| Distance to PanCK from CD3CD8 | Whole core | Naïve and Neoadjuvant | Neoadjuvant<br>Naïve | 72<br>436 | 0.54 (0.31-0.92)<br>0.83 (0.66-1.03) | 0.045 |
| Distance to PanCK from CD68 | Whole core | Naïve and Neoadjuvant | Neoadjuvant<br>Naïve | 72<br>436 | 0.39 (0.22-0.69)<br>0.79 (0.64-0.99) | 0.027 |
| Distance to CD3 from CD68 | Whole core | Naïve and Neoadjuvant | Neoadjuvant<br>Naïve | 72<br>436 | 0.45 (0.26-0.80)<br>1.38 (1.11-1.72) | 0.010 |
| Distance to FOXP3CD3 from CD68 | Whole core | Naïve and Neoadjuvant | Neoadjuvant<br>Naïve | 72<br>436 | 0.42 (0.24-0.73)<br>1.42 (1.14-1.78) | 0.003 |
| Distance to CD3CD8 from CD68 | Whole core | Naïve and Neoadjuvant | Neoadjuvant<br>Naïve | 72<br>436 | 2.19 (0.93-5.17)<br>1.33 (1.07-1.66) | 0.008 |
| Distance to PanCK from FOXP3CD3 | Whole core | Naïve and Neoadjuvant | Neoadjuvant<br>Naïve | 72<br>436 | 0.38 (0.21-0.70)<br>0.79 (0.62-1.02) | 0.028 |

**Table 4.6 Nearest neighbour patterns associated with disease specific survival in combined naïve and neoadjuvant cohorts looking at whole core**. *Nearest neighbour pattern reported per group and region, patient group indicated, along with number of patients in each group. Log Rank (Mantel-Cox) p value and Univariate cox regression hazard ratio (HR) shown with 95% confidence interval (CI).*

### 4.11.3 Prognostically favourable mutual nearest neighbour tumour immune landscape in naïve vs neoadjuvant patients

Significant differences were established in average distances between naïve and neoadjuvant patients for a range of mutual nearest neighbour pairs. These differences were mostly observed in CD68+ macrophages associated pairs. Decreased distance between CD68+ macrophages and αSMA+ (p<0.001), PanCk+ (p<0.001), CD3+ (p<0.001), CD3CD8+ (p<0.001), CD68+ (p<0.001) and FOXP3CD3+ (p<0.001) demonstrated in the neoadjuvant cohort (figure 4.11).

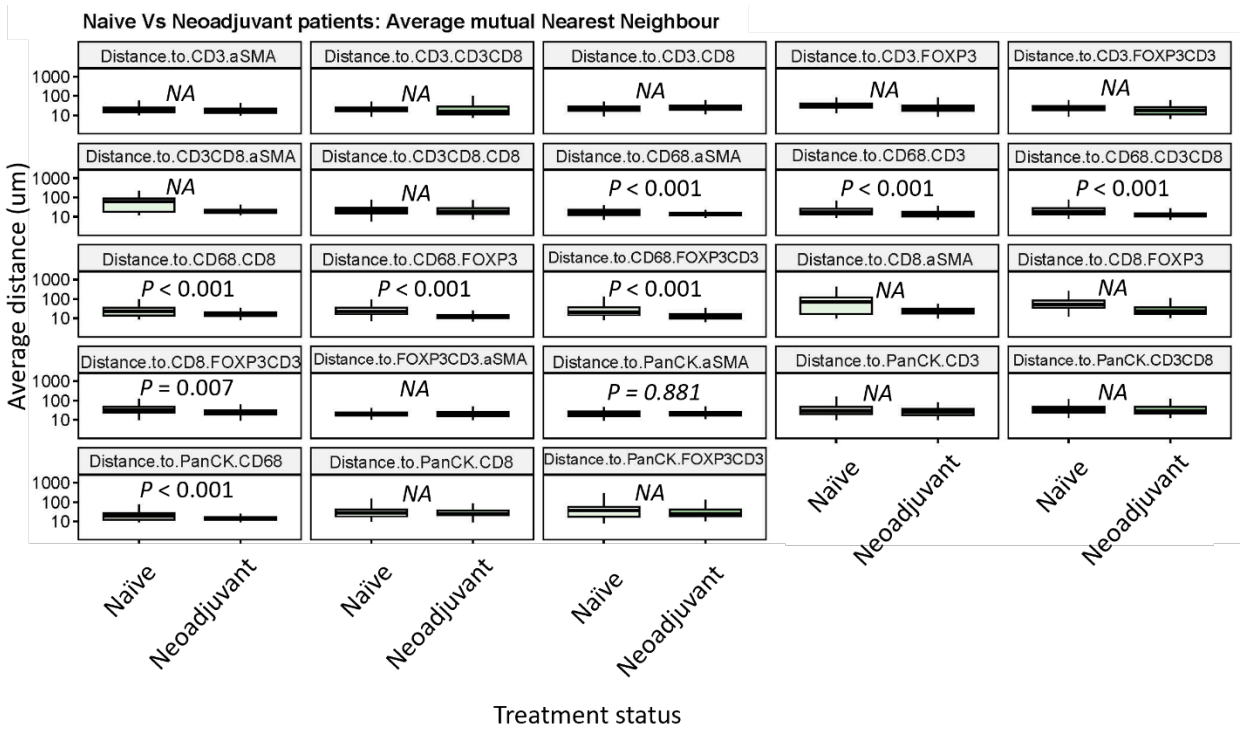


**Figure 4.11 Average mutual nearest neighbour distance of combined naïve and neoadjuvant pancreatic cancer cohort.** *Boxplots are faceted by mutual nearest neighbour relationship, with treatment cohort along the x axis, and average distance in μm along the y axis.*

When looking at mutual pairs, large amount of overlap between the high survival naïve and high survival neoadjuvant patients was seen. Large distances between FOXP3CD3-αSMA (p=0.012), CD68-αSMA (p=0.009), CD68-CD3CD8 (p=0.01), PanCk-CD68 (p=0.002), and CD3-αSMA (p=0.004) in both neoadjuvant and naïve patients correlated with better survival (table 4.7). Furthermore, large distances in neoadjuvant patients between CD68-FOXP3CD3 (p=0.025), PanCk-αSMA (p=0.003) and PanCk-CD3CD8 (p=0.01) positively correlated with improved DSS (table 4.7).

| Mutual nearest neighbour trends in disease specific survival in combined naïve and neoadjuvant cohorts | | | | | | |
|---|---|---|---|---|---|---|
| **Mutual nearest neighbour pair** | **Region** | **Cohort** | **Group** | **Number** | **HR (95% CI)** | **P value** |
| Distance to PanCK and CD68 | Whole core | Naïve and Neoadjuvant | Neoadjuvant | 72 | 0.28 (0.11-0.73) | 0.002 |
| | | | Naïve | 436 | 0.62 (0.48-0.81) | |
| Distance to PanCK and αSMA | Whole core | Naïve and Neoadjuvant | Neoadjuvant | 72 | 0.51 (0.30-0.87) | 0.003 |
| | | | Naïve | 436 | 0.64 (0.49-0.83) | |
| Distance to CD3 and αSMA | Whole core | Naïve and Neoadjuvant | Neoadjuvant | 72 | 0.48 (0.25-0.92) | 0.004 |
| | | | Naïve | 436 | 0.65 (0.50-0.85) | |
| Distance to CD68 and αSMA | Whole core | Naïve and Neoadjuvant | Neoadjuvant | 72 | 0.40 (0.22-0.73) | 0.009 |
| | | | Naïve | 436 | 0.69 (0.54-0.90) | |
| Distance to FOXP3CD3 and αSMA | Whole core | Naïve and Neoadjuvant | Neoadjuvant | 72 | 0.42 (0.23-0.76) | 0.012 |
| | | | Naïve | 436 | 0.70 (0.54-0.92) | |
| Distance to CD68 and FOXP3CD3 | Whole core | Naïve and Neoadjuvant | Neoadjuvant | 72 | 0.48 (0.28-0.81) | 0.025 |
| | | | Naïve | 436 | 0.76 (0.59-0.99) | |
| Distance to CD68 and CD3CD8 | Whole core | Naïve and Neoadjuvant | Neoadjuvant | 72 | 0.31 (0.16-0.62) | 0.017 |
| | | | Naïve | 436 | 0.81 (0.62-1.05) | |
| Distance to PanCK and CD3CD8 | Whole core | Naïve and Neoadjuvant | Neoadjuvant | 72 | 0.36 (0.21-0.62) | 0.01 |
| | | | Naïve | 436 | 0.83 (0.64-1.07) | |

**Table 4.7 Mutual nearest neighbour patterns associated with disease specific survival in combined naïve and neoadjuvant cohorts in whole core.** *Mutual nearest neighbour pair reported per group and region, along with number of patients in each group. Log Rank (Mantel-Cox) p value and univariate cox regression hazard ratio (HR) shown with 95% confidence interval (CI).*

### 4.11.4 Prognostically favourable tumour immune landscape at different radii in naïve vs neoadjuvant pancreatic cancer patients

Finally, phenotypic differences in the immediate microenvironment (50μm radius) for all cells in naïve and neoadjuvant patients were determined. Elevated levels of CD68+ (p=0.022), and reduced levels of αSMA+ cells (p<0.001) within the PanCk+ environment, and within the CD68+ environment, elevated CD3CD8+ (p=0.004), elevated FOXP3CD3+ (p=0.003), reduced PanCk+ (p<0.001), and reduced αSMA+ (p<0.001) were observed in neoadjuvant patients compared to naïve patients (figure 4.12). Furthermore, increased expression of CD3CD3+ (p<0.001), CD68+ (p<0.001), FOXP3CD3+ (p=0.008), and reduced PanCk+ (p<0.001) surrounding CD3+ cells was observed in neoadjuvant patients compared to naïve patients (figure 4.12).

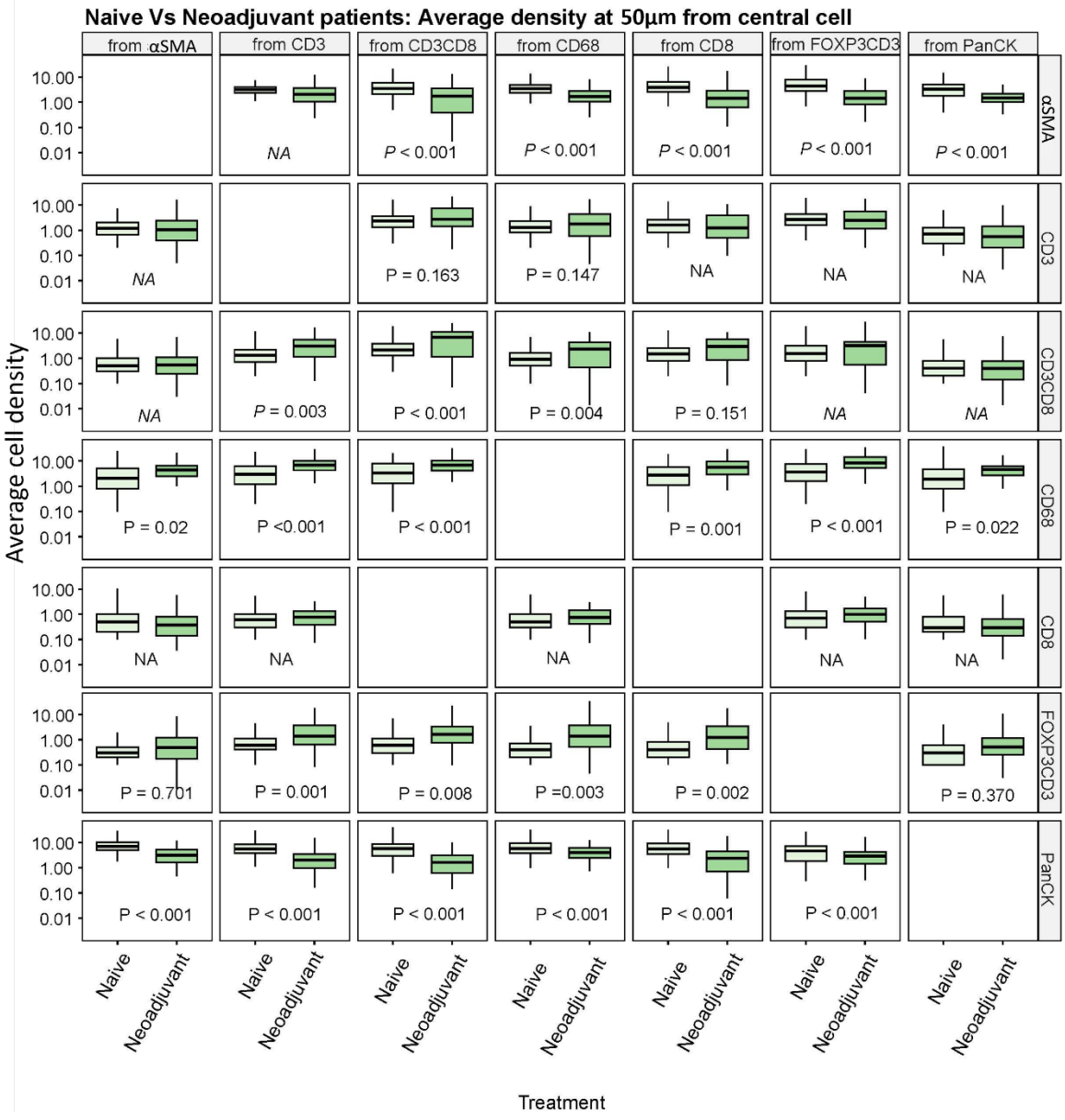


**Figure 4.12 Average immune cell population density at 50μm from central cell in combined**

**naïve and neoadjuvant cohorts** *Boxplots are faceted central cell ('from' phenotype), with each 'to' phenotype displayed along the right y axis, and average cellular density along the left y axis.*

To maintain the spatial aspect of this analysis, reporting is limited to significant survival relationships within 50μm. In the immediate surrounding environment of CD3+ cells (20μm radius), low density of FOXP3CD3+ (p=0.049) and CD3CD8+ (p=0.053) correlated with increased survival in neoadjuvant patients, and low density of CD68+ (p=0.009) in both neoadjuvant and naïve patients from CD3+ cells was associated with longer survival times (table 4.8). Matched tumour-macrophage trends were seen in naïve and neoadjuvant patients, with low density of CD68+ cells within 30μm from PanCk+ was associated with improved survival (table 4.8). Additionally, multiple macrophage associated trends demonstrated positive associations with prognosis. Neoadjuvant patients with low density of CD3+ (p=0.011), CD3CD8+ (p=0.018) and FOXP3CD3+ (p=0.044) within 40μm from CD68+ cells correlated with better prognosis (table 4.8).

| Radius trends in disease specific survival in combined naïve and neoadjuvant patients | | | | | | | |
|---|---|---|---|---|---|---|---|
| **From Phenotype** | **To Phenotype** | **Distance (μm)** | **Cohort** | **Group** | **Number** | **HR (95% CI)** | **P value** |
| CD3 | FOXP3CD3 | 20 | Naïve and Neoadjuvant | Neoadjuvant | 72 | 2.76 (1.59-4.78) | 0.049 |
| | | | | Naïve | 436 | 1.01 (0.66-1.55) | |
| CD3 | CD3CD8 | 20 | Naïve and Neoadjuvant | Neoadjuvant | 72 | 1.80 (1.09-2.99) | 0.053 |
| | | | | Naïve | 436 | 0.82 (0.61-1.08) | |
| CD3 | CD68 | 20 | Naïve and Neoadjuvant | Neoadjuvant | 72 | 2.53 (1.22-5.23) | 0.009 |
| | | | | Naïve | 436 | 1.49 (1.13-1.96) | |
| PanCk | CD68 | 30 | Naïve and Neoadjuvant | Neoadjuvant | 72 | 2.36 (1.23-4.54) | 0.011 |
| | | | | Naïve | 436 | 1.52 (1.14-2.01) | |
| CD68 | CD3 | 40 | Naïve and Neoadjuvant | Neoadjuvant | 72 | 1.64 (0.95-2.82) | 0.011 |
| | | | | Naïve | 436 | 0.68 (0.53-0.89) | |
| CD68 | CD3CD8 | 40 | Naïve and Neoadjuvant | Neoadjuvant | 72 | 1.99 (1.20-3.32) | 0.018 |
| | | | | Naïve | 436 | 0.72 (0.55-0.93) | |
| CD68 | FOXP3CD3 | 40 | Naïve and Neoadjuvant | Neoadjuvant | 72 | 2.61 (1.52-4.48) | 0.044 |
| | | | | Naïve | 436 | 0.82 (0.64-1.05) | |

**Table 4.8 Radii patterns associated with disease specific survival in combined naïve and neoadjuvant cohorts looking at whole core**. *Radii reported using 'from phenotype' column, indicating the central phenotype, and 'to phenotype' indicating the surrounding phenotype. Reported by distance (μm), cohort, group, along with number of patients in each group. Most significant radii is reported. Log Rank (Mantel-Cox) p value and Univariate cox regression hazard ratio (HR) shown with 95% confidence interval (CI).*

## 4.12 Discussion

To interrogate the spatial relationships within naïve and neoadjuvant PDAC at a single cell level, the base neoadjuvant landscape was established, using the same high-plex immune panel as was used in the naïve cohort. Subsequent comparisons were made between the different treatment types. Phenotypes were primarily established using biased cell typing, and subsequently validated with unbiased cell clustering using CytoMAP. Unbiased phenotyping confirmed all phenotypes categorized by biased phenotyping, except for one phenotype.

Data from the neoadjuvant cohort produced counterintuitive observations with regard to cellular densities. Notably, reduced CD3+ T cell infiltration significantly correlated with improved prognosis. Although neoadjuvant tumour immune cell profiling has been historically lacking in PDAC, of the studies generated, an immunogenic switch towards effector cells has been reported. Increased cytotoxic T cell, helper T cell (CD3+ and CD4+) infiltration has been observed, along with reduced Treg expression [8, 219, 251, 252, 257]. At first glance, the cellular density neoadjuvant results from this study contradict the literature. However, data from other solid cancers have been carried out documenting the alterations seen in immune cell count post neoadjuvant chemotherapy [216, 258-260]. In particular, a study investigating matched blood samples in oesophageal cancer demonstrated an initial reduction of CD8+ and CD4+, as well as B cell and natural killer cell populations post neoadjuvant therapy. Only the CD8+ count fully returned 8 weeks post neoadjuvant treatment and resection, with all other immune cells investigated never recovering [216]. An in-depth study in primary breast cancer observed depletion of all main T lymphocytes for up to 6 months, with CD4+ T cells significantly reduced 9 months post neoadjuvant treatment. Likewise, they found the functional state of cells present had altered, with increased memory CD4 T cells [259].

When comparing the naïve and neoadjuvant cohorts, an overall higher density of tumour and fibroblasts within the naïve cohort was observed, with higher infiltrates of macrophages and Tregs populations found in the neoadjuvant cohort. Moreover, naïve cohorts matched trends described in the literature (significant prognostic associations with elevated CD3+, CD3CD8+ and reduced CD68+ cells). In contrast, neoadjuvant patients with good outcomes presented with low density of T helper cells, cytotoxic T cells, and Tregs. Upon comparison with the naïve cohort, these patients remain the group with the highest median disease specific survival. This raises the question of whether increased expression of cytotoxic T cell markers alone is always a sufficient pseudo marker for cytotoxic activity. A study looking at the activation status of CD8+ T cells in treatment naïve and neoadjuvant treated PDAC found approximately 40-70% of infiltrating T cell

population expressed markers of dysregulation (PD-1 and/or TIM3) [261]. These cell types were predominantly found located within the tumour core and the invasive edge resulting in the loss of cytotoxic benefit, with elevated cytotoxic marker expression (GZMB) seen in the tumour adjacent pancreatic parenchyma. Intriguingly, a reduction of dysregulated T cells was observed when comparing histological regions with lower tumour cell presence [261, 262]. The ‘exhausted’ phenotype reportedly starts to occur almost immediately after tumour antigen exposure, with dysfunctional characteristics established in early-stage T cell activation [263]. This phenomenon may help disentangle the results seen within the neoadjuvant cohort. If the CD3CD8+ T cells found in the tumour core predominantly lack cytotoxic activity, their presence would not lead to apoptosis of tumour cells, thereby making elevated expression redundant. Furthermore, the reduced levels of these cells in the high survivor neoadjuvant group may be indicative of a ‘less active’ disease, with lower tumour cells present. Although, immune checkpoint inhibition of T cells via PD-L1/PD-1 interactions with tumour cells have been reported in pancreatic cancer, targeting this interaction has only proved beneficial in a small subset of microsatellite instability/mismatch repair deficient patients [264, 265]. Exploration of other histopathological regions, as well as activation status, would be required to fully explore the role of CD3CD8+ T cell density within the neoadjuvant cohort. Notably, the term exhausted has generated some controversy, with terms such as inactive or dysregulated perhaps being more appropriate.

Few IHC studies have focused on density ratios in neoadjuvant pancreatic cancer. Nejati et al investigated the T lymphocyte infiltration in neoadjuvant patients' post-neoadjuvant resection [256]. They found an increased ratio of CD8/FOXP3 cells significantly correlated with survival. In contrast, the neoadjuvant cohort expressed the opposite, demonstrating reduced levels of CD3CD8/FOXP3CD3 ratio correlated with survival [256]. The role of FOXP3+ T regulatory cells is not fully understood, with the vast majority of literature associating its expression with poor survival [266]. Moreover, in vivo reports have shown Tregs to specifically inhibit the cytotoxic function of CD8 T cells via TGF-β related pathways [267]. It is important to note that the neoadjuvant TMA was generated as a complex multi-regional, multi-core TMA with specific TMAs for defined regions e.g. tumour centre TMA, immune rich TMA. Consequently, comparisons were limited to tumour centre cores as this was the closest match to the histopathology found in naïve cohort TMAs. Thus, the results generated are strictly applicable to the direct tumour microenvironment, disregarding stromal rich areas, which may generate different patterns.

The major benefit of utilising multiplex immunofluorescence, is the ability to perform single cell spatial characteristic analysis to help deconvolute the complex tumour immune landscape of neoadjuvant treated pancreatic cancer. A large number of prognostically,

and potentially biologically, significant spatial metrics were observed. Patients with favourable prognosis presented with large distances to tumour cells from fibroblasts, from Tregs and from macrophages. These trends were emphasized in radius analysis of high survival patients, low densities of helper T cells, macrophages and Tregs were observed in the surrounding tumour cell environment. Reminiscent of cellular density analysis, studies focusing on neoadjuvant cohorts using multiplex analysis are relatively scarce. Within these studies, those that examine spatial metrics are even more uncommon. Heiduk et al explored the T cell infiltration in neoadjuvant chemotherapy treated patients. They found cytotoxic T cell infiltration was unchanged, and T regulatory cells significantly reduced. A switch form anti-inflammatory to pro-inflammatory cytokine secretion was linked with CD4 helper T cells, in addition to reduced inactive cytotoxic T cells [253]. Another study found similar results, increased abundance of cytotoxic T cells predominantly in stromal regions in neoadjuvant patients when compared to naïve patients, and a shift from M2 to M1 polarized macrophages, classed as CD68+ or CD163+ with co-expression of CD86+ and IRF5+ [252]. Curiously, limited survival analysis was shown in regard to immune cell densities. However, they found elevated numbers of M1 polarized macrophages within 20μm of tumour cells correlated with better prognosis in neoadjuvant treated patients [252]. Although this contradicts what was illustrated in the neoadjuvant cohort, it is important to note the differences in macrophage classification. Tumour microenvironment differences were also observed in important neoadjuvant clinical subgroups. Specifically, amongst FOLFIRINOX treated, and good regression patients, multiple prognostic significant density and spatial metrics were observed compared to their counterparts. Zwart et al examined immune variations across neoadjuvant treatment types and found differences between FOLFIRINOX and Gemcitabine-radiotherapy treated patients [268]. Though they found differences in cellular density across T cell and macrophage populations, no associations were established with disease specific or recurrence free survival.

Using several different models, the most important spatial relationships were extracted, demonstrating neoadjuvant patients with highest survival probability presented with varied patterns. These findings reinforce the need to establish multi-layered interactions to fully define the immune landscape in relation to survival. The naïve cohort yielded distinctly different trends associated with improved disease specific survival. These differences suggest an immunogenic switch following neoadjuvant treatment, implying the potential involvement of distinct biological pathways responsible for high survival rates within each treatment group. The neoadjuvant cohort yielded a blend of anticipated and unforeseen spatial trends. The spatial relationships seen linked to macrophages, fibroblasts, and T regulatory cells fall within the predominant hypotheses associated with these cell types,

whereas spatial relationships linked to CD3+ helper T cells and cytotoxic T cells were conflicting.

# 5 Chapter 5: Determining the Spatial Transcriptomic immune landscape in treatment naïve and neoadjuvant treated pancreatic cancer

## 5.1 Introduction

Transcriptomic exploration of cancer is an ever-expanding field that has led to the development of clinically relevant molecular subtypes, discovery of early detection biomarkers and identifying biological pathways driving oncogenesis [15, 63, 90, 100-102, 212, 269, 270]. This work has primarily been achieved via bulk RNA transcriptomic techniques, resulting in pooling of patient samples, reducing it to a homogenous averaged sample per patient. One of the biggest hurdles in cancer research is the vast inter and intra heterogeneity seen. Bulk RNA data often expresses the most dominant signature, loosing transcriptionally distinct subpopulations [271]. Single cell transcriptomics provides a solution to this limitation. This technique works by sequencing single cells, generating pure signatures, and allowing discovery of even rare transcriptionally distinct profiles [272, 273]. However, cancer cells do not exist in isolation, exhibiting complex, variable relationships with the tumour microenvironment. Both single cell and bulk transcriptomics omit this highly influential spatial architecture. Spatial Transcriptomics was developed to overcome this issue, providing highly specific regional transcriptomic profiles [274, 275]. Different platforms have been developed, each with their own benefits and limitations. Pancreatic cancer is a highly heterogenous and relatively poorly defined disease, which would benefit from techniques that allow maximum regional purity whilst maintaining tissue architecture to decipher its biology. The main advantages of Nanostrings® Spatial Transcriptome assay is its ability to work with TMAs and select areas of interest base on mIF staining, resulting in the generation of distinct signatures making it ideal for tissue compartment selection [113]. This is ideal for tissue compartment selection. Due to resolution limitations, this technique can be referred to as ‘mini-bulk’, and therefore should be considered as such when analysing and reporting data [113]. It is worth noting the current Spatial Transcriptomic landscape is continuously evolving, producing improved cell resolution, sequencing depth and transcript specificity, as well as the shifting focus to the development of assays applicable to 3D samples [108, 115, 116, 276].

Although current published Spatial Transcriptomic work, across all platforms, in pancreatic cancer remains limited, promising findings have emerged. Grunwald et al established three major sub-tumour microenvironments, demonstrating the location pattern of these regions correlated with survival, each with different immune and stromal features [277]. Transcriptional signatures identified immune cell subtypes associated with PDAC, including macrophages, and found they had differential locations [277]. Furthermore, insight can be drawn from other, similar cancers. A study on primary colorectal cancer demonstrated significantly different immune profiles at distinct histopathological regions between patients with good and poor survival [278].

To preserve compartment purity, Nanostrings® Whole Transcriptome Atlas (WTA) on the GeoMx® DSP platform was utilized on naïve and neoadjuvant TMA cohorts with associated extensive clinical data. Investigating the spatial transcriptomic profile of the TME in pancreatic cancer will assist in defining the molecular mechanisms underpinning this disease. Successful characterization of treatment naïve and treated patients will clarify the effect that chemotherapy has on immune pathways and may provide insight into novel biomarkers.

### 5.1.1 Aims

Investigate the Spatial Transcriptomic alterations in upfront resected PDAC patients, with consideration given to important clinical subgroups per treatment status. This was carried out in epithelium (PanCk+), fibroblast rich stromal (αSMA+) and immune (CD45+) regions. The naïve and neoadjuvant landscape will be individually established, and subsequent comparisons will be made. Focused analysis will be done on immune-related pathways and immune cell deconvolution. Explore the B7-H3 transcriptomic expression within the naïve and neoadjuvant landscape.

## 5.2 Clinical cohorts

The naive cohort consisted of a total of 62 pancreatic cancer specimens on a TMA with associated clinical data (table 5.1). These were a subset of the naïve cohort described in chapter 3. Median survival for these patients was 19.2 months. The neoadjuvant cohort consisted of 71 pancreatic cancer specimens split across 3 multi-regional TMAs (table 5.1). This cohort is the neoadjuvant cohort described in chapter 4 (n=58), with an additional clinical trial cohort (PRIMUS002, n=13). Median survival for this combined cohort was 20.4 months. Neoadjuvant whole sections consisted of clinical trial samples (PRIMUS002) including 2 matched biopsy and post chemotherapy resected cases. Clinical data associated with these cohorts are found in chapter 2.1.

| Study | Cohort name | Sample name | Sample number | Patient number | Treatment type |
|---|---|---|---|---|---|
| GeoMx WTA assay | Glasgow Naïve 2 | PDAC-PAN-TMA | 1 | 62 | Naïve |
| | Neoadjuvant combined | Neoadj-MAL-TMA batch1 | 1 | 58 | Neoadjuvant |
| | | Neoadj-MAL-TMA batch2 | 1 | | |
| | | PRIMUS-MAL | 1 | 13 | |
| | Primus whole section | PRIMUS002 | 4 | 2 | |

**Table 5.1 Naïve and neoadjuvant clinical cohorts and associated study.** *Summary table showing the study and associated neoadjuvant and naïve samples used, patient number and treatment type. The cohort name column refers to the cohort name in chapter 2.1. Primus whole section IDs found in chapter 2.1*

## 5.3 Spatial Transcriptomic landscape of Naïve PDAC

### 5.3.1 Whole transcriptome profiling in naïve pancreatic cancer

To elucidate the differences in primary resected and neoadjuvant pancreatic cancer, Spatial Transcriptomics using Nanostrings® WTA assay was performed. Three areas of illumination (AOIs) were selected; epithelium-rich, fibroblast-rich stroma and immune-rich tumour microenvironment, categorised by PanCk+, αSMA+ and CD45+ immunofluorescence antibodies respectively (figure 5.1.a). This selection method allowed for subsequent analysis of ‘pure’ tissue compartments within the naive PDAC cohorts, enabling molecular discovery between treatment types (figure 5.1.b).

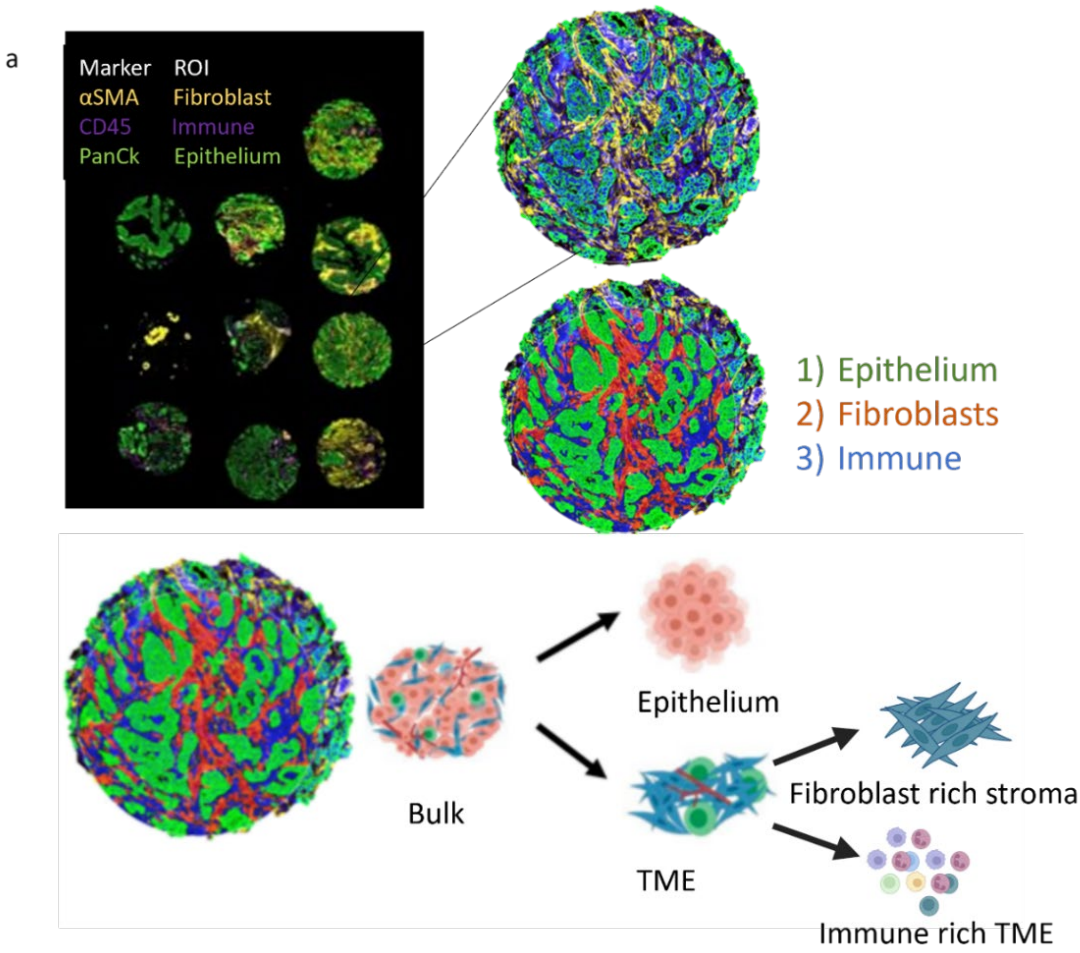


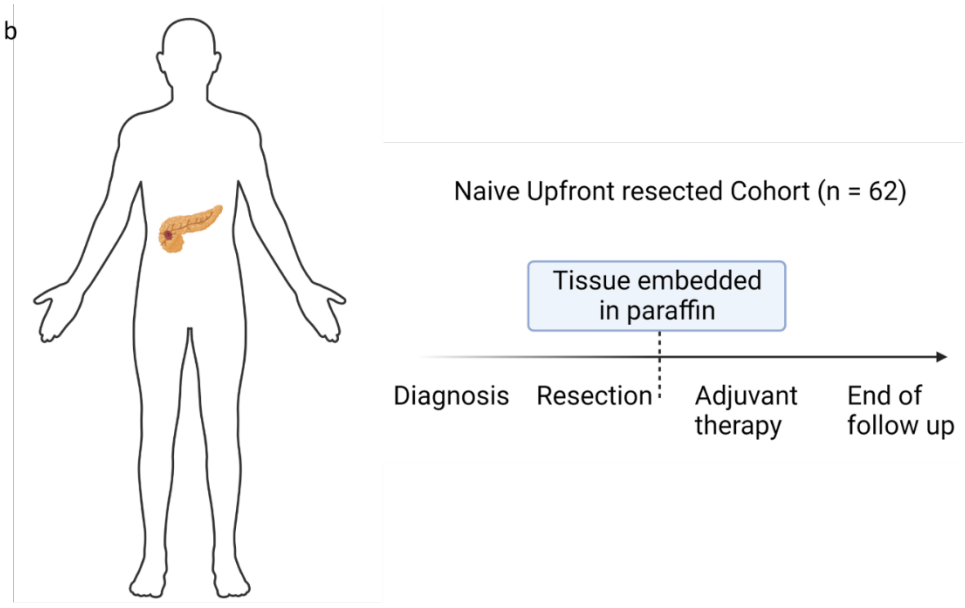


Naïve Upfront resected PDAC

**Figure 5.1.a-b GeoMx® Digital Spatial Profiler AOI selection in naïve PDAC TMAs**.

*a).Representative cores stained with immunofluorescent PanCk, αSMA and CD45. Schematic of epithelial, fibroblast rich and immune rich specific segments generated from immunofluorescence staining, b). Overview of upfront resected naïve PDAC cohort (n=62), from diagnosis to end of follow up. Samples are neoadjuvant treatment naïve, but will undergo adjuvant therapy, tissue is embedded in paraffin before treatment.*

## 5.3.2 Tumour compartments demonstrate distinct transcriptome profiles in naïve pancreatic cancer

### 5.3.2.1 Inter-tumoral heterogeneity

Comparison between AOIs within the naïve cohort was carried out to confirm that adjacent tumour compartments expressed distinct transcriptome profiles. Vast differences in differential expression between PanCk vs αSMA segments, and PanCk vs Immune segments were observed, and limited differences between αSMA vs Immune segments (figure 5.2).

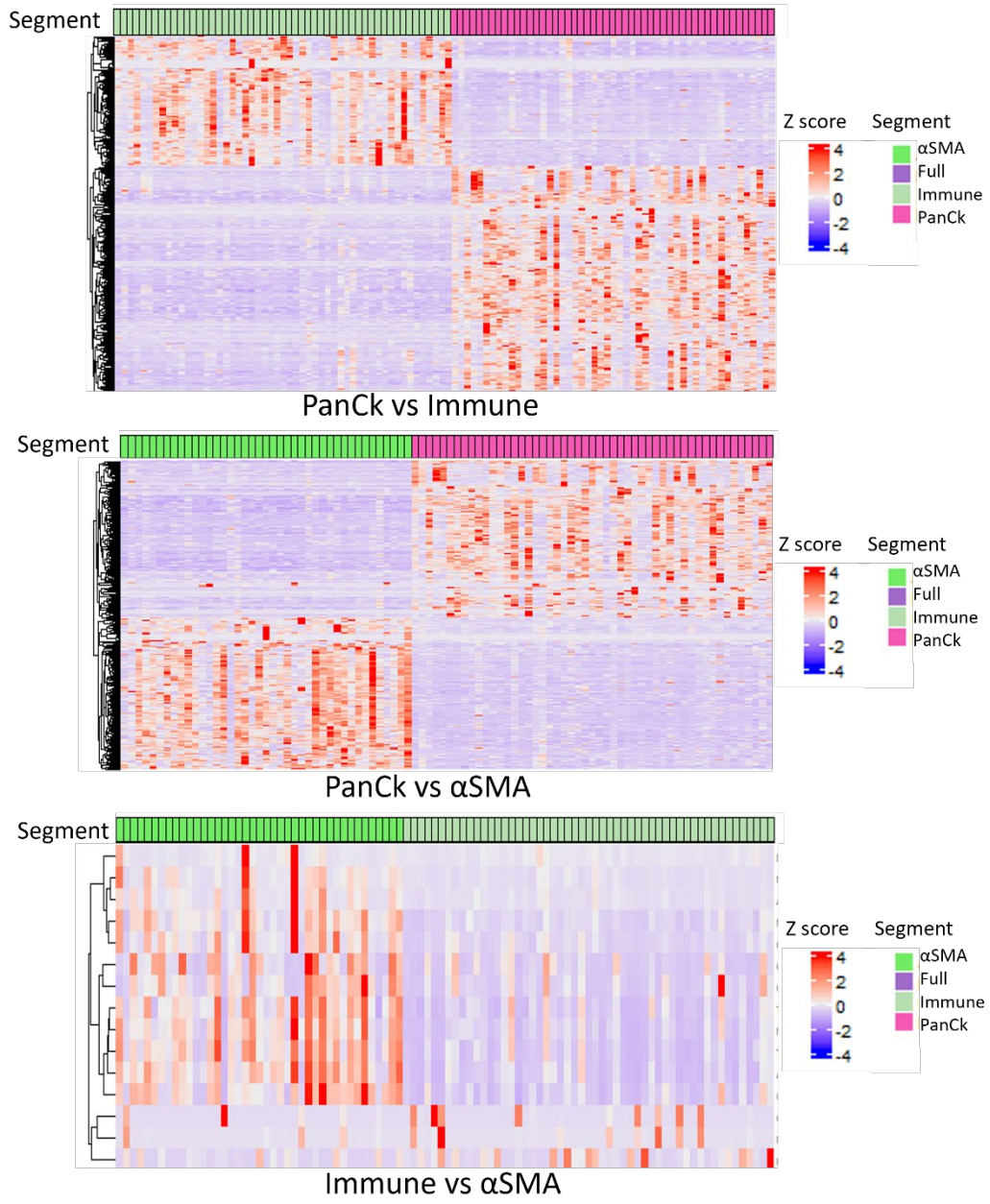


**Figure 5.2 Inter-compartment differential expression in naïve patients.** *Heatmap showing significant differentially expressed genes in all segment comparison. Segments comparisons carried out between PanCk vs immune, PanCk vs αSMA and immune vs αSMA*

Geneset enrichment analysis (GSEA) analysis demonstrated upregulation in a wide range of pathways when comparing all segments (supplementary 8.4.1.1). These results emphasize the need to separate the different compartments when investigating transcriptomic signatures that underlie biology. To validate the differences between segments, as described above, Principle Component Analysis (PCA) was performed on all naive segments. This analysis revealed distinct clustering by segments, in particular, clear grouping of PanCk and αSMA segments (figure 5.2). However, immune segments appeared relatively dispersed between PanCk and αSMA clusters. This phenomenon is perhaps due to the microenvironment in which the immune segments reside in, indicative of how influential the tumour and fibroblast-rich compartments are.

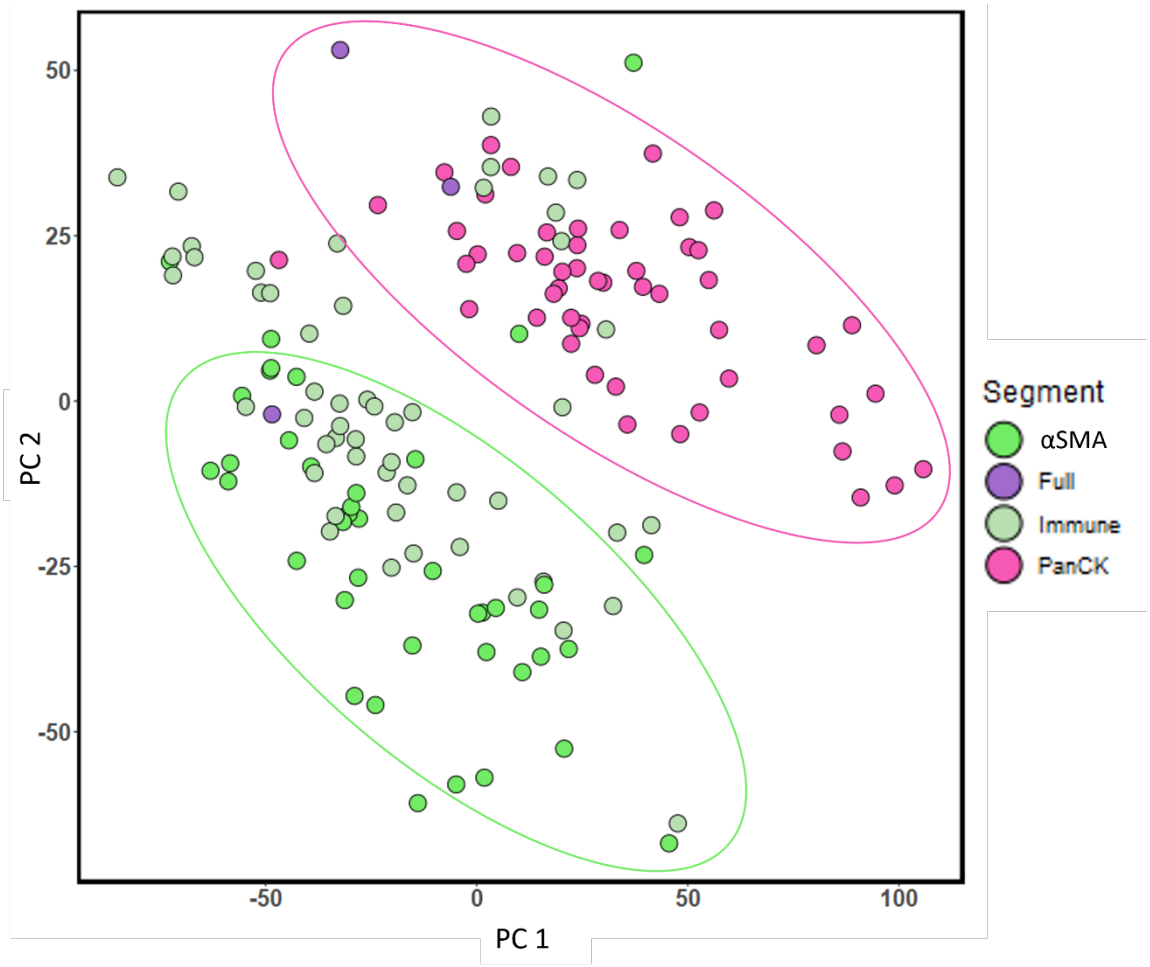


**Figure 5.2 GeoMx AOI segment PCA in naïve cohort**. *Clustering based on gene expression per AOI, annotated by segment. Clusters indicated by ellipses drawn*

### 5.3.2.2 Intra-compartment heterogeneity

Upon confirmation of discrete inter-compartment profiles, intra-compartment profiles were investigated. Hierarchical clustering was performed using PCA. This resulted in 2 distinct PanCk clusters, that demonstrated non-significant survival trends, with cluster 2 correlating with poor survival (p=0.075) (figure 5.3.a-b). The Kaplan-Meier curve, coupled with median survival between cluster 1 (21.2 months) and cluster 2 (14.7 months) were distinct enough to permit in-depth transcriptomic exploration.

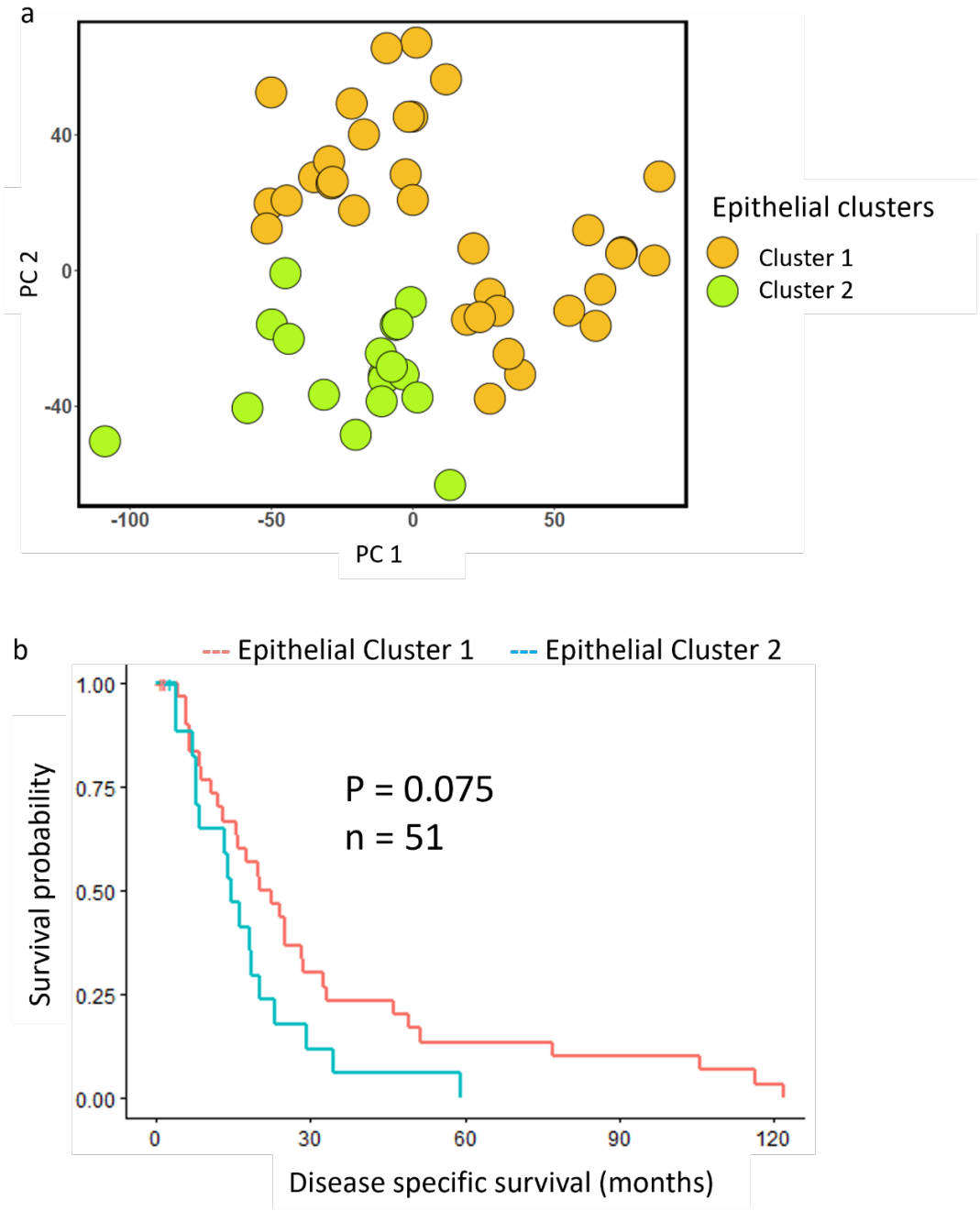


**Figure 5.3.a-b Epithelial intra-compartment heterogeneity in naïve cohort,** *a). PCA showing clustering of naïve epithelial segments b). Kaplan-Meier curve stratified by epithelial clusters for disease specific survival (months) (Log-Rank Mantel-Cox test).*

Of the differentially expressed genes, *HSPA6* (logFC = 1.8, padj <0.001) and *CST1* genes (logFC = 1.8, padj <0.001) were upregulated in the epithelial cluster 2 (figure 5.4.a). Although limited pathways were expressed, downregulated type I interferon (INF) pathway (NES = -2.0, padj = 0.007) and upregulated T cell pathways (NES = 1.7, padj = 0.003) were observed (figure 5.4.b).

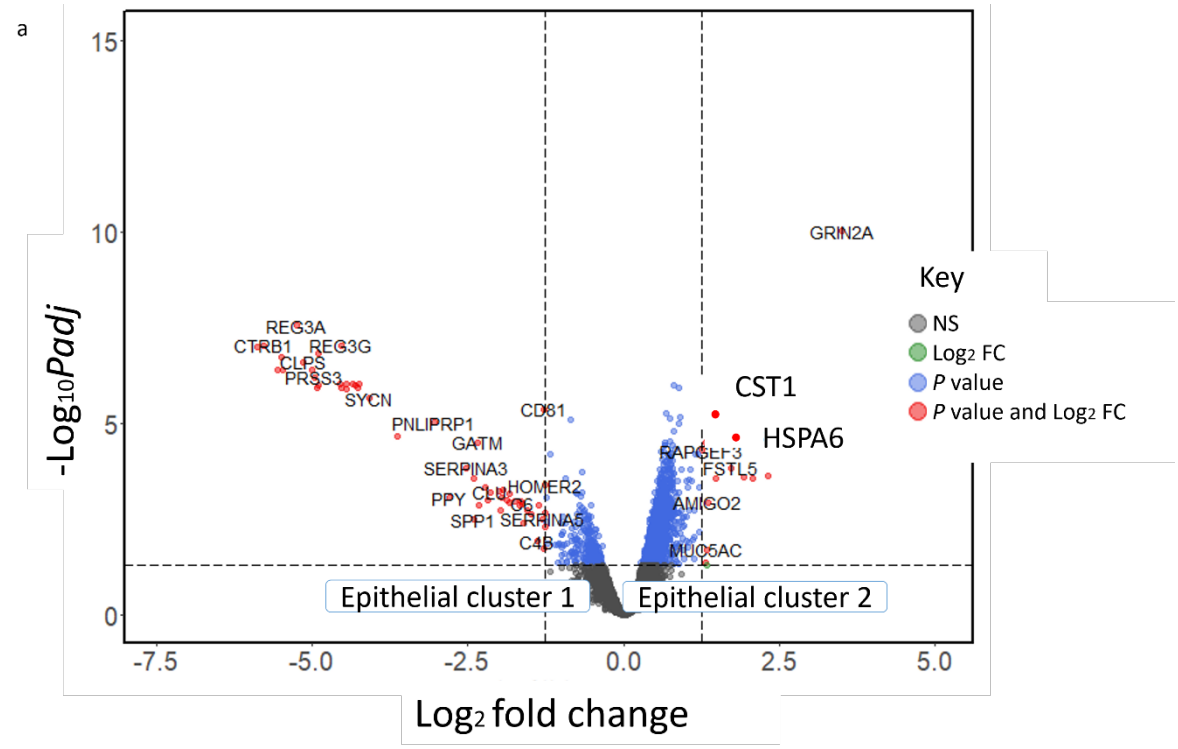


**Figure 5.4.a Spatial transcriptomic alterations between naïve epithelial clusters**, *a). Volcano plot demonstrating gene marker differential expression levels in epithelial cluster 1 vs epithelial cluster 2. Genes with log2 fold change above and below 1.5, and p adjusted value ≤0.05 were considered significant, important genes in bold. Dashed line indicates significance thresholds, NS = non-significant, FC = fold change.*

.

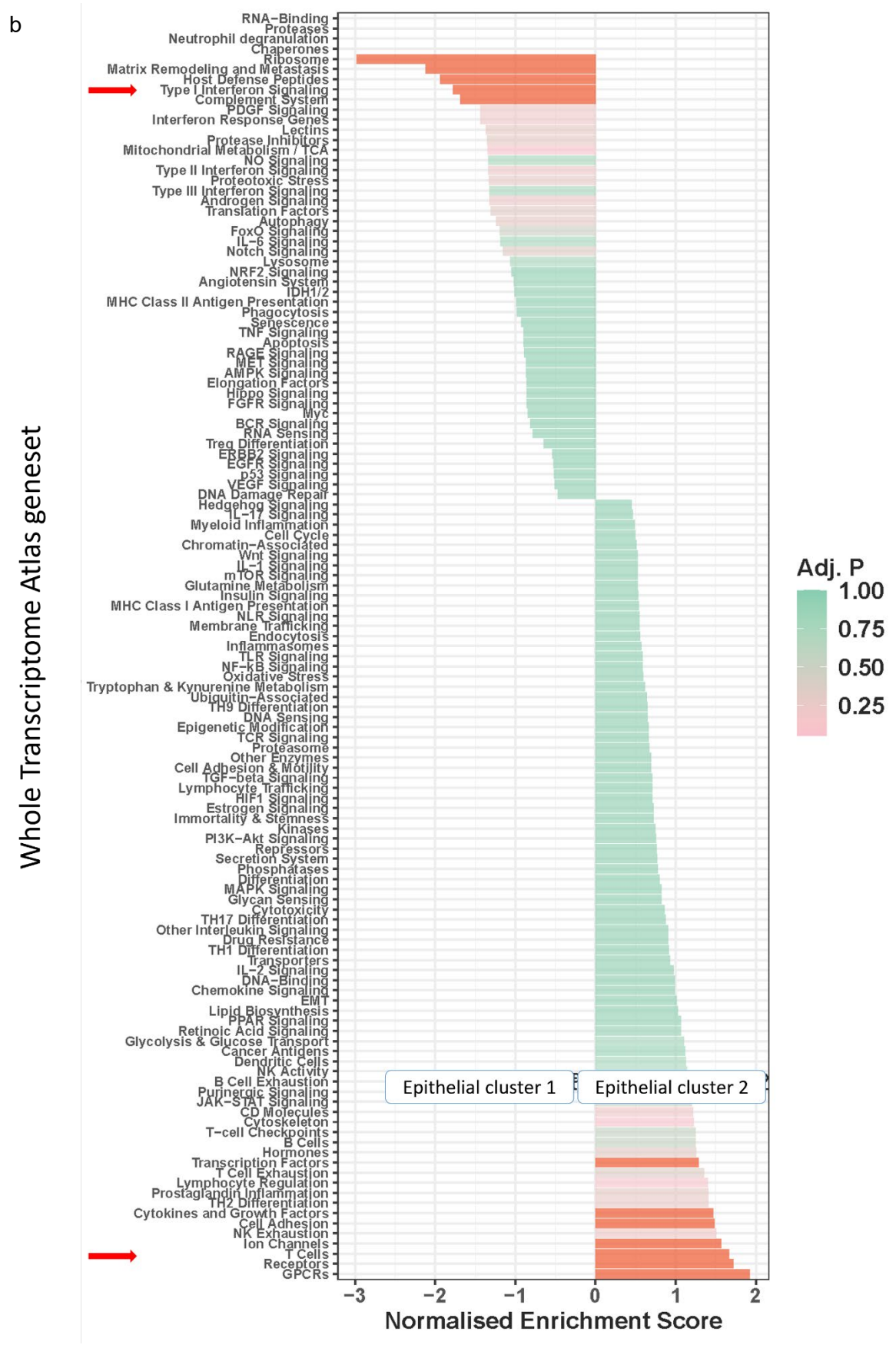


**Figure 5.4.b Spatial Transcriptomic alterations between naïve epithelial clusters**, *b). Geneset enrichment bar chart in epithelial cluster 1 vs epithelial cluster 2. Pathways with normalized enrichment score above and below 1.5, and p adjusted (Adj. P) value ≤ 0.05 were considered significant. Important pathways are indicated by an arrow.*

Spatial immune cell deconvolution comparing these clusters estimated decreased tumour infiltrating B cells (p=0.012), memory dendritic cells (p=0.007) and increased expression of monocytes (p=0.027), and neutrophils (p=0.02) in cluster 2 epithelium (figure 5.5.a). To ensure these epithelial clusters were not simply previously established transcriptomic signatures, the epithelial cluster gene set was compared to Collison et al, Moffit et al and Bailey et al gene sets [100-102], with minimal overlap seen (figure 5.5.b).

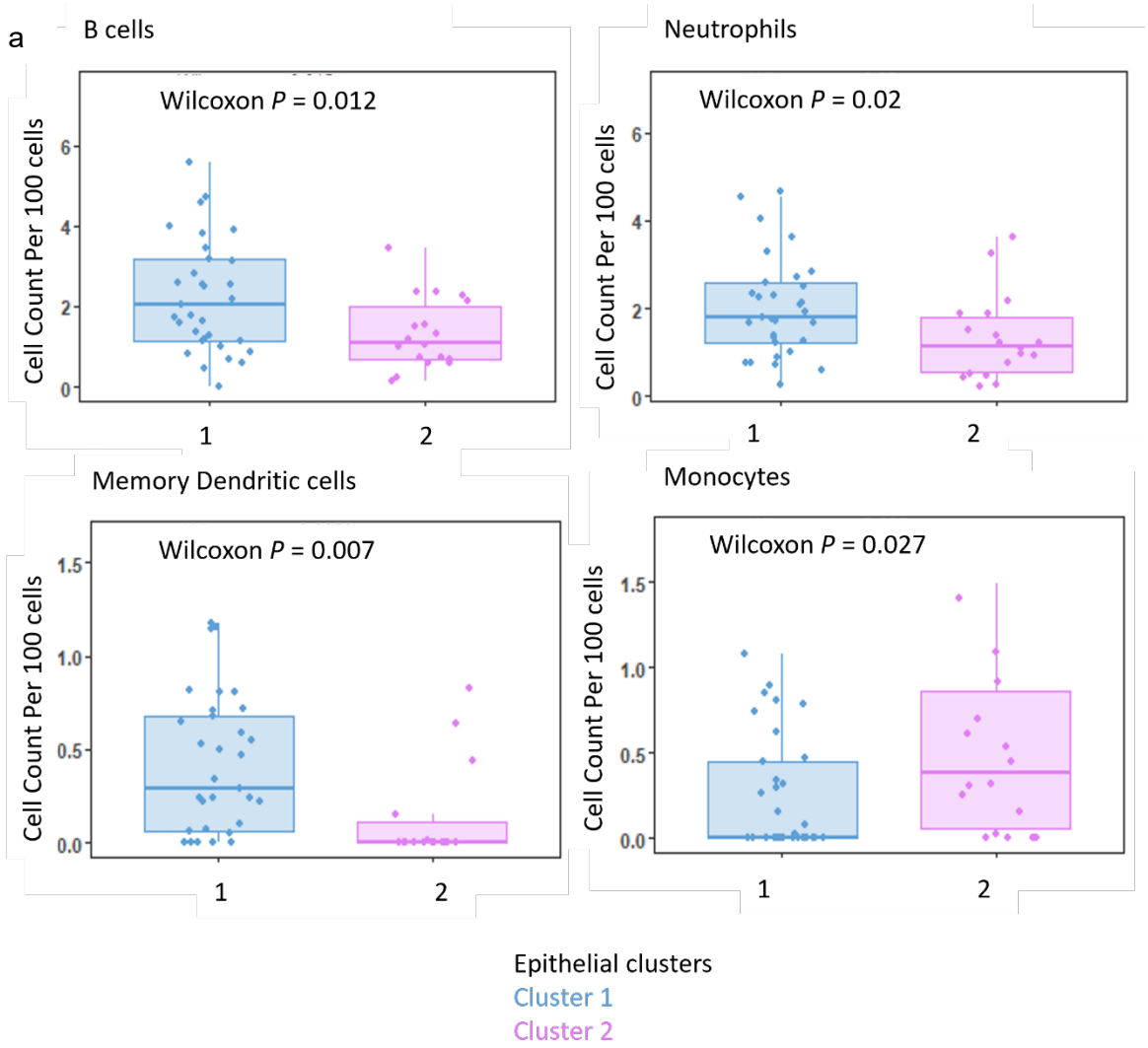


**Figure 5.5.a Epithelial cluster immune cell deconvolution and molecular subtype comparison,** *a). Boxplots demonstrate estimated immune cell expression per 100 cells in; B cells, neutrophils, memory dendritic cells and monocytes. Wilcoxon test with adjusted p value was used.*

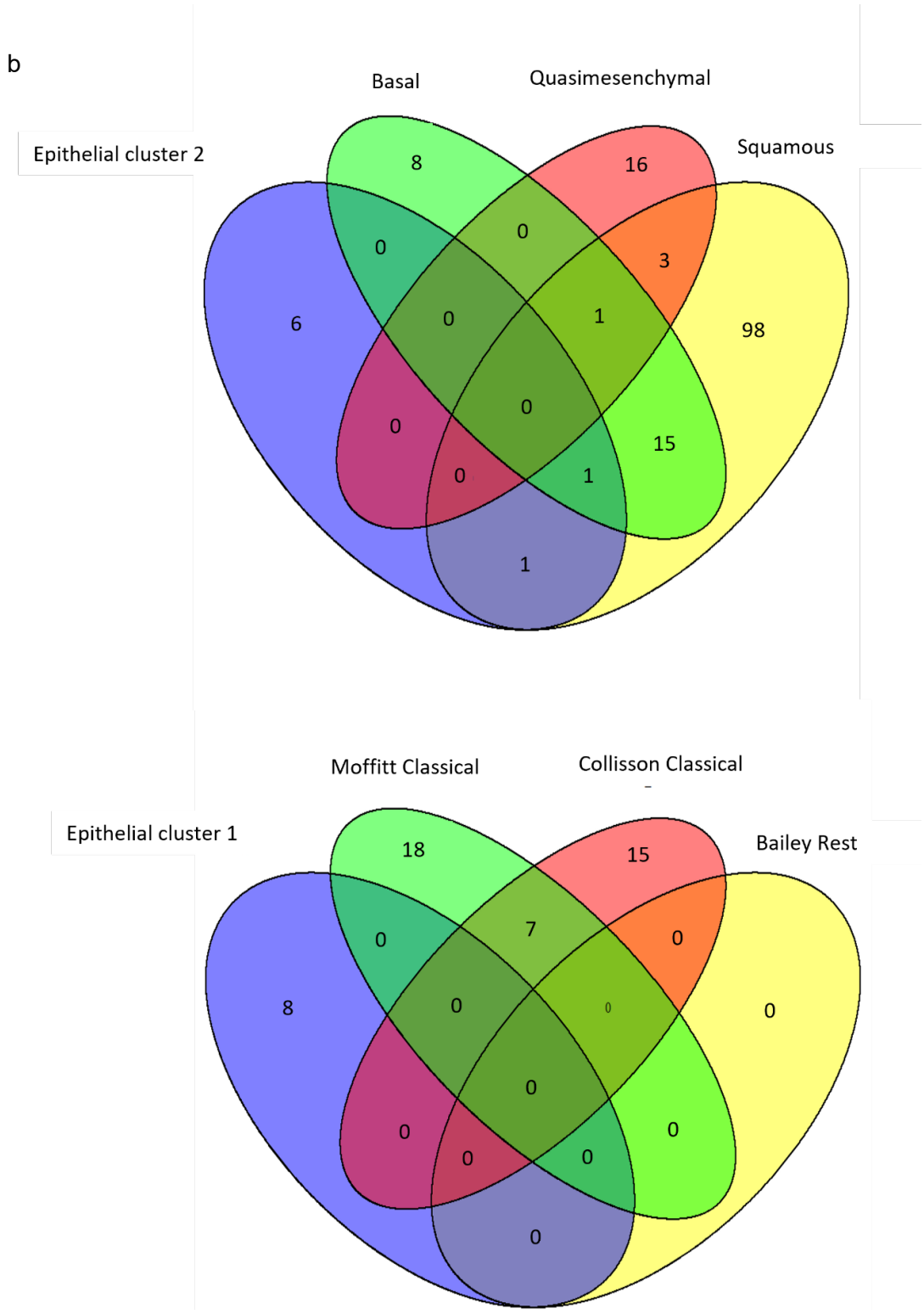


**Figure 5.5.b Epithelial cluster immune cell deconvolution and molecular subtype comparison,** *b). Venn diagram showing number of overlapping genes between molecular subtypes and epithelial cluster 1 and epithelial cluster 2.*

Tumour cells have symbiotic relationships with immune and stromal cells. Although individually, αSMA and immune clusters did not prove significant, combination of immune or αSMA clusters with the established epithelial clusters, displayed prognostically relevant subtypes (figure 5.6.a-d). Patients with epithelial cluster 2 combined with αSMA cluster 1 had significantly worse survival compared to all other combinations (p=0.02) (figure 5.6.c and table 5.2). When epithelial and immune clusters were combined, epithelial cluster 1 coupled with immune cluster 1 (epi-immune cluster 1) demonstrated improved survival compared to the other clusters (ignoring the purple cluster due to limited number) (p=0.047) (figure 5.6.d and table 5.2).

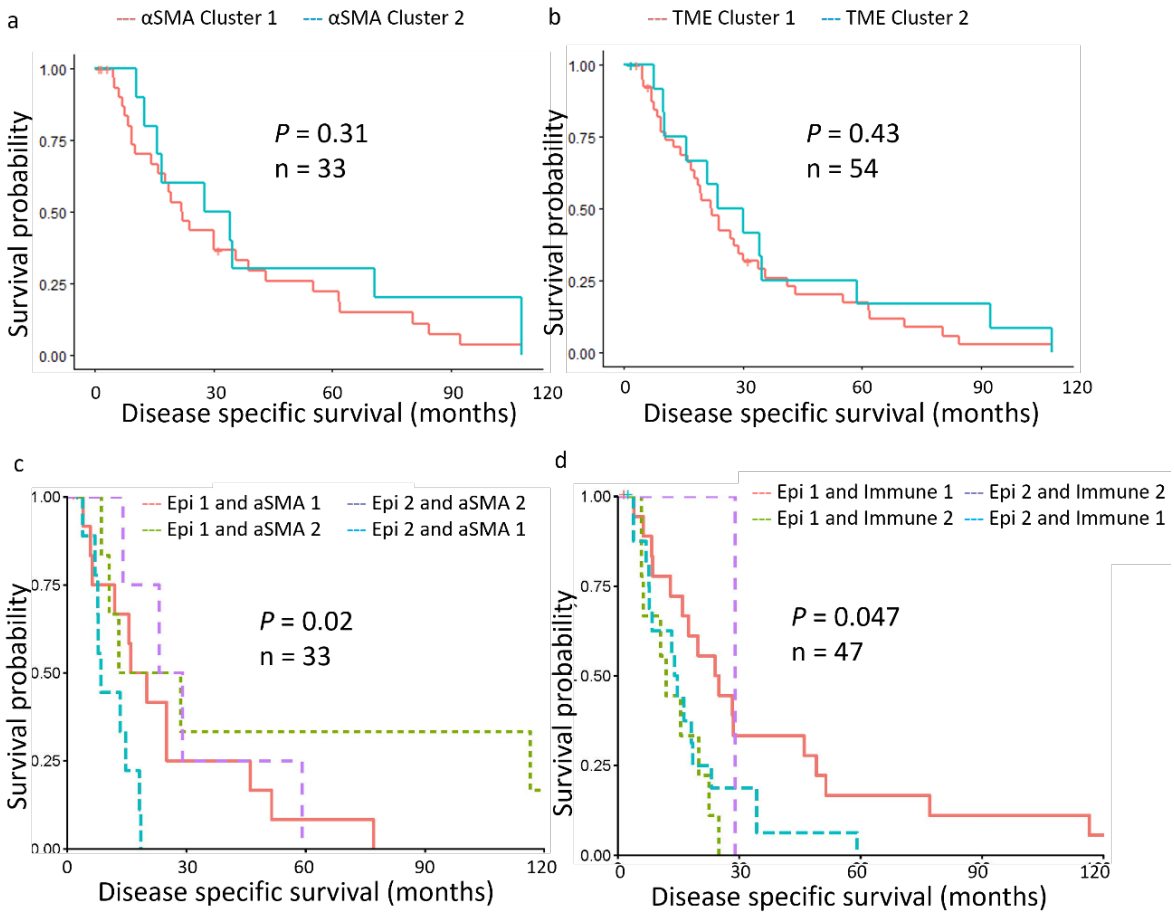


**Figure 5.6.a-d Individual and combined segment clusters associated with survival.** *Kaplan-Meier curves for disease specific survival (months) stratified by a). αSMA clusters b). TME clusters c). Epithelial and αSMA clusters, and d). epithelial and immune clusters. Log-rank (Mantel-Cox) test used.*

| Cluster comparison group | Cluster comparison pair 1 | Cluster comparison pair 2 | P value |
|---|---|---|---|
| Epithelial-αSMA cluster | Epi-cluster-1_αSMA-cluster-1 | Epi-cluster-1_αSMA-cluster-2 | 0.249 |
| | Epi-cluster-1_αSMA-cluster-1 | Epi-cluster-2_αSMA-cluster-1 | 0.029 |
| | Epi-cluster-1_αSMA-cluster-1 | Epi-cluster-2_αSMA-cluster-2 | 0.659 |
| | Epi-cluster-1_αSMA-cluster-2 | Epi-cluster-1_αSMA-cluster-1 | 0.249 |
| | Epi-cluster-1_αSMA-cluster-2 | Epi-cluster-2_αSMA-cluster-1 | 0.054 |
| | Epi-cluster-1_αSMA-cluster-2 | Epi-cluster-2_αSMA-cluster-2 | 0.801 |
| | Epi-cluster-2_αSMA-cluster-1 | Epi-cluster-1_αSMA-cluster-1 | 0.029 |
| | Epi-cluster-2_αSMA-cluster-1 | Epi-cluster-1_αSMA-cluster-2 | 0.054 |
| | Epi-cluster-2_αSMA-cluster-1 | Epi-cluster-2_αSMA-cluster-2 | 0.013 |
| | Epi-cluster-2_αSMA-cluster-2 | Epi-cluster-1_αSMA-cluster-1 | 0.659 |
| | Epi-cluster-2_αSMA-cluster-2 | Epi-cluster-1_αSMA-cluster-2 | 0.801 |
| | Epi-cluster-2_αSMA-cluster-2 | Epi-cluster-2_αSMA-cluster-1 | 0.013 |
| Epithelial-immune cluster | Epi-cluster-1_Immune-cluster-1 | Epi-cluster-1_Immune-cluster-2 | 0.012 |
| | Epi-cluster-1_Immune-cluster-1 | Epi-cluster-2_Immune-cluster-1 | 0.44 |
| | Epi-cluster-1_Immune-cluster-1 | Epi-cluster-2_Immune-cluster-2 | 0.922 |
| | Epi-cluster-1_Immune-cluster-2 | Epi-cluster-1_Immune-cluster-1 | 0.012 |
| | Epi-cluster-1_Immune-cluster-2 | Epi-cluster-2_Immune-cluster-1 | 0.477 |
| | Epi-cluster-1_Immune-cluster-2 | Epi-cluster-2_Immune-cluster-2 | 0.1 |
| | Epi-cluster-2_Immune-cluster-1 | Epi-cluster-1_Immune-cluster-1 | 0.044 |
| | Epi-cluster-2_Immune-cluster-1 | Epi-cluster-1_Immune-cluster-2 | 0.447 |
| | Epi-cluster-2_Immune-cluster-1 | Epi-cluster-2_Immune-cluster-2 | 0.607 |
| | Epi-cluster-2_Immune-cluster-2 | Epi-cluster-1_Immune-cluster-1 | 0.922 |
| | Epi-cluster-2_Immune-cluster-2 | Epi-cluster-1_Immune-cluster-2 | 0.1 |
| | Epi-cluster-2_Immune-cluster-2 | Epi-cluster-2_Immune-cluster-1 | 0.607 |

**Table 5.2 Pairwise comparison between naïve segment clusters** *taken from Kaplan Meier plots above (figure 5.6) Groups compared include epithelial-αSMA clusters (epi-αSMA) and epithelial-Immune clusters (epi-Immune). All comparison pairs reported using Log Rank (Mantel-Cox) pairwise comparison over strata*

The low survivor epithelial-αSMA cluster (named Epi-αSMA cluster 1 from now on) was extracted and spatial transcriptomic analysis was carried out in comparison with the remainder of the cluster groups (Epi-αSMA cluster 2). Epi-αSMA cluster 1 patients demonstrated upregulated *KIF4A* (logFC = 1.8, padj <0.001), *CXCL14* (logFC = 1.4, padj <0.001) and *MUC5AC* (logFC = 1.8, padj <0.001) (figure 5.7.a). Spatial deconvolution indicates increased expression of B cells (p=0.008) and memory dendritic cells (p=0.016) in cluster 2 patients (figure 5.7.b).

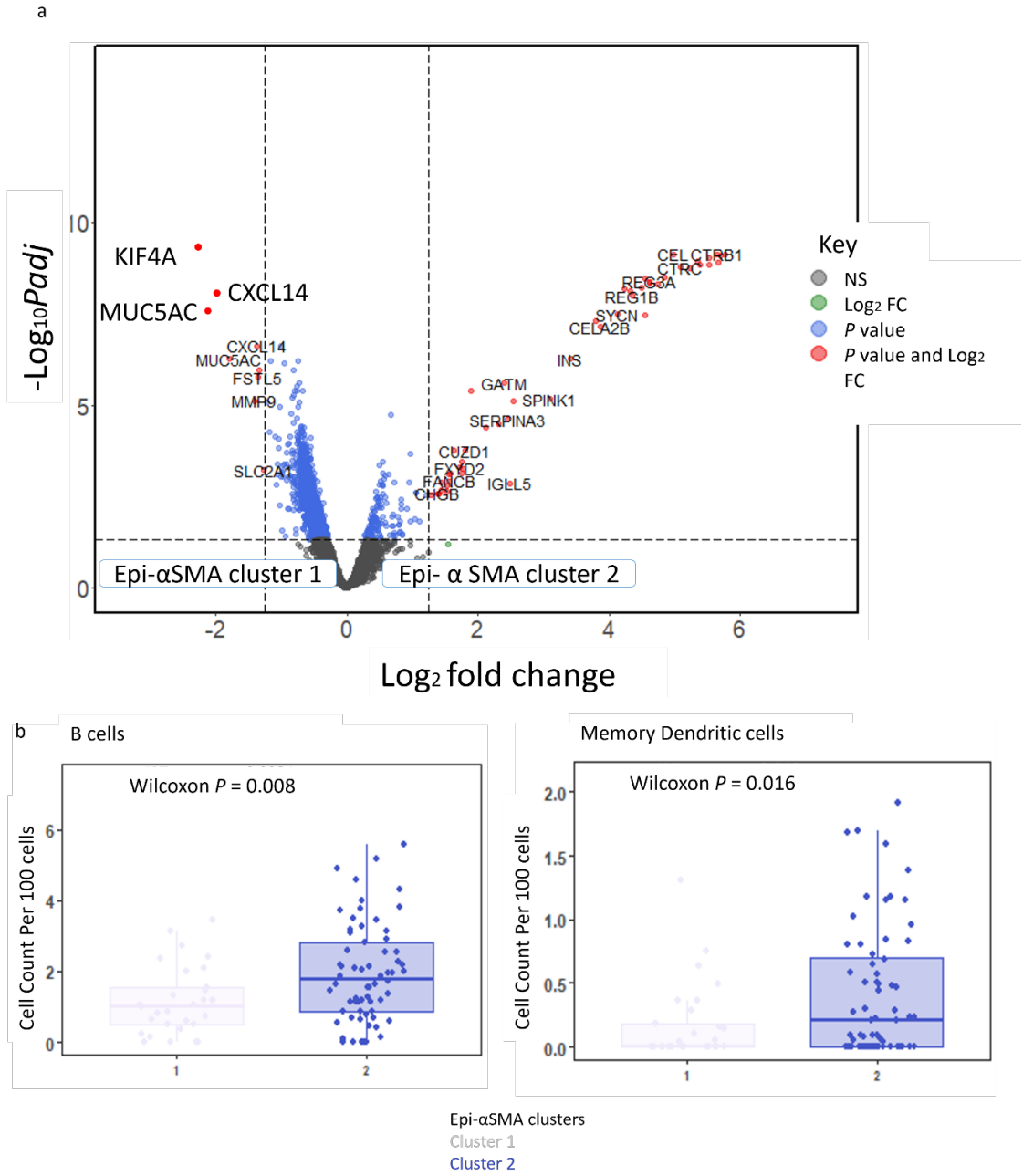


**Figure 5.7.a-b Spatial transcriptomic alterations between epithelial-αSMA combined clusters**, *a). Volcano plot demonstrating gene marker differential expression levels in epithelial-αSMA cluster 1 vs epithelial-αSMA cluster 2. Genes with log2 fold change above and below 1.5, and p adjusted value ≤0.05 were considered significant, important genes in bold, b). Boxplots demonstrate estimated differences between immune cell expression per 100 cells in; B cells and memory dendritic cells across epithelial-αSMA cluster 1 and cluster 2. Wilcoxon test with adjusted*

*p value was used. Dashed line indicates significance thresholds, NS = non-significant, FC = fold change.*

Finally, the high survivor epithelial-immune cluster (named epi-immune cluster 1) was extracted and compared to the other clusters (named epi-immune cluster 2). Cluster 2 patients demonstrated a distinct gene signature associated with upregulation of *REG3A* (logFC = 6.3, padj <0.001), *MT1G* (logFC = 2.6, padj <0.001) and *CPA2* (logFC = 5.3, padj <0.001) (figure 5.8.a). Moreover, a wide range of cell signalling, and immune related pathways were increased in cluster 2 including; MET (NES = 6.6, padj <0.001), EMT (NES = 2.1, padj <0.001), T cell exhaustion (NES = 1.6, padj = 0.03) and lymphocyte regulation (NES = 1.6, padj = 0.006) pathways (figure 5.8.b). Immune cell deconvolution estimates increased expression of B cells (p=0.011), cytotoxic T cells (p<0.001) and memory dendritic cells (p=0.024) in cluster 1 patients (figure 5.8.c).

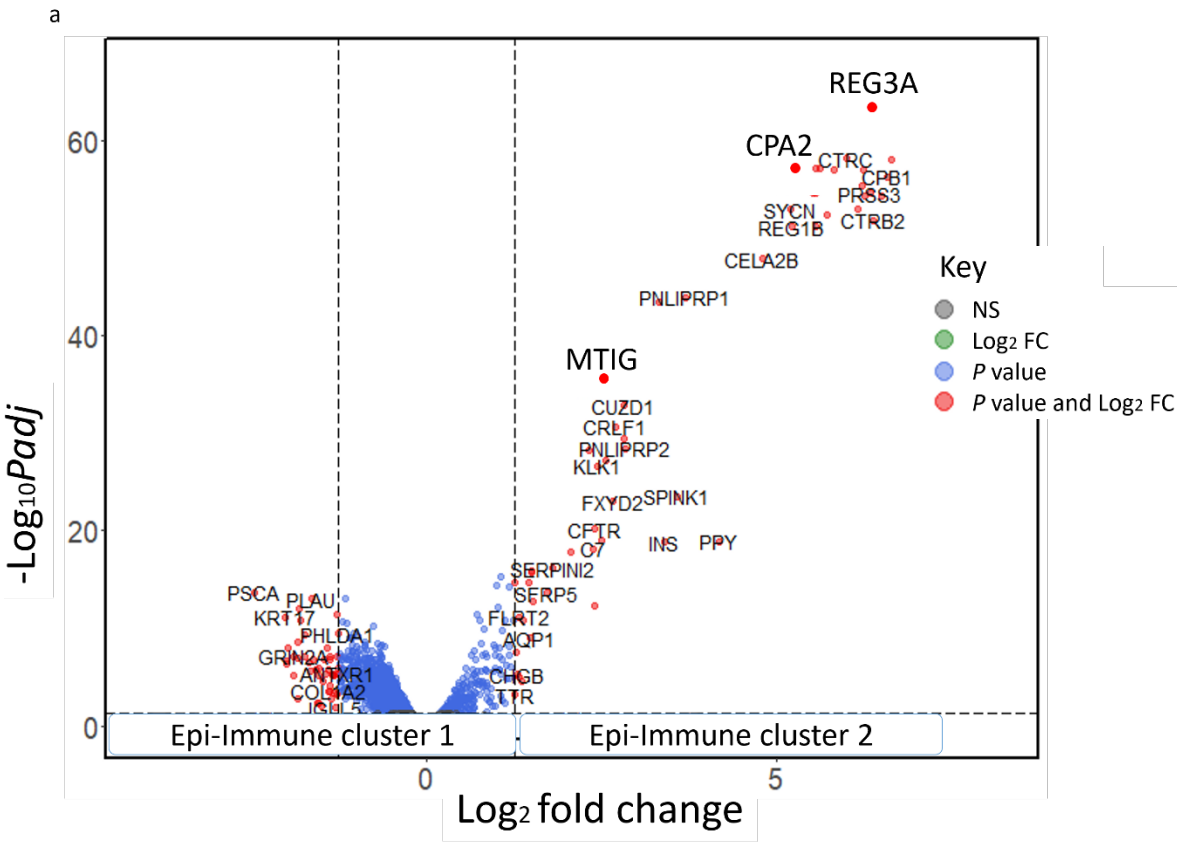


**Figure 5.8.a Spatial Transcriptomic alterations between epithelial-immune combined clusters**, *a). Volcano plot demonstrating gene marker differential expression levels in epithelial-immune cluster 1 vs epithelial-immune cluster 2. Genes with log2 fold change above and below 1.5, and p adjusted value ≤0.05 were considered significant, important genes in bold. Dashed line indicates significance thresholds, NS = non-significant, FC = fold change.*

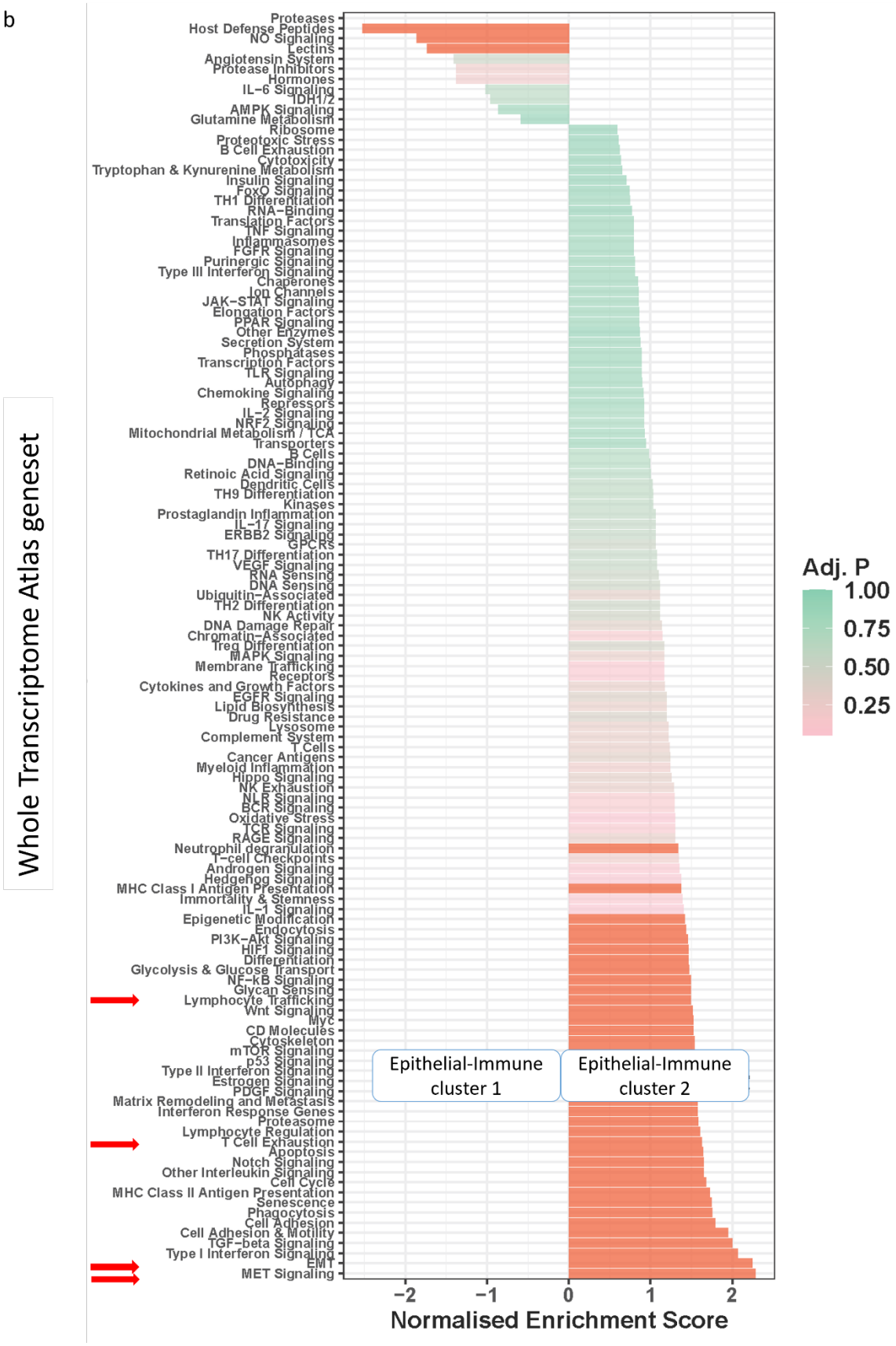


**Figure 5.8.b Spatial Transcriptomic alterations between epithelial-immune combined clusters**, *b). Geneset enrichment bar chart in in epithelial-immune cluster 1 vs epithelial-immune cluster 2. Pathways with normalized enrichment score above and below 1.5, and p adjusted (Adj. P) value ≤ 0.05 were considered significant. Important pathways are indicated by an arrow*

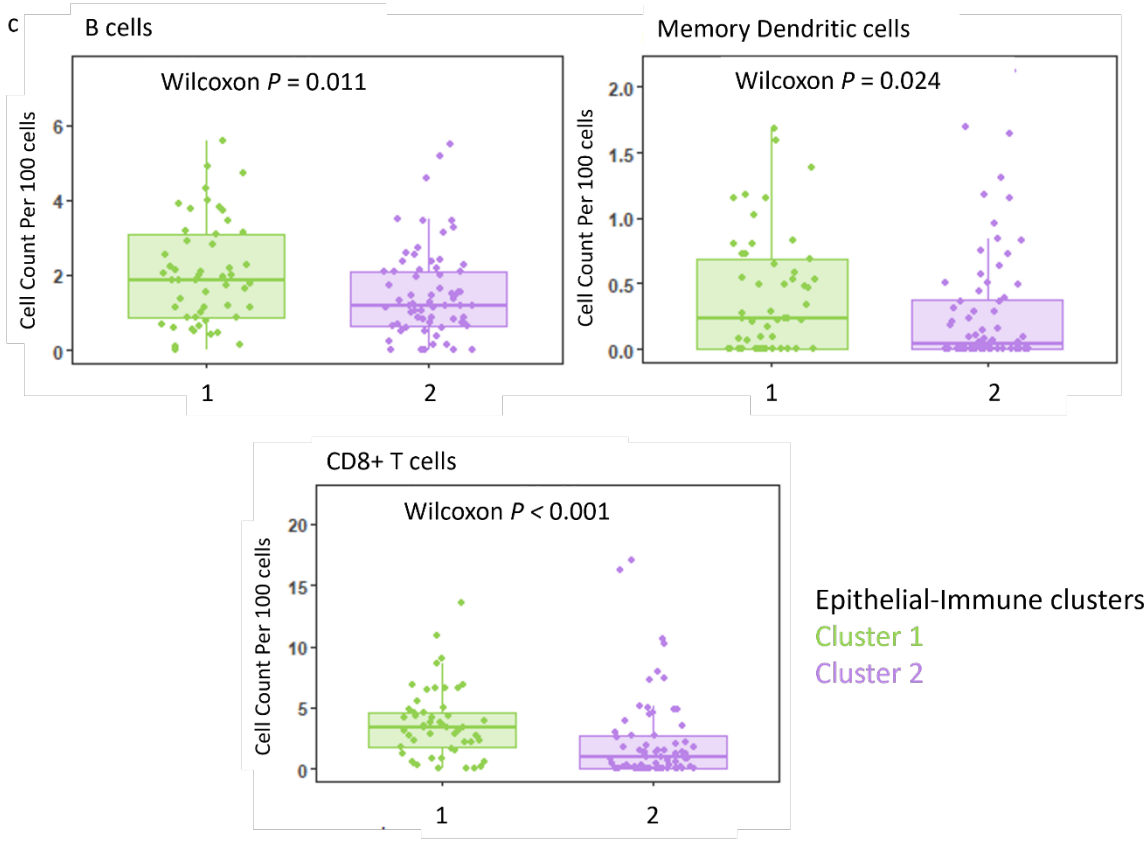


**Figure 5.8.c Spatial Transcriptomic alterations between epithelial-immune combined clusters**, *c). Boxplots demonstrate estimated differences between immune cell expression per 100 cells in; B cells, memory dendritic cells and CD8 T cells across epithelial-immune cluster 1 and cluster 2. Wilcoxon test with adjusted p value was used.*

### 5.3.3 Spatial Transcriptomic signatures across naïve molecular subtypes

As demonstrated in chapter 3, molecular subtypes can be powerful prognostic indicators, displaying high levels of heterogeneity between subtypes. Spatial Transcriptomic exploration of these subsets will establish the biological differences and may lead to biomarker discovery. Traditionally, molecular subtyping has been limited to whole section bulk transcriptomics. Using previously characterised molecular subtyping, an attempt was made to establish whether Spatial Transcriptomics can be utilised for molecular subtyping, by confirming the established subtypes in the naïve cohort, as well as categorising the remainder of the cases. Subtyping was restricted to Baileys Squamous and the Classical (rest) [102]. Epithelial regions were extracted and subtyped using a reduced geneset for Squamous and Rest (chapter 2.5.2.8). Clustering based on epithelial regions was not fully clear, therefore a subtype score was generated using geneset enrichment analysis of Squamous specific genes. This ranks AOIs according to the enrichment score of Squamous genes, splitting AOIs into very Squamous, mixed and very Classical. This roughly matched the clustering generated by the GeoMx® data, with Classical patients correctly subtyped according to the rank score (figure 5.9). To validate both the subtype score and ST subtyping, the established bulk transcriptomic subtypes were used for comparison. Unexpectedly, bulk subtypes also deviated from the subtype score generated, as well as from the subtype categorised by Spatial Transcriptomic regions (figure 5.9). Notably, molecular subtyping can be highly influenced to the sample set inputted.

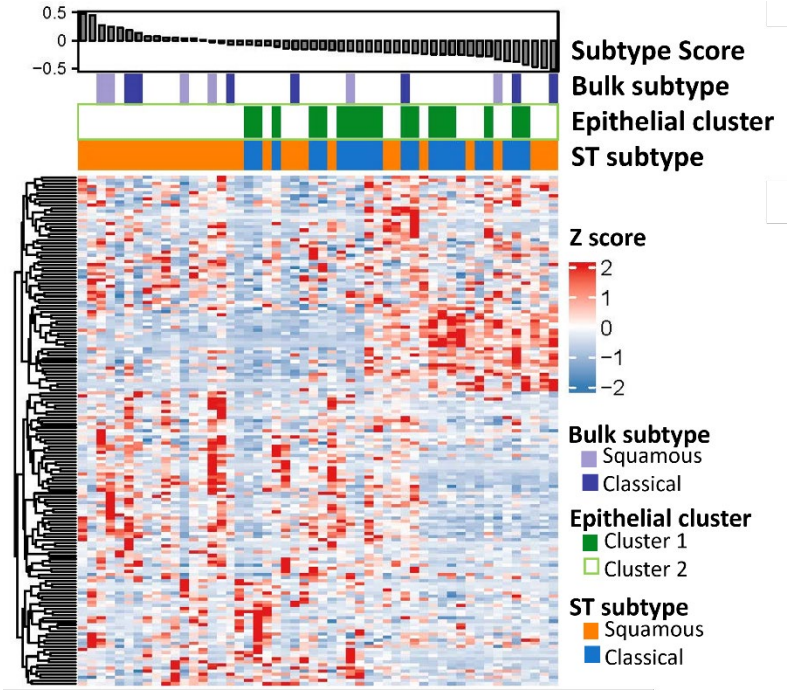


**Figure 5.9 Molecular subtyping across epithelial naïve segments.** *Heatmap showing Spatial Transcriptomic (ST) subtyped differentially expressed Squamous and Classical (rest) genes in epithelial naïve segments. Heatmap annotated with bulk subtypes, and epithelial clusters*

*established in chapter 5.3.2.2, and a ranked subtype score bar chart demonstrates the total squamous score for each epithelial segment.*

As molecular subtyping using the Spatial Transcriptome deviated from the subtypes generated from bulk, transcriptomic analysis of subtypes was limited to segments with associated bulk RNA sequencing (n=13). Few significant differences were seen between Squamous and Classical regions, possibly due to the limited number of available samples. On investigation, epithelial regions demonstrated the most meaningful differences. Squamous epithelium was enriched in *IGFBP3* (logFC = 3.3, padj = 0.004), *ADAM19* (logFC = 2.0, padj = 0.05) and *PGC* (logFC = 4.2, padj = 0.05) compared to Classical epithelium (figure 5.10.a). Pathway analysis revealed many significant gene sets. Of note, most pathways were cell signalling pathways, upregulation of MET (NES = 2.6, padj <0.001), IL-6 (NES = 1.9, padj = 0.02), PDGF (NES = 1.8, padj = 0.006) and TGF-β (NES = 1.8, padj <0.001) signalling among others were observed in Squamous epithelium (figure 5.10.b). Both stromal and immune segments revealed no significant DEA gene expression, and limited pathway insight. No estimated immune cell differences were seen across subtypes.

a

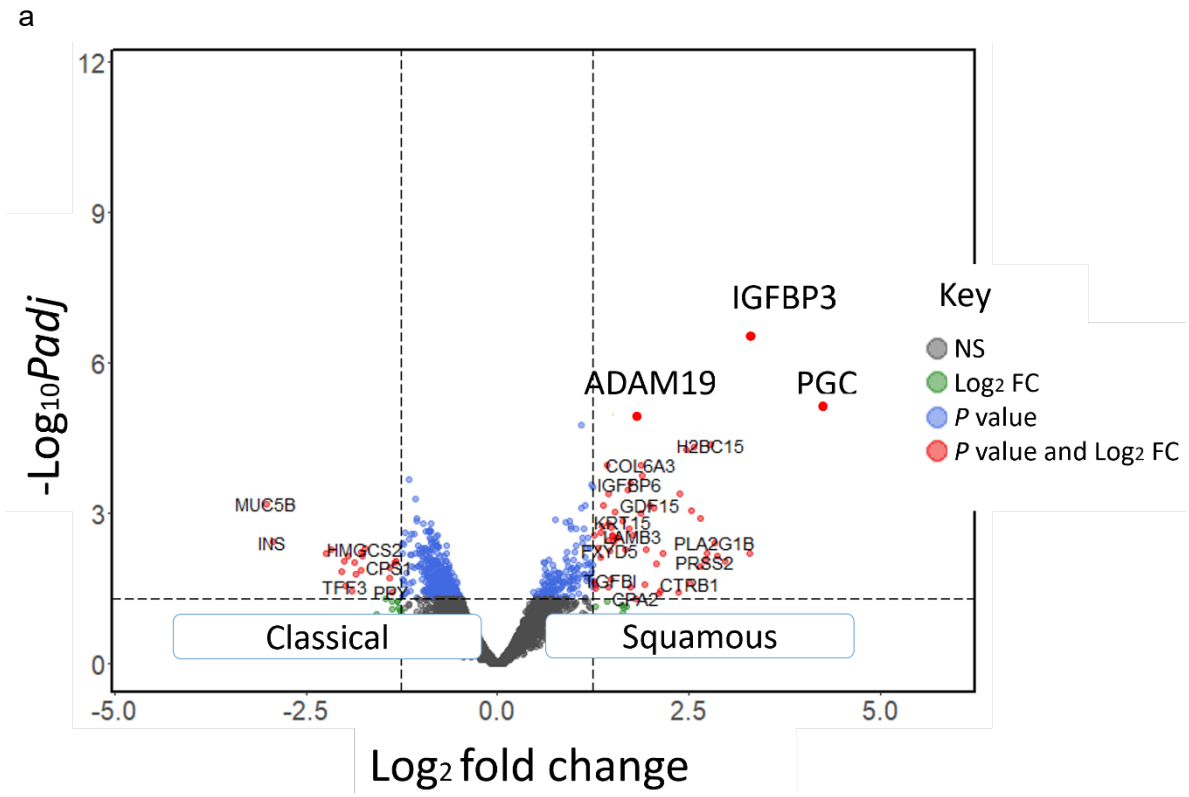


**Figure 5.10.a Spatial Transcriptomic alterations between molecular subtypes epithelium**, *a). Volcano plot demonstrating gene marker differential expression levels in Classical vs Squamous epithelial segments. Genes with log2 fold change above and below 1.5, and p adjusted value ≤0.05 were considered significant, important genes in bold. Dashed line indicates significance thresholds, NS = non-significant, FC = fold change.*

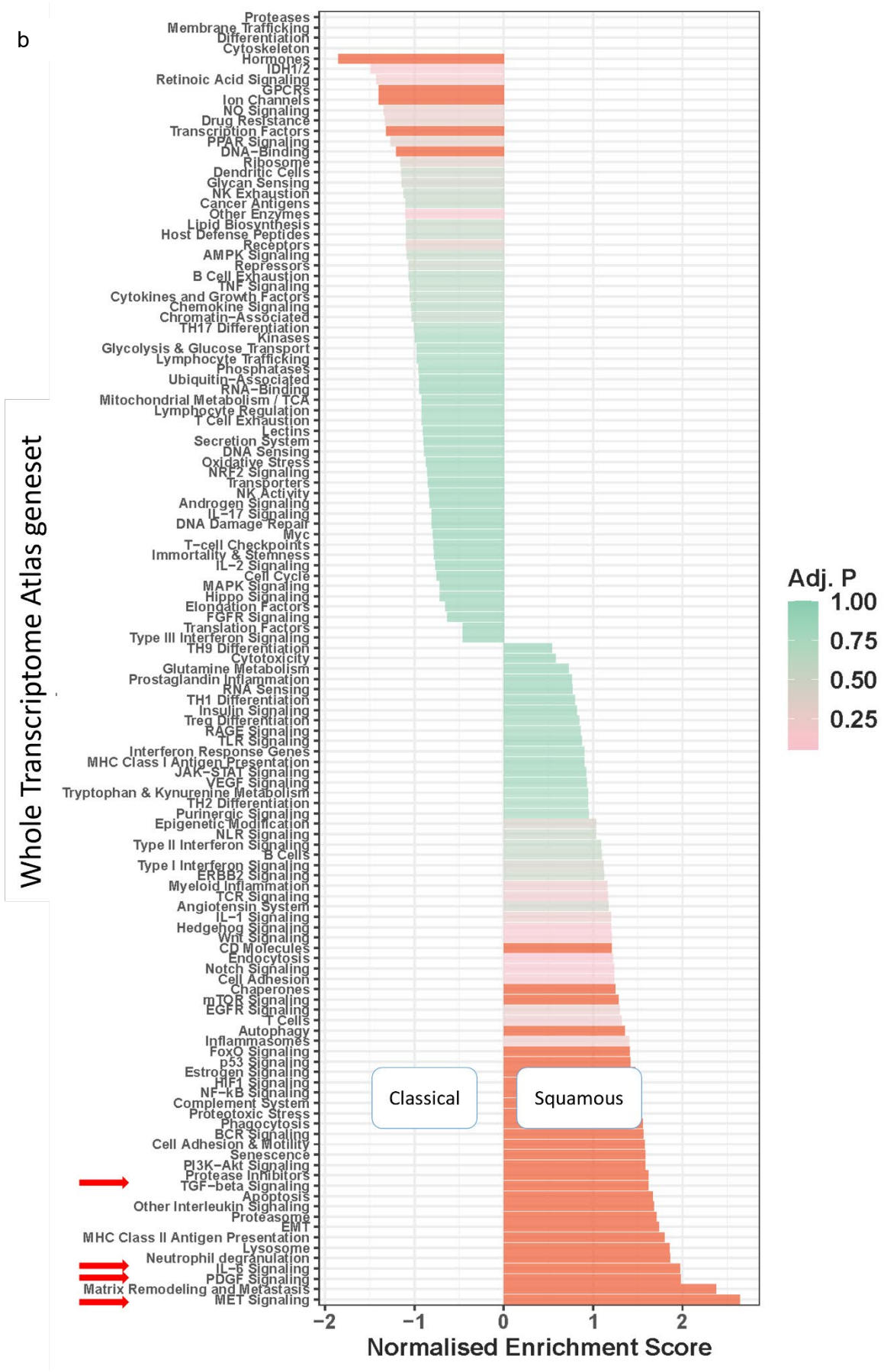


**Figure 5.10.b Spatial Transcriptomic alterations between molecular subtypes epithelium** *b). Geneset enrichment bar chart in Classical vs Squamous epithelial segments. Pathways with normalized enrichment score above and below 1.5, and p adjusted (Adj. P) value ≤ 0.05 were considered significant. Important pathways are indicated by an arrow.*

### 5.3.4 Spatial Transcriptomic signatures in naïve long-term survivors of pancreatic cancer

Pancreatic cancer has an abysmal survival rate; however, a small subset of patients tends to survive longer than expected. Transcriptomic assessment of these patients may elucidate the mechanisms behind this improved prognosis, in addition to potentially identifying predictive biomarkers for this subset. Within this naïve cohort, median survival was approximately 19 months, patients surviving over 36 months were classed as long-term survivors (LTS). Differential expression was carried out between the areas of illumination in LTS patients compared to the rest. Relatively few aberrations were observed between segments of the survivor groups. Of significance, high survivors expressed elevated *LYZ* (logFC = 3.2, padj <0.001) in epithelial compartments (figure 5.11.a), elevated *IGLL5* (logFC = 5.5, padj <0.001) and *NFKBID* (logFC = 1.9, padj = 0.01) in αSMA compartments (figure 5.11.b), and elevated *IGLL5* (logFC = 3.7, padj <0.001) and *IGHG1* (logFC = 3.7, padj <0.001) in immune compartments (figure 5.11.c).

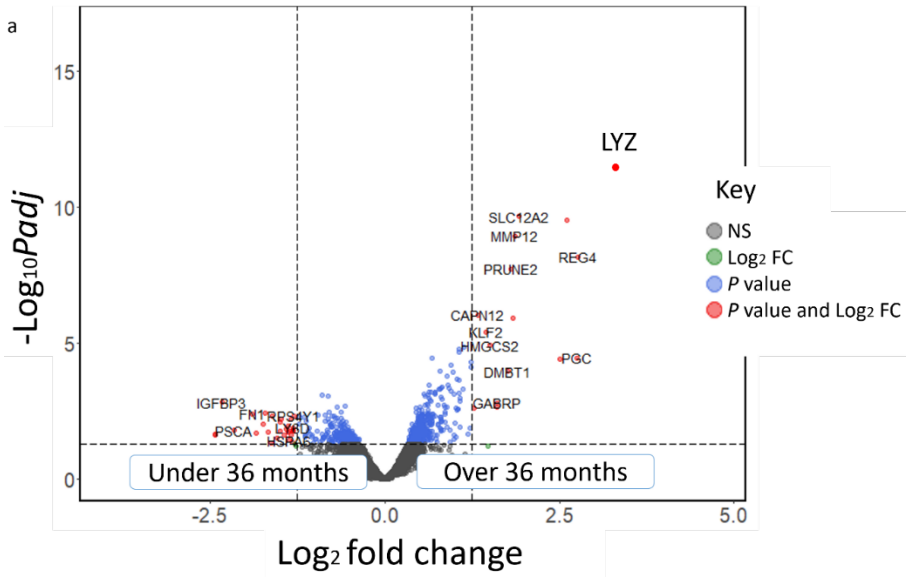


**Figure 5.11.a Differential expression alterations in long term survival naïve segments,** *volcano plot shows significantly expressed genes in patients surviving under 36 months vs over 36 months across a). Epithelium segments. Dashed line indicates significance thresholds, NS = non-significant, FC = fold change.*

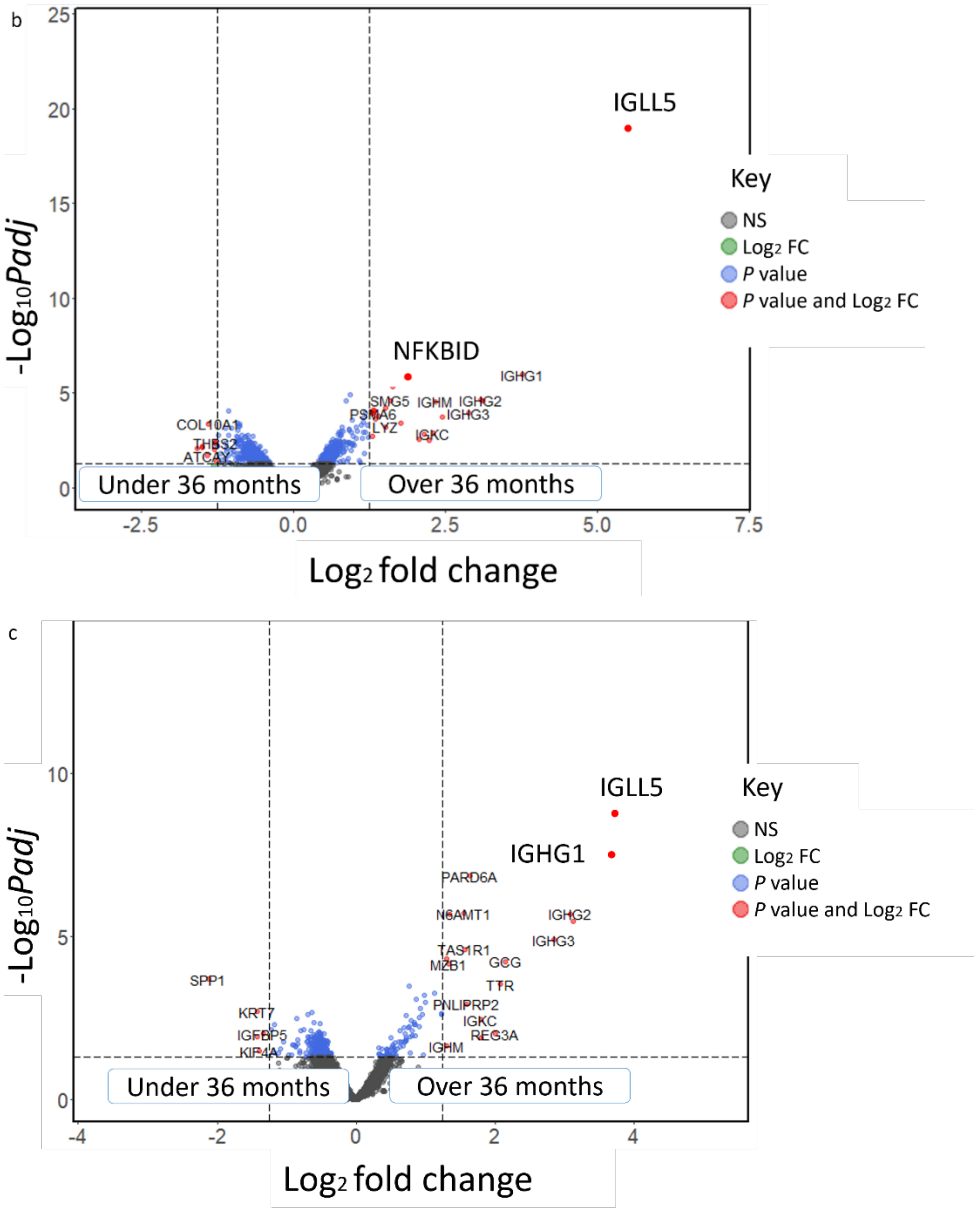


**Figure 5.11.b-c Differential expression alterations in long term survival naïve segments,** *volcano plot shows significantly expressed genes in patients surviving under 36 months vs over 36 months across b). αSMA segments c). Immune* segments. *Genes with log2 fold change above and below 1.5, and p adjusted value ≤0.05 were considered significant, important genes in bold. Dashed line indicates significance thresholds, NS = non-significant, FC = fold change.*

Although differential gene expression was relatively limited, an abundance of significant genesets were seen. Epithelial segments of LTS associated with downregulation of PDGF signalling (NES = -1.8, padj = 0.003), TGF-β signalling (NES = -1.8, padj <0.001), MET (NES = -1.8, padj = 0.004), PI3K-Akt (NES = -1.8, padj <0.001), and upregulated in TNF (NES = 1.7, padj = 0.005) and PPAR (NES = 1.8, padj <0.001) signalling (figure 5.12). Unexpectedly, almost no immune cell pathways appeared in the long-term survivor groups in either fibroblast rich or immune segment GSEA ((supplementary figure 8.4.a-b). Notably, the complement signalling pathway was downregulated in LTS epithelial regions but upregulated in stromal/immune segments, accentuating the importance of pure regional analysis. Immune cell population deconvolution estimated increased expression of B cells (p=0.024) and cytotoxic CD8 T cells (p=0.009) within immune regions in long term survivors (figure 5.13).

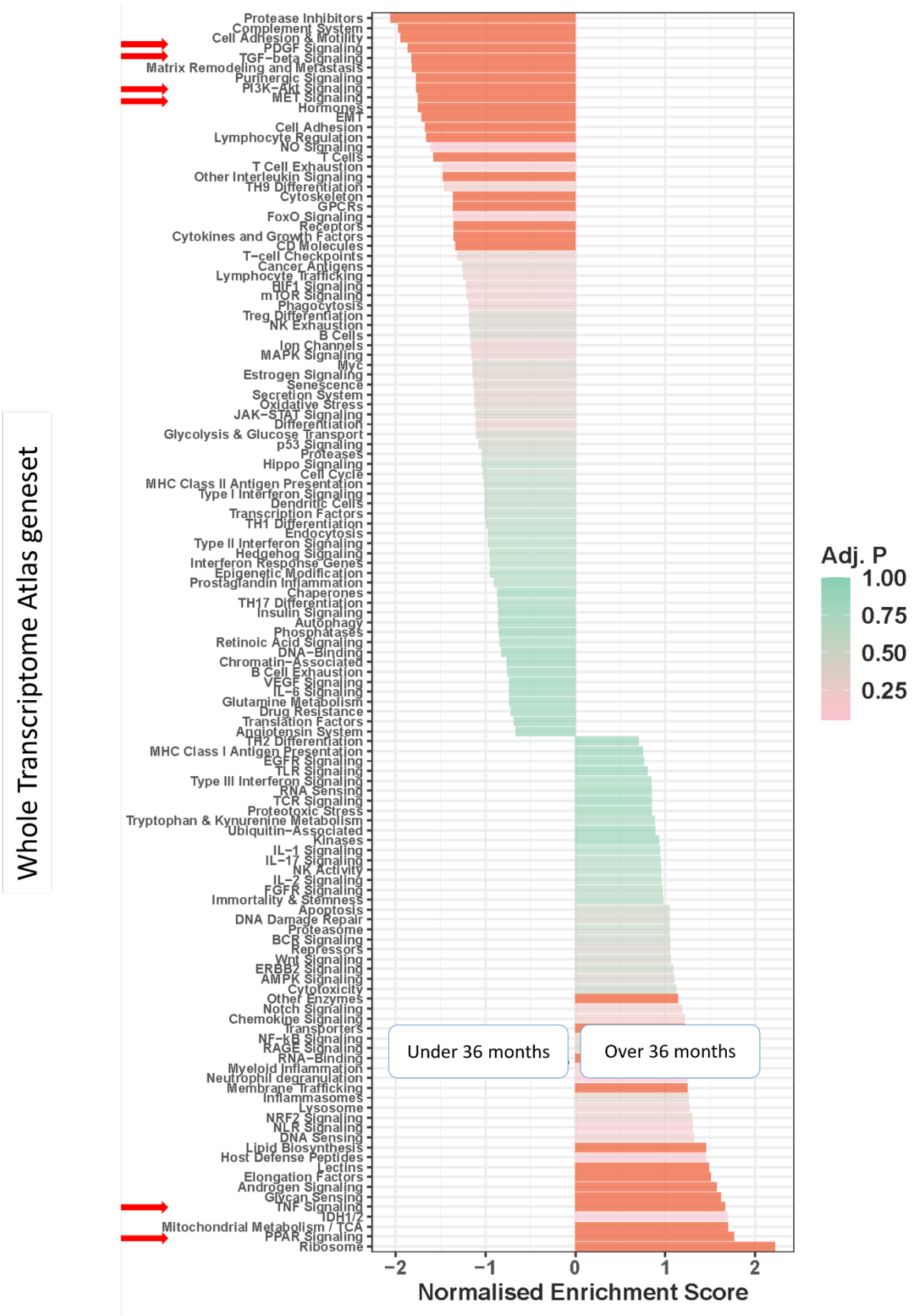


**Figure 5.12 Geneset enrichment of long-term survival naïve epithelial segments.** *Bar chart shows comparison between epithelial segments of patients surviving over 36 months and below. Pathways with normalized enrichment score above and below 1.5, and p adjusted (Adj. P) value ≤ 0.05 were considered significant. Important pathways are indicated by an arrow.*

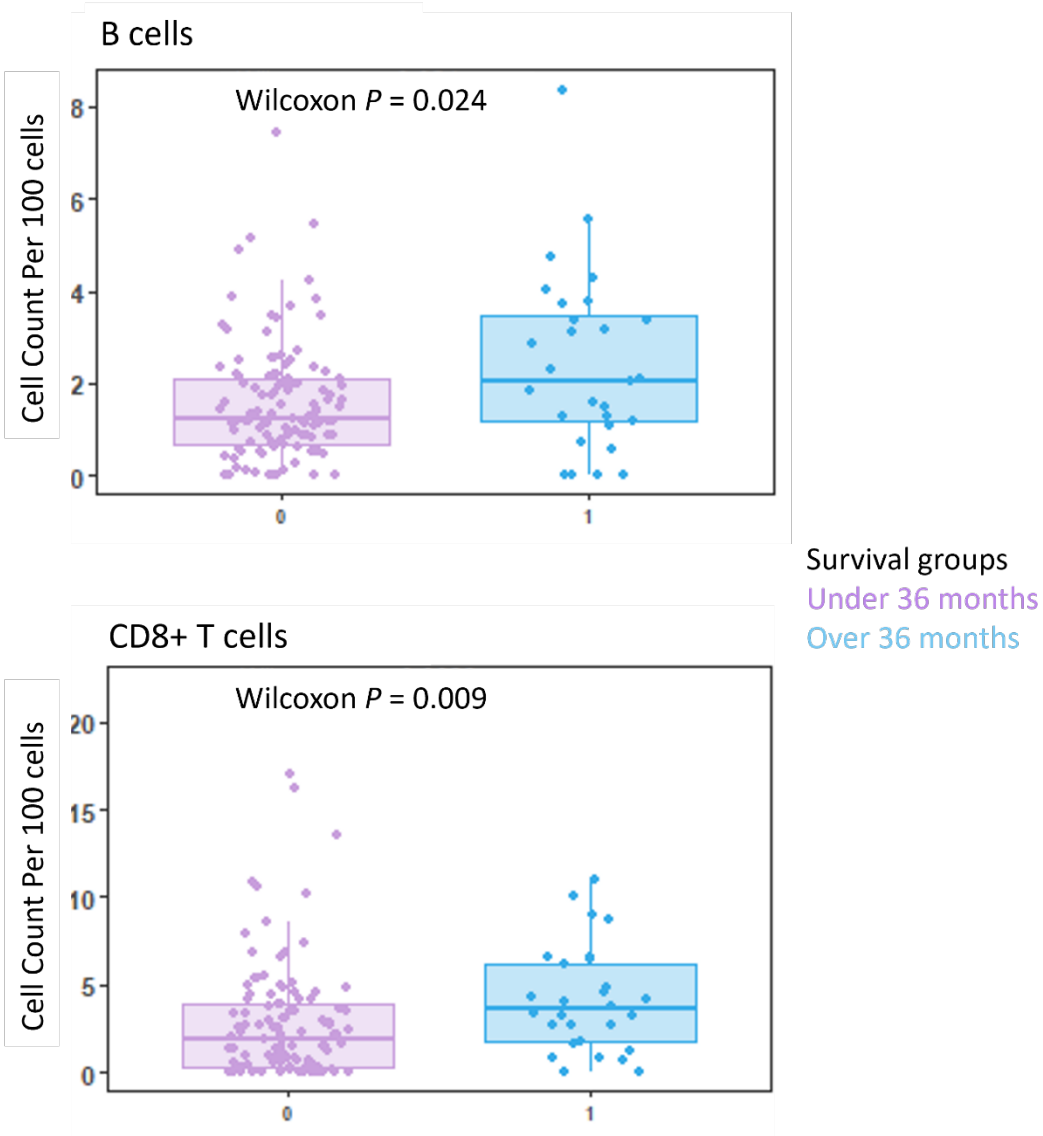


**Figure 5.13 Immune cell deconvolution of naïve long-term survivors.** *Boxplots demonstrate estimated immune cell expression per 100 cells in; B cells and CD8 T cells, across patients surviving over and under 36 months. Wilcoxon test with adjusted p value was used.*

### 5.3.5 B7-H3 signature in naïve pancreatic cancer

B7-H3 protein expression was demonstrated to be prognostic in naïve pancreatic cancer, with low expression in epithelial compartments significantly associating with disease specific survival (chapter 3.11). This pattern was replicated in a different naïve pancreatic TMA (table 5.1), using Spatial Transcriptomic expression. A prognostic pattern was observed when investigating average B7-H3 expression per patient, with low expression significantly correlating with improved survival (figure 5.14.a), and low epithelial expression demonstrating a non-significant trend towards improved survival (figure 5.14.b). Additionally, B7-H3 expression was upregulated in fibroblast-rich regions compared to epithelium, similar to the pattern observed in protein analysis (figure 5.14.c).

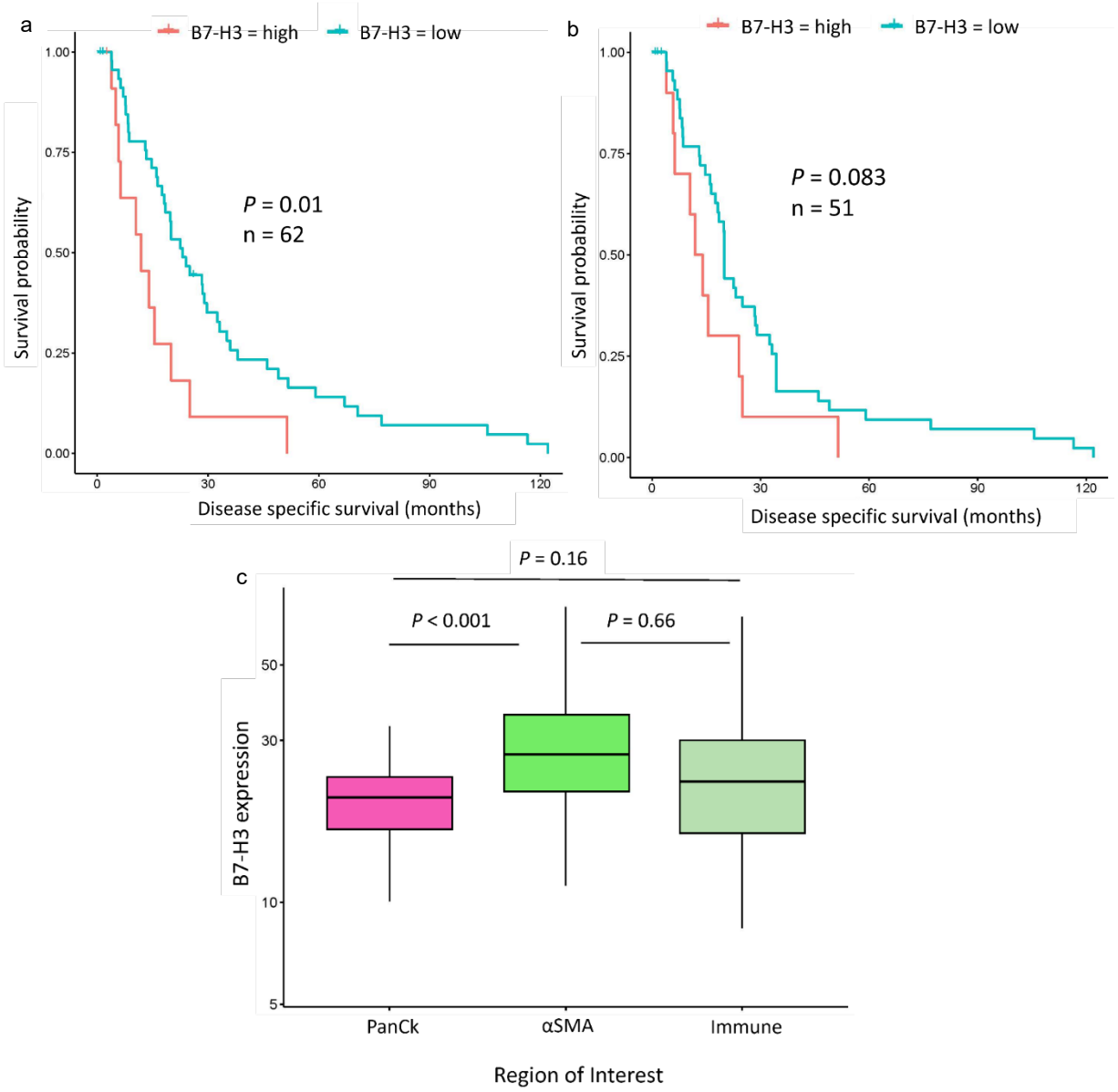


**Figure 5.14.a-c B7-H3 RNA expression in naïve pancreatic cancer.** *Kaplan-Meier curve stratified B7-H3 expression in disease specific survival (months) in a). whole core b). epithelial segments. Log-Rank (Mantel-Cox) test, replicating cutoff found in chapter 3.11, c). Boxplot showing B7-H3 expression across PanCk, αSMA and immune segments, Kruskal-Wallis test used.*

The Spatial Transcriptomic signature per ROI, associated with B7-H3 ranked expressions was investigated. A multitude of aberrated pathways were identified across all tissue compartments, with many cell signalling associated and immune related pathways, including downregulated B Cell Receptor (BCR) and T Cell Receptor (TCR) signalling, myeloid inflammation, and neutrophil degranulation among others (figure 5.15.a-c). Moreover, in B7-H3 low immune segments, decreased dendritic cell and T cell pathways were observed (figure 5.15.c), and fibroblast rich regions demonstrated reduced Treg differentiation pathways (figure 5.15.b). Of the pathways enriched, Nitric Oxide (NO) signalling and the complement system were seen in all three regions (figure 5.15.a-c), and epithelial regions demonstrated upregulation of the angiotensin system (figure 5.15.a).

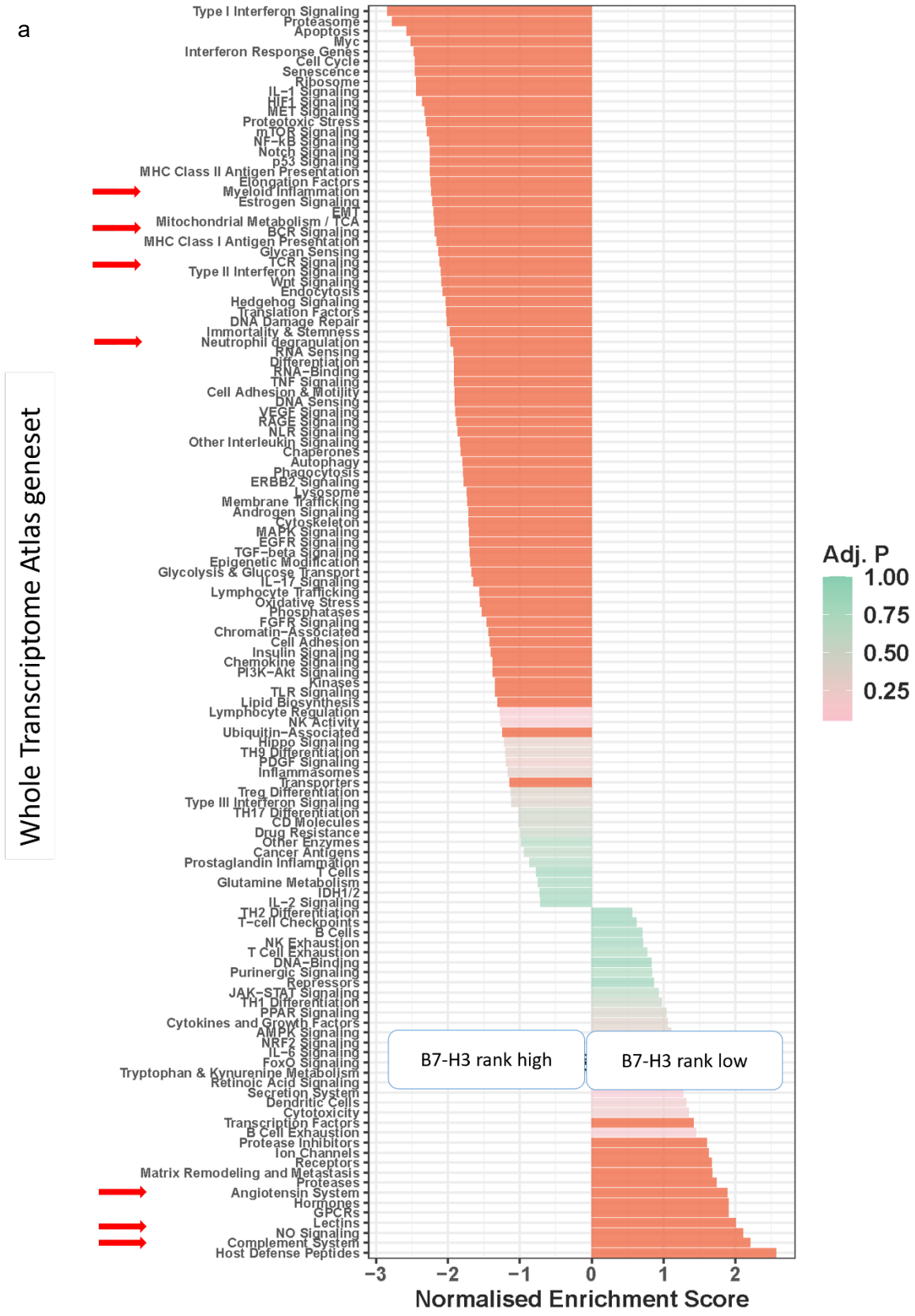


**Figure 5.15.a Geneset enrichment across B7-H3 ranked naïve segments.** *Bar charts demonstrate pathways differential expressed in B7-H3 high vs B7-H3 low a). epithelial segments. Pathways with normalized enrichment score above and below 1.5, and p adjusted (Adj. P) value ≤ 0.05 were considered significant. Important pathways are indicated by an arrow.*

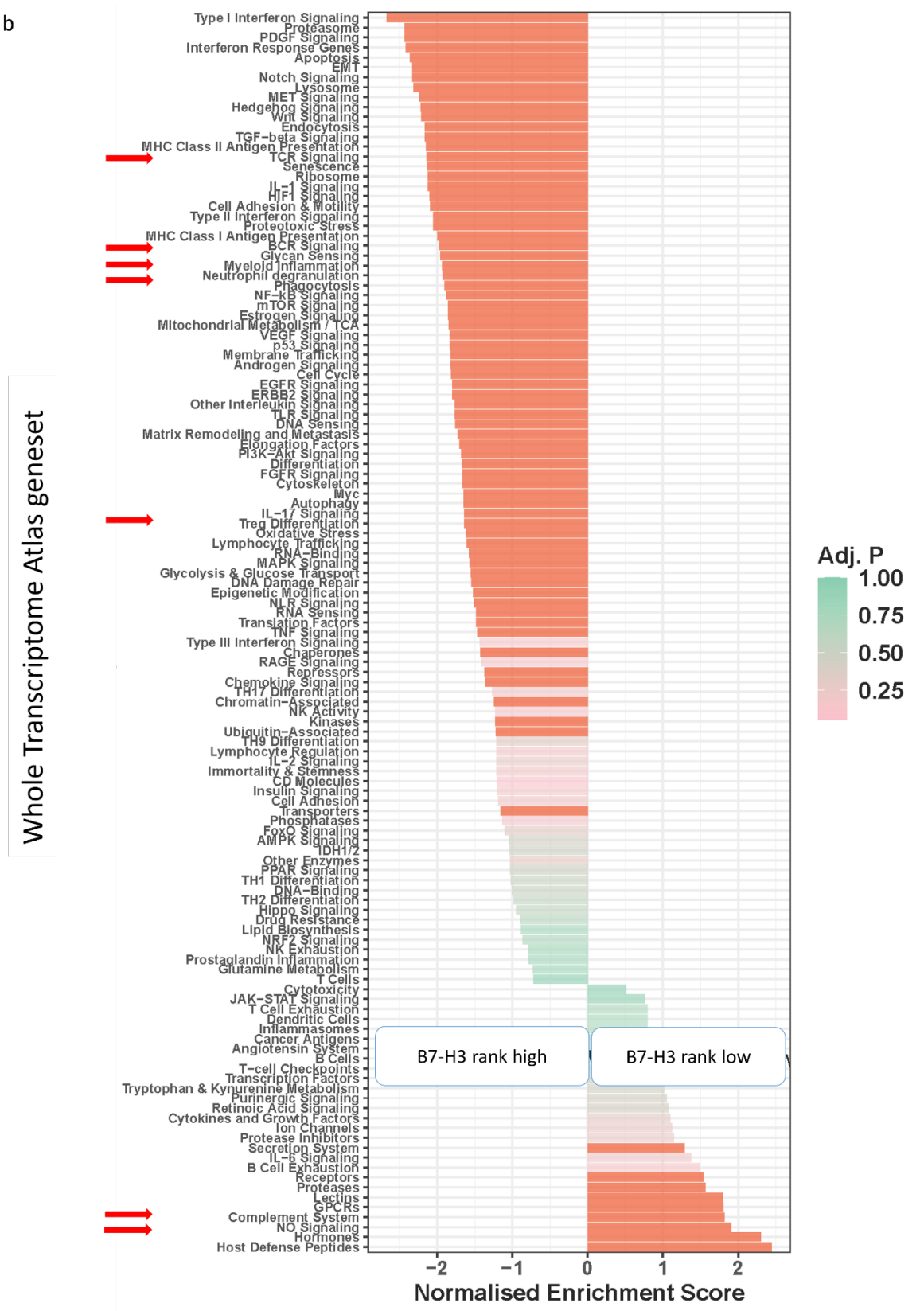


**Figure 5.15.b Geneset enrichment across B7-H3 ranked naïve segments.** *Bar charts demonstrate pathways differential expressed in B7-H3 high vs B7-H3 low b). αSMA segments. Pathways with normalized enrichment score above and below 1.5, and p adjusted (Adj. P) value ≤ 0.05 were considered significant. Important pathways are indicated by an arrow.*

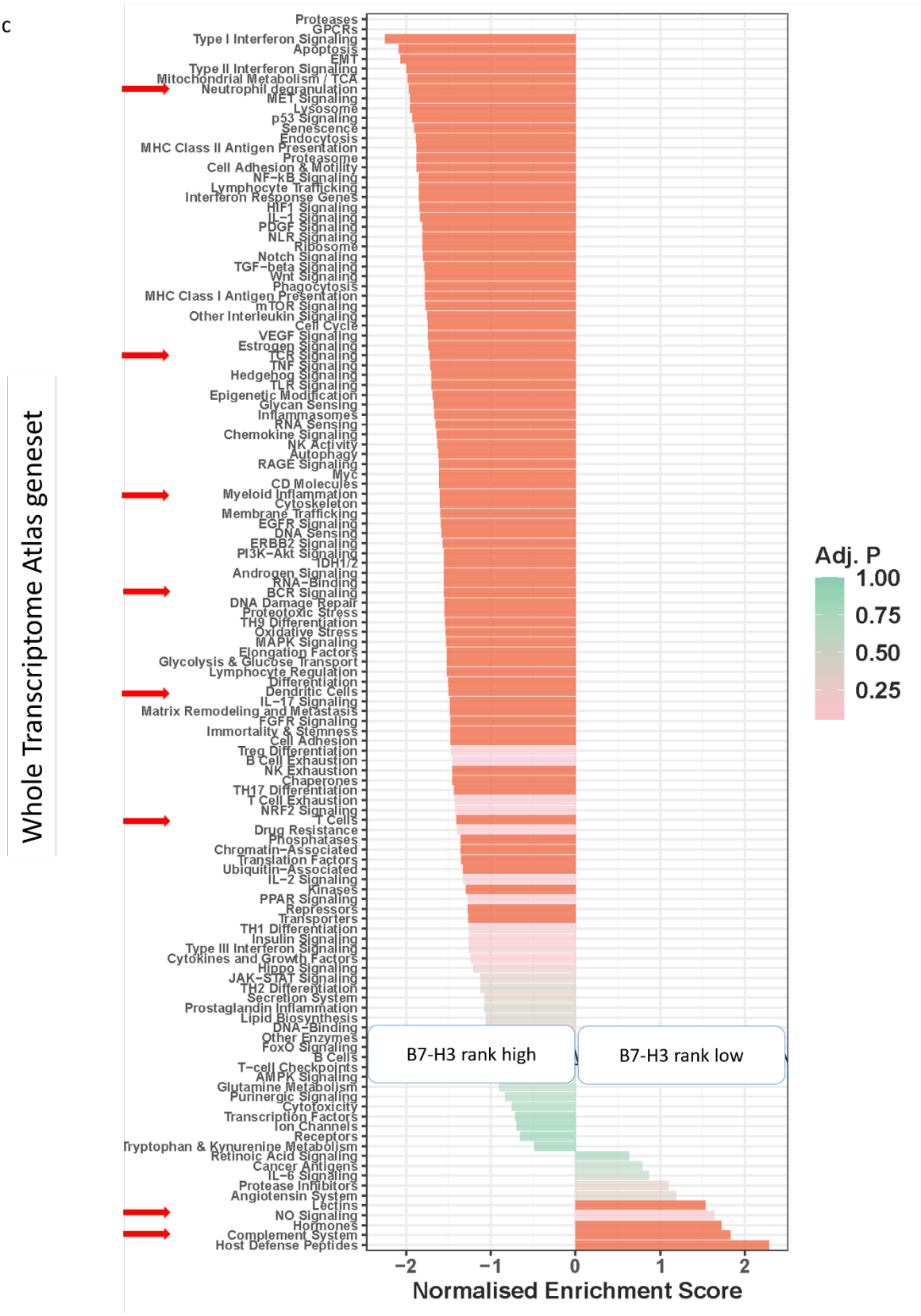


**Figure 5.15.c Geneset enrichment across B7-H3 ranked naïve segments.** *Bar charts demonstrate pathways differential expressed in B7-H3 high vs B7-H3 low c). immune segments. Pathways with normalized enrichment score above and below 1.5, and p adjusted (Adj. P) value ≤ 0.05 were considered significant. Important pathways are indicated by an arrow.*

## 5.4 Spatial Transcriptomic landscape of Neoadjuvant PDAC

### 5.4.1 Whole transcriptome profiling in neoadjuvant pancreatic cancer

To investigate the Spatial Transcriptomic profile of neoadjuvant treated pancreatic patients, Nanostrings whole transcriptome assay was used and replicated the segments found in the naïve cohort above (chapter 5.3.1). Of note, although the same segments were replicated, a deep learning algorithm was trained to generate these masks (chapter 2.5.2.1). The neoadjuvant cohort comprised of 58 archival Glasgow patients, and 13 clinical trial PRIMUS002 patients (figure 5.16 and table 5.1).

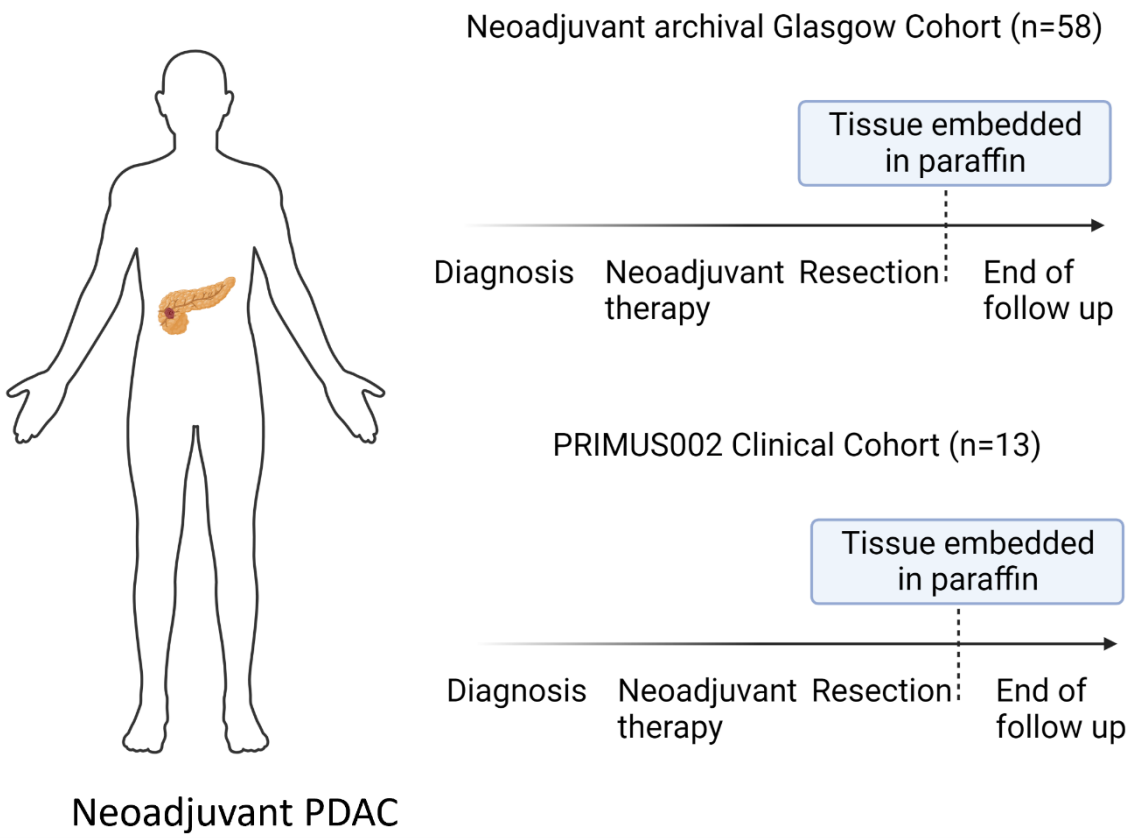


**Figure 5.16 Overview of neoadjuvant PDAC cohort**. *Schematic from diagnosis to end of follow up across archival Glasgow cohort (n=58) and PRECISION PANC PRIMUS002 clinical trial reduced cohort (n=13).*

## 5.4.2 Tumour compartments demonstrate distinct transcriptome profiles in neoadjuvant pancreatic cancer

### 5.4.2.1 Inter-compartment heterogeneity

Assessment between different areas of interest was repeated in the neoadjuvant cohort to establish specialised compartment signatures. Large DEA differences were seen between epithelial segments both immune and fibroblast-rich, whereas limited differences were seen between immune and αSMA segment comparisons (figure 5.17.a-c).

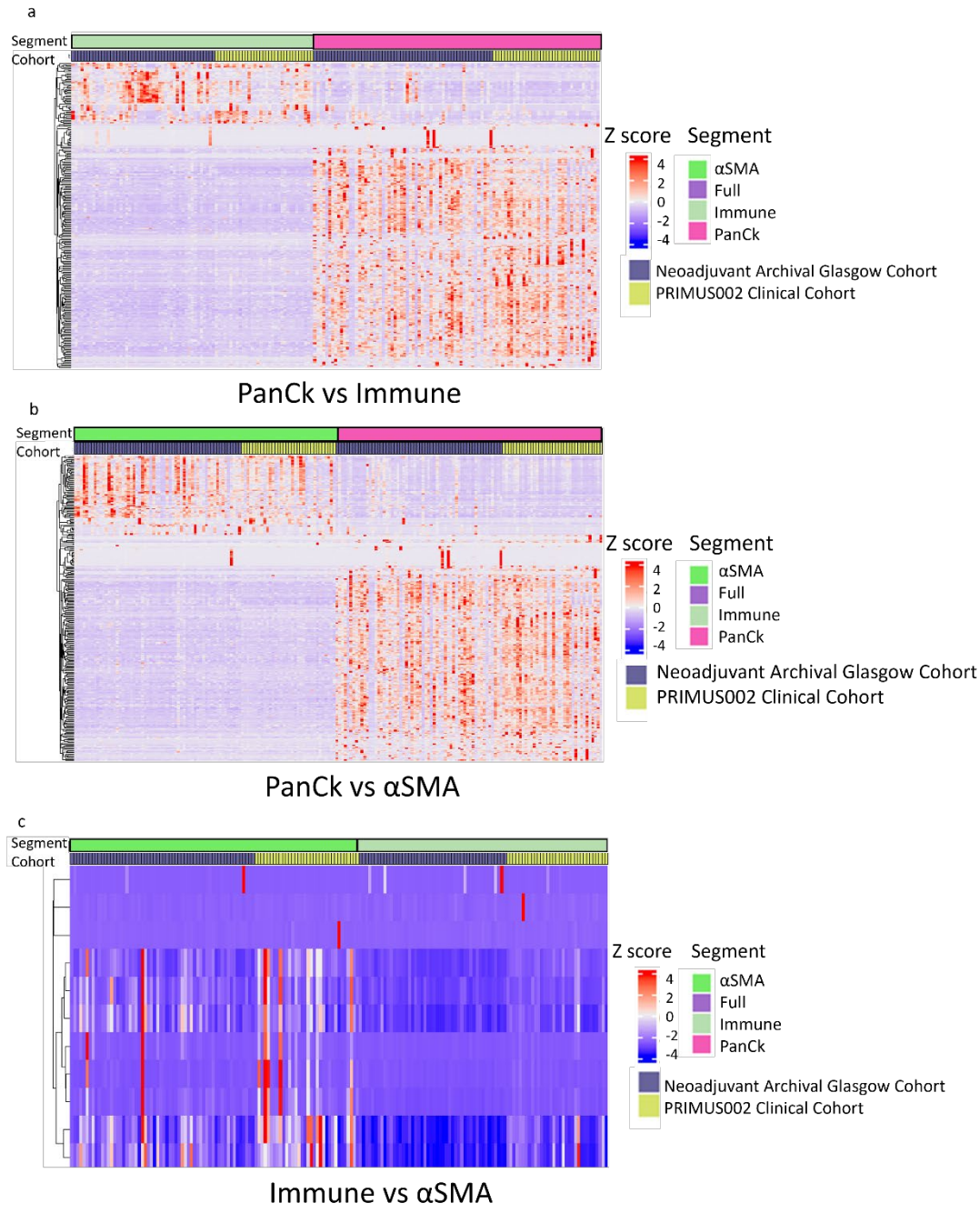


**Figure 5.17.a-c Inter-compartment differential expression in neoadjuvant patients.** *Heatmap showing significant differentially expressed genes in all segment comparison. Segments comparisons carried out between PanCk vs immune, PanCk vs αSMA and immune vs αSMA.*

As expected, geneset enrichment analysis showed many differences between all segment comparisons (supplementary 8.4.1.2). Spatial immune deconvolution estimated increased expression in a wide range of immune cells. Elevated macrophages (p<0.001), plasma cells (p=0.002), CD4 helper T cells (p<0.001), CD8 cytotoxic T cells (p<0.001) and memory DC (p<0.001), among others, were seen in immune compartments. As expected, αSMA regions were enriched with fibroblasts (p<0.001) (figure 5.18).

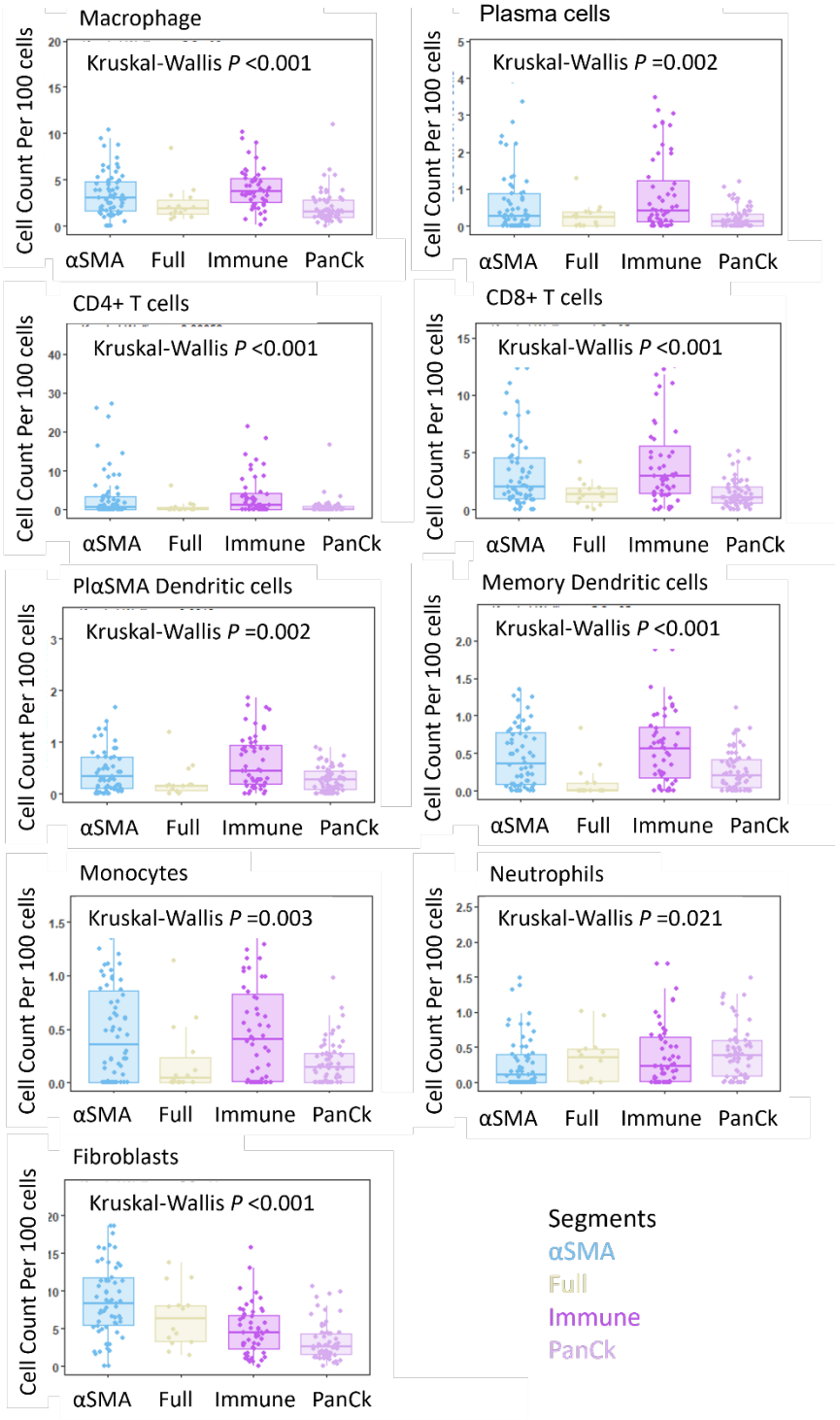


**Figure 5.18 Immune cell deconvolution across neoadjuvant segments.** *Boxplots demonstrate estimated immune cell expression per 100 cells in across PanCk, αSMA, immune and full neoadjuvant segments. Kruskal-Wallis test used.*

### 5.4.2.2 Histopathological region heterogeneity

The neoadjuvant TMAs were purpose built to include distinct histopathological regions, resulting in muti-regional samples taken from the tumour core (TC), presumed tumour bed (PTB) and lymph node metastasis to account for heterogeneity. The overall ROIs were compared per histopathological region, demonstrating large transcriptomic differences according to location. Pathway analysis displayed virtually all signalling pathways measured were significantly downregulated when the presumed tumour bed was compared to tumour core and lymph node metastasis (supplementary 8.4.1.3). Particular interest was given to the tumour core/lymph node comparison, as this represents a primary tumour/matched metastasis comparison. DEA showed upregulation of *CCL21* (logFC = 3.4, padj <0.001), *CXCL13* (logFC = 1.7, padj <0.001), *MMP9* (logFC = 1.5, padj <0.00), *MS4A1* (logFC = 1.5, padj <0.001) and *CD79A* (logFC = 1.5, padj <0.001) in LN regions (figure 5.19.a). In comparison, tumour core presented with elevated *SFRP2* (logFC = 1.6, padj <0.001) among others. LN core correlated with a considerable number of significant pathways. Multiple immune related pathways were seen in lymph node metastasis regions. Notably, increased pathways associated with aggressive disease phenotypes; immortality and stemness (NES = 1.8, padj <0.001), VEGF signalling (NES = 2.2, padj <0.001) and EMT (NES = 1.6, padj =0.001) (figure 5.19.b).

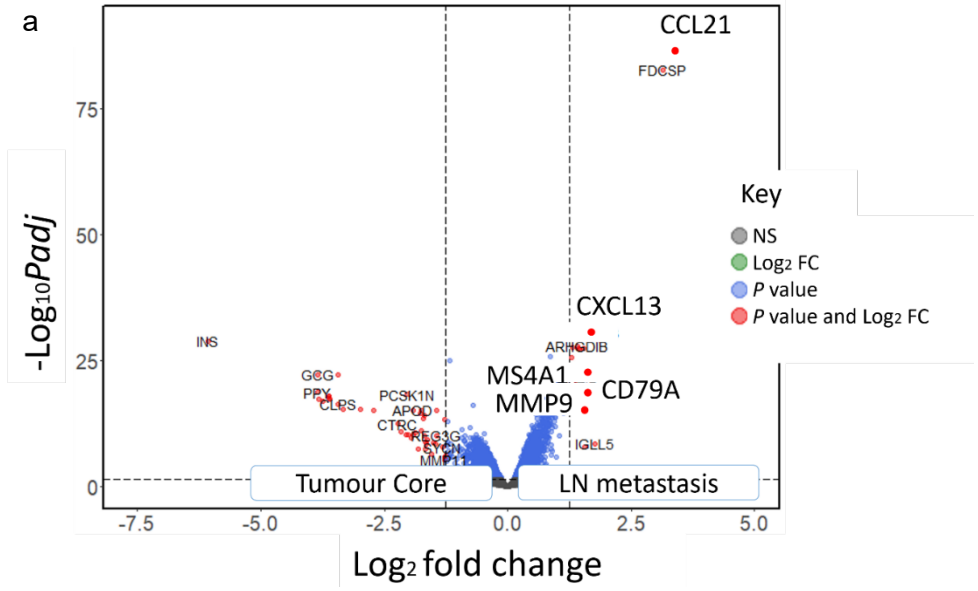


**Figure 5.19.a Spatial Transcriptomic alterations between distinct histopathology**, *a). Volcano plot demonstrating gene marker differential expression levels in tumour core vs LN metastasis. Genes with log2 fold change above and below 1.5, and p adjusted value ≤0.05 were considered significant, important genes in bold. Dashed line indicates significance thresholds, NS = non-significant, FC = fold change.*

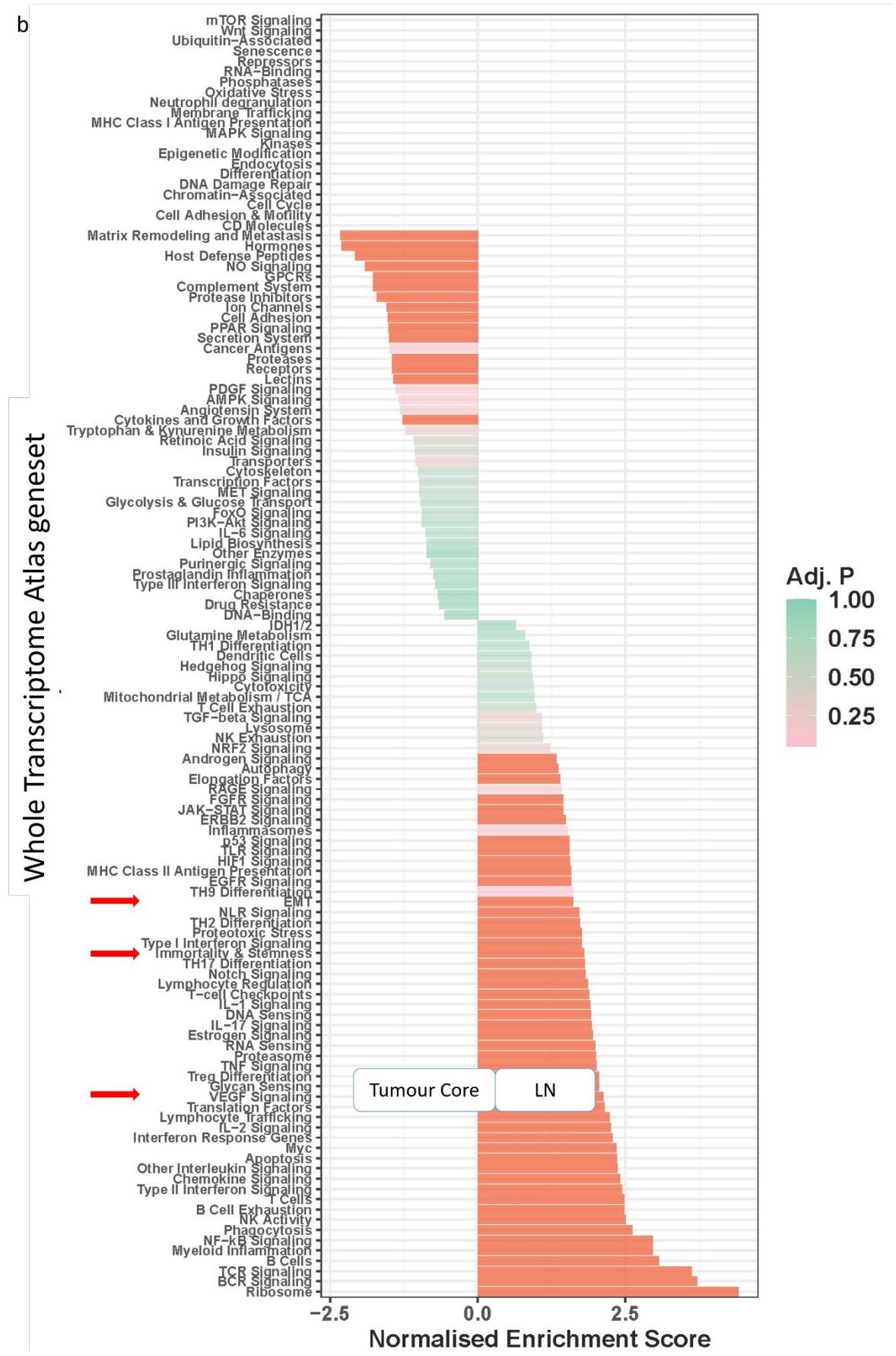


**Figure 5.19.b Spatial Transcriptomic alterations between distinct histopathology**, *b). Geneset enrichment bar chart in tumour core vs LN metastasis. Pathways with normalized enrichment score above and below 1.5, and p adjusted (Adj. P) value ≤ 0.05 were considered significant. Important pathways are indicated by an arrow*.

### 5.4.3 Survival profile

Introduction of neoadjuvant therapy for borderline and locally advanced pancreatic cancer has resulted in a significant increase in survival. A small subset of neoadjuvant patients have marked prognostic benefit. To investigate whether these differences could be explained using Spatial Transcriptomics, the neoadjuvant cohort was split using the same grouping as for the naïve analysis (chapter 5.3.4), long term survivors (over 36 months), compared to the rest. Pathway analysis in LTS epithelium showed downregulation of various signalling pathways including MYC (NES = -1.9, padj = 0.005), PPAR signalling (NES = -1.8, padj = 0.014), MET (NES = -1.8, padj = 0.014) and TNF (NES = -1.6, padj = 0.025) (figure 5.20.a). Patients surviving over 36months demonstrated fewer immune related pathways in immune and fibroblast segments, but elevated levels of NK activity (NES = 1.8, padj <0.001), IL-17 signalling (NES = 1.7, padj = 0.005) and B cells (NES = 1.6, padj = 0.043) in fibroblast segments (figure 5.20.b).

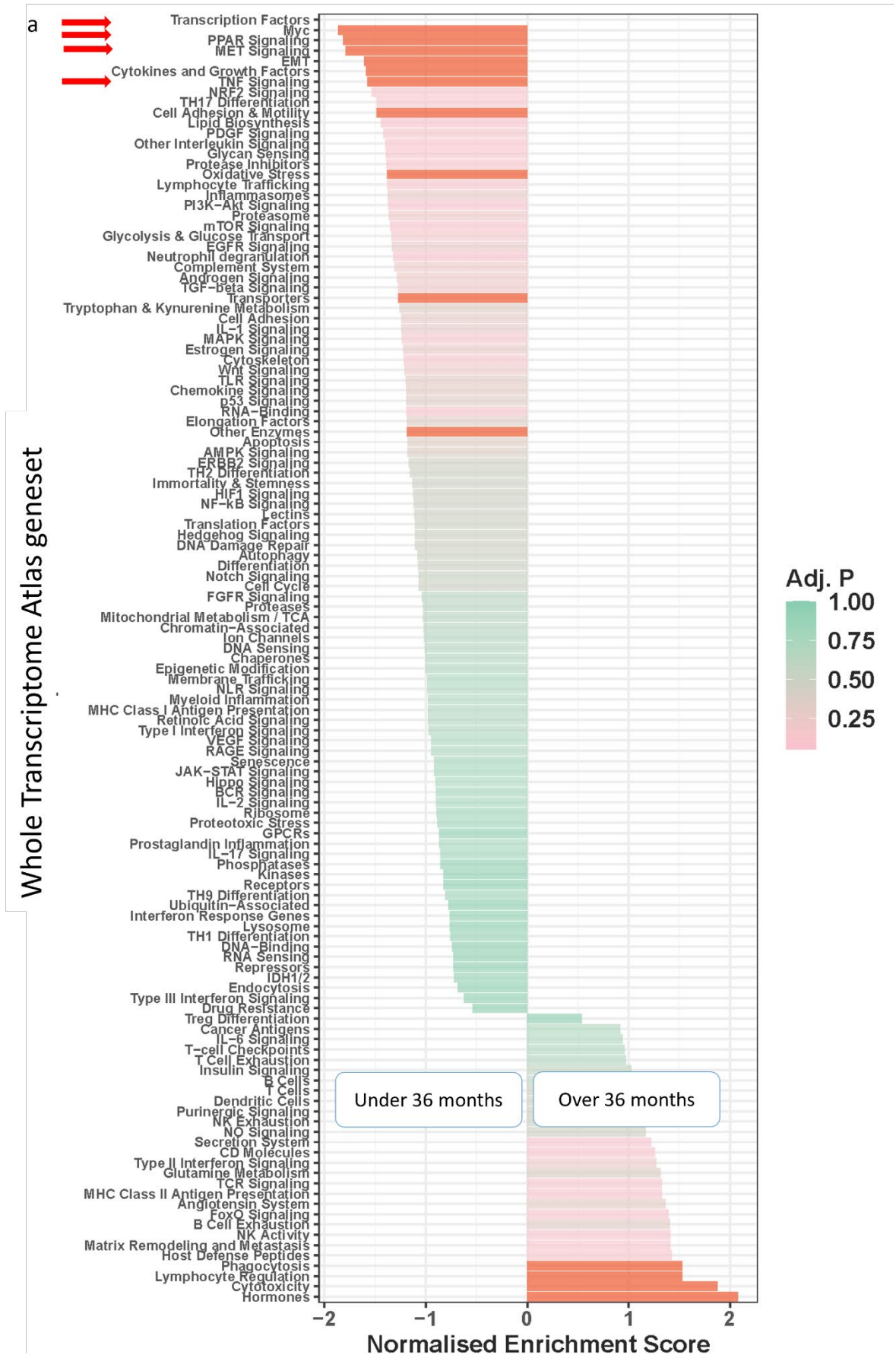


**Figure 5.20.a Geneset alterations in neoadjuvant long term survivors.** *Bar chart showing pathways enriched in patients surviving under and over 36 months in a). Epithelial segments.. Pathways with normalized enrichment score above and below 1.5, and p adjusted (Adj. P) value ≤ 0.05 were considered significant. Important pathways are indicated by an arrow*.

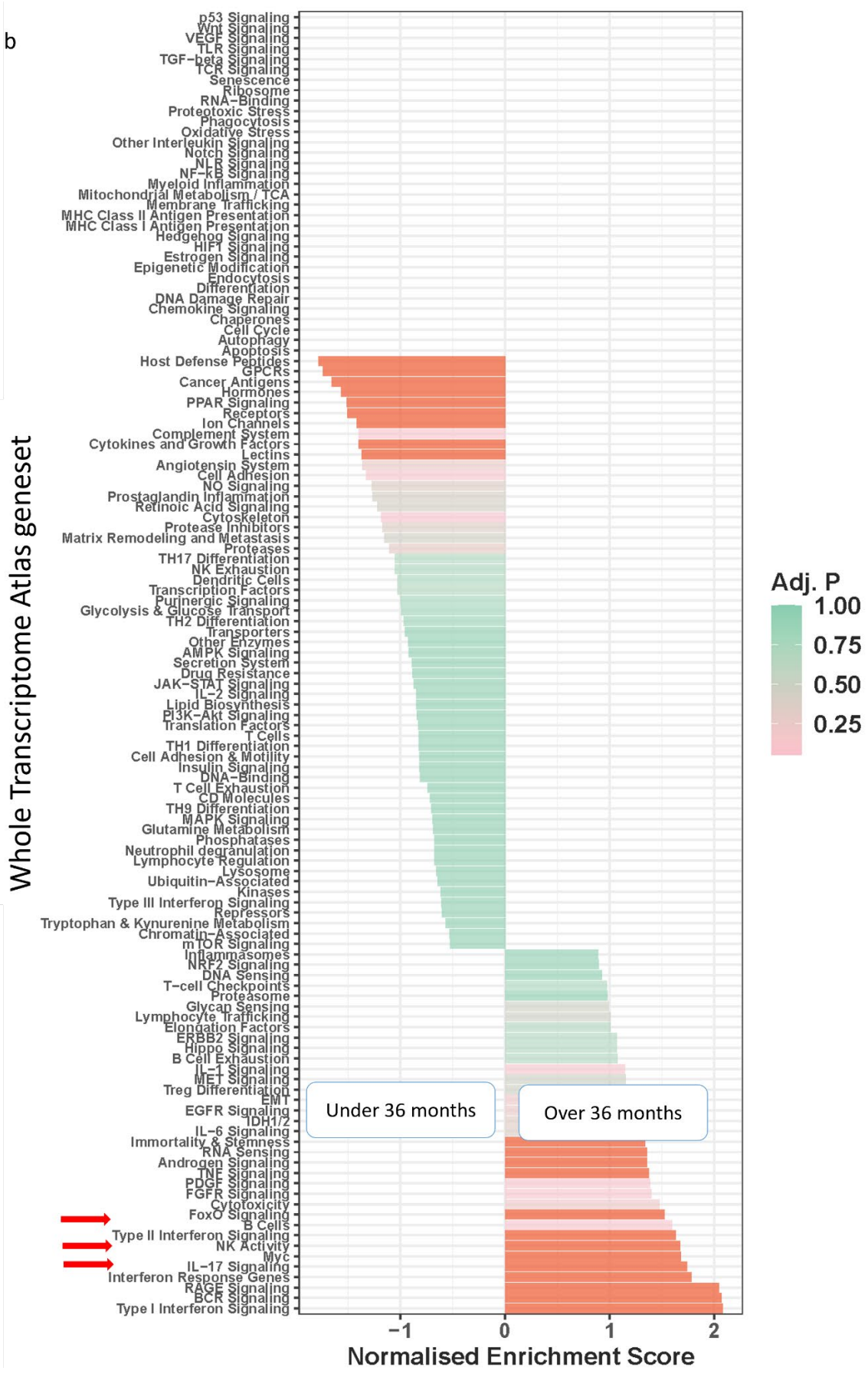


**Figure 5.20.b Geneset alterations in neoadjuvant long term survivors.** *Bar chart showing pathways enriched in patients surviving under and over 36 months in b). αSMA segments. Pathways with normalized enrichment score above and below 1.5, and p adjusted (Adj. P) value ≤ 0.05 were considered significant. Important pathways are indicated by an arrow*.

## 5.4.4 Neoadjuvant treatment types in neoadjuvant pancreatic cancer and their associated Spatial Transcriptomic profile

### 5.4.4.1 Types of neoadjuvant therapy and their associated signature

Patients eligible for neoadjuvant therapy can be administered chemotherapy or chemoradiotherapy. The biological differences produced between these two treatment methods is relatively unknown. To fully understand the effects neoadjuvant treatment has on pancreatic cancer, patients were split according to treatment type and matched tissue compartments compared. Further details on this subgroup can be found in chapter 2.1.1. Furthermore, regression pattern was fully explored (supplementary 8.4.2). Pathway analysis demonstrated varied aberrations in chemotherapy treated patients. Epithelial segments demonstrated a range of pathways including increased complement system (NES = 1.8, padj = 0.012) and neutrophil degranulation (NES = 1.8, padj <0.001), NO signalling (NES = 2.1, padj = 0.005), MET signalling (NES = 1.8, padj = 0.014) and autophagy (NES = 1.6, padj = 0.014) (figure 5.21.a). Immune segments showed relatively high numbers of aberrated immune pathways. Chemoradiotherapy segments showed increased levels of B cells (NES = 2.6, padj <0.001), coupled with elevated B cell exhaustion (NES = 2.4, padj <0.001) (figure 5.21.b). Elevated TCR signalling (NES = 1.9, padj <0.001) and myeloid inflammation (NES = 1.8, padj <0.001) were also observed (figure 5.21.b). Spatial immune cell deconvolution demonstrated increased memory dendritic cells in neoadjuvant chemotherapy treated patients (p=0.002) (figure 5.22).

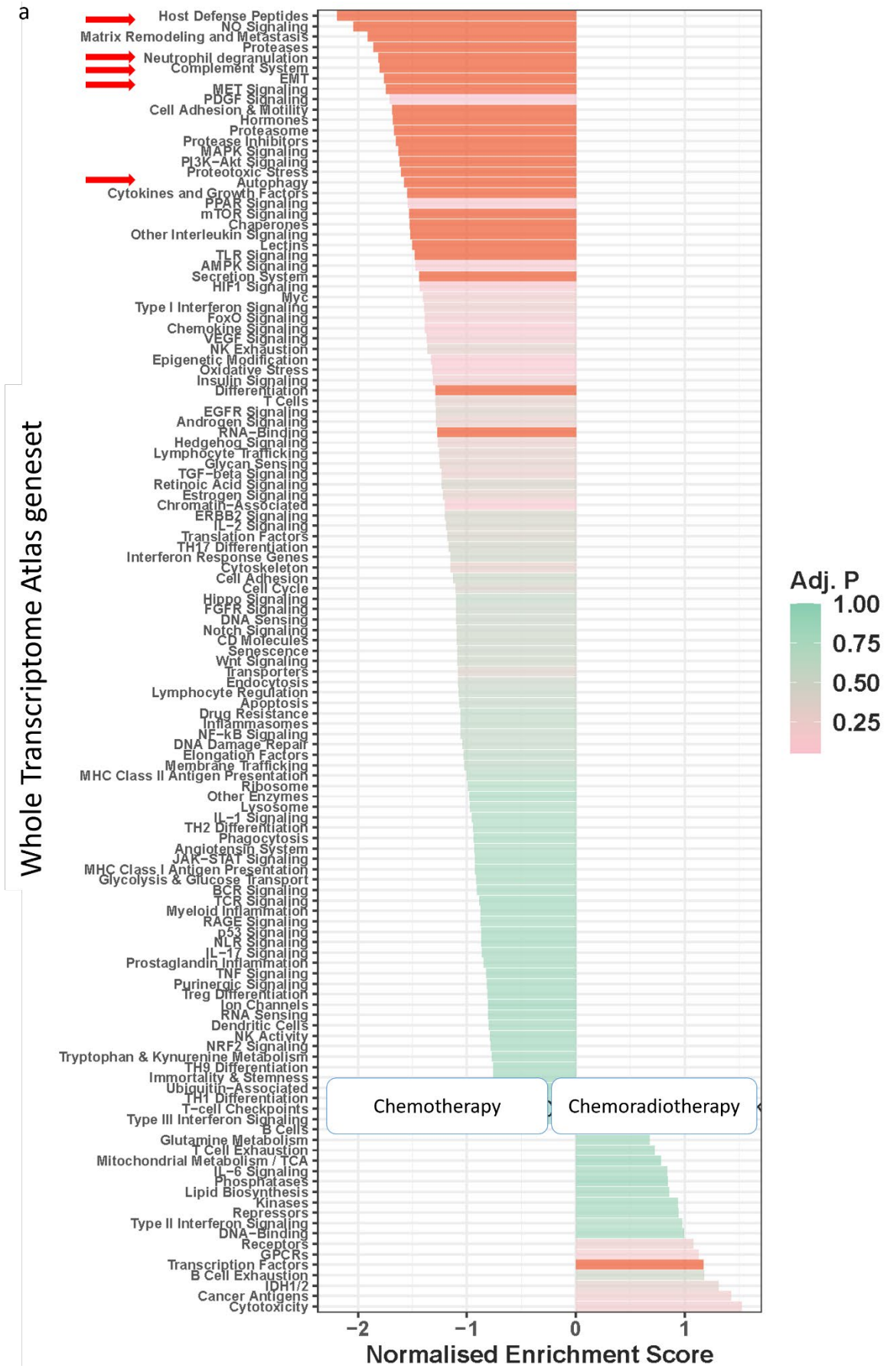


**Figure 5.21.a Geneset alterations in neoadjuvant treatment types.** *Bar chart showing pathways enriched in chemotherapy vs chemoradiotherapy in a). Epithelial segments. Pathways with normalized enrichment score above and below 1.5, and p adjusted (Adj. P) value ≤ 0.05 were considered significant. Important pathways are indicated by an arrow*.

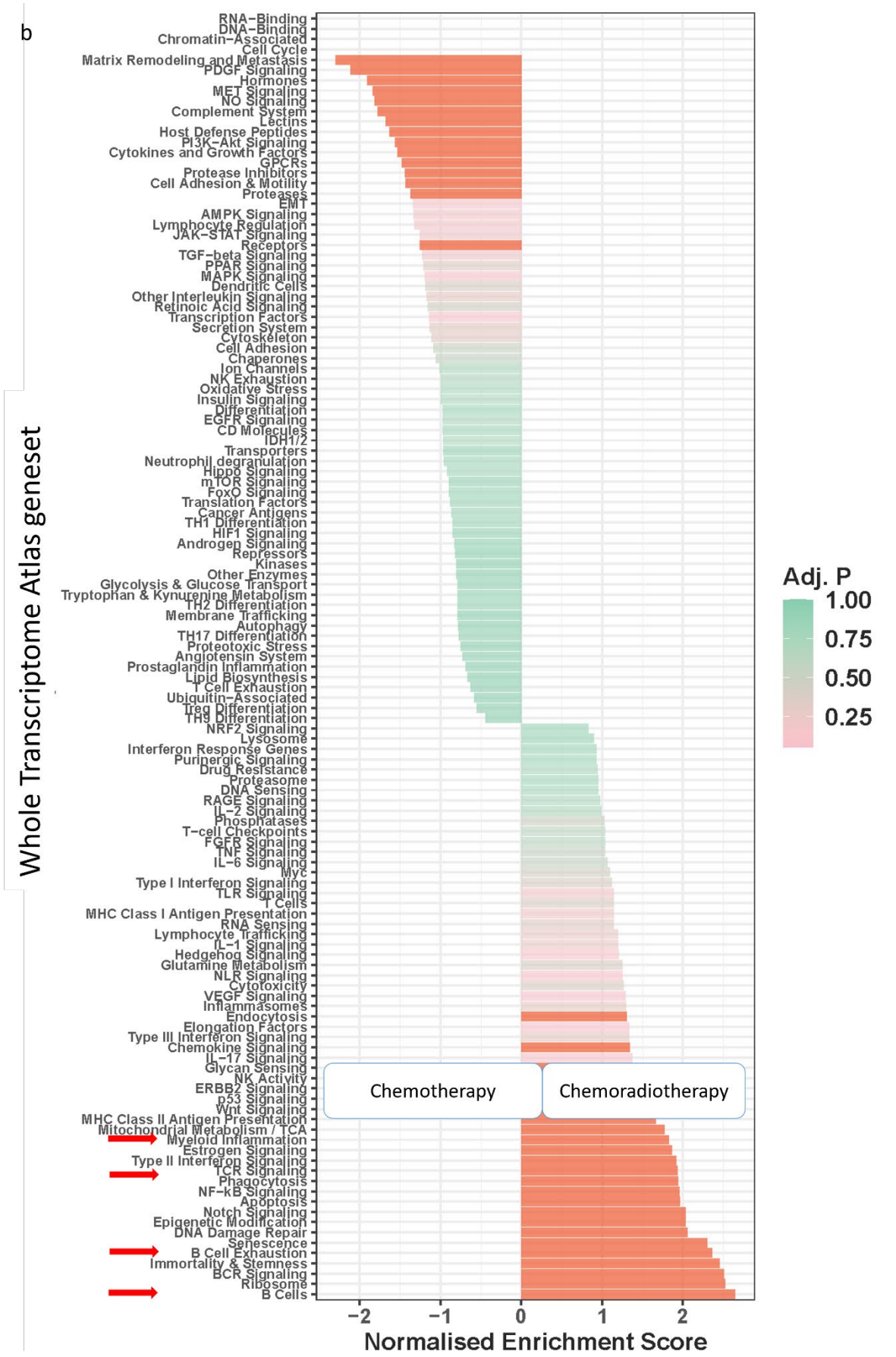


**Figure 5.21.b Geneset alterations in neoadjuvant treatment types.** *Bar chart showing pathways enriched in chemotherapy vs chemoradiotherapy in b). Immune segments. Pathways with normalized enrichment score above and below 1.5, and p adjusted (Adj. P) value ≤ 0.05 were considered significant. Important pathways are indicated by an arrow*.

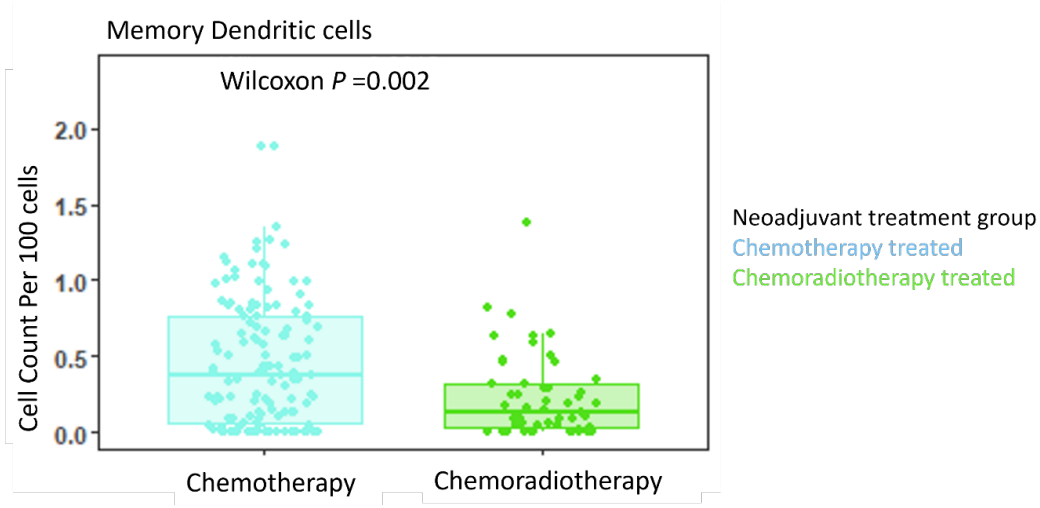


**Figure 5.22 Immune cell deconvolution in chemotherapy and chemoradiotherapy patients.** *Boxplots demonstrate estimated immune cell expression per 100 cells in memory dendritic cells across patients treated with chemotherapy or chemoradiotherapy. Wilcoxon test with adjusted p value was used.*

### 5.4.4.2 Types of neoadjuvant chemotherapy and their associated signature

Within chemotherapy, two main treatment types are utilised; FOLFIRINOX based and Gemcitabine based. Gemcitabine epithelium demonstrated elevated levels of *CA9* (logFC = 1.9, padj = 0.002), *IAPP* (logFC = 1.7, padj <0.001), and *CREB3* (logFC = 1.6, padj <0.001) genes, along with elevated B cell (NES = 2.0, padj = 0.020) and BCR signalling (NES = 1.8, padj <0.001) (figure 5.23.a-b). Comparatively, FFX had augmented levels of PPAR signalling (NES = 1.7, padj = 0.013) (figure 5.23.b).

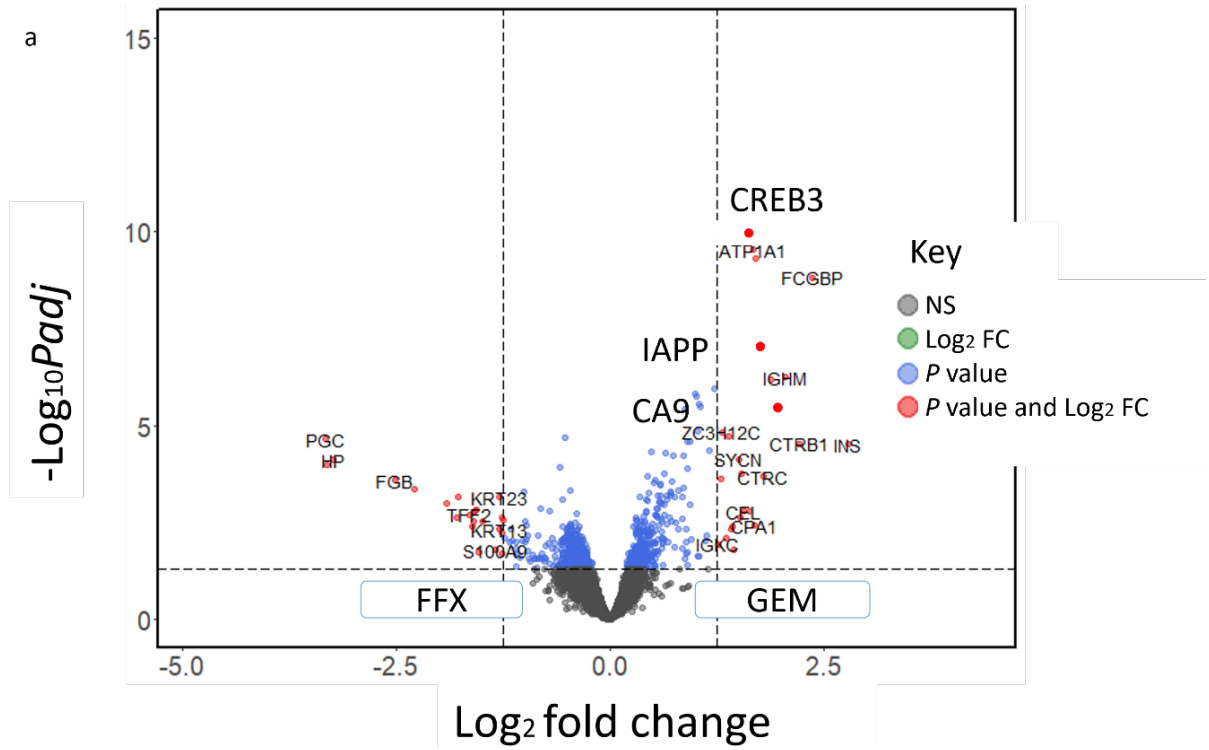


**Figure 5.23.a Epithelial Spatial Transcriptomic alterations between chemotherapy treatment type**, *a). Volcano plot demonstrating gene marker differential expression levels in FOLFIRINOX (FFX) vs Gemcitabine (GEM) epithelium. Genes with log2 fold change above and below 1.5, and p adjusted value ≤0.05 were considered significant, important genes in bold. Dashed line indicates significance thresholds, NS = non-significant, FC = fold change.*

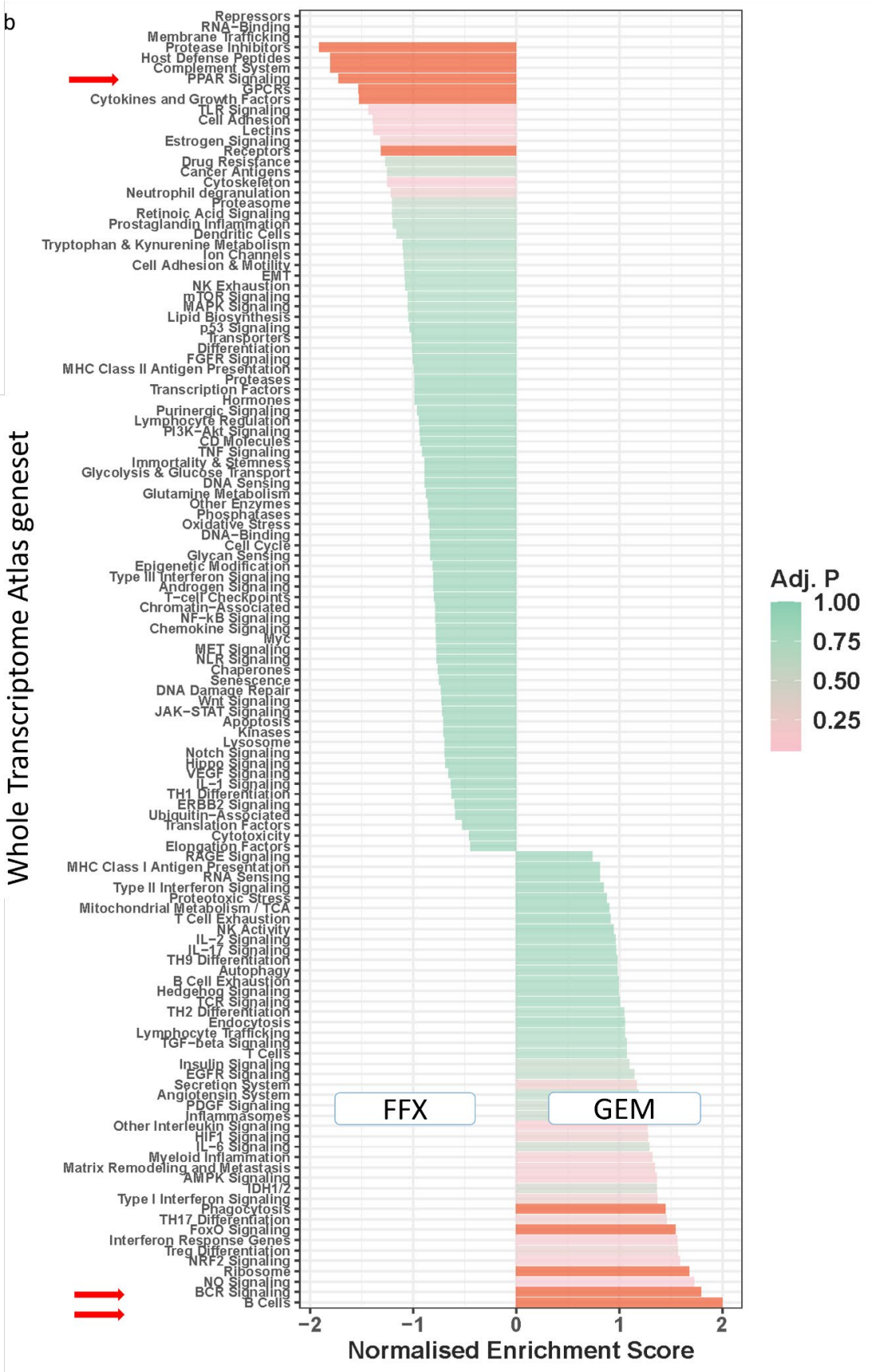


**Figure 5.23.b Epithelial Spatial Transcriptomic alterations between chemotherapy treatment type** *b). Geneset enrichment bar chart in FOLFIRINOX (FFX) vs Gemcitabine (GEM) epithelium. Pathways with normalized enrichment score above and below 1.5, and p adjusted (Adj. P) value ≤ 0.05 were considered significant. Important pathways are indicated by an arrow.*

Pathways enriched in αSMA segments were strongly immune related. Enriched B cell (NES = 3.2, padj <0.001) coupled with B cell exhaustion (NES = 2.1, padj = 0.006), T cell (NES = 2.0, padj <0.001) and T cell checkpoint (NES = 1.6, padj <0.001) were seen in Gemcitabine treated regions (figure 5.24). In contrast, FOLFIRINOX treated regions demonstrated cell signalling based pathways. These pathways include elevated NO signalling (NES = 1.9, padj <0.001), PDGF (NES = 1.7, padj = 0.003) and angiotensin system (NES = 1.6, padj = 0.039) among others (figure 5.24).

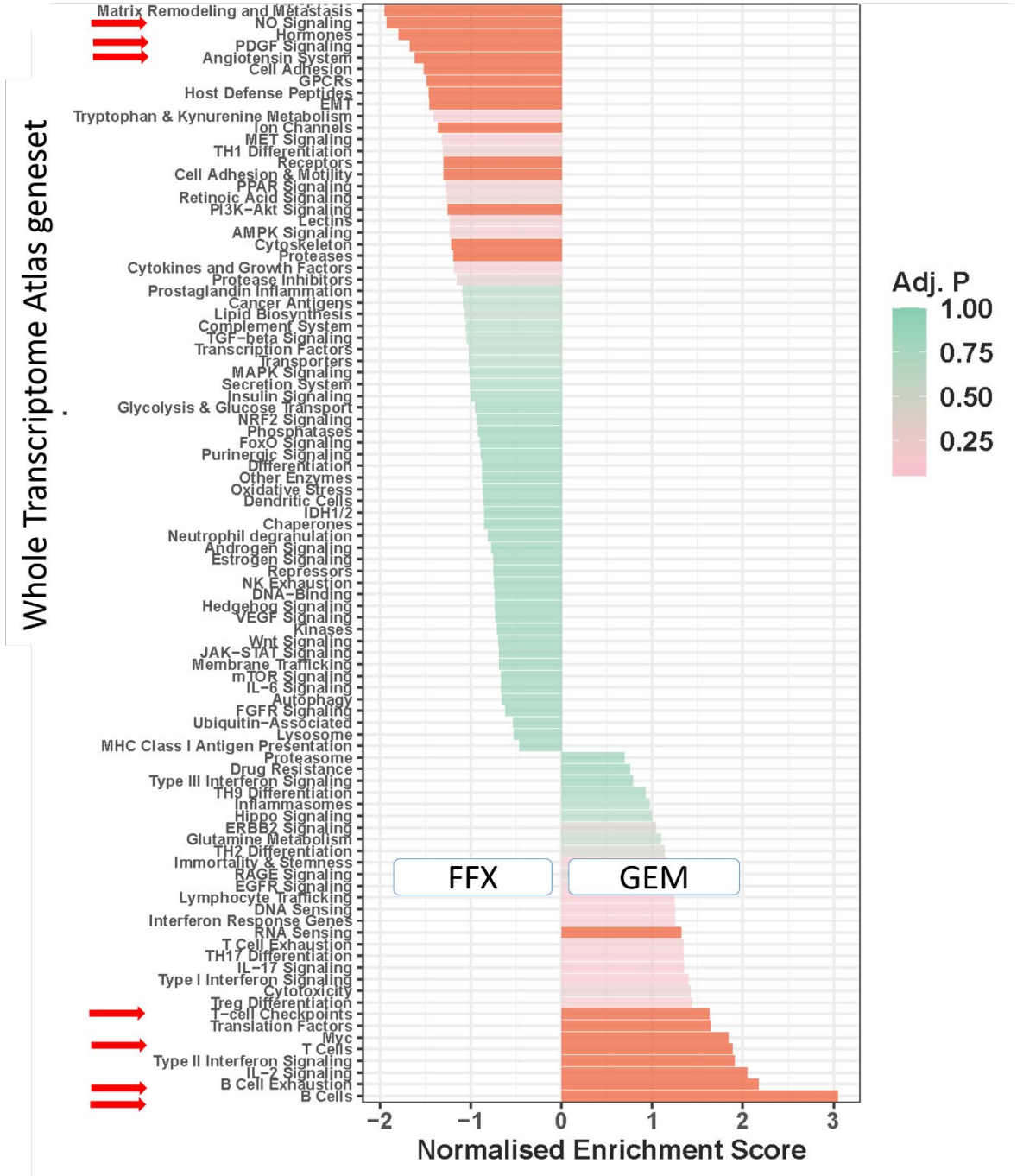


**Figure 5.24 Fibroblast Spatial Transcriptomic alterations between chemotherapy treatment type**. *Geneset enrichment bar chart in FOLFIRINOX (FFX) vs Gemcitabine (GEM) αSMA segments. Pathways with normalized enrichment score above and below 1.5, and p adjusted (Adj. P) value ≤ 0.05 were considered significant. Important pathways are indicated by an arrow.*

GSEA of immune areas demonstrated similar patterns as stromal regions. Augmented B cell (NES = 2.8, padj <0.001) coupled with B cell exhaustion (NES = 2.1, padj = 0.001), T cell (NES = 1.9, padj = 0.020) coupled with T cell exhaustion (NES = 2.6, padj <0.001), NK activity (NES = 1.6, padj = 0.005) and T cell checkpoints (NES = 1.8, padj = 0.02) were seen in Gemcitabine (figure 5.25). FOLFIRINOX treated immune segments demonstrated elevated neutrophil degranulation (NES = 1.9, padj <0.001) (figure 5.25).

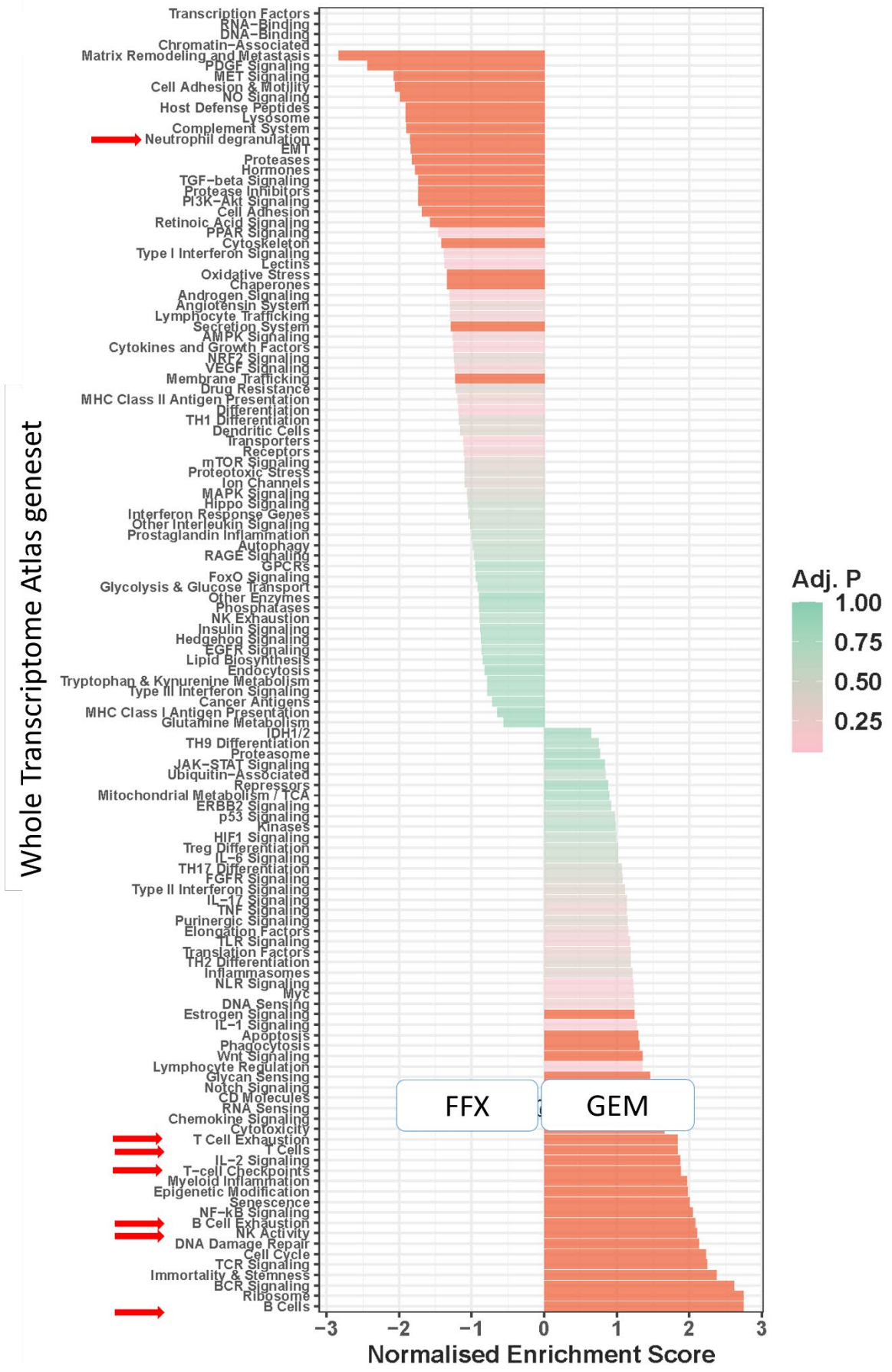


**Figure 5.25 Immune Spatial Transcriptomic alterations between chemotherapy treatment type**. *Geneset enrichment bar chart in FOLFIRINOX (FFX) vs Gemcitabine (GEM) immune segments. Pathways with normalized enrichment score above and below 1.5, and p adjusted (Adj. P) value ≤ 0.05 were considered significant. Important pathways are indicated by an arrow.*

Immune cell deconvolution confirmed the immune rich nature Gemcitabine treated samples have when compared to FFX treated samples. Elevated B cells (p=0.029), cytotoxic CD8 T cells (p=0.005), pDCs (p=0.043) and Tregs (p=0.003) were observed (figure 5.26).

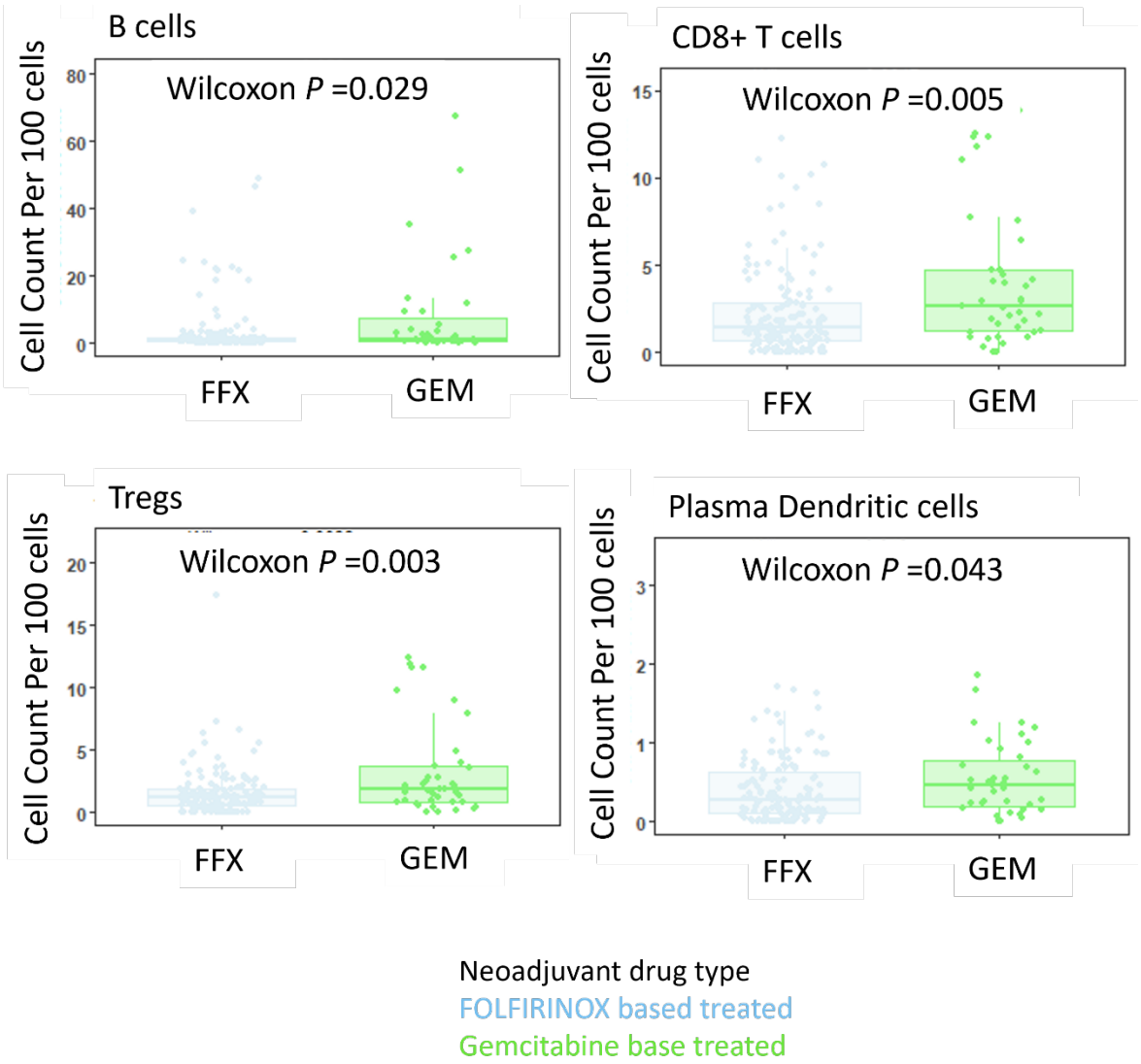


**Figure 5.26 Immune cell deconvolution between chemotherapy treatment type.** *Boxplots demonstrate estimated immune cell expression per 100 cells in; B cells, CD8 T cells, Tregs and plasma dendritic cells, across patients treated with FOLFIRINOX (FFX) or Gemcitabine (GEM). Wilcoxon test with adjusted p value was used.*

### 5.4.5 B7-H3 signature in neoadjuvant pancreatic cancer

Previous investigation demonstrated significant results for the cell checkpoint marker B7-H3 in the naïve Spatial Transcriptomic landscape. This analysis was repeated in the neoadjuvant cohort. Overall survival analysis demonstrated a significant correlation between low expression of B7-H3 and improved prognosis (p=0.050) (figure 5.27.a). A non-significant elevated expression was seen in PanCk segments, differing from what was observed in the naïve cohort (figure 5.27.b).

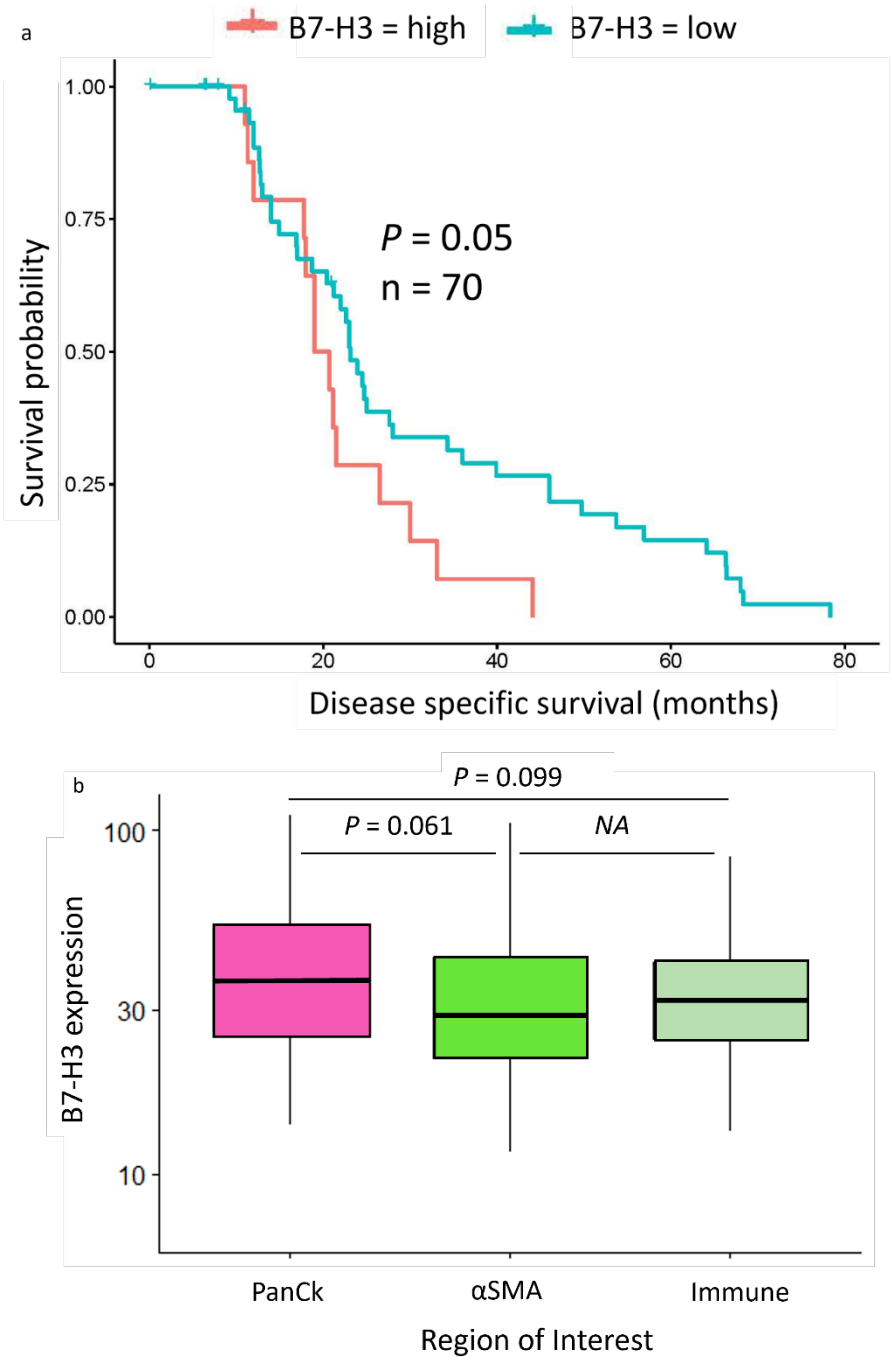


**Figure 5.27.a-b B7-H3 RNA expression in neoadjuvant pancreatic cancer.** *Kaplan-Meier curve stratified B7-H3 expression in disease specific survival (months) in a). whole core. Log-Rank (Mantel-cox) test, replicating cutoff found in chapter 3.11, b). Boxplot showing B7-H3 expression across PanCk, αSMA and immune segments, Kruskal-Wallis test used.*

The Spatial Transcriptomic signature across the segments was explored. Distinct pathways were displayed across αSMA and epithelial compartments (supplementary 8.4.3). Notably, the opposite immune trends were observed in the neoadjuvant cohort compared to the naïve cohort (chapter 5.3.5) within the immune segments. These include, low B7-H3 expressing patients presenting with elevated immune related pathways such as TCR signalling (NES = 1.7, padj = 0.001), BCR signalling (NES = 1.6, padj = 0.003), B cell exhaustion (NES = 2.0, padj = 0.008) and NK activity (NES = 1.7, padj = 0.004) in immune segments (figure 5.28).

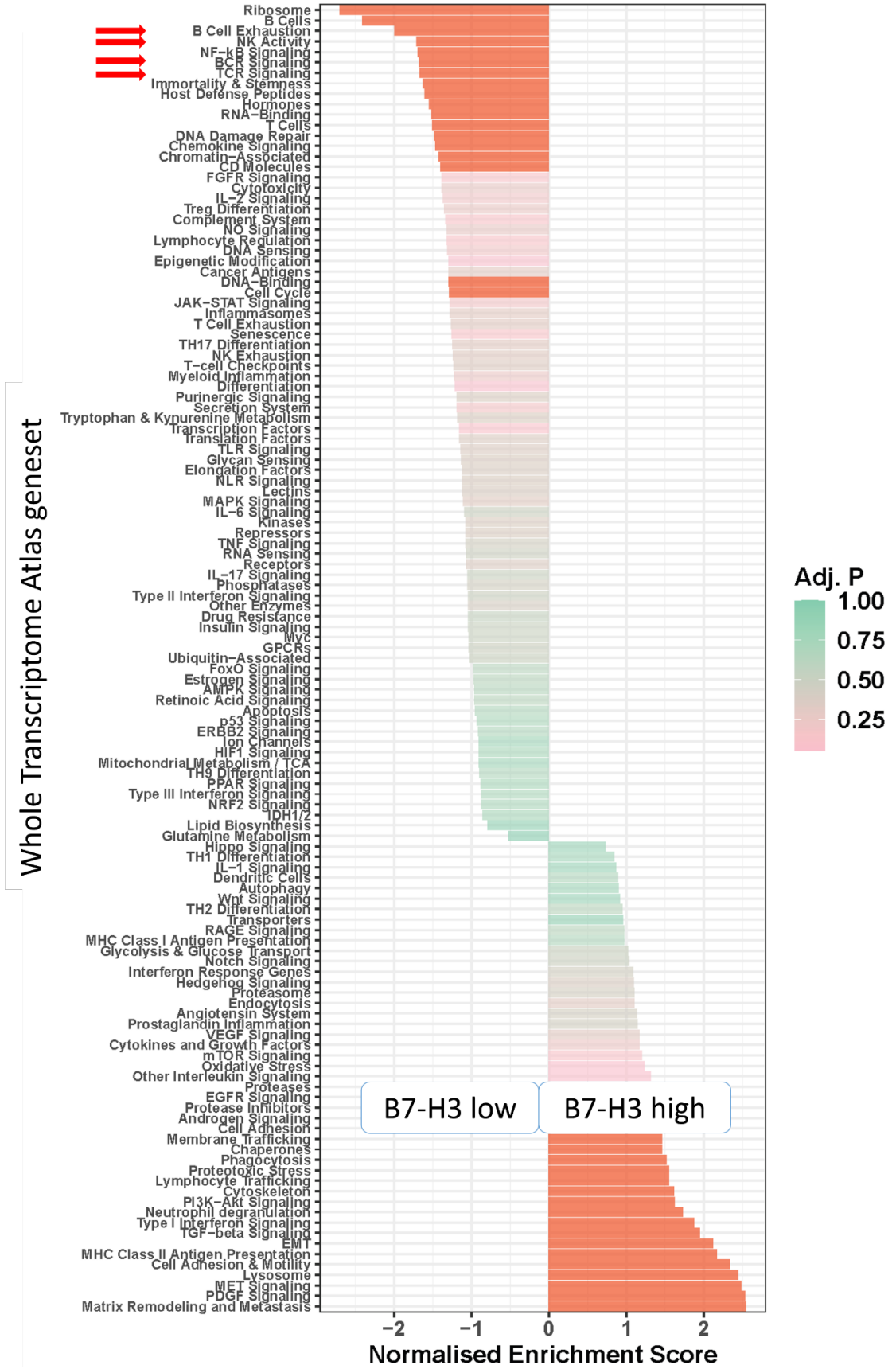


**Figure 5.28 Immune Spatial Transcriptomic alterations between B7-H3 ranked expression**. *Geneset enrichment bar chart in neoadjuvant B7-H3 low and high immune segments. Pathways with normalized enrichment score above and below 1.5, and p adjusted (Adj. P) value ≤ 0.05 were considered significant. Important pathways are indicated by an arrow.*

## 5.5 Spatial Transcriptomic alterations between naïve and neoadjuvant landscapes

To fully classify the effect of neoadjuvant chemotherapy, a direct comparison was made between treatment naïve and neoadjuvant treated patients.

### 5.5.1 Spatial Transcriptomic alterations across matched tissue compartments in naïve vs neoadjuvant PDAC

Matched epithelial comparison between naïve and neoadjuvant AOIs demonstrated distinct aberrated genes. Elevated levels of multiple IGHGs were observed in neoadjuvant epithelium, as well as elevated *COL3A1* (logFC = 1.7, padj <0.001), *ZNF830* (logFC = 2.4, padj <0.001) and *KRT6A* (logFC = 1.5, padj <0.001) (figure 5.29.a). Epithelial compartments displayed large numbers of geneset enrichment pathways from various cell signalling and immune cell pathways. Of note, enriched IL-2 (NES = 1.7, padj = 0.03) and MCH class II (NES = 1.6, padj = 0.016) signalling in neoadjuvant epithelium was observed (figure 5.29.b). The most enriched cell signalling pathways included MET (NES = 2.1, padj <0.001), PDGF (NES = 1.8, padj =0.004 ), MYC (NES = 1.8, padj <0.001) and TGF-β (NES = 1.7, padj <0.001) signalling (figure 5.29.b). In comparison, naïve epithelium was enriched for type I INF signalling (NES = 2.1, padj < 0.001) (figure 5.29.b).

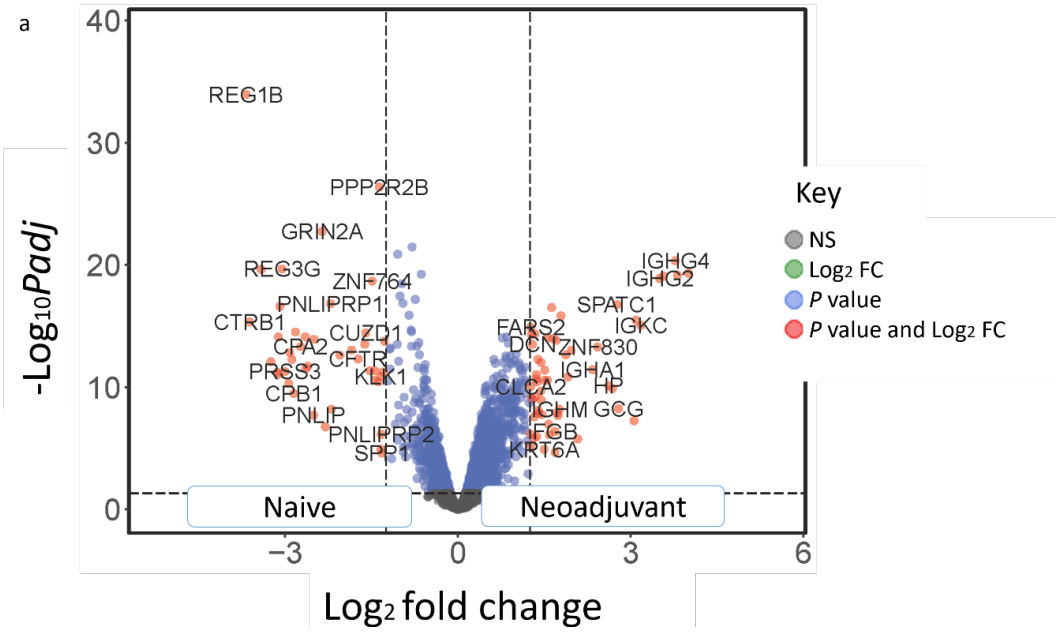


**Figure 5.29.a Spatial Transcriptomic alterations between naïve and neoadjuvant epithelial segments**, *a). Volcano plot demonstrating gene marker differential expression levels in naïve vs neoadjuvant epithelial segments. Genes with log2 fold change above and below 1.5, and p*

*adjusted value ≤0.05 were considered significant, important genes in bold. Dashed line indicates significance thresholds, NS = non-significant, FC = fold change.*

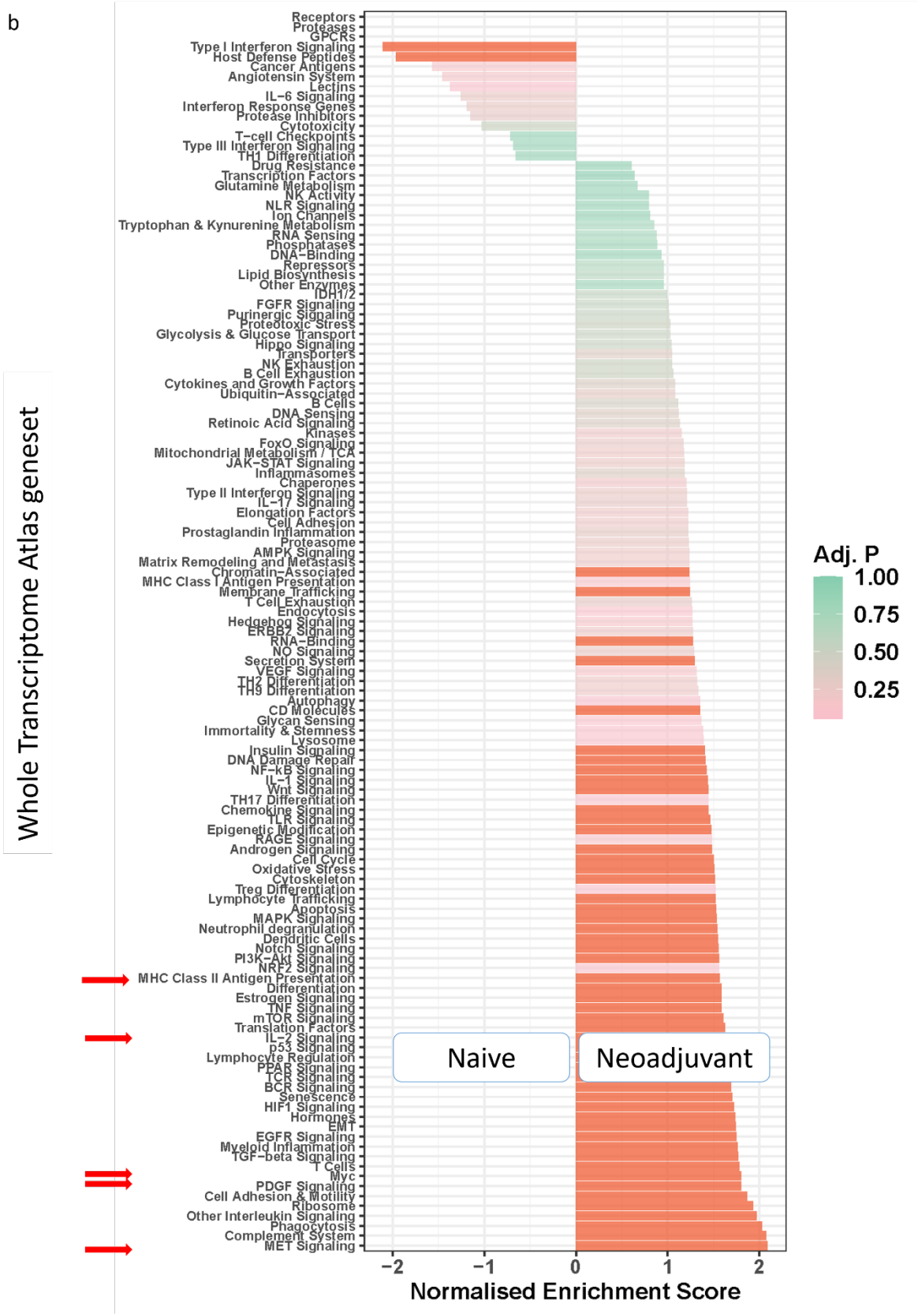


**Figure 5.29.b Spatial transcriptomic alterations between naïve and neoadjuvant epithelial segments**, *b). Geneset enrichment bar chart in naïve vs neoadjuvant epithelial segments. Pathways with normalized enrichment score above and below 1.5, and p adjusted (Adj. P) value ≤ 0.05 were considered significant. Important pathways are indicated by an arrow.*

αSMA regions also demonstrated distinct differential expression between treatment type, with numerous genes shown including downregulated *SPINK1* (logFC = -4.1, padj <0.001) and enriched *CCL19* (logFC = 1.8, padj <0.001) (figure 5.30.a). Multiple immune related pathways were shown in GSEA including augmented TCR (NES = 2.0, padj <0.001), BCR (NES = 2.0, padj <0.001), myeloid inflammation (NES = 1.8, padj <0.001) and Treg differentiation (NES = 1.8, padj = 0.003) and B cell exhaustion (NES = 1.6, padj =0.019) (figure 5.30.b).

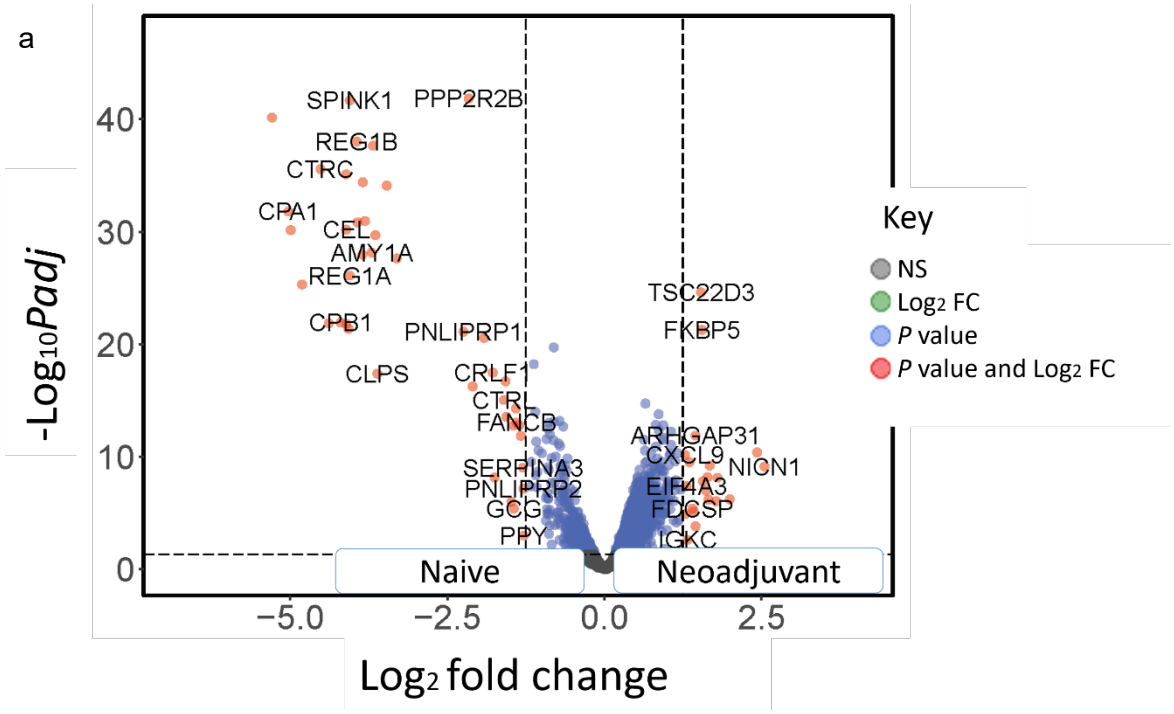


**Figure 5.30.a Spatial Transcriptomic alterations between naïve and neoadjuvant αSMA segments**, *a). Volcano plot demonstrating gene marker differential expression levels in naïve vs neoadjuvant αSMA segments. Genes with log2 fold change above and below 1.5, and p adjusted value ≤0.05 were considered significant, important genes in bold. Dashed line indicates significance thresholds, NS = non-significant, FC = fold change.*

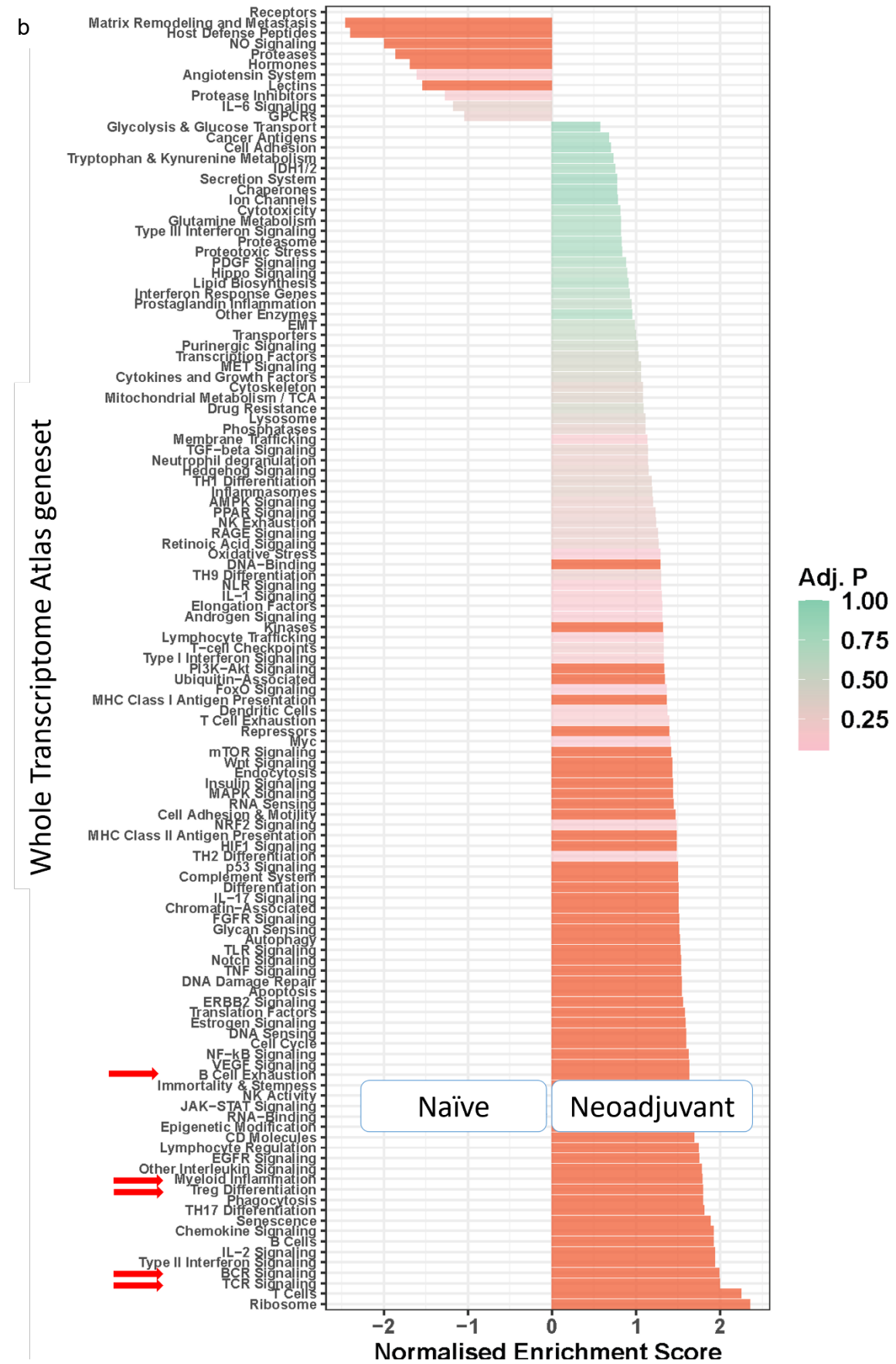


**Figure 5.30.b Spatial Transcriptomic alterations between naïve and neoadjuvant αSMA segments**. *b). Geneset enrichment bar chart in naïve vs neoadjuvant αSMA segments. Pathways with normalized enrichment score above and below 1.5, and p adjusted (Adj. P) value ≤ 0.05 were considered significant. Important pathways are indicated by an arrow.*

Neoadjuvant immune regions demonstrated enriched *IL7-R* (logFC = 1.5, padj <0.001) and reduced *SPINK1* (logFC = 4.6, padj <0.001) (figure 5.31.a). Elevated B cell (NES = 2.2, padj <0.001), B cell exhaustion (NES = 1.7, padj = 0.011), T cell (NES = 1.9, padj <0.001) and myeloid inflammation (NES = 1.6, padj <0.001) (figure 5.31.b). Cell signalling pathways included elevated IL-2 signalling (NES = 1.9, padj <0.001), type II INF signalling (NES = 1.6, padj =0.002) and NF-kB (NES = 1.5, padj =0.003) in neoadjuvant immune compartments (figure 5.31.b).

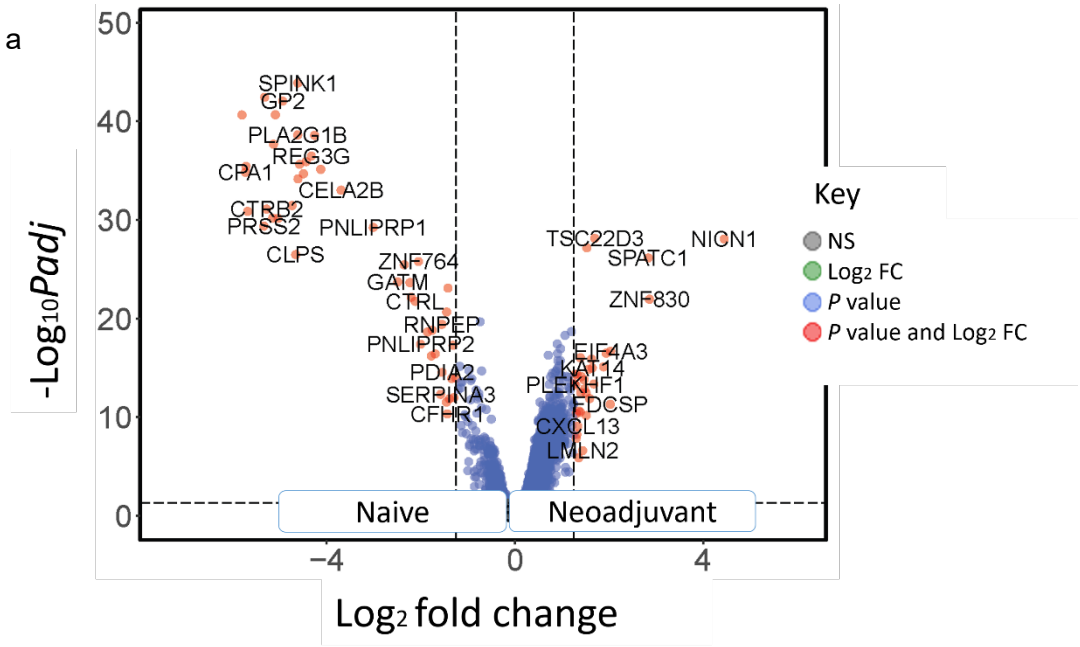


**Figure 5.31.a Spatial Transcriptomic alterations between naïve and neoadjuvant immune segments**, *a). Volcano plot demonstrating gene marker differential expression levels in naïve vs neoadjuvant immune segments. Genes with log2 fold change above and below 1.5, and p adjusted value ≤0.05 were considered significant, important genes in bold. Dashed line indicates significance thresholds, NS = non-significant, FC = fold change.*

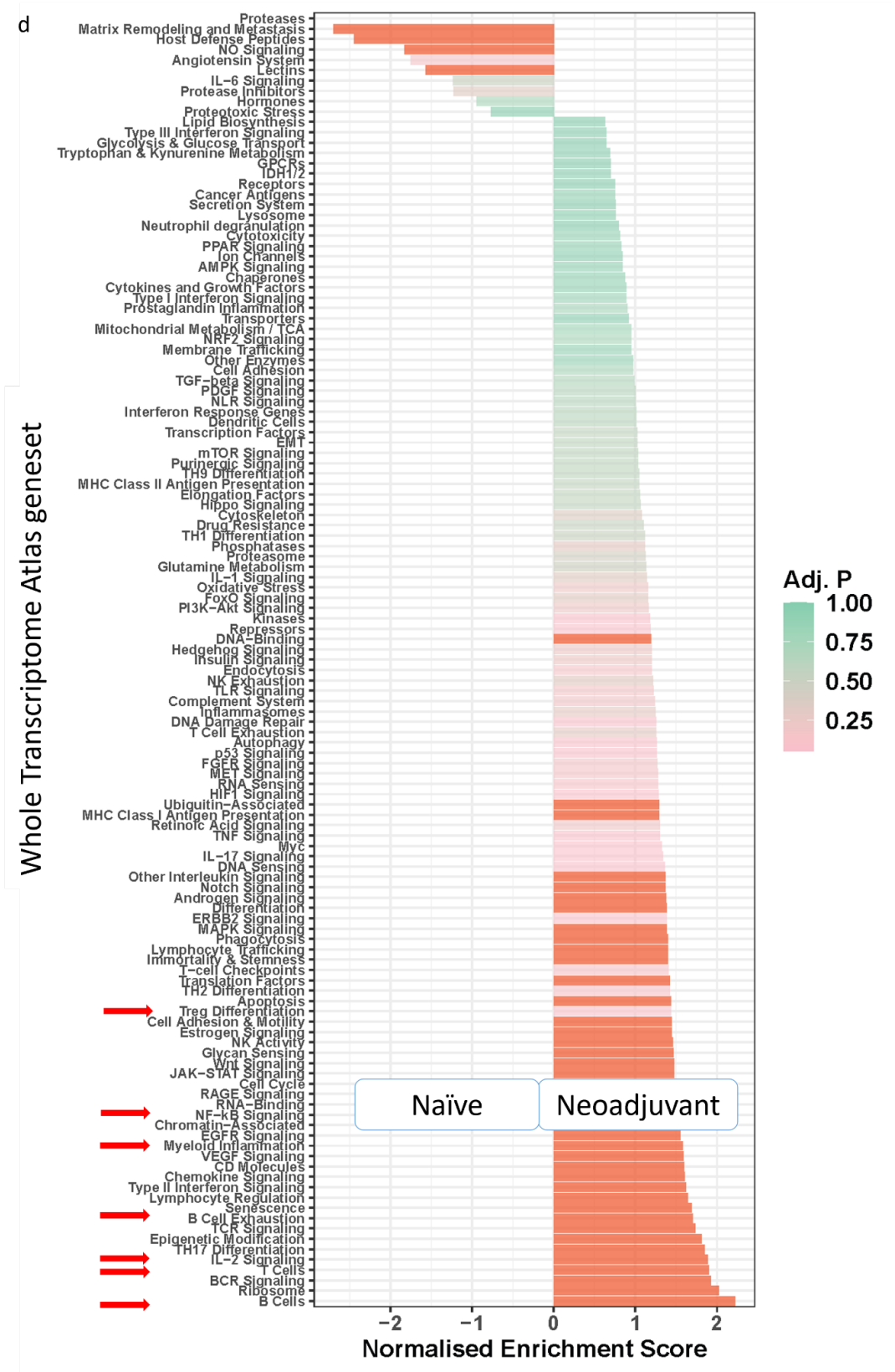


**Figure 5.31.b Spatial Transcriptomic alterations between naïve and neoadjuvant immune segments** *b). Geneset enrichment bar chart in naïve vs neoadjuvant immune segments. Pathways with normalized enrichment score above and below 1.5, and p adjusted (Adj. P) value ≤ 0.05 were considered significant. Important pathways are indicated by an arrow.*

Immune cell deconvolution found overall increased populations of multiple cells in neoadjuvant samples, including effector and suppressor cells. Suppressor cells elevated include macrophages (p=0.01) and Tregs (p=0.001) (figure 5.32). Additionally, enriched signatures for B cell (p<0.001), plasma cells (p<0.001), a range of dendritic cells including memory dendritic cells (p<0.001) were observed (figure 5.32). Elevated T cell signatures, CD4 T cells (p=0.017) and CD8 T cells (p<0.001) were also observed (figure 5.32). Notably, the only cell type elevated in naïve samples was neutrophils (p<0.001) (figure 5.32).

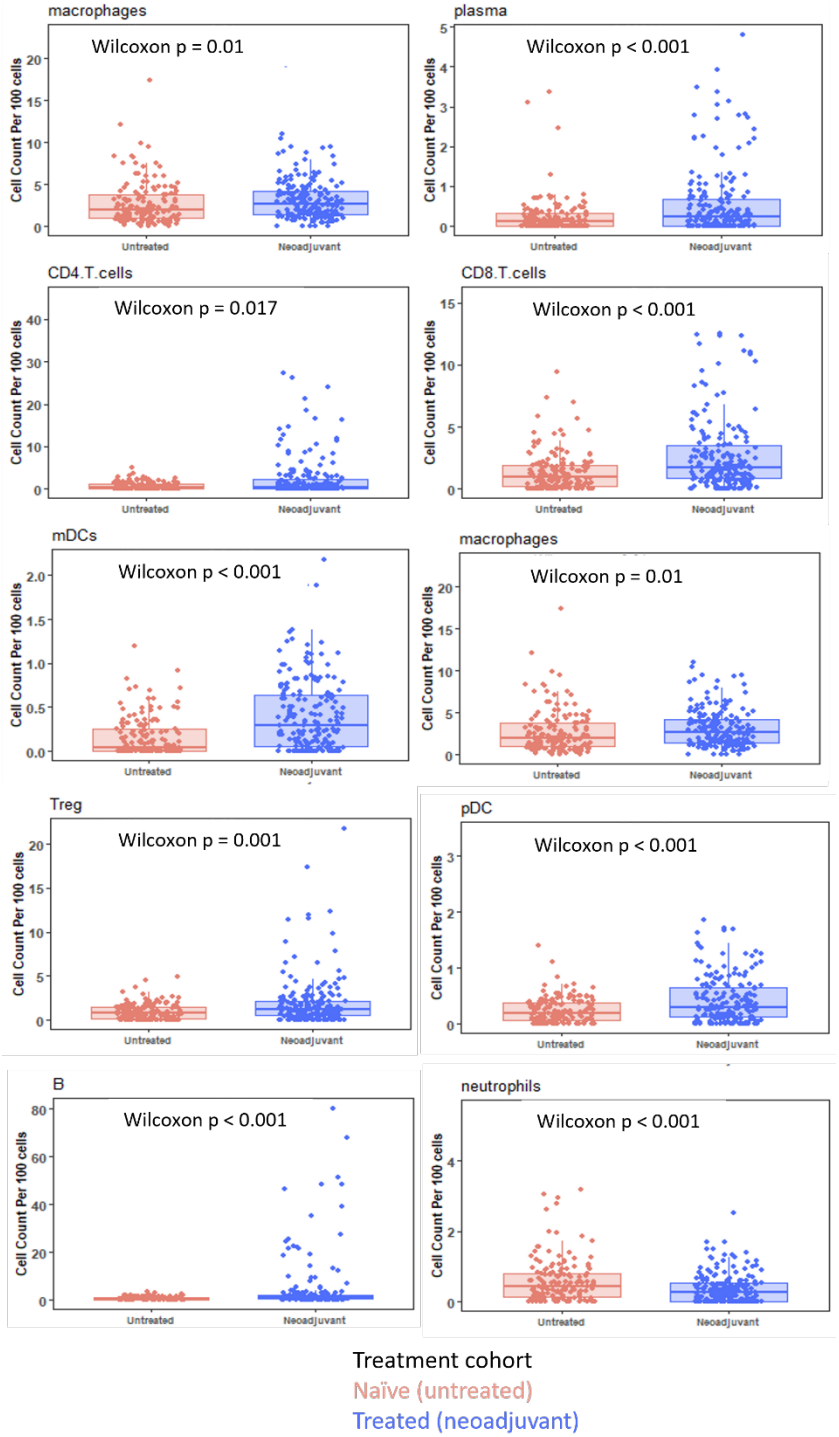


**Figure 5.32 Immune cell deconvolution across naïve and neoadjuvant AOIs.** *Boxplots demonstrate estimated immune cell expression per 100 cells in naïve (untreated) and neoadjuvant segments. Wilcoxon test used.*

## 5.5.2 Spatial Transcriptomic differences across treatment types

### 5.5.2.1 Neoadjuvant treatment type

Immune segments in both chemotherapy and chemoradiotherapy treated cohorts demonstrated upregulated immune related pathways, with chemoradiotherapy segments demonstrating increased variety. Elevated T cell (NES = 1.8, padj <0.001), B cell (NES = 2.1, padj <0.001), B cell exhaustion (NES = 1.7, padj = 0.019), and myeloid inflammation (NES = 1.5, padj = 0.003) were found in chemotherapy treated immune segments (figure 5.33.a). In comparison, chemoradiotherapy treated immune segments demonstrated upregulated B cell (NES = 2.3, padj <0.001), B cell exhaustion (NES = 1.9, padj <0.001), T cell (NES = 1.9, padj <0.001), myeloid inflammation (NES = 2.1, padj <0.001) and Treg differentiation (NES = 2.0, padj <0.001) (figure 5.33.b).

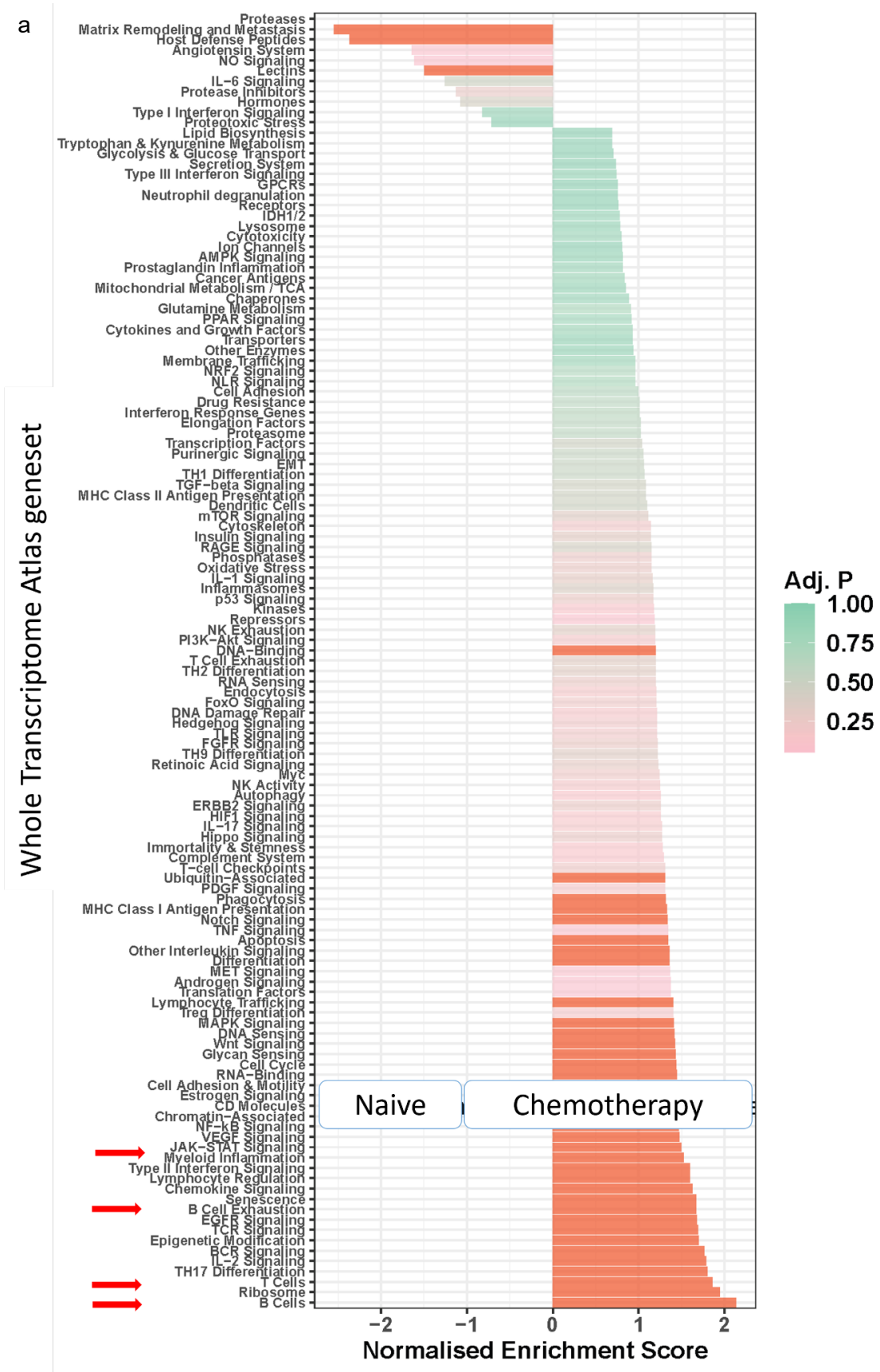


**Figure 5.33.a Immune Spatial Transcriptomic alterations between naïve and neoadjuvant treatment type.** *Geneset enrichment bar chart in immune segments across a). Naïve vs chemotherapy. Pathways with normalized enrichment score above and below 1.5, and p adjusted (Adj. P) value ≤ 0.05 were considered significant. Important pathways are indicated by an arrow.*

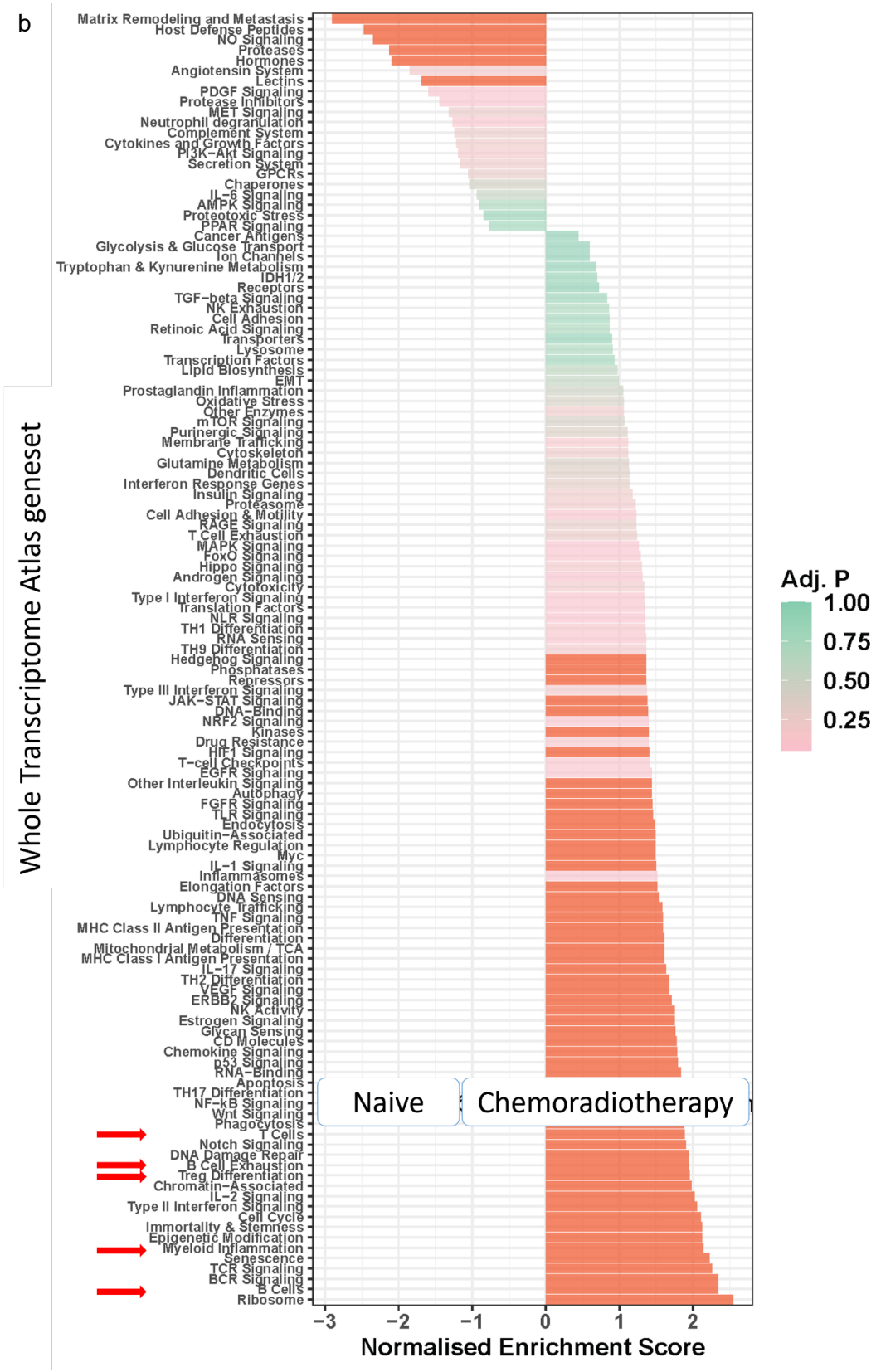


**Figure 5.33.b Immune Spatial Transcriptomic alterations between naïve and neoadjuvant treatment type.** *Geneset enrichment bar chart in immune segments across b). Naive vs chemoradiotherapy. Pathways with normalized enrichment score above and below 1.5, and p adjusted value ≤ 0.05 were considered significant. Important pathways are indicated by an arrow.*

#### 5.5.2.2 Types of neoadjuvant chemotherapy

Neoadjuvant treatment types were compared to naïve cohorts, demonstrating immune differences. In immune rich segments, elevated levels of T cells (NES = 1.8, padj <0.001), B cells (NES = 2.0, padj <0.001), and myeloid inflammation (NES = 1.6, padj = 0.001) were observed in FFX treated patients (figure 5.34.a). In comparison, Gemcitabine treated patients displayed a wide variety of immune related pathways. Elevated levels of B cells (NES = 2.3, padj <0.001), coupled with B cell exhaustion (NES = 1.9, padj <0.001), T cells (NES = 2.1, padj <0.001), coupled with T cell exhaustion (NES = 1.7, padj = 0.014), myeloid inflammation (NES = 1.9, padj <0.001), Treg (NES = 1.7, padj = 0.009) and NK activity (NES = 1.7, padj <0.001) were found in Gemcitabine compared to naïve immune segments (figure 5.34.b).

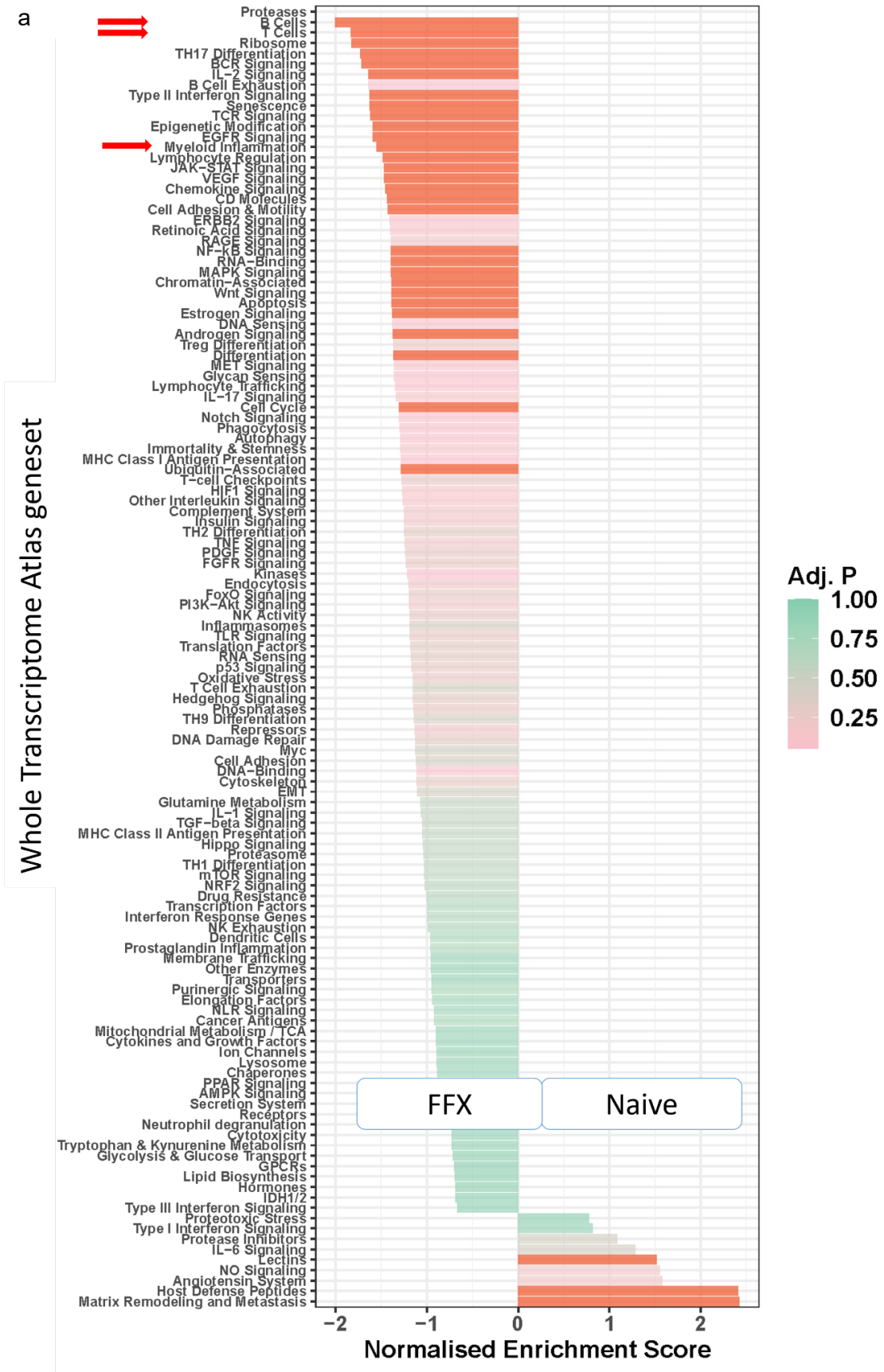


**Figure 5.34.a Immune Spatial Transcriptomic alterations between naïve and chemotherapy treatment type.** *Geneset enrichment bar chart in immune segments across a). FOLFIRINOX (FFX) vs naive. Pathways with normalized enrichment score above and below 1.5, and p adjusted (Adj. P) value ≤ 0.05 were considered significant. Important pathways are indicated by an arrow.*

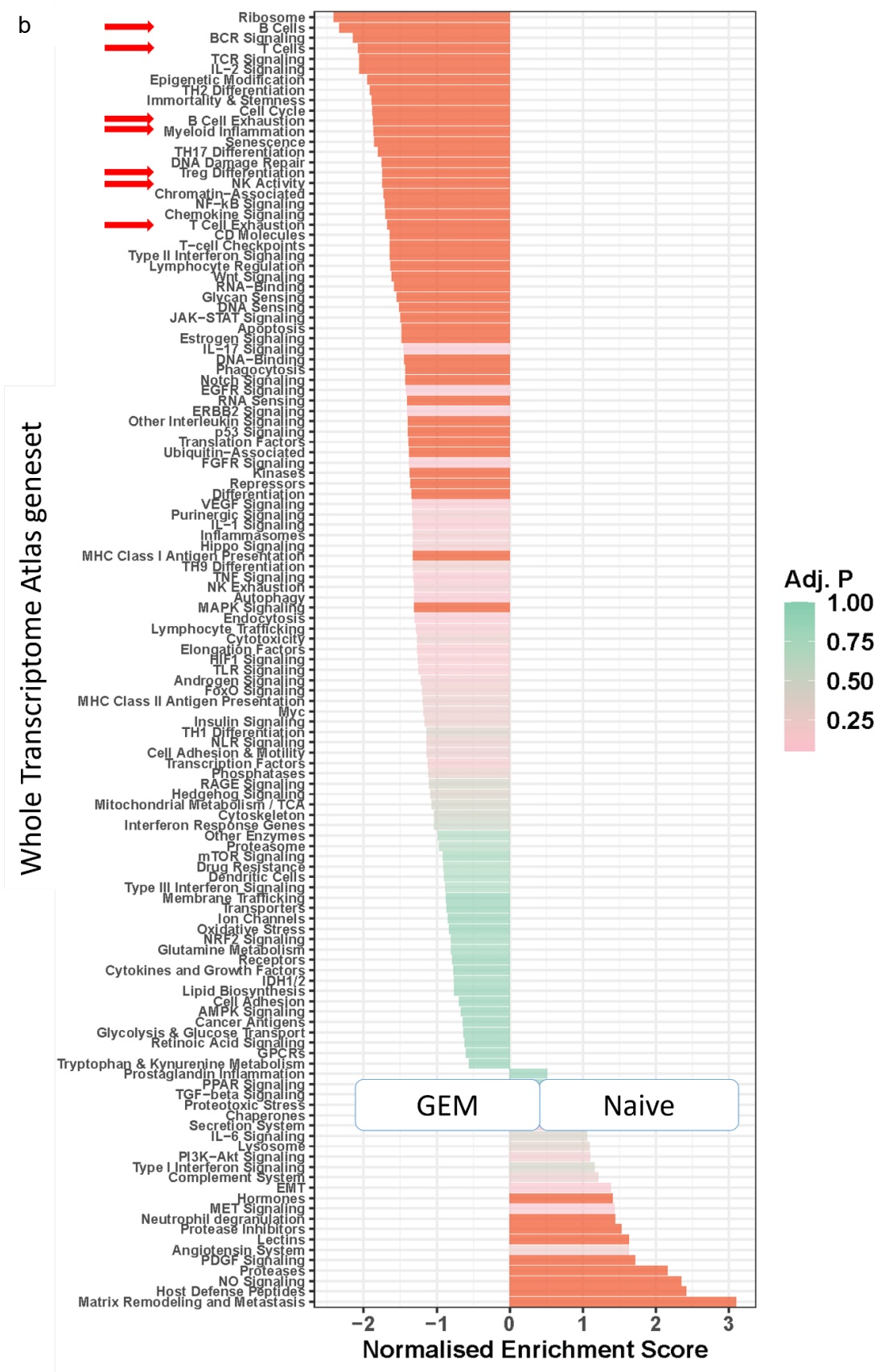


**Figure 5.34.b Immune Spatial Transcriptomic alterations between naïve and chemotherapy treatment type.** *Geneset enrichment bar chart in immune segments across b). Gemcitabine (GEM) vs naive. Pathways with normalized enrichment score above and below 1.5, and p adjusted (Adj. P) value ≤ 0.05 were considered significant. Important pathways are indicated by an arrow.*

### 5.5.3 Long term survival naïve vs neoadjuvant PDAC

As previously reported, long term survival for these cohorts was classed as above 36 months. When investigating differential expression between treatment status in long term survivors, large numbers of aberrated gene expression was seen in all three compartments. Of note, neoadjuvant patients demonstrated enriched *SPARCL1* (logFC = 1.5, padj <0.001) in epithelium, reduced *SPINK1* (logFC = 3.6, padj <0.001) in αSMA, and elevated *TSC22D3* (logFC = 1.9, padj = 0.004) in immune compartments (supplementary figure 8.4.4.a-c). Immune segments displayed augmented B cell exhaustion (NES = 2.0, padj <0.001), B cell (NES = 2.0, padj <0.001), T cell exhaustion (NES = 1.6, padj = 0.014), T cell (NES = 2.0, padj <0.001) and myeloid inflammation (NES = 1.6, padj <0.001) (figure 5.35.a). Finally, spatial immune cell deconvolution was performed on naïve and neoadjuvant patients grouped into long term survivors (over 36 months), and short-term survivors (under 36 months). Estimates showed elevated B cells(p=0.004), plasma cells (p=0.034), CD4 T cells (p=0.032) and cytotoxic T cells (p<0.001) in neoadjuvant long-term survivors (figure 5.35.b).

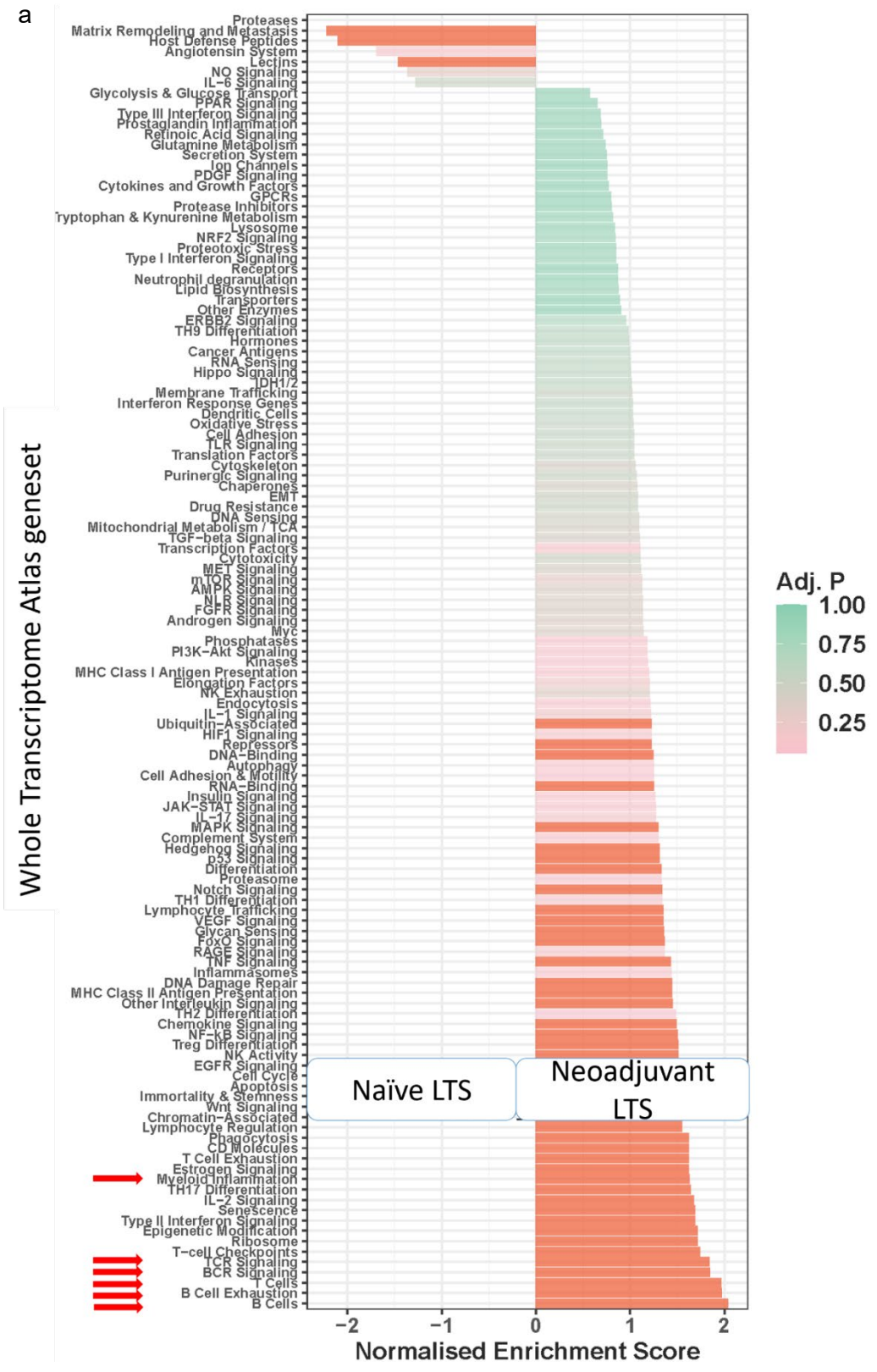


**Figure 5.35.a Immune Spatial Transcriptomic alterations between long term survival naïve and neoadjuvant** *a). Geneset enrichment bar chart in immune segments across naïve vs neoadjuvant long term survival (LTS), pathways with normalized enrichment score above and below 1.5, and p adjusted (Adj. P) value ≤ 0.05 were considered significant. Important pathways are indicated by an arrow.*

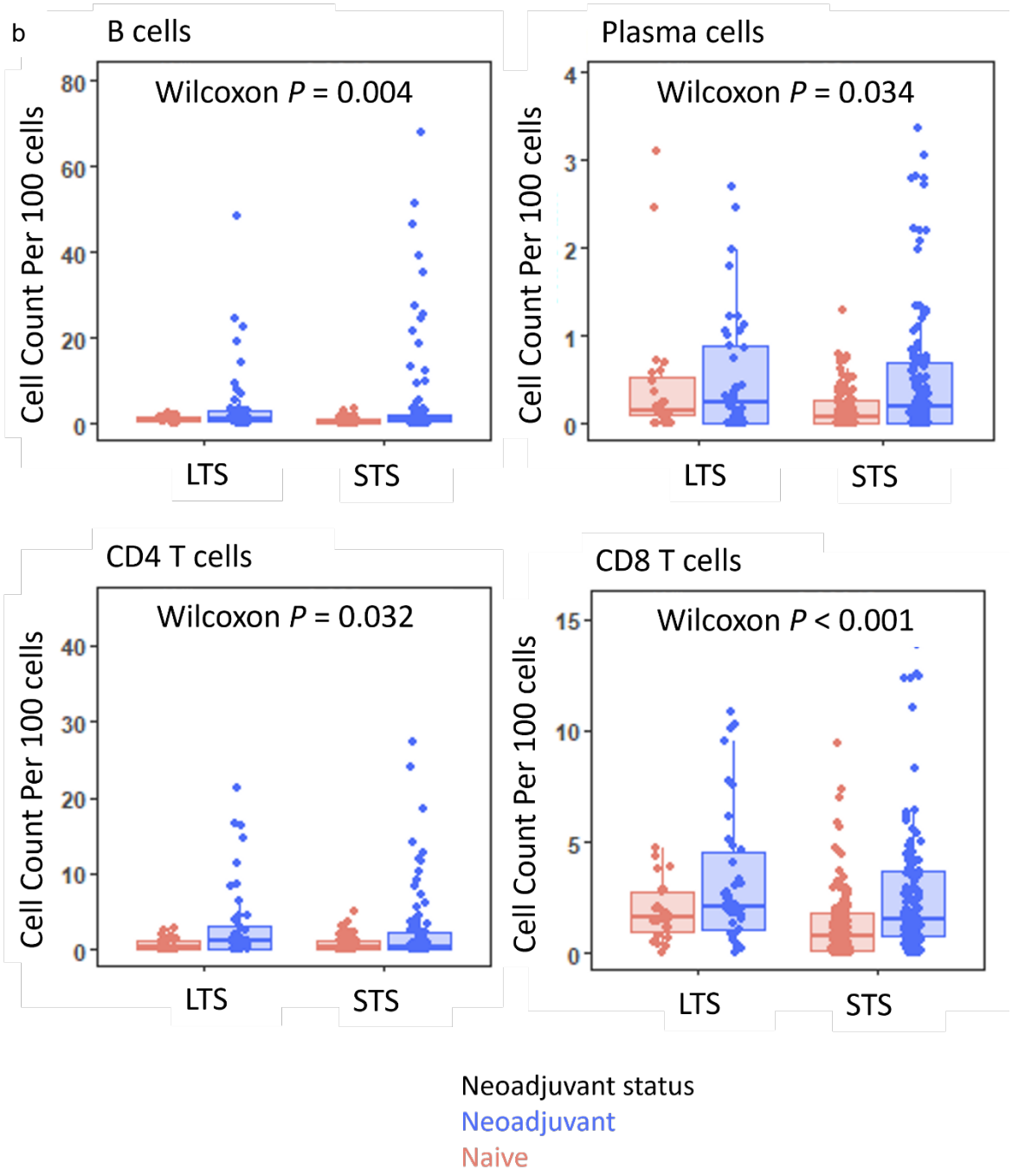


**Figure 5.35.b Immune Spatial Transcriptomic alterations between long term survival naïve and neoadjuvant** *b). Boxplots demonstrate estimated immune cell expression per 100 cells in; B cells, plasma cells, CD4 T cells and CD8 T cells across naïve vs neoadjuvant long term survival (LTS) and short term survival (STS). Wilcoxon test with adjusted p value was used.*

## 5.6 Whole section validation

In order to validate the effect of neoadjuvant therapy on the spatial transcriptome, analysis using whole sections was repeated on selected PRIMUS002 cases (table 5.1). This was done using biopsy and neoadjuvant whole sections with two matched cases. Non-epithelial regions were analysed to elucidate the treatment effect on the tumour microenvironment. Treatment naïve biopsies were compared to directly measure the effect of neoadjuvant chemotherapy. Multiple overlapping genes were observed when compared to single core TMA work, and completely new genes appeared. αSMA matched comparisons had overlap of 12/32 genes including *CXCL14*, *SYCN* and *CPA1/2* (supplementary table 8.3*)*. Matched biopsy vs treated comparison of immune regions demonstrated 8/41 overlapping DEA genes with naïve vs neoadjuvant comparison including downregulated *PLAG2G1B*, *CELA* related genes and *SYCN* among others (supplementary table 8.3*)*. Spatial immune cell deconvolution demonstrated a shift from high CD4 T cell, CD8 T cell and macrophage landscape in the biopsy samples, to a high B cell, CD4 T cell, CD8 T cell and Treg population dominating (figure 5.35).

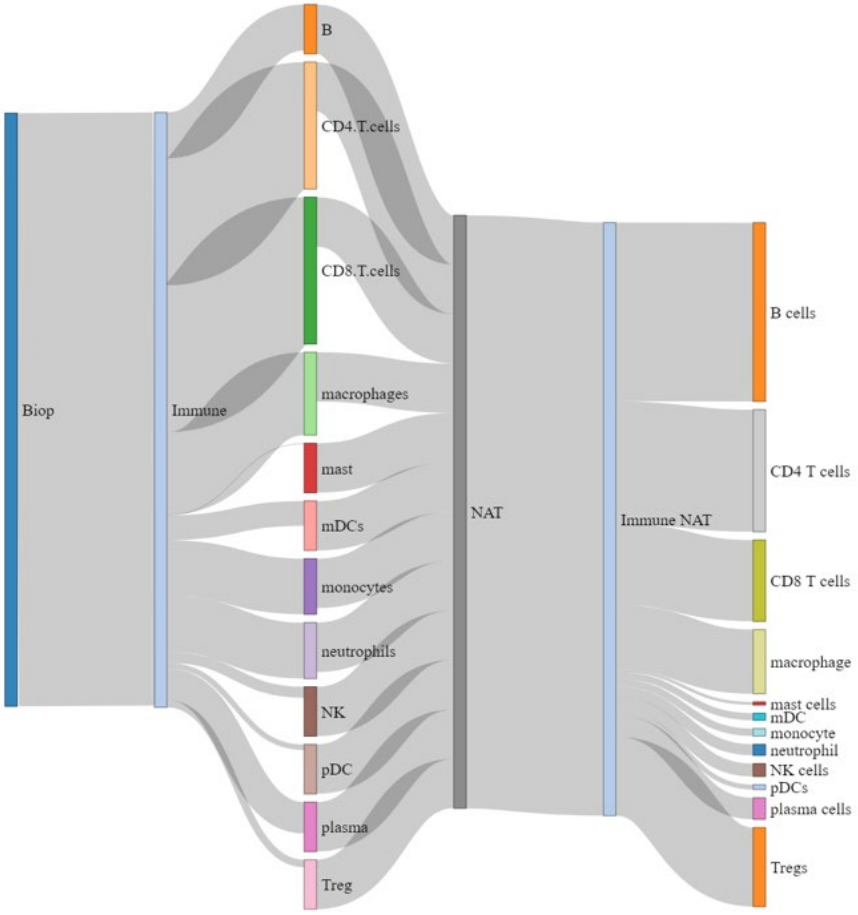


**Figure 5.36 Altering estimated immune cell landscape from biopsy to neoadjuvant treatment.** *Sankey plot shows the percentage estimated cell population from biopsy immune segments, flowing into the cell population of neoadjuvant treated (NAT) immune segments. Cell populations generated from Nanostring immune cell deconvolution algorithm.*

## 5.7 Discussion

The primary aim of this chapter was to establish the transcriptome within different compartments in base naïve and base neoadjuvant PDAC, and subsequently compare these two treatment groups. Highly specific representative regions (PanCk+ epithelium, αSMA+ fibroblasts and CD45+ immune regions) were obtained via the Spatial Transcriptomics GeoMx® WTA assay. To confirm if the use of bulk transcriptomics would be unsuitable, inter-tumoral heterogeneity in epithelial, stromal and immune rich compartments was determined. Results from both naive and neoadjuvant base analysis demonstrated vast gene signature differences when comparing the three tissue compartments, with distinct pathways aberrated. Although pancreatic cancer ST studies remain relatively limited, this compartment heterogeneity was also demonstrated by Ren et al using alternative techniques [279]. Notably, the αSMA+ and CD45+ regions were considerably distinct in the transcriptome within naïve and neoadjuvant cohorts. This is most likely due to the prevalent CAF population which has been shown to influence PDAC progression depending on the signature expressed [280].

Molecular subtyping of neoadjuvant naïve pancreatic cancer has led to multiple prognostic signatures being developed, providing considerable insight into PDAC mechanisms [100-102]. Using the naïve epithelium signature, intra-compartment heterogeneity was examined, successfully identifying two distinct refined epithelial clusters. Cluster 2 demonstrated non-significant association with poor prognosis. Augmented *HSPA6* and *CST1* gene expression, and decreased B cell estimates were seen in epithelial Cluster 2. Both genes have demonstrated potential roles as predictive biomarkers within the literature [281, 282]. *HSPA6* upregulation has previously been associated with intra-tumoral epithelial heterogeneity in pancreatic cancer. Using single cell transcriptomics, Xu et al found 5 distinct ductal cells, with *HSPA6* associated with type 4 [281]. Furthermore, *CST1* is a tumour specific biomarker used for early diagnosis in colorectal cancer, and correlates with proliferative and malignancy associated proteins [282]. Almost no overlap was observed between the main molecular subtypes and the ST epithelial cluster genes. Therefore, these clusters represent novel epithelial specific signatures, which should be fully explored in a larger cohort. When epithelial clusters were combined with either the αSMA cluster or immune clusters, a powerful prognostic trend was observed, indicative of the influence between these compartments. Epi-αSMA cluster 1 significantly associated with poor survival, and demonstrated elevated known invasive marker *KIF4A* and decreased B cell estimates [283]. Further work is required to fully classify these clusters and explore the relationship between the combined clusters.

Spatial Transcriptomic analysis of neoadjuvant chemotherapy type highlighted a disparate

landscape between FOLFIRINOX treated and Gemcitabine treated samples. Epithelial Gemcitabine segments demonstrated enriched *CA9* expression, and stromal segments demonstrated a wide range of immune cell related pathways. *CA9* have been linked to reports of targeted treatments. *CA9* combined inhibition results in reduced hypoxia, improved survival, and elevated levels correlated with tumour cell inhibition of cytotoxic T cells [284, 285]. The highly immunogenic landscape presented by the Gemcitabine samples mirrors reports seen in the literature [132, 213, 255, 257]. Comparatively, FFX samples retain the immune-desert phenotype traditionally associated with pancreatic cancer. The only immune cell pathway associated with FFX when compared to Gemcitabine was elevated neutrophil degranulation, found in αSMA regions. The role of these cells remains relatively controversial, although it is thought they play an immunosuppressive role on T cells [286]. This pattern was mirrored when both FFX and Gemcitabine treated segments were compared to naïve segments. A varied immune pathway signature was revealed in Gemcitabine treated segments, although this was also coupled with immune exhausted pathways.

Within the neoadjuvant cohort, chemoradiotherapy patients correlate with much longer survival. Multiple immune specific trends were associated in chemoradiotherapy patients when compared to chemotherapy treated patients. Specifically, elevated B cell pathways, B cell exhaustion and dendritic cells were observed. Dendritic populations within PDAC have a reportedly beneficial role in chemoradiotherapy response [287]. Protein validation is required to confirm the presence of these cells within the neoadjuvant PDAC microenvironment.

Considerable alterations were seen within matched compartment naïve vs neoadjuvant comparisons. Neoadjuvant cohort demonstrated multiple interesting and potentially targetable genes; upregulation of *COL3A1* in epithelium and a range of immune related pathways in immune segments including B cell, T cell and IL-2 signalling. Expression of *COL3A1* confirms these enriched immune pathway levels, with reports correlating elevated *COL3A1* with tumour infiltrating T cells, B cells and dendritic cells [288]. Furthermore, immune cell deconvolution of all neoadjuvant segments estimated elevated B cell and T cell populations. αSMA compartments showed enriched *CCL19*, which has been linked to improved memory CAR-T cell infiltration into the PDAC tumour core [289]. Notably, these immune associated pathways although considerably elevated in immune segments of neoadjuvant samples,  were often coupled with exhaustion pathways. Counterintuitively, elevated myeloid inflammation pathways and estimated macrophage population in αSMA neoadjuvant samples were observed when compared to naïve samples. CAF specific small nuclear RNA combined with Spatial Transcriptomic studies on neoadjuvant pancreatic cancer have shown 3 CAF expression profiles are significantly

upregulated in neoadjuvant cancers, and specific profiles associated with regression patterns [290]. These observations reinforce the need to consider immune cell subtypes, and activation status rather than solely relying on density analysis.

Prognosis in pancreatic cancer remains abysmal for the majority of patients. However, a small subset of patients survive for longer than expected. Naïve and neoadjuvant LTS patients associated with different pathways, indicative of different underlying biology resulting in better prognosis. Naïve patients associated with increased *LYZ*, a gene associated with the Classical subtype [291]. Neoadjuvant patients linked with enriched epithelial *SPARCL1* expression, reported for its anti-invasive properties in pancreatic cancer and reduced expression in metastasis [292]. Both treatment types had increased B cell and T cell expression. These immune cell deconvoluted populations are consistently associated with better performing groups and were by far the most statistically relevant.

Previous work has identified B7-H3 as a potential biomarker using a regional Spatial Protein assay in naïve pancreatic cancer (chapter 3.11). The same prognostic pattern was observed using Spatial Transcriptomics in naïve and neoadjuvant cohorts. Naïve PDAC demonstrated elevated expression in non-epithelial compartments, as shown in chapter 3.11. Reduced expression of B7-H3 associated with reduced T cell related pathways, dendritic cells, and an elevated angiotensin system within immune segments. This is of particular interest as studies have shown treatment with angiotensin system inhibitors and angiotensin blockade therapies in naive patients considerably improves prognosis [293-295]. Treatment appeared to trigger an immunogenic switch, resulting in elevated T cell activity pathways [295]. Furthermore B7-H3 itself has generated lots of interest as a potential immune checkpoint target, with clinical trials in a multitude of cancers ongoing [142-146]. Curiously, the opposite trends were observed in neoadjuvant associated with low expressing B7-H3 (high survivor) patients. Elevated levels of TCR and BCR signalling were seen, although this was offset by elevated B cell exhaustion pathways. Neoadjuvant patient comparison groups have repeatedly presented with exhausted pathways, a phenomenon that has been reported in the protein landscape [261].

Overall, Spatial Transcriptomics has uncovered intra-compartment heterogeneity within the naïve environment, revealing transcriptomic alterations in naïve and neoadjuvant settings. Distinct immune populations have consistently correlated with clinical groups with better outcomes. Combined with protein data this will determine whether transcriptomics signals translate into the protein landscape.

# 6 Chapter 6: Multi-omic, orthogonal characterisation of Pancreatic cancer

## 6.1 Introduction

High-plex single cell protein and Spatial Transcriptomic assays provide great insight into the tumour microenvironment. High plex phenotyping using immunofluorescence assays, although limited by its purely descriptive data, allows for robust immune cell characterisation at a single cell level whilst maintaining tissue integrity. Regional Spatial Transcriptomics provides indirect biological insight into differentially expressed genes, cell signalling pathways and estimation of immune cell populations. However, studies have shown a fluctuating range of protein translation rates from RNA, coupled with translational heterogeneity greatly effects the amount of protein actually expressed [296-299]. Orthogonal integration of multiplex protein and Spatial Transcriptomics data will provide complementary and data validation. While prognostic association with T cell and macrophage density within adjuvant treated pancreatic cancer is well documented, and similar trends were observed within the naïve cohort, comprehensive understanding of the fundamental underlying biological mechanisms remains elusive [8, 182, 237, 238]. At the time of writing, limited literature has been published combining high-plex protein data with Spatial Transcriptomic data in cancer [300, 301]. A more common approach utilises varying types of protein data with bulk or single cell transcriptomic analysis [302-305]. These integrative papers tend to focus on cell typing, neighbourhood discovery, cell-to-cell interactions, as well as establishing disease specific pathways. Exploration of transcriptomic alterations induced by neoadjuvant therapies in pancreatic cancer up until recently, was notably scarce, emphasizing a critical area of unmet research need [306, 307]. Although rare, orthogonal analysis methods focused on protein and transcriptomic analyses have enhanced knowledge of underlying immune mechanisms within the neoadjuvant setting, as well as identifying potential targeted therapy options [308].

The discovery nature of Spatial Transcriptomics experiments produces an enormous range of potentially interesting biomarkers and genesets. Validation using a single cell, deep phenotyping assay is required to confirm results observed. Notably, Spatial Transcriptomic T cell, B cell and dendritic cell signatures associated with important pancreatic groups in the naïve and neoadjuvant cohorts. These immune populations have been reported within the pancreatic literature, with links made to prognosis and neoadjuvant therapy response [11, 197, 253, 268, 287, 309]. Furthermore, B7-H3 expression retained its prognostic significance within the transcriptomic setting in naïve, as well as replicating the trend in the neoadjuvant cohort. Growing interest in using this immune checkpoint molecule as targeted therapy makes it important to characterise within pancreatic cancer. Phenotypic expression and cellular interactions of B7-H3 expressing cells are not fully understood, though reports indicate elevated expression is linked to immune evasion, metastasis and poor prognosis in pancreatic cancer amongst others [19,

310, 311] .To validate biomarkers generated from mIF led Spatial Transcriptomic results, two imaging based, oligonucleotide antibody assays were trialled (Akoyas PhenoCycler™ and Nanostrings CosMx™) with ultra-high plex immune panels [119, 312].

### 6.1.1 Aims

Integrate multiplex significant patterns with Spatial Transcriptomic data to explore the biological mechanisms underlying characterised phenotypes in treatment naïve and neoadjuvant pancreatic cancer. Confirmation of immune cell deconvolution patterns observed in Spatial Transcriptomic assays using super high-plex protein technologies. Validate single cell protein B7-H3 expression in the naïve and neoadjuvant pancreatic setting.

### 6.1.2 Clinical cohorts

Naive cohort (Glasgow naïve cohort 2) consisted of a total of 62 pancreatic cancer specimens within a TMA (table 6.1). These were a subset of the naïve cohort described in chapter 3 and the full naïve cohort utilised in chapter 5. Median survival for these patients was 19.2 months. Due to assay imaging gasket limitations, this naïve cohort was further reduced to 38 patients for chapter 6.4 onwards (table 6.1). Neoadjuvant cohort (neoadjuvant combined cohort) consisted of 71 pancreatic cancers split across 3 multi-regional TMAs (table 6.1). This cohort is the same neoadjuvant cohort as described in chapter 4 (n=58), with an additional clinical trial cohort (PRIMUS-MAL, n=13). Due to assay imaging gasket limitations, this neoadjuvant cohort was further reduced to 58 patients in total for chapter 6.4 onwards (table 6.1). Median survival for these patients was 20.4 months. Clinical data associated with these cohorts is found in chapter 2.1.

| Study | Cohort name | TMA | TMA number | Patient number | Treatment type |
|---|---|---|---|---|---|
| GeoMx | Glasgow naïve cohort 2 | PDAC-PAN-TMA | 1 | 62 | Naïve |
| | Neoadjuvant combined | Neoadj-MAL-TMA batch1 | 1 | | Neoadjuvant |
| | | Neoadj-MAL-TMA batch2 | 1 | 58 | |
| | | PRIMUS-MAL | 1 | 13 | |
| CosMx | Glasgow naïve cohort 2 | PDAC-PAN-TMA | 1 | 38 | Naïve |
| | Neoadjuvant combined | Neoadj-MAL-TMA batch1 | 1 | | Neoadjuvant |
| | | Neoadj-MAL-TMA batch2 | 1 | 45 | |
| | | PRIMUS-MAL | 1 | 13 | |

**Table 6.1 Naïve and neoadjuvant clinical cohorts and associated study.** *Summary table showing the study and associated TMAs used, patient number and treatment type. The cohort name column refers to the cohort name in chapter 2.1.*

# 6.2 Deep phenotypic comparisons in the Spatial Transcriptomic landscape of pancreatic cancer

## 6.2.1 Spatial Transcriptomic landscape of density phenotypes in naïve and neoadjuvant pancreatic cancer

Using a previously established deep phenotyping, naïve and neoadjuvant patients were categorized using the most important protein density variables (chapter 3.6 and chapter 4.5). Within the naïve cohort, this encompassed CD3 and CD68 density, and CD3CD8 density in the neoadjuvant cohort. Comparisons in matched regional Spatial Transcriptomics between phenotypic ranks was carried out to determine biological differences between them. CD3high density previously associated with increased survival in the naïve cohort (chapter 3.6). Relatively limited aberrated differences were observed in all three matched segments. Notably, CD3high patients presented with upregulated epithelial *SLC12A2* (logFC = 1.5, padj = 0.006) and *CXCL5* (logFC = 2.4, padj = 0.050), and downregulated *PRSS2* (logFC = -5.4, padj = 0.040) and *SPINK1* (logFC = -4.1, padj = 0.040) in αSMA regions (figure 6.1.a-b). Additionally, immune CD3high segments demonstrated elevated *CCN2* (logFC = 1.6, padj <0.001) and *PKN3* (logFC = 1.6, padj <0.001) (figure 6.1.c).

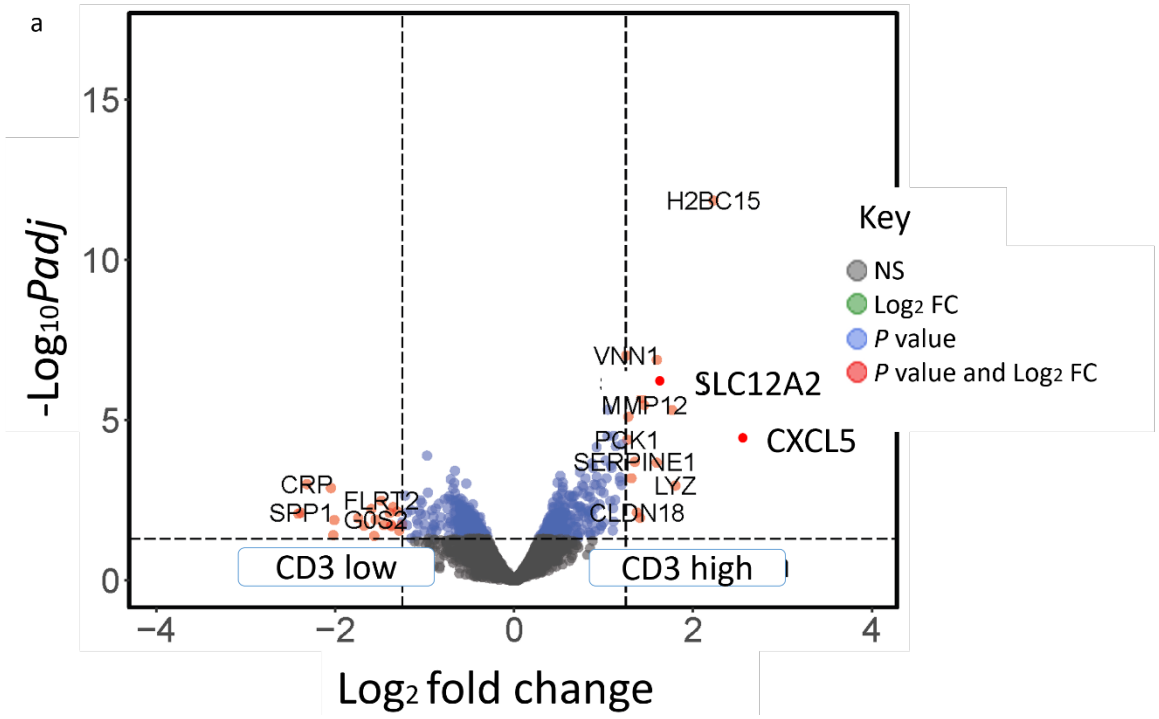


**Figure 6.1.a Volcano plot demonstrating gene marker differential expression levels in naive PDAC based on comparison of CD3low versus CD3high** *in* a). *Epithelial segments. Genes with log2 fold change above and below 1.5, and p adjusted value ≤0.05 were considered significant. Important genes in bold. Dashed line indicates significance thresholds, NS = non-significant, FC = fold change.*

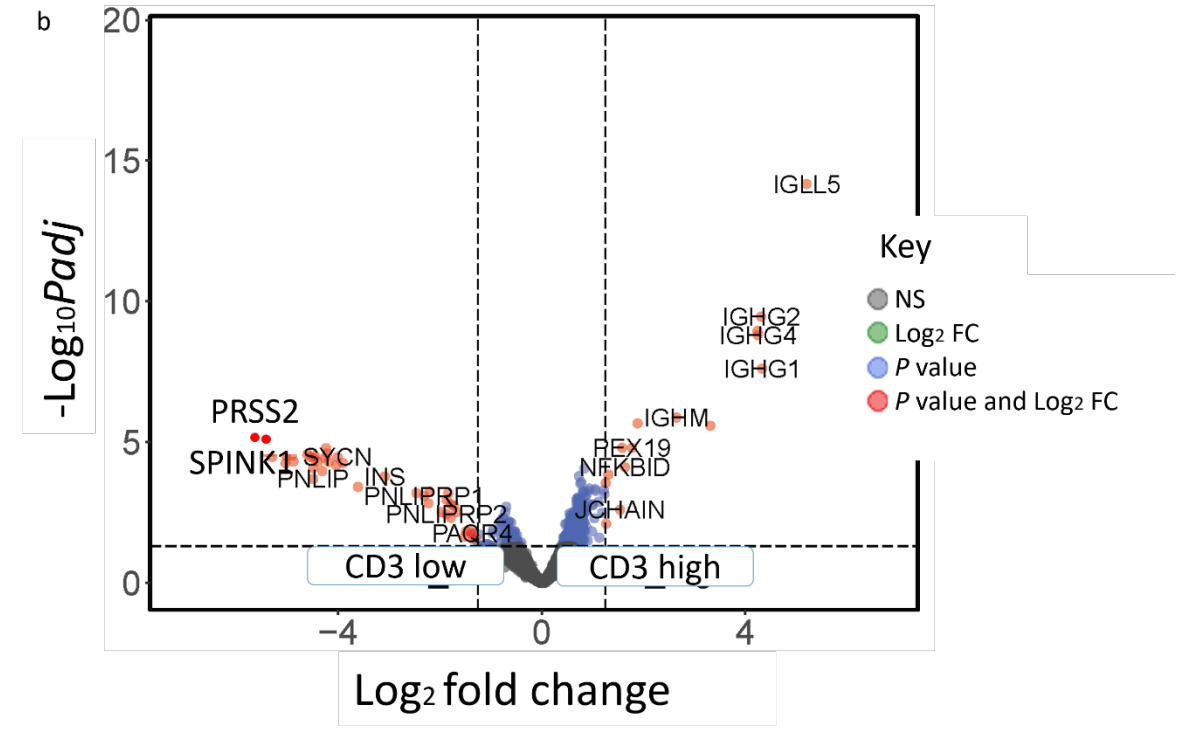


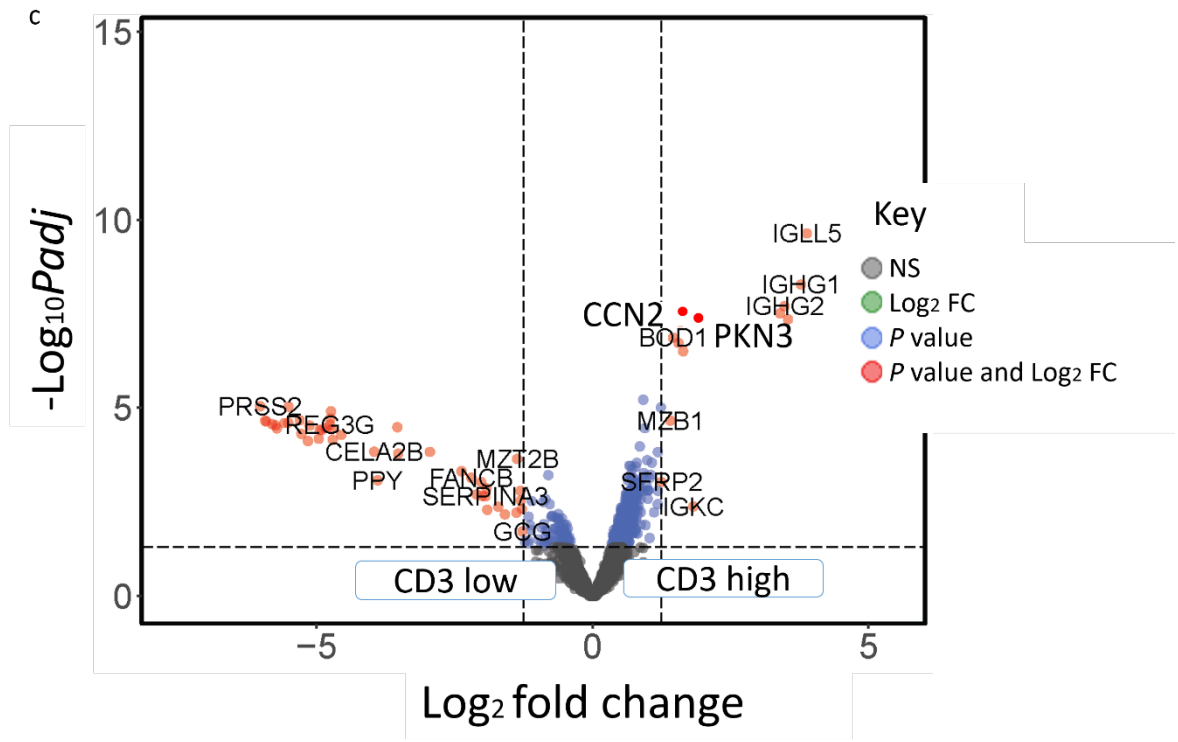


**Figure 6.1.b-c Volcano plot demonstrating gene marker differential expression levels in naïve PDAC based on comparison of CD3low versus CD3high** *in b). αSMA segments c). immune segments. Genes with log2 fold change above and below 1.5, and p adjusted value ≤0.05 were considered significant. Important genes in bold. Dashed line indicates significance thresholds, NS = non-significant, FC = fold change.*

Pathway analysis demonstrated epithelium of CD3high cases had elevated MYC (NES = 2.0, padj <0.001), PPAR (NES = 1.9, padj <0.001) and mTOR (NES = 1.6, padj <0.001) signalling, as well as reduced type I INF (NES = -1.8, padj = 0.008), PDGF (NES = -1.8, padj = 0.01), PI3K-Akt (NES = -1.5, padj <0.001) and JAK/STAT (NES = -1.5, padj = 0.04) signalling (figure 6.2.a). Unexpectedly, limited immune related pathways were observed in αSMA segments of CD3 ranked patients. GSEA demonstrated enriched complement (NES = 2.0, padj <0.001) and BCR signalling (NES = 1.5, padj = 0.035), as well as reduced matrix remodelling and metastasis (NES = -2.1, padj <0.001) (supplementary figure 8.10). CD3high immune segments displayed elevated cytotoxicity (NES = 1.6, padj = 0.047), lymphocyte regulation (NES = 1.6, padj = 0.01) and B cell (NES = 1.6, padj = 0.047), with reduced neutrophil degranulation (figure 6.2.b). Spatial immune cell deconvolution showed higher estimates of plasma cells (p=0.009) and CD8 T cells (p=0.029) in CD3high samples (figure 6.2.c).

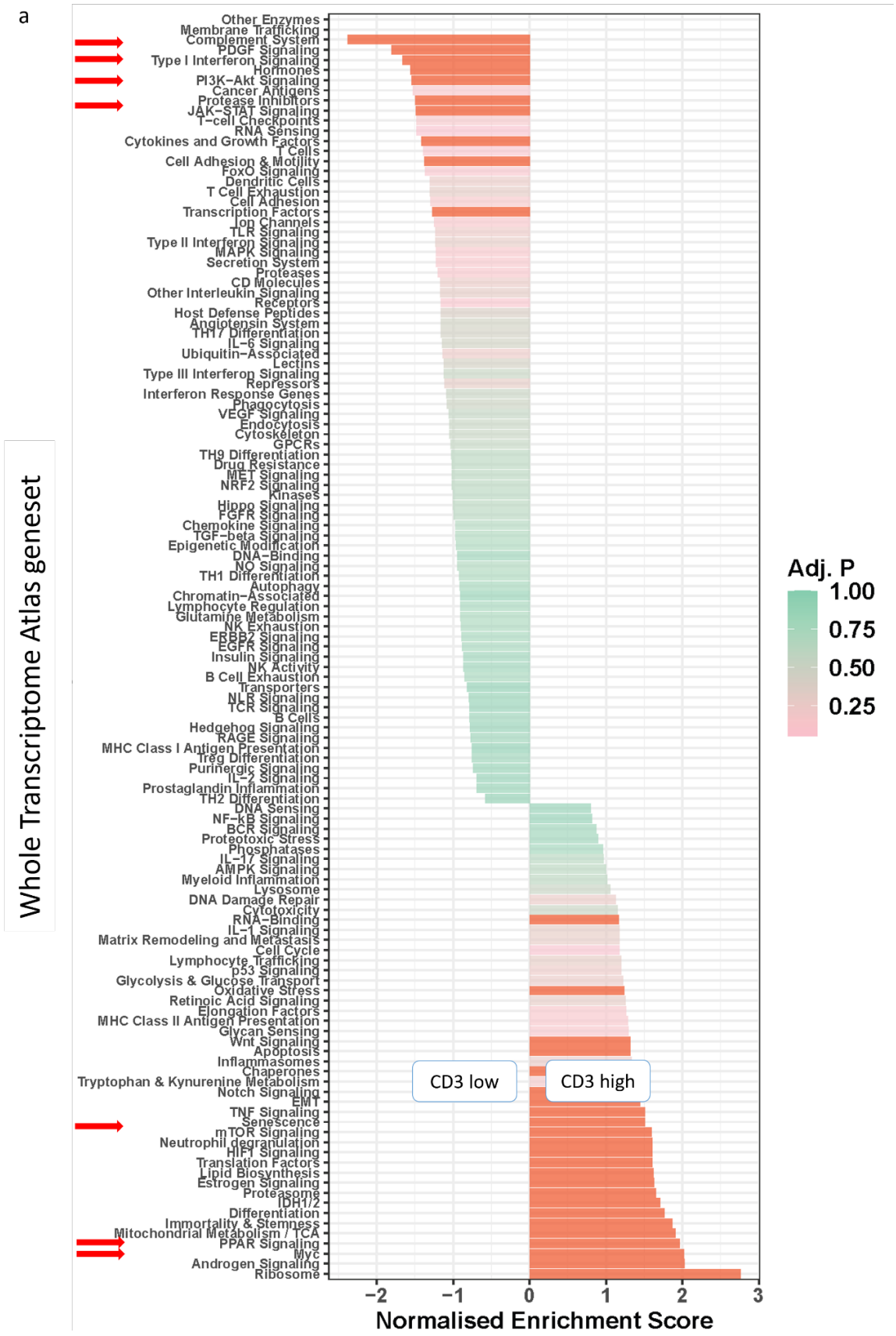


**Figure 6.2.a Geneset enrichment and immune cell deconvolution of naïve PDAC based on comparison of CD3low versus CD3high.** *Bar charts demonstrate pathways differential expressed in a). epithelial segments. Pathways with normalized enrichment score above and below 1.5, and p adjusted (Adj. P) value ≤0.05 were considered significant. Important pathways are indicated by an arrow.*

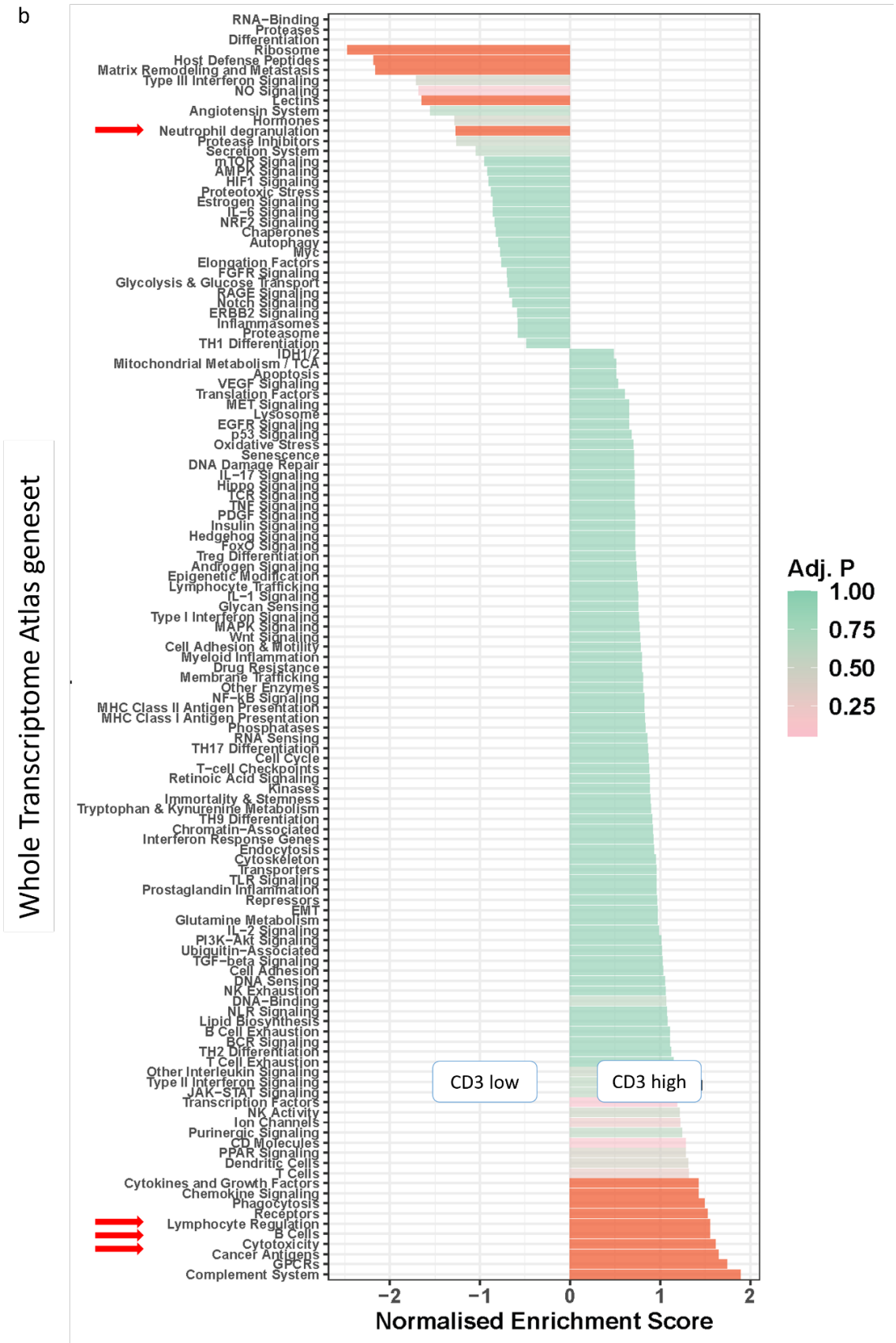


**Figure 6.2.b Geneset enrichment and immune cell deconvolution of naïve PDAC based on comparison of CD3low versus CD3high.** *Bar charts demonstrate pathways differential expressed in b). immune segments. Pathways with normalized enrichment score above and below 1.5, and p adjusted (Adj. P) value ≤0.05 were considered significant. Important pathways are indicated by an arrow.*

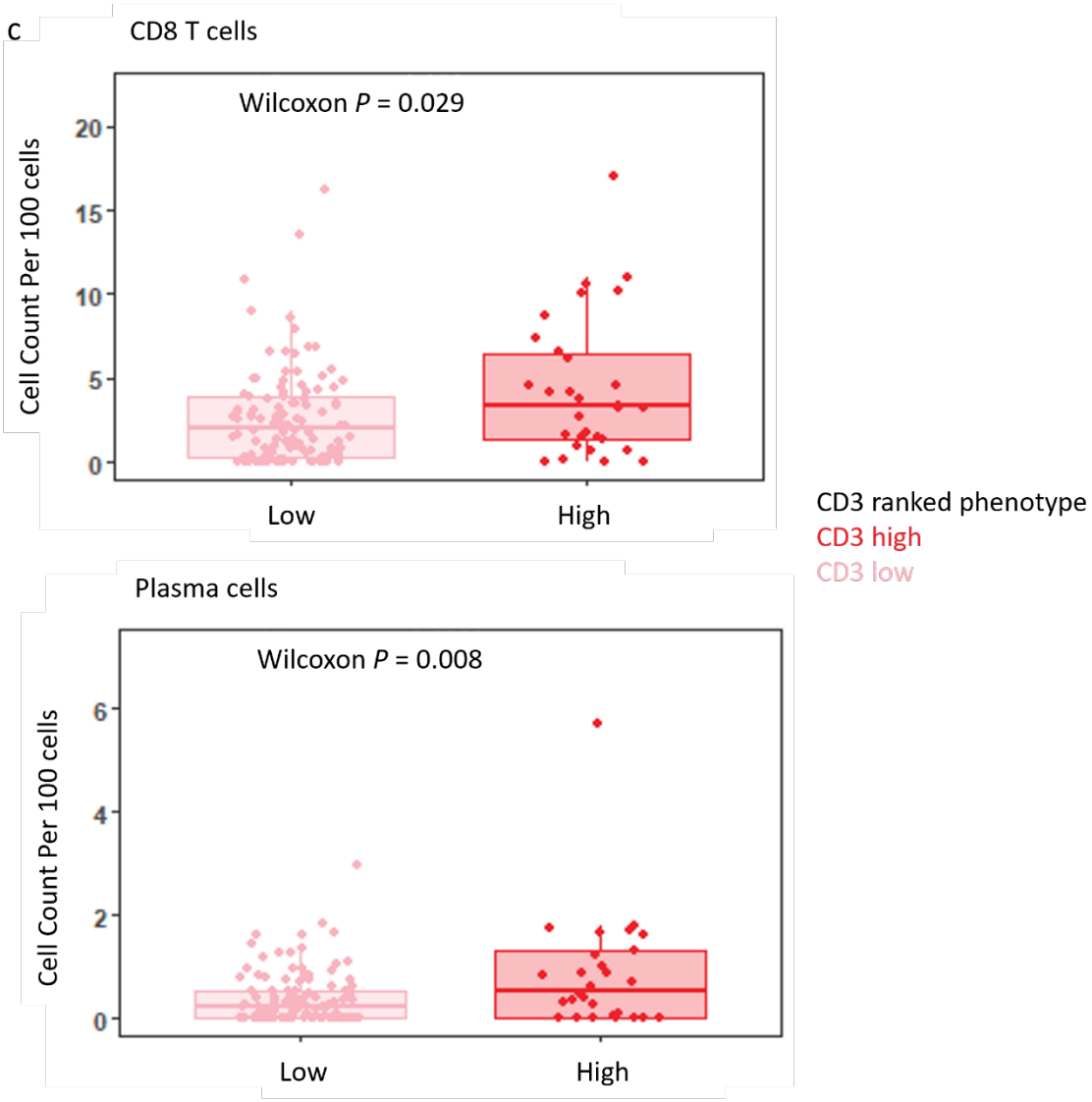


**Figure 6.2.c Geneset enrichment and immune cell deconvolution of naïve PDAC based on comparison of CD3low versus CD3high.** *Boxplots demonstrate estimated immune cell expression per 100 cells in c). CD3low and CD3high. Wilcoxon test with adjusted p value was used.*

Next CD68 ranked density was investigated, which negatively correlated with prognosis (chapter 3.6). Once again, relatively restricted gene signatures were produced for segment analysis (figure 6.3.a-b). Aberrated genes include elevated *IGLL5* (logFC = 4.6, padj <0.001) and *IGHG1* (logFC = 3.5, padj = 0.001) in αSMA segments (figure 6.3.a), and upregulated *POF1B* (logFC = 2.0, padj <0.0005) and *IGHG1* (logFC = 3.0, padj = 0.02) in CD68high immune segments (figure 6.3.b).

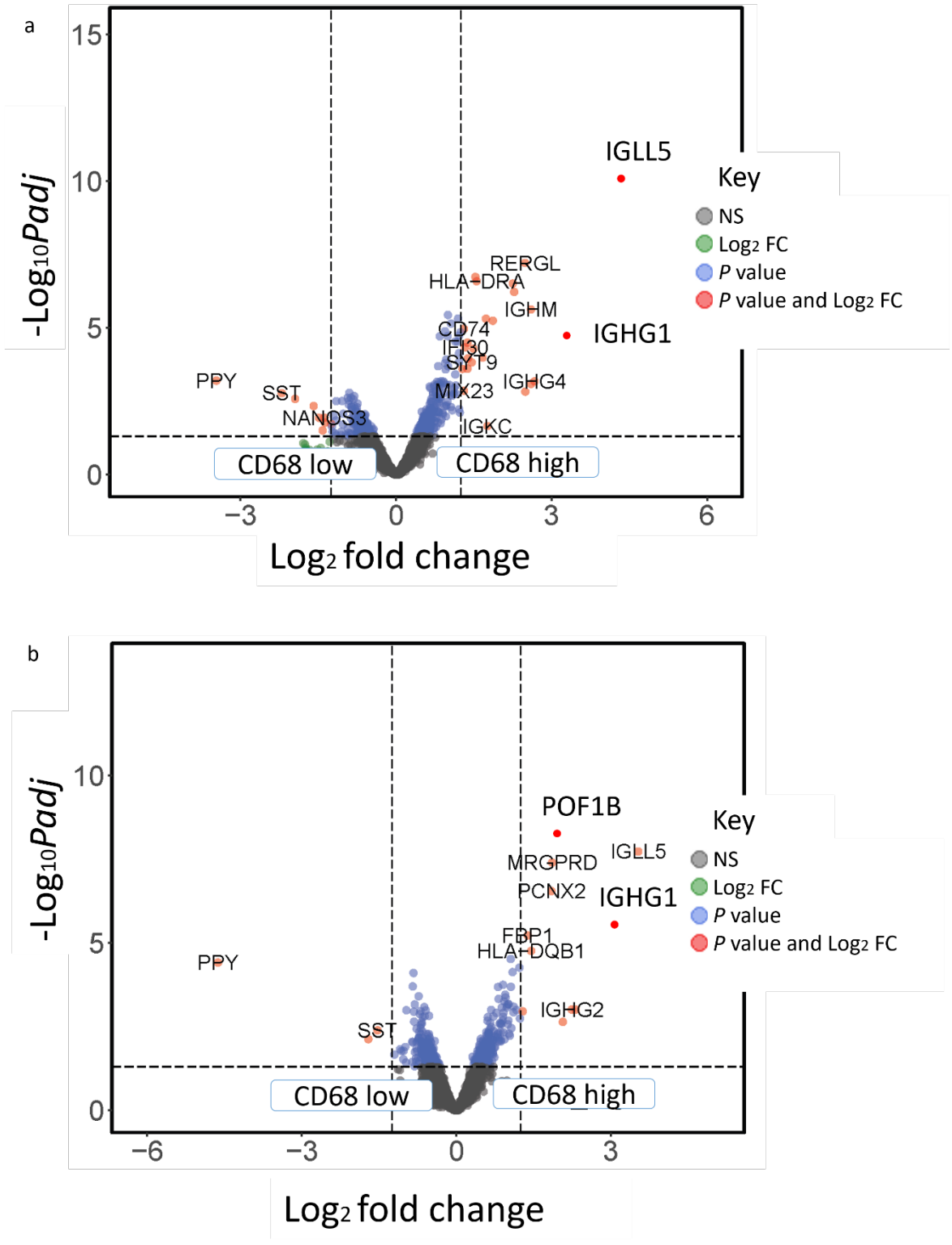


**Figure 6.3.a-b Volcano plot demonstrating gene marker differential expression levels in naïve PDAC based on comparison of CD68low versus CD68high** *in* a). *αSMA segments b).*

*immune segments. Genes with log2 fold change above and below 1.5, and p adjusted value ≤0.05 were considered significant. Important genes are in bold. Dashed line indicates significance thresholds, NS = non-significant, FC = fold change.*

Epithelial segments of CD68high cases demonstrated upregulation of matrix remodelling and metastasis pathways (NES = 2.3, padj <0.001), MET (NES = 2.0, padj <0.001) and NO (NES = 2.0, padj = 0.009) among others (figure 6.4.a). Upregulation of neutrophil degranulation (NES = 1.7, padj <0.001) was also seen (figure 6.4.a). Interestingly, CD68high immune segments, typically associated with poor survival, presented with a vast, diverse immune rich landscape. Increased T cells (NES = 2.2, padj <0.001), neutrophil degranulation (NES = 2.7, padj <0.001), dendritic cells (NES = 2.3, padj <0.001), NK activity (NES = 2.3, padj <0.001) and B cells (NES = 1.7, padj = 0.030) were observed in CD68high immune AOIs (figure 6.4.b). αSMA rich regions presented with similar patterns as demonstrate in the above immune segments (supplementary figure 8.11). Spatial deconvolution estimates demonstrated low macrophage estimates within the CD68low segments (p<0.001) as expected (figure 6.4.c). Furthermore, reduced estimated immune populations were seen for CD4 T cells (p=0.035), CD8 T cells (p=0.004), mDCs (p=0.003), monocytes (p=0.003) and fibroblasts (p=0.005) in CD68low patients (figure 6.4.c).

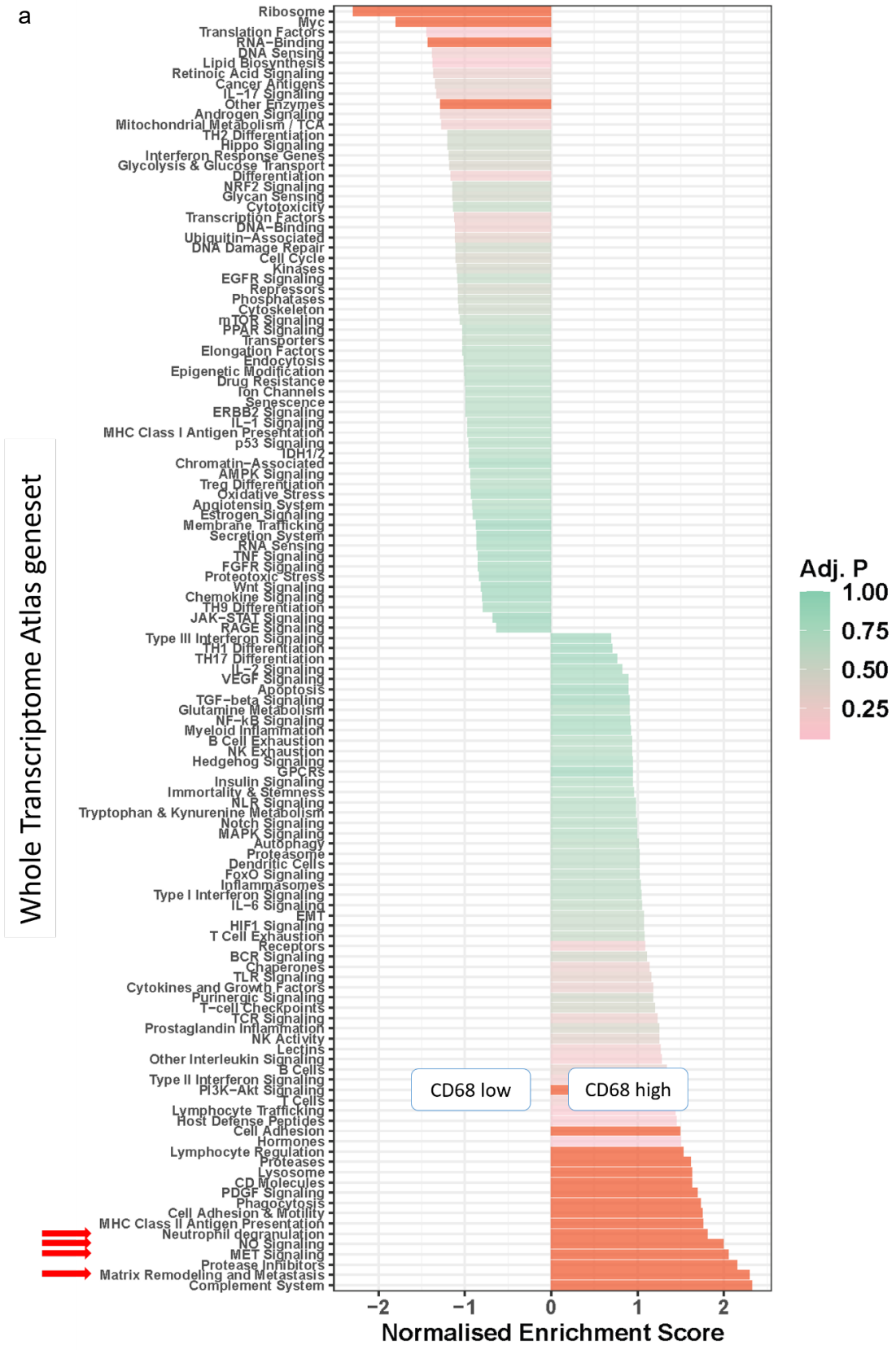


**Figure 6.4.a Geneset enrichment and immune cell deconvolution of naïve PDAC based on comparison of CD68low versus CD68high.** *Bar charts demonstrate pathways differential expressed in a). epithelial segments. Pathways with normalized enrichment score above and below 1.5, and p adjusted (Adj. P) value ≤0.05 were considered significant. Important pathways are indicated by an arrow.*

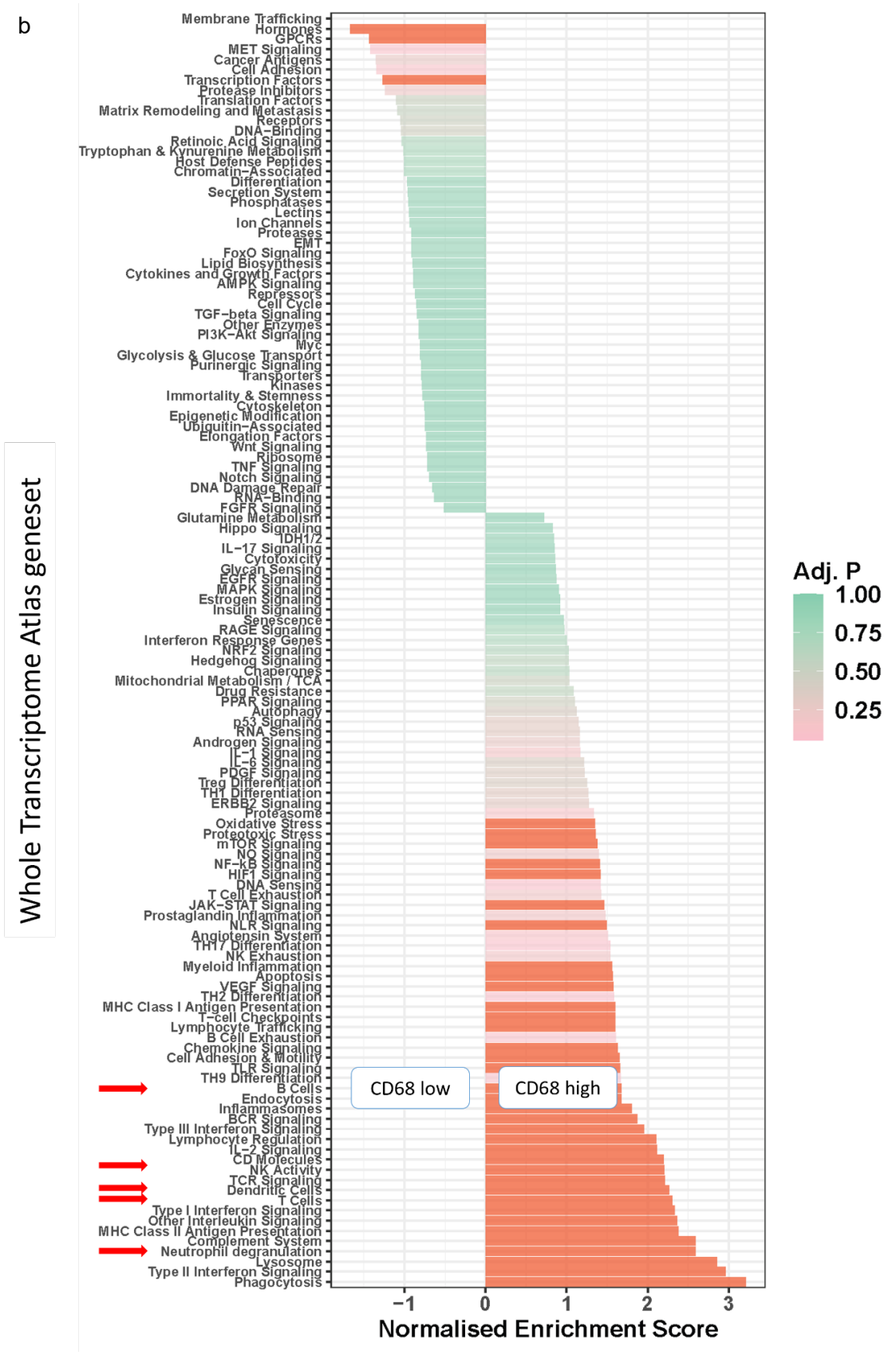


**Figure 6.4.b Geneset enrichment and immune cell deconvolution of naïve PDAC based on comparison of CD68low versus CD68high.** *Bar charts demonstrate pathways differential expressed in b). immune segments. Pathways with normalized enrichment score above and below 1.5, and p adjusted (Adj. P) value ≤0.05 were considered significant. Important pathways are indicated by an arrow.*

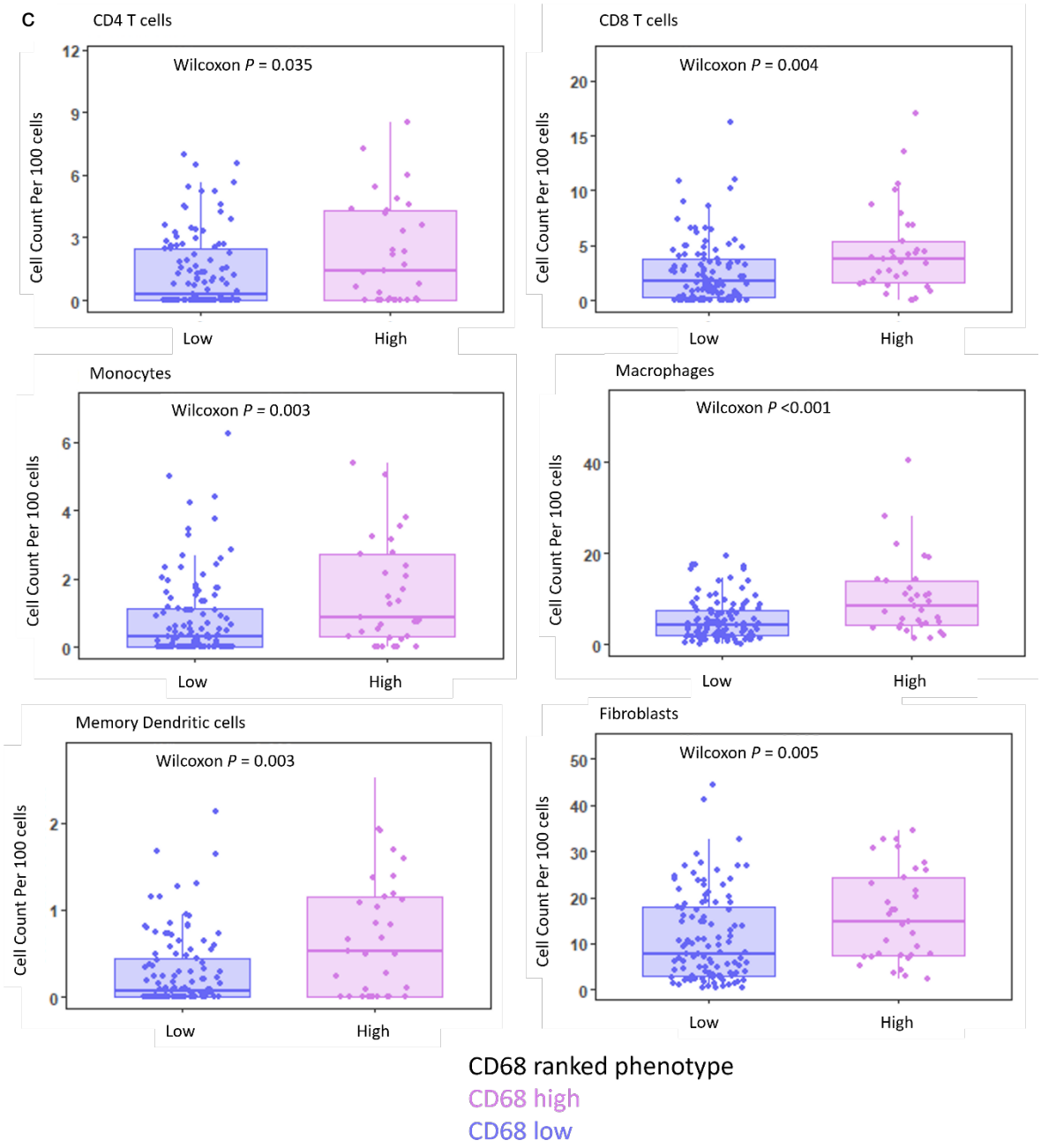


**Figure 6.4.c Geneset enrichment and immune cell deconvolution of naïve PDAC based on comparison of CD68low versus CD68high.** *Boxplots demonstrate estimated immune cell expression per 100 cells in c). CD68low and CD68high. Wilcoxon test with adjusted p value was used.*

Previous mIF analysis in neoadjuvant patients indicated CD3CD8 density correlated with survival. Contradictory to the central dogma, reduced levels of cytotoxic T cells correlated with better disease specific survival (chapter 4.5). In an attempt to explain this phenomenon, the transcriptomic differences between CD3CD8high and CD3CD8low ranked patients was investigated. Differential expression analysis demonstrated CD3CD8low epithelium was enriched with *DMBT1* (logFC = 1.9, padj = 0.007), CD3CD8low αSMA was enriched with *GREM2* (logFC = 1.9, padj = 0.007) and CD3CD8low immune had reduced *NOTCH1* expression (logFC = -1.8, padj = 0.04) (supplementary figure 8.12.a-c). Pathway analysis presented with many significant differences between ranked CD3CD8 density across all segments. Multiple cell signalling pathways were significantly reduced in CD3CD8low epithelium including NRF2 signalling (NES = -2.5, padj <0.001), p53 signalling (NES = -2.1, padj <0.001) and EMT (NES = -1.9, padj <0.001) signalling (figure 6.5.a). Additionally, CD3CD8 immune segments demonstrated downregulation of cell signalling and pro-tumorigenic pathways was seen involving type I INF (NES = -2.3, padj <0.001), NF-kB (NES = -1.9, padj = 0.002), immortality and stemness (NES = -1.5, padj = 0.014) and cell adhesion and motility (NES = -1.9, padj <0.001) (figure 6.5.b). Furthermore, reduced expression of B cells (NES = -2.4, padj <0.001), B cell exhaustion (NES = -2.0, padj = 0.005), T cells (NES = -2.3, padj <0.001) and T cell exhaustion (NES = -1.7, padj = 0.028) (figure 6.5.b).

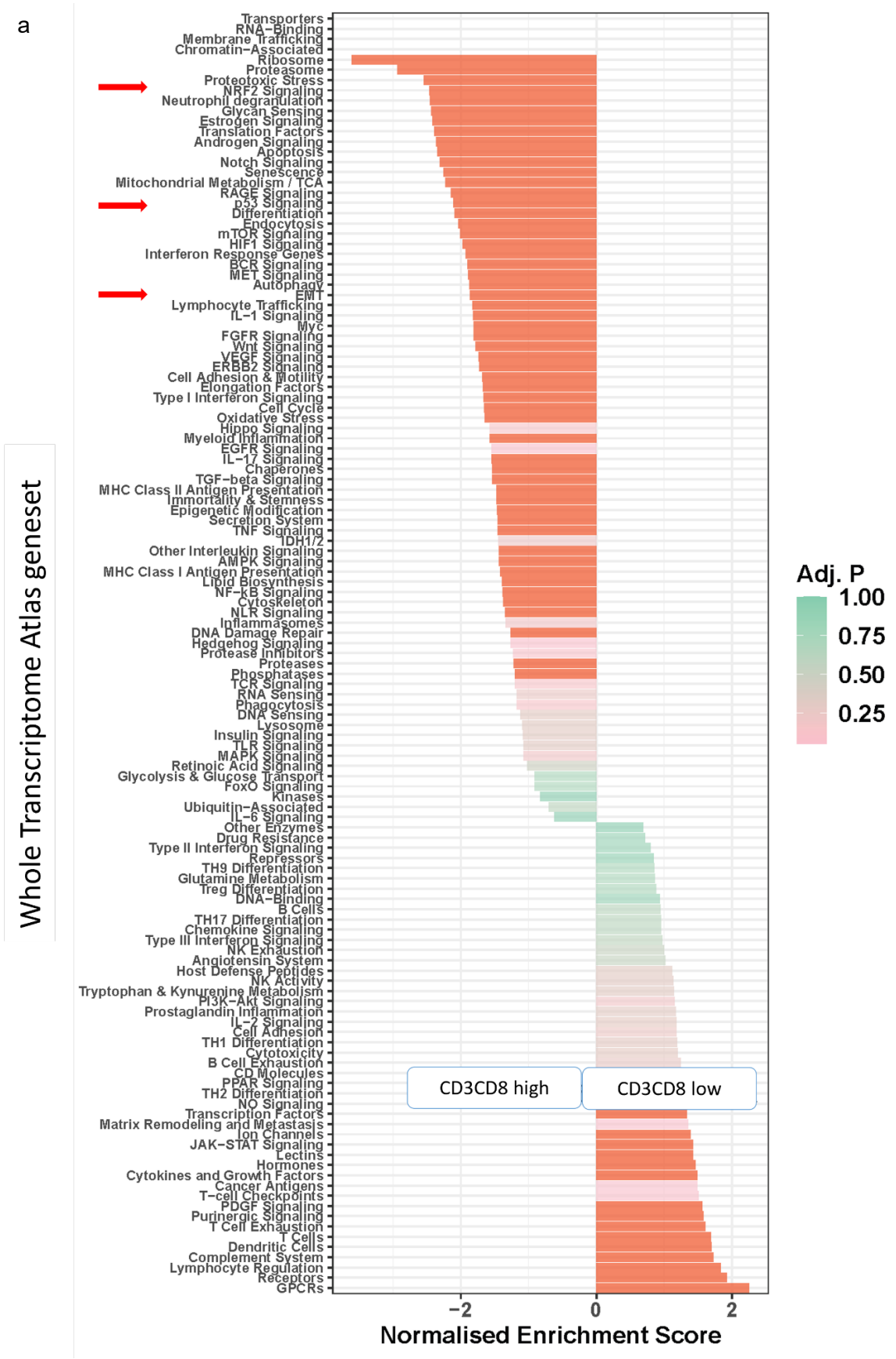


**Figure 6.5.a Geneset enrichment and immune cell deconvolution of neoadjuvant PDAC based on comparison of CD3CD8high versus CD3CD8low**. *Bar charts demonstrate pathways differential expressed in a). epithelial segments. Pathways with normalized enrichment score above and below 1.5, and p adjusted (Adj. P) value ≤0.05 were considered significant. Important pathways are indicated by an arrow.*

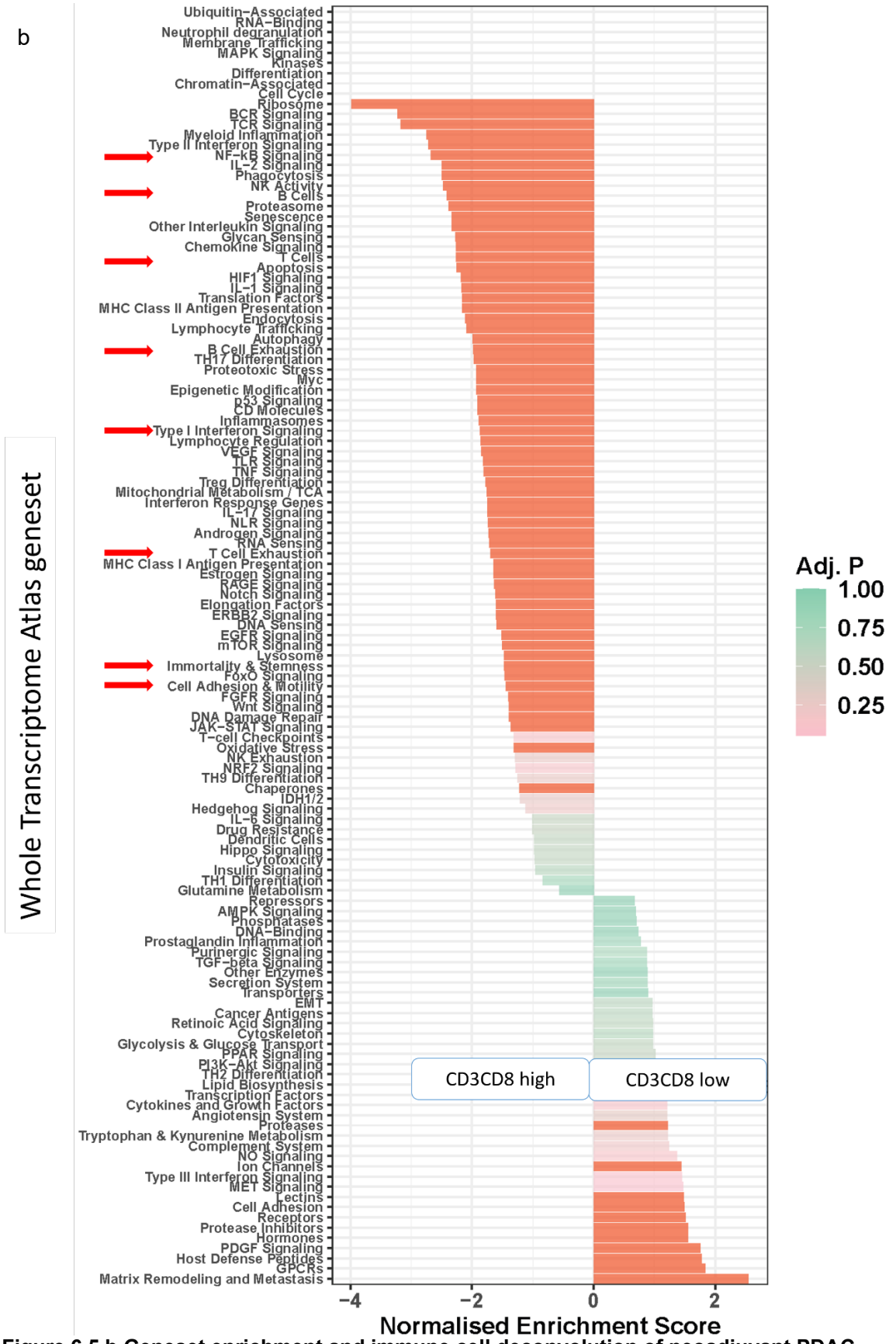


**Figure 6.5.b Geneset enrichment and immune cell deconvolution of neoadjuvant PDAC based on comparison of CD3CD8high versus CD3CD8low.** *Bar charts demonstrate pathways differential expressed in b). immune segments. Pathways with normalized enrichment score above and below 1.5, and p adjusted value ≤0.05 were considered significant. Important pathways are indicated by an arrow.*

### 6.2.2 Spatial Transcriptomic landscape of nearest neighbour phenotypes in naïve and neoadjuvant pancreatic cancer

Next, the most biologically interesting nearest neighbour relationships as characterised in chapter 3.8.1 and 4.7.1 were investigated. Within the naïve cohort, this encompassed distances from CD68 to CD3 and from CD68 to PanCk. The neoadjuvant cohort focuses on distances from CD3CD8 to PanCk. As above, comparisons in matched regional Spatial Transcriptomics were carried out to determine biological differences between nearest neighbour ranks.

Low distances from CD68+ to CD3+ (CD3near) correlate with better outcome in nearest neighbour analysis within the naïve cohort (chapter 3.8.1). Epithelial AOIs in CD3near cores had differential upregulation of *FCGBP* (logFC = 3.1, padj <0.001) and downregulation of *IGFBP3* (logFC = 2.2, padj = 0.02) (supplementary figure 8.13). Limited pathways were upregulated in CD3near epithelium with only PPAR signalling (NES = 1.6, padj = 0.02) and mitochondrial metabolism/tricarboxylic acid (NES = 1.6, padj = 0.001) being of note (figure 6.6.a). In contrast, numerous signalling pathways were decreased in CD3near epithelium with MET (NES = -2.2, padj <0.001), type I INF (NES = -2.2, padj <0.001), TGF-β (NES = -1.9, padj <0.001) seen (figure 6.6.a). Additionally, reduction of pro-tumorigenic pathways matrix remodelling and metastasis (NES = -2.0, padj <0.001) and EMT (NES = -2.0, padj <0.001) (figure 6.6.a) was observed. Additionally, CD3near immune segments were enriched in B cells (NES = 1.6, padj = 0.03) and reduced in angiotensin system (NES = -1.7, padj = 0.04), neutrophil degranulation (NES = -1.9, padj <0.001) and TCR signalling (NES = -1.4, padj = 0.036). Spatial immune cell deconvolution estimated increased B cell (p=0.011) and plasma (p=0.019) in CD3near samples (figure 6.6.b).

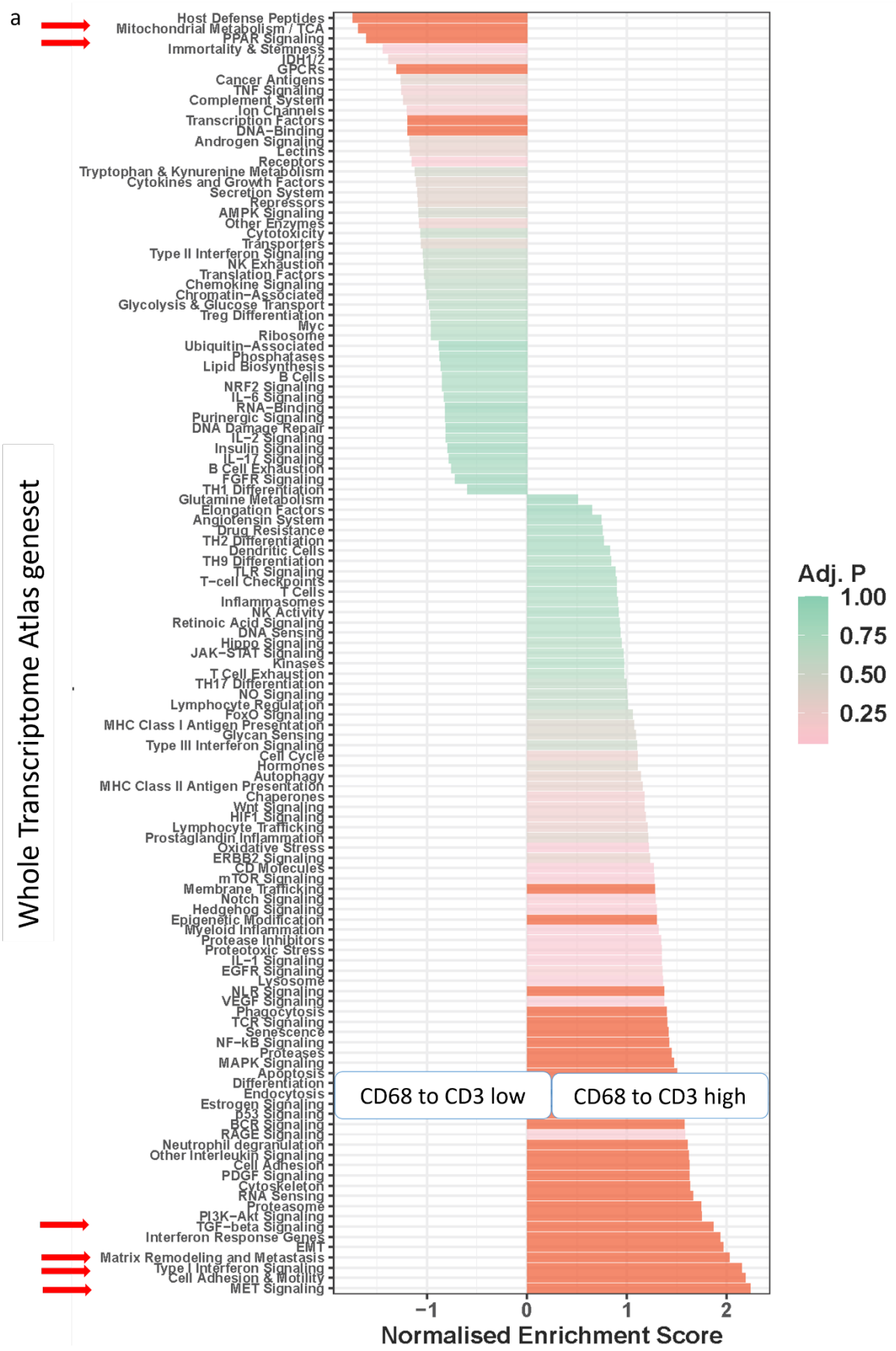


**Figure 6.6.a Geneset enrichment and immune cell deconvolution of neoadjuvant PDAC based on comparison of distance from CD68 to CD3low versus distance from CD68 to CD3high.** *Bar charts demonstrate pathways differential expressed in a). epithelial segments. Pathways with normalized enrichment score above and below 1.5, and p adjusted (Adj. P) value ≤0.05 were considered significant. Important pathways are indicated by an arrow.*


**Figure 6.6.b Geneset enrichment and immune cell deconvolution of neoadjuvant PDAC based on comparison of distance from CD68 to CD3low versus distance from CD68 to CD3high.** *Bar charts demonstrate pathways differential expressed in b). immune segments. Pathways with normalized enrichment score above and below 1.5, and p adjusted (Adj. P) value ≤0.05 were considered significant. Important pathways are indicated by an arrow.*

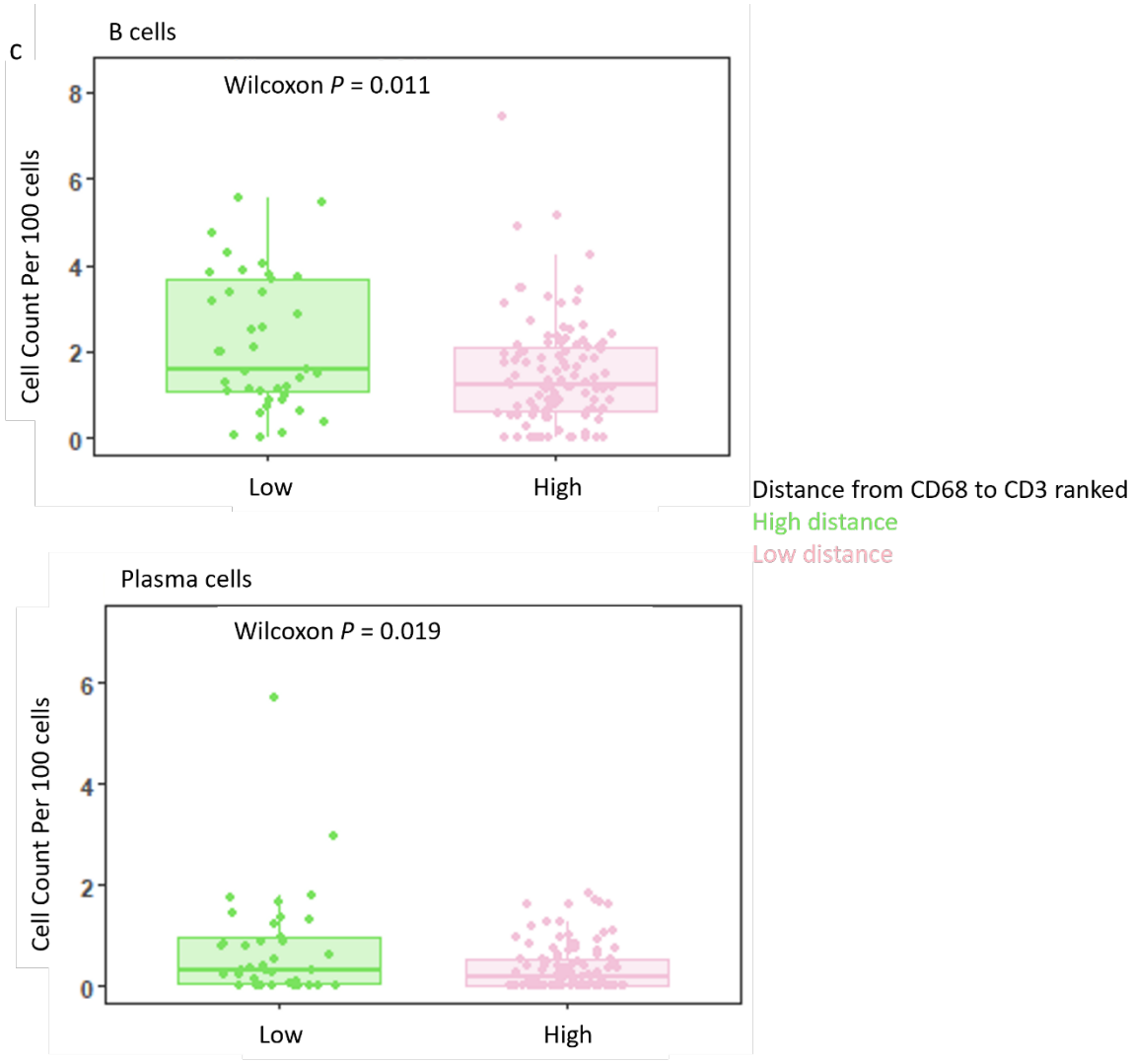


**Figure 6.6.c Geneset enrichment and immune cell deconvolution of naïve PDAC based on comparison of distance from CD68 to CD3low versus distance from CD68 to CD3high.** *Boxplots demonstrate estimated immune cell expression per 100 cells in c). low and high ranked distances from CD68 to CD3. Wilcoxon test with adjusted p value was used.*

Large distances from CD68 to PanCk (PanCkfar) correlated with better outcome in nearest neighbour analysis within the naïve cohort (chapter 3.8.1). PanCkfar epithelium differentially expressed *MMP12* (logFC = 2.4, padj <0.001), *SLC12A2* (logFC = 2.2, padj <0.001) and *CCL2* (logFC = 2.0, padj = 0.03) (supplementary figure 8.14.a). Limited aberrated pathways were seen, including elevated PDGF (NES = 2.4, padj <0.001), TNF (NES = 1.9, padj <0.001) and MET (NES = 1.6, padj = 0.03) signalling (figure 6.7.a). Furthermore, enriched type I INF (NES = 2.3, padj = 0.001), type II INF (NES = 2.1, padj = 0.003) and BCR (NES = 1.7, padj = 0.03) were observed in αSMA rich AOIs in PanCkfar (figure 6.7.b), although few differentially expressed genes were seen (supplementary figure 8.14.b). In contrast, immune PanCkfar segments had multiple significant genes, including fibroblast associated markers *ACTA2* (logFC = 1.7, padj <0.001) and *MYH11* (logFC = 1.8, padj <0.001) (supplementary figure 8.14.c).These segments saw reduced immune related pathways including dendritic cells (NES = -2.0, padj = 0.003), T cell (NES = -2.0, padj = 0.03), B cell exhaustion (NES = -2.1, padj = 0.005), BCR signalling (NES = -1.6, padj = 0.010) among others (figure 6.7.c). Elevated estimated neutrophil population was seen in PanCkfar samples (p=0.038) (figure 6.7.d).

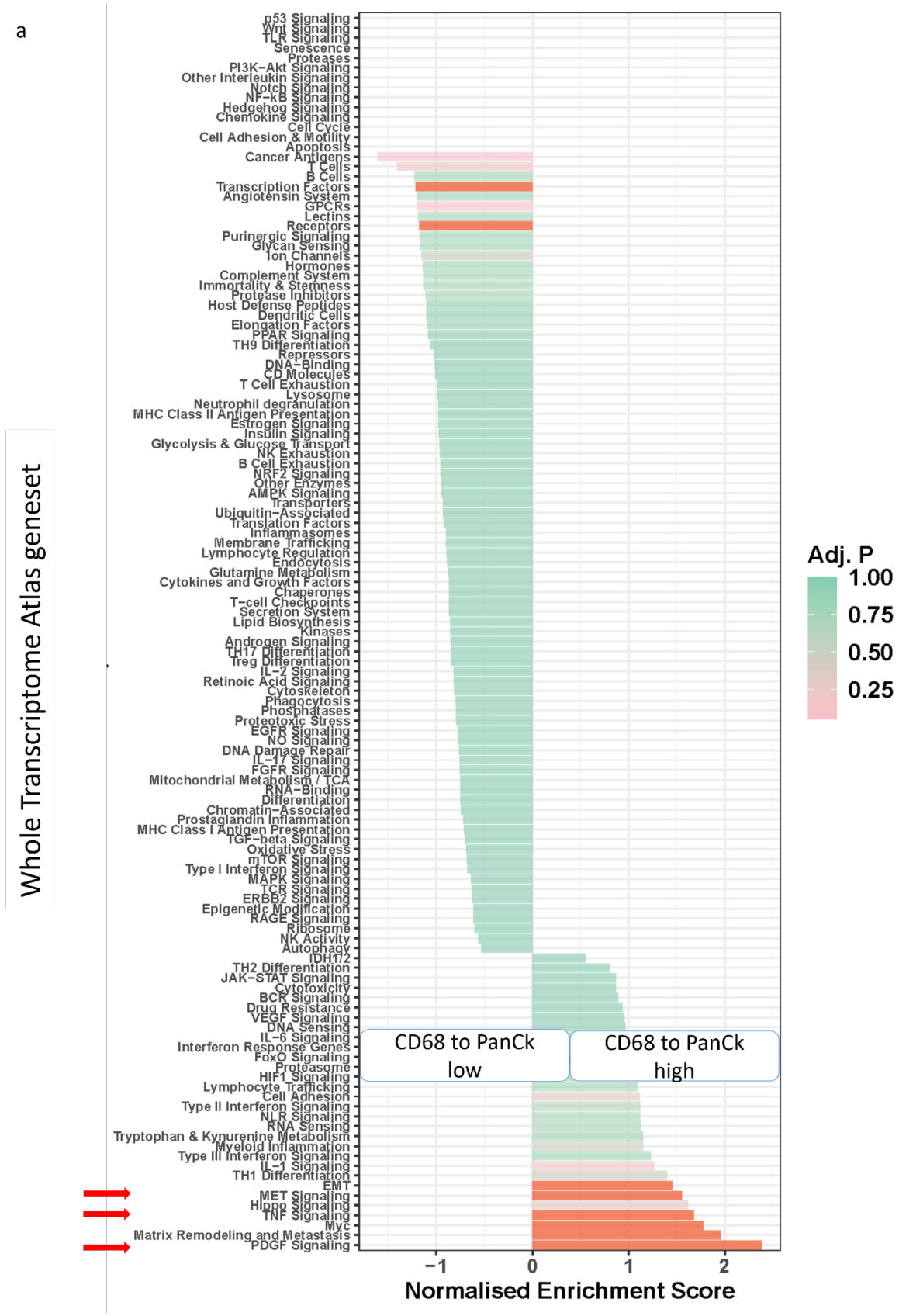


**Figure 6.7.a Geneset enrichment and immune cell deconvolution of neoadjuvant PDAC based on comparison of distance from CD68 to PanCklow versus distance from CD68 to PanCkhigh.** *Bar charts demonstrate pathways differential expressed in a). epithelial segments. Pathways with normalized enrichment score above and below 1.5, and p adjusted (Adj. P) value ≤0.05 were considered significant. Important pathways are indicated by an arrow.*

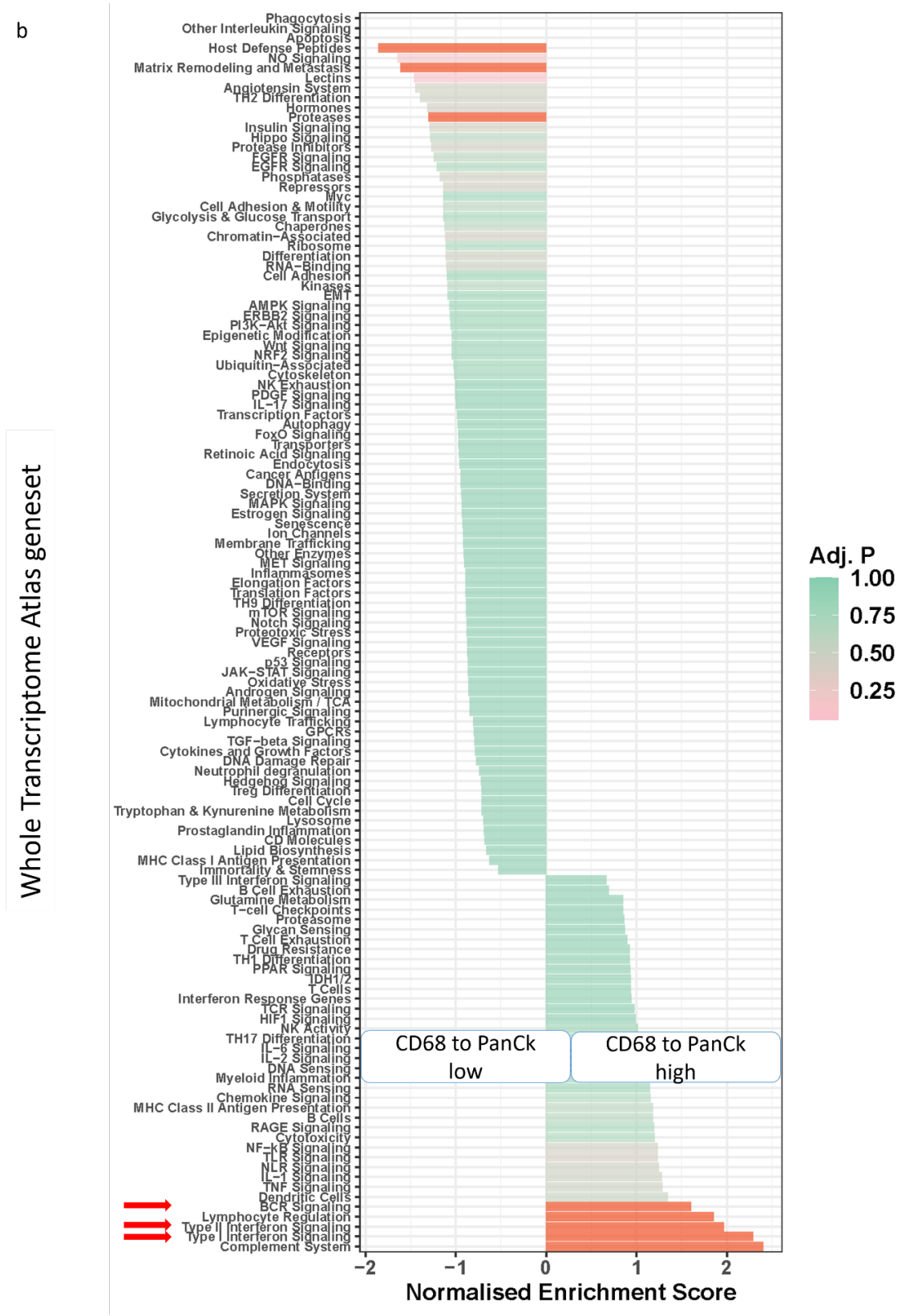


**Figure 6.7.b Geneset enrichment and immune cell deconvolution of neoadjuvant PDAC based on comparison of distance from CD68 to PanCklow versus distance from CD68 to PanCkhigh.** *Bar charts demonstrate pathways differential expressed in b). αSMA. Pathways with normalized enrichment score above and below 1.5, and p adjusted (Adj. P) value ≤0.05 were considered significant. Important pathways are indicated by an arrow.*

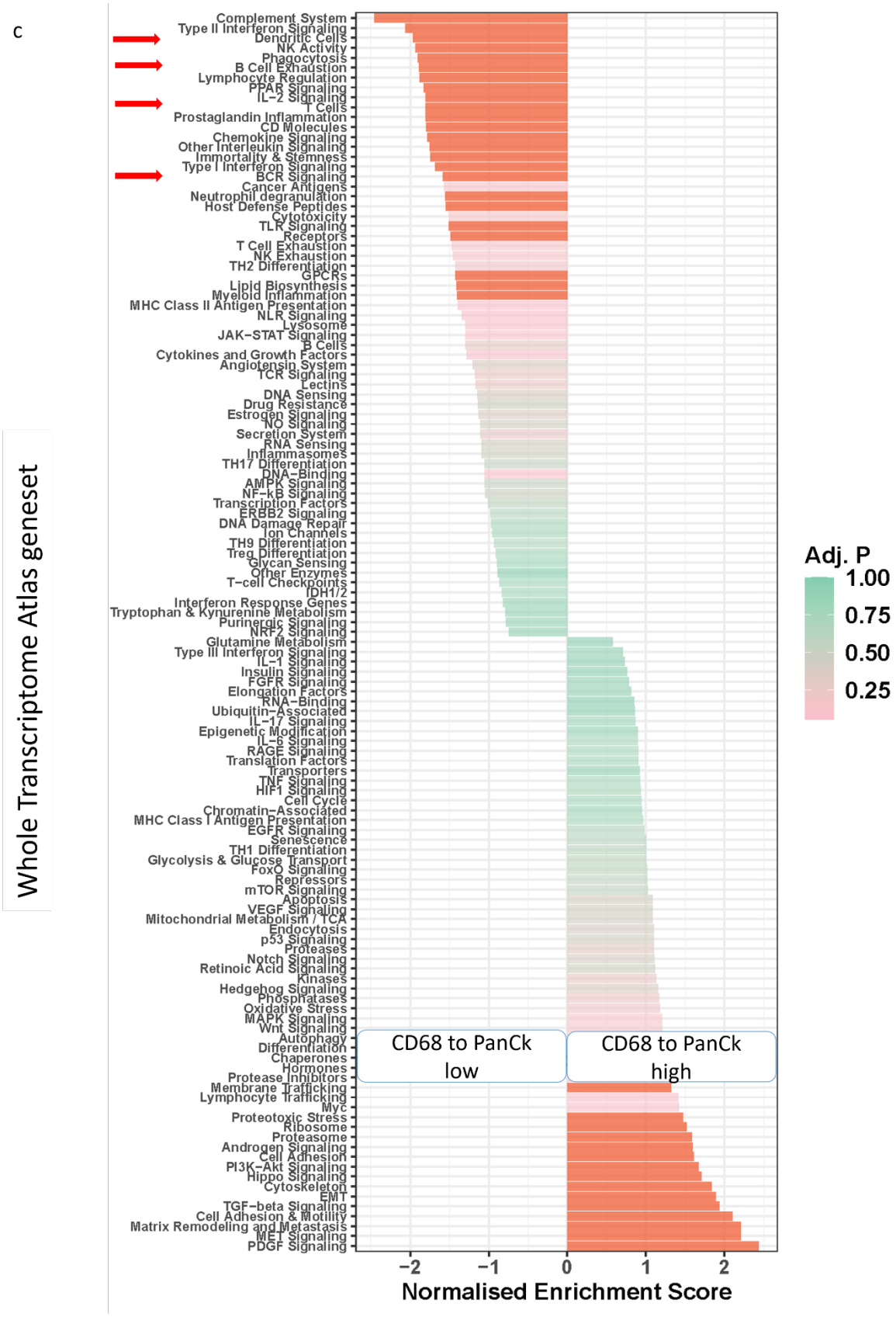


**Figure 6.7.c Geneset enrichment and immune cell deconvolution of neoadjuvant PDAC based on comparison of distance from CD68 to PanCklow versus distance from CD68 to PanCkhigh.** *Bar charts demonstrate pathways differential expressed in c). immune segments. Pathways with normalized enrichment score above and below 1.5, and p adjusted (Adj. P) value ≤0.05 were considered significant. Important pathways are indicated by an arrow.*

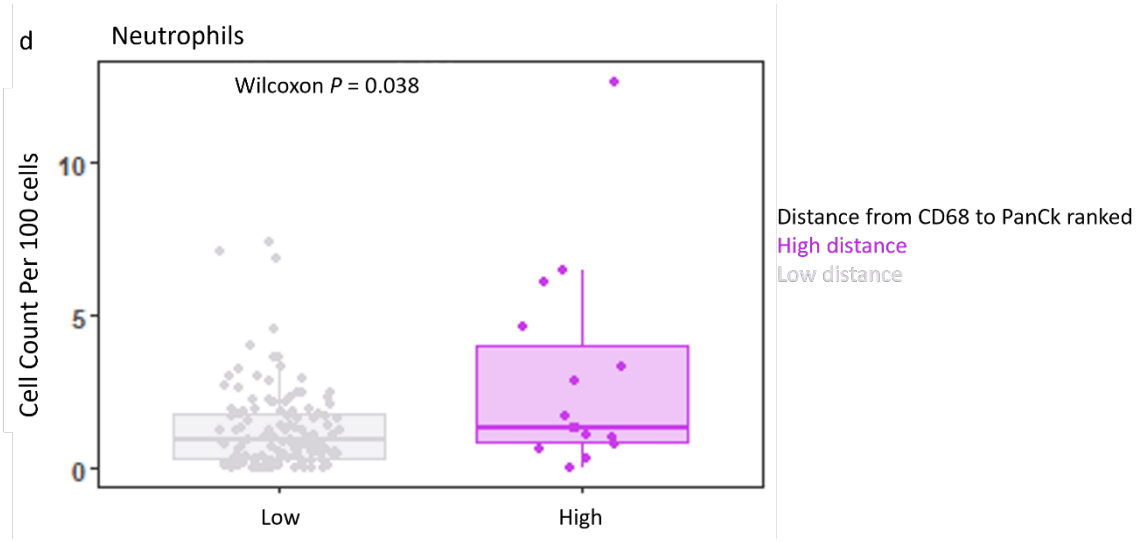


**Figure 6.7.d Geneset enrichment and immune cell deconvolution of neoadjuvant PDAC based on comparison of distance from CD68 to PanCklow versus distance from CD68 to PanCkhigh.** *Boxplots demonstrate estimated immune cell expression per 100 cells in d). low and high ranked distances from CD68 to PanCk. Wilcoxon test with adjusted p value was used.*

Finally, nearest neighbour protein expression of neoadjuvant patients with low distances from CD3CD8+ to PanCk+ (PanCknear) were explored. These patients had longer survival outcomes (chapter 4.7.1). Abundant aberrated pathways were observed in epithelial PanCknear segments, including elevated MET (NES = 2.6, padj <0.001), MYC (NES = 2.5, padj <0.001) and TGF-β (NES = 2.1, padj <0.001) signalling (figure 6.8.a). Additionally, multiple immune related pathways were significantly reduced (figure 6.8.a). αSMA segments mirrored this immune barren trend, with PanCknear regions presenting with reduced B cells (NES = -2.5, padj <0.001) and T cells (NES = -2.0, padj <0.001) (figure 6.8.b). In contrast, PanCknear immune segments demonstrated limited significant pathway differences between the ranked nearest neighbour groups (figure 6.8.c). Elevated type II INF signalling (NES = 2.0, padj <0.001), type I INF signalling (NES = 1.6, padj = 0.014) and Treg differentiation (NES = 2.0, padj = 0.033) was observed in PanCknear immune segments (figure 6.8.c). Enriched expression of mast cells (p=0.03) and NK cells (p=0.004) was estimated in patients with low distances from CD3CD8 to PanCk cells (figure 6.8.d).

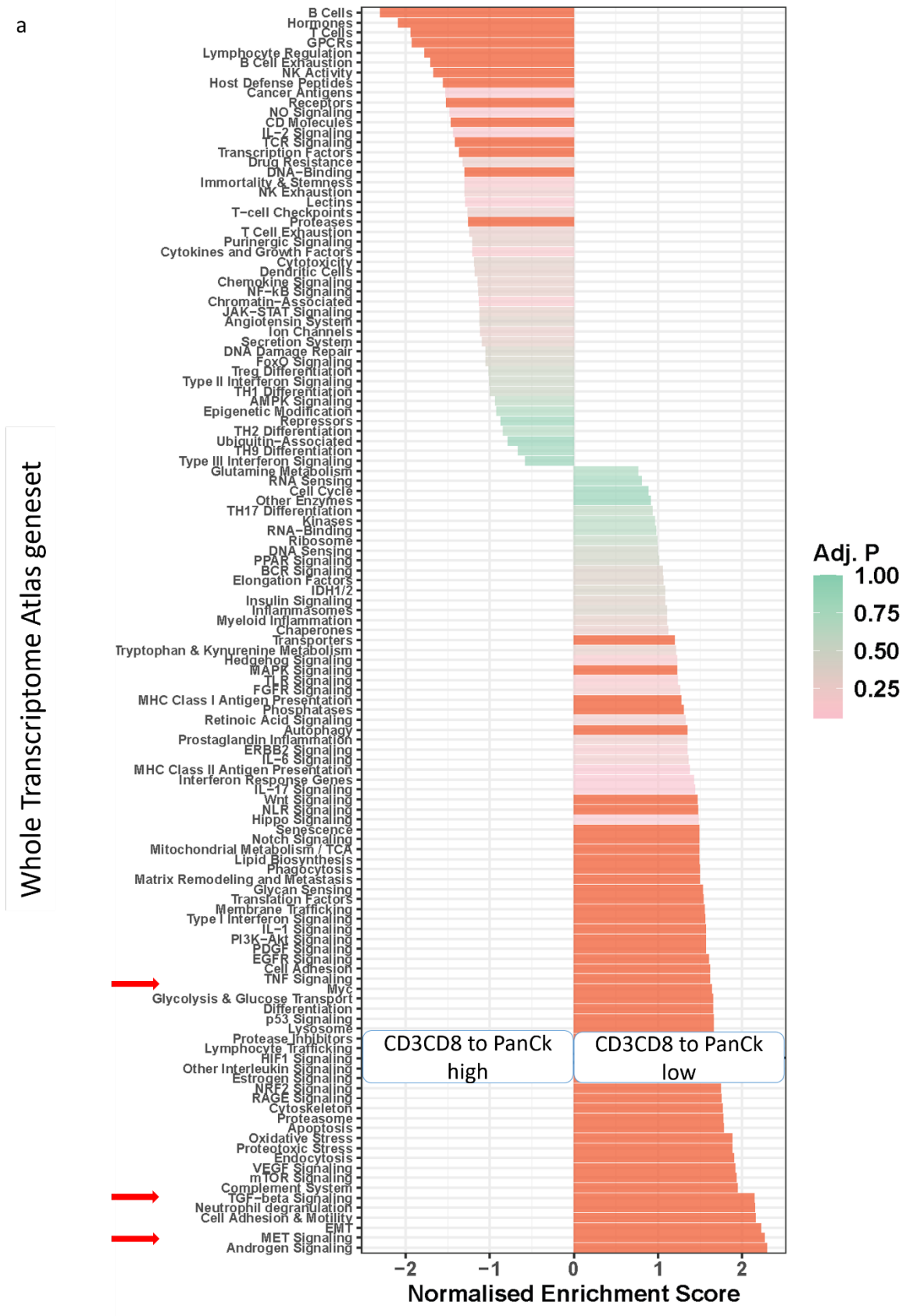


**Figure 6.8.a Geneset enrichment and immune cell deconvolution of neoadjuvant PDAC based on comparison of distance from CD3CD8 to PanCkhigh versus distance from CD3CD8 to PanCklow.** *Bar charts demonstrate pathways differential expressed in a). epithelial segments. Pathways with normalized enrichment score above and below 1.5, and p adjusted (Adj. P) value ≤0.05 were considered significant. Important pathways are indicated by an arrow.*

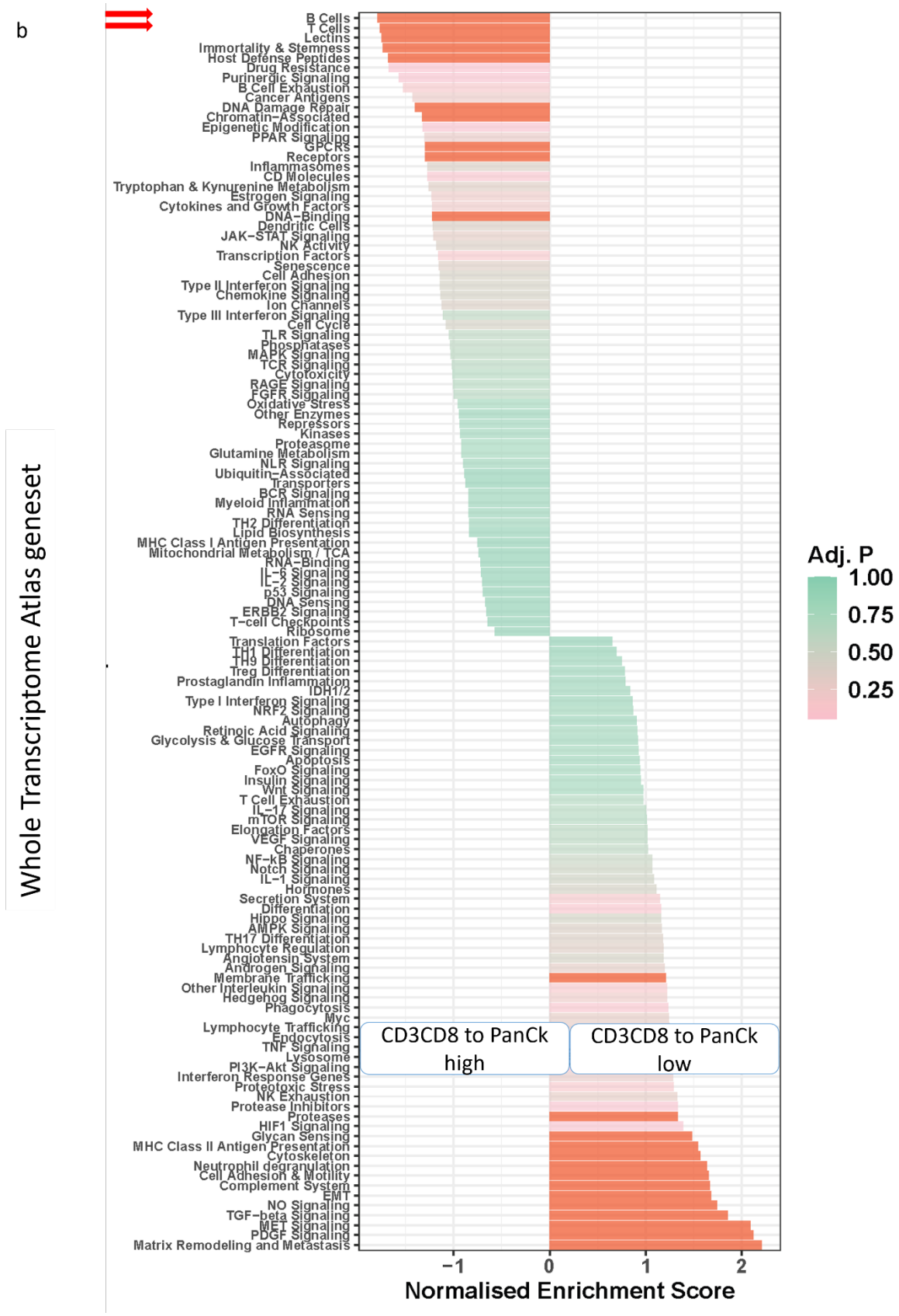


**Figure 6.8.b Geneset enrichment and immune cell deconvolution of neoadjuvant PDAC based on comparison of distance from CD3CD8 to PanCkhigh versus distance from CD3CD8 to PanCklow.** *Bar charts demonstrate pathways differential expressed in b). αSMA. Pathways with normalized enrichment score above and below 1.5, and p adjusted (Adj. P) value ≤0.05 were considered significant. Important pathways are indicated by an arrow.*

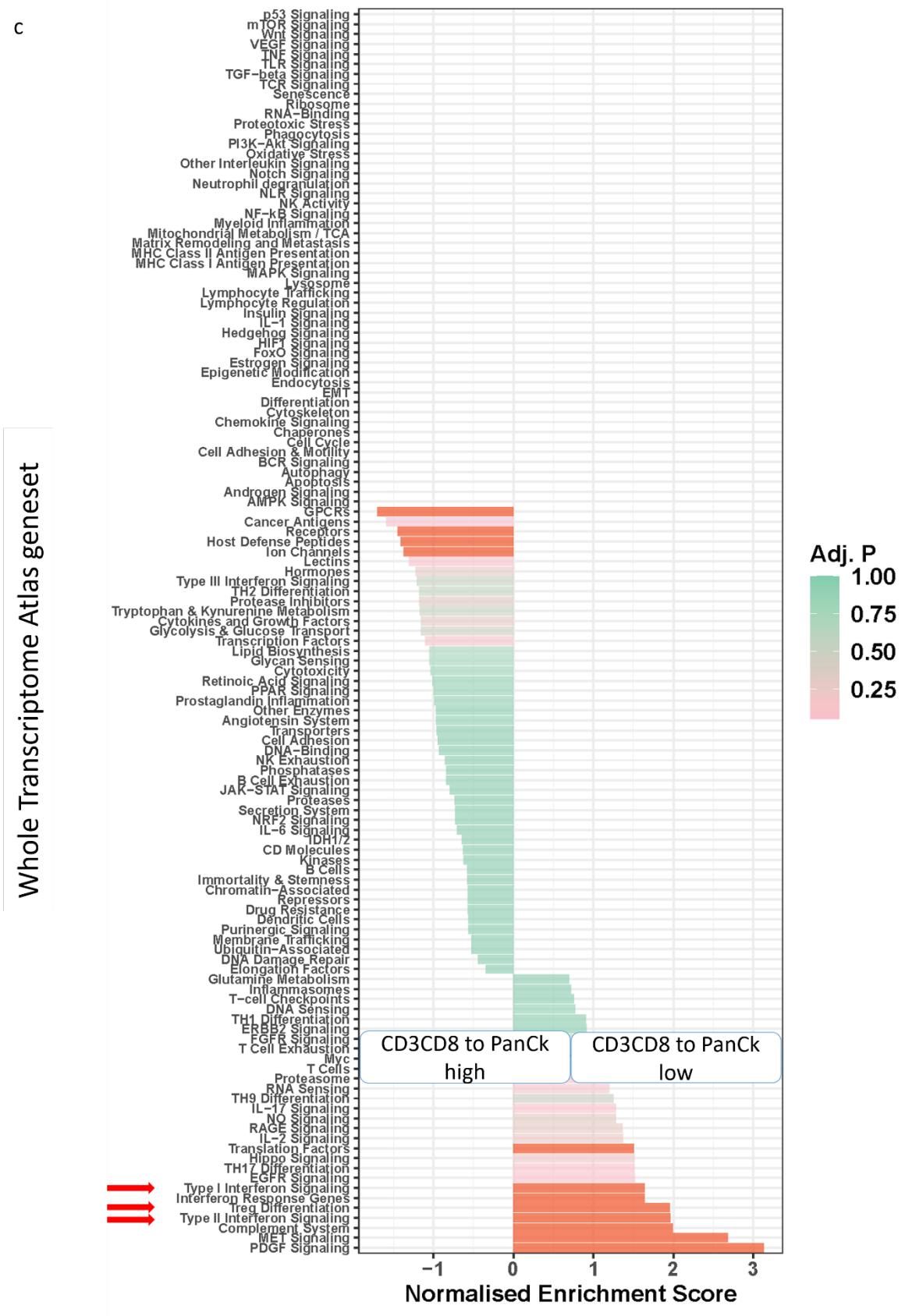


**Figure 6.8.c Geneset enrichment and immune cell deconvolution of neoadjuvant PDAC based on comparison of distance from CD3CD8 to PanCkhigh versus distance from CD3CD8 to PanCklow.** *Bar charts demonstrate pathways differential expressed in c). immune segments. Pathways with normalized enrichment score above and below 1.5, and p adjusted (Adj. P) value ≤0.05 were considered significant. Important pathways are indicated by an arrow.*

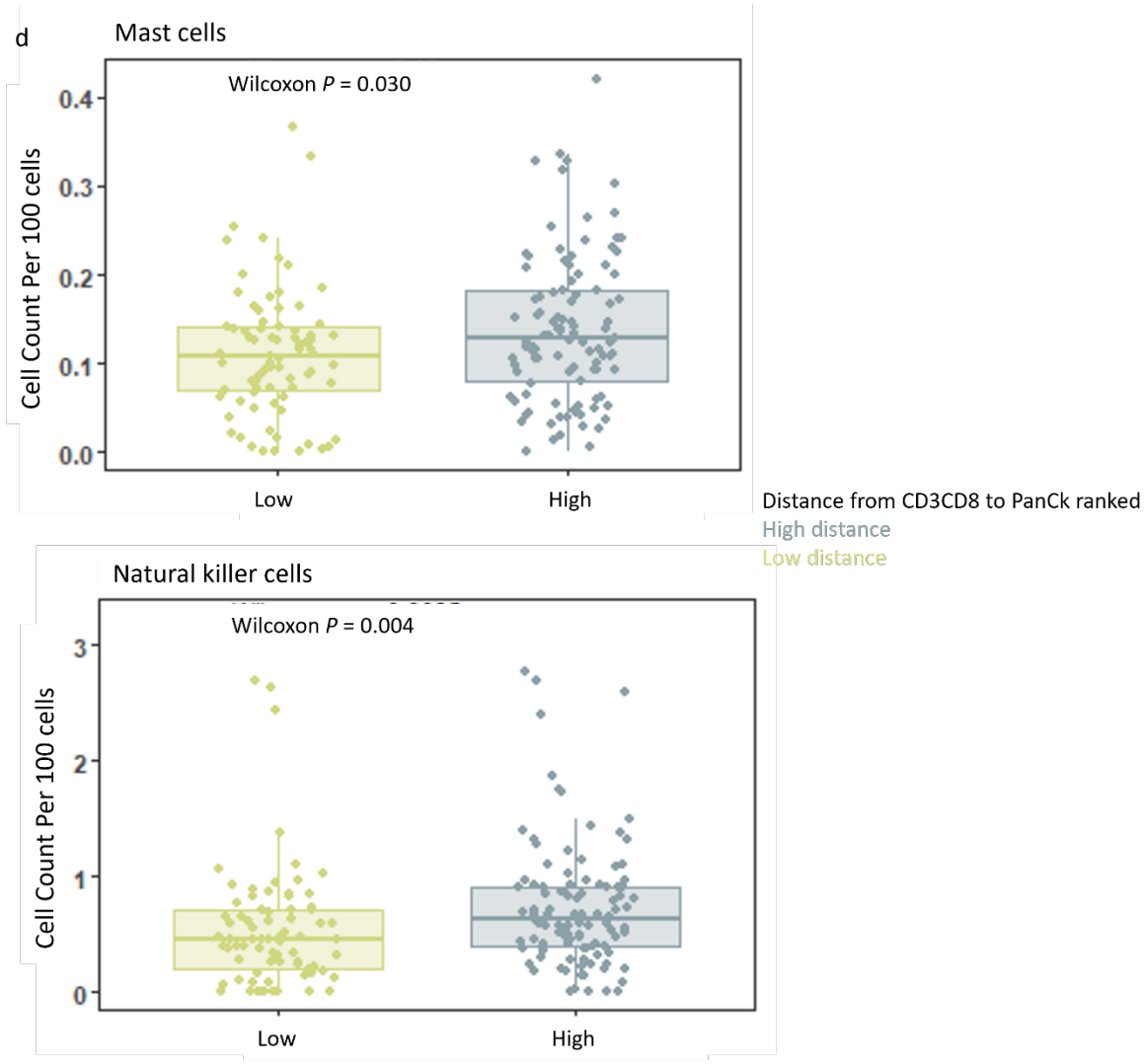


**Figure 6.8.d Geneset enrichment and immune cell deconvolution of neoadjuvant PDAC based on comparison of distance from CD3CD8 to PanCkhigh versus distance from CD3CD8 to PanCklow.** *Boxplots demonstrate estimated immune cell expression per 100 cells in d). low and high ranked distances from CD3CD8 to PanCk. Wilcoxon test with adjusted p value was used.*

## 6.3 Single cell B cell, T cell and dendritic cell signature across the naïve PDAC landscape

Previous Spatial Proteomic and Spatial Transcriptomic demonstrated recurrent immune cell trends within naïve pancreatic cancer (chapter 3, 6 and 6.2). Both geneset enrichment analysis and immune cell deconvolution estimates in the naïve pancreatic cancer cohort demonstrated a mixture of elevated B cells, T cells and dendritic cells repeatedly associated with subgroups associated with better outcome. Furthermore, regional Spatial Protein work in a separate naïve cohort demonstrated elevated T cell and B cell protein signature correlated with improved prognosis (chapter 3.12). Counterintuitively, two groups, B7-H3 ranked (chapter 6.3.5) and nearest neighbour distance from CD68 to PanCk ranked groups (chapter 6.2.2), presented with the opposite pattern within their respective high survivor associated subgroup. Concordance of regional protein signature landscape with single cell protein expression landscape was investigated. The three most biologically interesting immune cells, T cells, B cells and dendritic cells, were explored using the PhenoCycler™ assay on a direct serial section from the same naïve TMA used in chapter 6 (figure 6.9.a and table 6.1). Although this assay included a variety of markers, analysis was limited to cytotoxic T cells, helper T cells, B cells and dendritic cells (figure 6.9.b-c). Where possible, cell types were further subtyped into cell state using active/inactive markers (figure 6.9.c).

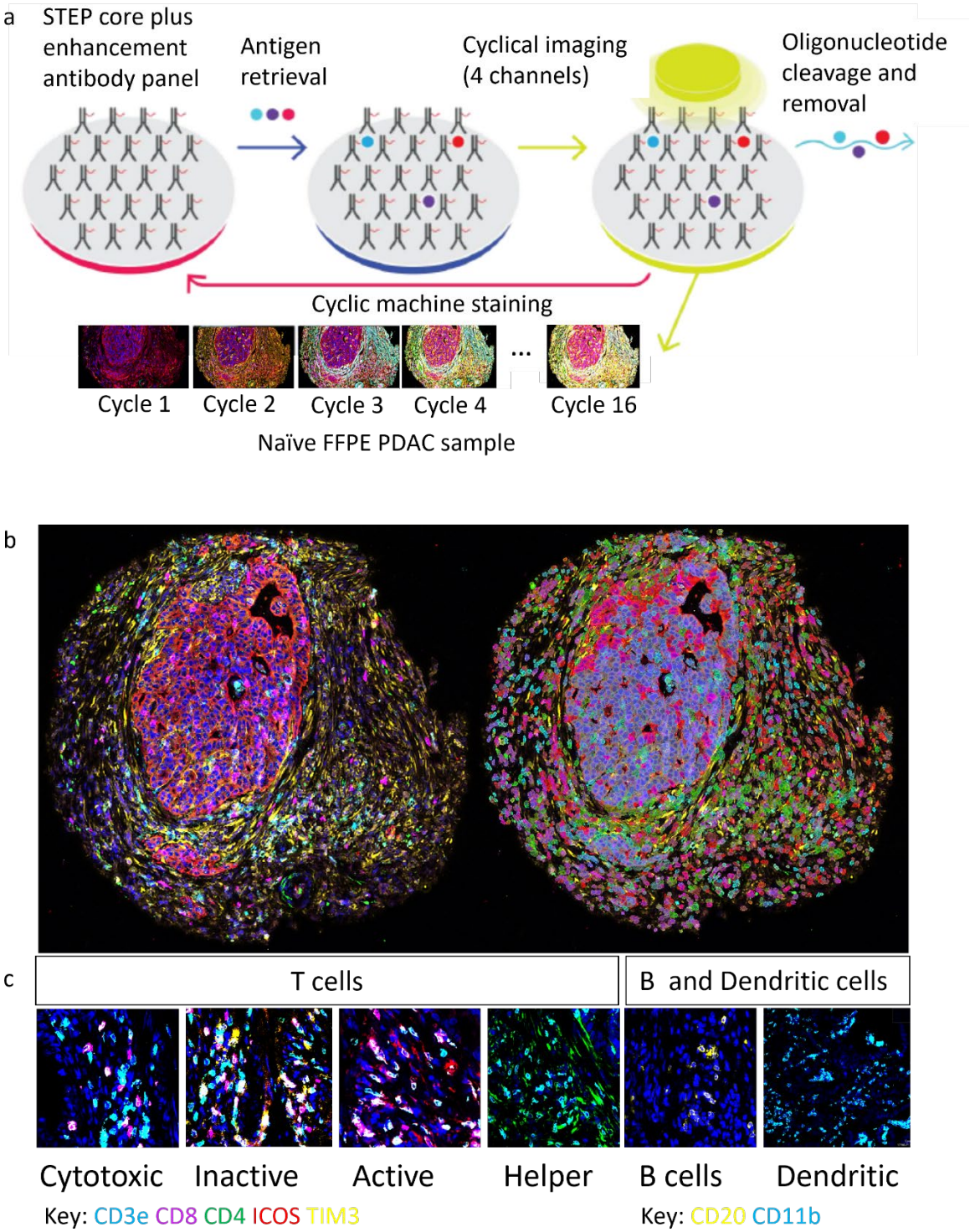


**Figure 6.9.a-c Deep single cell phenotyping in naïve pancreatic cancer using PhenoCycler.** *Technology access program using STEP core plus enhancement antibody panel a). PhenoCycler method overview schematic adapted with permission from Akoya®, showing cyclical oligonucleotide staining, including antibody panel, antigen retrieval, four channel imaging, cleavage and removal, cyclical process occurs up to 16 times, b). example naïve core with full panel shown (left) and false image overlay (right), c). phenotypes included in analysis, split into cytotoxic T cells (CD3e+CD8+), active T cells (CD3e+CD8+ICOS+), inactive T cells (CD3e+CD8+TIM3+), helper T cells (CD3e+CD4+), B cells (CD20) and dendritic cells (CD11b).*

Survival analysis confirmed high levels of B cells (CD20) (p=0.041) and helper T cells (CD3CD4) (p=0.004) correlated with increased disease specific survival (figure 6.10.a-b). Additionally, a non-significant correlation between high levels of dendritic cells (CD11b) and survival was observed (figure 6.10.c). This assay produced an unexpected oversaturated signal intensity, with high levels of background, making it difficult to confidently phenotype. Furthermore, it lacked a suitable B7-H3 protein marker, prompting exploration of an alternative high plex protein method.

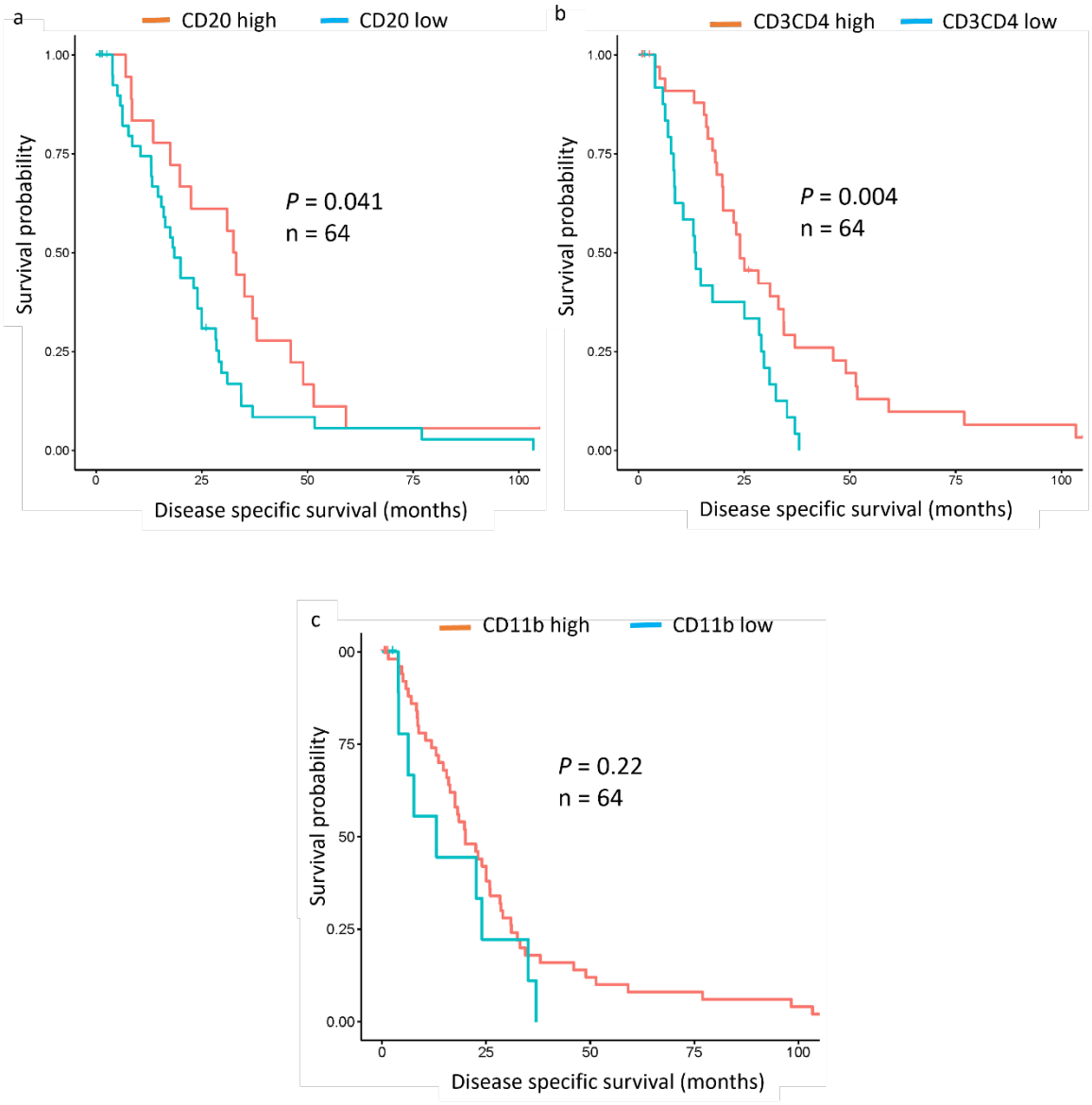


**Figure 6.10.a-c Naïve immune cell density association with DSS.** *Kaplan-Meier curves (disease specific survival in months) stratified by mIF protein marker expression (Log-Rank Mantel-cox test) for a). CD20 (B cells) b). CD3CD4 ( Helper T cells), and c). CD11b (neutrophils).*

## 6.4 Single cell protein analysis of T cell and B cell signatures across the naïve and neoadjuvant landscape

In late 2023, Nanostring® released a single cell, subcellar protein assay tailored for immune oncology. The panel consists of up to 60 markers, with well-defined T cell, B cell and dendritic subsets, as well as immune checkpoint marker B7-H3. This assay was performed to further explore the concordance between regional Spatial Transcriptomic and protein with single cell protein expression. The assay works relatively similarly to the cyclical fluorescent in situ hybridization imaging method as seen in the Phenocycler™ assay above (chapter 6.3), with the added benefit of robust probe design, automatic AI cell segmentation and instant expression readout (figure 6.11.a-b). This panel was applied on serial sections of the naïve cohort and neoadjuvant cohorts (table 6.1). Analysis was carried out in TMA cores.

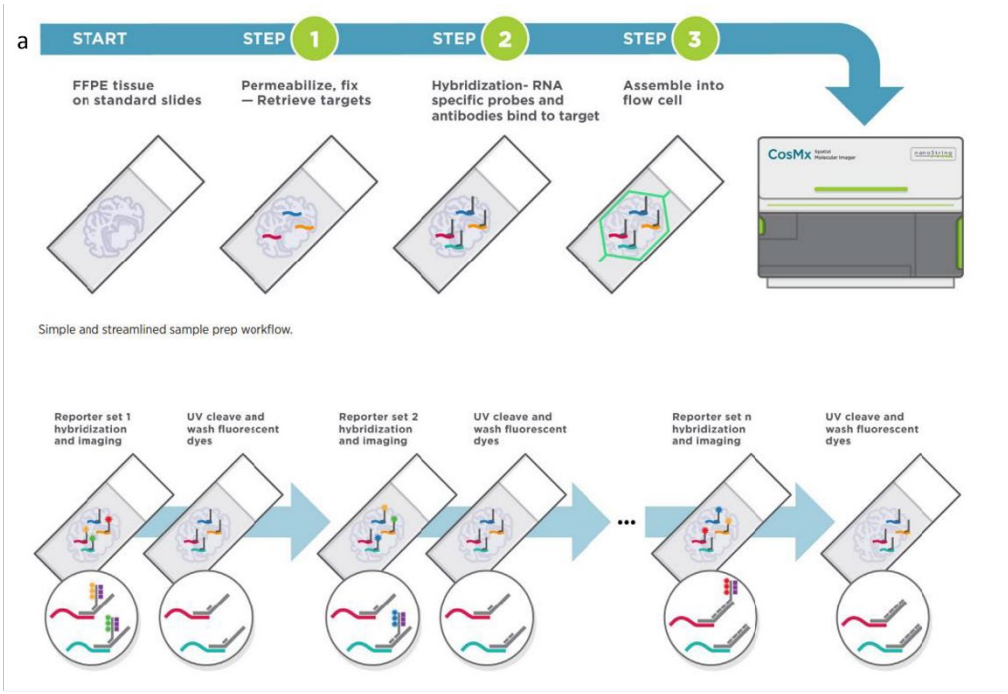


**Figure 6.11.a-b Deep single cell phenotyping in naïve pancreatic cancer using CosMx™ protein panel**, a). *CosMx™ Method overview schematic showing diagram with permission from Nanostring. FFPE slide undergo sample preparation workflow, exposing proteins for hybridization*

*and performing up to 5 plex immunofluorescence for visualisation. Flow cell is assembled and sample placed into the machine to undergo cyclical reporter set hybridisation, z stack imaging and ultraviolet cleavage/washing steps. This cycle repeats up to 16 times with count data per cell available as soon the run finishes b). example naïve core treated with 60 plex protein panel (left), markers shown include EpCAM+ (green), CD3+CD4+ (yellow), CD11b+CD11c+ (cyan), CD19+CD20+ (purple), CD8 (red) and B7-H3 (magenta), zoomed in cell segmentation (right) using native CosMx™ option, cellpose.*

### 6.4.1 Cell typing

Celesta is the recommended cell typing method for CosMx™ protein assays, however this algorithm lacks a B7-H3 based cell population. Instead, an exploratory phenotyping method using Seurat was trialled (chapter 2.6.6). Unsupervised dimensional reduction in naive samples demonstrated 34 distinct clusters (figure 6.12.a). B7-H3 expression appeared relatively dispersed, appearing in 3 ‘hotspots’ (figure 6.12.b). Distinct clusters associated with B cell, T cell, dendritic cell specific markers (figure 6.12.b). The top unique makers associated with each cluster were then used to classify the dominant cell type (figure 6.13). Initial cluster classification was limited to phenotypes of interest. This resulted in cluster 14 associated with B cells markers, cluster 4 associated with CD8 T cells and cluster 3 associated with CD4 T cells (figure 6.13). B7-H3 associated with 3 major clusters, cluster 5, cluster 12 and cluster 20 (figure 6.13). Unexpectedly, dendritic markers appeared in a range of clusters including cluster 0, making it more difficult to accurately cluster (figure 6.13).

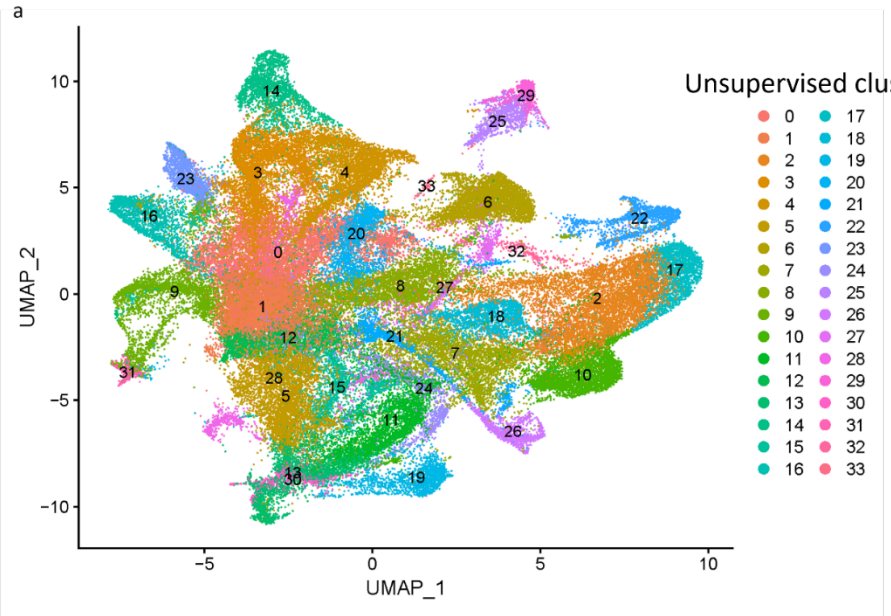


**Figure 6.12.a. Naïve single cell protein UMAP clustering with Seurat.** *Unbiased cell clustering UMAP in 2 dimensions showing a). cluster labels. Most common markers used to distinguish B cells (CD20, CD19, IgD), T cells (CD3, CD4, CD8), Dendritic cells (CD11b, CD11c, CD123) and B7-H3 are represented.*

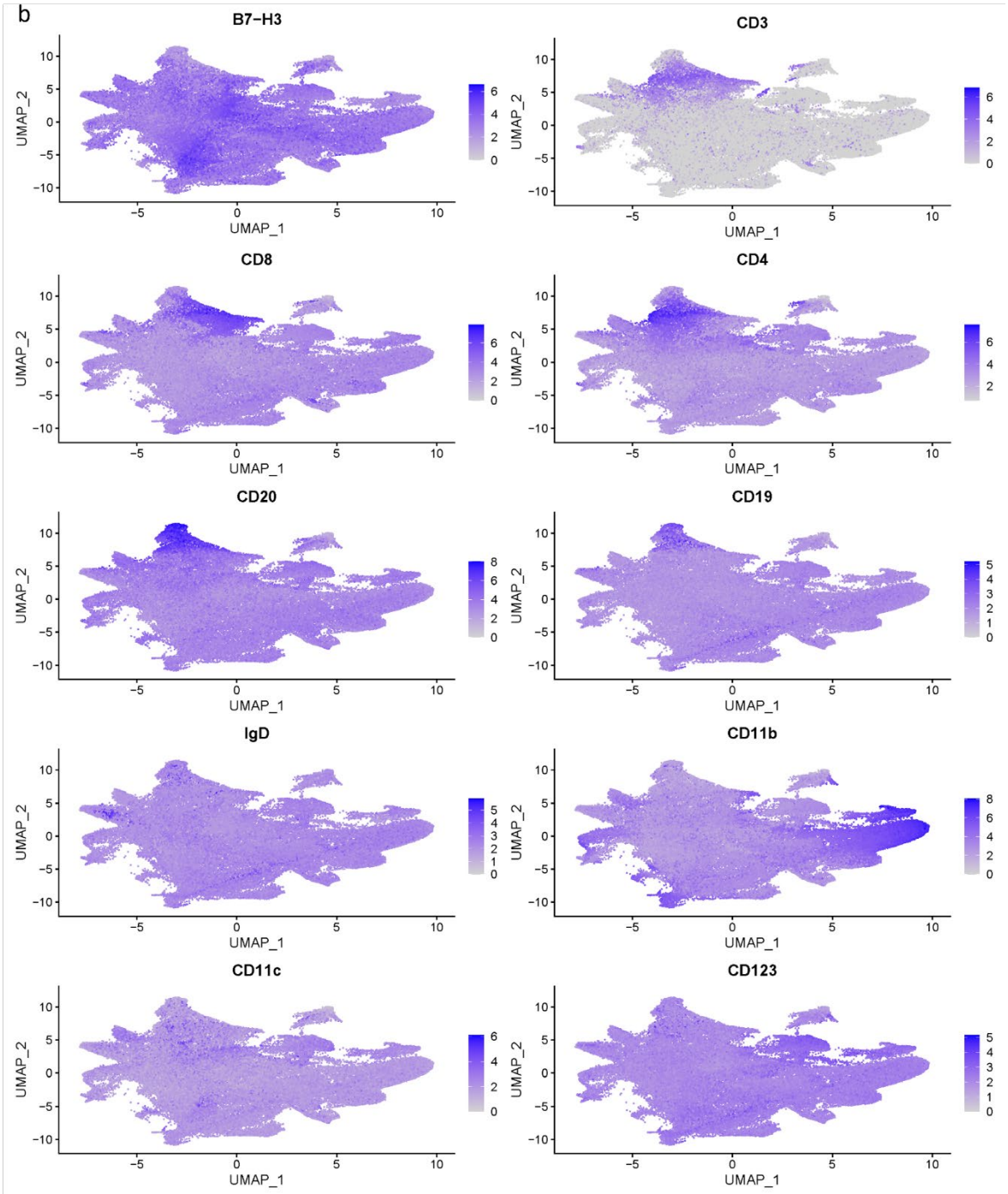


**Figure 6.12.b. Naïve single cell protein UMAP clustering with Seurat.** *Unbiased cell clustering UMAP in 2 dimensions showing b). phenotype specific marker density. Most common markers used to distinguish B cells (CD20, CD19, IgD), T cells (CD3, CD4, CD8), Dendritic cells (CD11b, CD11c, CD123) and B7-H3 are represented.*

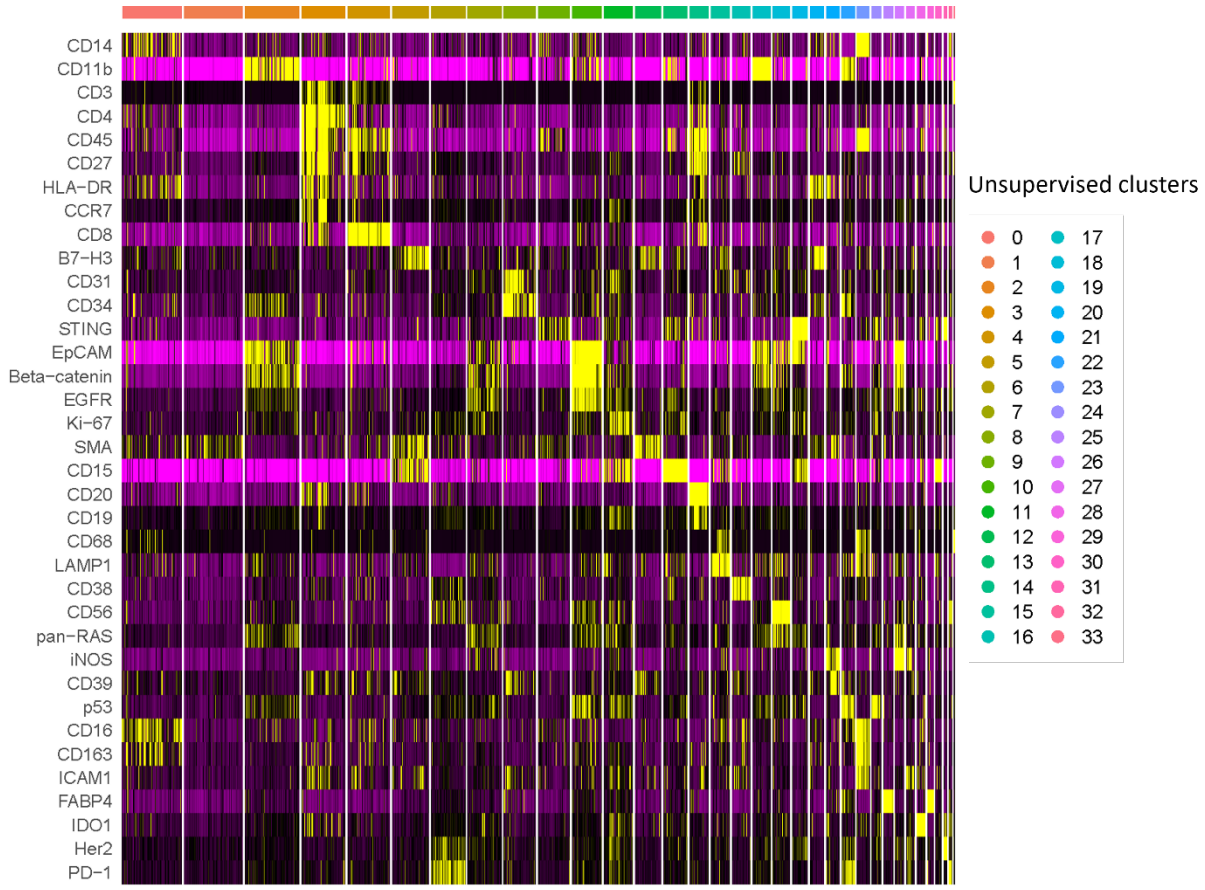


**Figure 6.13 Naïve single cell protein clustered heatmap with Seurat.** *Showing top differentially expressed markers that distinguish between each cluster. Cluster 14 was distinguished by B cell markers (CD20, CD19, CD27), cluster 4 was distinguished by T cell markers (CD3, CD8), cluster 3 was distinguished by T cell markers (CD3, CD4). B7-H3 associated with cluster 5, 12 and 20.*

The same methods were used to phenotype the combined neoadjuvant cohorts, showing 46 clustering patterns (figure 6.14.a). Compared to naïve samples (figure 6.12.a), distinct differences were observed between cluster number generated, space occupied, as well as discrete markers differentiating between the naïve and neoadjuvant clusters. In total, almost all top markers distinguishing naïve clusters, were also expressed in neoadjuvant samples. Comparatively, almost 1/3 of distinguishing markers within the neoadjuvant cohort were unique. As expected, neoadjuvant clusters were more complex, making it difficult to distinguish between the dominant signature within clusters. B cell markers were elevated in a wide range of clusters including clusters 2,10, 18, 24 and 34 (figure 6.14.b). CD8 T cell markers were enriched in cluster 8 and cluster 35, and CD4 T cell markers were enriched in cluster 9 and cluster 16. Dendritic markers were enriched in a wide range of clusters including 13, 15, 23, 36 among others (figure 6.14.b). Furthermore B7-H3 expression was upregulated in 4 different clusters, 4, 17, 27 and 41 (figure 6.14.b).

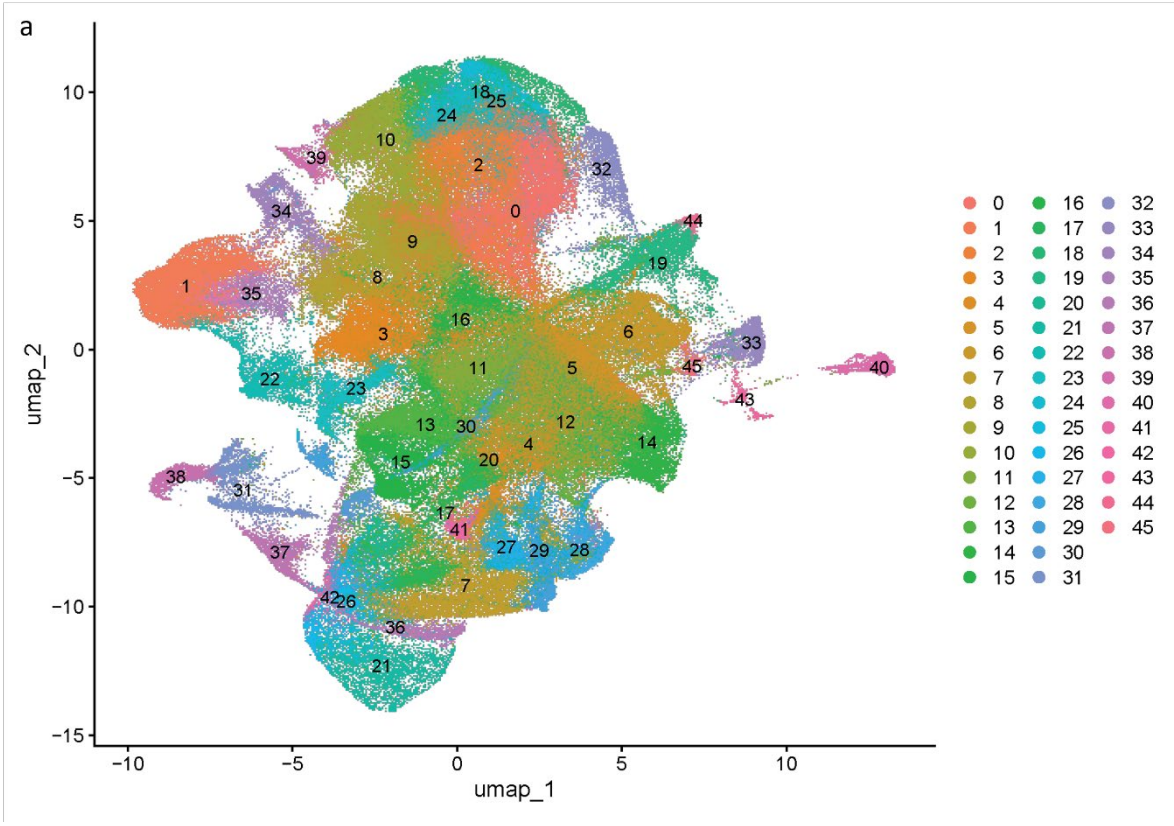


**Figure 6.14.a Neoadjuvant single cell protein clustering with Seurat.** *Unbiased cell clustering UMAP in 2 dimensions showing a). UMAP with cluster labels. B cell markers were enriched in clusters 2, 10, 18, 24 and 34, CD8 T cell markers were enriched in cluster 8 and 35, CD4 T cell markers were enriched in cluster 9 and 16, dendritic markers were enriched in cluster 13, 15, 23 and 36, and B7-H3 marker was enriched in cluster 4, 17, 27 and 41.*

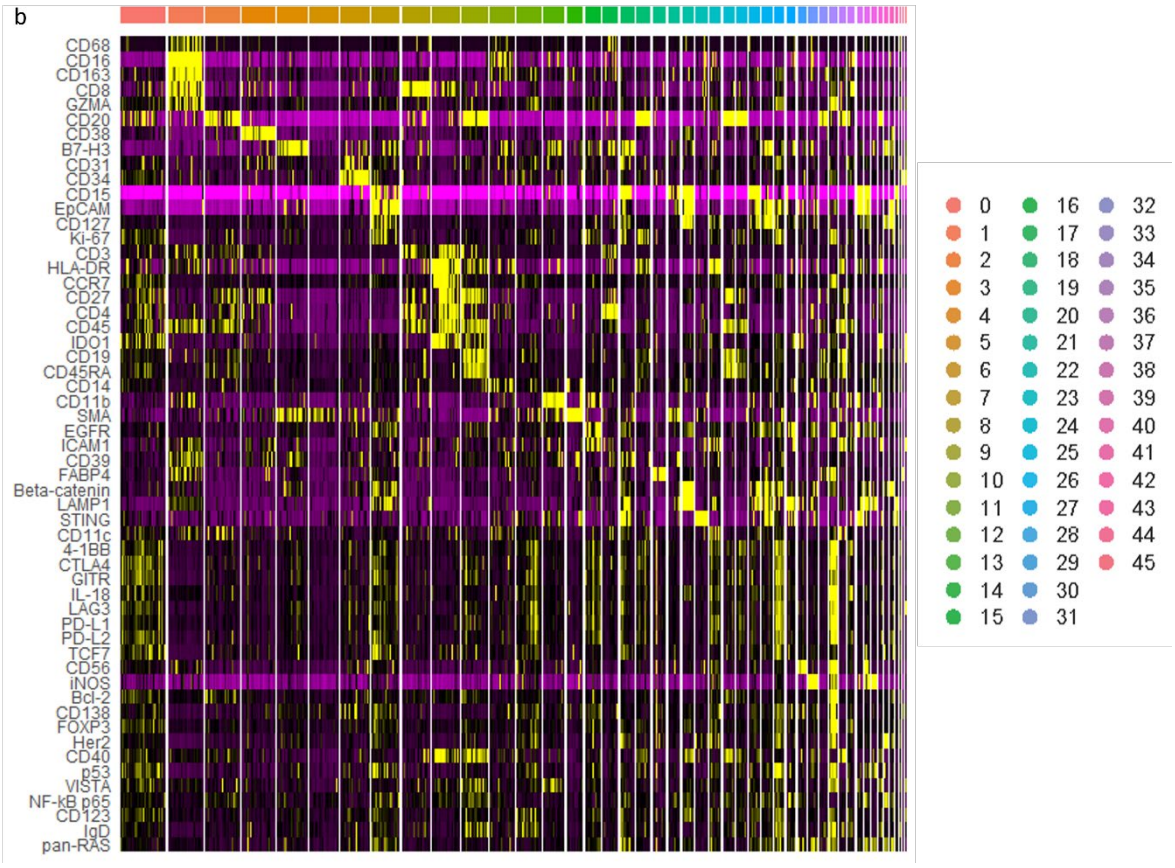


**Figure 6.14.b Neoadjuvant single cell protein clustering with Seurat.** *Unbiased cell clustering in 2 dimensions showing b). Clustered heatmap showing top unique protein markers that distinguish between each cluster. B cell markers were enriched in clusters 2, 10, 18, 24 and 34, CD8 T cell markers were enriched in cluster 8 and 35, CD4 T cell markers were enriched in cluster 9 and 16, dendritic markers were enriched in cluster 13, 15, 23 and 36, and B7-H3 marker was enriched in cluster 4, 17, 27 and 41.*

### 6.4.2 B7-H3 expression and associated cell types in naïve and neoadjuvant PDAC

Despite the vast intertest in B7-H3 as a potential target for checkpoint inhibition, little is known about the cell types it associates with. As shown above, B7-H3 appeared in 3 major clusters within the naïve cohort (figure 6.13). These clusters also presented with log fold increased expression of CD15 and αSMA (cluster 5), αSMA and CD39 (cluster 12), and HLA-DR with CD14 (cluster 20) (table 6.2). Additionally, neoadjuvant patients presented with 4 clusters where B7-H3 was amongst the highest expressing proteins (figure 6.14). These clusters associated with a varied range of markers. B7-H3 related clusters presented with B7-H3 alone (cluster 4), CD39 (cluster 17), STING, CD127, LAMP1 (cluster 27), and EpCAM, β-catenin, CD38, NF-κB p65 (cluster 41) (table 6.2).

| Cohort | Cluster | Protein marker | Log2 Fold change |
|---|---|---|---|
| Naïve | 5 | B7-H3 | 1.666 |
| Naïve | 5 | αSMA | 1.493 |
| Naïve | 5 | CD15 | 1.024 |
| Naïve | 12 | αSMA | 1.743 |
| Naïve | 12 | B7-H3 | 1.617 |
| Naïve | 12 | CD39 | 1.121 |
| Naïve | 20 | HLA-DR | 2.675 |
| Naïve | 20 | CD14 | 1.911 |
| Naïve | 20 | B7-H3 | 1.375 |
| Neoadjuvant | 4 | B7-H3 | 2.027 |
| Neoadjuvant | 17 | B7-H3 | 2.540 |
| Neoadjuvant | 17 | CD39 | 1.845 |
| Neoadjuvant | 27 | STING | 2.032 |
| Neoadjuvant | 27 | B7-H3 | 1.610 |
| Neoadjuvant | 27 | CD127 | 2.246 |
| Neoadjuvant | 27 | LAMP1 | 1.901 |
| Neoadjuvant | 41 | EpCAM | 2.487 |
| Neoadjuvant | 41 | B7-H3 | 1.501 |
| Neoadjuvant | 41 | Beta-catenin | 2.929 |
| Neoadjuvant | 41 | CD127 | 2.592 |
| Neoadjuvant | 41 | CD38 | 1.726 |
| Neoadjuvant | 41 | NF-κB p65 | 1.660 |

**Table 6.2 B7-H3 clusters and associated top differentially expressed proteins in naïve and neoadjuvant pancreatic cancer.** *Log2 fold change expression for each marker in naïve and neoadjuvant cohort demonstrated, with Seurat cluster is indicated.*

Next, visual co-expression with B7-H3 was explored. Naïve cluster 5 associated with B7-H3, CD15 and αSMA. Co-expression was seen often between B7-H3 and myofibroblast marker αSMA alone (figure 6.15.a bottom right), and with B7-H3, CD15 and αSMA together (figure 6.15.a). Cluster 12 associated with B7-H3, αSMA and CD39 markers, with co-expression seen between all three markers (figure 6.15.b). Finally, naïve cluster 20 marker co-expression was seen for B7-H3, HLA-DR and CD14 (figure 6.15.c), likewise frequent B7-H3 and HLA-DR co-expression without CD14 was also seen in naïve samples (figure 6.15.c bottom right). All three clusters are defined by immune rich markers. CD15 expression has been reported in neutrophil cells, CD39 expression with dysregulated T cell function, and both HLA-DR and CD14 expressed on macrophages [313, 314].

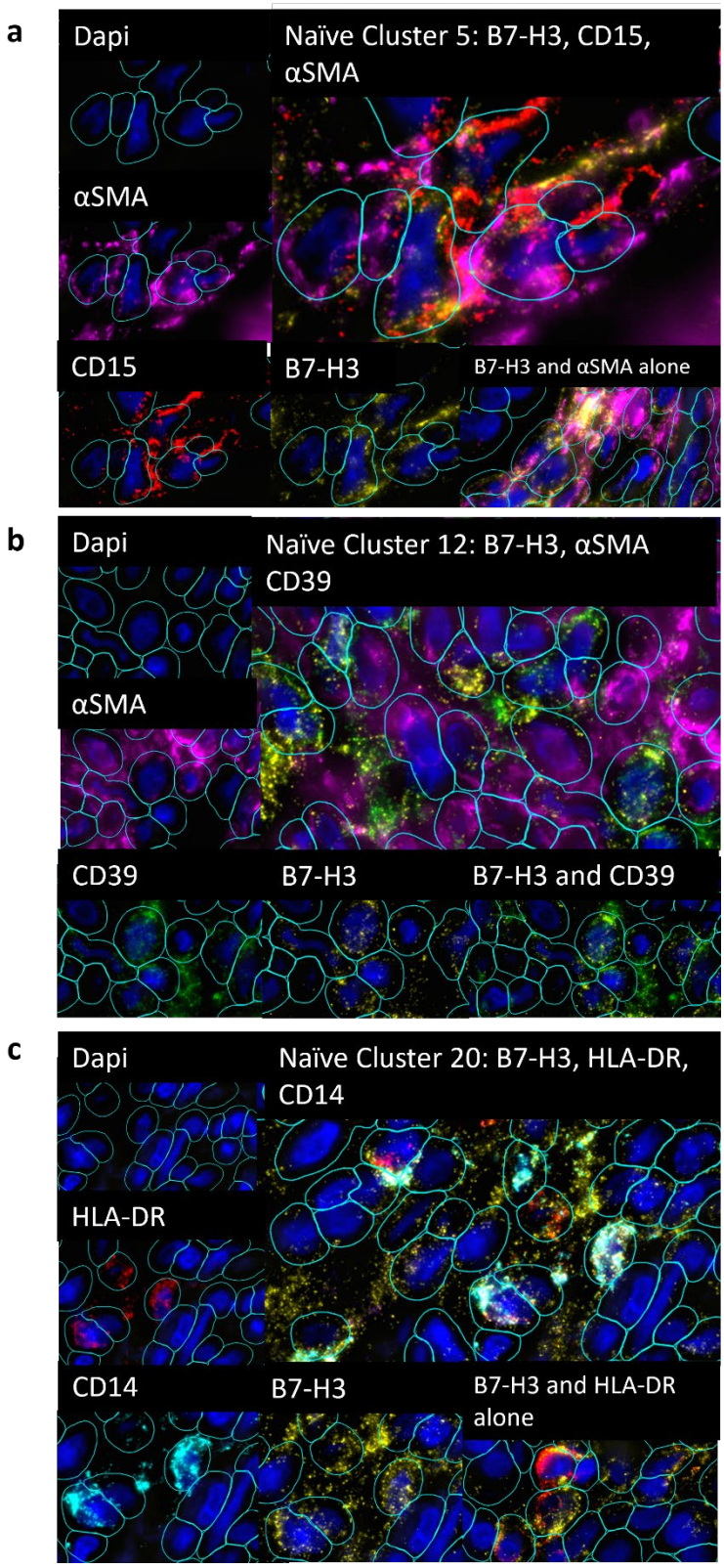


**Figure 6.15.a-c B7-H3 naïve cluster visual co-expression with top expressing markers** *in example images demonstrating a). Cluster 5, showing a fibroblast /neutrophil signature with B7-H3, αSMA and CD15, bottom right image 'B7-H3 and aSMA alone' shows different cells within the same core, only expressing B7-H3 and aSMA b). Cluster 12, showing fibroblast/exhausted T cell signature with B7-H3, αSMA and CD39 c). Cluster 20, showing macrophage signature B7-H3, HLA-DR and CD14, bottom right image 'B7-H3 and HLA-DR alone' shows different cells within the same core, only expressing B7-H3 and HLA-DR*

Within the neoadjuvant cohort, 4 major clusters were found, one of which (cluster 4) was only defined by B7-H3. In contrast, cluster 17 was defined by elevated B7-H3 and T cell dysregulation marker CD39, similarly to naïve cluster 12, with co-expression seen (figure 6.16.a). Varied protein markers were upregulated in Clusters 27 and 41 (table 6.1). Co-expression was confirmed with B7-H3, CD127 and STING as indicated by cluster 27 (figure 6.16.b). Furthermore, frequent co-expression was seen of B7-H3 cells with STING. Notably, CD127 and STING can all express in T lymphocytes [315-317]. Cluster 41 was defined by immune related and epithelial related markers, therefore these markers were investigated by cell lineage to check for B7-H3 co-localisation. Two distinct B7-H3 cell types were observed within this cluster. The first cell type presented as B7-H3/EpCAM/β-catenin positive cells, and were predominantly located in the epithelium, though not all EpCAM+β-catenin+ cells expressed B7-H3 (figure 6.16.c). The second cell type expressed as B7-H3/CD38/NF-κB p65 positive cells and were observed in the tumour microenvironment (figure 6.16.d). Both CD38 and NF-κB p65 expression have been related to B cells [318, 319]. Notably, naïve and neoadjuvant B7-H3 related clusters were characterised by distinctly different markers. The only overlap seen was between naïve cluster 12 and neoadjuvant cluster 17, with B7-H3 co-expressing associating with ‘exhausted’ T cell marker CD39.

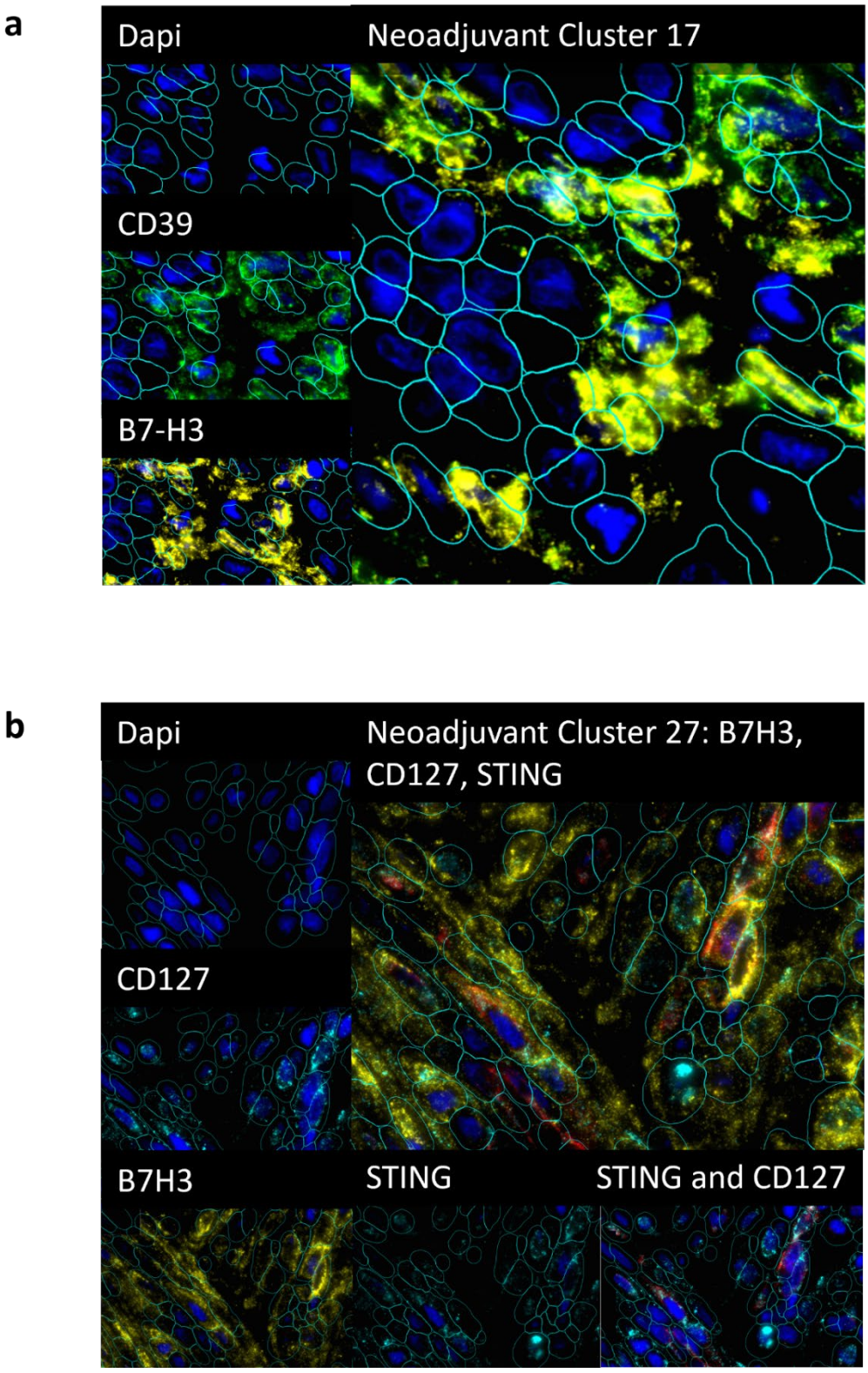


**Figure 6.16.a-b B7-H3 neoadjuvant cluster visual co-expression with top expressing markers** *in a). Cluster 17, showing an exhausted T cell signature with B7-H3 and CD39 b). Cluster 27, showing T lymphocyte signature B7-H3, CD127, and STING.*

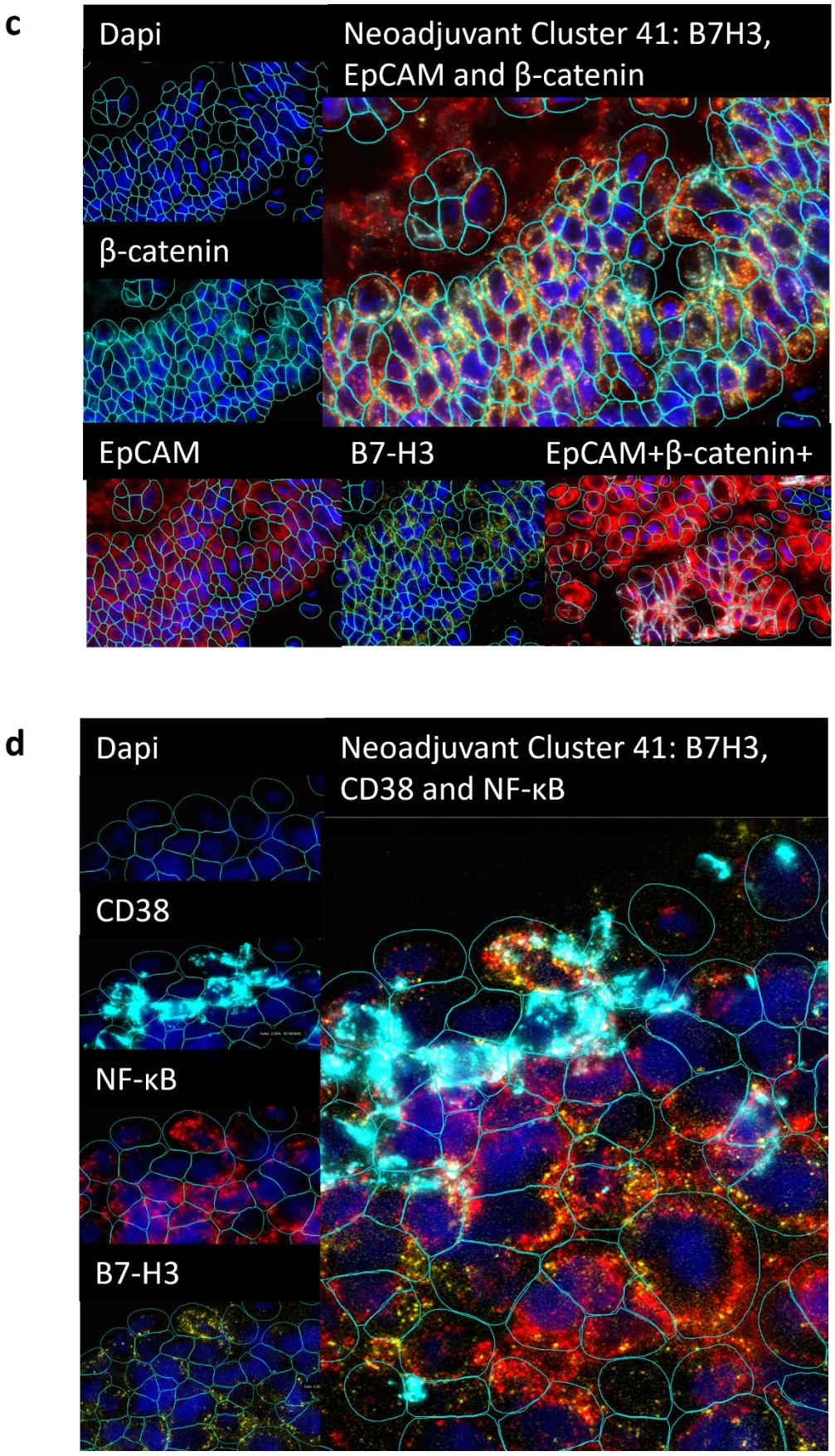


**Figure 6.16.c-d B7-H3 neoadjuvant cluster visual co-expression with top expressing markers** *in c). Cluster 41, showing an epithelial signature with B7-H3, EpCAM and β-catenin d). Cluster 41, showing B cell signature B7-H3, CD38 and NF-κB.*

### 6.4.3 NeoadjXRT subtyping

Assuming the differences in B7-H3 clusters observed above is in some-part related to a cell type or cell function switch triggered by treatment, the effect of neoadjuvant treatment type on clustering was investigated. Dimension reduction using Seurat native UMAP function demonstrated distinct clustering differences between chemotherapy treated and chemoradiotherapy treated pancreatic cancer, indicating possible cell type variances between the two groups (figure 6.17). Large differences are seen between neoadjuvant chemotherapy and chemoradiotherapy samples, indicated by cluster pattern, space occupation, as well as cluster generation. Overlap of 34 protein markers was observed between chemotherapy and chemoradiotherapy clusters, with 6 unique markers in both treatment subsets. Chemotherapy treated samples generated 31 clusters, 3 of which demonstrated significant differential elevated B7-H3 expression (clusters 26, 28 and 30) (figure 6.18.a). In contrast, chemoradiotherapy treated samples presented with 28 clusters, with 4 clusters (clusters 8, 13, 14 and 17) demonstrating increased B7-H3 expression (figure 6.18.b). Both treatment types associated with epithelial, T lymphocyte and macrophage heavy B7-H3 clusters, although the markers within each cluster differed considerably and were mixed.

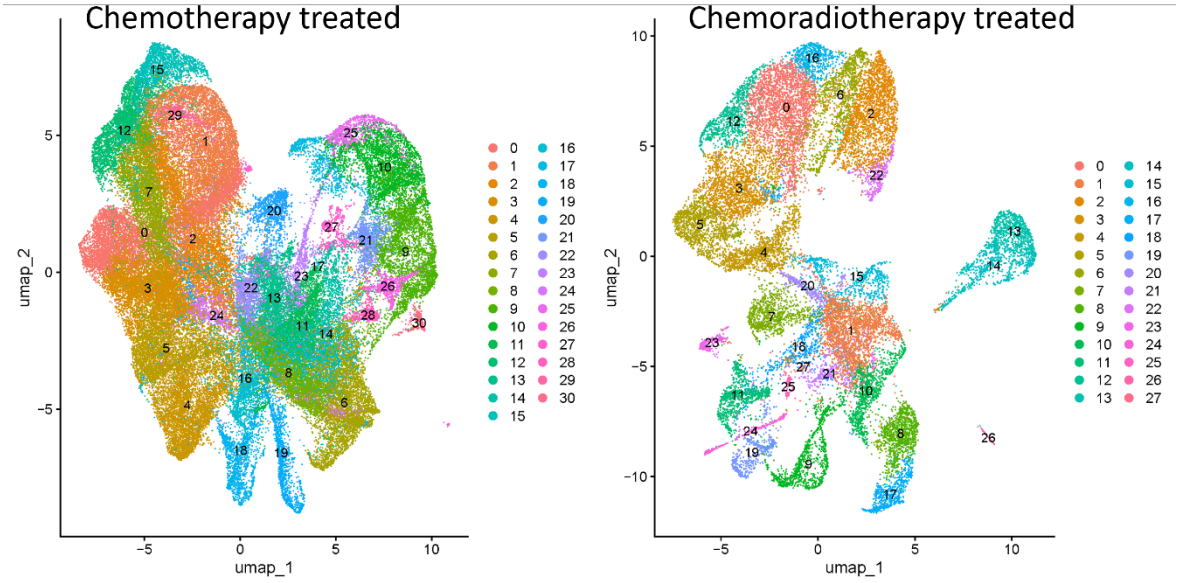


**Figure 6.17 Chemotherapy and chemoradiotherapy single cell protein UMAP clustering with Seurat.** *Unbiased cell clustering UMAP in 2 dimensions showing differences in clustering produced in chemotherapy treated (left) and chemoradiotherapy treated (right) samples.*

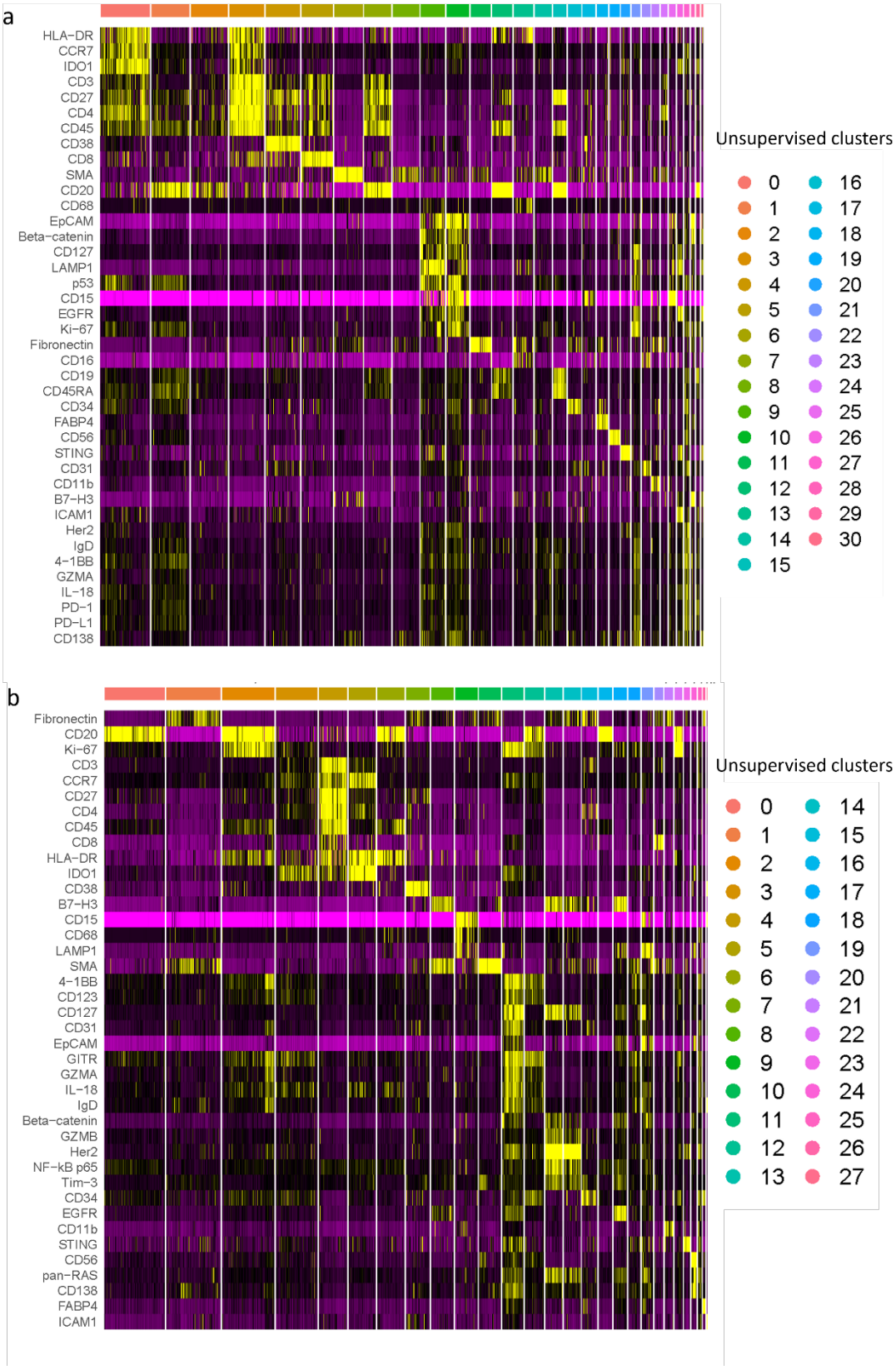


**Figure 6.18.a-b Neoadjuvant treatment single cell protein clustered heatmap with Seurat.** *Showing top differentially expressed markers that distinguish between each cluster in a). chemotherapy treated patients, b). chemoradiotherapy treated patients.*

## 6.4.4 Cluster density in naïve and neoadjuvant pancreatic cancer

Upon satisfactory cluster assignment, density of well-established cell types and the B7-H3 related clusters were investigated within naïve and neoadjuvant cohorts. The naïve cohort demonstrated a non-significant increased density of B cell related clusters (figure 6.19.a), along with significant elevated median density of T cell exhausted cluster 12 when compared to macrophage cluster 20 (figure 6.19.b). Within the neoadjuvant cohort, the highest density clusters seen were B cell and CD4 T cell clusters, as well as significantly elevated B cell related clusters compared to CD8 T cell clusters (figure 6.19.c). Furthermore, significant differences were observed between the two T cell related B7-H3 clusters, with elevated levels of exhausted T cell related cluster 17 seen. Additionally, cluster 41, associated with both epithelial and immune expression, has the smallest density within the neoadjuvant cohort, as well as being significantly reduced when compared to cluster 27 (figure 6.19.d). Moreover, non-significant elevated density of cluster 13 in chemoradiotherapy treated patients was observed (supplementary figure 8.15).

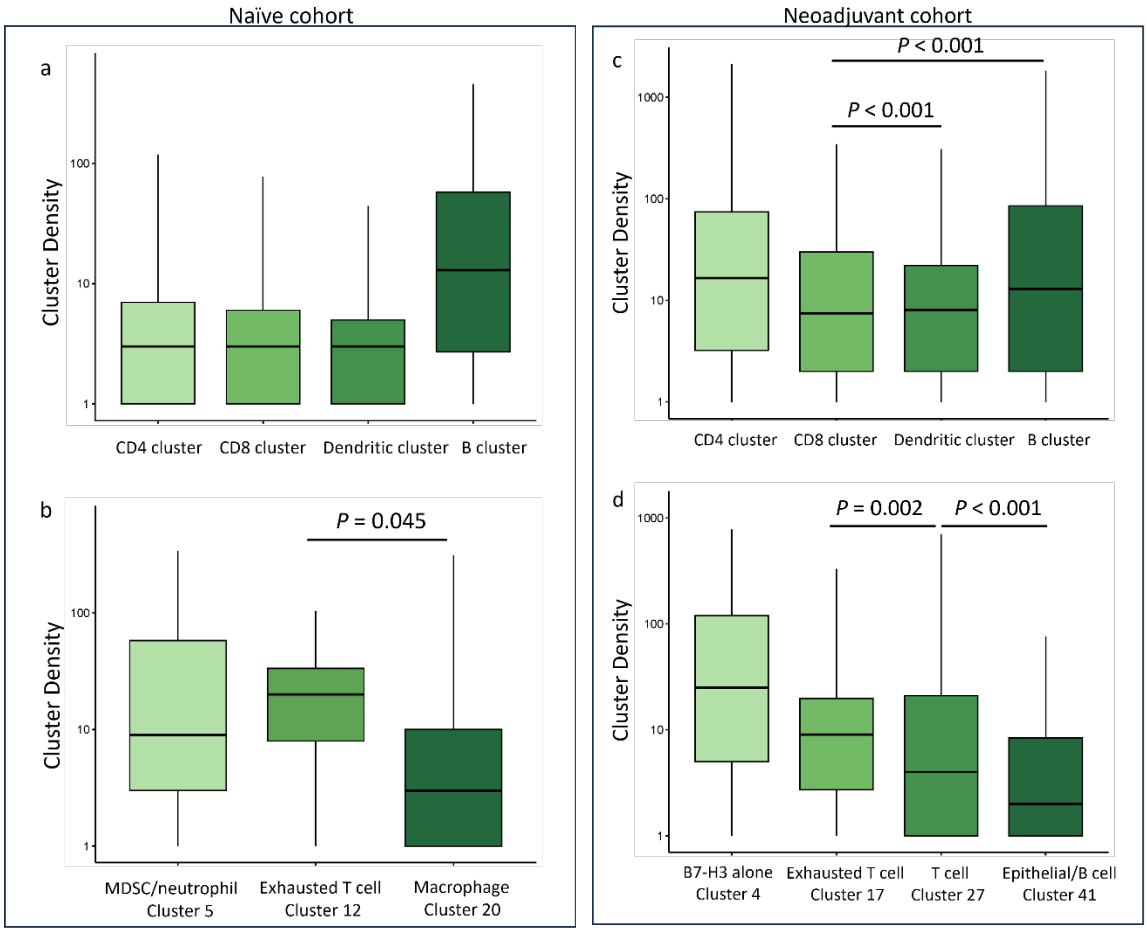


**Figure 6.19.a-d Density of Seurat clusters associated immune cell clusters** *in naïve and neoadjuvant pancreatic cancer cohorts. Boxplots shows density per grouped immune cluster in a). naïve B cell, CD4, CD8 and dendritic clusters, b). naïve B7-H3 related clusters, c). neoadjuvant B cell, CD4, CD8 and dendritic clusters, d). neoadjuvant B7-H3 related clusters. Statistics generated*

*by Kruskal-Wallis test, only significant p values shown.*

### 6.4.5 Nearest neighbours surrounding B7-H3

Previous protein based results have demonstrated density alone can be insufficient to characterise the tumour immune microenvironment (chapter 3 and 4). Using nearest neighbour metrics, immune cell environment surrounding B7-H3 related clusters was investigated. Location of B7-H3 in comparison to clusters enriched in tumour cells, T cells, B cells and dendritic cells was explored. Dendritic cells consistently remain amongst the top 2 closest neighbours for all naïve B7-H3 clusters, along with CD4 helper T cells for clusters 12 and 5, and CD8 cytotoxic T cells for cluster 20 (figure 6.20.a). B cells were the furthest from cluster 5 and 20, and epithelial cells were furthest from cluster 12 (figure 6.20.a). Furthermore, cluster 20 also presented as one of the furthest phenotypes from cluster 12 and cluster 5 (figure 6.20.a). A shift in the populations surrounding B7-H3 related clusters within the neoadjuvant cohort was observed. Epithelial and CD4 helper T cells presented as some of the nearest neighbours for cluster 17 and 41, and cluster 4 and 27 respectively (figure 6.20.b). Additionally, B cells were the furthest away from clusters 4, 17 and 27, and dendritic cells were furthest from cluster 41 (figure 6.20.b). Finally, nearest neighbours across treatment types were explored. As expected, distinct patterns emerged, the most predominant nearest neighbour in chemotherapy treated for all B7-H3 related clusters were epithelial cells. Moreover, the furthest neighbour presented as B cells for cluster 26, CD8T cells for cluster 28, and CD4 T cells, CD8 T cells and B cells for cluster 30 (figure 6.21.a). In contrast, chemoradiotherapy treated B7-H3 clusters seemed to reside together, as indicated by B7-H3 clusters being the closest nearest neighbours. Moreover, epithelial and CD8 T cells were the furthest neighbours for cluster 13/14, and cluster 8/17 respectively (figure 6.21.b). Notably, the chemoradiotherapy treated subgroup is limited in patient number (n=27).

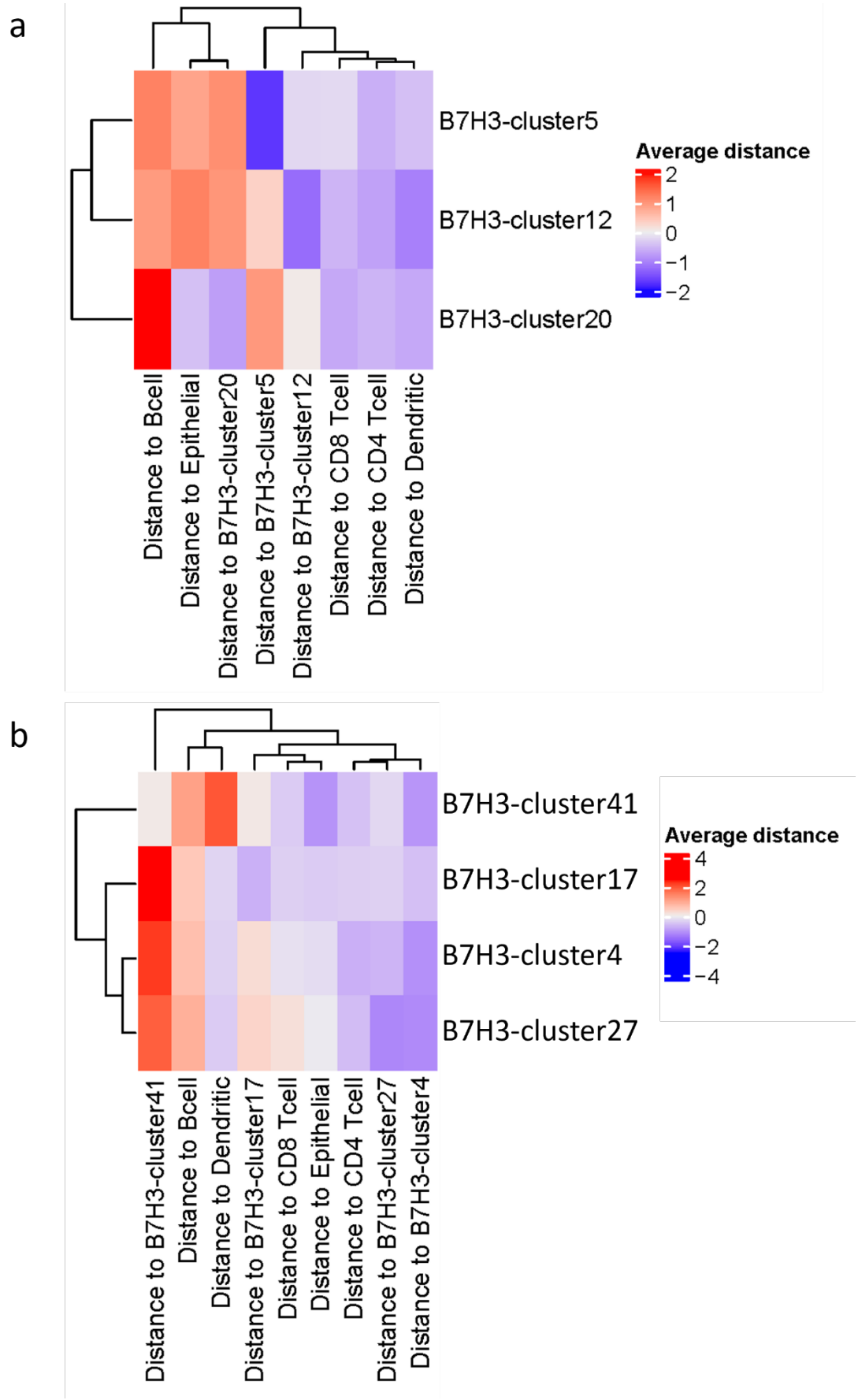


**Figure 6.20.a-b Average nearest neighbour distance for Seurat generated phenotypes in pancreatic cancer.** *Columns show the distance to phenotype, and rows show distance from phenotype. Filtered for B7-H3 related cluster nearest neighbour distances in a). Naïve cohort b). Neoadjuvant cohort. Average distance represented as a z score.*

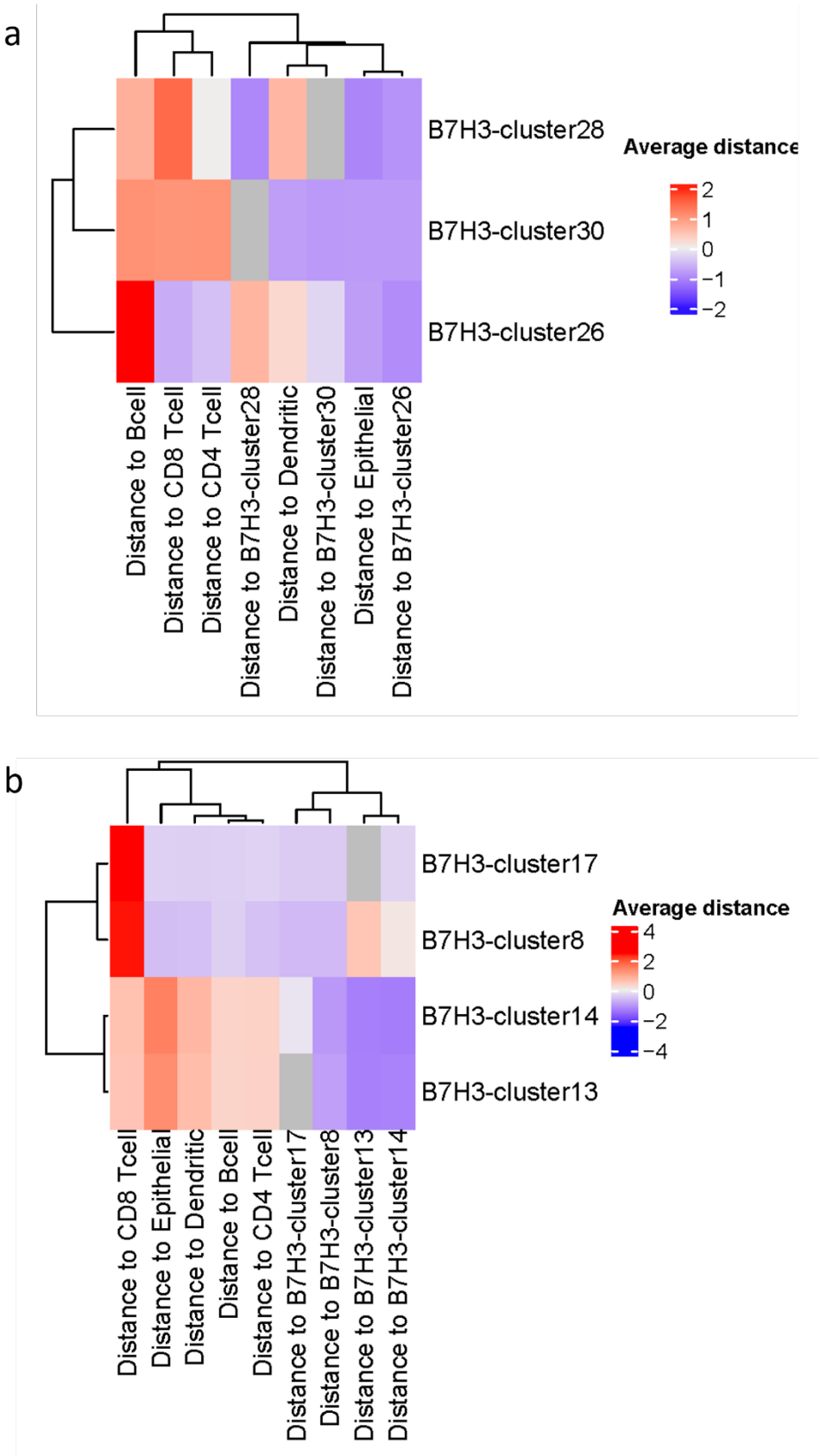


**Figure 6.21.a-b Average nearest neighbour distance for Seurat generated phenotypes in neoadjuvant pancreatic cancer.** *Columns show the distance to phenotype, and rows show distance from phenotype. Filtered for B7-H3 related cluster nearest neighbour distances in a). chemotherapy treated cohort b). chemoradiotherapy treated cohort. Average distance represented as a z score.*

## 6.4.6 Prognostic associations with cluster density

Upon satisfactory initial cluster characterisation, prognostic utility was investigated. Within the naïve cohort patients enriched in CD4 helper T cell (p=0.014) and CD8 cytotoxic T cells (p=0.007) had increased survival, replicating patterns seen in in chapter 3 and 6 (table 6.3). Likewise, reduction of B7-H3 enriched, T cell exhausted cluster 12 positively correlated with survival (p=0.003) (table 6.3). Mirroring chapter 4 trends, neoadjuvant patients with reduced levels of CD8 cytotoxic T cells (p<0.001) and CD4 helper T cells (p=0.006) associated with better prognosis (table 6.3). Furthermore, decreased density of B7-H3 cluster 4 (p=0.036) and B7-H3, T cell heavy cluster 27 (p=0.022) (table 6.3). Interestingly, only T cell related B7-H3 clusters demonstrated prognostic correlation in both naïve and neoadjuvant patients.

| Seurat clusters | Group | Cut-off method | Number | HR (95% CI) | P value |
|---|---|---|---|---|---|
| B cell cluster | Naïve | Rcutoff | 38 | 0.36(0.10-1.29) | 0.120 |
| CD4 T cell cluster | Naïve | Rcutoff | 38 | 0.07 (0.01-0.59) | 0.014 |
| CD8 T cell cluster | Naïve | Rcutoff | 38 | 0.14 (0.03-0.58) | 0.007 |
| Dendritic cell cluster | Naïve | Rcutoff | 38 | 2.06 (0.83-5.14) | 0.11 |
| Neutrophil/αSMA cluster 5 | Naïve | Rcutoff | 38 | 0.97 (0.43-2.21) | 0.46 |
| Exhausted T cell cluster 12 | Naïve | Rcutoff | 38 | 4.46 (1.67-11.9) | 0.003 |
| Macrophage cluster 20 | Naïve | Rcutoff | 38 | 0.49 (0.22-1.12) | 0.092 |
| B cell cluster | Neoadjuvant | Rcutoff | 61 | 2.04 (1.05-3.99) | 0.31 |
| CD4 T cell cluster | Neoadjuvant | Rcutoff | 61 | 2.43 (1.28-4.64) | 0.006 |
| CD8 T cell cluster | Neoadjuvant | Rcutoff | 61 | 2.81 (1.36-5.80) | <0.001 |
| Dendritic cell cluster | Neoadjuvant | Rcutoff | 61 | 1.68 (0.91-3.10) | 0.097 |
| B7-H3 cluster 4 | Neoadjuvant | Rcutoff | 61 | 1.89 (1.04-3.41) | 0.036 |
| Exhausted T cell cluster 17 | Neoadjuvant | Rcutoff | 61 | 1.49 (0.83-2.66) | 0.2 |
| T cell cluster 27 | Neoadjuvant | Rcutoff | 61 | 2.30 (1.13-4.68) | 0.022 |
| Epithelial/B cell cluster 41 | Neoadjuvant | Rcutoff | 61 | 1.69 (0.83-3.46) | 0.2 |

**Table 6.3 Summary of Seurat generated immune and B7-H3 related clusters for disease specific survival** *in whole core across naïve and neoadjuvant PDAC cohort. Cut-off method established (chapter 2.6.9). Log Rank (Mantel-Cox) p value and Univariate cox regression hazard ratio (HR) shown with 95% confidence interval (CI).*

## 6.5 Discussion

Immune cell density in pancreatic cancer remains one of the most consistently predictive prognostic tools within the research field. This trend repeated across the PDAC cohorts utilised within this study, notably CD3 and CD68 density in naïve patients, and CD3CD8 in neoadjuvant patients. To start unravelling biological differences between levels of immune cell expression, characterised phenotype groups were integrated with Spatial Transcriptomic data, allowing discovery of aberrated genes and pathways in epithelial, fibroblast, and immune rich segments. Relatively limited pathway differences were observed in αSMA-rich and immune-rich segments in CD3high and CD3low naïve patients. In particular, elevated cytotoxicity and B cell related pathways were observed. Interactions between T and B lymphocytes have been reportedly associated with prognostic benefit in cancer. This has been seen in terms of cellular location, triggering local inflammation in mouse models, as well as the presence of tertiary lymphoid structures within the tumour microenvironment [11, 171, 227]. Interestingly, epithelial CD3 ranked segments presented with a wide range of aberrated cell signalling pathways. In particular, JAK/STAT and type I INF signalling was reduced in CD3high epithelium. The JAK/STAT pathway is well reported to play an important role in the immune response, and chronic activation of this pathway promotes oncogenesis [80, 81, 320]. Comparatively, CD68 density in treatment-naïve patients presented with multiple significantly dysregulated pathways. Of note, epithelium from CD68low cases demonstrated reduced matrix remodelling and metastatic pathways, as well as MET and NO signalling. CD68low expression significantly correlates with improved survival amongst the naïve cohort as well as within the literature [238]. Upon investigating immune and αSMA segments, counterintuitive results were seen. CD68low segments presented with an immune barren landscape, whereas CD68high was enriched in various immune cell pathways. This pattern repeated when performing immune cell deconvolution, with macrophage expression being significantly reduced in CD68low samples, indicative of the concordance between deconvolution methods and actual protein expression. These results indicate that enrichment of immune pathway presence alone may be insufficient to predict outcome.
In the neoadjuvant cohort, CD3CD8+ T cells emerged as a significant predictive marker. Intriguingly, elevated levels correlated with poor survival, contradicting the central dogma [132, 255, 321]. This finding is not isolated; similar observations have been reported in similar cancer types, prompting investigation of pathways to help explain this phenomenon [322]. Interestingly, patients with elevated levels of CD3CD8 presented with increased EMT and p53 pathways in epithelial segments, as well as increased immortality and stemness in immune segments. Additionally, these patients demonstrated elevated T cell and B cell pathways, coupled with elevated T cell and B cell ‘exhaustion’.

Nearest neighbours were the most powerful spatial protein single cell metric within naïve and neoadjuvant cohorts as reported in chapter 3 and 4. The most prognostically significant categorised nearest neighbour patterns were extracted, comprising of distance from CD68+ to CD3+, and distance from CD68+ to PanCk+ within the naïve cohort, and distance from CD3CD8 to PanCk+ in the neoadjuvant cohort. Patients with short distances from CD68 to CD3 (CD3near) significantly correlated with improved survival (chapter 3.7). Epithelial segments of these patients demonstrated downregulation of pro-tumorigenic pathways such as matrix remodelling and metastasis, and EMT signalling pathways. Additionally, CD3near immune segments demonstrated elevated B cell and reduced angiotensin signalling pathways. B cell elevation was further confirmed using immune cell deconvolution. Multiple signalling pathways trigger angiogenesis in PDAC, promoting tumour development, metastasis and poor prognosis [323]. Aberrant expression of this phenomenon offers a potential targeted treatment option, something severely lacking in pancreatic cancer. Furthermore, immune segments in patients with large distance from CD68+ to PanCk+, present with upregulated dendritic cells, reportedly associated with improved survival and T cell immunity restoration [287]. Within the neoadjuvant cohort, short distances from CD3CD8+ to PanCk+ cells correlated with improved survival (chapter 4.7). Interestingly, αSMA and immune segments of these patients presented with reduced B cells and T cells. Although the T cell trend mirrors the rest of the neoadjuvant results, the reduced B cell pathway observed in the poor survival group contradicts the overall neoadjuvant trend. B cells remain a contradictory cell type in pancreatic cancer, with reports showing both anti-tumorigenic and pro-tumorigenic properties [11, 97, 203]. In particular, CD49CD73 co-expressing B cells promote angiogenesis, underlining the importance of robust subtyping in the context of biomarker discovery [97].

The variable rates of translation from RNA into protein imply that while Spatial Transcriptomics can offer estimates of immune cell deconvolution, it may not always serve as an accurate surrogate for direct protein expression [296-299]. These estimates should be validated against true protein data to ensure reliability. Initially, the Akoya Biosciences Phenocycler™ assay using the STEP core plus enhancement immune panel was trialled. This panel allows for a wide range of immune cells to be visualized including T, B and dendritic cells. Significant survival trends were found for helper T cells, B cells and dendritic cells. Notably, this assay was performed by the company as part of a beta technology access program. Images produced had high levels of background, with oversaturated and unspecific staining seen. Accurate phenotyping was difficult to robustly establish. Furthermore, a B7-H3 marker was not covered by the PhenoCycler™ panel.

To characterise the tumour immune microenvironment, Nanostrings CosMx™ was used, a

single cell protein assay suited to the investigative needs. The panel comprises of 60 markers, including epithelial, T cell, B cell, dendritic cell and B7-H3 markers. Although Celesta cell typing is the recommended method to phenotype CosMx™ protein experiments, this lacked a B7-H3 related cell type. Instead, a Seurat based approach was trialled, popular with bulk and single cell transcriptomic data, as well as being recommended for CosMx™ RNA assays [324]. This method generates clusters which dominant cell types can be assigned to via differential expression analysis. Further phenotyping methods would have to take place to validate cell clusters. Naïve and neoadjuvant samples generated distinct clusters, indicating the differences in cell types seen across these cohorts. Clear cluster cell assignment was carried out in naïve samples T and B lymphocytes, and overlap was seen in dendritic related clusters. Conversely, neoadjuvant clusters appeared heterogenous, demonstrating varied top differentially expressed markers, making clusters more difficult to assign a dominant cell type. This resulted in multiple clusters being combined to generate our three focused immune cells. Differential B7-H3 expression was observed in 3 naïve clusters and 4 neoadjuvant clusters along with other markers. Naïve B7-H3 related clusters were all immune related, with a neutrophil/myofibroblast heavy association (cluster 5), a T cell exhausted marker association (cluster 12) and a macrophage marker association (cluster 20). A more diverse B7-H3 clustering was seen within the neoadjuvant cohort, including a mixture of epithelial related (cluster 41), B cells (cluster 41), T cells (cluster 27) and exhausted T cells (cluster 17). Varied B7-H3 cluster density was seen in naïve and neoadjuvant, with the highest density presenting as the exhausted T cell cluster in both cohorts. Although B7-H3 is well known as an immune checkpoint molecule, it has yet to be fully characterised in terms of the cell type it expresses in, or the cells it interacts with. Contradictory reports have associated B7-H3 expression with a wide range of cell types including T cells, B cells, macrophages, as well as fibroblasts and tumour cells [325-327].

Regardless of the cell type associated with this checkpoint molecule, elevated expression correlates with poor prognosis [18]. Similar prognostic trends were observed in the two PDAC cohorts. Elevated exhausted T cell related clusters (cluster 5 and cluster 7) negatively correlated with the survival in naïve and neoadjuvant patients respectively. Reports linking B7-H3 to immune evasion via T cell inhibition may help explain this phenomenon [311]. These results reinforce the rationale in clinical trials testing B7-H3 inhibition in a multitude of cancers [142-144, 146]. These results validate those reported for Spatial Protein (chapter 3.11) and Spatial Transcriptomics (chapter 5.3.5 and chapter 5.4.5). Furthermore, increased B7-H3 expression in mouse models associates with invasion and metastasis via the NF-kB pathway, with increased angiogenesis marker VEGF being secreted [19], or via the JAK/STAT pathway with increased autophagy marker Mcl-1 being secreted [328, 329]. These reports also demonstrate inhibition of B7-

H3 results in increased treatment sensitivity [328, 329].

Assuming that the differences in B7-H3 clusters expressed in neoadjuvant compared to naïve is solely due to treatment type, it was hypothesised neoadjuvant treatment type would also present with distinct cell based clustering. Clear distinctions were demonstrated between chemotherapy treated and chemoradiotherapy treated patients, as seen by the UMAPs. Furthermore, an attempt was made to characterise the cell-to-cell interactions between B7-H3 clusters and phenotypes of interest. Future mechanistic studies should be performed to validate these results.

Multiplex led Spatial Transcriptomic analysis has revealed signalling pathways that are potentially pivotal in defining sub-grouped patients. This advanced, integrative approach not only aids in deciphering the fundamental mechanisms of disease, but it also potentially discovers new patient populations that could benefit from targeted therapies. Without this orthogonal approach, these insights may have remained undiscovered. Furthermore, the use on an ultra-high plex single cell protein assay has allowed us to begin characterising B7-H3 with the pancreatic cancer landscape, essential research if this checkpoint marker is to become a targeted treatment option.

# 7 Chapter 7: Final Discussion

## 7.1 General Discussion

Pancreatic cancer is the 5th most common cause of cancer related deaths, with a 5-year survival of <7% [1, 2]. Treatment options remain stagnant, with surgical resection being the best treatment option [21]. At diagnosis, most patients present with metastatic disease and are unsuitable for resection, thus the vast majority undergo adjuvant treatment. One of the few advancements within the last decade is the introduction of neoadjuvant therapy in borderline resectable and locally advanced disease, resulting in increased disease specific survival [5]. Despite the development of molecular subtype characterization, research underpinning the biology of PDAC is well behind that of similar solid tumours. This is partly attributed to its complex, heterogenous landscape, dominated by a rare mutational, and immune barren landscape [15]. This thesis aimed to characterise the tumour immune landscape of naive and neoadjuvant treated human pancreatic cancer in terms of cellular content, density and spatial orientation. Initial protein characterisation focused on the most common cells seen, T lymphocytes, macrophages and fibroblasts, using Akoya PhenoImager™. Subsequent regional 'omic' characterisation using the NanoString® immune-oncology panel was carried out for confirmation and discovery of rare protein signatures. Furthermore, the aim was to establish the Spatial Transcriptomic signature in distinct tissue compartments across treatment cohorts and appropriate clinical subgroups, using the NanoString® WTA panel. Finally, multi-'omic' characterization was performed using a combination of orthogonal data, to explore the underlying biology in prognostically relevant biomarkers, and validate transcriptomic signatures. Analysis was first carried out separately on naïve and neoadjuvant cohorts to establish the base landscape, then compared to characterize the immunogenic switch between these cohorts. The secondary aim was to characterize B7-H3 expression and determine its interaction within the naïve and neoadjuvant pancreatic landscape. This thesis primarily uses Spatial Biology, which can be categorized by two different methods; histological location, and single cell characterization. Histological location mainly refers to regional spatial biology, were an overall or 'mini-bulk' signature is generated per area of interest. Single cell characterization methods require a minimum of variable expression per cell and X-Y coordinates and is used for distance-based metrics. Both methods can be employed simultaneously

## 7.2 Deep protein characterization of the tumour immune microenvironment in PDAC

Immune cell protein characterization is relatively well established in naive, and less well established in neoadjuvant PDAC. However, the focus remains on the most common cell

types including T cells, macrophages and fibroblasts. In general, immunohistochemistry (IHC) studies demonstrate elevated CD8 cytotoxic T cells, CD3 T cells, and reduced CD68 macrophages and fibroblasts significantly correlates with improved prognosis in naïve [170-174] and neoadjuvant PDAC [132, 147, 213, 214]. To confirm these trends within the naïve cohort, IHC was carried out using antibodies to CD3, CD8, CD68 and CD163, demonstrating significant associations with prognosis and pattern of recurrence for CD3, CD8 and CD68. Upon confirmation that these markers were suitable, a 7 plex immunofluorescence panel was developed to investigate a range of T cell subsets, macrophages and myofibroblasts. This assay allows for in-depth characterization, co-expression analysis and establishing cell-to-cell interactions. This mIF assay generated many significant trends within naïve and neoadjuvant cohorts. Robust characterization demonstrated the naïve PDAC landscape was dominated by elevated PanCk, αSMA and CD68 expression, and survival outcome of naïve pancreatic cancer patients associated with specific density and spatial parameters. Elevated levels of CD3+ T cells and reduced CD68+ macrophages, along with increased distances from CD68+ macrophages to tumour cells, and shorter distances from CD68+ macrophages to CD3+ T cells correlates with improved DSS. Furthermore, elevated CD3CD8+ surrounding tumour cells were observed in patients with improved prognosis. Until recently, few papers have explored the spatial landscape. Carstens et al reported elevated T lymphocytes close to tumour cells significantly correlated with overall survival [219]. Active T cells scan their environment, detect and either kill neoplastic cells (CD8 T cells) or render them senescent (CD3 T cells) [330]. These results suggest distance plays an important role in the effect of T cells on surrounding cells, indicating that density alone is not enough to produce an anti-tumour response. Although region specific analysis was carried out, reporting was limited to novel trends not observed in the overall TMA core. Unusually, elevated FOXP3CD3+ cells in TME regions correlated with survival, although this was only seen in the discovery naïve cohort.

The naïve molecular subtype microenvironment was also explored. Classical patients demonstrated T cell specific density trends, with elevated CD3+ and CD3CD8+ T cells correlating with improved DSS. In contrast, Squamous patients demonstrated reduced tumour cell and macrophage populations correlated with DSS. Furthermore, significant nearest neighbour trends also differed between subtypes. Considering the heterogeneity of pancreatic cancer, it is highly unlikely that a single clinically relevant biomarker or targeted therapy will be employed in the clinic. However, characterisation of clinically relevant subgroups may reveal aberrations that can be exploited. The phenotypic differences observed between subtypes emphasizes this potential and should be further investigated.

The neoadjuvant mIF assay produced a mixture of expected and unexpected results. Similarly to naïve patients, the most predominant cell types remained tumour cells, αSMA+ fibroblasts, and CD68+ macrophages. Contrary to the hypothesis, reduced density of CD3CD8+ cells and CD3+ cells significantly correlated with longer DSS. Additionally, a reduction in CD68+ and FOXP3CD3+ cells also positively correlated with prognosis. Neoadjuvant patients have the added complexity of having an altered disease state with multiple factors that may influence the TME landscape and associated prognosis. These include treatment method, chemotherapy or chemoradiotherapy, the type of chemotherapy, FOLFIRINOX based or Gemcitabine based , and finally, the regression pattern, which scores how well the tumour has responded to neoadjuvant treatment and could be indicative of chemoresistance. These three main factors were investigated within the neoadjuvant cohort. Distinct density differences were seen between neoadjuvant subgroups. Notably, varied immune cell density in chemoradiotherapy and good regression status patients significantly correlated with prognosis, in contrast, only tumour cell densities were prognostic in chemotherapy and poor regression status. Although CD3CD8+ and CD68+ prognostic marker overlap was seen between FOLFIRINOX and Gemcitabine treatment, additional markers, CD3+, FOXP3CD3+ and PanCk+, were observed in the FOLFIRINOX cohort. Regardless of subgroup investigated, the general trend remained the same, reduced expression of any phenotype correlated with longer disease specific survival. Of the few papers investigating the neoadjuvant immune landscape, the general trends demonstrate an immunogenic switch towards increased effector cell populations including cytotoxic, helper, and a reduced Treg population [132, 147, 213, 214]. Although the neoadjuvant results seem to contradict the PDAC literature, similar trends have been reported for similar cancers. Reports in oesophageal and breast demonstrate an initial reduction in CD8 and CD4 populations, amongst others, for up to 9 months post neoadjuvant treatment [216, 258-260]. Furthermore, the functional state was altered in breast cancer, resulting in an increased proportion of activated memory CD4 T cells [259]. This poorly understood phenomenon highlights two fundamental questions;

1. What is the optimal time period for samples to be taken? Does this need to be taken into consideration when establishing the post treatment landscape?

2. Is cellular density alone a sufficient tool for prognosis, without taking into consideration activation status or in-depth cell subtyping?

Furthermore, multiple nearest neighbour trends appear in neoadjuvant patients. This includes large distances from CD68+ macrophages to tumour cells, large distances from cytotoxic T cells to CD3+ helper T cells and short distances to CD3CD8+ cells from Tregs.

CD68+ macrophages are thought to suppress the anti-tumour immune response, which may indicate that increased distance to tumour cells dampens this effect [331]. Tregs play a pivotal role in suppressing the immune response, and are associated with poor survival, both in the literature and within the neoadjuvant cohort [256]. Reduced distances to cytotoxic T cells may reduce the effect of Tregs. This may be done by either directly targeting and killing Tregs, or by consuming the amount of essential Treg cytokines such as IL-2 which is reportedly required for survival and suppressive capabilities [332].

The spatial prognostic patterns demonstrated by treatment naïve and neoadjuvant pancreatic cancer patients illustrate the potential effect of neoadjuvant therapy on the tumour microenvironment, and how these alterations may contribute to improved prognosis. Considering only the notable patterns observed between naïve and neoadjuvant multiplex analysis, stark differences between longer survivors were observed. Longer survivor treatment naïve patients presented with elevated CD3+ helper T cells, and longer distances from CD68+macrophages to both FOXP3CD3+ Tregs, and αSMA+ fibroblasts. Additionally, they presented with short distances from macrophages to CD3+ helper T cells. In contrast, longer survivor neoadjuvant patients presented with reduced tumour cells, as well as reduced FOXP3CD3+ Treg expression. Moreover, a diverse range of nearest neighbour metrics were identified in neoadjuvant patients with improved prognosis. This included short distances from CD68+ macrophages to cytotoxic T cells, short distances from cytotoxic T cells to αSMA+ fibroblasts and large distances to CD68+ macrophages from cytotoxic T cells. Furthermore, the neoadjuvant longer survival group, consistently outperformed the naïve longer survival group. These results emphasize investigation of phenotype alone, without functional status, produces limited characterisation of the tumour microenvironment, without accounting for biological interactions.

In addition to inter-phenotype spatial relationships, intra phenotype spatial patterns were investigated. All characterized cell types in naïve and neoadjuvant PDAC within a TMA setting presented with a clustered pattern of expression as defined by Ripley's K function. Increased clustering patterns were seen within tumour cells and cytotoxic T cells in the naïve and neoadjuvant landscape. Further analysis is required within whole sections to fully explore these patterns and to determine whether histological regions alter the patterns of expression.

To validate naïve prognostic biomarkers generated by high-plex mIF and explore more of the immune landscape, a regional immune-oncology GeoMx® assay was performed. Upon confirmation of adequate concordance between matched DSP and IHC markers, the overall immune landscape was investigated. This demonstrated an immune-rich and

immune-void naïve landscape, associated with DSS. Furthermore, a range of region specific biomarkers were observed. Notably, highly expressed B7-H3 in epithelial segments negatively correlated with DSS. This immune checkpoint marker has limited expression in normal tissue, making it an ideal targetable marker for the diseased state [17-19]. Subsequent Spatial Transcriptomic and single cell Spatial Proteomic confirmed and further explored these results, as discussed below.

## 7.3 Spatial Transcriptomic characterization of the tumour immune microenvironment in PDAC

Pancreatic cancer is complex disease, made up of highly dynamic compartments, resulting in a heterogenous landscape. Whilst previous gold standard techniques such as bulk or single cell transcriptomics may have characterised the dominant gene signature, they have failed to maintain the spatial architecture. This has resulted in a lack of understanding of PDAC biology compared to similar solid cancers, and almost no improvement in treatment and biomarker discovery. Similarly, findings from bulk transcriptomics are often from tissue samples with diverse histopathological regions, resulting in a mixed signature output, dominated by the strongest gene expressing compartment. Recent studies, including work from the Jamieson laboratory, have highlighted this phenomenon. A high percentage of tumour microenvironment input in bulk transcriptomic assays disproportionately impacted the overall expression signature, resulting in a confounded signal [271]. Controversially, this would imply that most of the tumour subtypes, are in fact, tumour microenvironment (TME) subtypes. Furthermore, the TME is highly dynamic and changeable compared to the tumour compartment, as tissue samples offer a snapshot view, these subtypes may only be reflective of a moment in time. The diverse nature of pancreatic cancer necessitates structural integrity to be maintained to understand the biology of this disease. Spatial Transcriptomics offers an elegant solution to begin solving these problems in pancreatic cancer. Naïve and neoadjuvant samples were first established separately, then compared.

To confirm the necessity of Spatial Transcriptomics, inter-segment heterogeneity was confirmed, demonstrating distinct aberrated differential genes and pathways between tumour vs fibroblast or immune rich segments. These results reinforce the hypothesis that mixed compartment signatures would be dominated by the strongest gene expression, limiting discovery of subtle signals. Furthermore, in an attempt to subtype naïve patients, discrepancies were found between previously established bulk subtyping, a ranked squamous score, and the subtype classes generated from epithelial segments. These discrepancies could be due to multiple factors. Importantly, Spatial Transcriptomics works with reduced tissue input, a robust signature can be generated from as little as 100 cells

per segment. This may not be an adequate amount for robust subtyping. As discussed above, molecular subtypes have mostly been generated from a confounded signal, with considerable tumour microenvironment input, resulting in a mixed signature rather than an epithelial based signature [271]. Furthermore, subtyping using differential expression is highly reliant on the sample set, and may force subtype clustering, resulting in inaccurate subtype clusters generated. A larger sample set would mitigate this.

Intra-segment heterogeneity was observed in epithelial segments, with limited gene overlap observed between well-established molecular subtypes, indicative of a novel epithelial specific signature. These clusters demonstrated a non-significant prognostic value, with epithelial cluster 2 correlating with reduced survival. Additionally, distinct transcriptomic differences were observed between them. Two targetable genes were upregulated in cluster 2, *HSPA6* and *CST1*, associated with PDAC epithelial heterogeneity in single cell transcriptomics, and correlated with proliferative and malignancy associated proteins in colorectal cancer [281, 282]. If validated in a larger cohort, these biomarkers could prove useful in predicting aggressive PDAC. Furthermore, immune cell deconvolution displayed a significant reduction of B cells and memory dendritic cell. These trends are repeated in multiple comparisons. Within the naïve study, long term survivors (over 36months) demonstrated elevated B cells, as well as CD8+ T cells estimates. Additionally, naïve long-term survivors (over 36months) presented with elevated B cell and CD8 T cell estimates, and differentially expressed Classical marker *LYZ* in epithelial segments [291]. This marker has also been reportedly upregulated in slow progressor intraductal grafted organoid PDAC mouse models [291].

Intra-tumour heterogeneity of neoadjuvant patients was examined using tumour core with matched lymph node metastasis. As expected, elevated B cell related genes including *MS4A1* and *CD79A* presented in LN samples, as well as elevated TCR and BCR signalling pathways. Additionally, these samples presented with an increased aggressive disease landscape demonstrated by elevated VEGF, immortality and stemness, and EMT signalling.

As outlined above, neoadjuvant PDAC biology can be affected by multiple factors. These were considered when characterizing the neoadjuvant transcriptomic immune landscape. Numerous transcriptomic differences were observed between FFX treated and Gemcitabine treated PDAC. Notably, Gemcitabine epithelium demonstrated enriched *CA9*. The presence of *CA9* indicates the potential for targeted immunotherapy, as observed in similar cancer types [333]. Gemcitabine has been reported to work synergistically with immunotherapy, partly due to its increased immunogenic nature [213, 334, 335]. This was demonstrated by elevated B cell, T cell and natural killer cell

pathways. In addition, exhaustion pathways, specifically B cell and T cell exhaustion were observed which are known to dampen the anti-tumour effect of immune cells [261, 262]. Similarly, chemoradiotherapy patients, positively associated with DSS, presented with increased B cell and B cell exhausted pathways, as well as T cell receptor (TCR) signalling pathways in immune segments. Furthermore, these patients demonstrated reduced autophagy signalling in epithelial segments. Autophagy has been reported to promote immune evasion, and tumour growth in PDAC, which may explain the elevated immune pathways seen [212, 336]. Additionally, increased memory dendritic cell expression was observed in chemoradiotherapy treated patients, reported to play a role in T cell immunity restoration, and improving radiotherapy response [287, 309]. Unexpectedly, differential expression analysis in regression group comparisons did not differ drastically. However, pathway analysis identified interesting immune related pathways. Poor regression demonstrated enriched T cell, B cell and B cell exhaustion pathways, as well as an estimated elevation of memory dendritic cells. This interchange between anti-tumour and pro-tumour effect in PDAC is a common phenomenon and is even more apparent in the neoadjuvant cohort. Notably, the term exhausted has generated some controversy, with terms such as inactive or dysregulated perhaps being more appropriate. However, as GSEA pathways are defined as exhaustion pathways, this term has been used.

Matched immune segment comparison between naïve and neoadjuvant cohorts displayed many alterations. Notably, immune associated pathways although considerably elevated in immune segments of neoadjuvant samples, were often coupled with exhaustion pathways. Specifically, both T cell coupled with T cell exhaustion, and B cell coupled with B cell exhaustion pathways were upregulated. This exhausted phenotype has been reported in treatment naïve PDAC cohorts, for CD4 and CD8 T cells, with consideration given to cell surface activation markers within the spatial landscape [337]. Additionally, pro-inflammatory cytokine IL-2 was elevated. This phenomenon has previously been reported to be triggered by neoadjuvant treatment [253]. This emphasizes that it is insufficient to simply look at the overall density of these immune cell populations, activation status needs to be considered to fully classify the neoadjuvant immune landscape.

Direct comparisons between the naïve and neoadjuvant transcriptome remains a niche, unmet research field in pancreatic ductal adenocarcinoma. Of the work undertaken, the majority remains focused on bulk transcriptomic techniques. Bailey et al found three specific cell phenotypes (GATA6, KRT17 and CYP3A) with neoadjuvant chemotherapy treated patients (mFOLFIRINOX or Gemcitabine treated), located within the epithelium [338]. Interestingly, they found an increased diverse, heterogenous neoplastic tumour

state associated with subtype specific WGCNA programs within neoadjuvant treated compared to naïve patients, which correlated with survival within the neoadjuvant cohort. Additionally, these neoplastic cell populations also potentially link with chemoresistance [338]. An attempt was made to replicate these cell types using Spatial Transcriptomics within the cohorts, however Spatial Transcriptomic expression did not appear sufficient to characterise these novel neoadjuvant specific cell types. Further work should be performed using Spatial Transcriptomics on whole sections to explore these phenotypes.

When comparing the naive cohort to different neoadjuvant treatment types or chemotherapy regimens, similar immune focused patterns were observed. Elevated T cell and B cell signalling pathways were constantly upregulated in chemotherapy treated, chemoradiotherapy treated, FFX and Gemcitabine treated immune segments when compared to naïve segments. Moreover, B cell exhaustion was also upregulated in chemoradiotherapy and Gemcitabine treated segments, along with a variety of other immune cell pathways. Interestingly, a similar trend is observed in neoadjuvant long-term survivors compared to their naïve counterparts, with the addition of the upregulation of B cell and T cell exhausted pathways. This exhausted landscape appears to be recurrent within the neoadjuvant cohort, indicating that the effect of matched immune cells may be redundant, as seen in the literature [261, 262]. Furthermore, these results seem to contradict the patterns found within high-plex protein investigation. However, approximately 20-50% of mRNA is translated into protein, therefore, to robustly characterise cells, protein expression should be examined [296-299]. This emphasizes the need for multi-omic studies. Whole section validation was carried out using two matched biopsies and neoadjuvant resected cases. This demonstrated a shift from a high CD4 T cell, CD8 T cell and macrophage population, into a high B cell, CD4 T cell, CD8 T cell and Treg population.

Regional protein naïve results demonstrated that reduced expression of epithelial B7-H3 positively correlated with survival. As this marker is specific to the disease state and has growing interest as a potentially targetable treatment option, in-depth Spatial Transcriptomic exploration was performed in naïve and neoadjuvant pancreatic cancer [19, 310, 311]. Although epithelial specific survival analysis failed to identify a significant correlation, reduced expression in whole core naïve and neoadjuvant cohorts significantly correlated with DSS. Expression was predominantly seen in non-epithelial tissue in naïve patients, and a slight non-significant increased expression in neoadjuvant epithelium. Reduced T cell pathways, and elevated angiotensin pathways were observed in B7-H3low immune segments. This indicates the possibility of using angiotensin targeted therapies, reported to considerably improve prognosis in naïve PDAC patients [99], as well as targeting B7-H3 itself. Pancreatic cancer is renowned for its aggressive innate and

adaptive treatment resistance, rendering most treatment options ineffective, or at the very least severely limiting their effectiveness [155, 159, 339]. If B7-H3 is validated as a biomarker, these patients could be stratified for combined targeted angiotensin system inhibitor treatment and B7-H3 inhibition. Extensive mechanistic action research would be required to test the viability of this hypothesis. Rationale for this treatment combination has been reported for colorectal cancer studies [340]. Interestingly, B7-H3low immune segments presented with elevated B cell and T cell signalling pathways, although this was coupled with B cell exhaustion pathways.

## 7.4 Multi-omic tumour immune microenvironment characterization in PDAC

Independently, high-plex immunofluorescence and regional Spatial Transcriptomics have provided insight into the tumour immune microenvironment across PDAC treatment cohorts. Single cell protein assay allows for robust characterization, although it is limited by its purely descriptive capability. Similarly, Spatial Transcriptomics offers indirect biological understanding, and immune cell estimates, however, it is limited by protein translation rates. Orthogonal integration of significant multiplex density and nearest neighbour trends with Spatial Transcriptomics helps deconvolute the underlying biology specific to the immune landscapes of patients that correlate with prognosis. Furthermore, concordance between true protein expression and estimated protein expression can be established.

CD3 density has proved prognostic in naïve PDAC across IHC, regional protein and multiplex assays. CD3high ranked immune and αSMA segments demonstrated elevated cytotoxicity and B cell signalling pathways. Furthermore, reduced JAK/STAT and type I INF signalling was observed in CD3high epithelium. Reports show type I INF activation of PD-L1 via the JAK/STAT pathway results in elevated expression on tumour cells in PDAC mouse models [81]. Furthermore, JAK/STAT inhibition resulted in increased T cell infiltration, and sensitized mouse models to anti-PD-L1 therapy [81]. Assuming this reported phenomenon is solely based on the role of JAK/STAT, it indicates the elevated CD3 levels seen within the naïve cohort are in part, due to this aberrated JAK/STAT signalling pathway. If validated, this indicates CD3high patients would benefit from combination JAK/STAT and PD-L1 inhibition treatment.

In the neoadjuvant cohort, high CD3CD8 density negatively correlated with survival in multiplex results. Immune segments of CD3CD8high demonstrated elevated T cell and B cells, as expected, coupled with elevated T cell and B cell exhausted signalling pathways.

In theory, this dysfunctional state results in a loss of tumour suppressor function, therefore elevated density of these cells is redundant, reportedly correlating with poor survival [261, 262]. This may explain why patients with fewer, but active immune cell populations correlate with improved survival within the neoadjuvant cohort.

Naïve patients with short distances from CD68 macrophages to CD3 T cells correlate with survival. Immune segments of these patients had upregulated B cell and reduced angiotensin signalling. Targeted inhibition of angiotensin has been explored in a range of cancers. VEGF-A inhibitor, bevacizumab, has shown promising results in treatment of similar cancers including non-small cell lung cancer subtype lung adenocarcinoma [341, 342]. However, single anti-VEGF inhibitor treatment has failed to produce the same effect in PDAC, most likely due to VEGF independent pathways being used [99]. Huang et al demonstrated blocking BICC1/LCN2 signalling, responsible for VEGF-independent angiogenesis via the JAK/STAT pathway, resulted in reduced microvessel density, and sensitized mouse models to Gemcitabine treatment [99]. Furthermore, use of angiotensin system inhibitors has correlated with PDAC survival in retrospective studies [293, 295]. Correlation between B cells and angiogenesis in cancer is poorly understood. However, subsets of B cell populations have been reported to promote angiogenesis, specifically those with elevated STAT3 signalling or CD49CD73 co-expressing cells [12, 97]. The opposite trend was observed in the naïve cohort, highlighting the need to robustly characterises immune cell subsets within spatial regions to improve the likelihood of successful targeted therapy implementation within the pancreatic cancer setting.

Although B cell estimated density and signalling pathway enrichment has mostly associated with the better outcome group within Spatial Transcriptomic comparisons, a nearest neighbour neoadjuvant metric contradicts this trend. A short distance from CD3CD8+ T cells to tumour cells correlates with improved survival in neoadjuvant patients. αSMA and immune segments of these patients displayed reduced B cell signalling pathways. B cells remain a contradictory cell type within PDAC, with reports associating them with both pro-tumorigenic pathways such as angiogenesis, and anti-tumour pathways [11, 12, 97]. Thus, relying solely on transcriptomics for immune cell characterisation can be insufficient, highlighting the need for robust single cell subtyping within the immune protein landscape.

Three main immune cell patterns appeared throughout Spatial Transcriptomic characterization, T cell, B cell and dendritic cells. To confirm this transcriptomic signature accurately represented true protein expression, a single cell ultra-plex protein assay was performed on a serial section of the naïve cohort. Initially, the PhenoCycler™ STEP core plus enhancement panel was trialled, however this lacked a B7-H3 marker, and produced

oversaturated images with high levels of background, making robust phenotyping difficult to establish. NanoStrings® protein CosMx™ panel encompassed a variety of immune cell and epithelial markers, along with a specific B7-H3 marker. Using Seurat clustering, a method frequently used in single cell transcriptomics, cell clusters were generated. Distinct clustering was seen for naïve (n= 34 clusters), and neoadjuvant (n= 46 clusters) cohorts, with further cluster generation in neoadjuvant subgroups, chemotherapy treated (n= 31) and chemoradiotherapy (n=28 clusters). T cell, B cell, dendritic cell and B7-H3 clusters were assigned by establishing the top differentially expressed proteins. This produced three B7-H3 heavy naïve, and four B7-H3 heavy neoadjuvant clusters. B7-H3 is reportedly expressed in a wide range of cells in the diseased state including T cells, B cells, macrophages and epithelial cells.

Visual co-expression confirmation was observed between B7-H3 and the other top expressing proteins within individual clusters. Naïve clusters generated a neutrophil/myofibroblast heavy cluster (cluster 5), with co-expression frequently seen between B7-H3, αSMA and CD15. Additionally, B7-H3 expressed with a T cell dysregulation marker, CD39, in cluster 12, and macrophage markers CD14 and HLA-DR, in cluster 20. Cluster 20 co-expression has been reported in NSCLC [343]. Furthermore, diverse clustering was observed in neoadjuvant samples. Co-expression was observed with epithelial markers EpCAM and β-catenin, in cluster 41 and potential B cell markers CD38, in cluster 41. Additionally, B7-H3 co-expressing T cell related clusters were observed, including a T cell dysregulation marker CD39 in cluster 17, and mixed T cell markers CD127, and STING, in cluster 27. Correlation between T cell exhaustion and B7-H3 has been reported in ovarian cancer and was seen in both naïve and neoadjuvant cohorts [344]. Notably, cluster 41 generated two signatures, although they were not expressed in the same cells. Furthermore, some markers including CD14, CD38 and HLA-DR, have been reported to express on multiple cell types, therefore further phenotyping and co-expression analyse should be performed. Notably, these co-expressing cells are called clusters rather than cell types, until robust phenotype validation is performed. Naïve median density of exhausted T cell cluster 12 was significantly increased compared to macrophage cluster 20. Neoadjuvant median density of exhausted T cell cluster 17 was increased compared to T cell cluster 27, and cluster 27 was elevated compared to cluster 41.

In an attempt to characterise the cells surrounding reported B7-H3 clusters, nearest neighbour analysis was performed. Dendritic cells appeared in the top 2 closest neighbour cells from all naïve B7-H3 clusters. Intriguingly, B7-H3 was first cloned from dendritic cells, and this may play a role in its immunosuppressive T cell function [243, 345]. Within the neoadjuvant cohort, a shift in the populations surrounding B7-H3 related clusters was

observed. Epithelial clusters were amongst the top nearest neighbours for exhausted T cell cluster 17 and epithelial/B cell cluster 41, and CD4 helper T cell clusters were the closest neighbours for B7-H3 cluster 4 and T cell cluster 27. T cell exhaustion or dysregulation can be triggered by overexposure to immunosuppressive factors secreted by tumour cells, this phenomenon may explain the proximity of B7-H3/exhausted T cell cluster to epithelium [346]. Additionally, previous mIF work demonstrated CD3+ cells significantly clustered together according to Ripley's K function. If CD3+CD8- cells are assumed to be a pseudo marker for CD4 T helper cells, a similar trend is apparent with neoadjuvant B7-H3 T cell cluster 27 being in close proximity to CD4 helper T cells.

Markers found within chemotherapy and chemoradiotherapy B7-H3 clusters were highly mixed, with potentially multiple cell types including epithelial cells, T cells and macrophages seen within these clusters. Additional deconvolution needs to be performed before confidently assigning these clusters. Close proximity was observed between all chemotherapy B7-H3 clusters and tumour cells, perhaps indicating a B7-H3 epithelial expressing phenotype. Furthermore, chemoradiotherapy B7-H3 clusters appeared to reside within similar locations, as indicated by the B7-H3 clusters consistently appearing as the closest neighbour cells.

Irrespective of the cell type, B7-H3 expression is prognostic in a wide range of cancers, a trend replicated in naïve and neoadjuvant cohorts as seen in chapter 5. Using Seurat clusters, naïve CD4 T cell and CD8 T cell clusters positively correlated with survival, replicating results found in previous IHC and mIF work. Similarly, neoadjuvant CD4 T cell and CD8 T cell clusters negatively correlated with survival, validating mIF work reported in chapter 4. B cell and dendritic cell Spatial Transcriptomic signatures consistently associated with better outcome subgroups, however failed to demonstrate prognostic value when using Seurat clusters. This may be due to the phenotyping methods used and should be confirmed using a stringent method. Intriguingly, T cell related B7-H3 cluster in naïve (cluster 12), and neoadjuvant (cluster 27) demonstrated a negative association with disease specific survival. The prognostic value of these B7-H3 clusters emphasize the possible clinical utility of this immune checkpoint marker, reinforcing the need for additional exploration into these clusters. Due to the highly novel nature of the single cell protein assay, analysis methods remain experimental in nature and therefore initial data presented is exploratory. Further work is needed to validate the results presented.

The Spatial Omic era is arguably at the stage where it produces more questions than solutions. However, much like for single cell transcriptomics, these will gradually be resolved. A combination of novel analysis method development, re-purposing "omic data" techniques, and employing non-life science methods will be required to fully exploit these

datasets. Undoubtedly, analysis methods will go through multiple iterations until a gold standard is established.

## 7.5 Limitations

There are several general limitations associated with this thesis. The most apparent one being the use of tissue microarrays for the majority of work. This may prevent robust characterisation of the entire protein and transcriptomic TME landscape. However, the TMAs used were multi-regional with at least 3 cores per patient and selected by expert pathologists to accurately depict the heterogeneity of pancreatic cancer. Furthermore, studies have reported that 3 cores per patient is sufficient to replicate whole section results in leiomyosarcoma [254]. Taking this into account, the mIF studies were performed with at least 3 cores per patient. However, only one core per patient was selected for most of the spatial transcriptomic and proteomic studies. These assay techniques are labour extensive, time consuming and expensive, making it unrealistic to produce a large sample number with multiple cores per patient or whole sections. Validation was carried out on a subset of neoadjuvant whole sections for spatial transcriptomics, however this was still limited by ROI selection. True whole section validation should be repeated for a small subgroup of naïve and neoadjuvant patients for mIF and Spatial Transcriptomic/Protein work.

The naïve combined cohort is considerably older with a tumour centre histology. TMAs were created using a macroscopic selection technique, resulting in a mixed histology. Conversely, the neoadjuvant combined cohort was custom built to represent distinct histology per TMA, comprising of a malignant rich, immune rich and benign TMA, with cores computationally selected by an expert pathologist using a TMA Grand Master™ (3DHISTECH, Budapest, Hungry). To directly compare the two treatment cohorts, the neoadjuvant malignant TMA was selected, as it represented the most similar histology. However, this implies that the entire neoadjuvant immune landscape was not captured, limiting observations to the direct tumour microenvironment. Finally, survival variable ranks were established using a range of exploratory cut-off methods, producing highly specific numbers. Although this is ideal in a digital world, it would not be suitable for manual scoring by pathologists. Cut-off validation should be carried out using the closest rounded number to test whether the results presented could be translated into the clinic.

The major limitation when using the PhenoImager™ assay is the possibility of spectral bleed through. This primarily occurs when two antibodies are bound to fluorophores that have overlapping absorption and emission spectra. This results in the stronger expressing

fluorophore bound antibody being picked up when a weaker expressing antibody is being imaged, usually because faint antibodies take longer to image. Although this can be mostly mitigated by spectral unmixing, occasionally bleed through is still present. Additionally, biased phenotyping was performed for mIF assays. To mitigate user bias, an unbiased phenotyping method using CytoMAP was used to validate phenotypes selected. All phenotypes were confirmed, with the addition of an unexpected FOXP3+CD3+PanCk+ cell type. This phenotype is most likely due to spectral bleed through rather than true co-expression. Finally, the PhenoImager™ assay does not account for functional states nor offer a biological mechanistic insight, resulting in a purely descriptive assay.

Spatial Transcriptomic work using the GeoMx® is limited by region selection and through-put. However, this assay was specifically selected for its region selection feature to make use of a large archival FFPE TMA resource available via the GTRF. Furthermore, TMA based studies offer a work around for the low through-put imposed by the machine. The resolution of this assay requires around 100 nuclei per segment for robust analysis, indicating rare signatures may not be detected. Likewise, although immune cell deconvolution offers immune cell estimates, these should be validated for a true protein signature due to variable protein translation rates. Although this assay provides insight into the underlying biological mechanisms in pancreatic cancer, it remains heavily descriptive, requiring further experiments to explore significant genes and signalling pathways observed. Spatial Biology has rapidly evolved in the last year, with the commercial introduction of NanoString® CosMx™ assays. Naturally, this novel technology has issues that are yet to be resolved. Cell segmentation is primarily generated using an adapted Cellpose algorithm that cannot be altered. This results in variable segmentation efficiency depending on the quality of the fluorescent image generated. However, this is currently being improved by NanoString®. Furthermore, analysis methods are still being explored, making initial results subject to change.

## 7.6 Further work

Further work following up the results generated from this thesis would aim to validate the mIF, Spatial Transcriptomics and Spatial Protein trends generated in naïve and neoadjuvant pancreatic cancer. Further investigation of mechanistic studies for important biological pathways demonstrated in subgroup specific Spatial Transcriptomics results is also required.

### 7.6.1 Whole section validation

Most of the work generated within this thesis has been carried out on TMAs. Although this was purposefully done for throughput and cost reasons, this may introduce core location bias. The multiplex panel and Spatial Transcriptomics WTA panel should be repeated using whole sections from representative naïve and neoadjuvant patients with a mixture of the appropriate clinical subgroups. This would confirm whether TMA utilisation is an appropriate surrogate for whole sections when employing these spatial biology assays.

### 7.6.2 Neodjuvant mIF validation

Certain prognostic trends demonstrated in mIF analysis of the neoadjuvant Glasgow cohort using tumour centre specific TMAs contradicted the hypothesis. An immunogenic switch towards effector cells was expected, however, a reduction of all mIF panel cell types, including cytotoxic T cells, was associated with patients with improved DSS. The mIF panel should be repeated on the matched immune rich TMAs, as well as a separate neoadjuvant cohort to ensure these results are not location or cohort specific.

### 7.6.3 B7-H3, biomarkers and targetable pathways

B7-H3 demonstrated prognostic relevance and distinct Spatial Transcriptomic landscapes in naïve and neoadjuvant patients. This indicates a potential targetable checkpoint marker, as seen in clinical trials with other solid tumours [142-144]. Furthermore, B7-H3low ranked epithelium demonstrated upregulation of the angiotensin system pathway in naïve pancreatic cancer. B7-H3 dependent angiogenesis has been reported in colorectal cancer, with studies reporting the rationale of combination targeted therapy [340]. Interestingly, angiotensin system inhibitors are one of the few targeted treatment options that show promise in PDAC [293, 295]. Confirmation of a positive association between protein expression of B7-H3 and angiogenesis markers e.g. FGFR or VEGFR, should be established via a small mIF panel [98]. To determine whether B7-H3 has a biological effect on angiogenesis in pancreatic cancer, in vitro cell culture assays could be used for B7-H3 siRNA knockdown, and western blots probed for FGFR or VEGFR to determine the effect. Finally, mouse models could be used to further validate B7-H3/angiogenesis effect, in addition to testing the validity of combination B7-H3/angiogenesis inhibition.

### 7.6.4 CosMx™ cell typing

CosMx™ cell types were established using a Seurat clustering method. Notably, this technique does not strictly phenotype cellular populations, rather it produces cell type heavy clusters, and is popular in single cell transcriptomic studies [324]. As clusters can

be composed up of mixed cell populations, robust phenotyping of clusters should be established. This could be done by in-depth cluster investigation using tools such as ROGUE, which determines single cell signature purity [347]. Once robust phenotyping is performed, B7-H3 co-expression should be confirmed, possibly using a multiplex immunofluorescence panel focused only of B7-H3 and the markers it associates with e.g. CD39. Additionally, the NanoString® recommended cell typing method, Celesta, could be trained to include pancreatic cancer cell types of interest such as B7-H3. Furthermore, B7-H3 cell types could be compared across naïve and neoadjuvant patients to validate the variety observed in the CosMx™ Seurat cluster results. Upon robust cell typing and survival analysis, significant trends can be integrated with Spatial Transcriptomics work to investigate the differential gene expression and biological pathway aberrations.

### 7.6.5 Cell-ligand interactions and subcellular work

To investigate biological spatial interaction, cell-ligand interaction analysis could be established using NanoStrings® single cell Spatial Transcriptomics CosMx™ panel. This panel includes markers for the cell types focused on throughout this thesis, B7-H3 expressing cells, T cells, macrophages, fibroblasts, B cells and dendritic cells. This would be especially interesting to explore potential targetable interactions in T cells, as most checkpoint inhibitors, including PD-1/PD-L1 immunotherapy, fail in the majority of pancreatic cancer [348]. Multiple clinical trials are investigating B7-H3 inhibition due to its lack of expression in normal tissue and association with an aggressive disease state [19, 310, 311]. Establishing the cell-ligand interactions within B7-H3 cell types would help clarify whether B7-H3 inhibitors would be an appropriate treatment option in PDAC. The CosMx™ assay can provide subcellular probe coordinates. At the time of writing, B7-H3 remains an orphan ligand, though some reports show interaction between TLT-2 on activated immune cells [349]. IHC studies have shown B7-H3 cellular localization on cellular membrane, cytoplasm and nucleus depending on the tissue type investigated [350-352]. It is possible that this variety is due to different B7-H3 expressing cell types. Exact protein and RNA location of B7-H3 could be established within distinct B7-H3 phenotyped cells.

### 7.6.6 3D spatial biology

Although 5µm FFPE tissue sections are required for GeoMx® and CosMx™ spatial biology assays, the images are ultimately flattened to produce a 2-dimensional (2D) image. As pancreatic cancer does not exist in a 2D plane, the results produced from these types of assays are limited to a single snapshot. To explore the pancreatic cancer tumour microenvironment whilst maintaining spatial, cellular and anatomical structural integrity,

the cutting-edge Stellaromics® multi-omic assays could be used. This allows for a highly representative omic discovery, down to subcellular resolution, in tissues up to 200μm thick [116]. Potential biomarker and drug target discovery using 3D assays would be more robust, as they take into account the complex, heterogenous pancreatic landscape.

## 7.7 Final conclusion

This thesis leverages innovative Spatial Biology to robustly characterize the tumour immune microenvironment protein and transcriptomic landscape within the treatment naïve and neoadjuvant pancreatic cancer. Individually, Spatial Protein and Spatial Transcriptomics are incredibly powerful tools for in-depth microenvironment analysis. Spatial Protein assays enable deep phenotyping, revealing unknown spatial interactions. Spatial Transcriptomics provides biological insight into specific regions of interest, identifying potential biomarkers and targetable pathways. Combined, these technologies represent a cutting-edge approach for deep characterisation of the diseased state. The identification of B7-H3, and other actionable pathways, if validated, holds a promise for novel pancreatic cancer treatments, an urgent need within this cancer.

# 8 Chapter 8: Supplementary

# 8.1 Chapter 2 supplementary: Spatial Transcriptomic filtering and normalization alternative

Spatial Transcriptomics has rapidly evolved in the last 3 years. At the start of this thesis project, Nanostring whole transcriptome assays were not commercially available, and only became so in 2020. Naturally, the technology, and therefore analysis methods, have advanced. At the time of analysis, an established filtering and normalization method was used. However, there is a shift to more stringent filtering methods, to maximise the purty of signature produced, as well as alternate normalization methods [353, 354]. A representative analysis work through has been carried out using this stringent filtering method. Complete overlap was observed between the filtering methods, indicative of significant signatures maintaining their power in lenient filtering, with the addition of more subtle, lower expressing signatures also being picked up. As robust biological characterisation of pancreatic cancer has yet to be fully established, lenient methods should initially be used, with subsequent stringent filtering applied when appropriate.

# 8.2 Chapter 3 supplementary

## 8.2.1 Prognostically favourable nearest neighbour tumour immune landscape in naïve patients across molecular subtypes

| Nearest neighbour trends within Molecular subtypes in Naive discovery cohorts | | | | | | | | |
|---|---|---|---|---|---|---|---|---|
| **Nearest neighbour pattern** | **Region** | **Cohort** | **Group** | **Cut-off method** | **Number** | **Time (months)** | **HR (95% CI)** | **P value** |
| Distance to CD3 from αSMA | Whole | Discovery | Classical | UQ | 122 | DSS | 0.62 (0.40-0.96) | 0.031 |
| Distance to CD3 from CD68 | Whole | Discovery | Classical | UQ | 122 | DSS | 0.43 (0.26-0.68) | <0.001 |
| Distance to CD3 from CD68 | Whole | Discovery | Classical | UQ | 122 | RFS | 0.50 (0.31-0.80) | 0.004 |
| Distance to CD3CD8 from CD68 | Whole | Discovery | Classical | UQ | 122 | DSS | 0.45 (0.28-0.72) | <0.001 |
| Distance to CD3CD8 from CD68 | Whole | Discovery | Classical | UQ | 122 | RFS | 0.46 (0.29-0.75) | 0.002 |
| Distance to CD68 from PanCk | Whole | Discovery | Squamous | LQ | 53 | DSS | 2.24 (1.14-4.42) | 0.018 |
| Distance to CD68 from PanCk | Whole | Discovery | Squamous | LQ | 53 | RFS | 2.09 (1.05-4.13) | 0.033 |
| Distance to CD68 from CD3CD8 | Whole | Discovery | Squamous | Med | 53 | DSS | 1.84 (1.00-3.38) | 0.046 |

**Supplementary table 8.1 Nearest neighbour patterns associated with disease specific survival in naïve cohorts across molecular subtypes in whole cores.** *Cut-off method established per pattern in discovery cohort. Nearest neighbour pattern reported per cohort and region, patient group indicated, along with number of patients in each group. Log Rank (Mantel-Cox) p value and Univariate cox regression hazard ratio (HR) shown with 95% confidence interval (CI).*

### 8.2.2 Multivariate Cox regression analysis naïve multiplex immunofluorescence

Density and nearest neighbour groups were split to avoid overloading the model. In density only models, CD3CD8+ and margin status were most significant in the discovery cohort. Low cellular density of CD3CD8+ (p=0.007, HR= 1.59 (1.13-2.23) was significantly associated with poor survival in treatment naïve pancreatic cancer (supplementary figure 8.1.a). When investigating the distances from tumour cells, CD8+ and margin status were most significant in the Discovery cohort. A short distance to CD8+ cells from PanCk+ (p=0.008, HR= 0.60 (0.41-0.87) was associated with better survival (supplementary figure 8.1.c). Short distance to αSMA cells from CD3+ (p=0.007, HR= 1.53 (1.13-2.08) and margin status 1, was observed in poor prognostic patients (supplementary figure 8.1.g). Although spatial metrics retain their prognostic significance, margin continuously outcompetes them. Unexpectedly, one validated spatial parameter seemed to equal margin status. Decreased distance to CD3+ cells from CD68+ (p<0.001, HR= 0.59 (0.43-0.80) was significantly associated with better survival (supplementary figure 8.1.e). These patterns were replicated in the Validation cohort (supplementary figure 8.1.b, supplementary figure 8.1.d, supplementary figure 8.1.f and supplementary figure 8.1.h).

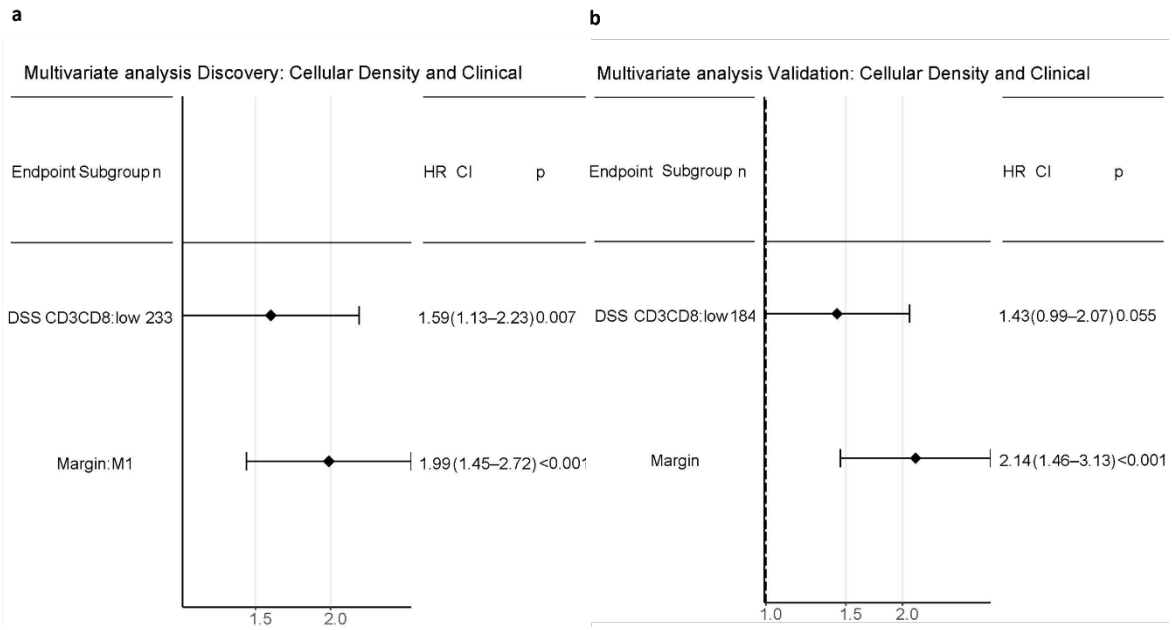


**Supplementary figure 8.1.a-b Final multivariate cox regression forest plot with clinical variables in discovery and validation naïve PDAC cohorts** *a) Density for discovery cohort b) Density for validation cohort. HR= Hazard ratio, CI = Confidence interval, n = number.*

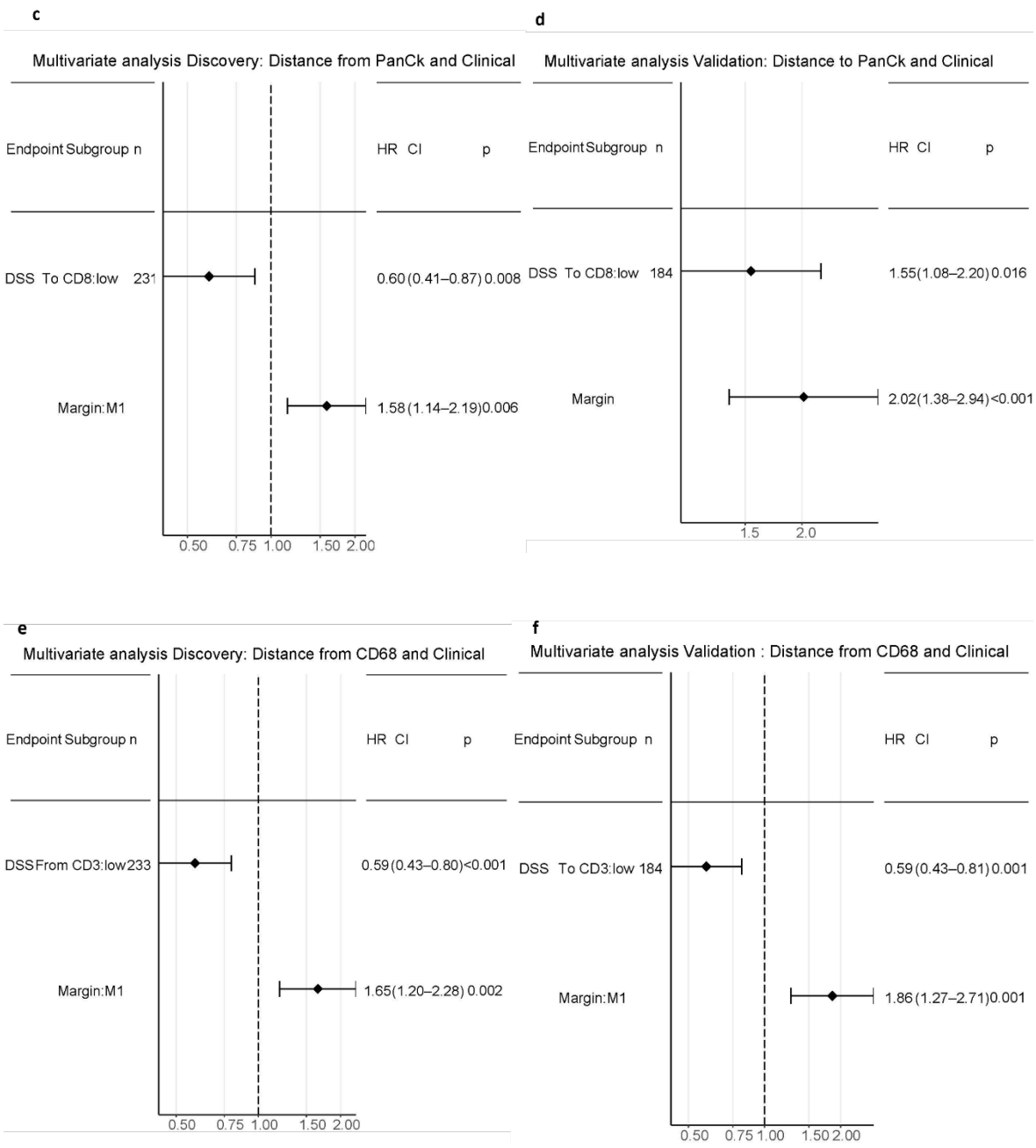


**Supplementary figure 8.1.c-f Final multivariate cox regression forest plot with clinical variables in discovery and validation naïve PDAC cohorts** *c). Distance from tumour cells in discovery cohort d). Distance from tumour in validation cohort e). Distance from macrophages cells in discovery cohort f). Distance from macrophages cells in validation cohort. HR= Hazard ratio, CI = Confidence interval, n = number*.

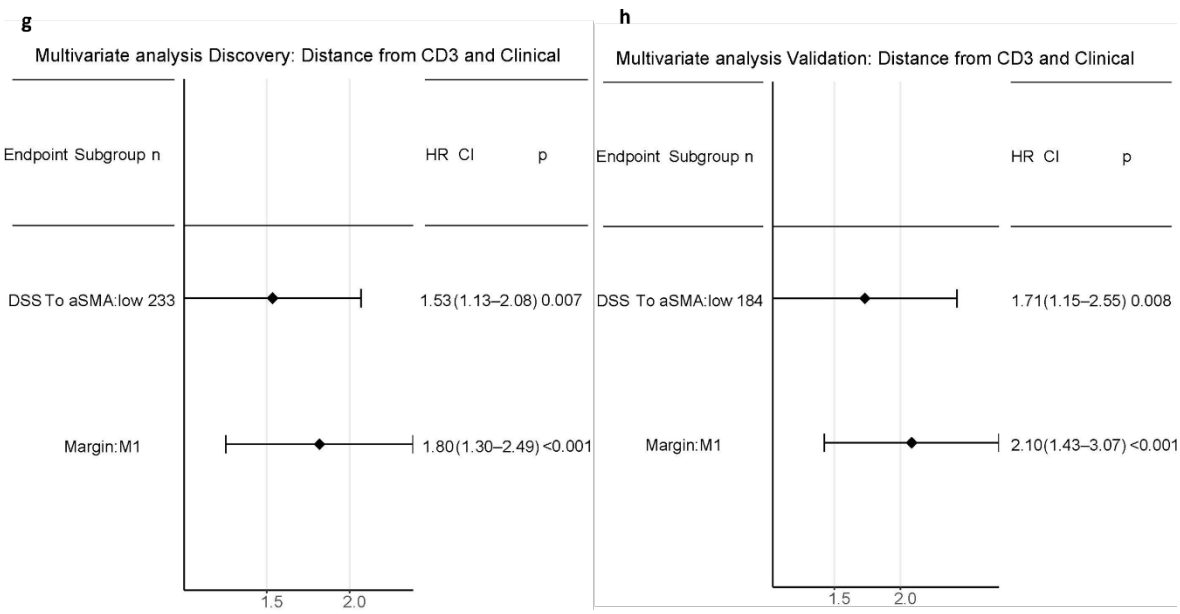


**Supplementary figure 8.1.g-h Final multivariate cox regression forest plot with clinical variables in discovery and validation naïve PDAC cohorts** *g). Distance from CD3 helper T cells in discovery cohort h). Distance from CD3 helper T cells in validation cohort. HR= Hazard ratio, CI = Confidence interval, n = number.*

# 8.3 Chapter 4 supplementary

## 8.3.1 Prognostically favourable nearest neighbour tumour immune landscape across clinical groups in neoadjuvant pancreatic cancer

Relevant clinical subgroups were investigated in the neoadjuvant cohort. Initially, different neoadjuvant treatment types were investigated. Chemotherapy treated patients with better outcome associated with short distance to CD3CD8+ (p=0.019), and large distances to PanCk+ (p<0.001) cells from αSMA+ (supplementary table 8.2). Furthermore, large distances from CD3CD8+ to PanCk+ (p=0.020), from CD3CD8+ to FOXP3CD3+ (p=0.037), from CD68+ to αSMA+ (p=0.045), and from FOPX3CD3+ to CD68+ (p=0.026) correlated with better prognosis (supplementary table 8.2). In comparison, longer survival chemoradiotherapy patients presented with different trends. Reduced distance from PanCk+ to αSMA+ (p=0.017), from CD3CD8+ to αSMA+ (p=0.011), and longer distances from CD3CD8+ to CD3+ (p=0.003), to CD68+ (p=0.002) and to FOXP3CD3+ (p=0.017) correlated with improved prognosis in chemoradiotherapy patients. Shorter distances to αSMA+ (p=0.008) and longer distances to CD3+ (p=0.005) from FOXP3CD3+ were also observed in better outcome patients (supplementary table 8.2).

Next, different types of chemotherapeutic drugs were investigated. Notably, FOLFIRINOX treated patients with better outcome correlated with more nearest neighbour phenotypic relationships compared to Gemcitabine treated longer survivors. Better outcome patients receiving Gemcitabine based treatment only demonstrated one significant pattern, specifically, short distances from CD3+ to αSMA+ cells (p=0.015) (supplementary table 8.2). In contrast, short distances from PanCk+ to CD3+ (p=0.001), and longer distances from αSMA+ to CD68+ (p=0.041), to PanCk+ (p=0.001), and from CD3+ to PanCk+ (p=0.041), to FOXP3CD3+ (p=0.002) and to CD68+ (p=0.010) all correlate with improved prognosis (supplementary table 8.2). In addition, multiple T regulatory related trends appear. Longer survivors displayed shorter distances from FOXP3CD3+ to αSMA+ (p=0.037), and larger distances from FOXP3CD3+ to PanCk+ (p=0.004), and to CD3CD8+ (p=0.002) (supplementary table 8.2).

Treatment response as defined by regression status was investigated. Good response patients associated with larger distances from PanCk+ cells to FOXP3CD3+ (p=0.005), from αSMA+ to PanCk+ (p=0.034) and to CD68+ (p=0.006) (supplementary table 8.2). Moreover, increased distances from CD3CD8+ cells to CD68+ (p=0.003) and to FOXP3CD3+ (p=0.010), and reduced distances to αSMA from CD3+ (p=0.020 presented in better survival, good response patients (supplementary table 8.2). Poor response patients presented with much fewer trends associated with survival, and those seen were replicated in the good response group. Reduced distance to CD3CD8+ from PanCk+ (p=0.045), and larger distances from FOXP3CD3+ to CD3CD8+ cells (p=0.012) and from CD68+ to PanCk+ cells (p=0.042) linked with significantly better survival (supplementary table 8.2). These findings, although counterintuitive, are not surprising considering results observed in chapter 4.5 and chapter 4.7.1.

| Nearest neighbour trends in disease specific survival in clinical subgroups of neoadjuvant cohort | | | | | | |
|---|---|---|---|---|---|---|
| **Phenotype** | **Region** | **Cohort** | **Group** | **Number** | **HR (95% CI)** | **P value** |
| Distance to CD8 from PanCK | Whole core | Neoadjuvant | Chemotherapy treated | 46 | 7.54 (2.17-26.2) | 0.001 |
| Distance to CD3CD8 from aSMA | Whole core | Neoadjuvant | Chemotherpay treated | 46 | 2.19 (1.13-4.24) | 0.019 |
| Distance to CD8 from aSMA | Whole core | Neoadjuvant | Chemotherpay treated | 46 | 5.80 (2.13-15.8) | <0.001 |
| Distance to PanCK from aSMA | Whole core | Neoadjuvant | Chemotherpay treated | 46 | 0.27 (0.13-0.56) | <0.001 |
| Distance to PanCk from CD3CD8 | Whole core | Neoadjuvant | Chemotherpay treated | 46 | 0.43 (0.21-0.87) | 0.020 |
| Distance to FOXP3CD3 from CD3CD8 | Whole core | Neoadjuvant | Chemotherpay treated | 46 | 0.38 (0.16-0.94) | 0.037 |
| Distance to aSMA from CD68 | Whole core | Neoadjuvant | Chemotherpay treated | 46 | 0.29 (0.09-0.97) | 0.045 |
| Distance to CD68 from FOXP3CD3 | Whole core | Neoadjuvant | Chemotherpay treated | 46 | 0.48 (0.25-0.92) | 0.026 |
| Distance to aSMA from PanCK | Whole core | Neoadjuvant | Chemoradiotherpay treated | 24 | 4.02 (1.29-12.5) | 0.017 |
| Distance to aSMA from CD3CD8 | Whole core | Neoadjuvant | Chemoradiotherpay treated | 24 | 4.11 (1.38-12.2) | 0.011 |
| Distance to CD3 from CD3CD8 | Whole core | Neoadjuvant | Chemoradiotherpay treated | 24 | 0.12 (0.03-0.49) | 0.003 |
| Distance to CD68 from CD3CD8 | Whole core | Neoadjuvant | Chemoradiotherpay treated | 24 | 0.16 (0.05-0.52) | 0.002 |
| Distance to FOXP3CD3 from CD3CD8 | Whole core | Neoadjuvant | Chemoradiotherpay treated | 24 | 0.08 (0.01-0.64) | 0.017 |
| Distance to aSMA from FOXP3CD3 | Whole core | Neoadjuvant | Chemoradiotherpay treated | 24 | 4.41 (1.48-13.1) | 0.008 |
| Distance to CD3 from FOXP3CD3 | Whole core | Neoadjuvant | Chemoradiotherpay treated | 24 | 0.10 (0.02-0.50) | 0.005 |
| Distance to CD3 from PanCK | Whole core | Neoadjuvant | FOLFIRINOX | 52 | 4.52(1.81-11.3) | 0.001 |
| Distance to PanCK from aSMA | Whole core | Neoadjuvant | FOLFIRINOX | 52 | 0.33 (0.16-0.65) | 0.001 |
| Distance to CD68 from aSMA | Whole core | Neoadjuvant | FOLFIRINOX | 52 | 0.53 (0.29-0.97) | 0.041 |
| Distance to PanCK from CD3 | Whole core | Neoadjuvant | FOLFIRINOX | 52 | 0.5 (0.26-0.97) | 0.041 |
| Distance to FOXP3CD3 from CD3 | Whole core | Neoadjuvant | FOLFIRINOX | 52 | 0.36 (0.19-0.69) | 0.002 |
| Distance to CD68 from CD3 | Whole core | Neoadjuvant | FOLFIRINOX | 52 | 0.31 (0.13-0.75) | 0.01 |
| Distance to aSMA from CD3CD8 | Whole core | Neoadjuvant | FOLFIRINOX | 52 | 2.01 (1.05-3.84) | 0.034 |
| Distance to FOXP3CD3 from CD3CD8 | Whole core | Neoadjuvant | FOLFIRINOX | 52 | 0.26 (0.13-0.52) | <0.001 |
| Distance to CD68 from CD3CD8 | Whole core | Neoadjuvant | FOLFIRINOX | 52 | 0.42 (0.23-0.78) | 0.006 |
| Distance to PanCK from CD68 | Whole core | Neoadjuvant | FOLFIRINOX | 52 | 0.38 (0.19-0.75) | 0.005 |
| Distance to CD3CD8 from CD68 | Whole core | Neoadjuvant | FOLFIRINOX | 52 | 0.43 (0.21-0.87) | 0.019 |
| Distance to FOXP3CD3 from CD68 | Whole core | Neoadjuvant | FOLFIRINOX | 52 | 0.40 (0.20-0.79) | 0.009 |
| Distance to CD3 from CD68 | Whole core | Neoadjuvant | FOLFIRINOX | 52 | 0.37 (0.19-0.72 | 0.003 |
| Distance to aSMA from FOXP3CD3 | Whole core | Neoadjuvant | FOLFIRINOX | 52 | 2.11 (1.05) | 0.037 |
| Distance to PanCK from FOXP3CD3 | Whole core | Neoadjuvant | FOLFIRINOX | 52 | 0.35 (0.17-0.72) | 0.004 |
| Distance to CD3CD8 from FOXP3CD3 | Whole core | Neoadjuvant | FOLFIRINOX | 52 | 0.34 (0.17-0.67) | 0.002 |
| Distance to aSMA from CD3 | Whole core | Neoadjuvant | Gemcitabine | 18 | 5.24 (1.37-20.0) | 0.015 |
| Distance to FOXP3CD3 from PanCK | Whole core | Neoadjuvant | Good response | 35 | 0.26 (0.10-0.67) | 0.005 |
| Distance to PanCK from aSMA | Whole core | Neoadjuvant | Good response | 35 | 0.40(0.17-0.93) | 0.034 |
| Distance to CD68 from aSMA | Whole core | Neoadjuvant | Good response | 35 | 0.31 (0.13-0.71) | 0.006 |
| Distance to CD68 from CD3CD8 | Whole core | Neoadjuvant | Good response | 35 | 0.24 (0.09-0.62) | 0.003 |
| Distance to FOXP3CD3 from CD3CD8 | Whole core | Neoadjuvant | Good response | 35 | 0.33 (0.14-0.77) | 0.01 |
| Distance to aSMA from CD3 | Whole core | Neoadjuvant | Good response | 35 | 2.51 (1.16-5.45) | 0.02 |
| Distance to CD3CD8 from PanCK | Whole core | Neoadjuvant | Poor response | 33 | 2.28 (1.02-5.12) | 0.045 |
| Distance to CD3CD8 from FOXP3CD3 | Whole core | Neoadjuvant | Poor response | 33 | 0.29 (0.11-0.76) | 0.012 |
| Distance to PanCK from CD68 | Whole core | Neoadjuvant | Poor response | 33 | 0.42 (0.18-0.97) | 0.042 |

**Supplementary table 8.2 Nearest neighbour patterns associated with disease specific survival in clinical subgroups in neoadjuvant cohorts looking at whole core**. *Cut off generated per nearest neighbour pattern, cohort, patient group and number indicated. Log Rank (Mantel-Cox) p value and Univariate Cox regression hazard ratio (HR) shown with 95% confidence interval (CI).*

## 8.3.2 Prognostically favourable tumour immune landscape in different neoadjuvant treatment types at different radii

In the neoadjuvant cohort, chemoradiotherapy treated patients tend to do better than chemotherapy alone. Focusing on chemotherapy treated patients, low density of αSMA+ (p=0.008) within 30μm from PanCk+ cells, and low density of CD68+ (p=0.045) from 10μm of FOXP3CD3+ was affiliated with longer survival (supplementary table 8.3). Interestingly, more trends were seen in chemoradiotherapy patients. Patients with low

levels of CD3+ (p=0.04) and FOXP3CD3+ (p=0.046) correlated with better DSS at 20μm from PanCk+ cells (supplementary table 8.3). Additionally, longer surviving patients presented with a low density of CD3+ cells (p=0.03), CD3CD8+ (p=0.027) and CD68+ (p=0.005) within 40μm of αSMA+ cells (supplementary table 8.3).

Different types of neoadjuvant chemotherapy were investigated. Similarly, to the nearest neighbour results (chapter 4.7.2), Gemcitabine based treated patients only showed one significant radius pattern. At 30μm from FOXP3CD3, low density of CD68+ cells (p=0.044) correlated with improved survival (supplementary table 8.3). Multiple trends were observed in longer survivor FOLFIRINOX treated patients, particularly, a reduced density of CD3CD8+ (p=0.022) and FOXP3CD3+ (p=0.044) within 30μm from PanCk+ cells, and low density of CD3CD8+ (p=0.009), CD68+ (p=0.032) and FOXP3CD3+ (p<0.001) within 30μm from CD3+ cells was observed in longer survivors. Interestingly, elevated levels of αSMA+ within 30μm from CD3+ (p=0.042), 30μm from CD3CD8+ (p=0.033), and 40μm from FOXP3CD3+ (p=0.019) is also seen in patients with better outcome (supplementary table 8.3).

Within the better response patients, there is a subgroup that does much better, most likely due to complete or partially complete pathological response. These patients presented with a low density of CD3+ (p=0.005), CD3CD8+ (p=0.022), CD68+ (p=0.037) and FOXP3CD3+ (p=0.017) within 30μm of PanCk+, and low density of CD3+ (p=0.004) and CD3CD8+ (p=0.048) within 30μm of αSMA+ cells (supplementary table 8.3). A low density of CD3CD8+ (p=0.047), CD68+ (p=0.007), PanCk+ (p=0.018) and FOXP3CD3+ (p=0.033) at 40μm from CD3+ was also observed (supplementary table 8.3).
Although patients may have a poor outcome, it is beneficial to characterise what differences are seen between those that do poorly and those that do slightly better. At 10μm, low density of PanCk+ (p=0.02) from CD3 helper T cells, and low density of FOXP3CD3+ (p=0.011) at 20μm from CD3CD8+ T cells were observed in better outcome patients (supplementary table 8.3).

| Radius trends in disease specific survival in clinical subgroups of neoadjuvant patients | | | | | | | |
|---|---|---|---|---|---|---|---|
| **From Phenotype** | **To Phenotype** | **Distance (um)** | **Cohort** | **Group** | **Number** | **HR (95% CI)** | **P value** |
| PanCK | aSMA | 30 | Neoadjuvant | Chemotherapy treated | 46 | 2.91 (1.33-6.36) | 0.008 |
| FOXP3CD3 | CD68 | 10 | Neoadjuvant | Chemotherpay treated | 46 | 2.03 (1.01-4.06) | 0.045 |
| PanCk | CD3 | 20 | Neoadjuvant | Chemoradiotherapy treated | 24 | 2.79 (1.05-7.42) | 0.04 |
| PanCk | FOXP3CD3 | 20 | Neoadjuvant | Chemoradiotherapy treated | 24 | 4.64 (1.03-21.0) | 0.046 |
| aSMA | CD3 | 40 | Neoadjuvant | Chemoradiotherapy treated | 24 | 3.85 (1.14-13.0) | 0.03 |
| aSMA | CD3CD8 | 40 | Neoadjuvant | Chemoradiotherapy treated | 24 | 3.24 (1.14-9.21) | 0.027 |
| aSMA | CD68 | 40 | Neoadjuvant | Chemoradiotherapy treated | 24 | 4.64 (1.59-13.6) | 0.005 |
| CD3 | CD3CD8 | 30 | Neoadjuvant | FOLFIRINOX | 52 | 2.21 (1.22-4.00) | 0.009 |
| CD3 | CD68 | 30 | Neoadjuvant | FOLFIRINOX | 52 | 2.78 (1.09-7.07) | 0.032 |
| CD3 | PanCk | 30 | Neoadjuvant | FOLFIRINOX | 52 | 2.40 (1.07-5.40) | 0.035 |
| CD3 | FOXP3CD3 | 30 | Neoadjuvant | FOLFIRINOX | 52 | 3.61 (1.80-7.25) | <0.001 |
| CD3 | aSMA | 30 | Neoadjuvant | FOLFIRINOX | 52 | 0.42 (0.19-0.97) | 0.042 |
| CD3CD8 | CD68 | 30 | Neoadjuvant | FOLFIRINOX | 52 | 2.78 (1.09-7.07) | 0.032 |
| CD3CD8 | FOXP3CD3 | 30 | Neoadjuvant | FOLFIRINOX | 52 | 2.25 (1.21-4.19) | 0.01 |
| CD3CD8 | aSMA | 30 | Neoadjuvant | FOLFIRINOX | 52 | 0.50 (0.27-0.95) | 0.033 |
| CD68 | CD3CD8 | 30 | Neoadjuvant | FOLFIRINOX | 52 | 2.97(1.56-5.64) | <0.001 |
| CD68 | PanCK | 30 | Neoadjuvant | FOLFIRINOX | 52 | 2.15 (1.05-4.40) | 0.037 |
| CD68 | FOXP3CD3 | 30 | Neoadjuvant | FOLFIRINOX | 52 | 2.56 (1.36-4.82) | 0.004 |
| PanCK | CD3CD8 | 30 | Neoadjuvant | FOLFIRINOX | 52 | 2.03 (1.11-3.73) | 0.022 |
| PanCK | FOXP3CD3 | 30 | Neoadjuvant | FOLFIRINOX | 52 | 1.97 (1.02-3.81) | 0.044 |
| FOXP3CD3 | CD3 | 40 | Neoadjuvant | FOLFIRINOX | 52 | 2.27 (1.03-4.98) | 0.041 |
| FOXP3CD3 | CD3CD8 | 40 | Neoadjuvant | FOLFIRINOX | 52 | 4.06 (2.01-8.20) | <0.001 |
| FOXP3CD3 | CD68 | 40 | Neoadjuvant | FOLFIRINOX | 52 | 2.54 (1.24-5.19) | 0.01 |
| FOXP3CD3 | PanCK | 40 | Neoadjuvant | FOLFIRINOX | 52 | 3.91 (1.19-12.8) | 0.024 |
| FOXP3CD3 | aSMA | 40 | Neoadjuvant | FOLFIRINOX | 52 | 0.45 (0.24-0.88) | 0.019 |
| aSMA | CD3 | 30 | Neoadjuvant | FOLFIRINOX | 52 | 1.89 (1.03-3.46) | 0.038 |
| aSMA | PanCK | 30 | Neoadjuvant | FOLFIRINOX | 52 | 2.39 (1.29-4.43) | 0.006 |
| aSMA | FOXP3CD3 | 30 | Neoadjuvant | FOLFIRINOX | 52 | 2.19 (1.01-4.77) | 0.047 |
| FOXP3CD3 | CD68 | 30 | Neoadjuvant | Gemcitabine | 18 | 3.37 (1.03-11.0) | 0.044 |
| PanCK | CD3 | 30 | Neoadjuvant | Good response | 35 | 355 (1.46-8.62) | 0.005 |
| PanCK | CD3CD8 | 30 | Neoadjuvant | Good response | 35 | 2.53 (1.14-5.58) | 0.022 |
| PanCK | CD68 | 30 | Neoadjuvant | Good response | 35 | 2.50 (1.05-5.92) | 0.037 |
| PanCK | FOXP3CD3 | 30 | Neoadjuvant | Good response | 35 | 2.75 (1.20-6.27) | 0.017 |
| aSMA | CD3 | 30 | Neoadjuvant | Good response | 35 | 3.81 (1.53-9.52) | 0.004 |
| aSMA | CD3CD8 | 30 | Neoadjuvant | Good response | 35 | 2.16 (1.01-4.64) | 0.048 |
| CD3 | CD3CD8 | 40 | Neoadjuvant | Good response | 35 | 2.14 (1.01-4.54) | 0.047 |
| CD3 | CD68 | 40 | Neoadjuvant | Good response | 35 | 10.7 (1.93-59.3) | 0.007 |
| CD3 | PanCk | 40 | Neoadjuvant | Good response | 35 | 3.30 (1.22-8.91) | 0.018 |
| CD3 | FOXP3CD3 | 40 | Neoadjuvant | Good response | 35 | 4.49 (1.79-11.3) | 0.001 |
| CD3 | PanCk | 10 | Neoadjuvant | Poor response | 33 | 2.76 (1.09-7.02) | 0.033 |
| CD3CD8 | FOXP3CD3 | 20 | Neoadjuvant | Poor response | 33 | 2.58 (1.13-5.88) | 0.024 |

**Supplementary table 8.3 Radii patterns associated with disease specific survival in clinical subgroups of neoadjuvant cohorts looking at whole core**. *Radii reported using 'from phenotype' column, indicating the central phenotype, and 'to phenotype' indicating the surrounding phenotype. Reported by distance (μm), cohort, patient group, along with number of patients in each group. Most significant radii is reported. Log Rank (Mantel-Cox) p value and Univariate Cox regression hazard ratio (HR) shown with 95% confidence interval (CI) for disease specific survival (DSS) and recurrence free survival (RFS).*

### 8.3.3 Multivariate Cox regression analysis in neoadjuvant multiplex immunofluorescence

Multivariate cox regression analysis was performed on significant density and nearest neighbour patterns and adjusted for lymph node status and resection margin status. Density and nearest neighbour patterns were compared separately. In the density model, only CD3CD8+ and PanCk+ remained significant. A low density of CD3CD8+ cells ($p<0.001$, HR = 0.26 (0.14-0.50)) and PanCk+ cells ($p=0.002$, HR = 0.41 (0.23-0.72)) correlated with better survival (supplementary figure 8.2.b). Interestingly, lymph node status and margin status did not appear in the final multivariate model (supplementary figure 8.2.a). Nearest neighbour pairs were split according to phenotype. Poor survivor neoadjuvant patients associated with shorter distance from CD3CD8+ to PanCk+ cells ($p=0.003$, HR=2.58 (1.38-4.83)) (supplementary figure 8.2.c) and shorter distance to CD3+ from CD3CD8+ cells ($p<0.001$, HR = 3.11 (1.71-5.64)) (supplementary figure 8.2.d). Additionally, a shorter distance to CD3CD8+ from FOXP3CD3+ correlated with improved survival in neoadjuvant patients ($p=0.003$, HR=0.2 (0.07-0.58)) (supplementary figure 8.2.e).

a

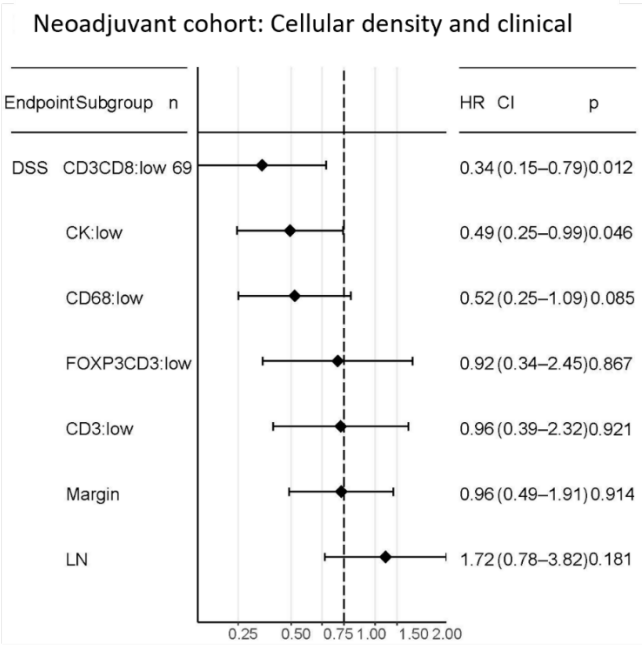


b

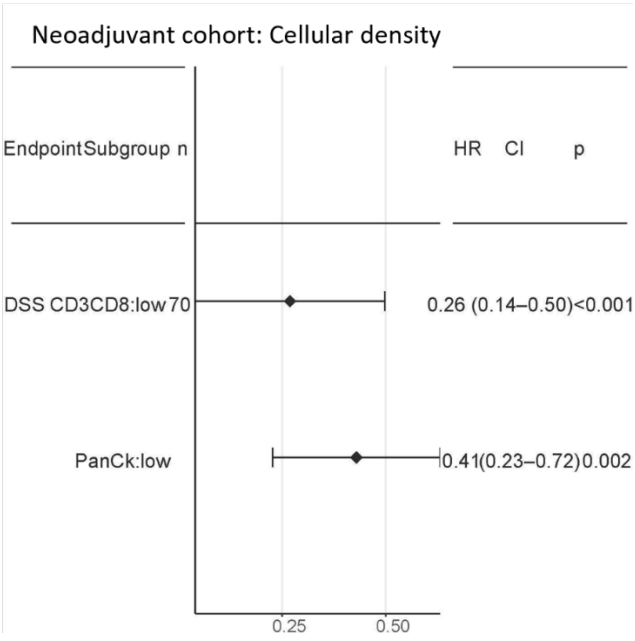


**Supplementary figure 8.2.a-b Final multivariate model cox regression models in neoadjuvant cohort** *a) All phenotype densities and clinical b). Final density model. HR= Hazard ratio, CI = Confidence interval n= number.*

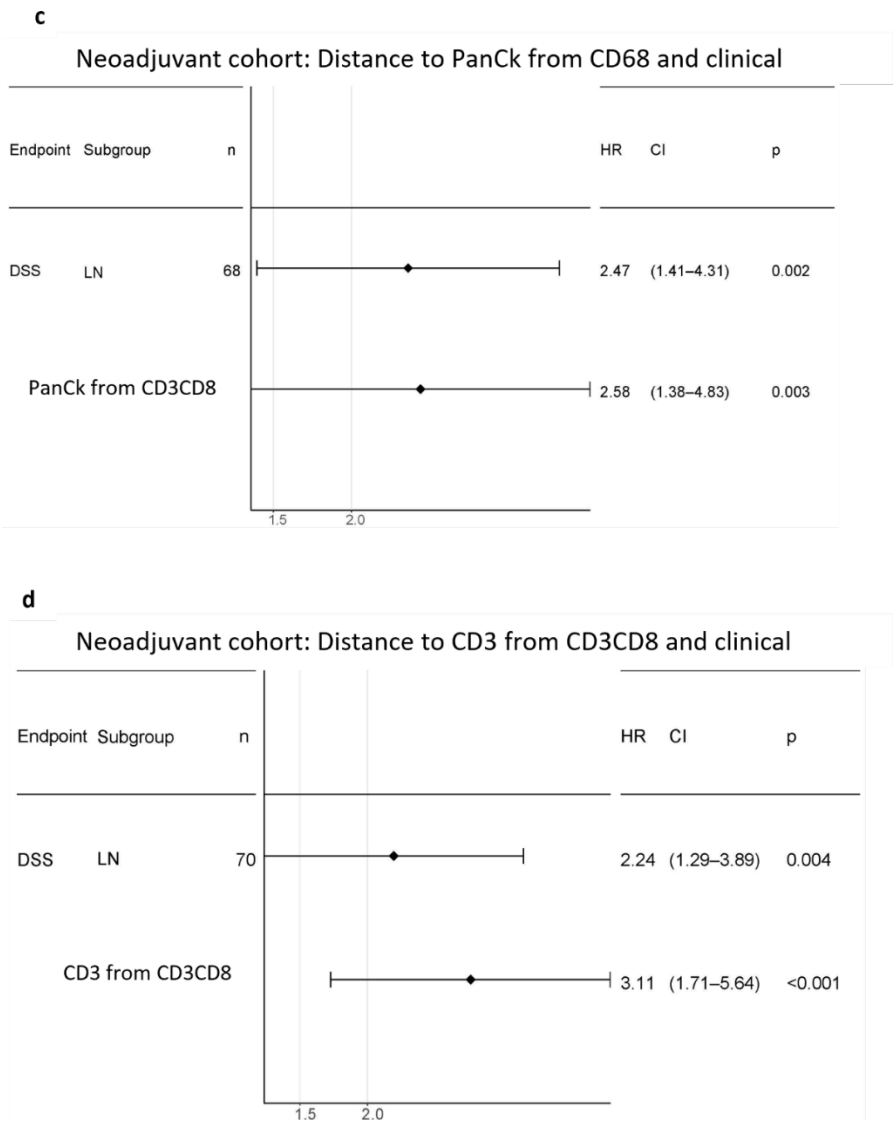


**Supplementary figure 8.2.c-d Final multivariate model cox regression models in neoadjuvant cohort.** *Nearest neighbour distance metric multivariate models split by central phenotype for c). From CD3CD8+ cells to PanCk+ cells d).From CD3CD8+ to CD3+ cells*

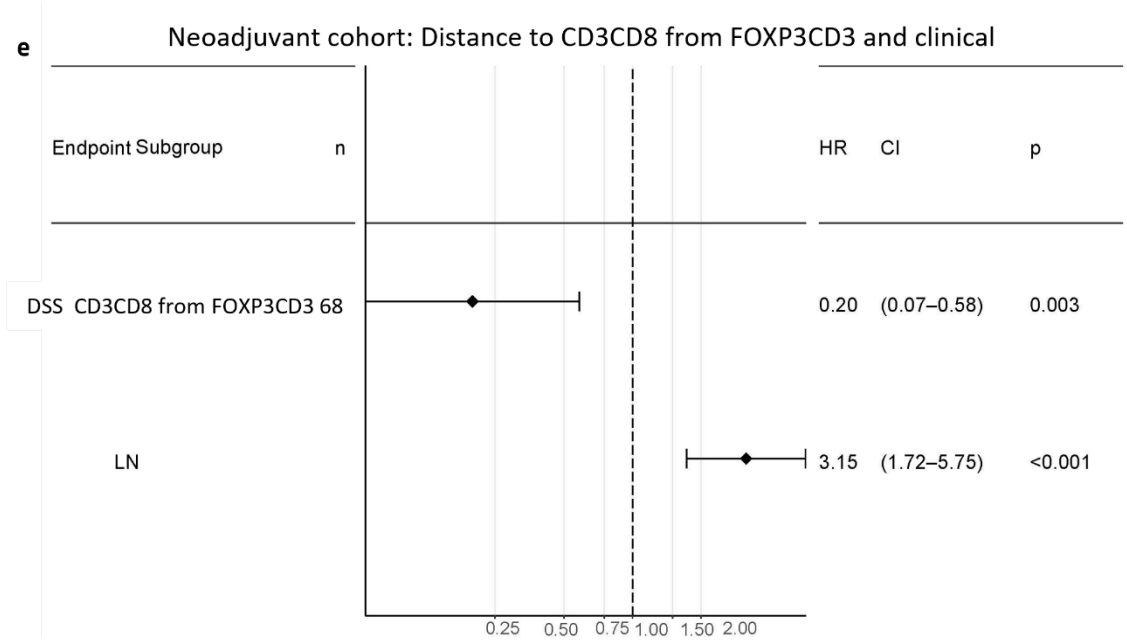


**Supplementary figure 8.2.e Final multivariate model cox regression models in neoadjuvant cohort.** *Nearest neighbour distance metric multivariate models split by central phenotype for e). From FOXP3CD3+ to CD3CD8+*

# 8.4 Chapter 5 supplementary

## 8.4.1 Tumour compartments demonstrate distinct transcriptome profiles in pancreatic cancer

#### 8.4.1.1 Naïve PDAC inter-tumoral heterogeneity

Numerous significant pathway aberrations were observed when comparing segments. Notable pathways observed included, B cell exhaustion (PanCk vs Immune: NES = 2.2, padj <0.0005), T cell exhaustion (PanCk vs Immune: NES = 1.9, padj = 0.01), and EMT (PanCk vs αSMA: NES = 1.6, padj = 0.015), as well as overlapping signalling pathways including PDGF signalling in both αSMA and immune segments (PanCk vs αSMA: NES = 2.3, padj < 0.001, and PanCk vs Immune: NES = 2.2, padj < 0.001) (supplementary figure 8.3.a-b). Furthermore, epithelial segments demonstrated enrichment of a wide range of signalling pathways such as Type 1 INF signalling (PanCk vs αSMA: NES = 2.0, padj <0.001) and NOTCH signalling (PanCk vs αSMA: NES = 1.9, padj <0.0005, and PanCk vs αSMA: NES = 1.9, padj <0.001) (supplementary figure 8.3.a-b).

GSEA differences were also observed between the fibroblast and immune segments, although this was considerably reduced. αSMA segments demonstrated enrichment of structural related pathways such as matrix remodelling and metastasis (NES = 1.7 , padj <0.0005) and cell adhesion and motility (NES = 1.6, padj <0.0005) (supplementary figure 8.3.c). Additionally, upregulation of a range of cell signalling pathways such as PDGF (NES = 2.1, padj <0.001) and MET (NES = 2.0, padj <0.001) signalling was observed. Conversely, immune segments maintained a marked enrichment of innate and adaptive immune pathways similar to the epithelial comparison (supplementary figure 8.3.c) Interestingly, dendritic cells (NES = 2.2, padj <0.001) and natural killer cell activity (NES = 2.1, padj <0.001) were the highest upregulated immune cell related geneset in immune segments (supplementary figure 8.3.c).

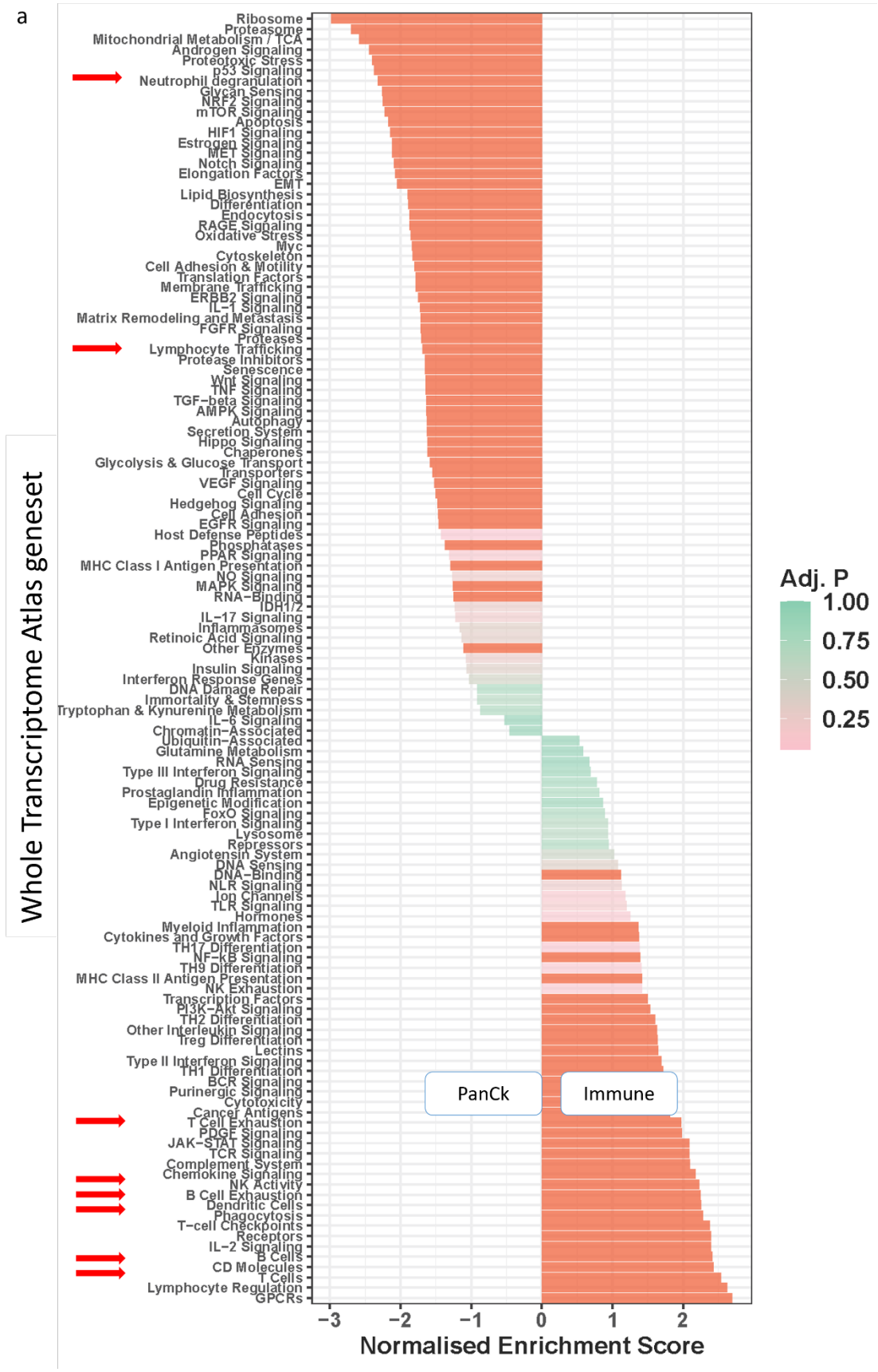


**Supplementary figure 8.3.a Spatial Transcriptomic alterations between naïve segments**, *a). Geneset enrichment bar chart comparing PanCk and immune segments. Pathways with normalized enrichment score above and below 1.5, and p adjusted (Adj. P) value ≤ 0.05 were considered significant. Important pathways are indicated by an arrow.*

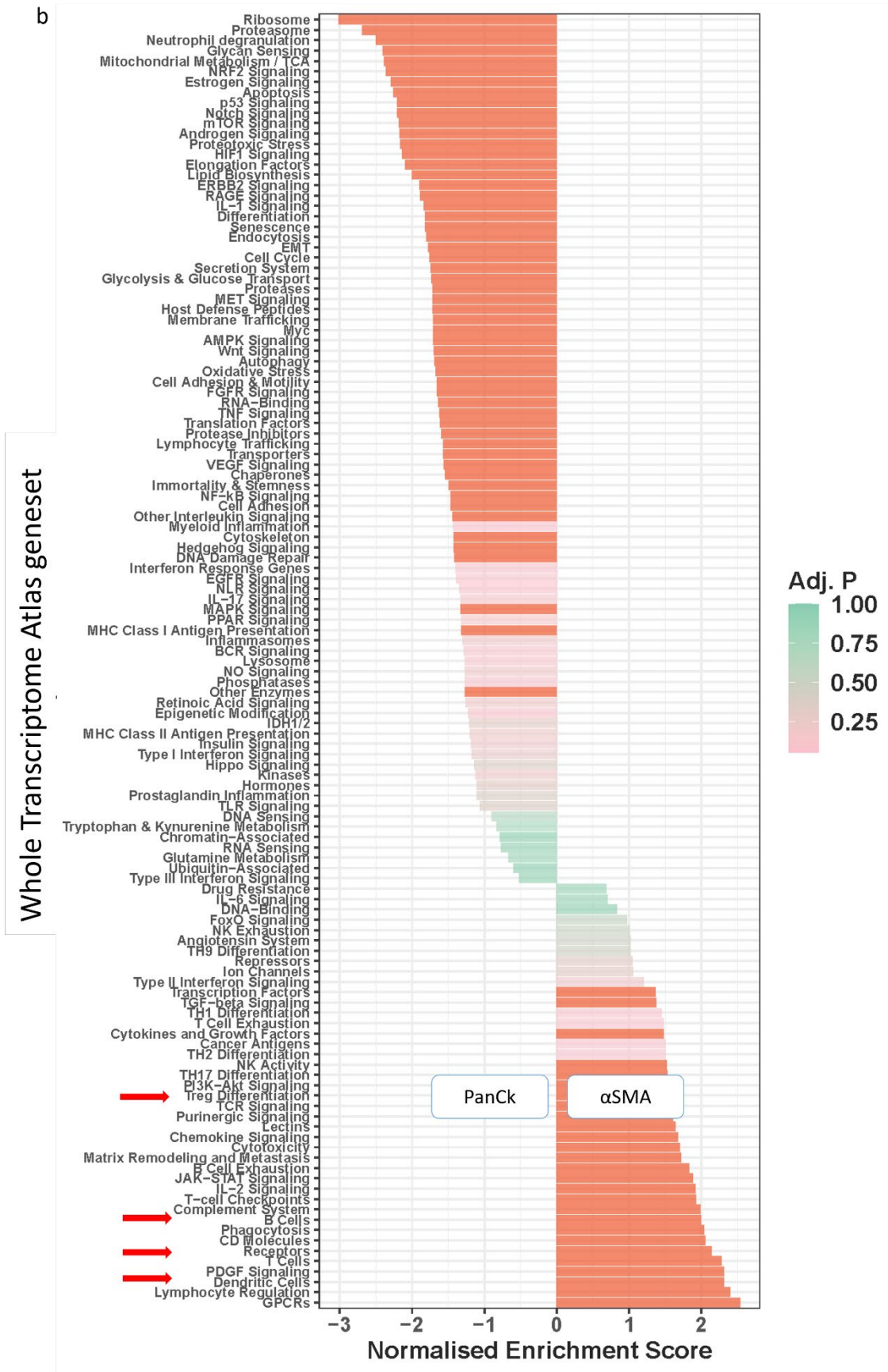


**Supplementary figure 8.3.b Spatial Transcriptomic alterations between naïve segments**. *b). Geneset enrichment bar chart comparing PanCk and αSMA segments. Pathways with normalized enrichment score above and below 1.5, and p adjusted (Adj. P) value ≤ 0.05 were considered significant. Important pathways are indicated by an arrow.*

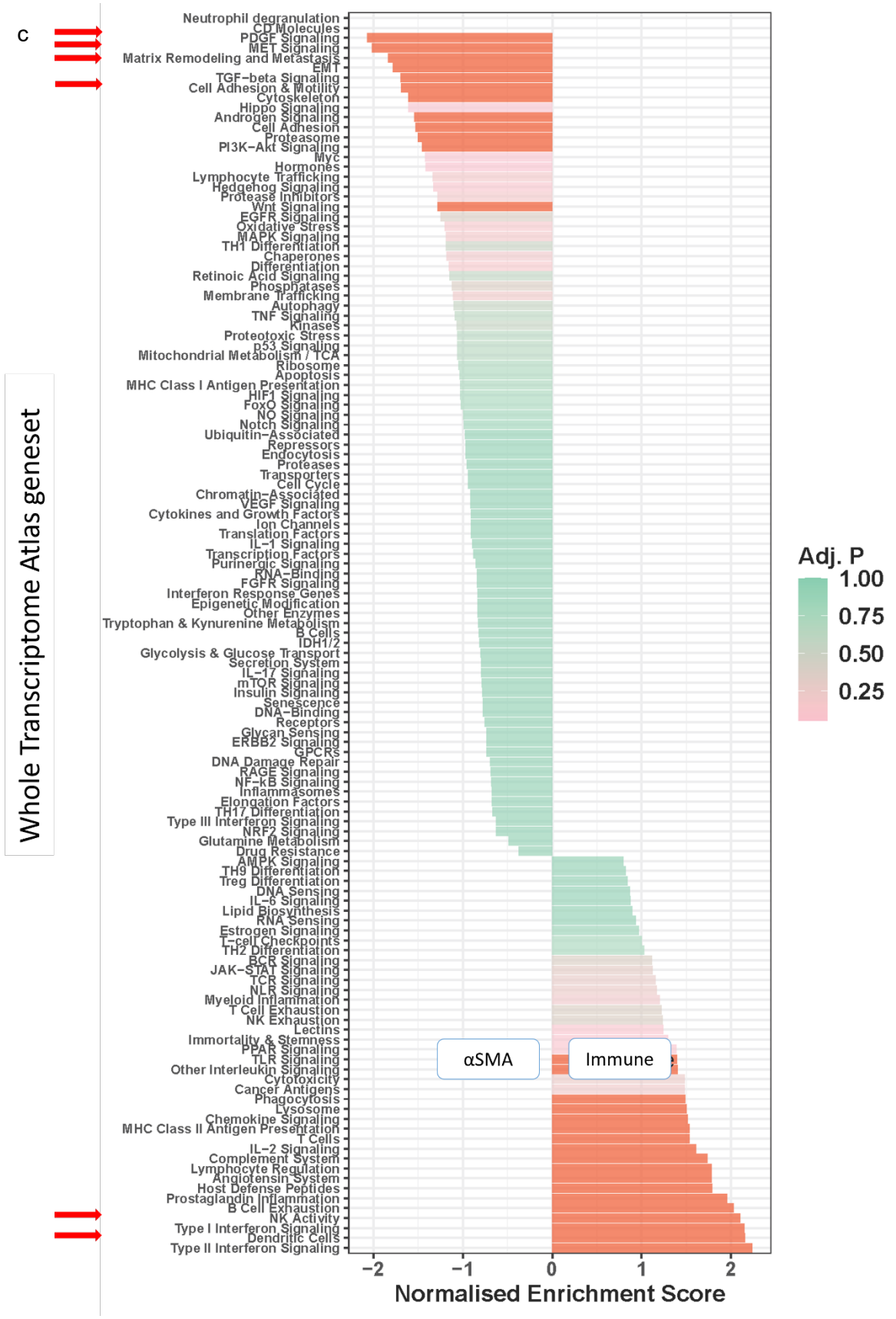


**Supplementary figure 8.3.c Spatial Transcriptomic alterations between naïve segments**. *c). Geneset enrichment bar chart comparing αSMA and immune segments. Pathways with normalized enrichment score above and below 1.5, and p adjusted (Adj. P) value ≤ 0.05 were considered significant. Important pathways are indicated by an arrow.*

Unexpectedly, almost no immune cell pathways appeared in the long-term survival naive groups in either fibroblast rich or immune segment GSEA (supplementary figure 8.4.a-b).

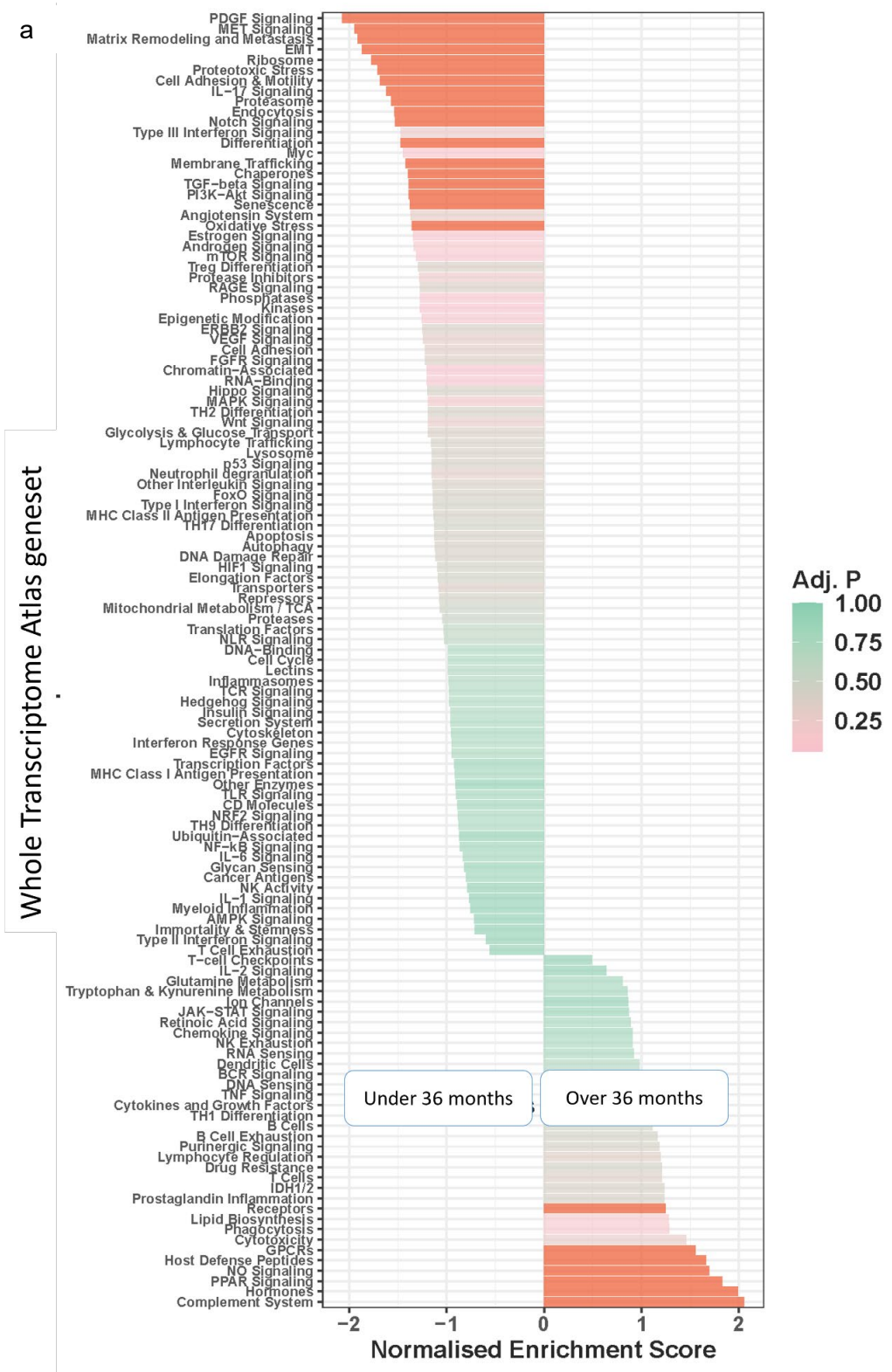


**Supplementary figure 8.4.a Spatial Transcriptomic alterations between LTS and STS segments** *a). Geneset enrichment bar chart comparing patients that survived under 36 months (STS) and over 36 months (LTS) in αSMA segments. Pathways with normalized enrichment score above and below 1.5, and p adjusted (Adj. P) value ≤ 0.05 were considered significant.*

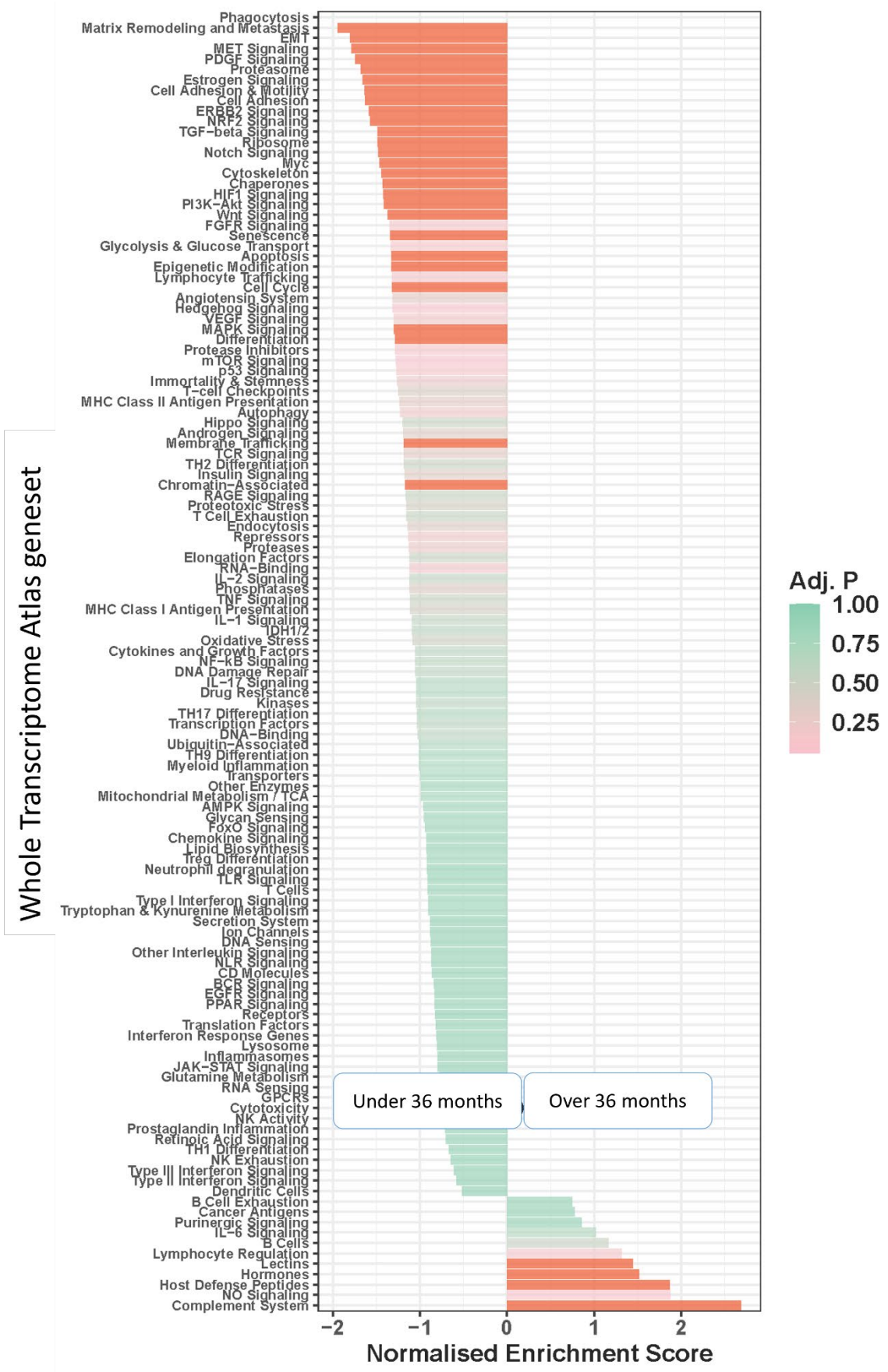


**Supplementary figure 8.4.b Spatial Transcriptomic alterations between LTS and STS segments** *b). Geneset enrichment bar chart comparing patients that survived under 36 months (STS ) and over 36 months (LTS) in immune segments. Pathways with normalized enrichment score above and below 1.5, and p adjusted (Adj. P) value ≤ 0.05 were considered significant.*

#### 8.4.1.2 Neoadjuvant PDAC inter-tumoral heterogeneity

Upregulation of T cells (NES = 2.5, padj <0.001), B cells (NES = 2.5, padj <0.001), dendritic cells (NES = 2.3, padj <0.001), and NK activity (NES = 2.3, padj <0.001) among others were observed in immune segments (supplementary figure 8.5.a). In contrast, dysregulated immune pathways such as B cell exhaustion (NES = 2.2, padj <0.001) and T cell exhaustion (NES = 2.0, padj <0.001) were also observed (supplementary figure 8.5.a). Epithelial regions were primarily upregulated with cell signalling pathways and a few immune pathways. Interestingly, neutrophil degranulation (NES = 2.3, padj <0.001) and lymphocyte trafficking (NES = 1.7, padj =0.008) pathways were upregulated (supplementary figure 8.5.a). Additionally, when comparing stromal and epithelial regions, αSMA regions presented with enriched immune related pathways including T cells (NES = 2.2, padj <0.001), dendritic cells (NES = 2.3, padj <0.001), B cells (NES = 2.0, padj <0.001), Treg differentiation (NES = 1.5, padj =0.05) among others (supplementary figure 8.5.b).

Although limited aberrations were observed at an individual gene level between αSMA and immune regions, distinct variations were observed when looking at pathway analysis. Fibroblast signatures demonstrated elevated MET (NES = 2.4, padj <0.001), PDGF (NES = 2.2, padj <0.001), TGF-b (NES = 2.1, padj <0.001) signalling, as well as lymphocyte trafficking (NES = 1.5, padj =0.04) (supplementary figure 8.5.c).

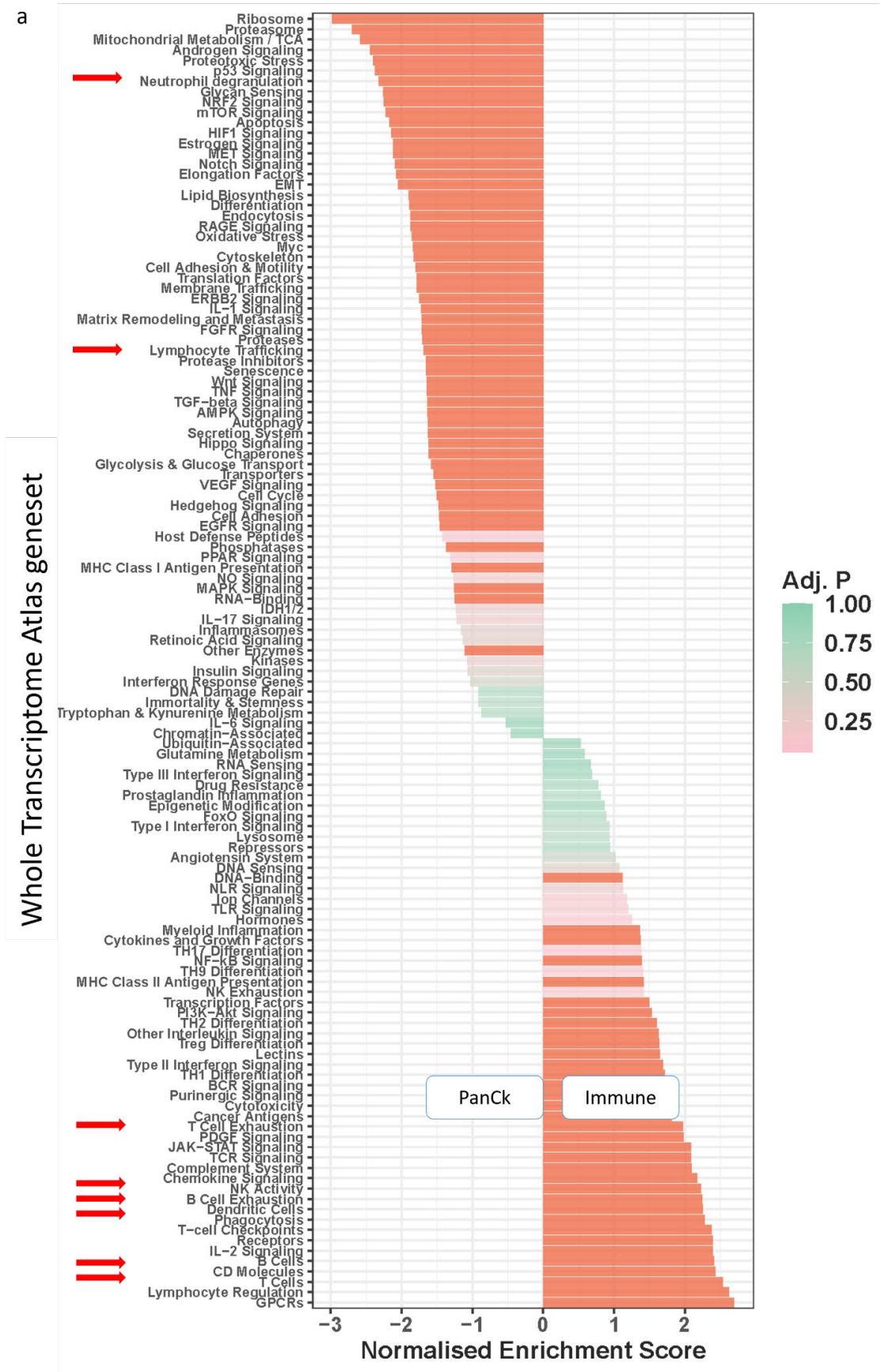


**Supplementary figure 8.5.a Spatial Transcriptomic alterations between neoadjuvant segments**. *a). Geneset enrichment bar chart comparing PanCk and immune segments. Pathways with normalized enrichment score above and below 1.5, and p adjusted (Adj. P) value ≤ 0.05 were considered significant. Important pathways are indicated by an arrow.*

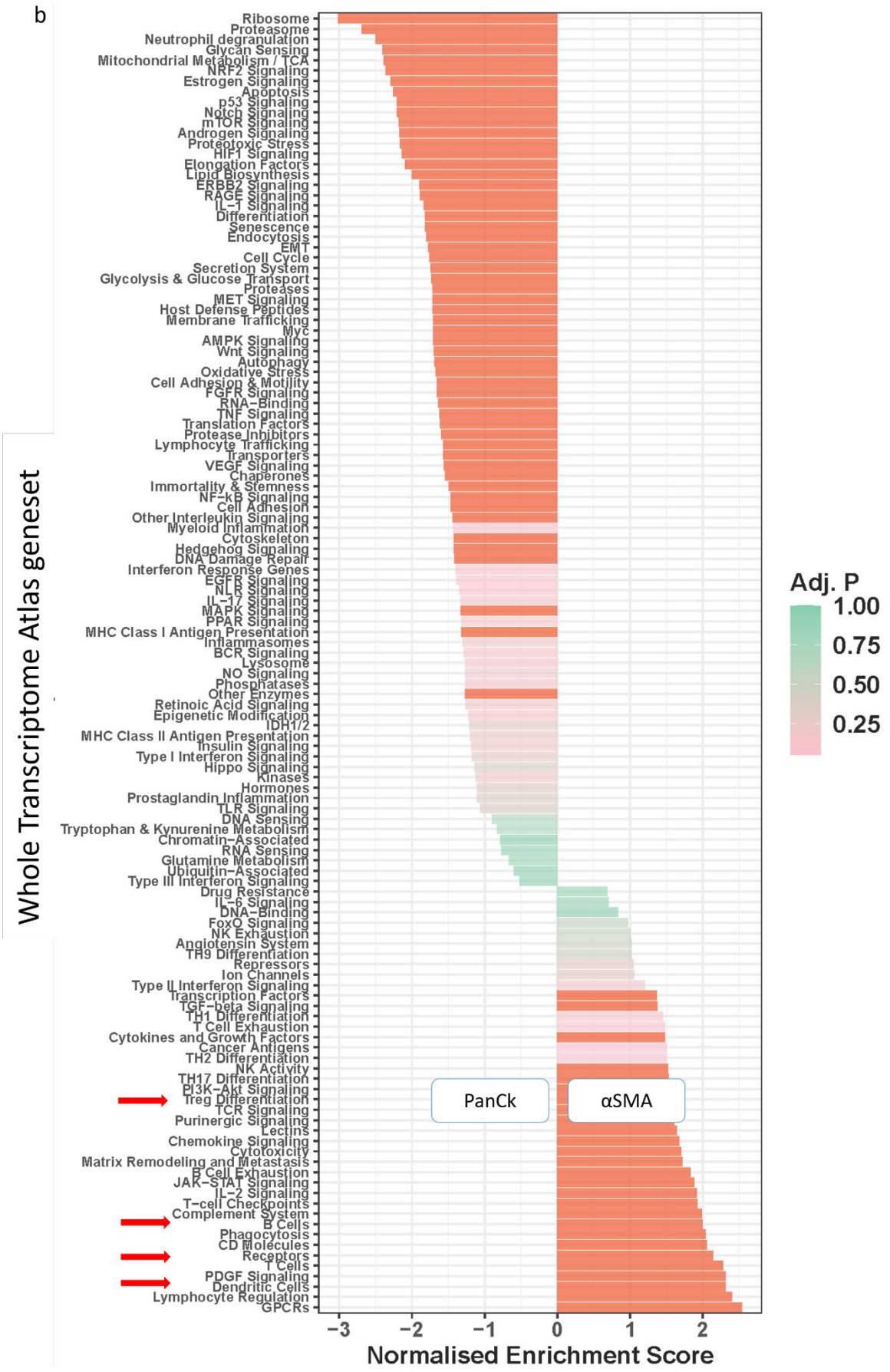


**Supplementary figure 8.5.b Spatial Transcriptomic alterations between neoadjuvant segments**. *b). Geneset enrichment bar chart comparing PanCk and αSMA segments. Pathways with normalized enrichment score above and below 1.5, and p adjusted (Adj. P) value ≤ 0.05 were considered significant. Important pathways are indicated by an arrow.*

c

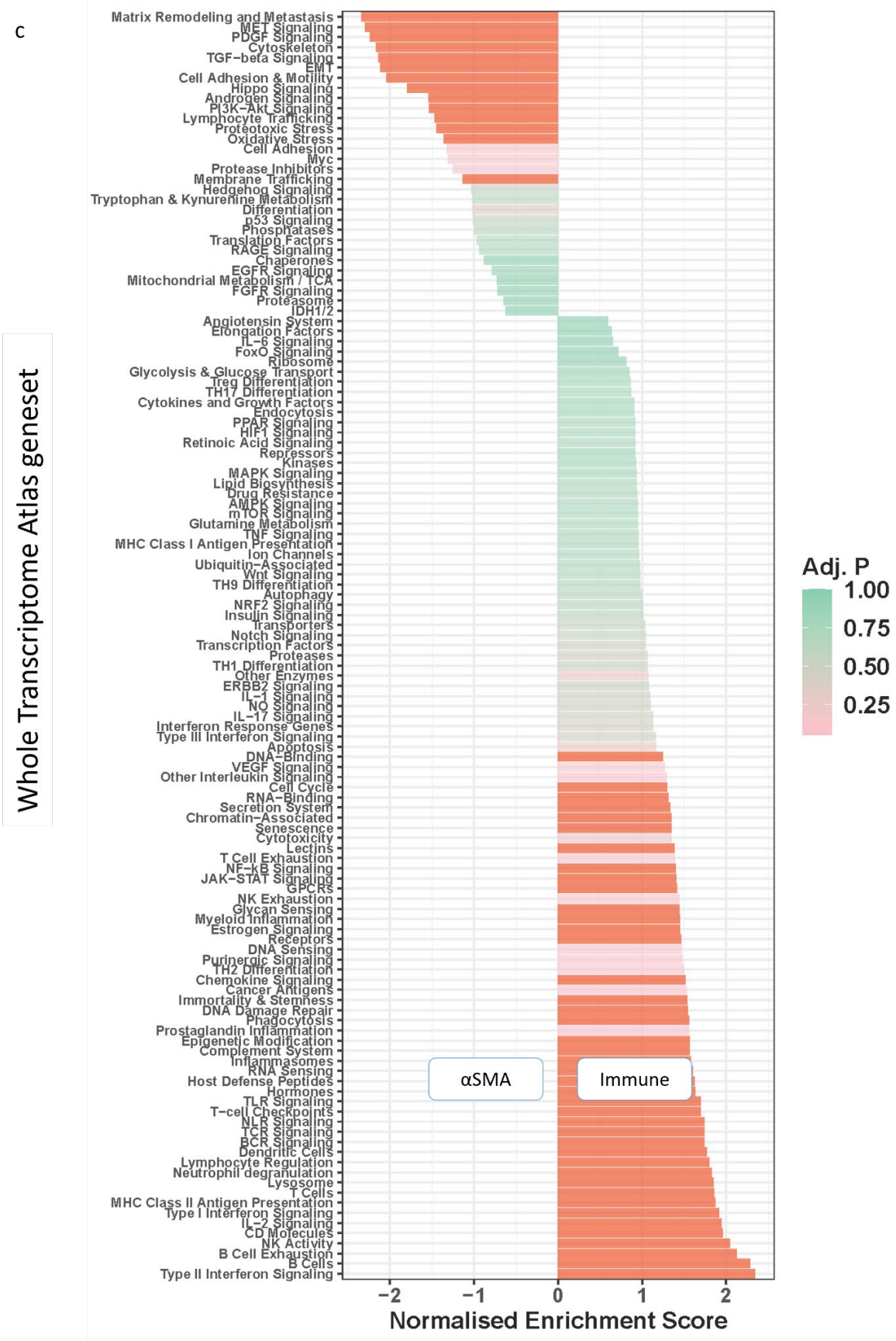


**Supplementary figure 8.5.c Spatial Transcriptomic alterations between neoadjuvant segments**. *c). Geneset enrichment bar chart comparing αSMA and immune segments. Pathways with normalized enrichment score above and below 1.5, and p adjusted (Adj. P) value ≤ 0.05 were considered significant.*

#### 8.4.1.3 Histopathological region heterogeneity in neoadjuvant pancreatic cancer

Pathway analysis illustrated that virtually all signalling pathways measured were significantly downregulated when comparing presumed tumour bed (PTB) to tumour core (supplementary figure 8.6).

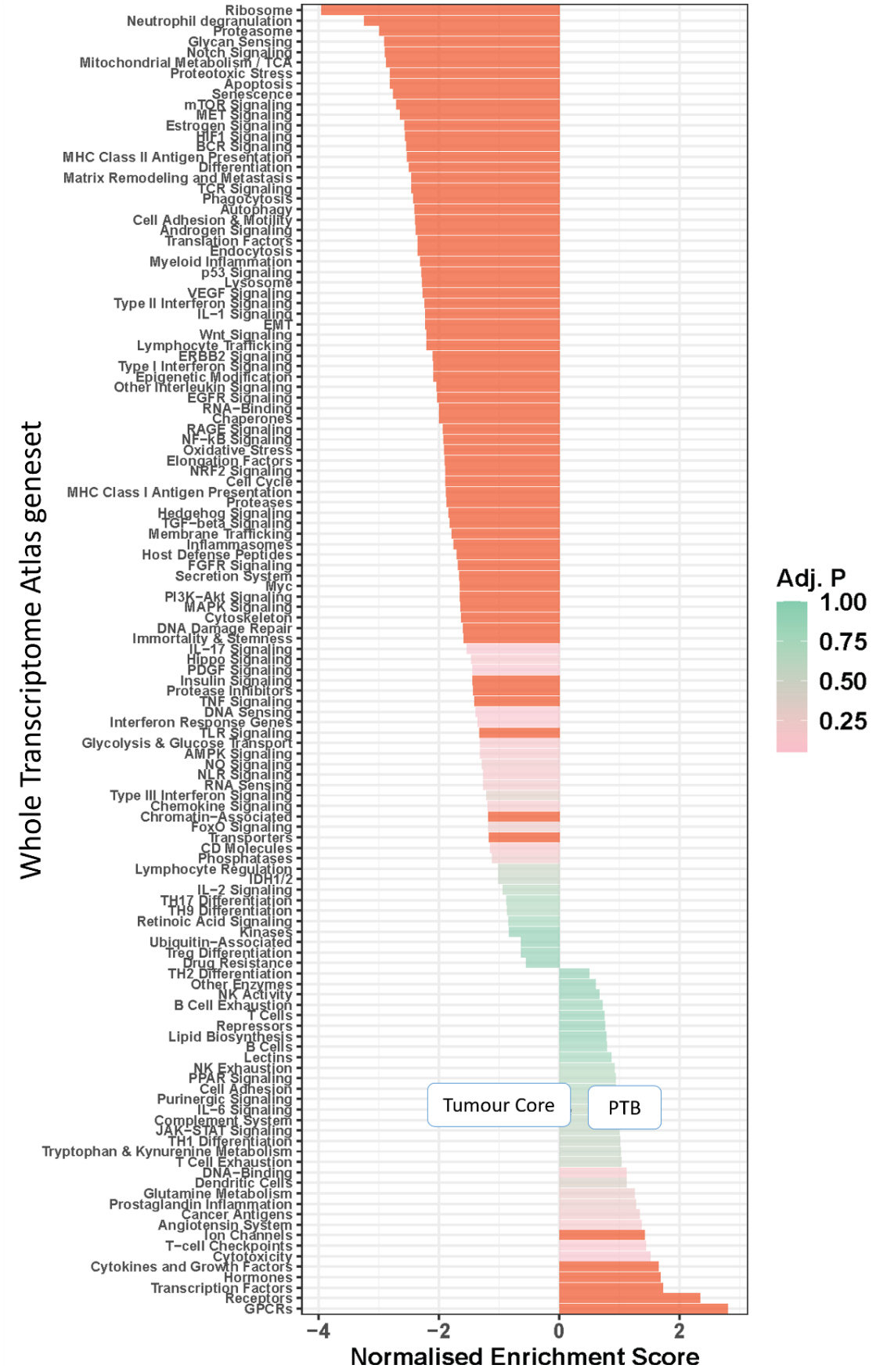


**Supplementary figure 8.6 Spatial Transcriptomic alterations between tumour core and presumed tumour bed**. *Geneset enrichment bar chart comparing overall tumour core and presumed tumour bed (PTB). Pathways with normalized enrichment score above and below 1.5, and p adjusted (Adj. P) value ≤ 0.05 were considered significant.*

### 8.4.2 Regression pattern in neoadjuvant pancreatic cancer demonstrates limited spatial transcriptomic differences

Neoadjuvant patients are categorised according to the regression pattern of the epithelium. The signatures associated with these groups were explored to determine if these response patterns were reflected in the transcriptome. Comparisons were made between samples grouped into good and poor regression. Upregulation of immune related pathways was mirrored in both αSMA and immune segments. Increased TCR signalling (NES = 2.5, padj < 0.001), BCR signalling (NES = 2.3, padj < 0.001), NK activity (NES = 2.0, padj < 0.001), T cell (NES = 1.5, padj = 0.014) and B cell (NES = 1.6, padj = 0.029) couple with B cell exhaustion (NES = 1.7, padj = 0.044) were seen in fibroblast segments of poor regression patients (supplementary figure 8.7.a). Furthermore, a large number of signalling pathways were elevated in the poor regression segments, in comparison, good response segments were void of any pathways apart from NO signalling (NES = 2.0, padj < 0.001) and complement system (NES = 2.0, padj < 0.001) (supplementary figure 8.7.a). Immune regions of poor regression patients also presented with elevated T cells (NES = 1.8, padj =0.003), TCR signalling (NES = 1.8, padj < 0.001), interferon response genes (NES = 1.6, padj = 0.031) and NK activity (NES = 1.5, padj =0.028) (supplementary figure 8.7.b). Regardless of the number of aberrated immune pathways, only one immune population was significant when spatial deconvolution was performed. Elevated levels of memory dendritic cells were demonstrated in poor regression patients (p=0.002) (supplementary figure 8.7.c). Although these findings have provided some insight into the differing treatment responses, protein analysis maybe more suited to characterize them.

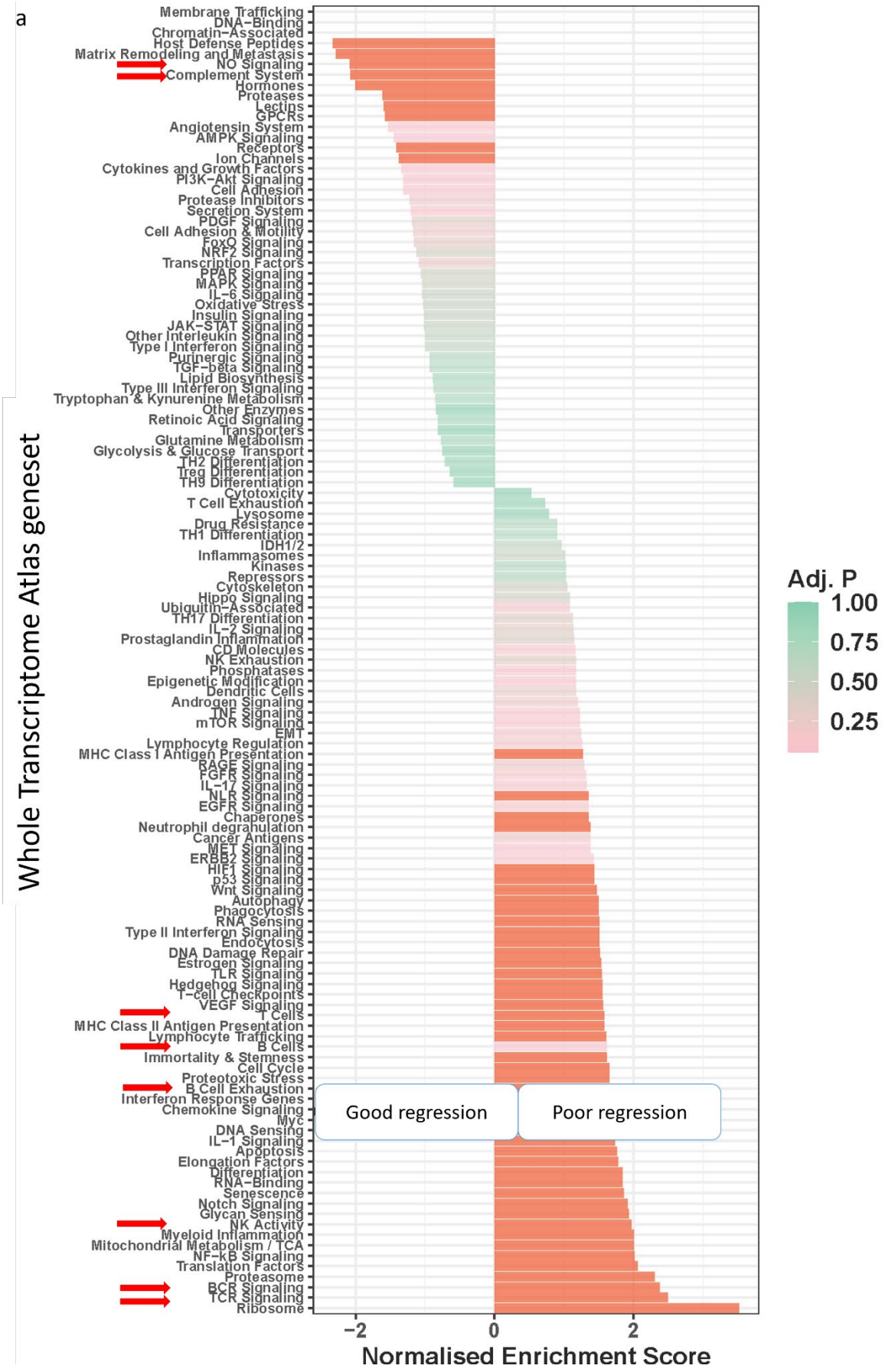


**Supplementary figure 8.7.a Spatial Transcriptomic alterations in neoadjuvant regression status** *a). Geneset enrichment bar chart comparing good and bad regression in αSMA+ segments. Pathways with normalized enrichment score above and below 1.5, and p adjusted (Adj. P) value ≤ 0.05 were considered significant. Important pathways are indicated by an arrow.*

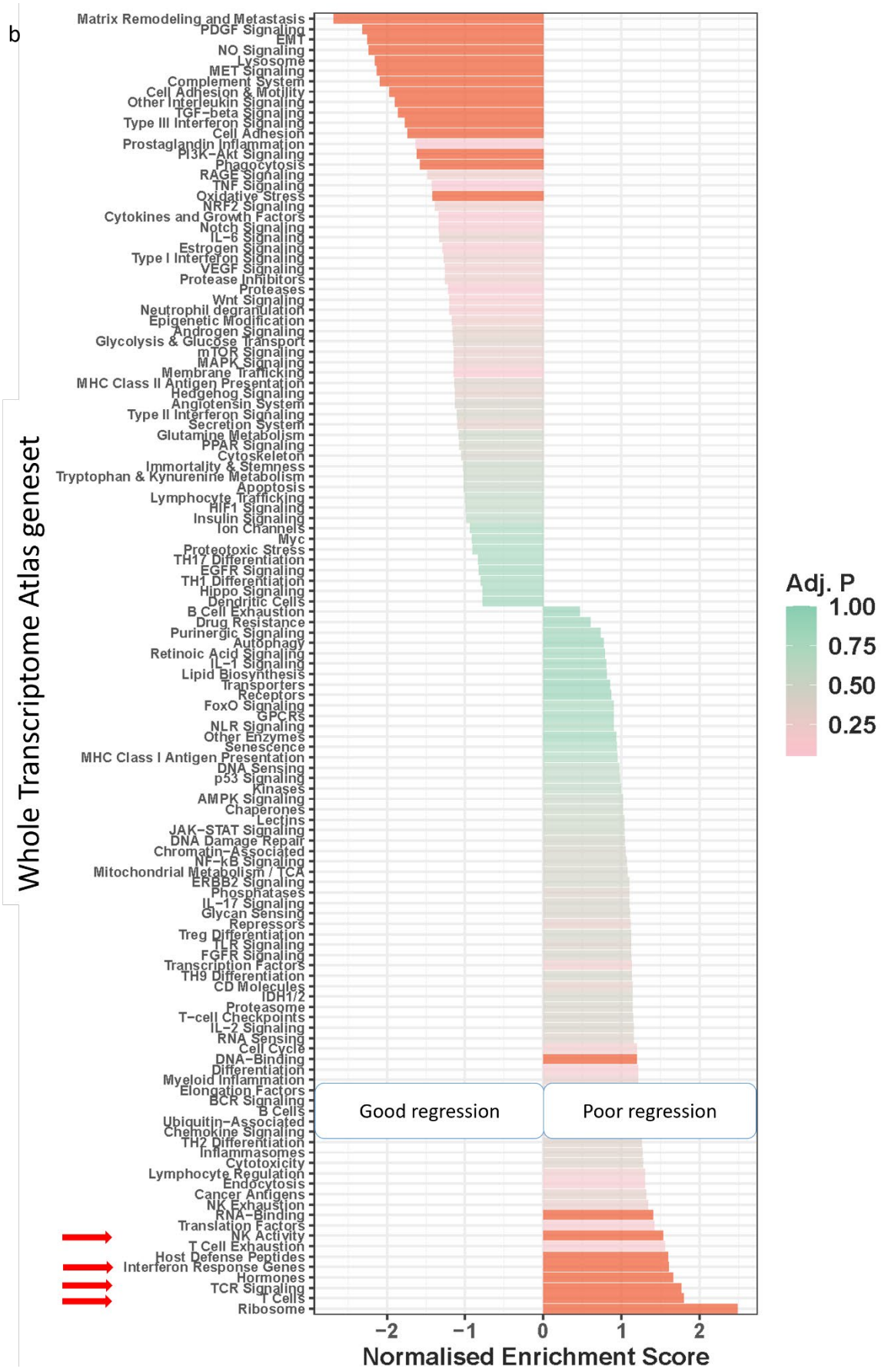


**Supplementary figure 8.7.b Spatial Transcriptomic alterations in neoadjuvant regression status** *b). Geneset enrichment bar chart comparing good and bad regression in immune segments. Pathways with normalized enrichment score above and below 1.5, and p adjusted (Adj. P) value ≤ 0.05 were considered significant. Important pathways are indicated by an arrow.*

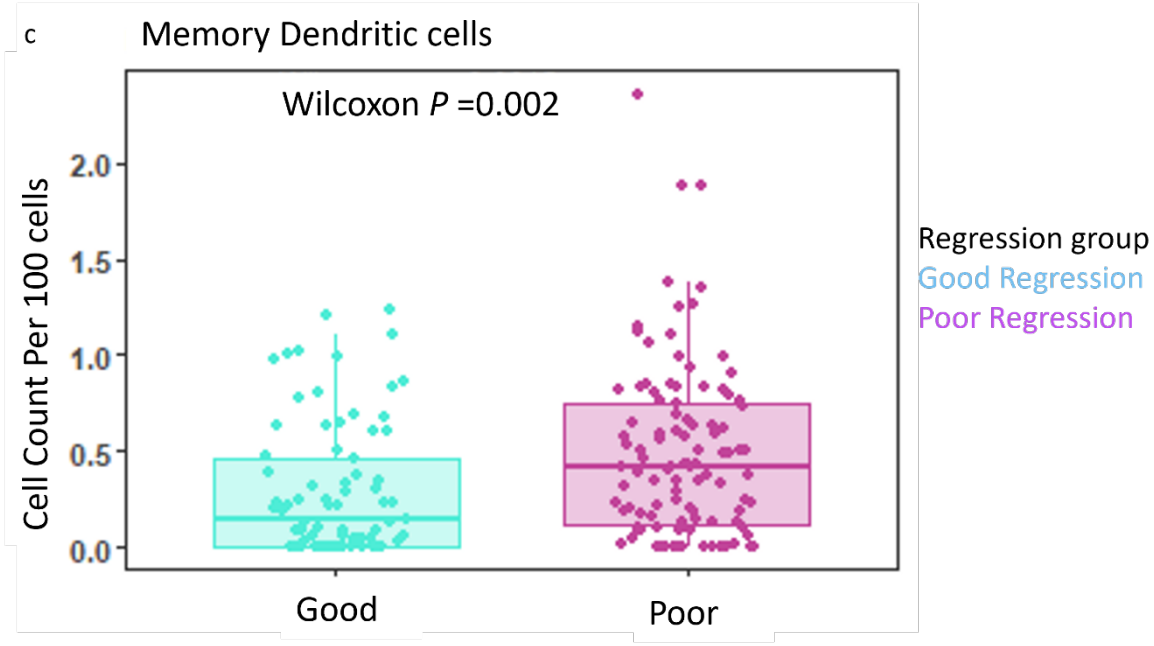


**Supplementary figure 8.7.c Spatial Transcriptomic alterations in neoadjuvant regression status,** *c). Boxplots demonstrate estimated memory dendritic cell expression per 100 cells in across neoadjuvant regression groups. Wilcoxon test used.*

## 8.4.3 B7-H3 signature in neoadjuvant pancreatic cancer

Numerous pathways were displayed across epithelial (supplementary figure 8.8.a) and αSMA (supplementary figure 8.8.b) compartments of ranked B7-H3 neoadjuvant patients.

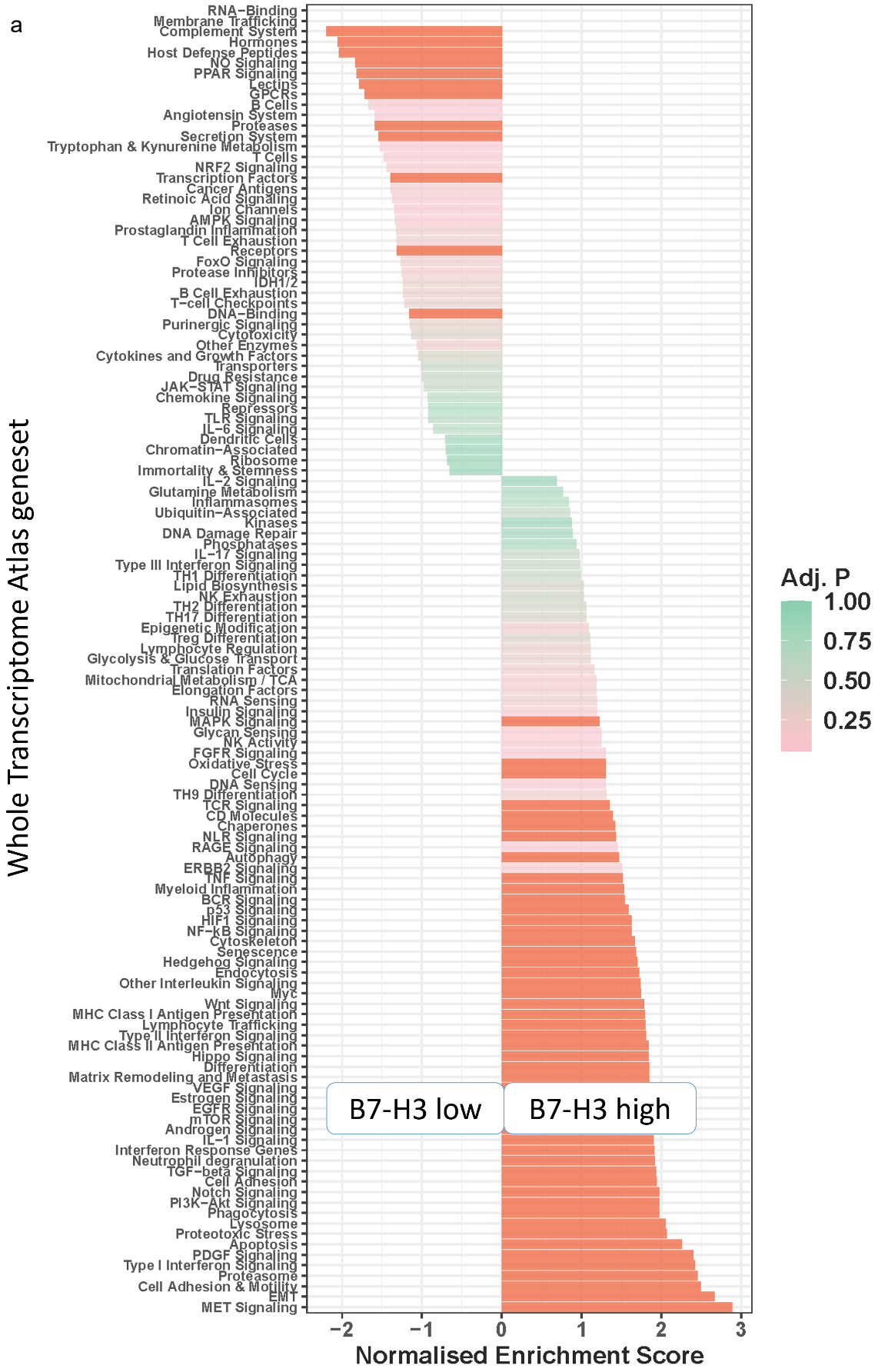


**Supplementary figure 8.8.a Spatial Transcriptomic alterations in B7-H3 ranked neoadjuvant patients** *a). Geneset enrichment bar chart comparing B7-H3 low and B7-H3 high in epithelial segments. Pathways with normalized enrichment score above and below 1.5, and p adjusted (Adj. P) value ≤ 0.05 were considered significant.*

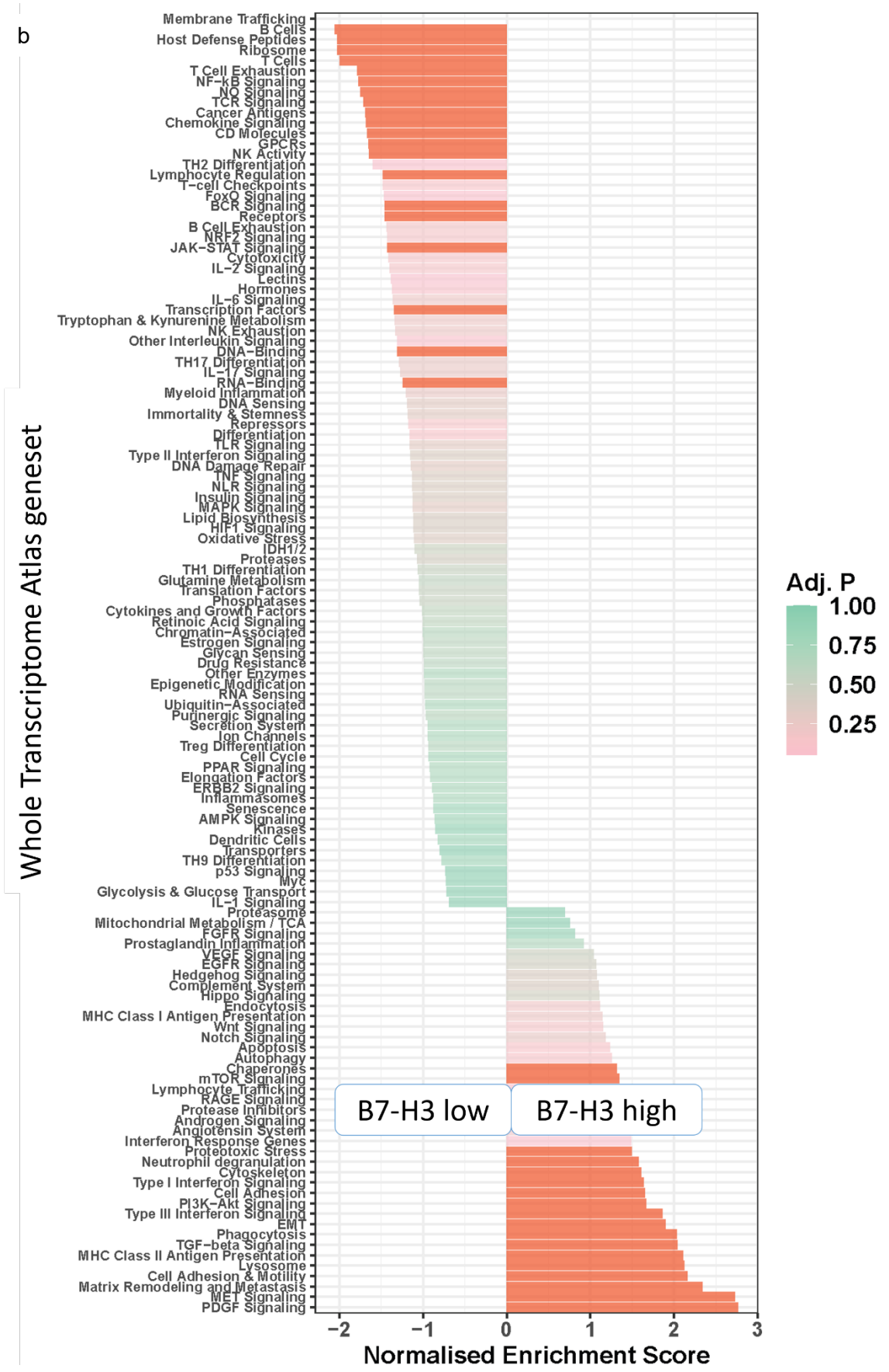


**Supplementary figure 8.8.b Spatial Transcriptomic alterations in B7-H3 ranked neoadjuvant patients** *b). Geneset enrichment bar chart comparing B7-H3 low and B7-H3 high in αSMA+ segments. Pathways with normalized enrichment score above and below 1.5, and p adjusted (Adj. P) value ≤ 0.05 were considered significant.*

## 8.4.4 Long term survival in naïve and neoadjuvant PDAC

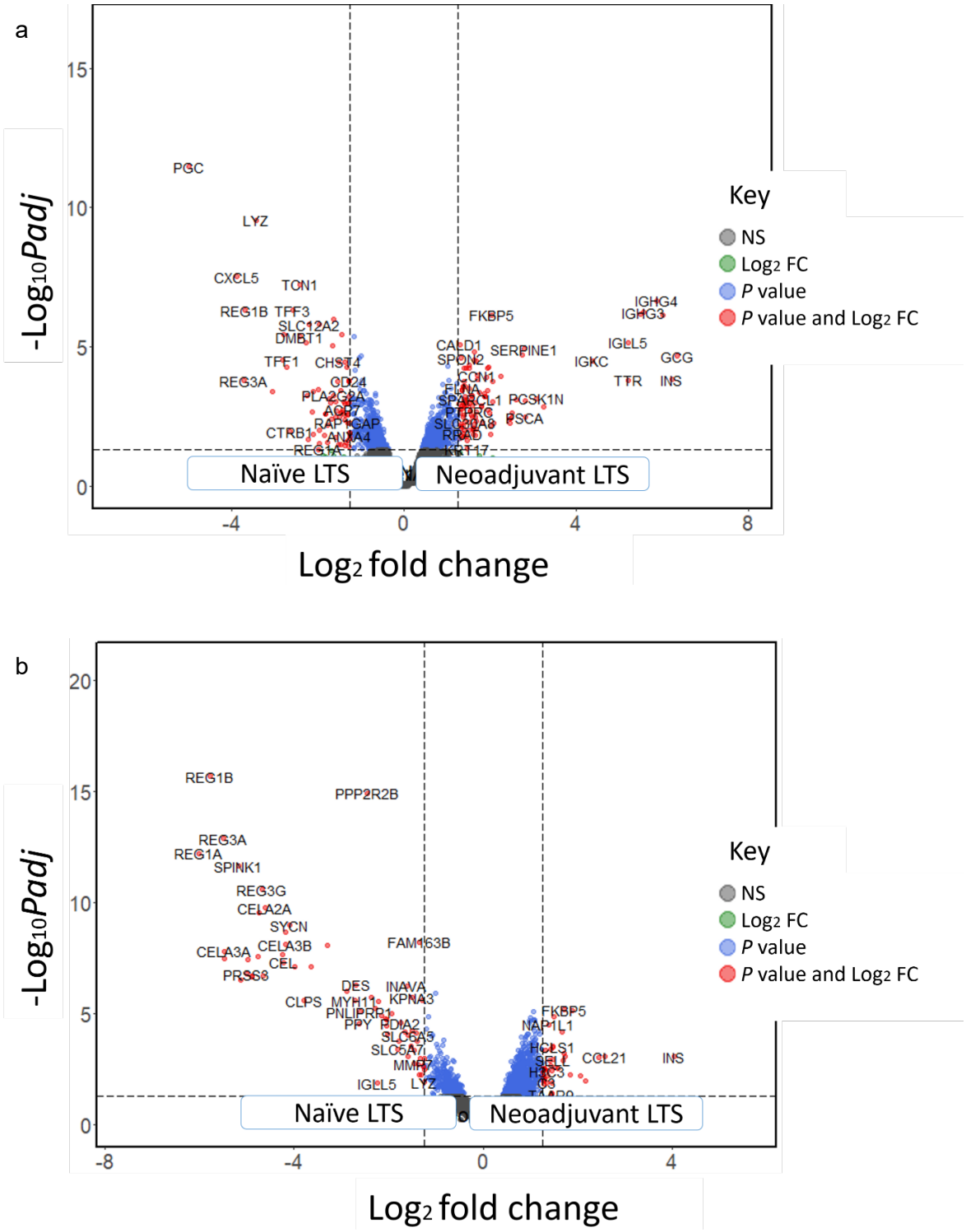


**Supplementary figure 8.9.a-b Spatial Transcriptomic gene alterations between naïve and neoadjuvant LTS segments**. *Volcano plot demonstrating gene marker differential expression levels in naive vs neoadjuvant long term survival (LTS) in a). epithelial segments, b). αSMA+ segments. Genes with log2 fold change above and below 1.5, and p adjusted value ≤0.05 were considered significant. Dashed line indicates significance thresholds, NS = non-significant, FC = fold change.*

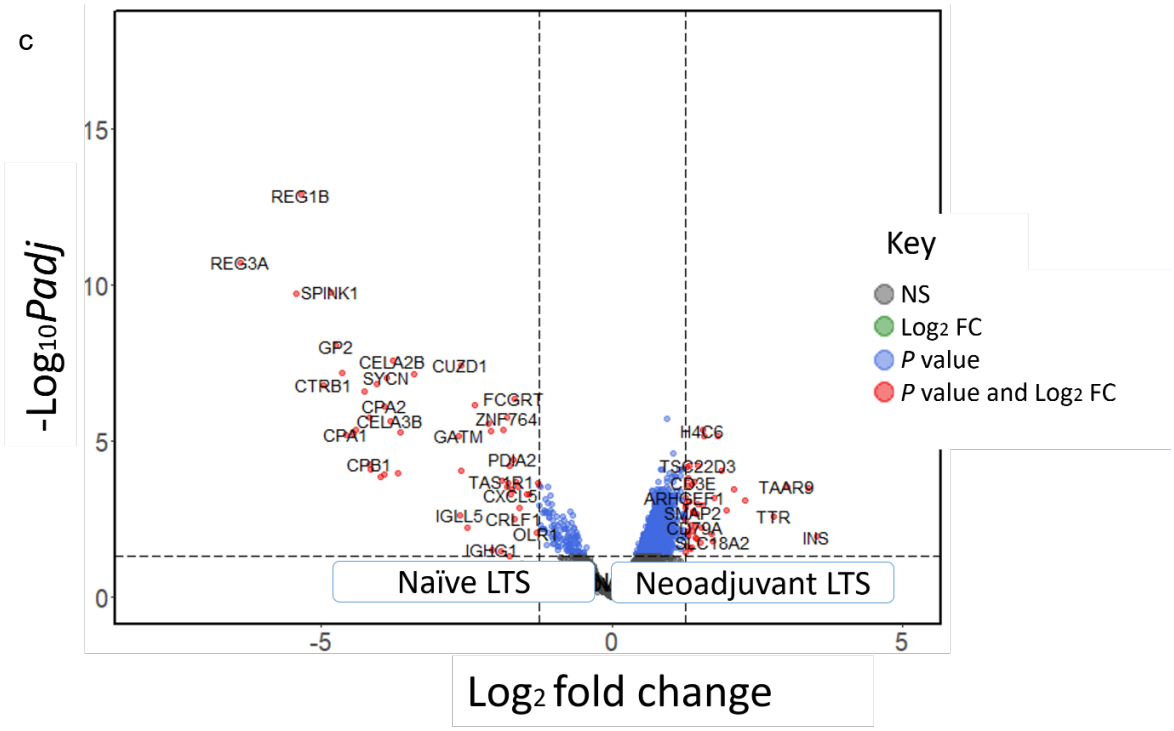


**Supplementary figure 8.9.c Spatial Transcriptomic gene alterations between naïve and neoadjuvant LTS segments**. *Volcano plot demonstrating gene marker differential expression levels in naive vs neoadjuvant long term survival (LTS) in c). immune segments. Genes with log2 fold change above and below 1.5, and p adjusted value ≤0.05 were considered significant. Dashed line indicates significance thresholds, NS = non-significant, FC = fold change.*

## 8.4.5 Neoadjuvant whole section vs TMA overlapping differential genes

| ROI | Comparison | Analysis method | Whole section | TMA | Matched |
|---|---|---|---|---|---|
| αSMA | Naïve vs Neoadjuvant | DEA | AMY1A | AMY1A | TRUE |
| αSMA | Naïve vs Neoadjuvant | DEA | CEL | CEL | TRUE |
| αSMA | Naïve vs Neoadjuvant | DEA | CELA2A | CELA2A | TRUE |
| αSMA | Naïve vs Neoadjuvant | DEA | CELA2B | CELA2B | TRUE |
| αSMA | Naïve vs Neoadjuvant | DEA | CELA3A | CELA3A | TRUE |
| αSMA | Naïve vs Neoadjuvant | DEA | CELA3B | CELA3B | TRUE |
| αSMA | Naïve vs Neoadjuvant | DEA | CPA1 | CPA1 | TRUE |
| αSMA | Naïve vs Neoadjuvant | DEA | CTRC | CTRC | TRUE |
| αSMA | Naïve vs Neoadjuvant | DEA | CXCL14 | CXCL14 | TRUE |
| αSMA | Naïve vs Neoadjuvant | DEA | GP2 | GP2 | TRUE |
| αSMA | Naïve vs Neoadjuvant | DEA | PLA2G1B | PLA2G1B | TRUE |
| αSMA | Naïve vs Neoadjuvant | DEA | REG1B | REG1B | TRUE |
| αSMA | Naïve vs Neoadjuvant | DEA | APCS | ARHGDIB | FALSE |
| αSMA | Naïve vs Neoadjuvant | DEA | BLCAP | ARHGEF1 | FALSE |
| αSMA | Naïve vs Neoadjuvant | DEA | CCN1 | C7 | FALSE |
| αSMA | Naïve vs Neoadjuvant | DEA | CCN2 | CCL19 | FALSE |
| αSMA | Naïve vs Neoadjuvant | DEA | COL11A1 | CCL21 | FALSE |
| αSMA | Naïve vs Neoadjuvant | DEA | CPLS | CPA2 | FALSE |
| αSMA | Naïve vs Neoadjuvant | DEA | CRLF1 | CTRB1 | FALSE |
| αSMA | Naïve vs Neoadjuvant | DEA | CTRL | CYTIP | FALSE |
| αSMA | Naïve vs Neoadjuvant | DEA | EEF1AKMT2 | FDCSP | FALSE |
| αSMA | Naïve vs Neoadjuvant | DEA | FGA | FKBP5 | FALSE |
| αSMA | Naïve vs Neoadjuvant | DEA | FNDC1 | HCFC2 | FALSE |
| αSMA | Naïve vs Neoadjuvant | DEA | IGFBP5 | HLA-DPA1 | FALSE |
| αSMA | Naïve vs Neoadjuvant | DEA | PGC | HLA-DPB1 | FALSE |
| αSMA | Naïve vs Neoadjuvant | DEA | PLA2G2A | IGHA1 | FALSE |
| αSMA | Naïve vs Neoadjuvant | DEA | PNLIP | IL7R | FALSE |
| αSMA | Naïve vs Neoadjuvant | DEA | PNLIPRP2 | JCHAIN | FALSE |
| αSMA | Naïve vs Neoadjuvant | DEA | PPY | PPP2R2B | FALSE |
| αSMA | Naïve vs Neoadjuvant | DEA | PRSS3 | REG1A | FALSE |
| αSMA | Naïve vs Neoadjuvant | DEA | PSCA | REG3A | FALSE |
| αSMA | Naïve vs Neoadjuvant | DEA | SYNC | REG3G | FALSE |
| αSMA | Naïve vs Neoadjuvant | DEA | | SMAP2 | FALSE |
| αSMA | Naïve vs Neoadjuvant | DEA | | SPINK1 | FALSE |
| αSMA | Naïve vs Neoadjuvant | DEA | | SST | FALSE |
| αSMA | Naïve vs Neoadjuvant | DEA | | STK17B | FALSE |
| αSMA | Naïve vs Neoadjuvant | DEA | | SYCN | FALSE |
| αSMA | Naïve vs Neoadjuvant | DEA | | TAAR9 | FALSE |
| αSMA | Naïve vs Neoadjuvant | DEA | | TRBC1 | FALSE |
| αSMA | Naïve vs Neoadjuvant | DEA | | TSC22D3 | FALSE |
| Immune | Naïve vs Neoadjuvant | DEA | AMY1A | AMY1A | TRUE |
| Immune | Naïve vs Neoadjuvant | DEA | CEL | CEL | TRUE |
| Immune | Naïve vs Neoadjuvant | DEA | CELA2A | CELA2A | TRUE |
| Immune | Naïve vs Neoadjuvant | DEA | CELA2B | CELA2B | TRUE |
| Immune | Naïve vs Neoadjuvant | DEA | CELA3B | CELA3B | TRUE |
| Immune | Naïve vs Neoadjuvant | DEA | CPA1 | CPA1 | TRUE |
| Immune | Naïve vs Neoadjuvant | DEA | GP2 | GP2 | TRUE |
| Immune | Naïve vs Neoadjuvant | DEA | PLA2G1B | PLA2G1B | TRUE |
| Immune | Naïve vs Neoadjuvant | DEA | ANTXR1 | ARHGDIB | FALSE |
| Immune | Naïve vs Neoadjuvant | DEA | BGN | CD79A | FALSE |
| Immune | Naïve vs Neoadjuvant | DEA | CALD1 | CELA3A | FALSE |
| Immune | Naïve vs Neoadjuvant | DEA | CAV1 | CORO1A | FALSE |
| Immune | Naïve vs Neoadjuvant | DEA | CD9 | CPA2 | FALSE |
| Immune | Naïve vs Neoadjuvant | DEA | CEACAN7 | CTRB1 | FALSE |
| Immune | Naïve vs Neoadjuvant | DEA | CLPS | CTRC | FALSE |
| Immune | Naïve vs Neoadjuvant | DEA | CRIPS3 | CXCL13 | FALSE |
| Immune | Naïve vs Neoadjuvant | DEA | CST1 | CXCR4 | FALSE |
| Immune | Naïve vs Neoadjuvant | DEA | CTRL | CYTIP | FALSE |
| Immune | Naïve vs Neoadjuvant | DEA | FBXO32 | FCMR | FALSE |
| Immune | Naïve vs Neoadjuvant | DEA | FGA | FDCSP | FALSE |
| Immune | Naïve vs Neoadjuvant | DEA | GCG | FKBP5 | FALSE |
| Immune | Naïve vs Neoadjuvant | DEA | GREM1 | H1-3 | FALSE |
| Immune | Naïve vs Neoadjuvant | DEA | HTRA3 | IL7R | FALSE |
| Immune | Naïve vs Neoadjuvant | DEA | IGFBP3 | IRF8 | FALSE |
| Immune | Naïve vs Neoadjuvant | DEA | KLK1 | MS4A1 | FALSE |
| Immune | Naïve vs Neoadjuvant | DEA | KRT5 | P2RX5 | FALSE |
| Immune | Naïve vs Neoadjuvant | DEA | LAMA4 | PNLIPRP1 | FALSE |
| Immune | Naïve vs Neoadjuvant | DEA | MMP11 | PRSS3 | FALSE |
| Immune | Naïve vs Neoadjuvant | DEA | MMP14 | PTPRC | FALSE |
| Immune | Naïve vs Neoadjuvant | DEA | MYL0 | REG1A | FALSE |
| Immune | Naïve vs Neoadjuvant | DEA | PLA2G2A | REG1B | FALSE |
| Immune | Naïve vs Neoadjuvant | DEA | PLAT | REG3A | FALSE |
| Immune | Naïve vs Neoadjuvant | DEA | PNLIP | REG3G | FALSE |
| Immune | Naïve vs Neoadjuvant | DEA | PNLIPRP2 | RPS27 | FALSE |
| Immune | Naïve vs Neoadjuvant | DEA | PPY | RPS27A | FALSE |
| Immune | Naïve vs Neoadjuvant | DEA | PSCA | SMAP2 | FALSE |
| Immune | Naïve vs Neoadjuvant | DEA | SIGLEC12 | SPINK1 | FALSE |
| Immune | Naïve vs Neoadjuvant | DEA | SYNC | STK17B | FALSE |
| Immune | Naïve vs Neoadjuvant | DEA | TGFB1 | SYCN | FALSE |
| Immune | Naïve vs Neoadjuvant | DEA | TTR | TSC22D3 | FALSE |

**Supplementary table 8.4 Differential genes expressed in neoadjuvant TMA and whole sections.** *Summary table showing all significant differentially expressed genes in αSMA and immune segments of neoadjuvant TMAs and whole sections. Column matched indicates whether the gene is seen in both tissue types.*

# 8.5 Chapter 6 supplementary

## 8.5.1 Spatial Transcriptomic landscape of density phenotypes in naïve and neoadjuvant pancreatic cancer

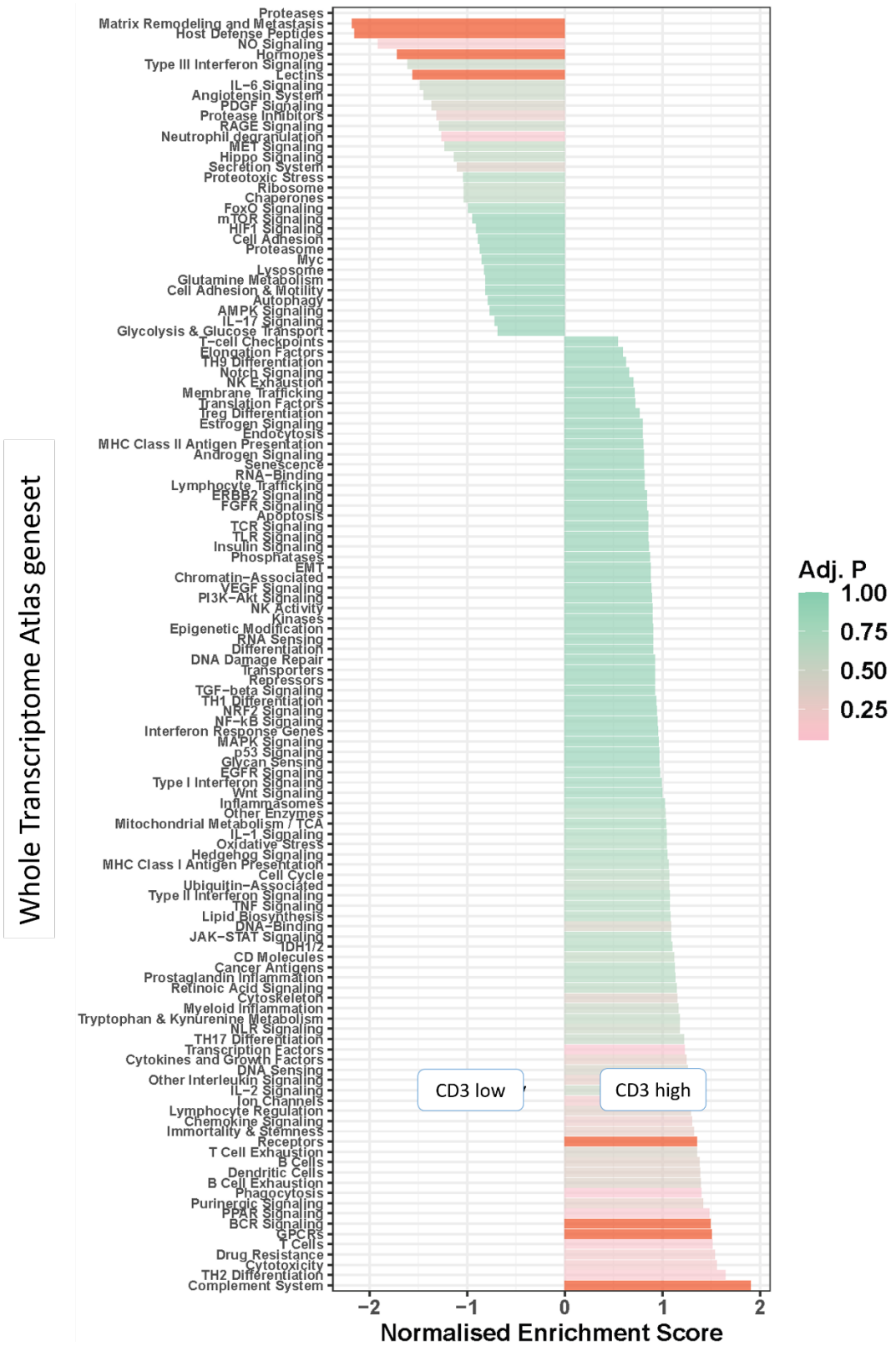


**Supplementary figure 8.10 Geneset enrichment of naïve PDAC based on CD3 ranked αSMA segments**. *Geneset enrichment bar chart comparing CD3low and CD3high in αSMA+ segments.*

*Pathways with normalized enrichment score above and below 1.5, and p adjusted (Adj. P) value ≤ 0.05 were considered significant.*

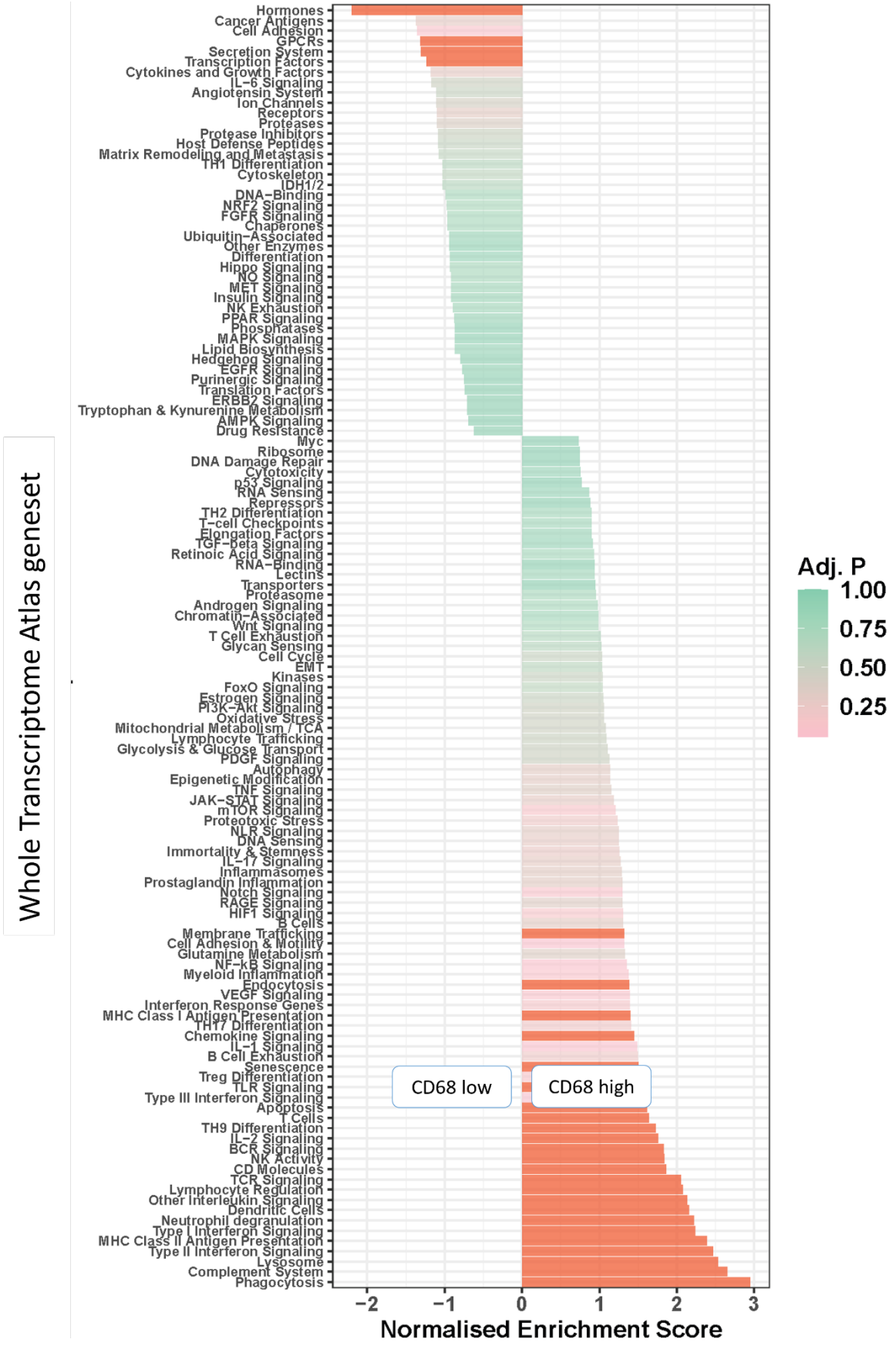


**Supplementary figure 8.11 Geneset enrichment of naïve PDAC based on CD68 ranked αSMA segments**. *Geneset enrichment bar chart comparing CD68low and CD68high in αSMA+*

*segments. Pathways with normalized enrichment score above and below 1.5, and p adjusted (Adj. P) value ≤ 0.05 were considered significant.*

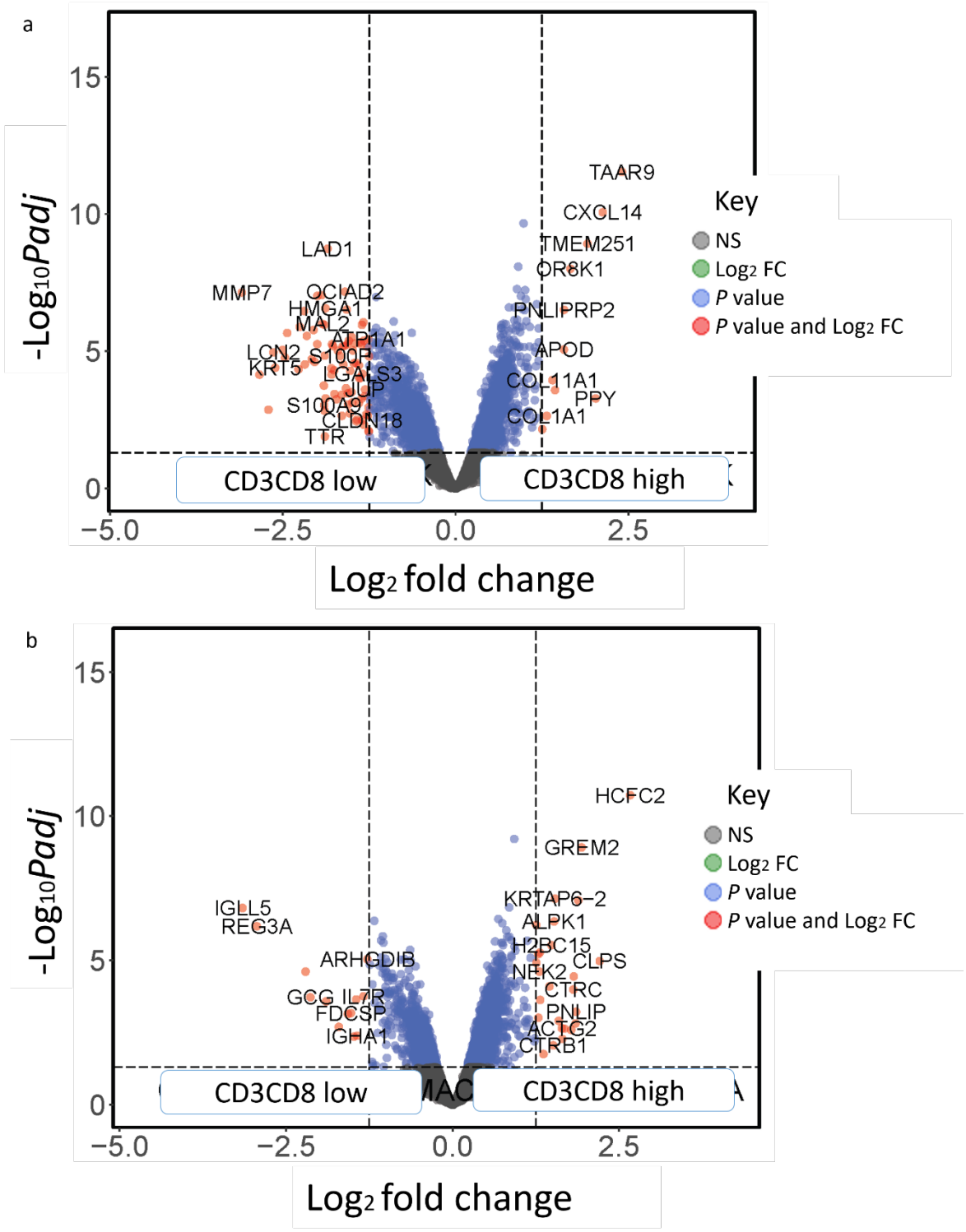


**Supplementary figure 8.12.a-b Spatial Transcriptomic alterations CD3CD8 ranked neoadjuvant PDAC**. *Volcano plot comparing CD3CD8low and CD3CD8high ranks in a). PanCk+ segments, b). αSMA+ segments. Genes with log2 fold change above and below 1.5, and p adjusted value ≤0.05 were considered significant. Dashed line indicates significance thresholds, NS = non-significant, FC = fold change.*

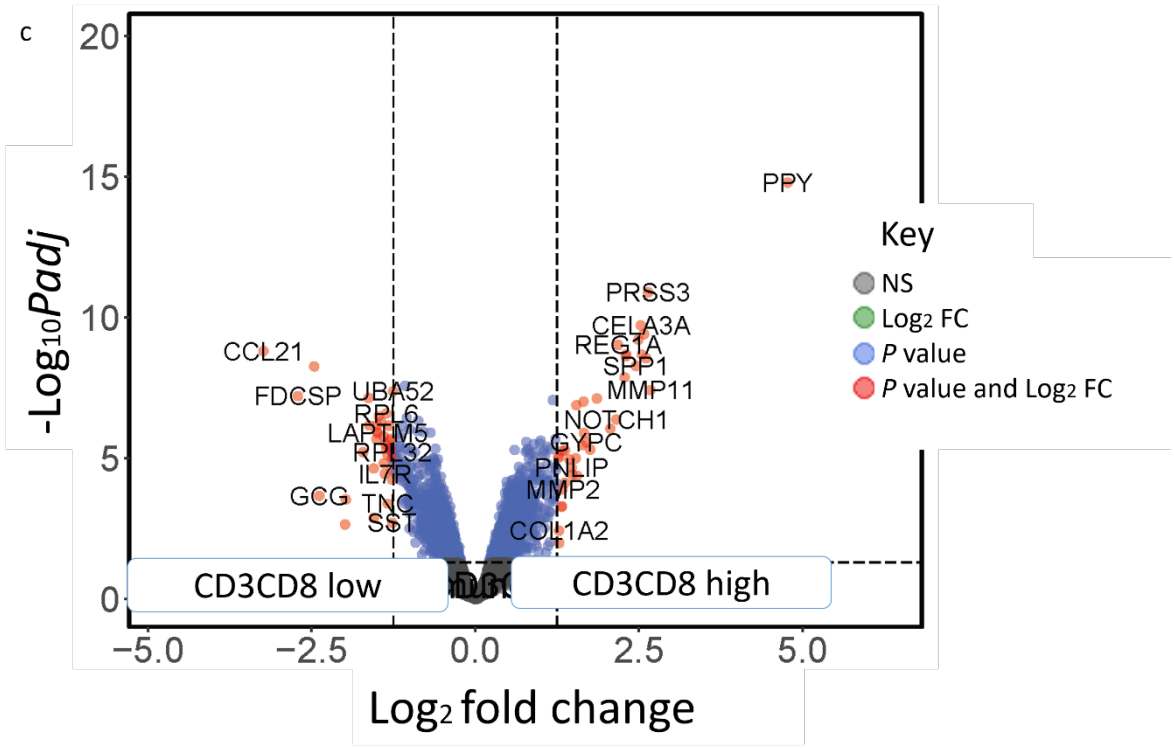


**Supplementary figure 8.12.c Spatial Transcriptomic alterations CD3CD8 ranked neoadjuvant PDAC**. *Volcano plot comparing CD3CD8low and CD3CD8high ranks in c). immune segments. Genes with log2 fold change above and below 1.5, and p adjusted value ≤0.05 were considered significant. Dashed line indicates significance thresholds, NS = non-significant, FC = fold change.*

## 8.5.2 Spatial Transcriptomic landscape of nearest neighbour phenotypes in naïve and neoadjuvant pancreatic cancer

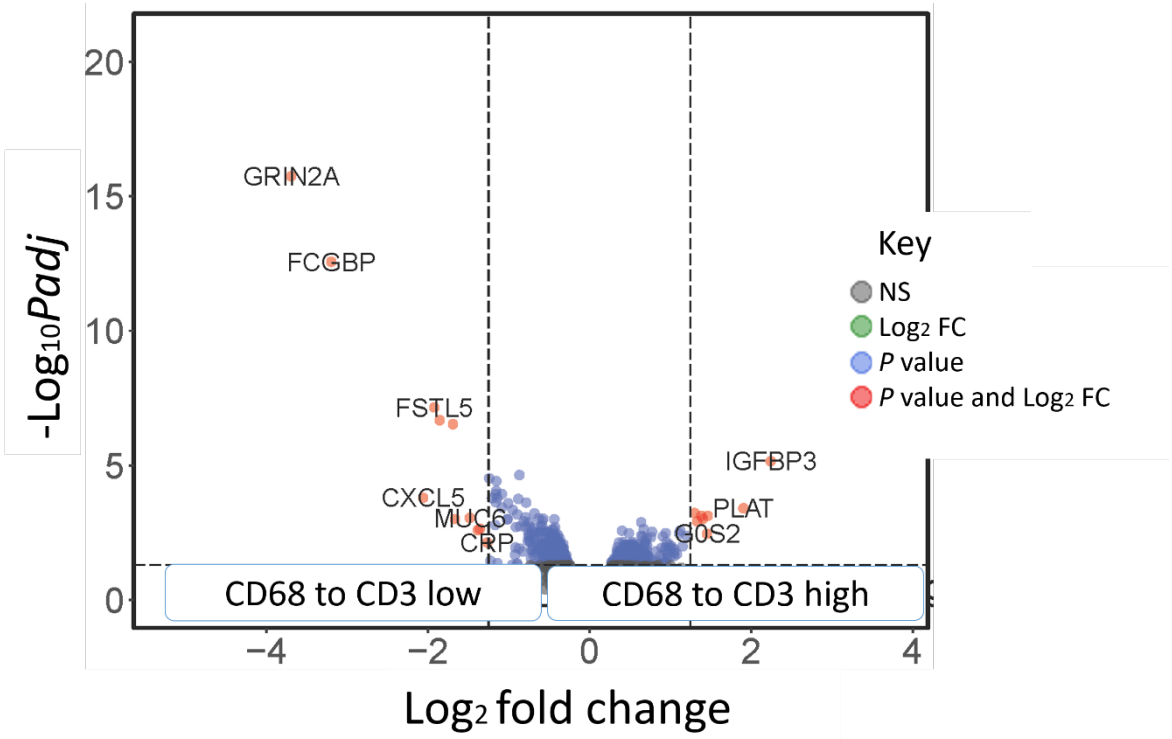


**Supplementary figure 8.13 Spatial Transcriptomic alterations in ranked distances from CD68 to CD3 in naïve PDAC**. *Volcano plot comparing from CD68 to CD3 low and from CD68 to CD3 high ranks in PanCk+ segments.. Genes with log2 fold change above and below 1.5, and p adjusted value ≤0.05 were considered significant. Dashed line indicates significance thresholds, NS = non-significant, FC = fold change.*

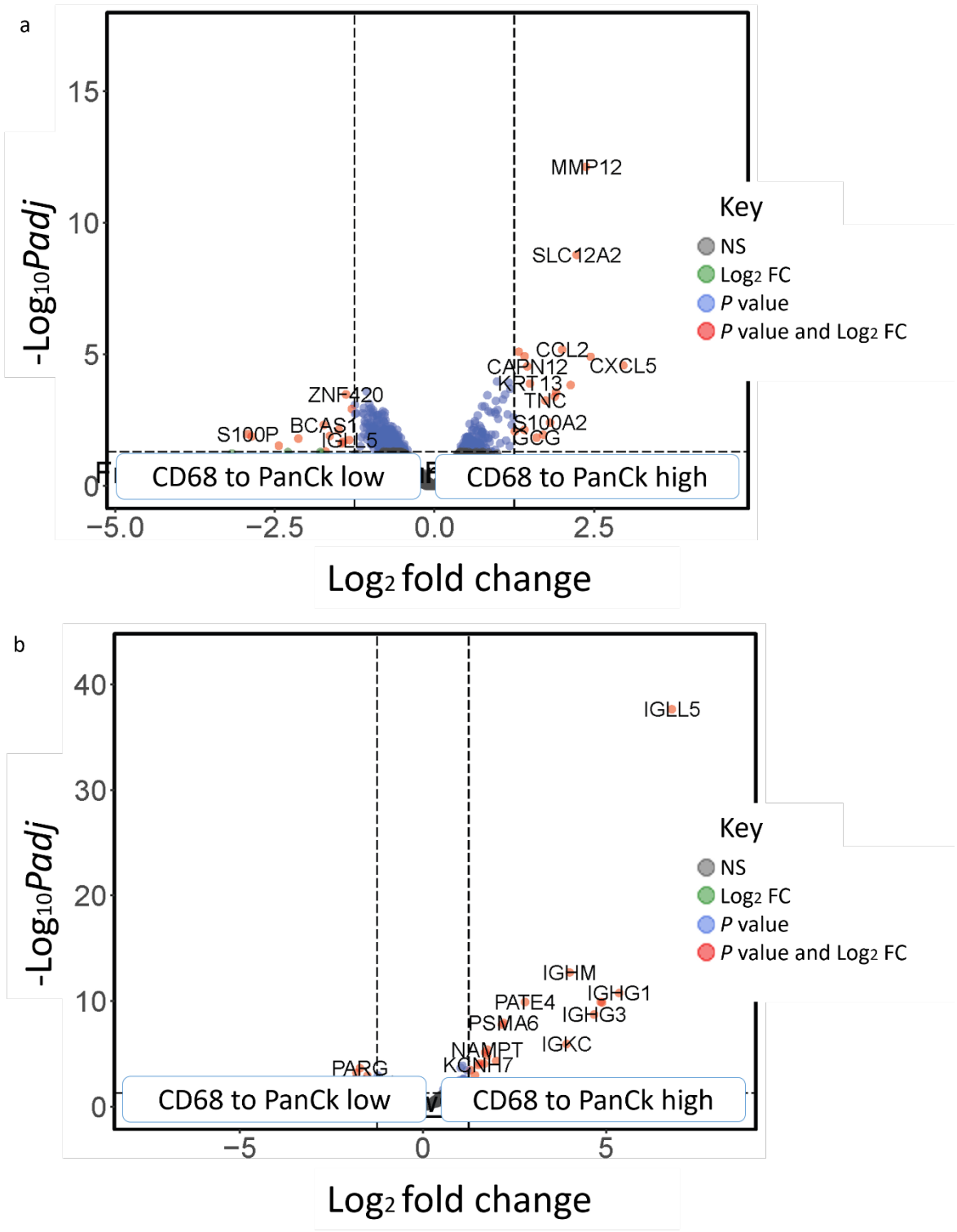


**Supplementary figure 8.14.a-b Spatial Transcriptomic alterations in ranked distances from CD68 to PanCk in naïve PDAC**. *Volcano plot comparing from CD68 to PanCk low and from CD68 to PanCk high ranks in a). PanCk+ segments, b). αSMA segments. Genes with log2 fold change above and below 1.5, and p adjusted value ≤0.05 were considered significant. Dashed line indicates significance thresholds, NS = non-significant, FC = fold change.*

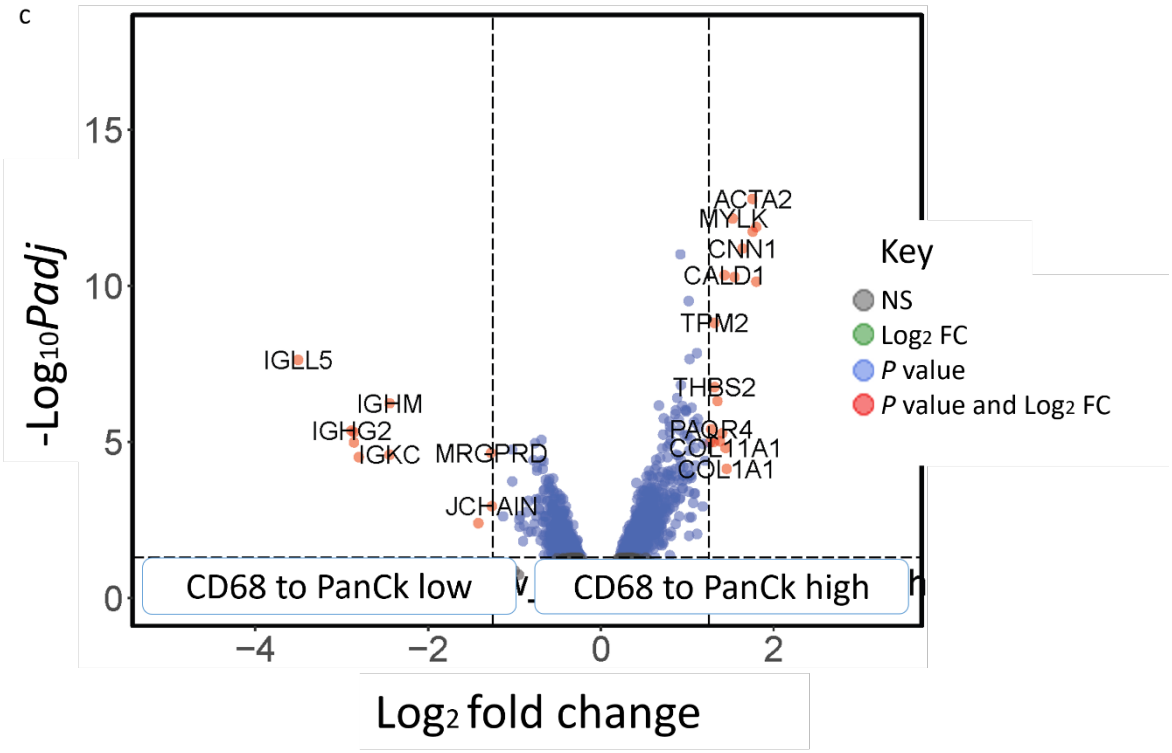


**Supplementary figure 8.14.c Spatial Transcriptomic alterations in ranked distances from CD68 to PanCk in naïve PDAC**. *Volcano plot comparing from CD68 to PanCk low and from CD68 to PanCk high ranks in c). immune segments. Genes with log2 fold change above and below 1.5, and p adjusted value ≤0.05 were considered significant. Dashed line indicates significance thresholds, NS = non-significant, FC = fold change.*

### 8.5.3 Cluster density in chemoradiotherapy treated pancreatic cancer

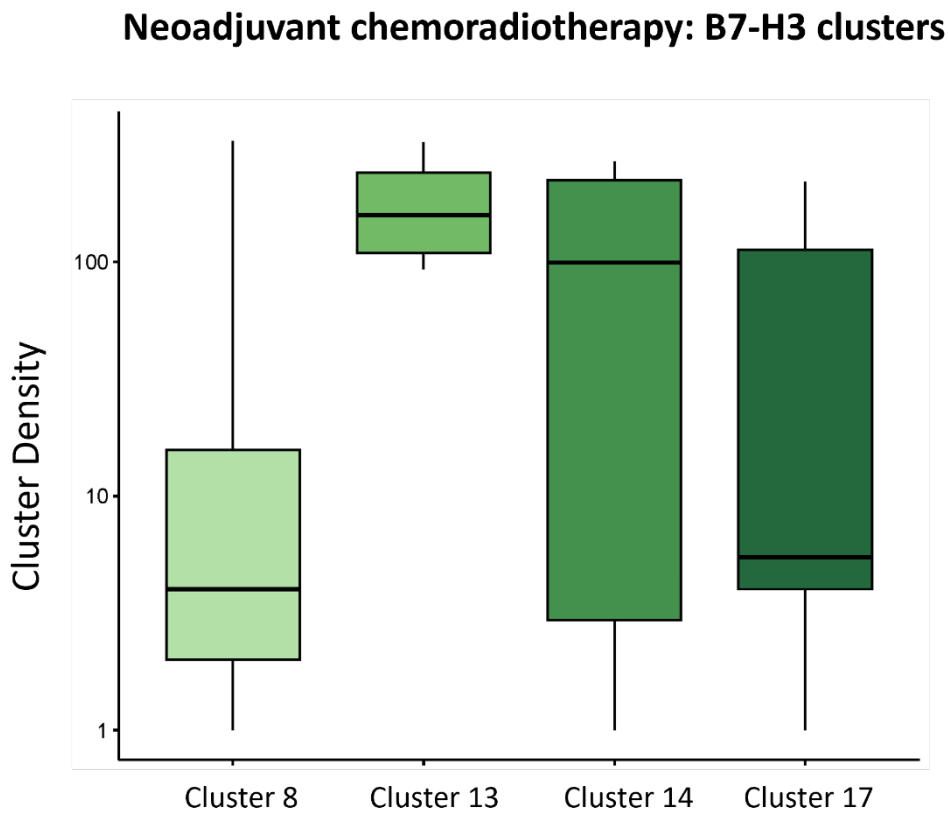


**Supplementary figure 8.15 Density of Seurat clusters associated B7-H3 clusters in chemoradiotherapy treated PDAC**. Boxplots shows density per grouped Seurat B7-H3 cluster in chemoradiotherapy treated neoadjuvant patients.

# References


1. Allemani, C., et al., *Global surveillance of trends in cancer survival 2000-14 (CONCORD-3): analysis of individual records for 37 513 025 patients diagnosed with one of 18 cancers from 322 population-based registries in 71 countries.* Lancet, 2018. **391**(10125): p. 1023-1075.
2. Rahib, L., et al., *Projecting Cancer Incidence and Deaths to 2030: The Unexpected Burden of Thyroid, Liver, and Pancreas Cancers in the United States.* Cancer Research, 2014. **74**(11): p. 2913-2921.
3. Conroy, T., et al., *FOLFIRINOX or gemcitabine as adjuvant therapy for pancreatic cancer.* New England Journal of Medicine, 2018. **379**(25): p. 2395-2406.
4. Gillen, S., et al., *Preoperative/neoadjuvant therapy in pancreatic cancer: a systematic review and meta-analysis of response and resection percentages.* PLoS medicine, 2010. **7**(4): p. e1000267.
5. Valeri, S., et al., *Complete pathological response after FOLFIRINOX for locally advanced pancreatic cancer. The beginning of a new era? Case report and review of the literature.* Pancreatology, 2014. **14**(5): p. 425-430.
6. Kunk, P.R., et al., *From bench to bedside a comprehensive review of pancreatic cancer immunotherapy.* Journal for Immunotherapy of Cancer, 2016. **4**: p. 12.
7. Carstens, J.L., et al., *Spatial computation of intratumoral T cells correlates with survival of patients with pancreatic cancer.* Nature communications, 2017. **8**(1): p. 15095.
8. Fukunaga, A., et al., *CD8(+) tumor-infiltrating lymphocytes together with CD4(+) tumor-infiltrating lymphocytes and dendritic cells improve the prognosis of patients with pancreatic adenocarcinoma.* Pancreas, 2004. **28**(1): p. E26-E31.
9. Ino, Y., et al., *Immune cell infiltration as an indicator of the immune microenvironment of pancreatic cancer.* British Journal of Cancer, 2013. **108**(4): p. 914-923.
10. Heger, U., et al., *Myofibroblastic CAF density, not activated stroma index, indicates prognosis after neoadjuvant therapy of pancreatic carcinoma.* Cancers, 2022. **14**(16): p. 3881.
11. Castino, G.F., et al., *Spatial distribution of B cells predicts prognosis in human pancreatic adenocarcinoma.* Oncoimmunology, 2016. **5**(4): p. 14.
12. van de Veen, W., et al., *A novel proangiogenic B cell subset is increased in cancer and chronic inflammation.* Science Advances, 2020. **6**(20): p. eaaz3559.
13. Senturk, Z.N., et al., *Pancreatic cancer: Emerging field of regulatory B-cell-targeted immunotherapies.* Frontiers in Immunology, 2023. **14**: p. 1152551.
14. Heining, C., et al., *NRG1 fusions in KRAS wild-type pancreatic cancer.* Cancer discovery, 2018. **8**(9): p. 1087-1095.
15. Waddell, N., et al., *Whole genomes redefine the mutational landscape of pancreatic cancer.* Nature, 2015. **518**(7540): p. 495-501.
16. Hofmeyer, K.A., A. Ray, and X. Zang, *The contrasting role of B7-H3.* Proceedings of the National Academy of Sciences, 2008. **105**(30): p. 10277-10278.
17. Zhao, X., et al., *B7-H3 overexpression in pancreatic cancer promotes tumor progression.* International journal of molecular medicine, 2013. **31**(2): p. 283-291.
18. Inamura, K., et al., *Tumor B7-H3 (CD276) expression and survival in pancreatic cancer.* Journal of clinical medicine, 2018. **7**(7): p. 172.
19. Xie, C., et al., *Soluble B7-H3 promotes the invasion and metastasis of pancreatic carcinoma cells through the TLR4/NF-κB pathway.* Scientific reports, 2016. **6**(1): p. 27528.
20. UK, C.R. *Pancreatic Cancer statistics*. Pancreatic cancer incidence statistics 2021 [cited 2023 03 March 2023]; Available from: https://www.cancerresearchuk.org/health-professional/cancer-statistics/statistics-by-cancer-type/pancreatic-cancer/incidence#heading-Zero.
21. Kamisawa, T., et al., *Pancreatic cancer.* The Lancet, 2016. **388**(10039): p. 73-85.
22. Sasaki, T., et al., *Improvement of treatment outcomes for metastatic pancreatic cancer: a real-world data analysis.* in vivo, 2019. **33**(1): p. 271-276.

23. Gaikwad, V., B. Sirohi, and S.V. Shrikhande, *Adjuvant and Neoadjuvant Therapy in Pancreatic Cancer.* ECAB Adjuvant and Neoadjuvant Therapy in Gastrointestinal Cancer-E-Book, 2014: p. 90.
24. Schmidt-Hansen, M., S. Berendse, and W. Hamilton, *Symptoms of pancreatic cancer in primary care: a systematic review.* Pancreas, 2016. **45**(6): p. 814-818.
25. Mizrahi, J.D., et al., *Pancreatic cancer.* The Lancet, 2020. **395**(10242): p. 2008-2020.
26. Artinyan, A., et al., *The anatomic location of pancreatic cancer is a prognostic factor for survival.* Hpb, 2008. **10**(5): p. 371-376.
27. Porta, M., et al., *Exocrine pancreatic cancer: symptoms at presentation and their relation to tumour site and stage.* Clinical and Translational Oncology, 2005. **7**: p. 189-197.
28. Barreto, S.G., P.J. Shukla, and S.V. Shrikhande, *Tumors of the pancreatic body and tail.* World Journal of Oncology, 2010. **1**(2): p. 52.
29. Treadwell, J.R., et al., *Imaging tests for the diagnosis and staging of pancreatic adenocarcinoma: a meta-analysis.* Pancreas, 2016. **45**(6): p. 789-795.
30. Wang, W., et al., *Use of EUS-FNA in diagnosing pancreatic neoplasm without a definitive mass on CT.* Gastrointestinal endoscopy, 2013. **78**(1): p. 73-80.
31. Ballehaninna, U.K. and R.S. Chamberlain, *The clinical utility of serum CA 19-9 in the diagnosis, prognosis and management of pancreatic adenocarcinoma: An evidence based appraisal.* Journal of gastrointestinal oncology, 2012. **3**(2): p. 105.
32. Lin, M.-S., J.-X. Huang, and H. Yu, *Elevated serum level of carbohydrate antigen 19-9 in benign biliary stricture diseases can reduce its value as a tumor marker.* International journal of clinical and experimental medicine, 2014. **7**(3): p. 744.
33. Shin, D.W. and J. Kim, *The American Joint Committee on Cancer 8th edition staging system for the pancreatic ductal adenocarcinoma: is it better than the 7th edition?* Hepatobiliary surgery and nutrition, 2020. **9**(1): p. 98.
34. Masuda, T., et al., *A comprehensive assessment of accurate lymph node staging and preoperative detection in resected pancreatic cancer.* Journal of Gastrointestinal Surgery, 2018. **22**: p. 295-302.
35. Morales-Oyarvide, V., et al., *Lymph node metastases in resected pancreatic ductal adenocarcinoma: predictors of disease recurrence and survival.* British journal of cancer, 2017. **117**(12): p. 1874-1882.
36. Schlitter, A.M. and I. Esposito, *Definition of microscopic tumor clearance (r0) in pancreatic cancer resections.* Cancers, 2010. **2**(4): p. 2001-2010.
37. Tummers, W., et al., *Impact of resection margin status on recurrence and survival in pancreatic cancer surgery.* Journal of British Surgery, 2019. **106**(8): p. 1055-1065.
38. Menon, K.V., et al., *Impact of margin status on survival following pancreatoduodenectomy for cancer: the Leeds Pathology Protocol (LEEPP).* Hpb, 2009. **11**(1): p. 18-24.
39. van Roessel, S., et al., *Pathological margin clearance and survival after pancreaticoduodenectomy in a US and European pancreatic center.* Annals of surgical oncology, 2018. **25**: p. 1760-1767.
40. Jamiyan, T., et al., *Clinical impacts of resection margin status and clinicopathologic parameters on pancreatic ductal adenocarcinoma.* World Journal of Surgical Oncology, 2020. **18**(1): p. 1-11.
41. Garcea, G., et al., *Survival following curative resection for pancreatic ductal adenocarcinoma. A systematic review of the literature.* Jop, 2008. **9**(2): p. 99-132.
42. Rochefort, M.M., et al., *Impact of tumor grade on pancreatic cancer prognosis: validation of a novel TNMG staging system.* Annals of surgical oncology, 2013. **20**: p. 4322-4329.
43. Wasif, N., et al., *Impact of tumor grade on prognosis in pancreatic cancer: should we include grade in AJCC staging?* Annals of surgical oncology, 2010. **17**: p. 2312-2320.
44. Hong, S.-M., et al., *Vascular invasion in infiltrating ductal adenocarcinoma of the pancreas can mimic pancreatic intraepithelial neoplasia: a histopathologic study of 209 cases.* The American journal of surgical pathology, 2012. **36**(2): p. 235.

45. Schorn, S., et al., *The influence of neural invasion on survival and tumor recurrence in pancreatic ductal adenocarcinoma–a systematic review and meta-analysis.* Surgical oncology, 2017. **26**(1): p. 105-115.
46. Crippa, S., et al., *Implications of perineural invasion on disease recurrence and survival after pancreatectomy for pancreatic head ductal adenocarcinoma.* Annals of surgery, 2022. **276**(2): p. 378-385.
47. Raimondi, S., et al., *Pancreatic cancer in chronic pancreatitis; aetiology, incidence, and early detection.* Best practice & research Clinical gastroenterology, 2010. **24**(3): p. 349-358.
48. Brentnall, T.A., *Cancer surveillance of patients from familial pancreatic cancer kindreds.* Medical Clinics of North America, 2000. **84**(3): p. 707-718.
49. Zhen, D.B., et al., *BRCA1, BRCA2, PALB2, and CDKN2A mutations in familial pancreatic cancer: a PACGENE study.* Genetics in Medicine, 2015. **17**(7): p. 569-577.
50. Van der Heijden, M.S., et al., *Fanconi anemia gene mutations in young-onset pancreatic cancer.* Cancer research, 2003. **63**(10): p. 2585-2588.
51. Bosetti, C., et al., *Cigarette smoking and pancreatic cancer: an analysis from the International Pancreatic Cancer Case-Control Consortium (Panc4).* Annals of oncology, 2012. **23**(7): p. 1880-1888.
52. Pandol, S., *The Exocrine Pancreas. San Rafeal (CA): Morgan & Claypool Life Sciences 2010. Anatomy*.
53. El Sayed, S.A. and S. Mukherjee, *Physiology, pancreas.* 2017.
54. Kleeff, J., et al., *Pancreatic cancer.* Nature reviews Disease primers, 2016. **2**(1): p. 1-22.
55. Cubilla, A.L. and P.J. Fitzgerald, *Morphological lesions associated with human primary invasive nonendocrine pancreas cancer.* Cancer research, 1976. **36**(7_Part_2): p. 2690-2698.
56. Lee, A.Y., et al., *Cell of origin affects tumour development and phenotype in pancreatic ductal adenocarcinoma.* Gut, 2019. **68**(3): p. 487-498.
57. Ferreira, R.M., et al., *Duct-and acinar-derived pancreatic ductal adenocarcinomas show distinct tumor progression and marker expression.* Cell reports, 2017. **21**(4): p. 966-978.
58. Ren, B., X. Liu, and A.A. Suriawinata, *Pancreatic ductal adenocarcinoma and its precursor lesions: histopathology, cytopathology, and molecular pathology.* The American journal of pathology, 2019. **189**(1): p. 9-21.
59. Peters, M.L.B., et al., *Progression to pancreatic ductal adenocarcinoma from pancreatic intraepithelial neoplasia: Results of a simulation model.* Pancreatology, 2018. **18**(8): p. 928-934.
60. Ying, H., et al., *Genetics and biology of pancreatic ductal adenocarcinoma.* Genes & development, 2016. **30**(4): p. 355-385.
61. Welsch, T., J. Kleeff, and H. Friess, *Molecular pathogenesis of pancreatic cancer: advances and challenges.* Current Molecular Medicine, 2007. **7**(5): p. 504-521.
62. Biankin, A.V., et al., *Pancreatic cancer genomes reveal aberrations in axon guidance pathway genes.* Nature, 2012. **491**(7424): p. 399-405.
63. Diehl, A.C., et al., *KRAS mutation variants and co-occurring PI3K pathway alterations impact survival for patients with pancreatic ductal adenocarcinomas.* The Oncologist, 2022. **27**(12): p. 1025-1033.
64. Bryant, K.L., et al., *KRAS: feeding pancreatic cancer proliferation.* Trends in biochemical sciences, 2014. **39**(2): p. 91-100.
65. Eibl, G. and E. Rozengurt. *KRAS, YAP, and obesity in pancreatic cancer: A signaling network with multiple loops*. in *Seminars in cancer biology*. 2019. Elsevier.
66. Huang, L., et al., *KRAS mutation: from undruggable to druggable in cancer.* Signal transduction and targeted therapy, 2021. **6**(1): p. 386.
67. Derynck, R. and Y.E. Zhang, *Smad-dependent and Smad-independent pathways in TGF-β family signalling.* Nature, 2003. **425**(6958): p. 577-584.
68. Tzavlaki, K. and A. Moustakas, *TGF-β Signaling.* Biomolecules, 2020. **10**(3): p. 487.

69. Roberts, A., et al., *Transforming growth factor-β: multifunctional regulator of differentiation and development.* Philosophical Transactions of the Royal Society of London. B, Biological Sciences, 1990. **327**(1239): p. 145-154.
70. David, C.J., et al., *TGF-β tumor suppression through a lethal EMT.* Cell, 2016. **164**(5): p. 1015-1030.
71. Hezel, A.F., et al., *TGF-β and αvβ6 integrin act in a common pathway to suppress pancreatic cancer progression.* Cancer research, 2012. **72**(18): p. 4840-4845.
72. Cave, D.D., et al., *TGF-β1 secreted by pancreatic stellate cells promotes stemness and tumourigenicity in pancreatic cancer cells through L1CAM downregulation.* Oncogene, 2020. **39**(21): p. 4271-4285.
73. Nolan-Stevaux, O., et al., *GLI1 is regulated through Smoothened-independent mechanisms in neoplastic pancreatic ducts and mediates PDAC cell survival and transformation.* Genes & development, 2009. **23**(1): p. 24-36.
74. Levy, L. and C.S. Hill, *Smad4 dependency defines two classes of transforming growth factor β (TGF-β) target genes and distinguishes TGF-β-induced epithelial-mesenchymal transition from its antiproliferative and migratory responses.* Molecular and cellular biology, 2005. **25**(18): p. 8108-8125.
75. Ren, X., et al., *lncRNA-PLACT1 sustains activation of NF-κB pathway through a positive feedback loop with IκBα/E2F1 axis in pancreatic cancer.* Molecular cancer, 2020. **19**(1): p. 1-19.
76. Sun, Q., et al., *Pin1 promotes pancreatic cancer progression and metastasis by activation of NF-κB-IL-18 feedback loop.* Cell Proliferation, 2020. **53**(5): p. e12816.
77. Matsusaka, T., et al., *Transcription factors NF-IL6 and NF-kappa B synergistically activate transcription of the inflammatory cytokines, interleukin 6 and interleukin 8.* Proceedings of the National Academy of Sciences, 1993. **90**(21): p. 10193-10197.
78. Rhim, A.D., et al., *EMT and dissemination precede pancreatic tumor formation.* Cell, 2012. **148**(1): p. 349-361.
79. Pramanik, K.C., et al., *Advancement of NF-κB signaling pathway: a novel target in pancreatic cancer.* International journal of molecular sciences, 2018. **19**(12): p. 3890.
80. O'Shea, J.J. and R. Plenge, *JAK and STAT signaling molecules in immunoregulation and immune-mediated disease.* Immunity, 2012. **36**(4): p. 542-550.
81. Lu, C., et al., *JAK-STAT-mediated chronic inflammation impairs cytotoxic T lymphocyte activation to decrease anti-PD-1 immunotherapy efficacy in pancreatic cancer.* Oncoimmunology, 2017. **6**(3): p. e1291106.
82. Song, Y., et al., *High JAK2 protein expression predicts a poor prognosis in patients with resectable pancreatic ductal adenocarcinoma.* Disease markers, 2020. **2020**.
83. Corcoran, R.B., et al., *STAT3 plays a critical role in KRAS-induced pancreatic tumorigenesis.* Cancer research, 2011. **71**(14): p. 5020-5029.
84. D'Amico, S., et al., *STAT3 is a master regulator of epithelial identity and KRAS-driven tumorigenesis.* Genes & development, 2018. **32**(17-18): p. 1175-1187.
85. Fukuda, A., et al., *Stat3 and MMP7 contribute to pancreatic ductal adenocarcinoma initiation and progression.* Cancer cell, 2011. **19**(4): p. 441-455.
86. Lesina, M., et al., *Stat3/Socs3 activation by IL-6 transsignaling promotes progression of pancreatic intraepithelial neoplasia and development of pancreatic cancer.* Cancer cell, 2011. **19**(4): p. 456-469.
87. Mengie Ayele, T., et al., *Role of JAK2/STAT3 signaling pathway in the tumorigenesis, chemotherapy resistance, and treatment of solid tumors: a systemic review.* Journal of Inflammation Research, 2022: p. 1349-1364.
88. Chen, J., et al., *Interleukin-32α inactivates JAK2/STAT3 signaling and reverses interleukin-6-induced epithelial–mesenchymal transition, invasion, and metastasis in pancreatic cancer cells.* OncoTargets and therapy, 2016: p. 4225-4237.
89. Trovato, R., et al., *Immunosuppression by monocytic myeloid-derived suppressor cells in patients with pancreatic ductal carcinoma is orchestrated by STAT3.* Journal for immunotherapy of cancer, 2019. **7**: p. 1-16.
90. Golan, T., et al., *Maintenance Olaparib for Germline BRCA-Mutated Metastatic Pancreatic Cancer.* New England Journal of Medicine, 2019. **381**(4): p. 317-327.

91. Alvarez, M.A., et al., *TGF-β inhibitors in metastatic pancreatic ductal adenocarcinoma.* Journal of gastrointestinal cancer, 2019. **50**: p. 207-213.
92. Krebs, A.M., et al., *The EMT-activator Zeb1 is a key factor for cell plasticity and promotes metastasis in pancreatic cancer.* Nature cell biology, 2017. **19**(5): p. 518-529.
93. Chouat, E., et al., *Tumor budding is a prognostic factor linked to epithelial mesenchymal transition in pancreatic ductal adenocarcinoma. Study report and literature review.* Pancreatology, 2018. **18**(1): p. 79-84.
94. Hanahan, D., *Hallmarks of cancer: new dimensions.* Cancer discovery, 2022. **12**(1): p. 31-46.
95. Provenzano, P.P., et al., *Enzymatic targeting of the stroma ablates physical barriers to treatment of pancreatic ductal adenocarcinoma.* Cancer cell, 2012. **21**(3): p. 418-429.
96. Jacobetz, M.A., et al., *Hyaluronan impairs vascular function and drug delivery in a mouse model of pancreatic cancer.* Gut, 2013. **62**(1): p. 112-120.
97. Yang, C., et al., *B cells promote tumor progression via STAT3 regulated-angiogenesis.* PloS one, 2013. **8**(5): p. e64159.
98. Craven, K.E., et al., *Angiogenic gene signature in human pancreatic cancer correlates with TGF-beta and inflammatory transcriptomes.* Oncotarget, 2016. **7**(1): p. 323.
99. Huang, C., et al., *BICC1 drives pancreatic cancer progression by inducing VEGF-independent angiogenesis.* Signal Transduction and Targeted Therapy, 2023. **8**(1): p. 271.
100. Collisson, E.A., et al., *Subtypes of pancreatic ductal adenocarcinoma and their differing responses to therapy.* Nature Medicine, 2011. **17**(4): p. 500-U140.
101. Moffitt, R.A., et al., *Virtual microdissection identifies distinct tumor-and stroma-specific subtypes of pancreatic ductal adenocarcinoma.* Nature genetics, 2015. **47**(10): p. 1168-1178.
102. Bailey, P., et al., *Genomic analyses identify molecular subtypes of pancreatic cancer.* Nature, 2016. **531**(7592): p. 47-+.
103. Raphael, B.J., et al., *Integrated genomic characterization of pancreatic ductal adenocarcinoma.* Cancer cell, 2017. **32**(2): p. 185-203. e13.
104. Puleo, F., et al., *Stratification of pancreatic ductal adenocarcinomas based on tumor and microenvironment features.* Gastroenterology, 2018. **155**(6): p. 1999-2013. e3.
105. Torres, C. and P.J. Grippo, *Pancreatic cancer subtypes: a roadmap for precision medicine.* Annals of medicine, 2018. **50**(4): p. 277-287.
106. Dreyer, S.B., et al., *Pancreatic Cancer Genomes: Implications for Clinical Management and Therapeutic Development.* Clinical Cancer Research, 2017. **23**(7): p. 1638-1646.
107. Wang, N., et al., *Spatial transcriptomics and proteomics technologies for deconvoluting the tumor microenvironment.* Biotechnology journal, 2021. **16**(9): p. 2100041.
108. Moses, L. and L. Pachter, *Museum of spatial transcriptomics.* Nature Methods, 2022. **19**(5): p. 534-546.
109. Marx, V., *Method of the Year: spatially resolved transcriptomics.* Nature methods, 2021. **18**(1): p. 9-14.
110. Shah, S., et al., *In situ transcription profiling of single cells reveals spatial organization of cells in the mouse hippocampus.* Neuron, 2016. **92**(2): p. 342-357.
111. Eng, C.-H.L., et al., *Profiling the transcriptome with RNA SPOTs.* Nature methods, 2017. **14**(12): p. 1153-1155.
112. Eng, C.-H.L., et al., *Transcriptome-scale super-resolved imaging in tissues by RNA seqFISH+.* Nature, 2019. **568**(7751): p. 235-239.
113. Merritt, C.R., et al., *Multiplex digital spatial profiling of proteins and RNA in fixed tissue.* Nature biotechnology, 2020. **38**(5): p. 586-599.
114. Ståhl, P.L., et al., *Visualization and analysis of gene expression in tissue sections by spatial transcriptomics.* Science, 2016. **353**(6294): p. 78-82.

115. Cheng, M., et al., *Spatially resolved transcriptomics: a comprehensive review of their technological advances, applications, and challenges.* Journal of Genetics and Genomics, 2023.
116. Wang, X., et al., *Three-dimensional intact-tissue sequencing of single-cell transcriptional states.* Science, 2018. **361**(6400): p. eaat5691.
117. Al-Amrani, S., et al., *Proteomics: Concepts and applications in human medicine.* World Journal of Biological Chemistry, 2021. **12**(5): p. 57.
118. Hoyt, C.C., *Multiplex immunofluorescence and multispectral imaging: forming the basis of a clinical test platform for immuno-oncology.* Frontiers in molecular biosciences, 2021. **8**: p. 674747.
119. Black, S., et al., *CODEX multiplexed tissue imaging with DNA-conjugated antibodies.* Nature protocols, 2021. **16**(8): p. 3802-3835.
120. Ben-Chetrit, N., et al., *Integration of whole transcriptome spatial profiling with protein markers.* Nature Biotechnology, 2023. **41**(6): p. 788-793.
121. Xu, Z., et al., *STOmicsDB: a comprehensive database for spatial transcriptomics data sharing, analysis and visualization.* Nucleic Acids Research, 2023: p. gkad933.
122. Plunkett, W., et al. *Gemcitabine: metabolism, mechanisms of action, and self-potentiation*. in *Seminars in oncology*. 1995.
123. Heinemann, V., et al., *Meta-analysis of randomized trials: evaluation of benefit from gemcitabine-based combination chemotherapy applied in advanced pancreatic cancer.* BMC cancer, 2008. **8**(1): p. 1-11.
124. Louvet, C., et al., *Gemcitabine in combination with oxaliplatin compared with gemcitabine alone in locally advanced or metastatic pancreatic cancer: results of a GERCOR and GISCAD phase III trial.* Journal of Clinical Oncology, 2005. **23**(15): p. 3509-3516.
125. Berlin, J.D., et al., *Phase III study of gemcitabine in combination with fluorouracil versus gemcitabine alone in patients with advanced pancreatic carcinoma: Eastern Cooperative Oncology Group Trial E2297.* Journal of Clinical Oncology, 2002. **20**(15): p. 3270-3275.
126. Neoptolemos, J.P., et al., *Comparison of adjuvant gemcitabine and capecitabine with gemcitabine monotherapy in patients with resected pancreatic cancer (ESPAC-4): a multicentre, open-label, randomised, phase 3 trial.* The Lancet, 2017. **389**(10073): p. 1011-1024.
127. Moore, M.J., et al., *Erlotinib plus gemcitabine compared with gemcitabine alone in patients with advanced pancreatic cancer: a phase III trial of the National Cancer Institute of Canada Clinical Trials Group.* Journal of clinical oncology, 2007. **25**(15): p. 1960-1966.
128. Cunningham, D., et al., *Phase III randomized comparison of gemcitabine versus gemcitabine plus capecitabine in patients with advanced pancreatic cancer.* Journal of Clinical Oncology, 2009. **27**(33): p. 5513-5518.
129. Yardley, D.A., *nab-Paclitaxel mechanisms of action and delivery.* Journal of Controlled Release, 2013. **170**(3): p. 365-372.
130. Siddiqui, N.S., et al., *Capecitabine for the treatment of pancreatic cancer.* Expert opinion on pharmacotherapy, 2019. **20**(4): p. 399-409.
131. Neoptolemos, J.P., et al., *Adjuvant chemoradiotherapy and chemotherapy in resectable pancreatic cancer: a randomised controlled trial.* Lancet, 2001. **358**(9293): p. 1576-1585.
132. Von Hoff, D.D., et al., *Increased Survival in Pancreatic Cancer with nab-Paclitaxel plus Gemcitabine.* New England Journal of Medicine, 2013. **369**(18): p. 1691-1703.
133. Nevala-Plagemann, C., M. Hidalgo, and I. Garrido-Laguna, *From state-of-the-art treatments to novel therapies for advanced-stage pancreatic cancer.* Nature reviews. Clinical oncology, 2019.
134. Golan, T., et al., *Overall survival and clinical characteristics of pancreatic cancer in BRCA mutation carriers.* British Journal of Cancer, 2014. **111**(6): p. 1132-1138.
135. Kowalewski, A., et al., *Emerging strategies in BRCA-positive pancreatic cancer.* Journal of Cancer Research and Clinical Oncology, 2018. **144**(8): p. 1503-1507.

136. Jan, I.-S. and H.J. Ch'ang, *Selection of patients with pancreatic adenocarcinoma who may benefit from radiotherapy.* Radiation Oncology, 2023. **18**(1): p. 137.
137. Wang, D., et al., *Effect of neoadjuvant radiotherapy on survival of non-metastatic pancreatic ductal adenocarcinoma: a SEER database analysis.* Radiation Oncology, 2020. **15**: p. 1-12.
138. Oba, A., et al., *Comparing neoadjuvant chemotherapy with or without radiation therapy for pancreatic ductal adenocarcinoma: National Cancer Database cohort analysis.* British Journal of Surgery, 2022. **109**(5): p. 450-454.
139. Johnson III, B.A., et al., *Strategies for increasing pancreatic tumor immunogenicity*. Clinical Cancer Research, 2017. **23**(7): p. 1656-1669.
140. Reck, M., et al., *Pembrolizumab versus chemotherapy for PD-L1–positive non–small-cell lung cancer.* New England Journal of Medicine, 2016. **375**(19): p. 1823-1833.
141. Birnbaum, D.J., et al., *Prognostic value of PDL1 expression in pancreatic cancer.* Oncotarget, 2016. **7**(44): p. 71198-71210.
142. Shenderov, E., et al., *620P MGC018, an anti-B7-H3 antibody-drug conjugate (ADC), in patients with advanced solid tumors: Preliminary results of phase I cohort expansion.* Annals of Oncology, 2021. **32**: p. S657-S659.
143. Yamato, M., et al., *DS-7300a, a DNA Topoisomerase I Inhibitor, DXd-Based Antibody–Drug Conjugate Targeting B7-H3, Exerts Potent Antitumor Activities in Preclinical Models.* Molecular Cancer Therapeutics, 2022. **21**(4): p. 635-646.
144. Doi, T., et al., *453O DS-7300 (B7-H3 DXd antibody-drug conjugate [ADC]) shows durable antitumor activity in advanced solid tumors: Extended follow-up of a phase I/II study.* Annals of Oncology, 2022. **33**: p. S744-S745.
145. Shenderov, E., et al., *Targeting B7-H3 in prostate cancer: phase 2 trial in localized prostate cancer using the anti-B7-H3 antibody enoblituzumab, with biomarker correlatives.* J Clin Oncol, 2022. **40**(16_suppl): p. 5015.
146. Powderly, J., et al., *Interim results of an ongoing Phase I, dose escalation study of MGA271 (Fc-optimized humanized anti-B7-H3 monoclonal antibody) in patients with refractory B7-H3-expressing neoplasms or neoplasms whose vasculature expresses B7-H3.* Journal for immunotherapy of cancer, 2015. **3**(2): p. 1-2.
147. Homma, Y., et al., *Changes in the immune cell population and cell proliferation in peripheral blood after gemcitabine-based chemotherapy for pancreatic cancer.* Clinical and Translational Oncology, 2014. **16**: p. 330-335.
148. Azad, A., et al., *PD-L1 blockade enhances response of pancreatic ductal adenocarcinoma to radiotherapy.* Embo Molecular Medicine, 2017. **9**(2): p. 167-180.
149. Mun, J.-Y., et al., *Dual relationship between stromal cells and immune cells in the tumor microenvironment.* Frontiers in Immunology, 2022. **13**: p. 864739.
150. Schlitter, A.M., et al., *Molecular, morphological and survival analysis of 177 resected pancreatic ductal adenocarcinomas (PDACs): Identification of prognostic subtypes.* Scientific reports, 2017. **7**(1): p. 41064.
151. Bulle, A. and K.-H. Lim, *Beyond just a tight fortress: contribution of stroma to epithelial-mesenchymal transition in pancreatic cancer.* Signal Transduction and Targeted Therapy, 2020. **5**(1): p. 249.
152. Feig, C., et al., *The Pancreas Cancer Microenvironment.* Clinical Cancer Research, 2012. **18**(16): p. 4266-4276.
153. Theocharis, A.D., et al., *Extracellular matrix structure.* Advanced drug delivery reviews, 2016. **97**: p. 4-27.
154. Karamanos, N.K., et al., *A guide to the composition and functions of the extracellular matrix.* The FEBS journal, 2021. **288**(24): p. 6850-6912.
155. Palamaris, K., E. Felekouras, and S. Sakellariou, *Epithelial to mesenchymal transition: key regulator of pancreatic ductal adenocarcinoma progression and chemoresistance.* Cancers, 2021. **13**(21): p. 5532.
156. Aiello, N.M., et al., *EMT subtype influences epithelial plasticity and mode of cell migration.* Developmental cell, 2018. **45**(6): p. 681-695. e4.

157. Uttamsingh, S., et al., *Synergistic effect between EGF and TGF-β1 in inducing oncogenic properties of intestinal epithelial cells.* Oncogene, 2008. **27**(18): p. 2626-2634.
158. Colomiere, M., et al., *Cross talk of signals between EGFR and IL-6R through JAK2/STAT3 mediate epithelial–mesenchymal transition in ovarian carcinomas.* British journal of cancer, 2009. **100**(1): p. 134-144.
159. Zhang, D., et al., *Tumor–stroma IL1β-IRAK4 feedforward circuitry drives tumor fibrosis, chemoresistance, and poor prognosis in pancreatic cancer.* Cancer research, 2018. **78**(7): p. 1700-1712.
160. Bussard, K.M., et al., *Tumor-associated stromal cells as key contributors to the tumor microenvironment.* Breast Cancer Research, 2016. **18**: p. 1-11.
161. Seager, R.J., et al., *Dynamic interplay between tumour, stroma and immune system can drive or prevent tumour progression.* Convergent science physical oncology, 2017. **3**(3): p. 034002.
162. Xu, Y., et al., *The co-expression of MMP-9 and Tenascin-C is significantly associated with the progression and prognosis of pancreatic cancer.* Diagnostic pathology, 2015. **10**: p. 1-8.
163. Tjomsland, V., et al., *The desmoplastic stroma plays an essential role in the accumulation and modulation of infiltrated immune cells in pancreatic adenocarcinoma.* Clinical and Developmental Immunology, 2011. **2011**.
164. Zhang, A., et al., *Cancer‐associated fibroblasts promote M2 polarization of macrophages in pancreatic ductal adenocarcinoma.* Cancer medicine, 2017. **6**(2): p. 463-470.
165. Cheng, Y., et al., *Cancer-associated fibroblasts induce PDL1+ neutrophils through the IL6-STAT3 pathway that foster immune suppression in hepatocellular carcinoma.* Cell death & disease, 2018. **9**(4): p. 422.
166. Freeman, P. and A. Mielgo, *Cancer-associated fibroblast mediated inhibition of CD8+ cytotoxic T cell accumulation in tumours: mechanisms and therapeutic opportunities.* Cancers, 2020. **12**(9): p. 2687.
167. Lin, S., et al., *Lactate-activated macrophages induced aerobic glycolysis and epithelial-mesenchymal transition in breast cancer by regulation of CCL5-CCR5 axis: a positive metabolic feedback loop.* Oncotarget, 2017. **8**(66): p. 110426.
168. Taylor, E.S., et al., *Functional impairment of infiltrating T cells in human colorectal cancer.* Oncoimmunology, 2016. **5**(11): p. e1234573.
169. Kouidhi, S., A.B. Elgaaied, and S. Chouaib, *Impact of metabolism on T-cell differentiation and function and cross talk with tumor microenvironment.* Frontiers in immunology, 2017. **8**: p. 270.
170. Muller, M., et al., *The immune landscape of human pancreatic ductal carcinoma: key players, clinical implications, and challenges.* Cancers, 2022. **14**(4): p. 995.
171. Hiraoka, N., et al., *Intratumoral tertiary lymphoid organ is a favourable prognosticator in patients with pancreatic cancer.* British journal of cancer, 2015. **112**(11): p. 1782-1790.
172. Miksch, R.C., et al., *Prognostic impact of tumor-infiltrating lymphocytes and neutrophils on survival of patients with upfront resection of pancreatic cancer.* Cancers, 2019. **11**(1): p. 39.
173. Fukunaga, A., et al., *CD8+ tumor-infiltrating lymphocytes together with CD4+ tumor-infiltrating lymphocytes and dendritic cells improve the prognosis of patients with pancreatic adenocarcinoma.* Pancreas, 2004. **28**(1): p. e26-e31.
174. Deicher, A., et al., *Targeting dendritic cells in pancreatic ductal adenocarcinoma.* Cancer cell international, 2018. **18**: p. 1-8.
175. Hoshikawa, M., et al., *NK cell and IFN signatures are positive prognostic biomarkers for resectable pancreatic cancer.* Biochemical and biophysical research communications, 2018. **495**(2): p. 2058-2065.
176. Hiraoka, N., et al., *Prevalence of FOXP3+ regulatory T cells increases during the progression of pancreatic ductal adenocarcinoma and its premalignant lesions.* Clinical cancer research, 2006. **12**(18): p. 5423-5434.

177. Tsujikawa, T., et al., *Quantitative Multiplex Immunohistochemistry Reveals Myeloid-Inflamed Tumor-Immune Complexity Associated with Poor Prognosis.* Cell Reports, 2017. **19**(1): p. 203-217.
178. Mantovani, A., et al., *The chemokine system in diverse forms of macrophage activation and polarization.* Trends in immunology, 2004. **25**(12): p. 677-686.
179. Fridlender, Z.G., et al., *Polarization of tumor-associated neutrophil phenotype by TGF-β:"N1" versus "N2" TAN.* Cancer cell, 2009. **16**(3): p. 183-194.
180. Lohneis, P., et al., *Cytotoxic tumour-infiltrating T lymphocytes influence outcome in resected pancreatic ductal adenocarcinoma.* European journal of cancer, 2017. **83**: p. 290-301.
181. Wang, Z., et al., *Prognostic significance of CD4 and interleukin-22 expression in pancreatic cancer.* International journal of clinical and experimental pathology, 2017. **10**(9): p. 9846.
182. Wang, Z., et al., *Infiltrating CD4/CD8 high T cells shows good prognostic impact in pancreatic cancer.* International journal of clinical and experimental pathology, 2017. **10**(8): p. 8820.
183. Teramatsu, K., et al., *Circulating CD8+ CD122+ T cells as a prognostic indicator of pancreatic cancer.* BMC cancer, 2022. **22**(1): p. 1-14.
184. Roth, S., et al., *Evolution of the immune landscape during progression of pancreatic intraductal papillary mucinous neoplasms to invasive cancer.* EBioMedicine, 2020. **54**.
185. Sierzega, M., et al., *Preoperative neutrophil-lymphocyte and lymphocyte-monocyte ratios reflect immune cell population rearrangement in resectable pancreatic cancer.* Annals of surgical oncology, 2017. **24**: p. 808-815.
186. Shan, T., et al., *Prometastatic mechanisms of CAF-mediated EMT regulation in pancreatic cancer cells.* International journal of oncology, 2017. **50**(1): p. 121-128.
187. Hwang, R.F., et al., *Cancer-associated stromal fibroblasts promote pancreatic tumor progression.* Cancer research, 2008. **68**(3): p. 918-926.
188. Xu, Z., et al., *Role of pancreatic stellate cells in pancreatic cancer metastasis.* The American journal of pathology, 2010. **177**(5): p. 2585-2596.
189. Menezes, S., et al., *Cancer-associated fibroblasts in pancreatic cancer: new subtypes, new markers, new targets.* The Journal of Pathology, 2022. **257**(4): p. 526-544.
190. Öhlund, D., et al., *Distinct populations of inflammatory fibroblasts and myofibroblasts in pancreatic cancer.* Journal of Experimental Medicine, 2017. **214**(3): p. 579-596.
191. Zhang, J., et al., *A cancer-associated fibroblast gene signature predicts prognosis and therapy response in patients with pancreatic cancer.* Frontiers in Oncology, 2022. **12**: p. 1052132.
192. Park, H., et al., *The prognostic significance of cancer-associated fibroblasts in pancreatic ductal adenocarcinoma.* Tumor Biology, 2017. **39**(10): p. 1010428317718403.
193. Erkan, M., et al., *The Activated Stroma Index Is a Novel and Independent Prognostic Marker in Pancreatic Ductal Adenocarcinoma.* Clinical Gastroenterology and Hepatology, 2008. **6**(10): p. 1155-1161.
194. Rhim, A.D., et al., *Stromal Elements Act to Restrain, Rather Than Support, Pancreatic Ductal Adenocarcinoma.* Cancer Cell, 2014. **25**(6): p. 735-747.
195. Duconseil, P., et al., *Transcriptomic Analysis Predicts Survival and Sensitivity to Anticancer Drugs of Patients with a Pancreatic Adenocarcinoma.* American Journal of Pathology, 2015. **185**(4): p. 1022-1032.
196. Mahajan, U.M., et al., *Immune Cell and Stromal Signature Associated With Progression-Free Survival of Patients With Resected Pancreatic Ductal Adenocarcinoma.* Gastroenterology, 2018. **155**(5): p. 1625-+.
197. Tong, D.N., et al., *Characterization of B cell-mediated PD-1/PD-L1 interaction in pancreatic cancer patients.* Clinical and Experimental Pharmacology and Physiology, 2020. **47**(8): p. 1342-1349.

198. Mirlekar, B., et al., *B cell–derived IL35 drives STAT3-dependent CD8+ T-cell exclusion in pancreatic cancer.* Cancer immunology research, 2020. **8**(3): p. 292-308.
199. Das, S. and D. Bar-Sagi, *BTK signaling drives CD1dhiCD5+ regulatory B-cell differentiation to promote pancreatic carcinogenesis.* Oncogene, 2019. **38**(17): p. 3316-3324.
200. Spear, S., et al., *Discrepancies in the tumor microenvironment of spontaneous and orthotopic murine models of pancreatic cancer uncover a new immunostimulatory phenotype for B cells.* Frontiers in immunology, 2019. **10**: p. 542.
201. Zhao, Y., et al., *Regulatory B cells induced by pancreatic cancer cell-derived interleukin-18 promote immune tolerance via the PD-1/PD-L1 pathway.* Oncotarget, 2018. **9**(19): p. 14803.
202. Jin, P., et al., *Circulating IL-35 in pancreatic ductal adenocarcinoma patients.* Human immunology, 2014. **75**(1): p. 29-33.
203. Pylayeva-Gupta, Y., et al., *IL35-producing B cells promote the development of pancreatic neoplasia.* Cancer discovery, 2016. **6**(3): p. 247-255.
204. Sautès-Fridman, C., et al., *Tertiary lymphoid structures in the era of cancer immunotherapy.* Nature Reviews Cancer, 2019. **19**(6): p. 307-325.
205. Lucchesi, D. and M. Bombardieri, *The role of viruses in autoreactive B cell activation within tertiary lymphoid structures in autoimmune diseases.* Journal of leukocyte biology, 2013. **94**(6): p. 1191-1199.
206. Dieu-Nosjean, M.-C., et al., *Tertiary lymphoid structures in cancer and beyond.* Trends in immunology, 2014. **35**(11): p. 571-580.
207. Gunderson, A.J., et al., *Germinal center reactions in tertiary lymphoid structures associate with neoantigen burden, humoral immunity and long-term survivorship in pancreatic cancer.* Oncoimmunology, 2021. **10**(1): p. 1900635.
208. Thomas, D. and P. Radhakrishnan, *Tumor-stromal crosstalk in pancreatic cancer and tissue fibrosis.* Molecular cancer, 2019. **18**: p. 1-15.
209. Biffi, G., et al., *IL1-induced JAK/STAT signaling is antagonized by TGFβ to shape CAF heterogeneity in pancreatic ductal adenocarcinoma.* Cancer discovery, 2019. **9**(2): p. 282-301.
210. Garg, B., et al., *NFκB in pancreatic stellate cells reduces infiltration of tumors by cytotoxic T cells and killing of cancer cells, via up-regulation of CXCL12.* Gastroenterology, 2018. **155**(3): p. 880-891. e8.
211. Ratnam, N.M., et al., *NF-κB regulates GDF-15 to suppress macrophage surveillance during early tumor development.* The Journal of clinical investigation, 2017. **127**(10): p. 3796-3809.
212. Yamamoto, K., et al., *Autophagy promotes immune evasion of pancreatic cancer by degrading MHC-I.* Nature, 2020. **581**(7806): p. 100-105.
213. Principe, D.R., et al., *Long-term gemcitabine treatment reshapes the pancreatic tumor microenvironment and sensitizes murine carcinoma to combination immunotherapy.* Cancer research, 2020. **80**(15): p. 3101-3115.
214. Mandili, G., et al., *In pancreatic cancer, chemotherapy increases antitumor responses to tumor-associated antigens and potentiates DNA vaccination.* Journal for Immunotherapy of Cancer, 2020. **8**(2).
215. Neoptolemos, J.P., et al., *Effect of adjuvant chemotherapy with fluorouracil plus folinic acid or gemcitabine vs observation on survival in patients with resected periampullary adenocarcinoma: the ESPAC-3 periampullary cancer randomized trial.* Jama, 2012. **308**(2): p. 147-156.
216. Westerterp, M., et al., *Differential responses of cellular immunity in patients undergoing neoadjuvant therapy followed by surgery for carcinoma of the oesophagus.* Cancer Immunology, Immunotherapy, 2008. **57**: p. 1837-1847.
217. Graeser, M., et al., *Immune cell composition and functional marker dynamics from multiplexed immunohistochemistry to predict response to neoadjuvant chemotherapy in the WSG-ADAPT-TN trial.* Journal for immunotherapy of cancer, 2021. **9**(5).

218. Candido, J.B., et al., *CSF1R(+) Macrophages Sustain Pancreatic Tumor Growth through T Cell Suppression and Maintenance of Key Gene Programs that Define the Squamous Subtype.* Cell Reports, 2018. **23**(5): p. 1448-1460.
219. Carstens, J.L., et al., *Spatial computation of intratumoral T cells correlates with survival of patients with pancreatic cancer.* Nature Communications, 2017. **8**.
220. Halse, H., et al., *Multiplex immunohistochemistry accurately defines the immune context of metastatic melanoma.* Scientific reports, 2018. **8**(1): p. 11158.
221. Choi, Y.-L., et al., *Distinct subset of immune cells assessed by multiplex immunohistochemistry correlates with immune phenotype classified by an artificial intelligence-powered tissue analyzer in advanced non-small cell lung cancer*. 2021, Wolters Kluwer Health.
222. MacNeil, T., et al., *Multiplex quantitative analysis of tumor-infiltrating lymphocytes, cancer-associated fibroblasts, and CD200 in pancreatic cancer.* Cancers, 2021. **13**(21): p. 5501.
223. Banik, G., et al., *High-dimensional multiplexed immunohistochemical characterization of immune contexture in human cancers*, in *Methods in enzymology*. 2020, Elsevier. p. 1-20.
224. Vennin, C., et al., *CAF hierarchy driven by pancreatic cancer cell p53-status creates a pro-metastatic and chemoresistant environment via perlecan.* Nature communications, 2019. **10**(1): p. 3637.
225. Helmink, B.A., et al., *B cells and tertiary lymphoid structures promote immunotherapy response.* Nature, 2020. **577**(7791): p. 549-+.
226. Germain, C., et al., *Presence of B cells in tertiary lymphoid structures is associated with a protective immunity in patients with lung cancer.* American journal of respiratory and critical care medicine, 2014. **189**(7): p. 832-844.
227. Garnelo, M., et al., *Interaction between tumour-infiltrating B cells and T cells controls the progression of hepatocellular carcinoma.* Gut, 2017. **66**(2): p. 342-351.
228. Simon, R., M. Mirlacher, and G. Sauter, *Immunohistochemical analysis of tissue microarrays.* Tissue Microarrays: Methods and Protocols, 2010: p. 113-126.
229. Levenson, R.M., A.D. Borowsky, and M. Angelo, *Immunohistochemistry and mass spectrometry for highly multiplexed cellular molecular imaging.* Laboratory Investigation, 2015. **95**(4): p. 397-405.
230. Kumar, B.V., T.J. Connors, and D.L. Farber, *Human T cell development, localization, and function throughout life.* Immunity, 2018. **48**(2): p. 202-213.
231. Raskov, H., et al., *Cytotoxic CD8+ T cells in cancer and cancer immunotherapy.* British journal of cancer, 2021. **124**(2): p. 359-367.
232. Masugi, Y., et al., *Characterization of spatial distribution of tumor-infiltrating CD8+ T cells refines their prognostic utility for pancreatic cancer survival.* Modern pathology, 2019. **32**(10): p. 1495-1507.
233. Luckheeram, R.V., et al., *CD4+ T cells: differentiation and functions.* Clinical and developmental immunology, 2012. **2012**.
234. Patterson, M.T., et al., *Tumor-specific CD4 T cells instruct monocyte fate in pancreatic ductal adenocarcinoma.* Cell reports, 2023. **42**(7).
235. Tang, Y., et al., *An increased abundance of tumor-infiltrating regulatory T cells is correlated with the progression and prognosis of pancreatic ductal adenocarcinoma.* PloS one, 2014. **9**(3): p. e91551.
236. Davies, L.C., et al., *Tissue-resident macrophages.* Nature immunology, 2013. **14**(10): p. 986-995.
237. Knudsen, E.S., et al., *Stratification of pancreatic ductal adenocarcinoma: combinatorial genetic, stromal, and immunologic markers.* Clinical Cancer Research, 2017. **23**(15): p. 4429-4440.
238. Diana, A., et al., *Prognostic role and correlation of CA9, CD31, CD68 and CD20 with the desmoplastic stroma in pancreatic ductal adenocarcinoma.* Oncotarget, 2016. **7**(45): p. 72819.
239. Jamieson, N.B., et al., *The relationship between tumor inflammatory cell infiltrate and outcome in patients with pancreatic ductal adenocarcinoma.* Annals of surgical oncology, 2012. **19**: p. 3581-3590.

240. Van Der Loos, C.M., *Chromogens in multiple immunohistochemical staining used for visual assessment and spectral imaging: the colorful future.* Journal of Histotechnology, 2010. **33**(1): p. 31-40.
241. Mi, H., et al., *Quantitative spatial profiling of immune populations in pancreatic ductal adenocarcinoma reveals tumor microenvironment heterogeneity and prognostic biomarkers.* Cancer research, 2022. **82**(23): p. 4359-4372.
242. Yamato, I., et al., *Clinical importance of B7-H3 expression in human pancreatic cancer.* British journal of cancer, 2009. **101**(10): p. 1709-1716.
243. Chapoval, A.I., et al., *B7-H3: a costimulatory molecule for T cell activation and IFN-γ production.* Nature immunology, 2001. **2**(3): p. 269-274.
244. Prasad, D.V., et al., *Murine B7-H3 is a negative regulator of T cells.* The Journal of Immunology, 2004. **173**(4): p. 2500-2506.
245. Suh, W.-K., et al., *The B7 family member B7-H3 preferentially down-regulates T helper type 1–mediated immune responses.* Nature immunology, 2003. **4**(9): p. 899-906.
246. Wang, C., et al., *CD276 expression enables squamous cell carcinoma stem cells to evade immune surveillance.* Cell stem cell, 2021. **28**(9): p. 1597-1613. e7.
247. Janssen, Q.P., et al., *Neoadjuvant treatment in patients with resectable and borderline resectable pancreatic cancer.* Frontiers in oncology, 2020. **10**: p. 41.
248. Ghaneh, P., et al., *Immediate surgery compared with short-course neoadjuvant gemcitabine plus capecitabine, FOLFIRINOX, or chemoradiotherapy in patients with borderline resectable pancreatic cancer (ESPAC5): a four-arm, multicentre, randomised, phase 2 trial.* The Lancet Gastroenterology & Hepatology, 2023. **8**(2): p. 157-168.
249. Versteijne, E., et al., *Preoperative chemoradiotherapy versus immediate surgery for resectable and borderline resectable pancreatic cancer: results of the Dutch randomized phase III PREOPANC trial.* Journal of Clinical Oncology, 2020. **38**(16): p. 1763.
250. Kunzmann, V., et al., *Nab-paclitaxel plus gemcitabine versus nab-paclitaxel plus gemcitabine followed by FOLFIRINOX induction chemotherapy in locally advanced pancreatic cancer (NEOLAP-AIO-PAK-0113): a multicentre, randomised, phase 2 trial.* The lancet Gastroenterology & hepatology, 2021. **6**(2): p. 128-138.
251. Liudahl, S.M., et al., *Leukocyte heterogeneity in pancreatic ductal adenocarcinoma: phenotypic and spatial features associated with clinical outcome.* Cancer discovery, 2021. **11**(8): p. 2014-2031.
252. Dias Costa, A., et al., *Neoadjuvant chemotherapy is associated with altered immune cell infiltration and an anti-tumorigenic microenvironment in resected pancreatic cancer.* Clinical cancer research, 2022. **28**(23): p. 5167-5179.
253. Heiduk, M., et al., *Neoadjuvant chemotherapy drives intratumoral T cells toward a proinflammatory profile in pancreatic cancer.* JCI insight, 2022. **7**(22).
254. Lee, A.T., et al., *The adequacy of tissue microarrays in the assessment of inter- and intra-tumoural heterogeneity of infiltrating lymphocyte burden in leiomyosarcoma.* Scientific Reports, 2019. **9**(1): p. 14602.
255. Homma, Y., et al., *Changes in the immune cell population and cell proliferation in peripheral blood after gemcitabine-based chemotherapy for pancreatic cancer.* Clinical & Translational Oncology, 2014. **16**(3): p. 330-335.
256. Nejati, R., et al., *Prognostic significance of tumor infiltrating lymphocytes in patients with pancreatic ductal adenocarcinoma treated with neoadjuvant chemotherapy.* Pancreas, 2017. **46**(9): p. 1180.
257. Reyes, C.M., et al., *Neoadjuvant Therapy Remodels the Pancreatic Cancer Microenvironment via Depletion of Protumorigenic Immune Cells.* Clinical Cancer Research, 2020. **26**(1): p. 220-231.
258. Verastegui, E.L., et al., *Long-term immune dysfunction after radiotherapy to the head and neck area.* International immunopharmacology, 2003. **3**(8): p. 1093-1104.
259. Verma, R., et al., *Lymphocyte depletion and repopulation after chemotherapy for primary breast cancer.* Breast Cancer Research, 2016. **18**(1): p. 1-12.

260. Lee, Y.J., et al., *Temporal changes in immune cell composition and cytokines in response to chemoradiation in rectal cancer.* Scientific reports, 2018. **8**(1): p. 7565.
261. Papalampros, A., et al., *Unique spatial immune profiling in pancreatic ductal adenocarcinoma with enrichment of exhausted and senescent T cells and diffused CD47-SIRPα expression.* Cancers, 2020. **12**(7): p. 1825.
262. Wherry, E.J., et al., *Viral persistence alters CD8 T-cell immunodominance and tissue distribution and results in distinct stages of functional impairment.* Journal of virology, 2003. **77**(8): p. 4911-4927.
263. Rudloff, M.W., et al., *Hallmarks of CD8+ T cell dysfunction are established within hours of tumor antigen encounter before cell division.* Nature Immunology, 2023. **24**(9): p. 1527-1539.
264. Gao, M., et al., *Direct therapeutic targeting of immune checkpoint PD-1 in pancreatic cancer.* British journal of cancer, 2019. **120**(1): p. 88-96.
265. Taïeb, J., et al., *Efficacy of immune checkpoint inhibitors in microsatellite unstable/mismatch repair-deficient advanced pancreatic adenocarcinoma: an AGEO European Cohort.* European Journal of Cancer, 2023. **188**: p. 90-97.
266. Orhan, A., et al., *The prognostic value of tumour-infiltrating lymphocytes in pancreatic cancer: a systematic review and meta-analysis.* European Journal of Cancer, 2020. **132**: p. 71-84.
267. Chen, M.-L., et al., *Regulatory T cells suppress tumor-specific CD8 T cell cytotoxicity through TGF-β signals in vivo.* Proceedings of the National Academy of Sciences, 2005. **102**(2): p. 419-424.
268. Zwart, E.S., et al., *The immune microenvironment after neoadjuvant therapy compared to upfront surgery in patients with pancreatic cancer.* Journal of Cancer Research and Clinical Oncology, 2023. **149**(16): p. 14731-14743.
269. Singh, K., et al., *Kras mutation rate precisely orchestrates ductal derived pancreatic intraepithelial neoplasia and pancreatic cancer.* Laboratory Investigation, 2021. **101**(2): p. 177-192.
270. Connor, A.A., et al., *Integration of genomic and transcriptional features in pancreatic cancer reveals increased cell cycle progression in metastases.* Cancer cell, 2019. **35**(2): p. 267-282. e7.
271. Fisher, N.C., et al., *Biological misinterpretation of transcriptional signatures in tumor samples can unknowingly undermine mechanistic understanding and faithful alignment with preclinical data.* Clinical Cancer Research, 2022. **28**(18): p. 4056-4069.
272. Fan, J., K. Slowikowski, and F. Zhang, *Single-cell transcriptomics in cancer: computational challenges and opportunities.* Experimental & Molecular Medicine, 2020. **52**(9): p. 1452-1465.
273. Tang, F., et al., *mRNA-Seq whole-transcriptome analysis of a single cell.* Nature methods, 2009. **6**(5): p. 377-382.
274. Fomitcheva-Khartchenko, A., et al., *Space in cancer biology: its role and implications.* Trends in Cancer, 2022.
275. Palla, G., et al., *Spatial components of molecular tissue biology.* Nature Biotechnology, 2022. **40**(3): p. 308-318.
276. Du, J., et al., *Advances in spatial transcriptomics and related data analysis strategies.* Journal of Translational Medicine, 2023. **21**(1): p. 1-21.
277. Grünwald, B.T., et al., *Spatially confined sub-tumor microenvironments in pancreatic cancer.* Cell, 2021. **184**(22): p. 5577-5592. e18.
278. Wood, C.S., et al., *Spatially Resolved Transcriptomics Deconvolutes Prognostic Histological Subgroups in Patients with Colorectal Cancer and Synchronous Liver Metastases.* Cancer Research, 2023. **83**(8): p. 1329-1344.
279. Ren, Z., et al., *Spatial transcriptomics reveals the heterogeneity and FGG+ CRP+ inflammatory cancer-associated fibroblasts replace islets in pancreatic ductal adenocarcinoma.* Frontiers in Oncology, 2023. **13**: p. 1112576.
280. Croft, W., et al., *Spatial determination and prognostic impact of the fibroblast transcriptome in pancreatic ductal adenocarcinoma.* Elife, 2023. **12**: p. e86125.

281. Xu, Q., et al., *Single-cell RNA transcriptome reveals the intra-tumoral heterogeneity and regulators underlying tumor progression in metastatic pancreatic ductal adenocarcinoma.* Cell Death Discovery, 2021. **7**(1): p. 331.
282. Jiang, J., et al., *Identification of cystatin SN as a novel biomarker for pancreatic cancer.* Tumor Biology, 2015. **36**: p. 3903-3910.
283. Chen, J., et al., *KIF4A Regulates the Progression of Pancreatic Ductal Adenocarcinoma through Proliferation and Invasion.* BioMed Research International, 2021. **2021**.
284. Logsdon, D.P., et al., *Blocking HIF signaling via novel inhibitors of CA9 and APE1/Ref-1 dramatically affects pancreatic cancer cell survival.* Scientific reports, 2018. **8**(1): p. 13759.
285. Yin, L., et al., *CA9-related acidic microenvironment mediates CD8+ T cell related immunosuppression in pancreatic cancer.* Frontiers in Oncology, 2022. **11**: p. 832315.
286. Patel, S., et al., *Unique pattern of neutrophil migration and function during tumor progression.* Nature immunology, 2018. **19**(11): p. 1236-1247.
287. Hegde, S., et al., *Dendritic cell paucity leads to dysfunctional immune surveillance in pancreatic cancer.* Cancer cell, 2020. **37**(3): p. 289-307. e9.
288. Zhang, H., et al., *Data mining-based study of collagen type III alpha 1 (COL3A1) prognostic value and immune exploration in pan-cancer.* Bioengineered, 2021. **12**(1): p. 3634-3646.
289. Hu, J.-f., et al., *Induced expression of CCL19 promotes the anti-tumor ability of CAR-T cells by increasing their infiltration ability.* Frontiers in Immunology, 2022. **13**: p. 958960.
290. Hwang, W.L., et al., *Single-nucleus and spatial transcriptome profiling of pancreatic cancer identifies multicellular dynamics associated with neoadjuvant treatment.* Nature genetics, 2022. **54**(8): p. 1178-1191.
291. Miyabayashi, K., et al., *Intraductal transplantation models of human pancreatic ductal adenocarcinoma reveal progressive transition of molecular subtypes.* Cancer discovery, 2020. **10**(10): p. 1566-1589.
292. Esposito, I., et al., *Tumor-suppressor function of SPARC-like protein 1/Hevin in pancreatic cancer.* Neoplasia, 2007. **9**(1): p. 8-17.
293. Liu, H., et al., *The use of angiotensin system inhibitors correlates with longer survival in resected pancreatic adenocarcinoma patients.* HPB, 2023. **25**(3): p. 320-329.
294. Keith, S.W., et al., *Angiotensin blockade therapy and survival in pancreatic cancer: a population study.* BMC cancer, 2022. **22**(1): p. 150.
295. Liu, H., et al., *Use of angiotensin system inhibitors is associated with immune activation and longer survival in nonmetastatic pancreatic ductal adenocarcinoma.* Clinical Cancer Research, 2017. **23**(19): p. 5959-5969.
296. Sonneveld, S., B.M. Verhagen, and M.E. Tanenbaum, *Heterogeneity in mRNA translation.* Trends in cell biology, 2020. **30**(8): p. 606-618.
297. Ingolia, N.T., et al., *Genome-wide analysis in vivo of translation with nucleotide resolution using ribosome profiling.* science, 2009. **324**(5924): p. 218-223.
298. Schwanhäusser, B., et al., *Global quantification of mammalian gene expression control.* Nature, 2011. **473**(7347): p. 337-342.
299. Le Large, T.Y., et al., *Microdissected pancreatic cancer proteomes reveal tumor heterogeneity and therapeutic targets.* JCI insight, 2020. **5**(15).
300. Janesick, A., et al., *High resolution mapping of the tumor microenvironment using integrated single-cell, spatial and in situ analysis.* Nature Communications, 2023. **14**(1): p. 8353.
301. Guo, J., et al., *High-plex spatial transcriptomic profiling reveals distinct immune components and the HLA class I/DNMT3A/CD8 modulatory axis in mismatch repair-deficient endometrial cancer.* Cellular Oncology, 2023: p. 1-13.
302. Tang, W., et al., *Integrated proteotranscriptomics of breast cancer reveals globally increased protein-mRNA concordance associated with subtypes and survival.* Genome medicine, 2018. **10**: p. 1-14.

303. Xu, S., et al., *Whole transcriptome and proteome analyses identify potential targets and mechanisms underlying tumor treating fields against glioblastoma.* Cell Death & Disease, 2022. **13**(8): p. 721.
304. Park, J., et al., *Transcriptome profiling-based identification of prognostic subtypes and multi-omics signatures of glioblastoma.* Scientific reports, 2019. **9**(1): p. 10555.
305. Orzan, F., et al., *A simplified integrated molecular and immunohistochemistry-based algorithm allows high accuracy prediction of glioblastoma transcriptional subtypes.* Laboratory Investigation, 2020. **100**(10): p. 1330-1344.
306. Farren, M.R., et al., *Immunologic alterations in the pancreatic cancer microenvironment of patients treated with neoadjuvant chemotherapy and radiotherapy.* Jci Insight, 2020. **5**(1): p. 13.
307. Werba, G., et al., *Single-cell RNA sequencing reveals the effects of chemotherapy on human pancreatic adenocarcinoma and its tumor microenvironment.* Nature Communications, 2023. **14**(1): p. 797.
308. Li, K., et al., *Multi-omic analyses of changes in the tumor microenvironment of pancreatic adenocarcinoma following neoadjuvant treatment with anti-PD-1 therapy.* Cancer cell, 2022. **40**(11): p. 1374-1391. e7.
309. Kaur, P., et al., *The role of dendritic cells in radiation-induced immune responses.* International Review of Cell and Molecular Biology, 2023. **378**: p. 61-104.
310. Peuker, K., et al., *Microbiota-dependent activation of the myeloid calcineurin-NFAT pathway inhibits B7H3-and B7H4-dependent anti-tumor immunity in colorectal cancer.* Immunity, 2022. **55**(4): p. 701-717. e7.
311. Liu, H.-J., et al., *mTORC1 upregulates B7-H3/CD276 to inhibit antitumor T cells and drive tumor immune evasion.* Nature Communications, 2023. **14**(1): p. 1214.
312. He, S., et al., *High-plex imaging of RNA and proteins at subcellular resolution in fixed tissue by spatial molecular imaging.* Nature Biotechnology, 2022. **40**(12): p. 1794-1806.
313. Canale, F.P., et al., *CD39 expression defines cell exhaustion in tumor-infiltrating CD8+ T cells.* Cancer research, 2018. **78**(1): p. 115-128.
314. Abeles, D., et al., *CD14, CD16 and HLA‐DR reliably identifies human monocytes and their subsets in the context of pathologically reduced HLA‐DR expression by CD14hi/CD16neg monocytes: Expansion of CD14hi/CD16pos and contraction of CD14lo/CD16pos monocytes in acute liver failure.* Cytometry Part A, 2012. **81**(10): p. 823-834.
315. Damasceno, L.E.A., et al., *STING is an intrinsic checkpoint inhibitor that restrains the TH17 cell pathogenic program.* Cell reports, 2022. **39**(8).
316. He, H., et al., *Interleukin-7 regulates CD127 expression and promotes CD8+ T cell activity in patients with primary cutaneous melanoma.* BMC immunology, 2022. **23**(1): p. 35.
317. Aktas, E., et al., *Relationship between CD107a expression and cytotoxic activity.* Cellular immunology, 2009. **254**(2): p. 149-154.
318. Zeng, F., et al., *Effect of CD38 on B‐cell function and its role in the diagnosis and treatment of B‐cell‐related diseases.* Journal of Cellular Physiology, 2022. **237**(7): p. 2796-2807.
319. Feng, B., et al., *NF-kB inhibitor blocks B cell development at two checkpoints.* Medical immunology, 2004. **3**(1): p. 1-16.
320. Denley, S.M., et al., *Activation of the IL-6R/Jak/stat pathway is associated with a poor outcome in resected pancreatic ductal adenocarcinoma.* Journal of gastrointestinal surgery, 2013. **17**: p. 887-898.
321. Von Hoff, D.D., et al., *Increased survival in pancreatic cancer with nab-paclitaxel plus gemcitabine.* New England Journal of Medicine, 2013. **369**(18): p. 1691-1703.
322. Matsuo, H., et al., *Association between high immune activity and worse prognosis in uveal melanoma and low-grade glioma in TCGA transcriptomic data.* BMC genomics, 2022. **23**(1): p. 351.
323. Zhang, Z., et al., *Role of angiogenesis in pancreatic cancer biology and therapy.* Biomedicine & Pharmacotherapy, 2018. **108**: p. 1135-1140.

324. Butler, A., et al., *Integrating single-cell transcriptomic data across different conditions, technologies, and species.* Nature biotechnology, 2018. **36**(5): p. 411-420.
325. Chen, Y., et al., *B7-H3: A promising therapeutic target for autoimmune diseases.* Cellular Immunology, 2020. **352**: p. 104077.
326. Kanchan, R.K., et al., *To kill a cancer: Targeting the immune inhibitory checkpoint molecule, B7-H3.* Biochimica et Biophysica Acta (BBA)-Reviews on Cancer, 2022: p. 188783.
327. Zhang, S., et al., *The anti-apoptotic effect on cancer-associated fibroblasts of B7-H3 molecule enhancing the cell invasion and metastasis in renal cancer.* OncoTargets and therapy, 2019. **12**: p. 4119.
328. Liu, H., et al., *B7-H3 silencing increases paclitaxel sensitivity by abrogating Jak2/Stat3 phosphorylation.* Molecular cancer therapeutics, 2011. **10**(6): p. 960-971.
329. Zhao, X., et al., *Silencing of B7-H3 increases gemcitabine sensitivity by promoting apoptosis in pancreatic carcinoma.* Oncology letters, 2013. **5**(3): p. 805-812.
330. Braumüller, H., et al., *T-helper-1-cell cytokines drive cancer into senescence.* Nature, 2013. **494**(7437): p. 361-365.
331. Komohara, Y., et al., *Role of tumor-associated macrophages in hematological malignancies.* Pathology international, 2015. **65**(4): p. 170-176.
332. Chinen, T., et al., *An essential role for the IL-2 receptor in Treg cell function.* Nature immunology, 2016. **17**(11): p. 1322-1333.
333. Giatromanolaki, A., et al., *Carbonic anhydrase 9 (CA9) expression in non-small-cell lung cancer: correlation with regulatory FOXP3+ T-cell tumour stroma infiltration.* British Journal of Cancer, 2020. **122**(8): p. 1205-1210.
334. Hirooka, Y., et al., *A combination therapy of gemcitabine with immunotherapy for patients with inoperable locally advanced pancreatic cancer.* Pancreas, 2009. **38**(3): p. e69-e74.
335. Chang, L.-S., et al., *Gemcitabine enhances antitumor efficacy of recombinant lipoimmunogen-based immunotherapy.* Oncoimmunology, 2016. **5**(3): p. e1095433.
336. Yang, S., et al., *Pancreatic cancers require autophagy for tumor growth.* Genes & development, 2011. **25**(7): p. 717-729.
337. Yousuf, S., et al., *Spatially resolved multi-omics single-cell analyses inform mechanisms of immune-dysfunction in pancreatic cancer.* Gastroenterology, 2023.
338. Zhou, X., et al., *Persister cell phenotypes contribute to poor patient outcomes after neoadjuvant chemotherapy in PDAC.* Nature Cancer, 2023. **4**(9): p. 1362-1381.
339. Zhang, J., et al., *Multi-omics analysis reveals the chemoresistance mechanism of proliferating tissue-resident macrophages in PDAC via metabolic adaptation.* Cell Reports, 2023. **42**(6).
340. Wang, R., et al., *B7-H3 promotes colorectal cancer angiogenesis through activating the NF-κB pathway to induce VEGFA expression.* Cell death & disease, 2020. **11**(1): p. 55.
341. Ferrara, N., et al., *Discovery and development of bevacizumab, an anti-VEGF antibody for treating cancer.* Nature reviews Drug discovery, 2004. **3**(5): p. 391-400.
342. Garcia, J., et al., *Bevacizumab (Avastin®) in cancer treatment: A review of 15 years of clinical experience and future outlook.* Cancer treatment reviews, 2020. **86**: p. 102017.
343. Zhang, G., et al., *A novel subset of B7-H3+ CD14+ HLA-DR−/low myeloid-derived suppressor cells are associated with progression of human NSCLC.* Oncoimmunology, 2015. **4**(2): p. e977164.
344. Cai, D., et al., *Tumor-expressed B7-H3 mediates the inhibition of antitumor T-cell functions in ovarian cancer insensitive to PD-1 blockade therapy.* Cellular & molecular immunology, 2020. **17**(3): p. 227-236.
345. Mahnke, K., et al., *Induction of immunosuppressive functions of dendritic cells in vivo by CD4+ CD25+ regulatory T cells: role of B7-H3 expression and antigen presentation.* European journal of immunology, 2007. **37**(8): p. 2117-2126.

346. Gallimore, A., et al., *Induction and exhaustion of lymphocytic choriomeningitis virus–specific cytotoxic T lymphocytes visualized using soluble tetrameric major histocompatibility complex class I–peptide complexes.* The Journal of experimental medicine, 1998. **187**(9): p. 1383-1393.
347. Liu, B., et al., *An entropy-based metric for assessing the purity of single cell populations.* Nature communications, 2020. **11**(1): p. 3155.
348. Feng, M., et al., *PD-1/PD-L1 and immunotherapy for pancreatic cancer.* Cancer letters, 2017. **407**: p. 57-65.
349. Zhang, G., et al., *B7-H3 augments the inflammatory response and is associated with human sepsis.* The Journal of Immunology, 2010. **185**(6): p. 3677-3684.
350. Sun, Y., et al., *B7-H3 and B7-H4 expression in non-small-cell lung cancer.* Lung cancer, 2006. **53**(2): p. 143-151.
351. Deng, J., et al., *Expression and clinical significance of immune checkpoint regulator B7-H3 (CD276) in human meningioma.* World neurosurgery, 2020. **135**: p. e12-e18.
352. Qin, X., et al., *Mifepristone inhibited the expression of B7-H2, B7-H3, B7-H4 and PD-L2 in adenomyosis.* Reproductive Biology and Endocrinology, 2021. **19**(1): p. 1-11.
353. Greenbaum, S., et al., *A spatially resolved timeline of the human maternal–fetal interface.* Nature, 2023. **619**(7970): p. 595-605.
354. van Hijfte, L., et al., *Alternative normalization and analysis pipeline to address systematic bias in NanoString GeoMx Digital Spatial Profiling data.* Iscience, 2023. **26**(1).